# Diagnostic Imaging for Thoracic Surgery

A Manual for Surgeons and Radiologists

Michele Anzidei
Marco Anile
*Editors*

Springer

Michele Anzidei · Marco Anile
Editors

# Diagnostic Imaging for Thoracic Surgery

## A Manual for Surgeons and Radiologists

Springer

*Editors*
Michele Anzidei
Sapienza Università di Roma
Policlinico Umberto I
Rome
Italy

Marco Anile
Department of Thoracic Surgery
University of Rome Sapienza
Policlinico Umberto I
Rome
Italy

ISBN 978-3-319-89892-6 ISBN 978-3-319-89893-3 (eBook)
https://doi.org/10.1007/978-3-319-89893-3

Library of Congress Control Number: 2018946700



Printed on acid-free paper

This Springer imprint is published by the registered company Springer International Publishing AG part of Springer Nature
The registered company address is: Gewerbestrasse 11, 6330 Cham, Switzerland

# Foreword

Today, medical imaging is no longer the same as twenty or even ten years ago. The slice war in CT, the race to higher magnetic fields in MR and the development of novel contrast agents represent challenges of the past. The future of medical imaging now lies in artificial intelligence, machine learning, data mining and automation of diagnosis and interventions. And this is not a far future, rather the very next present.

To preserve our role in medicine, we will be called to reshape our professional skills and compensate automation rigidity with human adaptability. In this scenario, cross-specialty contamination is one of the human strength points as well as one of the daily challenges in clinical practice: the often over-animated debate between medical specialists in multidisciplinary teams represents in most of the cases the key to achieve optimal results for patients and will never be replaced by any software.

This is the inspiring concept at the very base of *Diagnostic Imaging for Thoracic Surgery*, in which the editors and authors aimed at conjoining shared points of view on non-vascular thoracic diseases with a large amount of high-quality images and line art, tables and updated guidelines, including latest 8th TNM for thoracic cancers and updated thoracic imaging guidelines.

Mostly written by enthusiastic and extremely competent radiologists, the aim of the book of providing an open and clear view on the role of medical imaging to thoracic surgeons, oncologists and pulmonologists is clearly and successfully reached, encouraging informed discussion in the daily clinical practice. As long as this continues to happen in our hospitals, we will be a step ahead of any machine.

Rome, Italy

Carlo Catalano
Department of Radiology
Sapienza University of Rome

# Contents

# Preoperative and Postoperative Chest X-Ray

1

Michele Anzidei, Vincenzo Noce, and Carola Palla

**Abstract**

CXR is a first-line diagnostic tool for many clinical scenarios, since it is available in every hospital unit and is cheap in terms of costs and patients dose. Furthermore, it represents a wide-ranging point of view for the thoracic surgeon, allowing either pre-interventional evaluation and post-surgical monitoring.

Principal indication of chest X-Ray in the field of thoracic surgery include:

- Pre-operative assessment, the utility of which has been validated only for patients that present new\unstable cardiopulmonary disease;
- Post-operative follow-up, in order to evaluate surgery complications such as persistent air leakage, pneumonia, parenchymal atelectasis, empyema;
- Monitoring medical devices (pleural, esophageal, tracheal etc.)

By knowing specific chest X-Ray semiology, the physician is able to interpret the images obtaining clinical information.

**Keywords**

Chest X-Ray · Radiology · Chest imaging · Thoracic surgery · Cardiac surgery

Chest radiograph, or chest X-ray (CXR) in colloquial language, is the most frequently performed radiographic examination.

CXR is a first-line diagnostic tool for many clinical scenarios, since it is available in every hospital unit and is cheap in terms of costs and patient dose. Furthermore, it represents a wide-ranging point of view for the thoracic surgeon, allowing either pre-interventional evaluation or postsurgical monitoring [1].

This chapter briefly reviews CXR technique and addresses the pathological conditions assessable through chest radiograph which are considered of surgical interest.

## 1.1 Technical Considerations

Radiography utilizes electromagnetic high-frequency X-radiations, generated by a so-called X-ray tube (or generator) and captured by a photosensitive film or a digital detector.

High-voltage radiations (120–130 kVp) are advised to guarantee proper contrast resolution and to assure correct visualization of areas with complex anatomical structure (e.g., retro-cardiac

M. Anzidei (✉) · V. Noce · C. Palla
Department of Radiological, Oncological and Anatomopatological Sciences, Sapienza, University of Rome, Rome, Italy
e-mail: michele.anzidei@uniroma1.it


M. Anzidei, M. Anile (eds.), *Diagnostic Imaging for Thoracic Surgery*,
https://doi.org/10.1007/978-3-319-89893-3_1

region). Since high kVp significantly increases image noise, filtering devices integrated to X-ray generator have been introduced.

A chest radiographic exam may possibly comprehend many projections.

The classical ones are a posteroanterior view (PA) and a laterolateral view (LL), both obtained in end-inspiratory breath-hold (Fig. 1.1). For optimal reproduction of anatomical proportions, the more suitable distance between source and object should be at least 180 cm.

Inpatient radiographs are often performed bedside with portable X-ray tubes. This technology has significantly increased imaging feasibility for acutely ill subjects and posttreatment monitoring; on the other hand, portable CXR has lower diagnostic accuracy. In fact, anteroposterior view (AP) holds projective defects, especially regarding cardiac shape visualization (Fig. 1.2).

To better realize this issue, remind that cardiac shadow represents a significant part in CXR image and, if acquired on AP projection, it appears considerably magnified covering other structures and leading to misinterpretation of cardiac size (false cardiomegaly).

Furthermore, the absence of LL view makes accurate localization of lung findings extremely difficult and actually blinds radiologist's eye to some areas, as posterior pleural recesses.

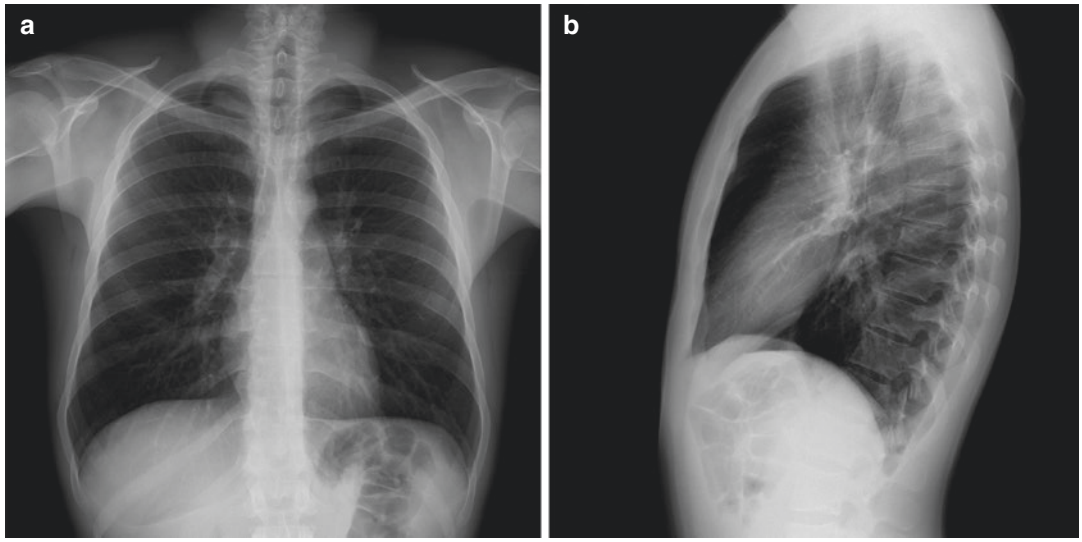


**Fig. 1.1** Standard chest X-Ray PA (**a**) and LL (**b**) projections

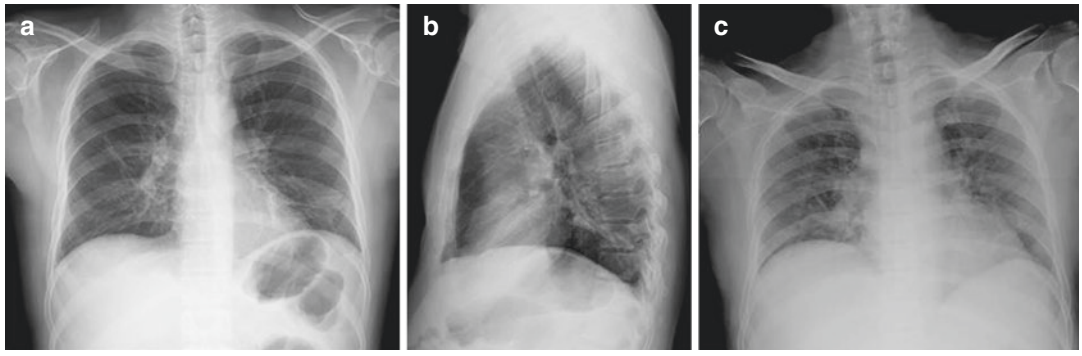


**Fig. 1.2** Chest X-Ray projections: PA (**a**), LL (**b**) and AP (**c**)

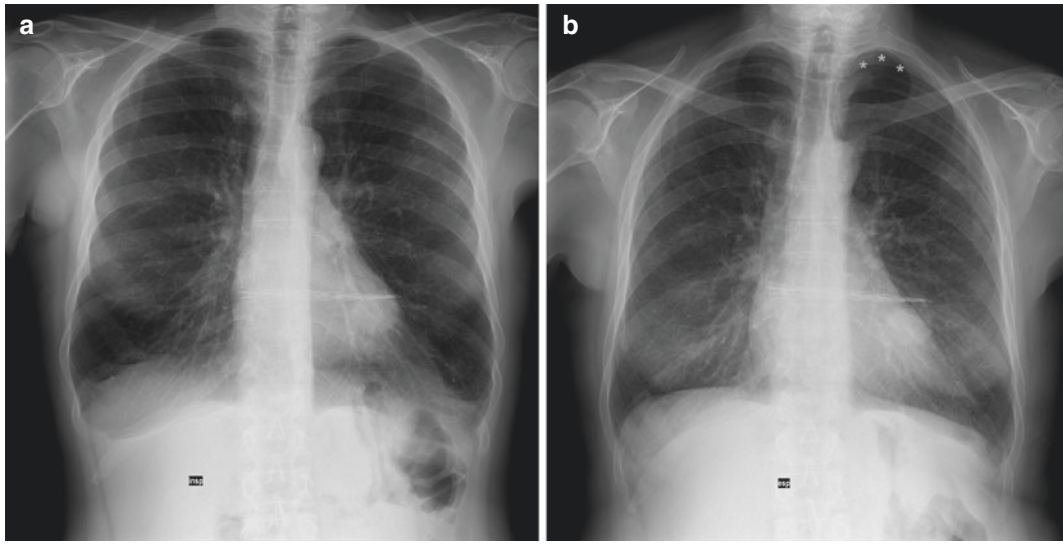


**Fig. 1.3** Technical adequacy of CXR: uncorrect **(a)** and correct **(b)** image acquisition, with optimal visualization of bony structures, thoracic vessels and lung apices

As general principle, in routine imaging a double-view standard chest X-ray should always be preferred to a AP single-view exam. Portable radiographs are of basic importance in emergency and intensive care units, but in post-surgery patients a standard exam should be performed as possible.

Some dedicated projections comprehend:

- "Expiratory view" (Fig. 1.3), acquired in end-expiratory breath-hold to better evaluate the presence of pneumothorax.
- "Apical view," with superoinferior direction of X-radiation to show more clearly apical areas.
- "Oblique view," with 45° rotation of the patient between X-ray beam and cassette, useful for sternum and rib evaluation.

Technical adequacy of CXR exams is assessed, apart from a complete inclusion of the rib cage in the radiogram, by evaluation of X-ray's effective penetration across the thoracic structures (bony structures and pulmonary vessels are used as references), patient's rotation (clavicle heads should be equidistant to vertebral bodies), and inspiration (8th–10th posterior costal arches should be seen).

## 1.2 Lung Cancer Detection

Lung cancer is one of the leading causes of mortality in the world and its early diagnosis has demonstrated to relate with better prognosis; in light of this, screening programs of population at risk (heavy smokers) have been proposed by CXR and computed tomography (CT) imaging.

Chest radiograph has poor sensitivity on lung nodule detection (54%) despite its low cost and wide availability; on the other hand, volumetric CT, even with low-dose acquisition, encountered significantly higher sensitivity but still no evidence has pointed towards reduction of mortality for the populations screened by CT.

In modern practice, a negative CXR alone should not be interpreted as absence of neoplastic disease to lungs. In fact, pulmonary cancer detection on radiographs depends on some factors: lesion size, tumor localization, and density and secondary parenchymal changes.

The most challenging presentation of lung cancer in chest X-ray is as solitary nodule, the detection of which is deeply related to lesion location and volume. The main perceptive

difficult for solitary nodule is anatomical structure superimposition that might hide pathologic findings; in this sense dangerous zones are represented by lung apices, diaphragmatic domes, and pericardiac and peri-hilar areas (Fig. 1.4).

Obstructive pneumonia/consolidation, hilar enlargement, and mediastinal enlargement are the main CXR findings that may highlight the presence of a central pulmonary neoplasm.

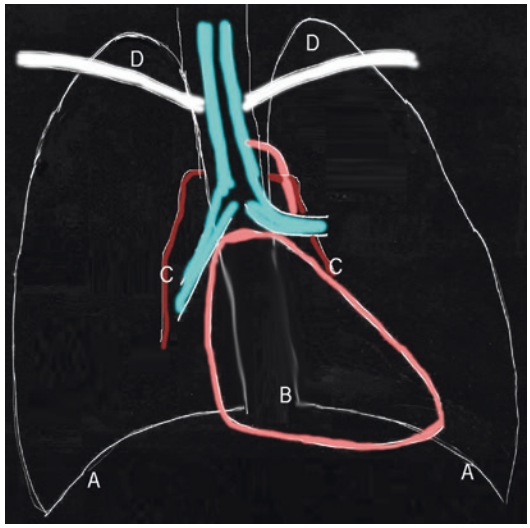


**Fig. 1.4** Schematic representation of hardly evaluable anatomical zones on CXR: (**a**) diaphragmatic domes, (**b**) pericardiac areas, (**c**) peri hilar areas, (**d**) lung apices

Obstructive parenchymal consolidation is due to bronchus obliteration by central located cancer (Fig. 1.5). Obstructive pneumonia affects more commonly a segment or a lobe and more rarely an entire lung; moreover it has been frequently associated to squamous cell carcinoma than adenocarcinoma.

Hilar enlargement is another radiological sign of central lung cancer and it is due to direct neoplastic infiltration, metastatic involvement of hilar lymph nodes, or both (Fig. 1.6). Notice that when metastatic lymph nodes are small in size, the only radiographic sign of hilar involvement may be an increment in density of its radiographic shadow.

Mediastinal direct invasion or enlargement of paratracheal and paraesophageal lymphnodes may cause another sign of central lung cancer, mediastinal shadow widening. Mediastinal involvement by cancer may determine paralysis of phrenic nerve with subsequent diaphragm relaxation that is assessable by CXR.

Peripheral lung cancer less frequently causes involvement of airways or other mediastinal structures; thus its diagnosis often occurs as an incidental finding of solitary

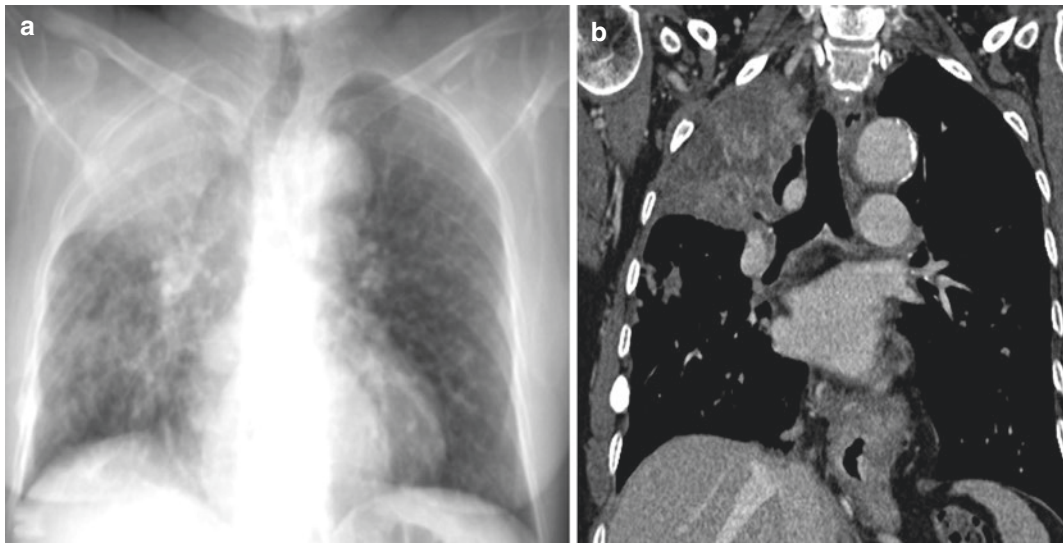


**Fig. 1.5** Obstructive parenchimal consolidation on CXR (**a**) and CT (**b**) examination

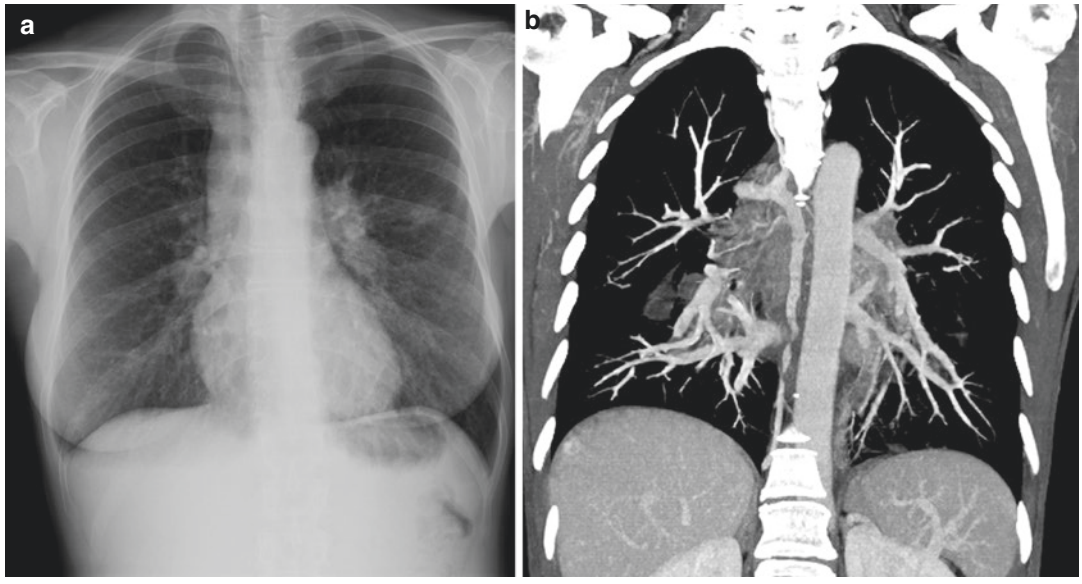


**Fig. 1.6** Hilar enlargment on CXR (**a**) and CT (**b**) examination

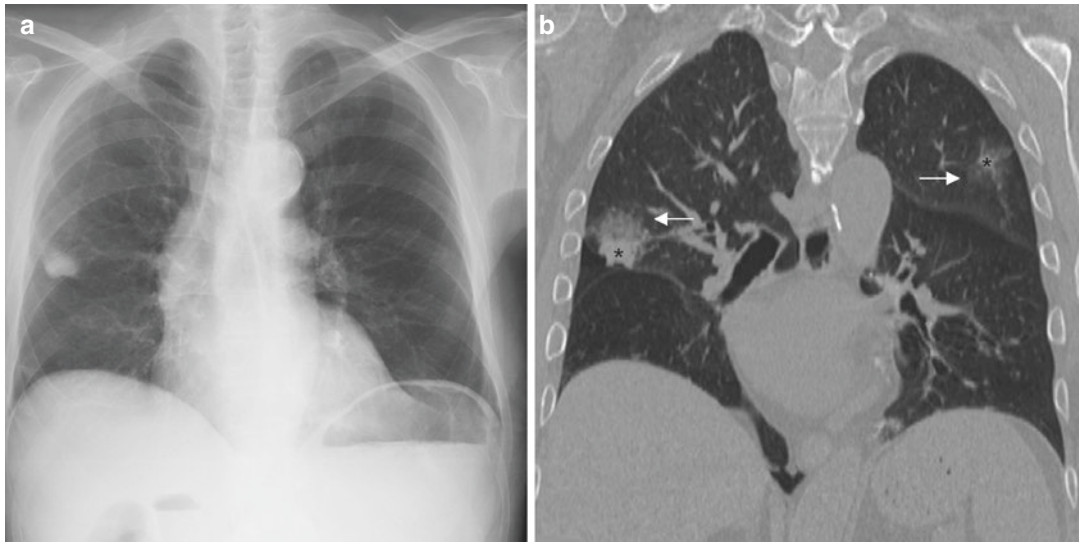


**Fig. 1.7** Peripheral lung cancer on CXR (**a**) and CT (**b**) examination

nodule. Peripheral neoplasms are often more than 1 cm in diameter at the time of first diagnosis; nonetheless even larger sub-solid tumors may be overlooked due to their low-attenuation structure (Fig. 1.7).

Pleural effusion is associated with 10% of lung neoplasms (Fig. 1.8) and may reveal a hidden peripheral cancer that invades pleural layers.

## 1.3 Preoperative Screening

Historically a chest radiography was routinely acquired for any patient admitted to hospital to rule out asymptomatic tubercular infection. In modern surgical practice no significant benefit has been associated with preoperative screening CXR for asymptomatic patients with no cardiopulmonary disease history or risk factors.

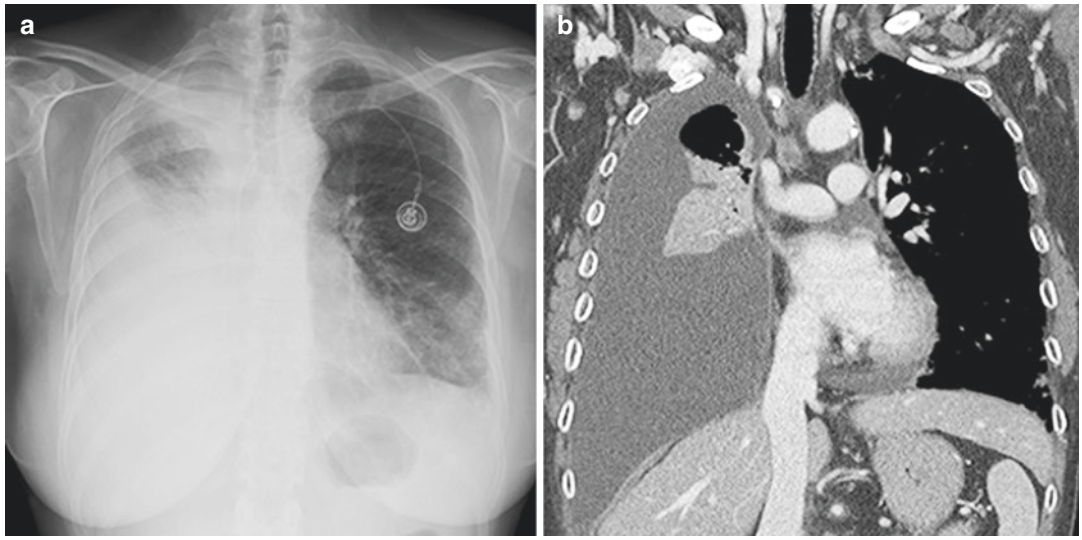


**Fig. 1.8** Lung cancer- associated pleural effusion on CXR (**a**) and CT (**b**) examination

Even if some discordance is encountered among physicians' societies, guidelines generally agree that a pre-surgery chest radiograph is clearly indicated in patients with new or unstable cardiopulmonary signs or symptoms on physical examination (Table 1.1).

In daily practice, preoperative CXR is often advised on the basis of general performance status of the patient and grading of surgical intervention. American Society of Anesthesiologists (ASA) patients' classification is considered the most useful tool to standardize performance status into three classes (1 = healthy patient; 2 = patient with mild systemic disease; 3 = patient with severe systemic disease).

Abnormal findings at preoperative screening CXR are considered rare and often they are represented by chronic disease alterations, suspected on the basis of physical exam and history. Moreover, only rarely CXR findings are able to modify perioperative management of the patient or alter outcomes and clinical history of subjects at risk.

Thus, preoperative CXR rarely adds material to physical examination and anamnestic info in order to stratify surgical risk.

In conclusion, current statement on screening preoperative CXR does not warrant routine use of radiography to predict the risk of postoperative pulmonary complications; only patients with new/unstable cardiopulmonary disease should be

**Table 1.1** Pre-operative chest radiography: guidelines

| | |
|---|---|
| American College of Radiology, 2008 | Chest radiography is usually appropriate for:<br>- Patients with acute cardiopulmonary findings on history or physical examination<br>- Patients older than 70 years who have chronic cardiopulmonary disease and have not had chest radiography in the previous 6 months |
| American Society of Anesthesiologists, 2002 | Consider chest radiography for:<br>- Patients who smoke<br>- Patients with a history of recent upper respiratory infection patients with chronic obstructive pulmonary disease<br>- Patients with cardiac disease<br>However, if these conditions are chronic and stable, preoperative chest radiography is not necessarily indicated |
| Institute for Clinical Systems Improvement, 2012 | Chest radiography may be considered for patients with signs or symptoms suggesting new or unstable cardiopulmonary disease |

examined, if CXR findings may alter perioperative management.

## 1.4 Postoperative Chest X-Ray

The principal aim for radiologists who operate in a cardiothoracic surgical environment is to highlight every complication that may arise after an intervention. During postoperative course, complications of different nature and severity can arise and can be classified as immediate, early, or late, depending on the time of onset.

Approximately 16% of patients undergoing major surgical interventions will suffer from a complication within 30 days. In the field of thoracic surgery, incidence of pulmonary complications varies from 5% to 80% between different hospitals. Moreover, patients undergoing thoracic surgery are usually high-risk patients with a poor physical status [2].

Another routine use of chest X-ray after thoracic surgery is monitoring lung tube position; even though this evaluation is daily assessed for every patient in many institutions, no significant difference in terms of mortality, intensive care unit stay, or hospital length of stay has been demonstrated with CXR performed in selected cases [3].

## 1.5 Chest X-Ray Imaging of Lung Surgery Complications

In the immediate postoperative period, patients' imaging follow-up is assessed with portable equipment [4].

In case of major lung interventions (pneumonectomy/lobe resections) [5], CXR is usually performed in first and second postoperative days; then at the removal of the former and second drainage (fourth and fifth postoperative days); at discharge; and the at varying intervals depending on the clinical evolution (Table 1.2).

In patients undergoing sub-lobar resection (segmental or atypical) monitoring is performed with lower frequency, using X-ray evaluation in the first postoperative day, at removal of the single drainage (3–4 postoperative days), at discharge, and later in accordance with the clinical evolution (Table 1.3).

However, when radiographic findings are subtle or equivocal, CT frequently allows more accurate identification of the disease process as well as prompt and appropriate treatment [6].

### 1.5.1 Persistent Air Leak

Air leaks following major pulmonary resection are a well-known entity. Nearly all patients undergoing lobectomy or sub-lobar resection can be expected to experience some degree of postoperative air leakage. This condition is usually related to small parenchymal gaps produced during surgery, typically in the lysis of pleuroparenchimal adhesions or in the interlobar fissure completion; a higher incidence rate is observed in case of incomplete/absent interlobar fissures and in older patients with emphysema.

Most air leaks will stop within the first 1–2 days postoperatively; an air leakage lasting beyond 5 days is defined as persistent or

**Table 1.2** Timing of chest x-ray evaluation after major lung interventions (pneumonectomy/lobe resections)

| 1st p.o.day | 2nd p.o.day | 3rd p.o.day | 4th p.o.day 1st drainage removal | 5th p.o.day 2nd drainage removal | discharge | Later in accordance with clinical evolution |
|---|---|---|---|---|---|---|
| • | • | | • | • | • | • |

**Table 1.3** Timing of chest x-ray evaluation after minor lung interventions (segmental/atypical resection)

| 1st p.o.day | 2nd p.o.day | 3rd p.o.day | 4th p.o.day drainage removal | 5th p.o.day | discharge | Later in accordance with clinical evolution |
|---|---|---|---|---|---|---|
| • | | | • | | • | • |

prolonged and shows an incidence ranging from 5% to 10% [7, 8].

Chest radiography is able to depict persistent pneumothorax, pneumomediastinum, or subcutaneous emphysema.

Pneumothorax is defined as the presence of air in the pleural cavity, with secondary lung collapse.

The elective exam for the diagnosis of pneumothorax is standard CXR, performed in orthostatic position, with the additional acquisition of a forced-expiration imaging. However, the detection of the specific signs of this condition has a low sensitivity when CXR is performed in the supine position at bedside.

The characteristic sign on CXR is visceral pleural detection (as a radiopaque line) at the apex in orthostatic situation, with no evidence of pulmonary vasculature beyond the pleural edge (Fig. 1.9). The displacement of mediastinal structures, contralateral to the affected side, is evidence of hypertensive pneumothorax that is caused by pleural tear acting as one-way valve and requires urgent drainage.

On supine CXR diagnosis is more difficult because air moves up and medially between the lung and the heart; pneumothorax in supine position may be suspected in case of lucency at the hypochondria or at costophrenic angles (deep sulcus sign), and appearance of sharp edges of mediastinum, heart, and subcutaneous tissues (Fig. 1.10). When an air leak occurs in a preexisting pleural effusion it determines a specific finding, called hydro-pneumothorax, characterized by an air-fluid level inside the pleural space (Fig. 1.11).

Pneumomediastinum is a challenging radiological diagnosis; most common findings are represented by lucent streaks, bubbles of air outlining mediastinal structures, and visible mediastinal pleura [9].

### 1.5.2 Atelectasis

Postoperative atelectasis is a common issue following any major surgical intervention [10]. Thoracic surgical procedures increase the risk of this complication occurrence because pain, thoracic muscle injury, chest wall instability, and diaphragmatic dysfunction impair clearance of secretions by cough. In addition, patients with lung diseases are prone to increased bronchial secretions.

A wide range of incidence of this complication has been reported following pulmonary resection [11]. Incidence of lobar and segmental atelectasis after pulmonary lobectomy is reported

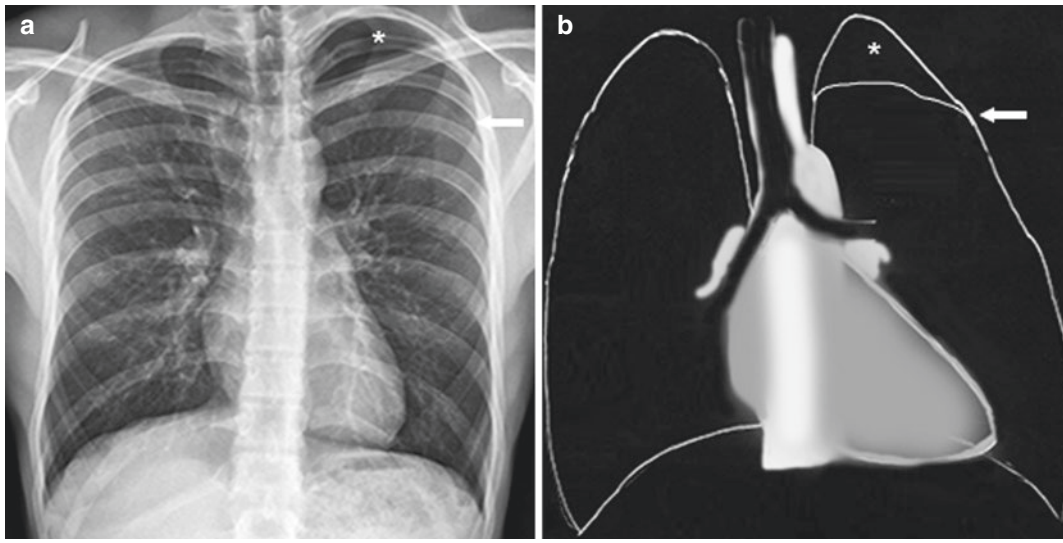


**Fig. 1.9** Pneumothorax: standard CXR appearance (**a**) and schematic representation (**b**)

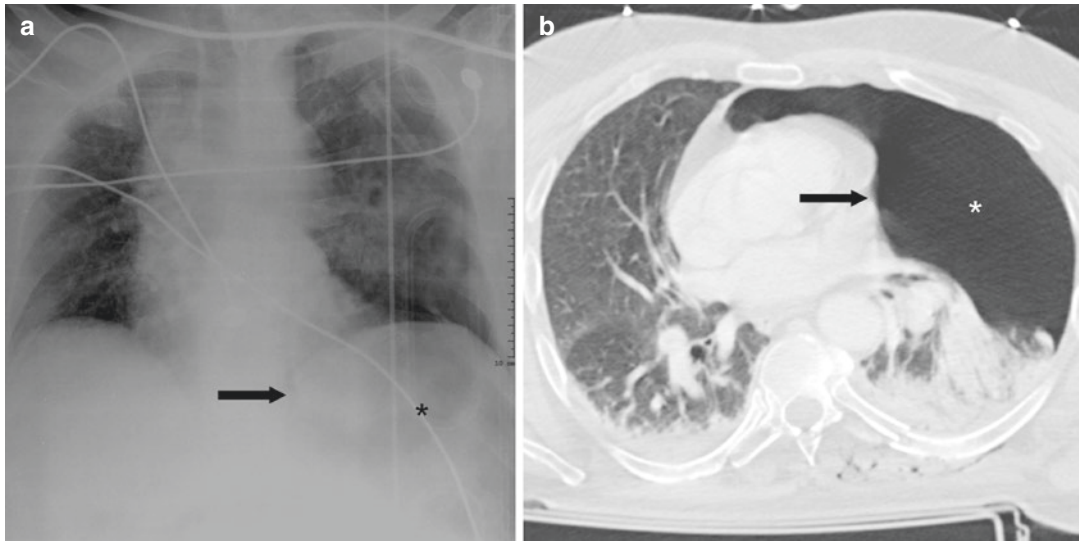


**Fig. 1.10** Pneumothorax appearance on supine CXR **(a)** and CT **(b)** examination

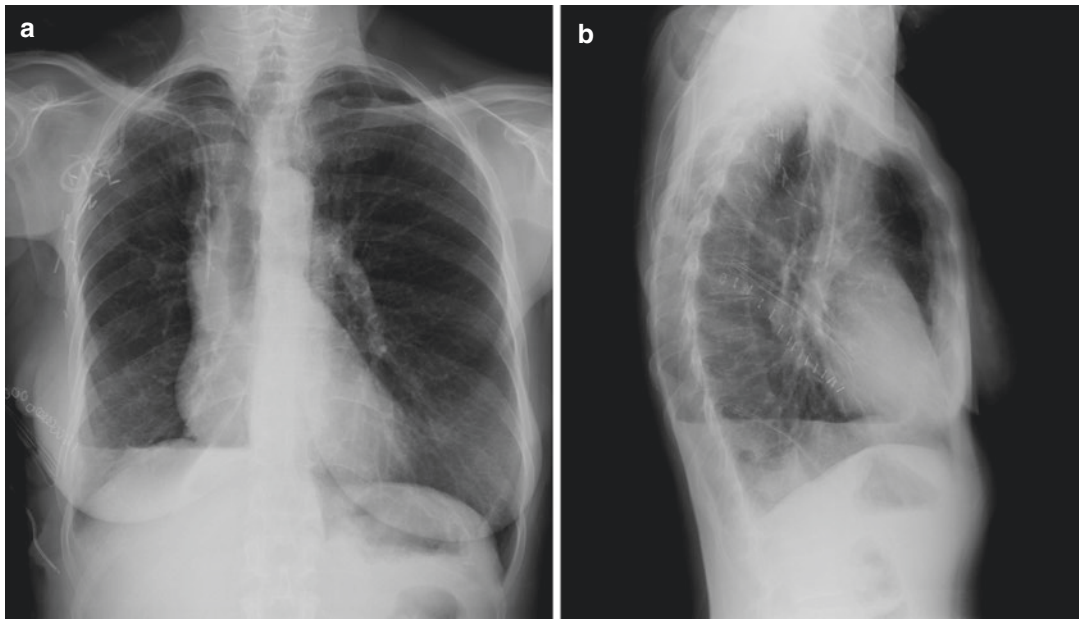


**Fig. 1.11** Hydro-pneumothorax on standard CXR PA (**a**) and LL (**b**) projections

to be about 5–7%. Limited atelectasis is usually well tolerated and easily reversible. However, complete atelectasis of the remaining lung following partial lung resection may be poorly tolerated.

Classic chest X-ray findings include opacification of the remaining lung parenchyma and general signs of atelectasis relate to volume loss, as displacement of the interlobar fissures, hemidiaphragm rise, and attractive mediastinal shift. Usually, there is compensatory overinflation of the remaining aerated segments in the affected lobe, while collapsed area demonstrates sharp (often linear) borders.

### 1.5.3 Pneumonia

Postoperative pulmonary infection is observed in 2–22% of patients undergoing partial or total lung resection [12]. The main cause of this event is aspiration of gastric secretions and bacterial colonization of an atelectasis portion of residual lung, with intubation and mechanical ventilation representing predisposing factors [13]. In hospitalized patients the most common etiological agents are gram-negative, highly virulent organisms.

Radiographic findings may vary from patchy bronchopneumonic pattern to lobar airspace consolidation and necrotizing evolution of inflammatory collections (underlined by appearance of air-fluid level in the background of lung consolidations) (Fig. 1.12).

### 1.5.4 Bronchopleural Fistula

Bronchopleural fistula (BPF) is a pathologic communication between the pleural space and the bronchial tree and potentially represents a fatal complication of major thoracic surgery. Its incidence has decreased over the last few decades from 28% to 4%, but its mortality rate remains high (25–71%) due to aspiration pneumonia and subsequent acute respiratory distress syndrome.

BPF is frequently associated with postoperative mechanical ventilation [14].

Bronchopleural fistula is classified into immediate postoperative (due to faulty closure of the bronchus) and delayed postoperative (secondary to infection or recurrent tumor of the bronchial stump).

CXR may depict BPF as a localized collection with air-fluid level adjacent to bronchial stump (more commonly in the right hemithorax) or as decreases and increases over time of an already present air-fluid level (Fig. 1.13). Other radiological findings are represented by persistent pneumothorax despite drainage tube, progressive subcutaneous/mediastinal emphysema, and affected hemithorax volume enlargement.

### 1.5.5 Empyema

Empyema is a serious but uncommon complication of pulmonary resection, occurring in 2–16% of patients with high mortality rates (16–71%) and usually observed as bronchopleural fistula consequence [15]. Empyema is often associated with total pneumonectomy, preoperative irradiation,

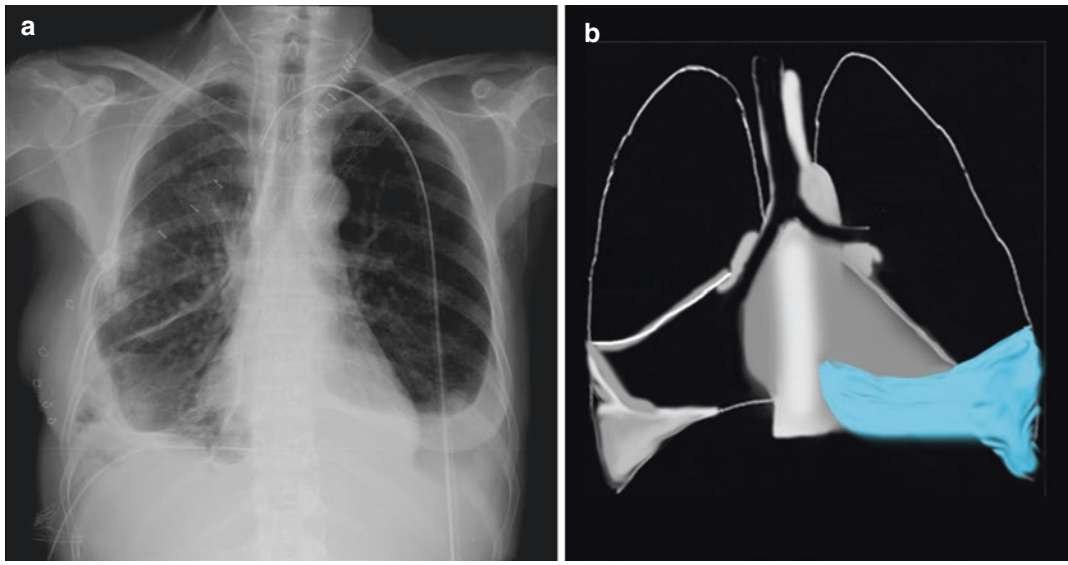


**Fig. 1.12** Pneumonia: different radiographic findings (**a**) and schematic representation (**b**)

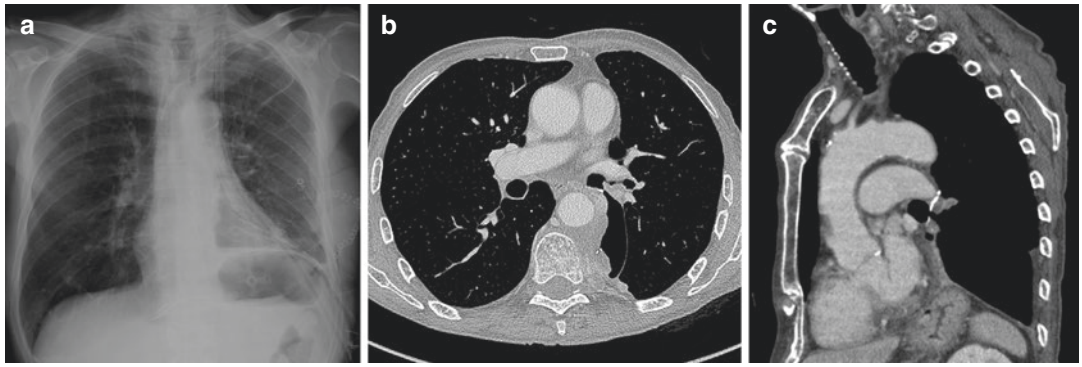


**Fig. 1.13** BPF in the left hemithorax on CXR (**a**) and CT (**b**, **c**) examination

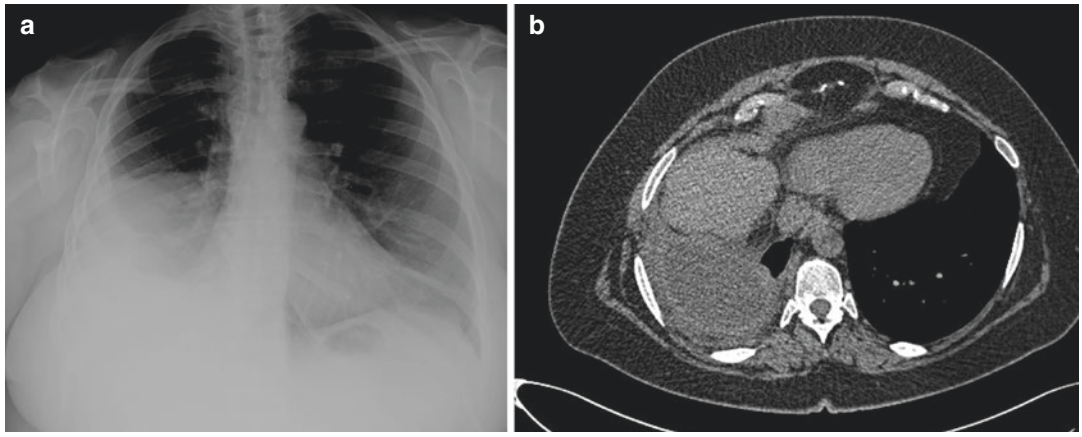


**Fig. 1.14** Empyema appearance on CXR (**a**) and CT (**b**) examination

gross contamination of the pleura, long bronchial stump, and mechanical ventilation. It usually occurs in the early postoperative period, but can develop months or even years after surgery.

Postsurgical empyema is detected on CXR as a large radiopaque collection, often with multiple air-fluid levels. In chronic phase empyema is demonstrated by contralateral deviation of mediastinal structures (Fig. 1.14). Even the appearance of an air-fluid level in already opacified pleural space may be indicative of empyema.

### 1.5.6 Hemothorax

In the absence of deficiency of coagulation, the postoperative bleeding has an extremely low incidence, lower than 1%. Major hemorrhage following thoracotomy and resection is most commonly the result of inadequate hemostasis of a bronchial artery or systemic vessels in the chest wall. It infrequently results from the slipping of a ligature from a major pulmonary vessel or an unrecognized injury to a systemic vein.

CXR findings of hemothorax are nonspecific, mainly represented by significant amount of pleural effusion with fast onset and growth.

### 1.5.7 Chylothorax

Postoperative chylothorax is a rare but well-known complication of general thoracic surgery. It results from a massive chyle fluid leak (rich of rich triglycerides and chylomicrons) in the pleura, caused by thoracic duct injury [16].

Sites of potential thoracic duct injury during pneumonectomy include the inferior right hemithorax in the paravertebral area during extrapleural resection, the pericarinal and subaortic areas during radical nodal dissection, and the inferior pulmonary ligaments on either side during standard resection.

Radiographic findings are nonspecific and overlap with hemothorax appearance: pleural effusion with fast occurrence and expansion [17].

### 1.5.8 Acute Pulmonary Edema and Acute Respiratory Distress Syndrome

Acute pulmonary edema (APE) is defined as an abnormal accumulation of fluid in the extravascular compartment of the lung. It is a life-threatening complication that can develop 2–3 days after pulmonary resection, usually after pneumonectomy, lobectomy, or bilobectomy [18].

The most common cause of pulmonary edema in postsurgical period is an increased fluid overload.

APE is classified into two main groups, depending on different pathogenetic mechanisms: cardiogenic APE, due to increased hydrostatic pressure in pulmonary capillaries during congestive heart failure or fluid excess, and non-cardiogenic APE, due to increased capillary permeability during acute respiratory distress syndrome (ARDS).

In cardiogenic APE chest X-ray may show cardiomegaly, pulmonary venous hypertension, and pleural effusions [19]. Moreover, radiographic signs of cardiogenic APE include redistribution of blood flow to the nondependent portions of the lungs and the upper lobes (stage I), interstitial fluid collection with ill-defined vessels and peribronchial cuffing, as well as interlobular septal thickening (stage II) and peri-hilar and lower lobe airspace filling with features typical of consolidation (stage III) (Fig. 1.15).

ARDS is considered the most severe form of lung injury that can occur in patients who underwent thoracic surgery. Its overall incidence, observed after pulmonary resection, varies from 2% to 15% with a mortality rate reaching 80% [20].

This pathologic condition consists of an acute respiratory failure due to increased capillary permeability and usually occurs in the early postoperative days; however ARDS may also occur in association with other complications such as pneumonia or bronchopleural fistula.

Possible risk factors of ARDS after lung resection can be classified as preoperative (chronic obstructive pulmonary disease, chronic suppura-

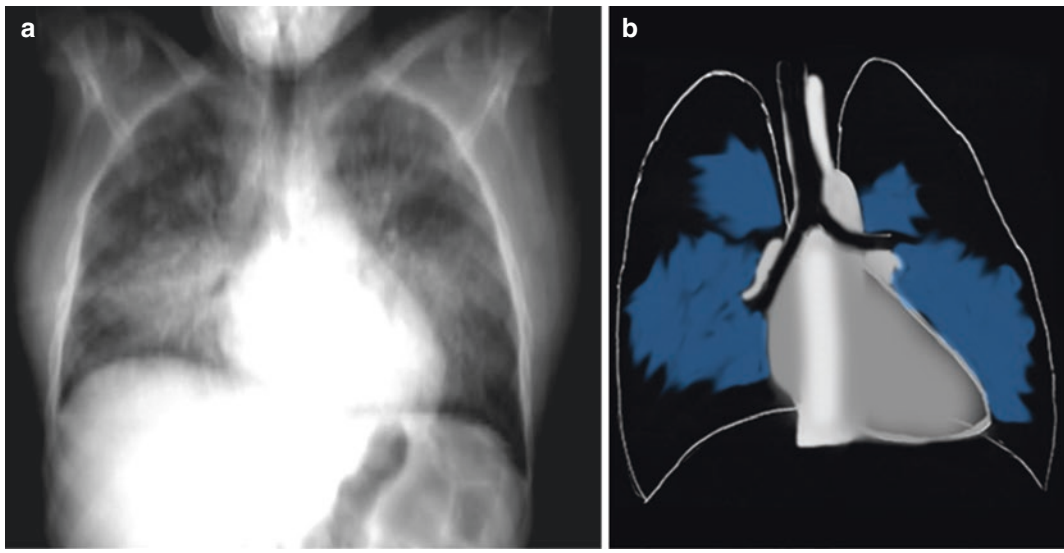


**Fig. 1.15** Acute pulmonary edema (stage III): CXR appearance (**a**) and schematic representation (**b**)

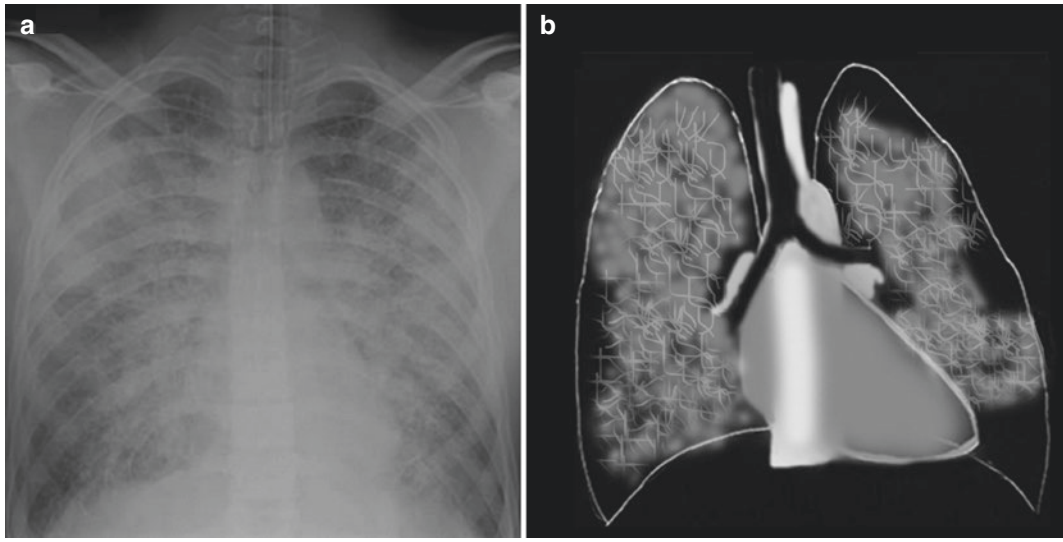


**Fig. 1.16** ARDS: CXR appearance (**a**) and schematic representation (**b**)

tive disease, concurrent cardiac disease, low diffusion capacity for carbon monoxide, prior therapy), intraoperative (pneumonectomy, excessive perioperative intravascular volume, duration of operation), and postoperative (nonbalanced drainage of hemithorax after pneumonectomy.

Chest X-ray, more often negative in the first 24 h after the onset of clinical symptoms, shows the rapid development of extensive opacities with homogeneous or asymmetric and "patchy" distribution that don't spare the periphery of the mid or upper lungs, as observed in hydrostatic pulmonary edema. In non-cardiogenic causes, moreover, cardiomegaly and pleural effusions are usually less evident (Fig. 1.16).

## 1.6 Chest X-Ray Imaging After Cardiac Surgery

Post-cardiac surgery chest radiograph is routinely used to detect hemothorax or other pleural effusion. After removal of the chest tube, radiographs have traditionally been obtained to exclude pneumothorax or any other abnormality requiring intervention.

However, many studies demonstrate that chest radiography after chest tube removal following cardiac surgery is necessary only if the patient has respiratory or hemodynamic changes or if there are problems with the technical aspect of chest tube removal.

There is evidence presented that routine post-drain removal chest radiography provides no diagnostic or therapeutic advantage over clinically indicated chest radiography or simple clinical assessment [21, 22].

On the other hand, minimally invasive cardiac surgery patients represent a population that might benefit from routine CXRs after surgery, permitting prompt diagnosis of pathological condition related to the place of surgical access (pneumothorax, subcutaneous emphysema), temporary one-lung ventilation technique (atelectasis), less surgical field visualization and hemostasis (hemothorax), or need for invasive device placement (pulmonary artery catheter, temporary transvenous pacing wire) [23].

## 1.7 Chest X-Ray Imaging of Thoracic Surgery Devices

In postsurgical chest X-ray several medical devices may be encountered; radiologist ought to recognize each of them assessing their proper positioning.

Medical devices can be classified into pleural, tracheal, esophageal, and cardiovascular.

### 1.7.1 Pleural Devices

Pleural drainage catheters, often referred as chest tubes, are placed lying inside the space between parietal and visceral pleura through thoracostomy access. Their function is to evacuate effusion or air collections.

Notice that fluid effusion is often evacuated by tubes placed at lung bases while pneumothorax requires a drain placed at apices (Fig. 1.17). Not infrequently pigtail and flexible catheters are used to drain loculated collections.

Chest tube erroneous positioning must be recognized utilizing proper radiographic views (e.g., latero-lateral projection) and clinical information. Other technical complications following drain catheter insertion may be intra-fissure or extrapleural placement (even in thoracic wall structures) and tube kinking.

### 1.7.2 Tracheal Devices

Endotracheal tubes (ETT) are fundamental to guarantee assisted ventilation, a lifesaving care. Two different types are recognizable by CXR: endotracheal cannula and tracheostomy tube (Fig. 1.18). They are cuffed and placed in the

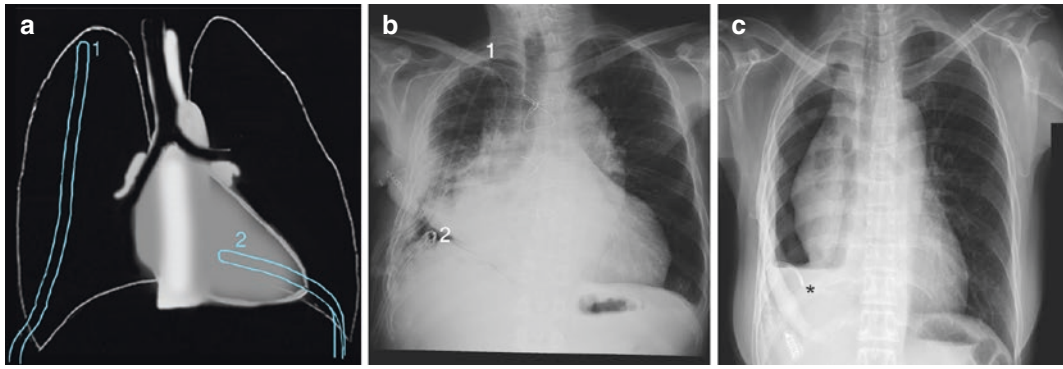


**Fig. 1.17** Drainage tubes placed at lung apices (1) or at lung bases (2): schematic representation (**a**) and CXR appearance (**b**); flexible catheter at right lung base in a case of hydro-pneumothorax on CXR (**c**)

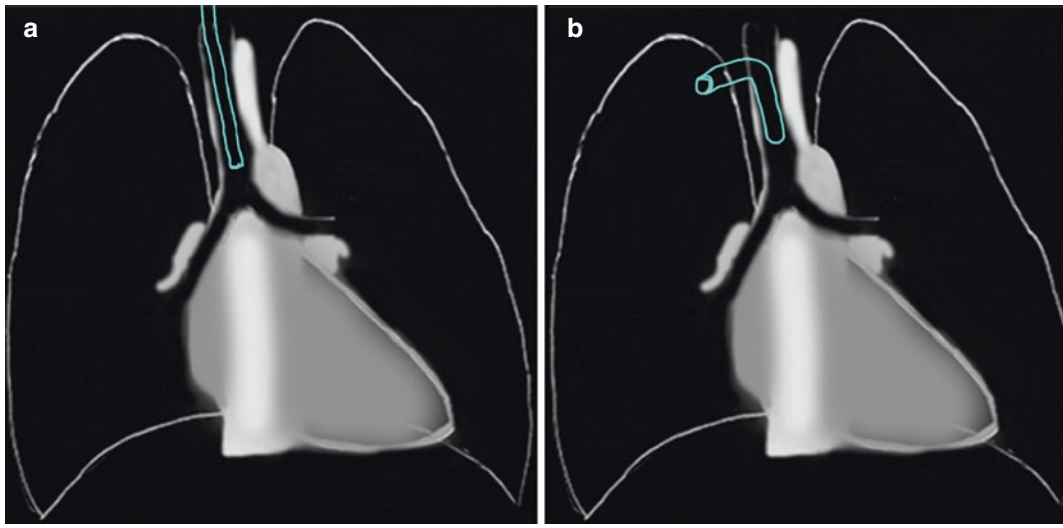


**Fig. 1.18** Schematic representation of endotracheal cannula (**a**) and tracheostomy tube (**b**)

trachea, either via the oropharynx or introduced surgically through a tracheostomy; the latter method is preferred in long-period mechanical ventilation.

Tip of endotracheal cannula might be 5 cm above carina, approximatively at T4–T5 intervertebral space. Notice that sometimes a double-lumen device approach is utilized to control ventilation for each lung.

CXR is able to depict the misplacement of ET devices that often migrate to right main bronchus determining combination of overinflation and atelectasis. Other possible misplacements of ETT detectable by CXR are endo-laryngeal site, where its cuff can injure vocal cords, and intraesophageal location [24].

### 1.7.3 Esophageal Devices

Nasogastric (NG) catheter is employed for enteral nutrition or gastric aspiration in particular clinical conditions. CXR is rarely used for feeding tube assessment (Fig. 1.19) with the exception of unconscious patients. The lower tip of nasogastric tube should preferably be placed in the upper small bowel (distal duodenum), as assessable through abdominal X-ray [25].

### 1.7.4 Cardiovascular Devices

Central venous catheters may insert through either subclavian or internal jugular vein of both sides or occasionally via the femoral vein, particularly in babies. These devices have been developed to monitor central venous pressures and to safe deliver large volumes of fluids over long periods [26]. Correct placement of CVC tip is recognizable by CXR and it is considered between the most proximal venous valves of the subclavian or jugular veins and the right atrium (Fig. 1.20); if the tip of the catheter is placed inside right cardiac chambers, it may cause arrhythmias or cardiac perforation.

Other complications of CVC placement are pneumothorax (Fig. 1.21) and injury to venous walls with secondary thrombosis. Ultrasound-guided CVC positioning has permitted to significantly decrease complication rates [27].

Swan-Ganz (SG) catheters are used to monitor pulmonary capillary wedge pressure; the tip is placed in pulmonary artery when measurements are assessed. CXR may assess correct positioning of SG tip that may project within the mediastinal shadow (Fig. 1.22).

Malpositioning of Swan-Ganz catheters may occur in a quarter of the patients, resulting in

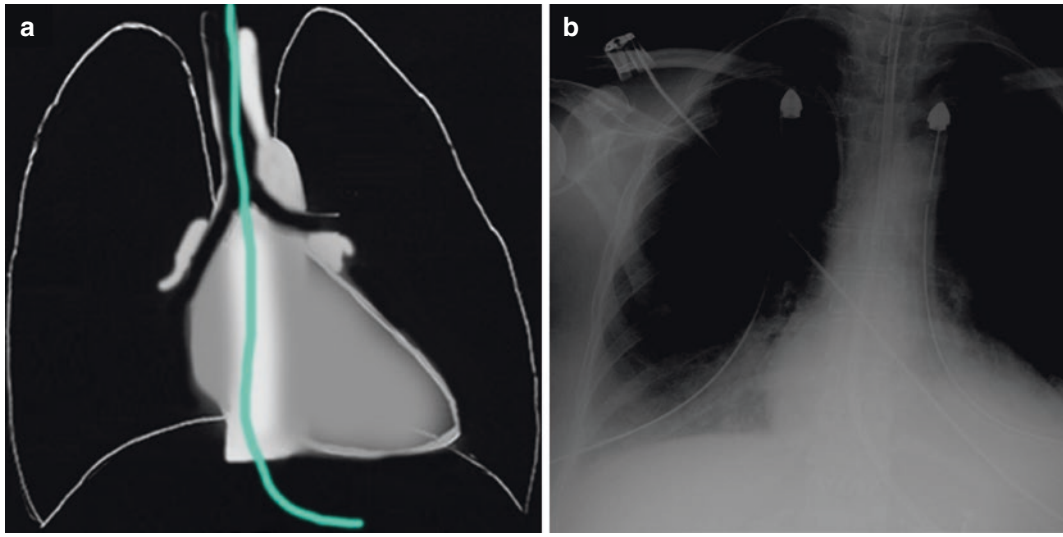


**Fig. 1.19** Nasogastric catheter: schematic representation (**a**) and CXR appearance (**b**)

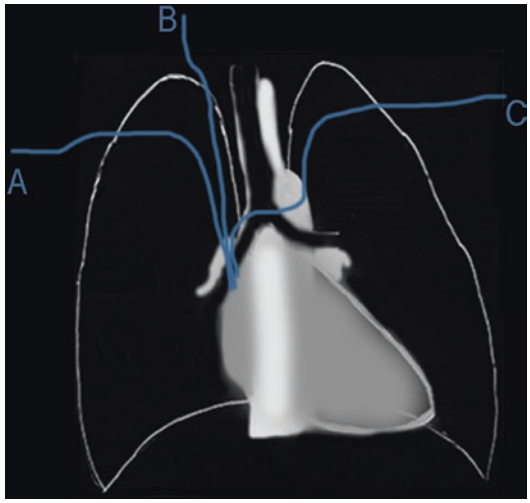


**Fig. 1.20** Schematic representation of correct CVC placement

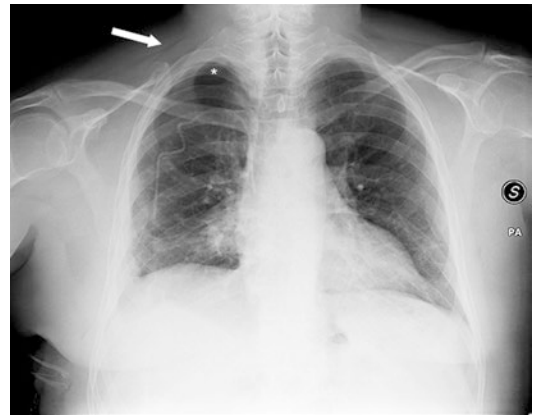

**Fig. 1.21** Post CVC placement right lung pneumothorax on CXR

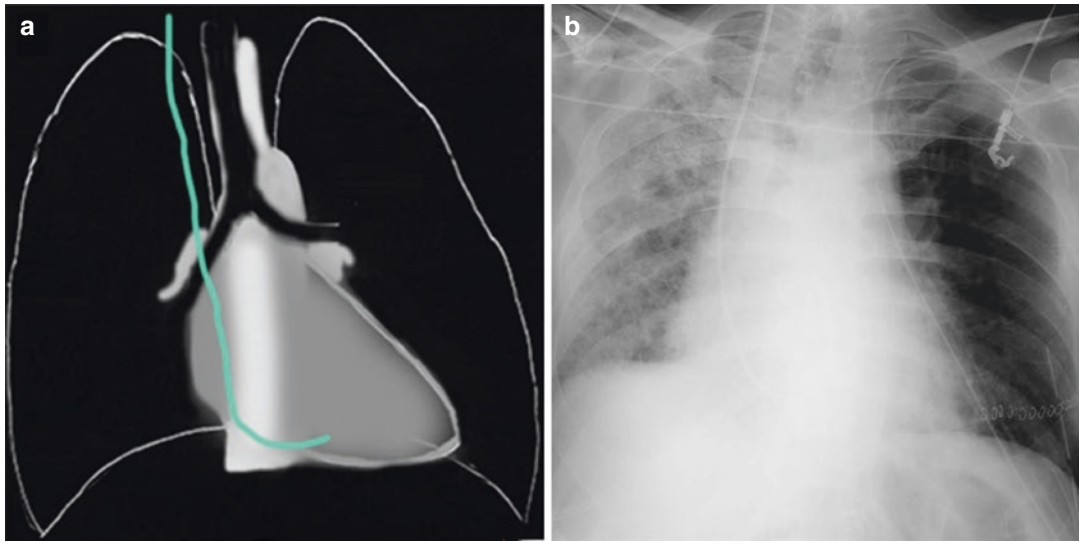


**Fig. 1.22** Swan-Ganz catheter: schematic representation (**a**) and CXR appearance (**b**)

false pulmonary capillary wedge pressure readings, risk for pulmonary infarction, pulmonary artery perforation, cardiac arrhythmias, and endocarditis.

## References

1. Richard Webb W, Higgins CB. Thoracic imaging: pulmonary and cardiovascular radiology. Philadelphia, PA: Lippincott Williams & Wilkins; 2010.
2. Bello SO, Page A, Sadat U, et al. Chest X-ray and electrocardiogram in post-cardiac surgery follow-up clinics: should this be offered routinely or when clinically indicated? Interact Cardiovasc Thorac Surg. 2013;16(6):725–30. https://doi.org/10.1093/icvts/ivt017.
3. French DG, Dilena M, LaPlante S, et al. Optimizing postoperative care protocols in thoracic surgery: best evidence and new technology. J Thorac Dis. 2016;8(Suppl 1):S3–S11. https://doi.org/10.3978/j.issn.2072-1439.2015.10.67.
4. Alloubi I, Jougon J, Delcambre F, et al. Early complications after pneumonectomy: retrospective

study of 168 patients. Interact Cardiovasc Thorac Surg. 2010;11(2):162–5. https://doi.org/10.1510/icvts.2010.232595.
5. Pool KL, Munden RF, Vaporciyan A, et al. Radiographic imaging features of thoracic complications after pneumonectomy in oncologic patients. Eur J Radiol. 2012;81:165–72. https://doi.org/10.1016/j.ejrad.2010.08.040.
6. Kim EA, Lee KS, Shim YM. Radiographic and CT findings in complications following pulmonary resection. Radiographics. 2002;22(1):67–86.
7. Paramasivam E, Bodenham A. Air leaks, pneumothorax, and chest drains. Contin Educ Anaesth Crit Care Pain. 2008;8(6):204–9. https://doi.org/10.1093/bjaceaccp/mkn038.
8. Venuta F, Rendina EA, Giacomo TD, et al. Technique to reduce air leaks after pulmonary lobectomy. Eur J Cardiothorac Surg. 1998;13:361–4.
9. Kouritas VK, Papagiannopoulos K, Lazaridis G, et al. Pneumomediastinum. J Thorac Dis. 2015;7(Suppl 1):S44–9. https://doi.org/10.3978/j.issn.2072-1439.2015.01.11.
10. Massard G, Wihlm JM. Postoperative atelectasis. Chest Surg Clin N Am. 1998;8(3):503–28, viii.
11. Restrepo RD, Braverman J. Current challenges in the recognition, prevention and treatment of perioperative pulmonary atelectasis. Expert Rev Respir Med. 2015;9(1):97–107. https://doi.org/10.1586/17476348.2015.996134.
12. Schweizer A, Perrot MD, Hohn L, Spiliopoulos A, Licker M. Massive contralateral pneumonia following thoracotomy for lung resection. J Clin Anesth. 1998;10:678–80.
13. Franquet T, Giménez A, Rosón N, et al. Aspiration diseases: findings, pitfalls, and differential diagnosis. Radiographics. 2000;20(3):673–85. https://doi.org/10.1148/radiographics.20.3.g00ma01673.
14. Asamura H, Naruke T, Tsuchiya R. Bronchopleural fistulas associated with lung cancer operations. Univariate and multivariate analysis of risk factors, management, and outcome. J Thorac Cardiovasc Surg. 1992;104(5):1456–64.
15. Ng CS, Wan S, Lee TW, et al. Post-pneumonectomy empyema: current management strategies. ANZ J Surg. 2005;75(7):597–602. https://doi.org/10.1111/j.1445-2197.2005.03417.x.
16. Nair SK, Petko M, Hayward MP. Aetiology and management of chylothorax in adults. Eur J Cardiothorac Surg. 2007;32:362–9. https://doi.org/10.1016/j.ejcts.2007.04.024.
17. Kuhlman JE, Singha NK. Complex disease of the pleural space: radiographic and CT evaluation. Radiographics. 1997;17:63–79. https://doi.org/10.1148/radiographics.17.1.9017800.
18. Gluecker T, Capasso P, Schnyder P. Clinical and radiologic features of pulmonary edema. Radiographics. 1999;19(6):1507–31; discussion 1532–3. https://doi.org/10.1148/radiographics.19.6.g99no211507.
19. Cardinale L, Volpicelli G, Lamorte A. Revisiting signs, strengths and weaknesses of standard chest radiography in patients of acute dyspnea in the emergency department. J Thorac Dis. 2012;4(4):398–407. https://doi.org/10.3978/j.issn.2072-1439.2012.05.05.
20. Kutlu CA, Williams EA, Evans TW, et al. Acute lung injury and acute respiratory distress syndrome after pulmonary resection. Ann Thorac Surg. 2000;69:376–8.
21. Eisenberg RL, Khabbaz KR. Are chest radiographs routinely indicated after chest tube removal following cardiac surgery? AJR Am J Roentgenol. 2011;197(1):122–4. https://doi.org/10.2214/AJR.10.5856.
22. Sepehripour AH, Farid S, Shah R. Is routine chest radiography indicated following chest drain removal after cardiothoracic surgery? Interact Cardiovasc Thorac Surg. 2012;14(6):834–8. https://doi.org/10.1093/icvts/ivs037.
23. Tolsma M, Bentala M, Rosseel PM, et al. The value of routine chest radiographs after minimally invasive cardiac surgery: an observational cohort study. J Cardiothorac Surg. 2014;9:174. https://doi.org/10.1186/s13019-014-0174-9.
24. Kwiatt M, Tarbox A, Seamon MJ, et al. Thoracostomy tubes: a comprehensive review of complications and related topics. Int J Crit Illn Inj Sci. 2014;4(2):143–55. https://doi.org/10.4103/2229-5151.134182.
25. Metheny NA, Meert KL. Monitoring feeding tube placement. Nutr Clin Pract. 2004;19:487–95. https://doi.org/10.1177/0115426504019005487.
26. Khan AN, Al-Jahdali H, Al-Ghanem S, et al. Reading chest radiographs in the critically ill (Part I): normal chest radiographic appearance, instrumentation and complications from instrumentation. Ann Thorac Med. 2009;4(2):75–87. https://doi.org/10.4103/1817-1737.49416.
27. Pikwer A, Baath L, Davidson B, et al. The incidence and risk of central venous catheter malpositioning: a prospective cohort study in 1619 patients. Anaesth Intensive Care. 2008;36:30–7.

# 2 Indications to the Use of Computed Tomography in Thoracic Pathologies

Francesco Lavra and Luca Saba

**Abstract**

During the past decades, improvement in computed tomography (CT) technology and post-processing techniques have favoured its wide use in the clinical practice.

Nowadays, CT does not only provide a mere anatomical assessment but is also capable to give information regarding the chemical composition, as well as the blood flow of the scanned tissue. The rapid coverage of large anatomic volumes and its high spatial and temporal resolution also make CT particularly suitable in the assessment of criticaly ill patients. Moreover, CT allows a detailed assessment of lung parenchyma, interstitium, and airways, as well as the thoracic vasculature and coronary arteries. Because of these technical and diagnostic characteristics CT has gained a crucial role in the assessment of thoracic pathologies.

Given the risk associated with radiation exposure and contrast media administration, it is of paramount importance to appropriately use CT in the clinical situations in which this technique has the proper diagnostic yield.

The purpose of this chapter is to explain the clinical indication of CT in thoracic pathologies to establish the appropriateness criteria for use of this technique in standard diagnostic care.

**Keywords**

Computed tomography · Thoracic pathology · Anatomical assessment · Neoplastic disease · Vascular disease · Lung disease

## 2.1 Basic Technical Principles

In the past decade, the improvement in CT scanner technologies has allowed rapid coverage of large anatomic volumes, submillimeter isotropic spatial resolution, and temporal resolution as low as 66 ms [1] with a limited requirement for sedation and anesthesia in patients unable to cooperate with a short breath hold [2, 3].

CT enables visualization of the lung parenchyma, interstitium, and airways with great anatomic details; ECG gating allows delineation of the aortic root and of coronary artery involvement minimizing imaging artifacts caused by cardiac motion [1].

A variety of post-processing techniques can be retrospectively utilized by radiologists depending on a specific clinical question [4]:

- Two-dimensional multiplanar reformations allow to visualize the acquired images in any spatial plane.

F. Lavra · L. Saba (✉)
Department of Radiology, Azienda Ospedaliero Universitaria (A.O.U.), Cagliari, Italy
e-mail: lucasaba@tiscali.it


M. Anzidei, M. Anile (eds.), *Diagnostic Imaging for Thoracic Surgery*,
https://doi.org/10.1007/978-3-319-89893-3_2

- Maximum intensity projections (MIPs) are used to increase the sensitivity and efficiency of pulmonary nodule detection and to assess the morphology and spatial extent of micronodular disease within the lungs. This technique displays the highest attenuation voxels on every view throughout the volume onto a two-dimensional slice, also allowing radiologists to select the thickness and position of the section.
- Minimum intensity projection (minIP) is a technique that projects the voxel with the lowest attenuation value on every view throughout the volume onto a 2D image; it is used for evaluation of the airways or distribution of emphysema.
- Three-dimensional (3D) volume-rendered images can be used to depict a volume of tissue in three dimensions, highlighting the spatial relationships of the different anatomical structures comprised in the scan [4].
- Virtual endoscopy utilizes 3D reconstructions to generate images that recreate the endoscopic perspective with great detail. This technique can be applied to the majority of luminal structures in the human body [5].

Dual-energy CT (DECT) scan consists in a simultaneous acquisition of two X-ray energy spectra at different tube voltages, providing information regarding the chemical composition of the scanned tissue taking advantage of the material-specific difference in attenuation, based on the spectral properties of the detected radiation [6]. This technique provides virtual non-contrast medium-enhanced and iodine-enhanced image series from a single contrast-enhanced scan with a low quantity of contrast material, limiting the radiation dose by obviating the need for routine non-contrast scans; as a matter of fact, it has been shown that DECT techniques are radiation-dose neutral compared with conventional single-energy CT examinations [7, 8]. DECT can also generate monochromatic X-ray beams, which are composed by photons with a single, constant energy, obtaining virtual monochromatic images that can provide more quantitatively accurate attenuation measurements and reduce beam-hardening artifacts [9].

Computer-aided detection (CAD) system is a computer technology used to assist radiologists to decrease observational oversights when examining digital medical images, and thus reduce diagnostic errors [10]. This technology is experiencing a wide diffusion, spreading from the automated detection of lung nodules [11] to the coronary artery disease [12].

Radiogenomics is a radiological field in which images are correlated with genomic variations and CT is demonstrating to have a potential important role in this investigation [13, 14].

Finally, perfusion CT imaging is demonstrating to be a useful tool in lung imaging, especially in lung tumor diagnosis and follow-up [15, 16].

#### 2.1.1 Advantages and Disadvantages

Its noninvasive nature, its high spatial and temporal resolution, and wide availability have conferred to CT a pivotal role in the assessment of thoracic pathologies allowing an exhaustive and accurate evaluation of all chest structures in both stable patients and emergency situations.

Limitations of CT include the exposure to ionizing radiation and the intravenous administration of iodinated contrast due to the risk of contrast material-induced nephropathy in patients with a poor renal function.

## 2.2 Clinical Indications and Guidelines

### 2.2.1 Neoplastic Diseases

#### 2.2.1.1 Neoplastic: Low-Dose CT in Lung Cancer Screening

The advent of low-dose helical computed tomography (CT) altered the landscape of lung cancer screening as it has proved to detect many tumors at early stages [17]. Table 2.1 shows a comparison between standard and ultralow-dose acquisition in a phantom study that demonstrated that these two techniques had a similar detection rate of pulmonary nodules [18].

The National Lung Screening Trial (NLST) demonstrated a relative reduction in mortality from lung cancer of 20.0% with low-dose CT screening, compared to the chest radiograph screening, for patients who have no signs or symptoms suggestive of underlying cancer, an age that ranges between 55 and 80 years with at least a 30 pack-year history of cigarette smoking (and if former smoker, quit date is within previous 15 years) and do not have a health problem that substantially limits life expectancy or the ability/willingness to undergo an intervention with curative intent. The acquisition variables were chosen to reduce exposure to an average effective dose of 1.5 mSv [19]. The rate of death from any cause was reduced by 6.7% in the low-dose CT group as compared with the radiography group, and this evidence suggests that such screening is not, on the whole, deleterious [19].

**Table 2.1** CTD1 (volume CT dose index); DLP (dose length product)

| | Standard acquisition | Ultra-dose |
|---|---|---|
| Dose | CTD1vol 3.15 mGy/DLP 126 mGy cm (40 cm scan length) | CTD1vol 0.22 mGy/DLP: 9 mGy cm (40 cm scan length) |
| Tube voltage | 100 kVp | 80 kVp |
| Tube current-time product | 100 reference mAs | 6 mAs |
| Primary collimation | 0.6 mm | |
| Gantry rotation time | 0.28 s | |
| Pitch | 2.2 | |

From Huber A, Landau J, Ebner L, Butikofer Y, et al. Performance of ultralow-dose CT with iterative reconstruction in lung cancer screening: limiting radiation exposure to the equivalent of conventional chest X-ray imaging. Eur Radiol. 2016;26(10):3643–52

During lung cancer screening programs, the large number of images acquired by MDCT scanners that need to be interpreted may lead to increased observational oversights of pulmonary nodules. CAD systems have proved to be a useful tool that helps radiologists in the detection of pulmonary nodules in lung cancer screening; as a matter of fact the use of CAD systems can improve the performance of radiologists, helping in the detection of nodules that are undetected [11] (Fig. 2.1).

#### 2.2.1.2 Neoplastic: CT in the Management of Small Pulmonary Nodules

Lung nodules are detected more and more frequently on chest CT scans with each new generation scanner. The rationale for recommending serial follow-up studies for all indeterminate small nodules is that some of them will turn out to be cancers and that early intervention will provide an opportunity for cure. On the contrary this

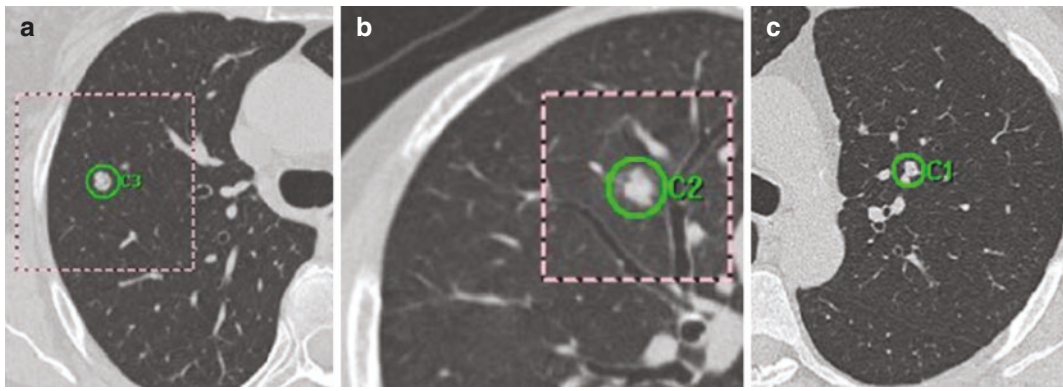


**Fig. 2.1** Images (**a**) and (**b**) show a pulmonary nodule in the upper right lobe detected by CAD and by the radiologist. Image (**c**) shows a nodule in the peribronchial zone of the upper left pulmonary lobe detected by CAD but not by the radiologist. From the Departments of Radiological Sciences and Medical Oncology, University of Rome "La Sapienza," Rome

policy may lead to a potential increase of morbidity and mortality from surgery for false-positive findings, increased healthcare costs and radiation exposure for the affected population [20–23].

The Fleischner Society in 2005 has established the following recommendations for follow-up and management of solid nodules smaller than 8 mm detected incidentally at non-screening CT (Table 2.2). For patients less than 35 years of age, a single follow-up exam in 6–12 months may be considered [24]. Patients older than 35 years of age are divided into high-risk patients (minimal or absent history of smoking and of other known risk factors) and low-risk patients (history of smoking or of other known risk factors) [24]. Additionally, the Fleischner Society has complemented the original recommendations for incidentally detected solid nodules by proposing a set of recommendations specifically aimed at subsolid nodules [25] (Table 2.3).

**Table 2.2** Size effect management rules for pulmonary nodules

| Nodule size mm | Low-risk patients | High-risk patients |
|---|---|---|
| Smaller or equal to 4 mm | No follow-up needed | Follow-up CT at 12 months; if unchanged, no further follow-up |
| Bigger than 4–6 mm | Follow-up CT at 12 months; if unchanged, no further follow-up | Initial follow-up CT at 6–12 months then at 18–24 months if no change |
| Bigger than 6–8 mm | Initial follow-up CT at 6–12 months then at 18–24 months if no change | Initial follow-up CT at 3–6 months then at 9–12 and 24 months if no change |
| Bigger than 8 mm | Follow-up CT at around 3, 9, and 24 months, dynamic contrast-enhanced CT, PET, and/or biopsy | Same as for low-risk patient |

From Heber MacMahon, MB, BCh, BAO, John H. M. Austin, MD et al. Guidelines for Management of Small Pulmonary Nodules Detected on CT Scans: A Statement from the Fleischner Society. Radiology November 2005

**Table 2.3** Size effect management rules for non solid pulmonary nodules

| Solitary pure ground-glass nodules (GGNs) | Management recommendations | Additional remarks |
|---|---|---|
| Smaller than 5 mm | No CT follow-up required | Obtain contiguous 1-mm-thick sections to confirm that nodule is truly a pure GGN |
| Bigger than 5 mm | Initial follow-up CT at 3 months to confirm persistence and then annual surveillance CT for a minimum of 3 years | FDG PET is of limited value, potentially misleading, and therefore not recommended |
| Solitary part-solid nodules | Initial follow-up CT at 3 months to confirm persistence. If persistent and solid component <5 mm, then yearly surveillance CT for a minimum of 3 years. If persistent and solid component larger or equal to 5 mm, then biopsy or surgical resection | Consider PET/CT for part-solid nodules of >10 mm |
| *Multiple subsolid nodules* | | |
| Pure GGNs smaller than 5 mm | Obtain follow-up CT at 2 and 4 years | Consider alternate causes for multiple GGNs smaller or equal to 5 mm |
| Pure GGNs bigger than 5 mm without a dominant lesion(s) | Initial follow-up CT at 3 months to confirm persistence and then annual surveillance CT for a minimum of 3 years | FDG PET is of limited value, potentially misleading, and therefore not recommended |
| Dominant nodule(s) with part-solid or solid component | Initial follow-up CT at 3 months to confirm persistence. If persistent, biopsy or surgical resection is recommended, especially for lesions with >5 mm solid component | Consider lung-sparing surgery for patients with dominant lesion(s) suspicious for lung cancer |

From David P. Naidich, MD, Alexander A. Bankier, MD, PhD et al. Management of Subsolid Pulmonary Nodules Detected at CT: A Statement from the Fleischner Society. Radiology: Volume 266: Number 1—January 2013

#### 2.2.1.3 Neoplastic: CT in Lung Cancer Staging

Lung cancer is a leading cause of cancer mortality in men and women in the United States [26]. The staging (TNM), which defines the extent of disease, is fundamental to guide the treatment and to define prognosis.

The CT diagnostic algorithm of a solitary pulmonary nodule (SPN), which is the most common manifestation of lung cancer, consists of two major parts: the calcification detection and characterization on a non-enhanced study and the assessment of the SPN enhancement on an enhanced scan [27]. The detection of calcification is important because the presence of particular patterns of calcification is attributed to benignity while evaluating tumor vascularity by the measure of its contrast enhancement is useful in distinguishing malignant nodules from benign nodules in contrast-enhanced dynamic CT [27].

By leveraging the DECT capability of differentiating the iodine, we can obtain a perfusion map depicting the distribution of iodine contrast material throughout the lung parenchyma; combining the perfusion status assessment of lung nodule and lobe we can obtain useful information to predict the postoperative lung function in candidates for surgical resection [6].

Chest CT alone is satisfactory for staging patients with pure ground-glass opacities, with peripheral IA disease or an otherwise normal study [28]. CT is the paramount imaging technique to depict additional tumor nodules and separate tumor nodule in the contralateral lung as the initial evaluation is the first moment when nodules are generally detected [29]; it can also depict separate masses that are likely to be technically resectable (no invasion or focal limited invasion) although in some cases it cannot confirm mediastinal invasion with certainty [30]. Tumor extension can be suggested by CT delineating its endobronchial component or demonstrating associated secondary changes such as postobstructive pneumonitis or atelectasis. CT can reliably detect the invasion of the chest wall only in cases with gross soft tissue or osseous involvement; magnetic resonance imaging (MRI) and positron emission tomography (PET) scanning may also provide additional important information for accurate classification in certain cases [31].

Perfusion CT is experiencing a progressive increase in interest and acceptance among the radiologic community for the diagnosis and follow-up of lung cancer. Specifically it has demonstrated its utility in follow-up studies of patients with inoperable lung cancer that underwent chemotherapy with antiangiogenic biologic drugs (bevacizumab), depicting early changes in tumor vascularity after biologic therapy and thus paving the way for an eventual complementary use with RECIST (Response Evaluation Criteria in Solid Tumors) criteria [15] (Fig. 2.2).

Additionally, CT characterization of lung tumors is showing to potentially have the capability to provide information about genetic alterations involved in the cancerogenesis: as a matter of fact, in preliminary radiogenomic studies, CT features of pulmonary nodules (ground-glass opacity and CT gray-level texture analysis) have shown to be connected with the expression of epidermal growth factor receptor in lung adenocarcinoma [13, 14].

#### 2.2.1.4 Neoplastic: CT in Lymphoma Staging

The World Health Organization International Classification of Disease (2008) identifies more than 50 types of lymphoma on the basis of histopathologic, immunohistochemical, cytogenetic, and molecular analyses [32]. The Lugano classification (2014) is the most recent system proposed for staging and response assessment of both Hodgkin's and non-Hodgkin's lymphoma, fully utilizing fluorodeoxyglucose (FDG) PET/CT in the staging and response evaluation of FDG-avid lymphoma [33].

Lymphomas with low or variable FDG uptake should still be staged with CT [33]. In the purpose of achieving an optimal anatomic assessment, a diagnostic contrast-enhanced CT, which may be completed as part of the FDG PET/CT, should still be performed at initial staging of FDG-avid lymphomas [34]. Contrast-enhanced CT allows a more accurate measurement of node size and helps to discern adenopathy from

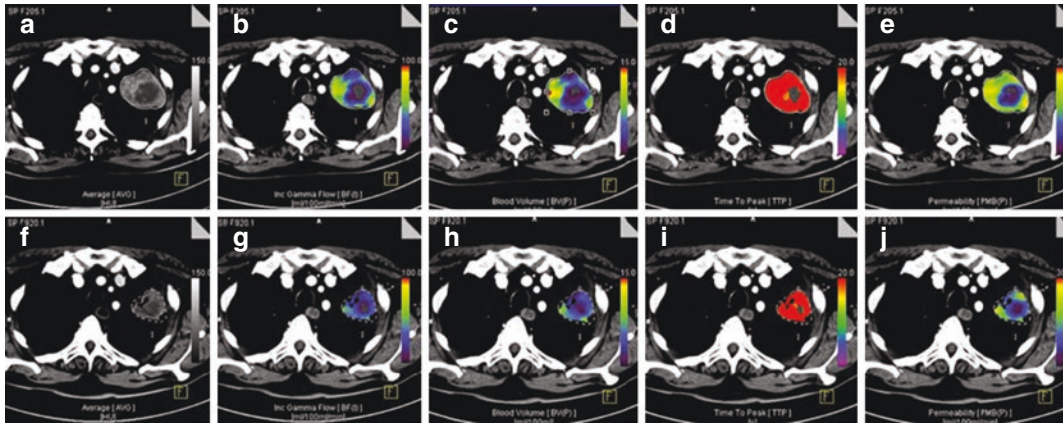


**Fig. 2.2** Image of a 56-year-old man with stage IV adenocarcinoma. Morphologic axial images (**a**, **f**), blood flow map (**b**, **g**), blood volume map (**c**, **h**), time to peak map (**d**, **i**), and permeability map (**e**, **j**) before therapy (top row) and after biologic antiangiogenic therapy (bottom row) showing a good lesion response according to RECIST criteria with a substantial stability of its vascularity. In this patient, perfusion CT shows no response to the antiangiogenic therapy despite a reduction in tumor size. From the Departments of Radiological Sciences and Medical Oncology, University of Rome "La Sapienza," Rome

surrounding soft-tissue structures better than the low-dose non-enhanced CT previously routinely performed for FDG PET/CT [35]. Surveillance CT imaging is still widely performed but may not be necessary in all patients [36].

The Lugano criteria do not advise the routine use of FDG PET/CT scans on follow-up imaging in asymptomatic patients and recommend CT surveillance scans on the basis of clinical signs or symptoms or as required by a clinical trial; it is also advised to limit the radiation exposure [33].

#### 2.2.1.5 Neoplastic: CT in Esophageal Cancer

Esophageal cancer is the third most common gastrointestinal malignancy and is among the ten most prevalent cancers worldwide; CT is the most commonly used modality in the initial staging of this disease [37]. The most important role of CT in the determination of T status is the exclusion of T4 disease, as indicated by the preservation of fat planes between the esophageal cancer and adjacent structures [38].

Contrast-enhanced CT is the mainstay to rule out distant metastasis because it allows the assessment of the three most common sites involved in secondary disease (in descending order of prevalence the liver, lungs, and bones), permitting immediate triage to systemic therapy or other multimodality treatments [39]. Additionally, 3D images and virtual endoscopy can be added to conventional protocol, improving the diagnostic accuracy of CT in this pathology [5]. Panebianco et al. showed that the 3D images could be useful to surgeons in the preoperative planning while virtual endoscopy, that can be performed in case of exophytic malignant narrowing impeding the passage of the endoscope, can characterize endoluminal tumors, assess the grade of stenosis, and visualize the rest of the esophagus and the stomach beyond the stricture [5].

An important limitation of CT in the esophageal cancer staging is its lack of sensitivity for detecting lymph node metastases and for determining the exact depth of tumor infiltration of the esophageal wall [37]. Currently, the combination of CT, endoscopic ultrasonography (US), and positron-emission tomography (PET) determines whether a patient should be treated with surgery, chemotherapy, or an association of chemotherapy and radiation therapy [37].

#### 2.2.1.6 Neoplastic: CT in Thymoma

Thymoma is the most common primary neoplasm of the anterior mediastinum [40]; it is characterized by a slow growth and may show

aggressive behavior, invading the adjacent structures and involving the pleura and pericardium, although distant metastases are rare [41]. Chest pain, dyspnea, or cough are present in up to one-third of patients with thymoma [42]. The secretion of hormones, antibodies, or cytokines by the tumor may cause systemic complaints and paraneoplastic syndromes [43].

CT is the mainstay of the assessment of this pathology and can help defining the differential diagnosis with other anterior mediastinal abnormalities. Vessel evaluation is important for staging and therefore intravenous contrast material, if not contraindicated, should be administered [44].

The International Thymic Malignancy Interest Group (ITMIG) recommends that in the follow-up, since late recurrences are not uncommon, patients should undergo a chest CT examination annually for 5 years after surgical resection, then alternated with annual chest radiography until year 11, and subsequently followed by annual chest radiography alone. In the surveillance of stage III or IVa thymoma, thymic carcinoma, incomplete resection, or other high-risk tumors, patients should undergo a CT scan every 6 months for 3 years [45].

#### 2.2.1.7 Neoplastic: CT in Chest Wall Neoplasms

Chest wall neoplasms are uncommon lesions that represent approximately 5% of all thoracic malignancies [46]; in more than 50% of cases they are malignant, typically resulting from direct invasion by or metastasis from thoracic tumors, even if they can also arise from the chest wall as primary tumors [47]. An accurate identification and characterization of chest wall malignancies are achieved through cross-sectional imaging techniques, such as multidetector CT and MRI.

CT readily reveals the presence of a lesion, the site and tissue origin (bone, cartilage, or soft tissues such as muscle, fat, or skin), morphologic features, and internal components [48, 49]. The intravenous administration of contrast material can be used to identify tumor vascularity [50]. CT has shown to be the best tool for the characterization of bone involvement and mineralization; this feature is particularly useful in the assessment of tumors of chondro-osseous origin, in radiation-associated malignancies and also in osseous metastatic disease [51]. Osseous metastasis may appear in many different ways, with some metastasis demonstrating imaging characteristics specific to the primary malignancies from which they are derived, some of which may be predominantly sclerotic (breast or prostate cancer), lytic and expansile (renal cell carcinoma), or lytic lesions (multiple myeloma) [51].

A disadvantage of MDCT is the use of ionizing radiation and the reduced soft-tissue contrast.

### 2.2.2 Vascular Diseases

#### 2.2.2.1 Vascular: CT in Congenital Heart Diseases

Congenital heart disease (CHD) is the most common congenital anomaly and currently almost all patients survive until adulthood [52–60]. Nevertheless, residual hemodynamic lesions require repeat interventions during the life and close surveillance with an important utilization of healthcare resources [61, 62].

Nowadays diagnostic techniques are primarily noninvasive and cardiovascular CT (cCT) is becoming a complement to echocardiography when cardiac magnetic resonance (cMR) is contraindicated, or when it is too risky or when it is not capable to provide images with the quality required for the clinical question [63, 64].

cCT is advised in the following conditions:

- In the presence of cMR-incompatible implant or foreign body or in the case in which a poor image quality is expected due to metallic artifact.
- In patients that are unfit to MR scan (obese, claustrophobic, or critically ill patients who may not tolerate breath holding or the length of cMR scan), in high-risk neonate, or young patients who require sedation or anesthesia to perform cMR for the evaluation of complex anatomy.
- In the evaluation of ventricular assist device or extracorporeal membrane oxygenation (ECMO) cannula positioning.

- When extra-cardiac anatomy evaluation is needed in addition to CHD (lung parenchyma, airway, skeletal abnormality).
- In the preoperative evaluations of sternal reentry in patients who may be susceptible to vascular injury due to an anterior coronary artery, conduit, or sternal adhesions.
- In the evaluation of the function or structural integrity of prosthetic valve (presence of calcifications, stenosis, coaptation defect, leaflet immobility, paravalvular leak, endocarditis or clot).
- Before undergoing catheter-based intervention in the evaluation of calcification within vessels and surgical conduits.
- In coronary artery imaging in CHD:
  - In the evaluation of patient who needs a detailed preoperative coronary artery evaluation in addition to assessment of complex cardiac anatomy.
  - Patients with a history of CHD, coronary intervention, or high-risk Kawasaki disease who experience symptoms and signs suggestive of atherosclerotic coronary disease.
  - In the presence or suspicion of coronary anomaly in young symptomatic patients especially when cMR is improbable to provide complete assessment without requiring anesthesia.
  - To define coronary anatomy in the preoperative evaluation of surgical or percutaneous pulmonary valve implantation.
  - In the postoperative evaluation after coronary artery manipulation or reimplantation [1].

When performed by experienced users with modern CT scanners, paying particular attention to scan parameters, CT delivers 10–15-fold less radiation than cardiac catheterization (less than 1 millisievert (mSv) for the majority congenital cardiac applications) [63, 65]; the examination is quick, without the need of specialized equipment, and patients are more accessible compared to a CMR scan and can return to the intensive care unit within 15–30 min [66].

#### 2.2.2.2 Vascular: CT in Pulmonary Embolism

Acute pulmonary embolism is a common clinical problem that is related to considerable morbidity and mortality [67]. The leading cause of death in patients with acute pulmonary embolism is its recurrence, with a mortality rate without treatment of approximately 30% [68]. Currently, CT angiography (CTA) has almost completely replaced scintigraphy and conventional angiography (ICA) for the diagnosis of this pathology (Fig. 2.3) and it is endorsed by both the American College of Radiology and the Fleischner Society as the reference standard for diagnosis of acute pulmonary embolism [69, 70], having proved to have a negative predictive value of 99% [71]. It is interesting to note that CTA, when combined with lower extremity US and D-dimer test, has also shown to be the most cost-effective option for all pretest clinical likelihoods [72].

The incomplete resolution of pulmonary thromboembolism is the main cause of chronic pulmonary thromboembolism that may secondarily lead to pulmonary hypertension [73]. Misdiagnosis is frequent due to the nonspecific symptoms related to pulmonary hypertension [74] and conventional pulmonary angiography is the traditional cornerstone for evaluation of this disease [75, 76].

CTA is a useful alternative not only for the diagnosis but also for the pre- and postoperative evaluation [73, 76, 77] being more sensitive than ICA in the depiction of central thrombotic disease [77]. It is also as sensitive as MR angiography in depicting the disease at the segmental level and more sensitive in the recognition of patent subsegmental arteries and intraluminal webs, for the direct visualization of thrombotic wall thickening even if it is unable to assess the severity of functional impairment [78]. CTA may also be useful in the definition of the differential diagnosis or of different causes of pulmonary hypertension and may provide futures that are predictive of a good response to pulmonary thromboendarterectomy [79–81].

Acute pulmonary embolism is one of the main applications of chest DECT; an optimal pulmonary enhancement, triggered with bolus-tracking

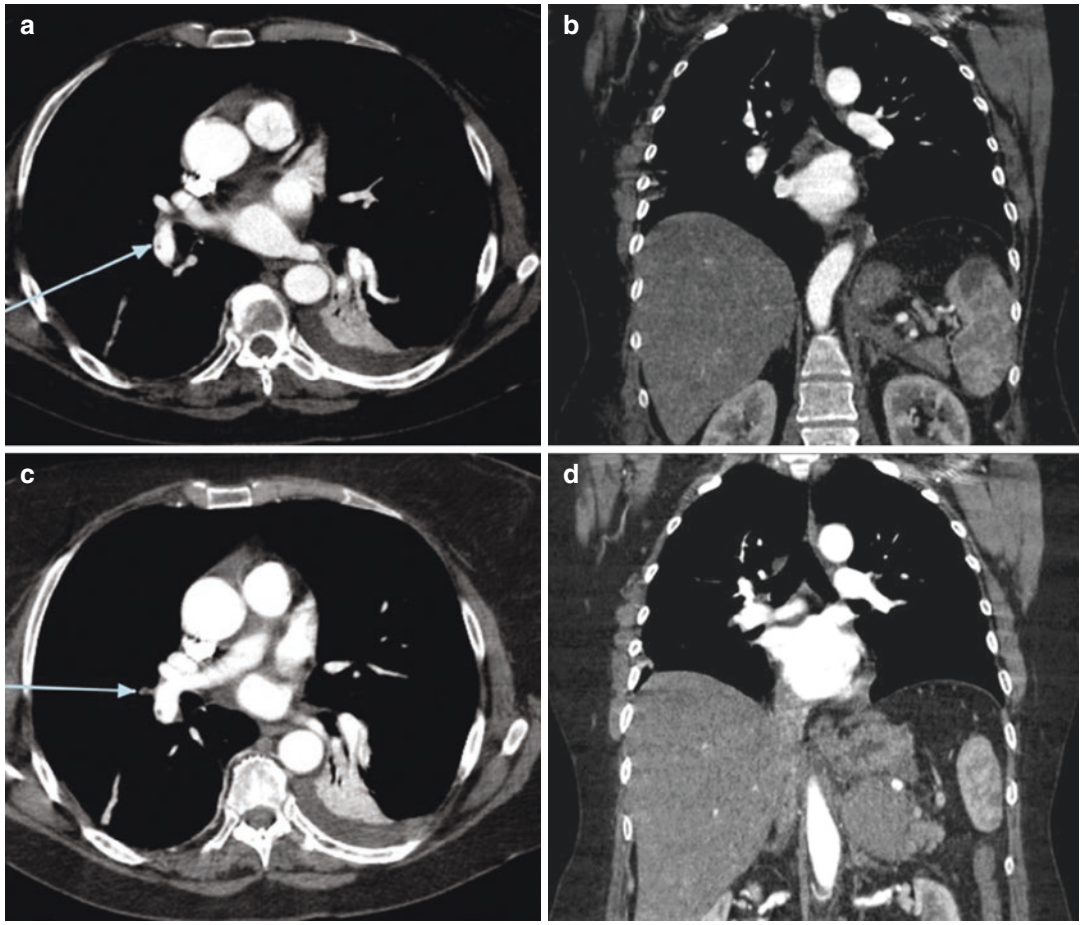


**Fig. 2.3** Acute pulmonary embolism in a 57-year-old patient (images **a** to **d**). A pulmonary arterial band is shown in the adjacent pulmonary branch (*blue arrow* in **a**) in relation to chronic pulmonary embolism. Complete obstruction in a segmental branch of right pulmonary artery (*blue arrow* in **c**). From the department of Radiology, Università degli studi di Cagliari, Cagliari

techniques, is required to make an accurate diagnosis; in particular, the acquisition of low-energy monochromatic DECT images can increase the arterial enhancement, improving the confidence in interpretation of pulmonary CTA images compared to single-energy CTA and a higher kilovoltage (100–140 kV), in which it is not possible to improve image contrast [82]. Low-energy virtual monochromatic images (≤60 keV) are acquired to ensure high attenuation in pulmonary vessels, even to the subsegmental level, with a reduced volume of contrast material allowing patients with an intermediate risk for contrast material-induced nephropathy (eGFR, 30–60 mL/min/1.73 $m^2$) to undergo the examination with only 25–35 mL of iodinated contrast (iodine concentration, 370 mg/mL) [83]. DECT pulmonary angiography has also many potentials in the assessment of suspected pulmonary embolism and pulmonary arterial hypertension [84]; as a matter of fact the perfusion imaging has reported a sensitivity of 100% and a specificity of 92%, which is superior to the diagnostic performance of scintigraphy, for the recognition of chronic thromboembolic pulmonary hypertension [85]. The peripheral decrease in lung parenchymal enhancement with increased enhancement of the main pulmonary artery has been reported in patients with pulmonary artery hypertension [86].

#### 2.2.2.3 Vascular: CT in Diseases of the Aorta

Aortic aneurysm and acute aortic syndrome are the most common aortic diseases encountered in daily practice. An aneurysm is defined as a permanent dilatation of the aorta exceeding the normal measurements by more than 2 SDs at a given anatomic level [87].

CTA have essentially replaced diagnostic ICA being routinely used to diagnose and evaluate thoracic aortic aneurysms (TAAs) [88]. ICA can demonstrate only the lumen of aneurysm while CTA can also study its wall and content, thereby allowing to measure accurately its size and to evaluate the morphologic features and surrounding structures [89, 90]. In the presence of a stent graft that may mimic endoleak after contrast administration, unenhanced scanning can be performed in order to detect aortic calcifications while delayed scans (usually in 2 min) are useful in the visualization of late filling of the false lumen, endoleaks, or contrast extravasations from rupture [91]. CTA is the gold standard to evaluate the thoracic aorta in the planning for endograft repair of the TAA because it helps assessing the great vessels in order to define the proximal landing zone, the patency of the vertebral vessels (stent graft covering the subclavian artery), and the common femoral artery access [92]. Arch evaluation with CTA has reduced the occurrence of "unusual" maneuvers during stent placement in patients who underwent CTA before carotid stenting [92].

CTA, by the means of direct planimetric measurement of the aortic valve regurgitant orifice area, has proved to be an accurate, noninvasive technique in the detection and quantification of aortic regurgitation [93], providing aortic valve area in addition to ejection fraction and coronary artery anatomy [94].

CTA is also routinely performed in the postoperative evaluation of the aorta and, compared to ICA, is relatively noninvasive and provides superior image quality, including multiplanar and 3D reformation capabilities [95]. Moreover, it may depict the mediastinum, allowing diagnosis of alternative intrathoracic complications or abnormalities [95]. Postoperative complications seen at CTA that require further intervention include pseudoaneurysms, anastomotic stenoses, dissections, and aneurysms [96].

CTA is the technique of choice for evaluation of suspected aortic rupture because of its fast speed, widespread availability, and excellent sensitivity and specificity for this complication [97]. "Triple-rule out" describes an ECG-gated CTA study used to evaluate patients with acute chest pain for three potential causes: aortic dissection, pulmonary embolism, and coronary artery dissection [98]. Unlike uncomplicated aneurysms, acute aortic diseases, including aortic dissection, intramural hematoma, and penetrating aortic ulcer, are usually diagnosed in patients with acute chest pain.

Aortic dissection is the most common acute aortic disease, in which an intimal tear in the aortic wall forms a dissection membrane creating a true and a false intramural lumen [99], with an incidence up to 0.2–0.8% and the highest mortality rate [100]. CT is the most commonly imaging technique performed for evaluation of suspected acute aortic syndrome with a sensitivity and specificity of 100% for the detection of aortic dissection [60]; it can also reliably predict its progression [101, 102]. The advantage is the capability to rapidly and simultaneously investigate the main sources of acute chest pain (thoracic aorta, pulmonary arteries, and coronary arteries) with a high negative predictive value [103].

The bleeding of the vasa vasorum in the medial layer of the aorta without blood flow within the media is defined intramural hematoma [104] and it can be a precursor of aortic dissection, representing either an early stage or a variant [105]. An unenhanced acquisition, followed by a contrast-enhanced one, is associated with a sensitivity as high as 96% for detection of intramural hematoma [106]. Several findings on initial CT examination have been shown to predict progression [107] and during the first 30 days of presentation close follow-up imaging is recommended for all patients treated medically [108].

Contrast-enhanced CT, including axial and multiplanar reformations, is the technique of choice for diagnosis of penetrating aortic ulcer

that is a pathology caused by the ulceration of an atherosclerotic plaque that disrupts the intima with subsequent extension of the blood into the media [109]. As for the dissection, close imaging follow-up within the first 30 first days of presentation is strongly advised in medically treated patients.

Aortic diseases are also another application of the multispectral imaging. The use of low monochromatic images increases enhancement of the systemic vasculature, as well as the pulmonary arteries, with fewer opportunities to miss incidental aortic abnormalities while material decomposition DECT images can help in the differentiation of the several aortic diseases [110]. As a matter of fact, virtual non-enhanced imaging (VNC that represents iodine subtraction) has the capability to replace true unenhanced CT for depiction and surveillance of real endoleaks after aortic aneurysm repair [111, 112]. On the other hand, PBV (pulmonary blood volume, iodine map) images determine intense iodine distribution in vasculature and in vascular malformations [110].

#### 2.2.2.4 Vascular: CT in Vasculitis

Pulmonary vasculitides are defined as noninfectious inflammatory disorders that primarily affect the blood vessels of the lung, from the main pulmonary artery to alveolar capillaries [113, 114]. The integration of clinical, laboratory, and imaging findings is mandatory for making a specific diagnosis of various pulmonary vasculitides [115].

Considering that the key important imaging findings of pulmonary abnormalities include pulmonary artery aneurysm, stenosis, nodules, or multifocal consolidation with or without cavity (Fig. 2.4), diffuse or extensive opacities and

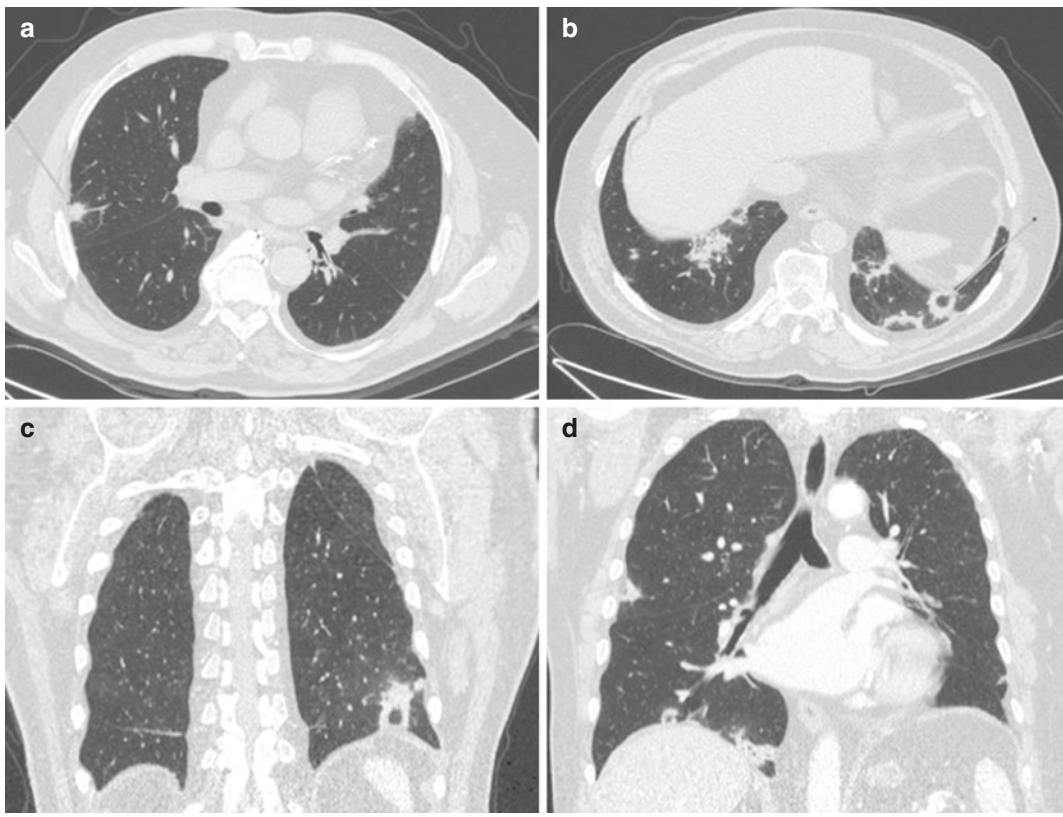


**Fig. 2.4** Wegener granulomatosis in a 40-year-old patient (images **a** to **d**). Multiple nodules with irregular margins (*blue arrow* in **a**); some of them show cavitation (*blue arrow* in **b**). From Department of Radiology, Università degli studi di Cagliari, Cagliari

tree-in-bud sign, chest CT, and CTA play a central role in the diagnostic algorithm, especially in extracranial arteries that are affected in large-vessel giant-cell arteritis, Takayasu arteritis, and idiopathic aortitis [116].

### 2.2.3 Infectious Diseases

#### 2.2.3.1 Infectious: CT in Human Immunodeficiency Virus/Acquired Immunodeficiency Syndrome

Pulmonary manifestations of human immunodeficiency virus (HIV)/acquired immunodeficiency syndrome (AIDS) are the major causes of morbidity and mortality in this group of patients and the great majority of lung complications derive from infections, neoplasms, interstitial pneumonias, Kaposi sarcoma (KS), and lymphomas [117].

Chest radiography is usually the first line and often the only imaging investigation, having demonstrated to be an accurate tool to diagnose common infectious complications [118].

High-resolution computed tomography (HRCT) is both more sensitive and more accurate, with a 93% negative predictive value in excluding active pulmonary disease [119]. However, CT is not routinely indicated because it only affords a modest diagnostic improvement [120]. Specific indications include the detection of occult disease in symptomatic patients, characterization of nonspecific radiographic disease patterns, assessment of the mediastinum and complications (particularly pleural disease), staging of malignancies, and guidance in invasive procedures [117]. CT has also shown to be a helpful tool to discriminate between a potential infectious and neoplastic causes in patients with AIDS who have multiple pulmonary nodules [121].

#### 2.2.3.2 Infectious: CT in Acute Mediastinitis after Cardiac Surgery

Mediastinitis following thoracic surgery is an infection of organs and tissues in the mediastinal space, with an incidence ranging between 0.4% and 5% of cases and high rates of morbidity and mortality [122–125].

A CT should be performed after the first two postoperative weeks in patients with clinical suspicion of mediastinitis or surgical wound infection, to investigate the presence of mediastinal collections and densification/edema of adjacent soft tissues and to determinate the extent of disease [126]. When there is a spontaneous drainage from the surgical wound, CT plays an important role in the identification of the superficial or deep collection origin, besides defining its nature. CT-guided percutaneous drainage is performed only when bacterial culture is required [127]. Curved multiplanar reconstructions are crucial to visualize the sternum; particularly the sagittal plane is useful to define the disease extent and to characterize the communication between mediastinal and parietal compartments [127].

CT is a useful tool in the medium- and long-term surveillance and for the clinical management after introduction of antibiotic therapy, besides confirming the resolution of the inflammatory process. After the debridement surgery, follow-up CT can depict debris and possible infection recidivation [128].

### 2.2.4 Occupational Diseases

#### 2.2.4.1 Occupational: CT in Occupational Lung Disease

A multidisciplinary approach, including the occupational medicine physician, radiologist, industrial hygienist, pulmonologist, and pathologist, is required for the diagnosis of occupational lung disease. Radiography, often in conjunction with the International Labor Organization (ILO) classification system, remains the most widely used method for diagnosis and monitoring of many occupational lung diseases [129].

Although CT has shown to be more sensitive and accurate than chest radiography in the evaluation of nonoccupational diffuse lung diseases [130, 131], no country has adopted it as a primary screening modality for pneumoconiosis, presumably because of its high cost and radia-

tion dose [132]. CT is commonly used as a secondary screening modality in symptomatic or physiologically impaired workers with normal or equivocal chest radiograph findings [133], being also particularly useful in the identification and characterization of the atypical presentations of occupational lung disease. A standardized system, analogous to the ILO radiographic classification, is increasingly used to score the extent of disease on CT scans [133–136] and has been shown to be associated with moderate inter-reader and intra-reader agreement for all categories of abnormality except ground-glass lesions [137].

Low-dose CT (1.5 mSv) is starting to be utilized in the screening of lung cancer in patients with occupational exposures to increased risk for malignancy (particularly asbestos exposure) [138, 139] as it may also be used for screening pneumoconiosis.

#### 2.2.4.2 Occupational: CT in Mesothelioma and Other Asbestos-Related Pleural Diseases

The inhalation or ingestion of asbestos has an established causal relationship with some types of cancer (lung, mesothelioma, larynx, and certain gastrointestinal cancers) and causes asbestosis, a progressive fibrotic disease of the lung, and several types of benign pleural diseases [140].

Chest CT is considered the primary imaging study to evaluate and assess patients with malignant pleural mesothelioma as it provides significant anatomic and pre-operatory information [141]. However, it has distinct limitations in distinguishing simple contiguity of tumor with chest wall or mediastinum from actual invasion [142, 143] while MRI can help in this purpose. In relation to the asbestos-related benign lung and pleural lesions, CT has shown to be useful in eliminating false-positive diagnoses of noncalcified plaques caused by subpleural fat and prominent intercostal muscles [144]; the role of HRCT in the clinical diagnosis of asbestosis and idiopathic pulmonary fibrosis is increasing in importance [145].

### 2.2.5 Others

#### 2.2.5.1 Others: CT in Interstitial Lung Disease

Over 100 different forms of interstitial lung disease (ILD) have been described [146] and the successful management of patients with this disease depends on the establishment of an accurate and specific diagnosis [146, 147]. Although a probable diagnosis may be achieved through the combination of history, physical examination, chest radiography, and other appropriate laboratory testing (such as peripheral blood tests and lung physiologic testing), additional examinations are needed to reach a confident diagnosis of a specific ILD [146].

HRCT has become a standard test for the evaluation of patients with possible ILD, providing invaluable information that strongly supports a specific diagnosis such that further testing with bronchoscopy or surgical lung biopsy may not be required [148]. In general, a normal HRCT scan virtually excludes the presence of ILD, although it may rarely still be present when a microscopic involvement of the lungs does not reach the threshold necessary to detect it by HRCT. Multidetector spiral CT is even better than HRCT in the imaging of ILD as it allows the use of an algorithmic approach to facilitate the differentiation among UIP, NSIP, and chronic HP patterns [149].

A recently published American Thoracic Society Task Force Report on bronchoalveolar lavage (BAL) for the diagnosis of ILD recommends using recently obtained HRCT imaging to choose an appropriate segment of the lung in which to perform BAL from a wedge position [150]. HRCT can also be used to score the extent/severity of fibrosis that is correlated to prognosis, even if the serial HRCT scanning has not been validated as a useful indicator of disease progression for idiopathic pulmonary fibrosis over time as it presents a significant radiation risk to the patient [131, 151].

Additionally, interstitial lung disease and pulmonary arterial hypertension represent the two thoracic manifestations of collagen vascular diseases that are responsible for a large part of the

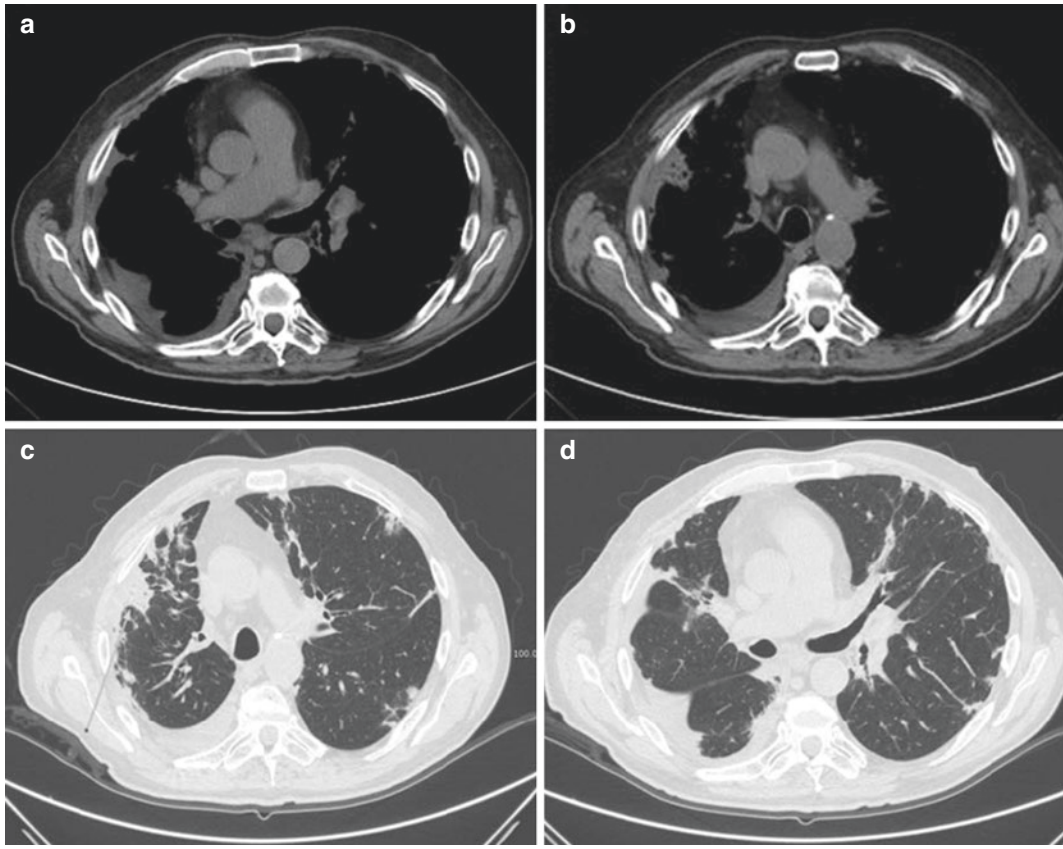


**Fig. 2.5** Methotrexate lung disease in a 65-year-old patient affected by rheumatoid arthritis (images **a** to **d**): diffuse and subpleural parenchymal opacification; some of them show air bronchogram (*blue arrow* in **c**); pleural effusion is also associated. Symptoms that were unresponsive to antibiotics, started after 2 months of therapy. From the Department of Radiology, Università degli studi di Cagliari, Cagliari

mortality and morbidity caused by this group of pathologies. Rheumatoid arthritis, progressive systemic sclerosis, systemic lupus erythematosus, polymyositis and dermatomyositis, mixed connective tissue disease, and Sjögren syndrome are the most common collagen vascular diseases that involve the lung (Fig. 2.5) [152]. Although chest radiography represents the most commonly used tool to screen and monitor thoracic alterations, HRCT can provide additional information about lung involvement that is particularly helpful for the differentiation of specific disease patterns in the lung [153].

#### 2.2.5.2 Others: CT in Airway Diseases

Small airway disease includes a heterogeneous group of pathologic conditions that are centered on small conducting airways; small airway disease involves the bronchioles primarily and varies in their etiology, clinical settings, and pathologic features [154]. Chest radiography and physiologic testing hardly detect small airway disease in its early stage.

The utilization of thin section and HRCT, in combination with clinical and pathologic features, has greatly heightened the diagnostic accuracy in the evaluation of patients suspected of being affected by this pathology [155]. The imaging evaluation should include inspiratory and expiratory HRCT obtained using thin collimation (1.25 mm or less) acquired as either noncontiguous images at 1 or 2 cm intervals or reconstructed from a spiral/helical volumetric acquisition. The volumetric acquisition, even if it implies a higher radiation dose, utilizing reconstructed multiplanar or post-processed images,

allows for evaluation of larger airways for the presence of bronchiectasis and optimizes the detection and characterization of airway abnormalities [156].

Between these large-airway abnormalities, tracheobronchomalacia (TBM) represents the most common congenital disease; however, it is still underdiagnosed in the pediatric patients because it escapes detection on routine end-inspiratory CT images [157]. Infants and children with known risk factors for TBM [157–159] who complain symptoms of impaired exercise tolerance, recurrent lower airway infection, and therapy-resistant, irreversible, and/or atypical asthma [158] are generally indicated to be evaluated for this pathology. The excessive (50%) collapsibility of trachea and bronchi is the characteristic feature of TBM and it is detected through dedicated expiratory-phase CT imaging [160], and multiplanar and 3D reconstructions [157, 161–168].

There are two main CT techniques to assess TBM: paired end-inspiratory and end-expiratory CT and paired end-inspiratory and dynamic expiratory CT; cine CT combined with a coughing maneuver is an alternative technique that may be helpful in this purpose [169]. The use of low-dose techniques is important for imaging infants and children who are very susceptible to the potentially harmful effects of ionizing radiation [169]. Intravenous contrast material is unnecessary for the routine assessment of TBM [166] even if it should be considered in certain settings, including known or suspected central airway neoplasms or mediastinal vascular anomalies [166, 170].

The presence of a mediastinal disease may also manifest as vocal cord paralysis (VCP) due to recurrent laryngeal nerve (RLN) dysfunction [171, 172]; the most common mediastinal causes of VCP include lung cancer, aortic dissection, metastatic disease, tuberculosis, esophageal cancer, and a variety of other conditions, including pulmonary embolism and amyloidosis [173]. Considering that RLN has a long course and extends inferiorly below the vocal cords, the cause of VCP may be overlooked using a CT protocol that does not include the extralaryngeal region, in particular the upper mediastinum [174]. Hence, if incidental findings of VCP are seen at neck CT, it is necessary to continue the scan to the upper mediastinum, including the aorticopulmonary window in the presence of left VCP [175], or complete the examination with a thorax scan later [176, 177].

#### 2.2.5.3 Others: CT in Chronic Obstructive Pulmonary Disease

Chronic obstructive pulmonary disease (COPD) is likely caused by the exposure to noxious inhaled particles and consists of an incompletely reversible expiratory airflow obstruction [178].

CT is the primary imaging modality in patients with suspected COPD, with an accuracy similar to histopathologic assessment, allowing a noninvasive qualitative and quantitative assessment of relative contribution and severity of the different pathologic changes [179]. The quantification of airway disease and emphysema at CT can allow clinically meaningful phenotyping of COPD [180].

Because variations in image acquisition parameters can affect both qualitative and even more quantitative assessment of COPD, it is required to adhere to a standard CT protocol for precise evaluation of the image data (0.5–1 mm reconstructions [181], non-contrast-enhanced end-inspiratory and end-expiratory volumetric acquisitions, standard reconstruction algorithm for computerized analysis with two separate sets of reconstructions for CT assessment [182]). The identification of the main causes of airflow limitation in patients with COPD is decisive for determining the appropriate therapeutic strategy [180, 183].

CT has also proved to be an accurate tool in the pre- and postoperative evaluation of emphysema patients treated with endobronchial valve placement (one-way valves that allow the air to flow out but not to flow in, resulting in collapse of the non-ventilated parenchyma [184, 185]) (Fig. 2.6). As a matter of fact, the semiautomated lung volume assessment with MDCT, by means of dedicated software, enables the radiologist to calculate the volume of a single lobe or lung region and to determine the real morphologic and functional improvement with good correlation with spirometric data [186] (Fig. 2.7).

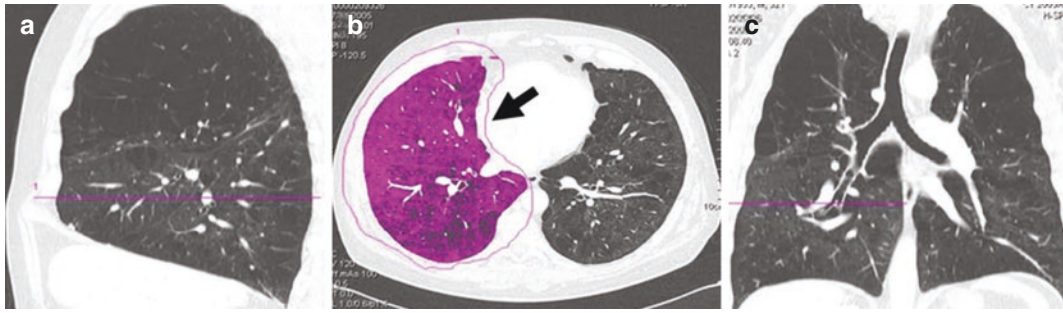


**Fig. 2.6** (**a**) Sagittal, (**b**) axial, and (**c**) coronal CT pretreatment post-processing images for the semiautomated evaluation of right upper lobe volume by manual tracing (*arrow* in **b**) of the lobe profile. From the Departments of Radiological Sciences and Medical Oncology, University of Rome "La Sapienza," Rome

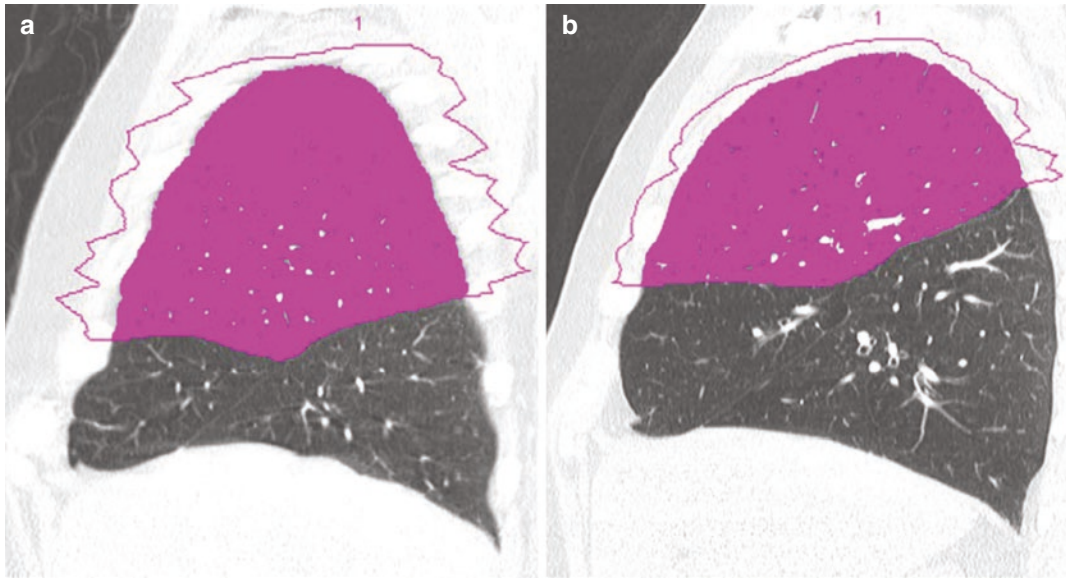


**Fig. 2.7** Sagittal post-processing images with semiautomated evaluation of upper pulmonary lobe. The comparison between preoperative (**a**) and postoperative (**b**) images shows volume reduction (respectively, 1801 $cm^3$ vs. 1207 $cm^3$). From the Departments of Radiological Sciences and Medical Oncology, University of Rome "La Sapienza," Rome

#### 2.2.5.4 Others: CT in Radiation Therapy Planning

Radiation therapy is one of the three most important aspects of cancer treatment with surgery and chemotherapy. The primary goal of treatment planning is to precisely calculate the radiation dose to the tumor in order to improve the outcome and reduce toxicity [187].

CT is the only three-dimensional imaging modality used for dose calculation due to its geometric fidelity and short acquisition time; moreover, CT allows the identification of the mass attenuation coefficient ($\mu/\rho$ ($m^2$/Kg)) or attenuation characteristics for high-energy photons, X-rays, and gamma-rays that are all critical factors for precise dose calculation [187]. Newly developed algorithms calculate the radiation absorption and scatter of different tissue densities and apply that to the dose calculation, although this is only possible because the tissue density is obtained using a table that relates the Hounsfield number to density [187].

Four-dimensional CT (4DCT) is another development used to quantify respiratory and

organ motion and it is normally applied in thoracic and abdominal sites in which respiratory motion can cause incorrect information regarding the size and position of a tumor and critical organs [188].

#### 2.2.5.5 Others: CT in Intensive Care Unit

The intensive care unit (ICU) is a difficult environment to perform a physical examination and to interpret a portable ICU radiograph; this is due to the patients' condition, the limitations of applying optimal radiographic technique, as well as the presence of monitoring and other devices that might hide portions of the chest [189].

CT is particularly useful when radiographic findings are equivocal or in discordance with the clinical scenario; CT provides high sensitivity for evaluating lung pathology, including recognition and characterization of pulmonary, pleural, and mediastinal abnormalities [190, 191]. The major categories in which chest CT has proven to be useful are pleural diseases, pulmonary disease, complications of life support devices and mechanical ventilation, and pulmonary embolism [192, 193].

Critically ill patients with trauma and surgical patients are deeply different from medical patients, especially because they require therapeutic interventions and raise diagnostic challenges that are easier to manage with chest CT evaluation, such as evaluation for infection, dislodged pleural cavity tubes, and/or post-op complications [191]. The accurate identification of these processes is fundamental because postoperative bleeding in patients with trauma is associated with high morbidity and mortality and because an untreated traumatic hemothorax may lead to empyema [194–196].

In medically critically ill patients it is possible to significantly limit the use of chest CTs, avoiding useless risks deriving from the intrahospital transport and from the intravenous contrast media use. Chest CTs have proven to be primarily useful in assisting with chest tube management and evaluating for PE (only 23.9% of a cohort of medically critically ill patients who underwent a chest CT scan received changes in management which could be clearly linked to the CT findings); this issues necessitate a CT scan, as bedside diagnostic modalities are not as helpful [197].

#### 2.2.5.6 Others: CT in Blunt Thoracic Trauma

Thorax injuries are the third most common injuries in trauma patients with an overall fatality rate of 10.1%, which is higher in patients with cardiac or tracheobronchial-esophageal injuries [198]. In the initial imaging investigation conventional radiology is generally used even when CT is subsequently performed [198]; as a matter of fact CT may depict significant diseases in patients with normal initial radiographs [199] and it has been credited with changing management in up to 20% of chest trauma patients with abnormal initial radiographs [200].

CT is more accurate than radiography for the evaluation of the several lesions that may occur in blunt thoracic trauma. These abnormalities include injuries of the pleural space (pneumothorax, hemothorax) [201, 202], lungs (pulmonary contusion (Fig. 2.8), pulmonary laceration, traumatic lung herniation) [203], airways (bronchial lacerations, tracheal lacerations, Macklin effect) [204–206], esophagus, heart (pericardial injuries, injuries to the heart valves and chambers), aorta and great vessels (thoracic aortic injury, injury to the internal mammary artery, injuries to the aortic arch branches), diaphragm [207, 208], and chest wall (rib fracture, flail chest, fractures of the scapula, sternal fractures, sternoclavicular dislocations) [198]. CT is also useful in the diagnosis of fractures of the thoracic spine, especially at the cervicothoracic junction, which are misevaluated with conventional radiography and it also aids in ruling out thoracic aortic injury, thereby limiting the number of catheter aortographic examinations [209].

#### 2.2.5.7 Others: CT in Fibrosing Mediastinitis

Fibrosing mediastinitis is a rare benign disorder characterized by the proliferation of dense fibrous tissue within the mediastinum [210]. The most common signs or symptoms are related to obstruction or compression of vital mediastinal structures such as the central airways, superior

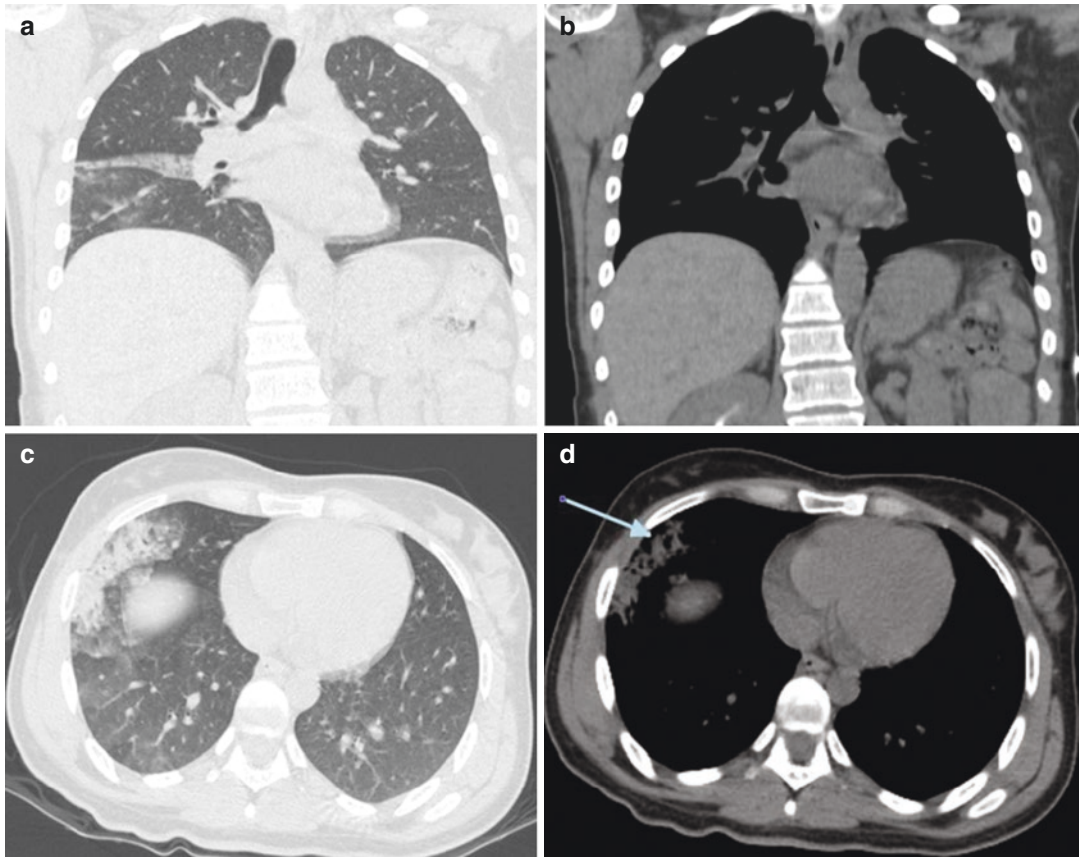


**Fig. 2.8** Pulmonary contusion after a car accident in a 30-year-old patient. Middle-lobe ground-glass opacity (panel **a** and panel **c**) with subpleural sparing (panel **b** and *blue arrow* in **d**). From the Department of Radiology, Università degli studi di Cagliari

vena cava (it is most common benign cause of the superior vena cava syndrome), pulmonary veins, pulmonary arteries, and esophagus [210–213].

CT is the imaging technique of choice in the diagnostic evaluation of patients with known or suspected fibrosing mediastinitis, especially because chest radiographic features are nonspecific and because MRI does not accurately depict calcifications [214].

Contrast material injection is useful when superior vena cava obstruction is suspected as it helps depicting the extent, level, and length of stenosis and also nicely shows collateral vessels within the mediastinum and chest wall. Contrast-enhanced CT may also determine the presence of encasement or obstruction of pulmonary arteries and veins. Two or 3D reconstruction techniques facilitate either surgical planning or local therapy [214]. CT also allows the assessment of the site, length, and severity of airway stenosis, particularly through thin collimation and 2D or 3D reconstruction techniques [215–219]; such techniques are also useful in the dilation planning and stent placement procedures.

#### 2.2.5.8 Others: CT in Thoracic Outlet Syndrome

The thoracic outlet includes three confined anatomic spaces: the interscalene triangle, the costoclavicular space, and the retropectoralis minor space [220, 221]. Thoracic outlet syndrome (TOS) consists of a dynamically induced com-

pression of the neural, arterial, or venous structures crossing one of these tunnels, leading to three distinct syndromes that depend on the injured component of the neurovascular bundle: neurogenic syndrome, arterial syndrome, and venous syndrome [222].

The clinical evaluation is the mainstay of the diagnosis, particularly if patient's symptoms can be reproduced when various dynamic maneuvers, including elevation of the arm, are undertaken. Mechanical compression or direct irritation of the neurovascular structures may be caused by anatomic abnormalities or acquired disease of the skeletal and soft-tissue structures forming or bordering on the three compartments [222].

In case of suspected TOS, a CT scan is performed first with the arms alongside the body and then with the arms elevated. Contrast media must be injected into a vein on the side opposite of that being examined in order to obtain CT angiographs (start scan 15–20 s after the start of a monophasic injection of 90 mL of iodinated contrast medium at a rate of 4 mL/s) opacifying the subclavian and axillary arteries only, without producing any venous artifacts [219, 223]. Arterial cross sections produced by sagittal reformations of data obtained both in the neutral position and after postural maneuvers allow an accurate assessment of arterial compression; volume-rendered images of the thoracic outlet before and after postural maneuvers allow simultaneous analysis of bones and vascular bundles [224]. Venous compression is very difficult to incriminate because such compression is frequently observed in asymptomatic individuals in all the compartments of the thoracic outlet after arm elevation. TC may also demonstrate venous thrombosis and collateral circulation that constitutes objective signs of venous TOS [223, 225].

CT limitations include the difficulty of carrying out a fine analysis of the brachial plexus (which can be analyzed by MRI) due to the limited contrast resolution, limited abduction of the shoulder by the size of the CT tunnel itself, and need to carry out the study in the supine position (32% of false-negative results reported were related to use of the supine position during the examination) [225].

## 2.3 Future Perspectives

CT represents a noninvasive, reliable tool in the diagnosis and follow-up of many thoracic pathologies. With the development of new techniques, such as the perfusion studies, and new radiologic fields, such as the radiogenomic, CT is changing its characteristics from a mere morphological investigation to a functional and molecular one.

These evolutions may allow radiologists to early assess in a noninvasive way the nature of a pulmonary lesion, to forecast the effectiveness of a therapy, or to give clinicians useful insights about the genetic alterations that are present in a certain tumor; this information is of paramount importance to choose a tailored treatment that can specifically interact with these involved molecular anomalies.

The development of machine learning and artificial intelligence, applied to the medical imaging, is also a promising field, particularly in the radiogenomic studies; in fact, machine learning and artificial intelligence potentially allow the discovery of new imaging features connected to genetic alterations that human eye and brain are not able to detect. Moreover, these new computer technologies may also be applied in the decision-making algorithm in order to state the optimal treatment for each pathology and specifically for each patient.

## References

1. Han BK, Rigsby CK, Leipsic J, Bardo D, Abbara S, Ghoshhajra B, et al. Computed tomography imaging in patients with congenital heart disease, Part 2: Technical recommendations. An expert consensus document of the society of cardiovascular computed tomography (SCCT): endorsed by the society of pediatric radiology (SPR) and the North American Society of Cardiac Imaging (NASCI). J Cardiovasc Comput Tomogr. 2015;9(6):493–513. https://doi.org/10.1016/j.jcct.2015.07.007.

2. Han BK, Lindberg J, Grant K, Schwartz RS, Lesser JR. Accuracy and safety of high pitch computed tomography imaging in young children with complex congenital heart disease. Am J Cardiol. 2011;107(10):1541–6. https://doi.org/10.1016/j.amjcard.2011.01.065.
3. Lell MM, May M, Deak P, Alibek S, Kuefner M, Kuettner A, et al. High-pitch spiral computed tomography: effect on image quality and radiation dose in pediatric chest computed tomography. Investig Radiol. 2011;46(2):116–23. https://doi.org/10.1097/RLI.0b013e3181f33b1d.
4. Little BP. Approach to chest computed tomography. Clin Chest Med. 2015;36(2):127–45, vii. https://doi.org/10.1016/j.ccm.2015.02.001.
5. Panebianco V, Grazhdani H, Iafrate F, Petroni M, Anzidei M, Laghi A, et al. 3D CT protocol in the assessment of the esophageal neoplastic lesions: can it improve TNM staging? Eur Radiol. 2006;16(2):414–21. https://doi.org/10.1007/s00330-005-2851-5.
6. Johnson TR, Krauss B, Sedlmair M, Grasruck M, Bruder H, Morhard D, et al. Material differentiation by dual energy CT: initial experience. Eur Radiol. 2007;17(6):1510–7. https://doi.org/10.1007/s00330-006-0517-6.
7. Hartman R, Kawashima A, Takahashi N, Silva A, Vrtiska T, Leng S, et al. Applications of dual-energy CT in urologic imaging: an update. Radiol Clin N Am. 2012;50(2):191–205. https://doi.org/10.1016/j.rcl.2012.02.007.
8. Kaza RK, Platt JF, Megibow AJ. Dual-energy CT of the urinary tract. Abdom Imaging. 2013;38(1):167–79. https://doi.org/10.1007/s00261-012-9901-7.
9. Remy-Jardin M, Faivre JB, Pontana F, Molinari F, Tacelli N, Remy J. Thoracic applications of dual energy. Semin Respir Crit Care Med. 2014;35(1):64–73. https://doi.org/10.1055/s-0033-1363452.
10. Castellino RA. Computer aided detection (CAD): an overview. Cancer Imaging. 2005;5:17–9. https://doi.org/10.1102/1470-7330.2005.0018.
11. Fraioli F, Bertoletti L, Napoli A, Pediconi F, Calabrese FA, Masciangelo R, et al. Computer-aided detection (CAD) in lung cancer screening at chest MDCT: ROC analysis of CAD versus radiologist performance. J Thorac Imaging. 2007;22(3):241–6. https://doi.org/10.1097/RTI.0b013e318033aae8.
12. Versteylen MO, Kietselaer BL, Dagnelie PC, Joosen IA, Dedic A, Raaijmakers RH, et al. Additive value of semiautomated quantification of coronary artery disease using cardiac computed tomographic angiography to predict future acute coronary syndrome. J Am Coll Cardiol. 2013;61(22):2296–305. https://doi.org/10.1016/j.jacc.2013.02.065.
13. Bashir U, Siddique MM, McLean E, Goh V, Cook GJ. Imaging heterogeneity in lung cancer: techniques, applications, and challenges. AJR Am J Roentgenol. 2016;207(3):534–43. https://doi.org/10.2214/AJR.15.15864.
14. Hong SJ, Kim TJ, Choi YW, Park JS, Chung JH, Lee KW. Radiogenomic correlation in lung adenocarcinoma with epidermal growth factor receptor mutations: imaging features and histological subtypes. Eur Radiol. 2016;26(10):3660–8. https://doi.org/10.1007/s00330-015-4196-z.
15. Fraioli F, Anzidei M, Zaccagna F, Mennini ML, Serra G, Gori B, et al. Whole-tumor perfusion CT in patients with advanced lung adenocarcinoma treated with conventional and antiangiogenetic chemotherapy: initial experience. Radiology. 2011;259(2):574–82. https://doi.org/10.1148/radiol.11100600.
16. Yuan X, Zhang J, Quan C, Cao J, Ao G, Tian Y, et al. Differentiation of malignant and benign pulmonary nodules with first-pass dual-input perfusion CT. Eur Radiol. 2013;23(9):2469–74. https://doi.org/10.1007/s00330-013-2842-x.
17. Doria-Rose VP, White MC, Klabunde CN, Nadel MR, Richards TB, McNeel TS, et al. Use of lung cancer screening tests in the United States: results from the 2010 National Health Interview Survey. Cancer Epidemiol Biomark Prev. 2012;21(7):1049–59. https://doi.org/10.1158/1055-9965.EPI-12-0343.
18. Huber A, Landau J, Ebner L, Butikofer Y, Leidolt L, Brela B, et al. Performance of ultralow-dose CT with iterative reconstruction in lung cancer screening: limiting radiation exposure to the equivalent of conventional chest X-ray imaging. Eur Radiol. 2016;26(10):3643–52. https://doi.org/10.1007/s00330-015-4192-3.
19. National Lung Screening Trial Research T, Aberle DR, Adams AM, Berg CD, Black WC, Clapp JD, et al. Reduced lung-cancer mortality with low-dose computed tomographic screening. N Engl J Med. 2011;365(5):395–409. https://doi.org/10.1056/NEJMoa1102873.
20. Brenner DJ. Radiation risks potentially associated with low-dose CT screening of adult smokers for lung cancer. Radiology. 2004;231(2):440–5. https://doi.org/10.1148/radiol.2312030880.
21. Imhof H, Schibany N, Ba-Ssalamah A, Czerny C, Hojreh A, Kainberger F, et al. Spiral CT and radiation dose. Eur J Radiol. 2003;47(1):29–37.
22. Kalra MK, Maher MM, Toth TL, Hamberg LM, Blake MA, Shepard JA, et al. Strategies for CT radiation dose optimization. Radiology. 2004;230(3):619–28. https://doi.org/10.1148/radiol.2303021726.
23. Mayo JR, Aldrich J, Muller NL, Fleischner S. Radiation exposure at chest CT: a statement of the Fleischner Society. Radiology. 2003;228(1):15–21. https://doi.org/10.1148/radiol.2281020874.
24. MacMahon H, Austin JH, Gamsu G, Herold CJ, Jett JR, Naidich DP, et al. Guidelines for management of small pulmonary nodules detected on CT scans: a statement from the Fleischner Society. Radiology. 2005;237(2):395–400. https://doi.org/10.1148/radiol.2372041887.
25. Naidich DP, Bankier AA, MacMahon H, Schaefer-Prokop CM, Pistolesi M, Goo JM, et al. Recommendations for the management of subsolid pulmonary nodules detected at CT: a statement from the Fleischner Society. Radiology. 2013;266(1):304–17. https://doi.org/10.1148/radiol.12120628.
26. Siegel R, Naishadham D, Jemal A. Cancer statistics, 2012. CA Cancer J Clin. 2012;62(1):10–29. https://doi.org/10.3322/caac.20138.

27. Chae EJ, Song JW, Krauss B, Song KS, Lee CW, Lee HJ, et al. Dual-energy computed tomography characterization of solitary pulmonary nodules. J Thorac Imaging. 2010;25(4):301–10. https://doi.org/10.1097/RTI.0b013e3181e16232.
28. Silvestri GA, Gonzalez AV, Jantz MA, Margolis ML, Gould MK, Tanoue LT, et al. Methods for staging non-small cell lung cancer: diagnosis and management of lung cancer, 3rd ed: American College of Chest Physicians evidence-based clinical practice guidelines. Chest. 2013;143(5 Suppl):e211S–e50S. https://doi.org/10.1378/chest.12-2355.
29. Nair A, Klusmann MJ, Jogeesvaran KH, Grubnic S, Green SJ, Vlahos I. Revisions to the TNM staging of non-small cell lung cancer: rationale, clinicoradiologic implications, and persistent limitations. Radiographics. 2011;31(1):215–38. https://doi.org/10.1148/rg.311105039.
30. Glazer HS, Kaiser LR, Anderson DJ, Molina PL, Emami B, Roper CL, et al. Indeterminate mediastinal invasion in bronchogenic carcinoma: CT evaluation. Radiology. 1989;173(1):37–42. https://doi.org/10.1148/radiology.173.1.2781028.
31. Detterbeck FC, Figueroa AS. Lung cancer staging: the value of PET depends on the clinical setting. J Thorac Dis. 2014;6(12):1714–23. https://doi.org/10.3978/j.issn.2072-1439.2014.11.16.
32. Campo E, Swerdlow SH, Harris NL, Pileri S, Stein H, Jaffe ES. The 2008 WHO classification of lymphoid neoplasms and beyond: evolving concepts and practical applications. Blood. 2011;117(19):5019–32. https://doi.org/10.1182/blood-2011-01-293050.
33. Johnson SA, Kumar A, Matasar MJ, Schoder H, Rademaker J. Imaging for staging and response assessment in lymphoma. Radiology. 2015;276(2):323–38. https://doi.org/10.1148/radiol.2015142088.
34. Pinilla I, Gomez-Leon N, Del Campo-Del Val L, Hernandez-Maraver D, Rodriguez-Vigil B, Jover-Diaz R, et al. Diagnostic value of CT, PET and combined PET/CT performed with low-dose unenhanced CT and full-dose enhanced CT in the initial staging of lymphoma. Q J Nucl Med Mol Imaging. 2011;55(5):567–75.
35. Cheson BD, Fisher RI, Barrington SF, Cavalli F, Schwartz LH, Zucca E, et al. Recommendations for initial evaluation, staging, and response assessment of Hodgkin and non-Hodgkin lymphoma: the Lugano classification. J Clin Oncol. 2014;32(27):3059–68. https://doi.org/10.1200/JCO.2013.54.8800.
36. Hartridge-Lambert SK, Schoder H, Lim RC, Maragulia JC, Portlock CS. ABVD alone and a PET scan complete remission negates the need for radiologic surveillance in early-stage, nonbulky Hodgkin lymphoma. Cancer. 2013;119(6):1203–9. https://doi.org/10.1002/cncr.27873.
37. Kim TJ, Kim HY, Lee KW, Kim MS. Multimodality assessment of esophageal cancer: preoperative staging and monitoring of response to therapy. Radiographics. 2009;29(2):403–21. https://doi.org/10.1148/rg.292085106.
38. Rice TW. Clinical staging of esophageal carcinoma. CT, EUS, and PET. Chest Surg Clin N Am. 2000;10(3):471–85.
39. Quint LE, Hepburn LM, Francis IR, Whyte RI, Orringer MB. Incidence and distribution of distant metastases from newly diagnosed esophageal carcinoma. Cancer. 1995;76(7):1120–5.
40. Morgenthaler TI, Brown LR, Colby TV, Harper CM Jr, Coles DT. Thymoma. Mayo Clin Proc. 1993;68(11):1110–23.
41. Regnard JF, Magdeleinat P, Dromer C, Dulmet E, de Montpreville V, Levi JF, et al. Prognostic factors and long-term results after thymoma resection: a series of 307 patients. J Thorac Cardiovasc Surg. 1996;112(2):376–84. https://doi.org/10.1016/S0022-5223(96)70265-9.
42. Lewis JE, Wick MR, Scheithauer BW, Bernatz PE, Taylor WF. Thymoma. A clinicopathologic review. Cancer. 1987;60(11):2727–43.
43. Osserman KE, Genkins G. Studies in myasthenia gravis: review of a twenty-year experience in over 1200 patients. Mt Sinai J Med. 1971;38(6):497–537.
44. Rosado-de-Christenson ML, Strollo DC, Marom EM. Imaging of thymic epithelial neoplasms. Hematol Oncol Clin North Am. 2008;22(3):409–31. https://doi.org/10.1016/j.hoc.2008.03.011.
45. Huang J, Detterbeck FC, Wang Z, Loehrer PJ Sr. Standard outcome measures for thymic malignancies. J Thorac Oncol. 2010;5(12):2017–23. https://doi.org/10.1097/JTO.0b013e3181f13682.
46. Incarbone M, Pastorino U. Surgical treatment of chest wall tumors. World J Surg. 2001;25(2):218–30.
47. David EA, Marshall MB. Review of chest wall tumors: a diagnostic, therapeutic, and reconstructive challenge. Semin Plast Surg. 2011;25(1):16–24. https://doi.org/10.1055/s-0031-1275167.
48. Athanassiadi K, Kalavrouziotis G, Rondogianni D, Loutsidis A, Hatzimichalis A, Bellenis I. Primary chest wall tumors: early and long-term results of surgical treatment. Eur J Cardiothorac Surg. 2001;19(5):589–93.
49. Jeung MY, Gangi A, Gasser B, Vasilescu C, Massard G, Wihlm JM, et al. Imaging of chest wall disorders. Radiographics. 1999;19(3):617–37. https://doi.org/10.1148/radiographics.19.3.g99ma02617.
50. Tateishi U, Gladish GW, Kusumoto M, Hasegawa T, Yokoyama R, Tsuchiya R, et al. Chest wall tumors: radiologic findings and pathologic correlation: part 1. Benign tumors. Radiographics. 2003;23(6):1477–90. https://doi.org/10.1148/rg.236015526.
51. O'Sullivan P, O'Dwyer H, Flint J, Munk PL, Muller NL. Malignant chest wall neoplasms of bone and cartilage: a pictorial review of CT and MR findings. Br J Radiol. 2007;80(956):678–84. https://doi.org/10.1259/bjr/82228585.
52. Afilalo J, Therrien J, Pilote L, Ionescu-Ittu R, Martucci G, Marelli AJ. Geriatric congenital heart disease: burden of disease and predictors of mor-

tality. J Am Coll Cardiol. 2011;58(14):1509–15. https://doi.org/10.1016/j.jacc.2011.06.041.
53. Khairy P, Ionescu-Ittu R, Mackie AS, Abrahamowicz M, Pilote L, Marelli AJ. Changing mortality in congenital heart disease. J Am Coll Cardiol. 2010;56(14):1149–57. https://doi.org/10.1016/j.jacc.2010.03.085.
54. Marelli AJ, Ionescu-Ittu R, Mackie AS, Guo L, Dendukuri N, Kaouache M. Lifetime prevalence of congenital heart disease in the general population from 2000 to 2010. Circulation. 2014;130(9):749–56. https://doi.org/10.1161/CIRCULATIONAHA.113.008396.
55. Marelli AJ, Mackie AS, Ionescu-Ittu R, Rahme E, Pilote L. Congenital heart disease in the general population: changing prevalence and age distribution. Circulation. 2007;115(2):163–72. https://doi.org/10.1161/CIRCULATIONAHA.106.627224.
56. Stulak JM, Dearani JA, Burkhart HM, Ammash NM, Phillips SD, Schaff HV. Coronary artery disease in adult congenital heart disease: outcome after coronary artery bypass grafting. Ann Thorac Surg. 2012;93(1):116–22; discussion 22–3. https://doi.org/10.1016/j.athoracsur.2011.09.013.
57. Warnes CA, Williams RG, Bashore TM, Child JS, Connolly HM, Dearani JA, et al. ACC/AHA 2008 guidelines for the management of adults with congenital heart disease: a report of the American College of Cardiology/American Heart Association task force on practice guidelines (writing committee to develop guidelines on the Management of Adults with Congenital Heart Disease). Developed in collaboration with the American Society of Echocardiography, Heart Rhythm Society, International Society for Adult Congenital Heart Disease, Society for Cardiovascular Angiography and Interventions, and Society of Thoracic Surgeons. J Am Coll Cardiol. 2008;52(23):e143–263. https://doi.org/10.1016/j.jacc.2008.10.001.
58. Tutarel O, Kempny A, Alonso-Gonzalez R, Jabbour R, Li W, Uebing A, et al. Congenital heart disease beyond the age of 60: emergence of a new population with high resource utilization, high morbidity, and high mortality. Eur Heart J. 2014;35(11):725–32. https://doi.org/10.1093/eurheartj/eht257.
59. van der Bom T, Zomer AC, Zwinderman AH, Meijboom FJ, Bouma BJ, Mulder BJ. The changing epidemiology of congenital heart disease. Nat Rev Cardiol. 2011;8(1):50–60. https://doi.org/10.1038/nrcardio.2010.166.
60. Warnes CA. The adult with congenital heart disease: born to be bad? J Am Coll Cardiol. 2005;46(1):1–8. https://doi.org/10.1016/j.jacc.2005.02.083.
61. Holst KA, Dearani JA, Burkhart HM, Connolly HM, Warnes CA, Li Z, et al. Risk factors and early outcomes of multiple reoperations in adults with congenital heart disease. Ann Thorac Surg. 2011;92(1):122–8; discussion 9–30. https://doi.org/10.1016/j.athoracsur.2011.03.102.
62. Mackie AS, Pilote L, Ionescu-Ittu R, Rahme E, Marelli AJ. Health care resource utilization in adults with congenital heart disease. Am J Cardiol. 2007;99(6):839–43. https://doi.org/10.1016/j.amjcard.2006.10.054.
63. Gherardi GG, Iball GR, Darby MJ, Thomson JD. Cardiac computed tomography and conventional angiography in the diagnosis of congenital cardiac disease in children: recent trends and radiation doses. Cardiol Young. 2011;21(6):616–22. https://doi.org/10.1017/S1047951111000485.
64. Han BK, Lesser AM, Vezmar M, Rosenthal K, Rutten-Ramos S, Lindberg J, et al. Cardiovascular imaging trends in congenital heart disease: a single center experience. J Cardiovasc Comput Tomogr. 2013;7(6):361–6. https://doi.org/10.1016/j.jcct.2013.11.002.
65. Watson TG, Mah E, Joseph Schoepf U, King L, Huda W, Hlavacek AM. Effective radiation dose in computed tomographic angiography of the chest and diagnostic cardiac catheterization in pediatric patients. Pediatr Cardiol. 2013;34(3):518–24. https://doi.org/10.1007/s00246-012-0486-2.
66. Greenberg SB. Rebalancing the risks of computed tomography and magnetic resonance imaging. Pediatr Radiol. 2011;41(8):951–2. https://doi.org/10.1007/s00247-011-2159-3.
67. Carson JL, Kelley MA, Duff A, Weg JG, Fulkerson WJ, Palevsky HI, et al. The clinical course of pulmonary embolism. N Engl J Med. 1992;326(19):1240–5. https://doi.org/10.1056/NEJM199205073261902.
68. Horlander KT, Mannino DM, Leeper KV. Pulmonary embolism mortality in the United States, 1979-1998: an analysis using multiple-cause mortality data. Arch Intern Med. 2003;163(14):1711–7. https://doi.org/10.1001/archinte.163.14.1711.
69. Bettmann MA, Baginski SG, White RD, Woodard PK, Abbara S, Atalay MK, et al. ACR appropriateness criteria(R) acute chest pain—suspected pulmonary embolism. J Thorac Imaging. 2012;27(2):W28–31. https://doi.org/10.1097/RTI.0b013e31823efeb6.
70. Remy-Jardin M, Pistolesi M, Goodman LR, Gefter WB, Gottschalk A, Mayo JR, et al. Management of suspected acute pulmonary embolism in the era of CT angiography: a statement from the Fleischner society. Radiology. 2007;245(2):315–29. https://doi.org/10.1148/radiol.2452070397.
71. Quiroz R, Kucher N, Zou KH, Kipfmueller F, Costello P, Goldhaber SZ, et al. Clinical validity of a negative computed tomography scan in patients with suspected pulmonary embolism: a systematic review. JAMA. 2005;293(16):2012–7. https://doi.org/10.1001/jama.293.16.2012.
72. Perrier A, Nendaz MR, Sarasin FP, Howarth N, Bounameaux H. Cost-effectiveness analysis of diagnostic strategies for suspected pulmonary embolism including helical computed tomography. Am J Respir Crit Care Med. 2003;167(1):39–44. https://doi.org/10.1164/rccm.2106128.

73. Schwickert HC, Schweden F, Schild HH, Piepenburg R, Duber C, Kauczor HU, et al. Pulmonary arteries and lung parenchyma in chronic pulmonary embolism: preoperative and postoperative CT findings. Radiology. 1994;191(2):351–7. https://doi.org/10.1148/radiology.191.2.8153305.
74. Lang IM. Chronic thromboembolic pulmonary hypertension—not so rare after all. N Engl J Med. 2004;350(22):2236–8. https://doi.org/10.1056/NEJMp048088.
75. Auger WR, Fedullo PF, Moser KM, Buchbinder M, Peterson KL. Chronic major-vessel thromboembolic pulmonary artery obstruction: appearance at angiography. Radiology. 1992;182(2):393–8. https://doi.org/10.1148/radiology.182.2.1732955.
76. Tardivon AA, Musset D, Maitre S, Brenot F, Dartevelle P, Simonneau G, et al. Role of CT in chronic pulmonary embolism: comparison with pulmonary angiography. J Comput Assist Tomogr. 1993;17(3):345–51.
77. Bergin CJSC, Hauschildt JP, Huynh TV, Auger WR, Fedullo PF, Kapelanski DP. Chronic thromboembolism: diagnosis with helical CT and MR imaging with angiographic and surgical correlation. Radiology. 1997;204(3):695–702. https://doi.org/10.1148/radiology.204.3.9280245.
78. Ley S, Kauczor HU, Heussel CP, Kramm T, Mayer E, Thelen M, et al. Value of contrast-enhanced MR angiography and helical CT angiography in chronic thromboembolic pulmonary hypertension. Eur Radiol. 2003;13(10):2365–71. https://doi.org/10.1007/s00330-003-1878-8.
79. Bergin CJ, Sirlin C, Deutsch R, Fedullo P, Hauschildt J, Huynh T, et al. Predictors of patient response to pulmonary thromboendarterectomy. AJR Am J Roentgenol. 2000;174(2):509–15. https://doi.org/10.2214/ajr.174.2.1740509.
80. Heinrich M, Uder M, Tscholl D, Grgic A, Kramann B, Schafers HJ. CT scan findings in chronic thromboembolic pulmonary hypertension: predictors of hemodynamic improvement after pulmonary thromboendarterectomy. Chest. 2005;127(5):1606–13. https://doi.org/10.1378/chest.127.5.1606.
81. Oikonomou A, Dennie CJ, Muller NL, Seely JM, Matzinger FR, Rubens FD. Chronic thromboembolic pulmonary arterial hypertension: correlation of postoperative results of thromboendarterectomy with preoperative helical contrast-enhanced computed tomography. J Thorac Imaging. 2004;19(2):67–73.
82. Apfaltrer P, Sudarski S, Schneider D, Nance JW Jr, Haubenreisser H, Fink C, et al. Value of monoenergetic low-kV dual energy CT datasets for improved image quality of CT pulmonary angiography. Eur J Radiol. 2014;83(2):322–8. https://doi.org/10.1016/j.ejrad.2013.11.005.
83. Delesalle MA, Pontana F, Duhamel A, Faivre JB, Flohr T, Tacelli N, et al. Spectral optimization of chest CT angiography with reduced iodine load: experience in 80 patients evaluated with dual-source, dual-energy CT. Radiology. 2013;267(1):256–66. https://doi.org/10.1148/radiol.12120195.
84. Ameli-Renani S, Rahman F, Nair A, Ramsay L, Bacon JL, Weller A, et al. Dual-energy CT for imaging of pulmonary hypertension: challenges and opportunities. Radiographics. 2014;34(7):1769–90. https://doi.org/10.1148/rg.347130085.
85. Dournes G, Verdier D, Montaudon M, Bullier E, Riviere A, Dromer C, et al. Dual-energy CT perfusion and angiography in chronic thromboembolic pulmonary hypertension: diagnostic accuracy and concordance with radionuclide scintigraphy. Eur Radiol. 2014;24(1):42–51. https://doi.org/10.1007/s00330-013-2975-y.
86. Ameli-Renani S, Ramsay L, Bacon JL, Rahman F, Nair A, Smith V, et al. Dual-energy computed tomography in the assessment of vascular and parenchymal enhancement in suspected pulmonary hypertension. J Thorac Imaging. 2014;29(2):98–106. https://doi.org/10.1097/RTI.0000000000000061.
87. Litmanovich D, Bankier AA, Cantin L, Raptopoulos V, Boiselle PM. CT and MRI in diseases of the aorta. AJR Am J Roentgenol. 2009;193(4):928–40. https://doi.org/10.2214/AJR.08.2166.
88. Agarwal PP, Chughtai A, Matzinger FR, Kazerooni EA. Multidetector CT of thoracic aortic aneurysms. Radiographics. 2009;29(2):537–52. https://doi.org/10.1148/rg.292075080.
89. Litmanovich D, Zamboni GA, Hauser TH, Lin PJ, Clouse ME, Raptopoulos V. ECG-gated chest CT angiography with 64-MDCT and triphasic IV contrast administration regimen in patients with acute non-specific chest pain. Eur Radiol. 2008;18(2):308–17. https://doi.org/10.1007/s00330-007-0739-2.
90. Yoshioka K, Niinuma H, Ehara S, Nakajima T, Nakamura M, Kawazoe K. MR angiography and CT angiography of the artery of Adamkiewicz: state of the art. Radiographics. 2006;26(Suppl 1):S63–73. https://doi.org/10.1148/rg.26si065506.
91. Abbara S, Kalva S, Cury RC, Isselbacher EM. Thoracic aortic disease: spectrum of multidetector computed tomography imaging findings. J Cardiovasc Comput Tomogr. 2007;1(1):40–54. https://doi.org/10.1016/j.jcct.2007.04.003.
92. Morales JP, Greenberg RK, Lu Q, Cury M, Hernandez AV, Mohabbat W, Moon MC, Morales CA, Bathurst S, Schoenhagen P. Endoleaks following endovascular repair of thoracic aortic aneurysm: etiology and outcomes. J Endovasc Ther. 2008;15(6):631–8. https://doi:10.1583/08-2551.1. PubMed PMID: 19090634.
93. Jassal DS, Shapiro MD, Neilan TG, Chaithiraphan V, Ferencik M, Teague SD, et al. 64-slice multidetector computed tomography (MDCT) for detection of aortic regurgitation and quantification of severity. Investig Radiol. 2007;42(7):507–12. https://doi.org/10.1097/RLI.0b013e3180375556.
94. Laissy JP, Messika-Zeitoun D, Serfaty JM, Sebban V, Schouman-Claeys E, Iung B, et al. Comprehensive evaluation of preoperative patients with aortic valve stenosis: usefulness of cardiac multidetector

computed tomography. Heart. 2007;93(9):1121–5. https://doi.org/10.1136/hrt.2006.107284.
95. Batra P, Bigoni B, Manning J, Aberle DR, Brown K, Hart E, et al. Pitfalls in the diagnosis of thoracic aortic dissection at CT angiography. Radiographics. 2000;20(2):309–20. https://doi.org/10.1148/radiographics.20.2.g00mc04309.
96. Prescott-Focht JA, Martinez-Jimenez S, Hurwitz LM, Hoang JK, Christensen JD, Ghoshhajra BB, et al. Ascending thoracic aorta: postoperative imaging evaluation. Radiographics. 2013;33(1):73–85. https://doi.org/10.1148/rg.331125090.
97. Novelline RA, Rhea JT, Rao PM, Stuk JL. Helical CT in emergency radiology. Radiology. 1999;213(2):321–39. https://doi.org/10.1148/radiology.213.2.r99nv01321.
98. White CS, Kuo D, Kelemen M, Jain V, Musk A, Zaidi E, et al. Chest pain evaluation in the emergency department: can MDCT provide a comprehensive evaluation? AJR Am J Roentgenol. 2005;185(2):533–40. https://doi.org/10.2214/ajr.185.2.01850533.
99. Meinel FG, Nikolaou K, Weidenhagen R, Hellbach K, Helck A, Bamberg F, et al. Time-resolved CT angiography in aortic dissection. Eur J Radiol. 2012;81(11):3254–61. https://doi.org/10.1016/j.ejrad.2012.03.006.
100. Sommer T, Fehske W, Holzknecht N, Smekal AV, Keller E, Lutterbey G, et al. Aortic dissection: a comparative study of diagnosis with spiral CT, multiplanar transesophageal echocardiography, and MR imaging. Radiology. 1996;199(2):347–52. https://doi.org/10.1148/radiology.199.2.8668776.
101. Kaji S, Akasaka T, Horibata Y, Nishigami K, Shono H, Katayama M, et al. Long-term prognosis of patients with type a aortic intramural hematoma. Circulation. 2002;106(12 Suppl 1):I248–52.
102. Kaji S, Nishigami K, Akasaka T, Hozumi T, Takagi T, Kawamoto T, et al. Prediction of progression or regression of type a aortic intramural hematoma by computed tomography. Circulation. 1999;100(19 Suppl):II281–6.
103. Johnson TR, Nikolaou K, Wintersperger BJ, Knez A, Boekstegers P, Reiser MF, et al. ECG-gated 64-MDCT angiography in the differential diagnosis of acute chest pain. AJR Am J Roentgenol. 2007;188(1):76–82. https://doi.org/10.2214/AJR.05.1153.
104. Choi SH, Choi SJ, Kim JH, Bae SJ, Lee JS, Song KS, et al. Useful CT findings for predicting the progression of aortic intramural hematoma to overt aortic dissection. J Comput Assist Tomogr. 2001;25(2):295–9.
105. Cho KR, Stanson AW, Potter DD, Cherry KJ, Schaff HV, Sundt TM 3rd. Penetrating atherosclerotic ulcer of the descending thoracic aorta and arch. J Thorac Cardiovasc Surg. 2004;127(5):1393–9; discussion 9–401. https://doi.org/10.1016/j.jtcvs.2003.11.050.
106. O'Gara PT, DeSanctis RW. Acute aortic dissection and its variants. Toward a common diagnostic and therapeutic approach. Circulation. 1995;92(6):1376–8.
107. Sueyoshi E, Imada T, Sakamoto I, Matsuoka Y, Hayashi K. Analysis of predictive factors for progression of type B aortic intramural hematoma with computed tomography. J Vasc Surg. 2002;35(6):1179–83.
108. Tittle SL, Lynch RJ, Cole PE, Singh HS, Rizzo JA, Kopf GS, et al. Midterm follow-up of penetrating ulcer and intramural hematoma of the aorta. J Thorac Cardiovasc Surg. 2002;123(6):1051–9.
109. Hayashi H, Matsuoka Y, Sakamoto I, Sueyoshi E, Okimoto T, Hayashi K, et al. Penetrating atherosclerotic ulcer of the aorta: imaging features and disease concept. Radiographics. 2000;20(4):995–1005. https://doi.org/10.1148/radiographics.20.4.g00jl01995.
110. Godoy MC, Naidich DP, Marchiori E, Leidecker C, Schmidt B, Assadourian B, et al. Single-acquisition dual-energy multidetector computed tomography: analysis of vascular enhancement and postprocessing techniques for evaluating the thoracic aorta. J Comput Assist Tomogr. 2010;34(5):670–7. https://doi.org/10.1097/RCT.0b013e3181e10627.
111. Numburi UD, Schoenhagen P, Flamm SD, Greenberg RK, Primak AN, Saba OI, et al. Feasibility of dual-energy CT in the arterial phase: imaging after endovascular aortic repair. AJR Am J Roentgenol. 2010;195(2):486–93. https://doi.org/10.2214/AJR.09.3872.
112. Stolzmann P, Frauenfelder T, Pfammatter T, Peter N, Scheffel H, Lachat M, et al. Endoleaks after endovascular abdominal aortic aneurysm repair: detection with dual-energy dual-source CT. Radiology. 2008;249(2):682–91. https://doi.org/10.1148/radiol.2483080193.
113. Brown KK. Pulmonary vasculitis. Proc Am Thorac Soc. 2006;3(1):48–57. https://doi.org/10.1513/pats.200511-120JH.
114. Hansell DM. Small-vessel diseases of the lung: CT-pathologic correlates. Radiology. 2002;225(3):639–53. https://doi.org/10.1148/radiol.2253011490.
115. Chung MP, Yi CA, Lee HY, Han J, Lee KS. Imaging of pulmonary vasculitis. Radiology. 2010;255(2):322–41. https://doi.org/10.1148/radiol.10090105.
116. Schmidt WA. Imaging in vasculitis. Best Pract Res Clin Rheumatol. 2013;27(1):107–18. https://doi.org/10.1016/j.berh.2013.01.001.
117. Allen CM, Al-Jahdali HH, Irion KL, Al Ghanem S, Gouda A, Khan AN. Imaging lung manifestations of HIV/AIDS. Ann Thorac Med. 2010;5(4):201–16. https://doi.org/10.4103/1817-1737.69106.
118. Boiselle PM, Tocino I, Hooley RJ, Pumerantz AS, Selwyn PA, Neklesa VP, et al. Chest radiograph interpretation of pneumocystis carinii pneumonia, bacterial pneumonia, and pulmonary tuberculosis in HIV-positive patients: accuracy, dis-

tinguishing features, and mimics. J Thorac Imaging. 1997;12(1):47–53.
119. Hartman TE, Primack SL, Muller NL, Staples CA. Diagnosis of thoracic complications in AIDS: accuracy of CT. AJR Am J Roentgenol. 1994;162(3):547–53. https://doi.org/10.2214/ajr.162.3.8109494.
120. Kang EY, Staples CA, McGuinness G, Primack SL, Muller NL. Detection and differential diagnosis of pulmonary infections and tumors in patients with AIDS: value of chest radiography versus CT. AJR Am J Roentgenol. 1996;166(1):15–9. https://doi.org/10.2214/ajr.166.1.8571866.
121. Edinburgh KJ, Jasmer RM, Huang L, Reddy GP, Chung MH, Thompson A, et al. Multiple pulmonary nodules in AIDS: usefulness of CT in distinguishing among potential causes. Radiology. 2000;214(2):427–32. https://doi.org/10.1148/radiology.214.2.r00fe22427.
122. Tortoriello TA, Friedman JD, McKenzie ED, Fraser CD, Feltes TF, Randall J, et al. Mediastinitis after pediatric cardiac surgery: a 15-year experience at a single institution. Ann Thorac Surg. 2003;76(5):1655–60.
123. Braxton JH, Marrin CA, McGrath PD, Ross CS, Morton JR, Norotsky M, et al. Mediastinitis and long-term survival after coronary artery bypass graft surgery. Ann Thorac Surg. 2000;70(6):2004–7.
124. Akman C, Kantarci F, Cetinkaya S. Imaging in mediastinitis: a systematic review based on aetiology. Clin Radiol. 2004;59(7):573–85. https://doi.org/10.1016/j.crad.2003.12.001.
125. Abboud CS, Wey SB, Baltar VT. Risk factors for mediastinitis after cardiac surgery. Ann Thorac Surg. 2004;77(2):676–83. https://doi.org/10.1016/S0003-4975(03)01523-6.
126. Jolles H, Henry DA, Roberson JP, Cole TJ, Spratt JA. Mediastinitis following median sternotomy: CT findings. Radiology. 1996;201(2):463–6. https://doi.org/10.1148/radiology.201.2.8888241.
127. Macedo CABM, Uezumi KK, Castro CC, Lucarelli CL, Cerri GG. Acute mediastinitis: multidetector computed tomography findings following cardiac surgery. Radiol Bras. 2008;41(4):269–73.
128. Merrill WH, Akhter SA, Wolf RK, Schneeberger EW, Flege JB Jr. Simplified treatment of postoperative mediastinitis. Ann Thorac Surg. 2004;78(2):608–12; discussion -12. https://doi.org/10.1016/j.athoracsur.2004.02.089.
129. Henry DA. International labor office classification system in the age of imaging: relevant or redundant. J Thorac Imaging. 2002;17(3):179–88.
130. Hansell DM. Computed tomography of diffuse lung disease: functional correlates. Eur Radiol. 2001;11(9):1666–80. https://doi.org/10.1007/s003300100880.
131. Lynch DA, Godwin JD, Safrin S, Starko KM, Hormel P, Brown KK, et al. High-resolution computed tomography in idiopathic pulmonary fibrosis: diagnosis and prognosis. Am J Respir Crit Care Med. 2005;172(4):488–93. https://doi.org/10.1164/rccm.200412-1756OC.
132. Cox CW, Rose CS, Lynch DA. State of the art: imaging of occupational lung disease. Radiology. 2014;270(3):681–96. https://doi.org/10.1148/radiol.13121415.
133. Hering KG, Tuengerthal S, Kraus T. Standardized CT/HRCT-classification of the German Federal Republic for work and environmental related thoracic diseases. Radiologe. 2004;44(5):500–11. https://doi.org/10.1007/s00117-004-1027-7.
134. Huuskonen O, Kivisaari L, Zitting A, Taskinen K, Tossavainen A, Vehmas T. High-resolution computed tomography classification of lung fibrosis for patients with asbestos-related disease. Scand J Work Environ Health. 2001;27(2):106–12.
135. Kraus T, Borsch-Galetke E, Elliehausen HJ, Frank K, Hering KG, Hieckel HG, et al. Recommendations for reporting benign asbestos-related findings in chest X-ray and CT to the accident insurances. Pneumologie. 2009;63(12):726–32. https://doi.org/10.1055/s-0029-1215322.
136. Suganuma N, Kusaka Y, Hering KG, Vehmas T, Kraus T, Parker JE, et al. Selection of reference films based on reliability assessment of a classification of high-resolution computed tomography for pneumoconioses. Int Arch Occup Environ Health. 2006;79(6):472–6. https://doi.org/10.1007/s00420-005-0067-2.
137. Suganuma N, Kusaka Y, Hering KG, Vehmas T, Kraus T, Arakawa H, et al. Reliability of the proposed international classification of high-resolution computed tomography for occupational and environmental respiratory diseases. J Occup Health. 2009;51(3):210–22.
138. Das M, Muhlenbruch G, Mahnken AH, Hering KG, Sirbu H, Zschiesche W, et al. Asbestos surveillance program Aachen (ASPA): initial results from baseline screening for lung cancer in asbestos-exposed high-risk individuals using low-dose multidetector-row CT. Eur Radiol. 2007;17(5):1193–9. https://doi.org/10.1007/s00330-006-0426-8.
139. Tiitola M, Kivisaari L, Zitting A, Huuskonen MS, Kaleva S, Tossavainen A, et al. Computed tomography of asbestos-related pleural abnormalities. Int Arch Occup Environ Health. 2002;75(4):224–8. https://doi.org/10.1007/s00420-001-0297-x.
140. Landrigan PJ. Asbestos--still a carcinogen. N Engl J Med. 1998;338(22):1618–9. https://doi.org/10.1056/NEJM199805283382209.
141. Cavallazzi KG. Mesothelioma and other asbestos-related pleural diseases. Pulm Dis. 2008;13:5.
142. Rusch VW, Godwin JD, Shuman WP. The role of computed tomography scanning in the initial assessment and the follow-up of malignant pleural mesothelioma. J Thorac Cardiovasc Surg. 1988;96(1):171–7.
143. Wang ZJ, Reddy GP, Gotway MB, Higgins CB, Jablons DM, Ramaswamy M, et al. Malignant pleural mesothelioma: evaluation with CT, MR imag-

ing, and PET. Radiographics. 2004;24(1):105–19. https://doi.org/10.1148/rg.241035058.
144. Friedman AC, Fiel SB, Fisher MS, Radecki PD, Lev-Toaff AS, Caroline DF. Asbestos-related pleural disease and asbestosis: a comparison of CT and chest radiography. AJR Am J Roentgenol. 1988;150(2):269–75. https://doi.org/10.2214/ajr.150.2.269.
145. Akira M, Yamamoto S, Inoue Y, Sakatani M. High-resolution CT of asbestosis and idiopathic pulmonary fibrosis. AJR Am J Roentgenol. 2003;181(1):163–9. https://doi.org/10.2214/ajr.181.1.1810163.
146. Meyer KC. Diagnosis and management of interstitial lung disease. Transl Respir Med. 2014;2:4. https://doi.org/10.1186/2213-0802-2-4.
147. Meyer KC. Interstitial lung disease in the elderly: pathogenesis, diagnosis and management. Sarcoidosis Vasc Diffuse Lung Dis. 2011;28(1):3–17.
148. Kanne JP. Interstitial lung disease (ILD): imaging finding, and the role of imaging in evaluating the patient with known or suspected ILD. Semin Roentgenol. 2010;45(1):3. https://doi.org/10.1053/j.ro.2009.09.001.
149. Hodnett PA, Naidich DP. Fibrosing interstitial lung disease. A practical high-resolution computed tomography-based approach to diagnosis and management and a review of the literature. Am J Respir Crit Care Med. 2013;188(2):141–9. https://doi.org/10.1164/rccm.201208-1544CI.
150. Meyer KC, Raghu G, Baughman RP, Brown KK, Costabel U, du Bois RM, et al. An official American Thoracic Society clinical practice guideline: the clinical utility of bronchoalveolar lavage cellular analysis in interstitial lung disease. Am J Respir Crit Care Med. 2012;185(9):1004–14. https://doi.org/10.1164/rccm.201202-0320ST.
151. Edey AJ, Devaraj AA, Barker RP, Nicholson AG, Wells AU, Hansell DM. Fibrotic idiopathic interstitial pneumonias: HRCT findings that predict mortality. Eur Radiol. 2011;21(8):1586–93. https://doi.org/10.1007/s00330-011-2098-2.
152. Woodhead F, Wells AU, Desai SR. Pulmonary complications of connective tissue diseases. Clin Chest Med. 2008;29(1):149–64, vii. https://doi.org/10.1016/j.ccm.2007.11.009.
153. Capobianco J, Grimberg A, Thompson BM, Antunes VB, Jasinowodolinski D, Meirelles GS. Thoracic manifestations of collagen vascular diseases. Radiographics. 2012;32(1):33–50. https://doi.org/10.1148/rg.321105058.
154. Visscher DW, Myers JL. Bronchiolitis: the pathologist's perspective. Proc Am Thorac Soc. 2006;3(1):41–7. https://doi.org/10.1513/pats.200512-124JH.
155. Abbott GF, Rosado-de-Christenson ML, Rossi SE, Suster S. Imaging of small airways disease. J Thorac Imaging. 2009;24(4):285–98. https://doi.org/10.1097/RTI.0b013e3181c1ab83.
156. Lynch DA. Imaging of small airways disease and chronic obstructive pulmonary disease. Clin Chest Med. 2008;29(1):165–79, vii. https://doi.org/10.1016/j.ccm.2007.11.008.
157. Boiselle PM, Feller-Kopman D, Ashiku S, Weeks D, Ernst A. Tracheobronchomalacia: evolving role of dynamic multislice helical CT. Radiol Clin N Am. 2003;41(3):627–36.
158. Carden KA, Boiselle PM, Waltz DA, Ernst A. Tracheomalacia and tracheobronchomalacia in children and adults: an in-depth review. Chest. 2005;127(3):984–1005. https://doi.org/10.1378/chest.127.3.984.
159. Lee KS, Ernst A, Trentham DE, Lunn W, Feller-Kopman DJ, Boiselle PM. Relapsing polychondritis: prevalence of expiratory CT airway abnormalities. Radiology. 2006;240(2):565–73. https://doi.org/10.1148/radiol.2401050562.
160. Hein E, Rogalla P, Hentschel C, Taupitz M, Hamm B. Dynamic and quantitative assessment of tracheomalacia by electron beam tomography: correlation with clinical symptoms and bronchoscopy. J Comput Assist Tomogr. 2000;24(2):247–52.
161. Boiselle PM. Multislice helical CT of the central airways. Radiol Clin N Am. 2003;41(3):561–74.
162. Boiselle PM. Imaging of the large airways. Clin Chest Med. 2008;29(1):181–93, vii. https://doi.org/10.1016/j.ccm.2007.11.002.
163. Boiselle PM, Ernst A. State-of-the-art imaging of the central airways. Respiration. 2003;70(4):383–94.
164. Boiselle PM, Lee KS, Ernst A. Multidetector CT of the central airways. J Thorac Imaging. 2005;20(3):186–95.
165. Boiselle PM, Reynolds KF, Ernst A. Multiplanar and three-dimensional imaging of the central airways with multidetector CT. AJR Am J Roentgenol. 2002;179(2):301–8. https://doi.org/10.2214/ajr.179.2.1790301.
166. Lee EY, Siegel MJ. MDCT of tracheobronchial narrowing in pediatric patients. J Thorac Imaging. 2007;22(3):300–9. https://doi.org/10.1097/RTI.0b013e3180cab6e8.
167. Lee EY, Siegel MJ, Hildebolt CF, Gutierrez FR, Bhalla S, Fallah JH. MDCT evaluation of thoracic aortic anomalies in pediatric patients and young adults: comparison of axial, multiplanar, and 3D images. AJR Am J Roentgenol. 2004;182(3):777–84. https://doi.org/10.2214/ajr.182.3.1820777.
168. Siegel MJ. Multiplanar and three-dimensional multidetector row CT of thoracic vessels and airways in the pediatric population. Radiology. 2003;229(3):641–50. https://doi.org/10.1148/radiol.2293020999.
169. Lee EY, Boiselle PM. Tracheobronchomalacia in infants and children: multidetector CT evaluation. Radiology. 2009;252(1):7–22. https://doi.org/10.1148/radiol.2513081280.
170. Lee EY, Boiselle PM, Cleveland RH. Multidetector CT evaluation of congenital lung anomalies. Radiology. 2008;247(3):632–48. https://doi.org/10.1148/radiol.2473062124.
171. Ramadan HH, Wax MK, Avery S. Outcome and changing cause of unilateral vocal cord paralysis.

Otolaryngol Head Neck Surg. 1998;118(2):199–202. https://doi.org/10.1016/S0194-5998(98)80014-4.
172. Yumoto E, Minoda R, Hyodo M, Yamagata T. Causes of recurrent laryngeal nerve paralysis. Auris Nasus Larynx. 2002;29(1):41–5.
173. Bando H, Nishio T, Bamba H, Uno T, Hisa Y. Vocal fold paralysis as a sign of chest diseases: a 15-year retrospective study. World J Surg. 2006;30(3):293–8. https://doi.org/10.1007/s00268-005-7959-x.
174. Glazer HS, Aronberg DJ, Lee JK, Sagel SS. Extralaryngeal causes of vocal cord paralysis: CT evaluation. AJR Am J Roentgenol. 1983;141(3):527–31. https://doi.org/10.2214/ajr.141.3.527.
175. Paquette CM, Manos DC, Psooy BJ. Unilateral vocal cord paralysis: a review of CT findings, mediastinal causes, and the course of the recurrent laryngeal nerves. Radiographics. 2012;32(3):721–40. https://doi.org/10.1148/rg.323115129.
176. Pretorius PM, Milford CA. Investigating the hoarse voice. BMJ. 2008;337:a1726. https://doi.org/10.1136/bmj.a1726.
177. Robinson S, Pitkaranta A. Radiology findings in adult patients with vocal fold paralysis. Clin Radiol. 2006;61(10):863–7. https://doi.org/10.1016/j.crad.2006.02.016.
178. Rabe KF, Hurd S, Anzueto A, Barnes PJ, Buist SA, Calverley P, et al. Global strategy for the diagnosis, management, and prevention of chronic obstructive pulmonary disease: GOLD executive summary. Am J Respir Crit Care Med. 2007;176(6):532–55. https://doi.org/10.1164/rccm.200703-456SO.
179. Litmanovich DE, Hartwick K, Silva M, Bankier AA. Multidetector computed tomographic imaging in chronic obstructive pulmonary disease: emphysema and airways assessment. Radiol Clin N Am. 2014;52(1):137–54. https://doi.org/10.1016/j.rcl.2013.09.002.
180. Matsuoka S, Yamashiro T, Washko GR, Kurihara Y, Nakajima Y, Hatabu H. Quantitative CT assessment of chronic obstructive pulmonary disease. Radiographics. 2010;30(1):55–66. https://doi.org/10.1148/rg.301095110.
181. Mayo JR. CT evaluation of diffuse infiltrative lung disease: dose considerations and optimal technique. J Thorac Imaging. 2009;24(4):252–9. https://doi.org/10.1097/RTI.0b013e3181c227b2.
182. Hackx M, Gyssels E, Severo Garcia T, De Meulder I, Alard S, Bruyneel M, et al. Chronic obstructive pulmonary disease: CT quantification of airway dimensions, numbers of airways to measure, and effect of bronchodilation. Radiology. 2015;277(3):853–62. https://doi.org/10.1148/radiol.2015140949.
183. Albert P, Agusti A, Edwards L, Tal-Singer R, Yates J, Bakke P, et al. Bronchodilator responsiveness as a phenotypic characteristic of established chronic obstructive pulmonary disease. Thorax. 2012;67(8):701–8. https://doi.org/10.1136/thoraxjnl-2011-201458.
184. Venuta F, de Giacomo T, Rendina EA, Ciccone AM, Diso D, Perrone A, et al. Bronchoscopic lung-volume reduction with one-way valves in patients with heterogenous emphysema. Ann Thorac Surg. 2005;79(2):411–6; discussion 6–7. https://doi.org/10.1016/j.athoracsur.2004.07.048.
185. Wood DE, McKenna RJ Jr, Yusen RD, Sterman DH, Ost DE, Springmeyer SC, et al. A multicenter trial of an intrabronchial valve for treatment of severe emphysema. J Thorac Cardiovasc Surg. 2007;133(1):65–73. https://doi.org/10.1016/j.jtcvs.2006.06.051.
186. Fraioli F, Calabrese FA, Venuta F, Anile M, Bertoletti L, Carbone I, et al. MDCT assessment of lung volume in patients undergoing bronchial stenting for treatment of pulmonary emphysema: correlation with respiratory tests and personal experience. Radiol Med. 2006;111(6):749–58. https://doi.org/10.1007/s11547-006-0078-4.
187. Pereira GC, Traughber M, Muzic RF Jr. The role of imaging in radiation therapy planning: past, present, and future. Biomed Res Int. 2014;2014:231090. https://doi.org/10.1155/2014/231090.
188. Keall P. 4-dimensional computed tomography imaging and treatment planning. Semin Radiat Oncol. 2004;14(1):81–90. https://doi.org/10.1053/j.semradonc.2003.10.006.
189. Soo E, Edey AJ. The role of thoracic imaging in the intensive care unit. Br J Hosp Med (Lond). 2012;73(11):612–9.
190. Hill JR, Horner PE, Primack SL. ICU imaging. Clin Chest Med. 2008;29(1):59–76, vi. https://doi.org/10.1016/j.ccm.2007.11.005.
191. Miller WT Jr, Tino G, Friedburg JS. Thoracic CT in the intensive care unit: assessment of clinical usefulness. Radiology. 1998;209(2):491–8. https://doi.org/10.1148/radiology.209.2.9807579.
192. Miller WT Sr. The chest radiograph in the intensive care unit. Semin Roentgenol. 1997;32(2):89–101.
193. Mirvis SE, Tobin KD, Kostrubiak I, Belzberg H. Thoracic CT in detecting occult disease in critically ill patients. AJR Am J Roentgenol. 1987;148(4):685–9. https://doi.org/10.2214/ajr.148.4.685.
194. DuBose J, Inaba K, Okoye O, Demetriades D, Scalea T, O'Connor J, et al. Development of posttraumatic empyema in patients with retained hemothorax: results of a prospective, observational AAST study. J Trauma Acute Care Surg. 2012;73(3):752–7. https://doi.org/10.1097/TA.0b013e31825c1616.
195. Hirshberg A, Wall MJ Jr, Ramchandani MK, Mattox KL. Reoperation for bleeding in trauma. Arch Surg. 1993;128(10):1163–7.
196. Karmy-Jones R, Holevar M, Sullivan RJ, Fleisig A, Jurkovich GJ. Residual hemothorax after chest tube placement correlates with increased risk of empyema following traumatic injury. Can Respir J. 2008;15(5):255–8.
197. Awerbuch E, Benavides M, Gershengorn HB. The impact of computed tomography of the chest on the management of patients in a medical intensive

care unit. J Intensive Care Med. 2015;30(8):505–11. https://doi.org/10.1177/0885066614540122.
198. Kaewlai R, Avery LL, Asrani AV, Novelline RA. Multidetector CT of blunt thoracic trauma. Radiographics. 2008;28(6):1555–70. https://doi.org/10.1148/rg.286085510.
199. Exadaktylos AK, Sclabas G, Schmid SW, Schaller B, Zimmermann H. Do we really need routine computed tomographic scanning in the primary evaluation of blunt chest trauma in patients with "normal" chest radiograph? J Trauma. 2001;51(6):1173–6.
200. Omert L, Yeaney WW, Protetch J. Efficacy of thoracic computerized tomography in blunt chest trauma. Am Surg. 2001;67(7):660–4.
201. de Moya MA, Seaver C, Spaniolas K, Inaba K, Nguyen M, Veltman Y, et al. Occult pneumothorax in trauma patients: development of an objective scoring system. J Trauma. 2007;63(1):13–7. https://doi.org/10.1097/TA.0b013e31806864fc.
202. Miller LA. Chest wall, lung, and pleural space trauma. Radiol Clin N Am. 2006;44(2):213–24, viii. https://doi.org/10.1016/j.rcl.2005.10.006.
203. Wanek S, Mayberry JC. Blunt thoracic trauma: flail chest, pulmonary contusion, and blast injury. Crit Care Clin. 2004;20(1):71–81.
204. Chen JD, Shanmuganathan K, Mirvis SE, Killeen KL, Dutton RP. Using CT to diagnose tracheal rupture. AJR Am J Roentgenol. 2001;176(5):1273–80. https://doi.org/10.2214/ajr.176.5.1761273.
205. Scaglione M, Romano S, Pinto A, Sparano A, Scialpi M, Rotondo A. Acute tracheobronchial injuries: impact of imaging on diagnosis and management implications. Eur J Radiol. 2006;59(3):336–43. https://doi.org/10.1016/j.ejrad.2006.04.026.
206. Wintermark M, Schnyder P. The Macklin effect: a frequent etiology for pneumomediastinum in severe blunt chest trauma. Chest. 2001;120(2):543–7.
207. Larici AR, Gotway MB, Litt HI, Reddy GP, Webb WR, Gotway CA, et al. Helical CT with sagittal and coronal reconstructions: accuracy for detection of diaphragmatic injury. AJR Am J Roentgenol. 2002;179(2):451–7. https://doi.org/10.2214/ajr.179.2.1790451.
208. Mirvis SE, Shanmuganagthan K. Imaging hemidiaphragmatic injury. Eur Radiol. 2007;17(6):1411–21. https://doi.org/10.1007/s00330-006-0553-2.
209. Downing SW, Sperling JS, Mirvis SE, Cardarelli MG, Gilbert TB, Scalea TM, et al. Experience with spiral computed tomography as the sole diagnostic method for traumatic aortic rupture. Ann Thorac Surg. 2001;72(2):495–501; discussion -2.
210. Loyd JE, Tillman BF, Atkinson JB, Des Prez RM. Mediastinal fibrosis complicating histoplasmosis. Medicine (Baltimore). 1988;67(5):295–310.
211. Hanley PC, Shub C, Lie JT. Constrictive pericarditis associated with combined idiopathic retroperitoneal and mediastinal fibrosis. Mayo Clin Proc. 1984;59(5):300–4.
212. Klisnick A, Fourcade J, Ruivard M, Baud O, Souweine B, Boyer L, et al. Combined idiopathic retroperitoneal and mediastinal fibrosis with pericardial involvement. Clin Nephrol. 1999;52(1):51–5.
213. Mole TM, Glover J, Sheppard MN. Sclerosing mediastinitis: a report on 18 cases. Thorax. 1995;50(3):280–3.
214. Rossi SE, McAdams HP, Rosado-de-Christenson ML, Franks TJ, Galvin JR. Fibrosing mediastinitis. Radiographics. 2001;21(3):737–57. https://doi.org/10.1148/radiographics.21.3.g01ma17737.
215. Ferretti GR, Knoplioch J, Bricault I, Brambilla C, Coulomb M. Central airway stenoses: preliminary results of spiral-CT-generated virtual bronchoscopy simulations in 29 patients. Eur Radiol. 1997;7(6):854–9. https://doi.org/10.1007/s003300050218.
216. Kauczor HU, Wolcke B, Fischer B, Mildenberger P, Lorenz J, Thelen M. Three-dimensional helical CT of the tracheobronchial tree: evaluation of imaging protocols and assessment of suspected stenoses with bronchoscopic correlation. AJR Am J Roentgenol. 1996;167(2):419–24. https://doi.org/10.2214/ajr.167.2.8686619.
217. Lee KS, Yoon JH, Kim TK, Kim JS, Chung MP, Kwon OJ. Evaluation of tracheobronchial disease with helical CT with multiplanar and three-dimensional reconstruction: correlation with bronchoscopy. Radiographics. 1997;17(3):555–67.; ; discussion 68–70. https://doi.org/10.1148/radiographics.17.3.9153696.
218. Quint LE, Whyte RI, Kazerooni EA, Martinez FJ, Cascade PN, Lynch JP 3rd, et al. Stenosis of the central airways: evaluation by using helical CT with multiplanar reconstructions. Radiology. 1995;194(3):871–7. https://doi.org/10.1148/radiology.194.3.7862994.
219. Remy J, Remy-Jardin M, Artaud D, Fribourg M. Multiplanar and three-dimensional reconstruction techniques in CT: impact on chest diseases. Eur Radiol. 1998;8(3):335–51. https://doi.org/10.1007/s003300050391.
220. Luoma A, Nelems B. Thoracic outlet syndrome. Thoracic surgery perspective. Neurosurg Clin N Am. 1991;2(1):187–226.
221. Poitevin LA. Thoraco-cervico-brachial confined spaces an anatomic study. Ann Chir Main. 1988;7(1):5–13.
222. Boezaart AP, Haller A, Laduzenski S, Koyyalamudi VB, Ihnatsenka B, Wright T. Neurogenic thoracic outlet syndrome: a case report and review of the literature. Int J Shoulder Surg. 2010;4(2):27–35. https://doi.org/10.4103/0973-6042.70817.
223. Matsumura JS, Rilling WS, Pearce WH, Nemcek AA Jr, Vogelzang RL, Yao JS. Helical computed tomography of the normal thoracic outlet. J Vasc Surg. 1997;26(5):776–83.
224. Remy-Jardin M, Remy J, Masson P, Bonnel F, Debatselier P, Vinckier L, et al. Helical CT angiography of thoracic outlet syndrome: functional anatomy. AJR Am J Roentgenol. 2000;174(6):1667–74. https://doi.org/10.2214/ajr.174.6.1741667.
225. Demondion X, Bacqueville E, Paul C, Duquesnoy B, Hachulla E, Cotten A. Thoracic outlet: assessment with MR imaging in asymptomatic and symptomatic populations. Radiology. 2003;227(2):461–8. https://doi.org/10.1148/radiol.2272012111.

# PET Hybrid Imaging of the Thorax

3

Deena Neriman, Ali Vahedi, Stefan Voo, James Connelly, and Francesco Fraioli

**Abstract**

For many years scintigraphy, planar imaging of radioactive emission using a large area detector, formed the backbone of nuclear medicine techniques with low spatial resolution but high sensitivity. Combined with the properties of a tracer, a substance labelled with a radioactive element (radionuclide), the technique could be used for imaging tissue properties or physiological processes. Advances in engineering and computing technology allowed the technique to move into 3-dimensional image reconstruction and then combined with radiological techniques, particularly CT, to provide state-of-the-art hybrid imaging techniques. Positron-emission tomography (PET) is fast becoming the dominant nuclear medicine technique, due to its higher sensitivity and resolution than single-photon-emission computed tomography (SPECT). It has been widely used for investigating malignant diseases and increasingly used for inflammatory diseases and infection. Whilst computed tomography (CT) images represent a snapshot of patient anatomy, radiopharmaceuticals and PET provide the means to image pathophysiology.

D. Neriman (✉) · A. Vahedi · S. Voo · J. Connelly
F. Fraioli
University College London Hospitals, London, UK
e-mail: deena.neriman@nhs.net

**Keywords**

PET SUV · PET tracers · PET lymphoma
PET mesothelioma · PET oesophagus
PET lung · PET thymoma · PET infection
PET PUO · PET immunodeficiency · PET Vasculitis · PET Sarcoidosis · PET ILD · PET autoimmune · Nuclear MPS · Nuclear MPI
Nuclear chest · PET cardiac · PET chest

## 3.1 Introduction

For many years scintigraphy, planar imaging of radioactive emission using a large area detector, formed the backbone of nuclear medicine techniques with low spatial resolution but high sensitivity. By imaging a tracer, a substance labelled with a radioactive element (radionuclide), scintigraphy could be used to image tissue properties or physiological processes. Advances in engineering and computing technology allowed the technique to move into three-dimensional image reconstruction and then to combine with radiological techniques, particularly computed tomography (CT), to provide state-of-the-art hybrid imaging techniques.

Positron-emission tomography (PET) is fast becoming the dominant nuclear medicine technique, due to its higher sensitivity and resolution than single-photon emission computed tomography (SPECT). It has become widely used for


M. Anzidei, M. Anile (eds.), *Diagnostic Imaging for Thoracic Surgery*,
https://doi.org/10.1007/978-3-319-89893-3_3

investigating malignant diseases and is increasingly used for inflammatory diseases and infection. Whilst CT images represent a snapshot of patient anatomy, radiopharmaceuticals and PET provide the means to image pathophysiology.

In this book chapter we review the theory of PET, the main radiopharmaceutical drugs, and the clinical applications in the most important areas of thoracic imaging.

## 3.2 Theory

Radionuclides used in PET imaging have a neutron deficiency within the nucleus, corresponding to a lower mass number than the most common stable isotope, and typically a short half-life in the order of minutes up to a couple of hours [1]. PET radionuclides decay whereby a proton transforms into a neutron, a neutrino, and a positron (positive electron), which is ejected. The positron particle is an antimatter counterpart of an electron. The positron travels a short distance (positron range), dependent on emitted energy of the positron, before interacting with a nearby electron and both undergoing annihilation. This process results in the conversion of both particles into a pair of gamma ray photons (511 keV) that travel in opposite directions. Coincident detection of these two photons forms the basis of PET scanning [2].

## 3.3 PET Imaging Equipment

### 3.3.1 PET Camera

A clinical PET camera typically comprises a ring of detectors which surround a section of the patient. Following a nuclide decay and positron annihilation with an electron, the two annihilation photons travelling in opposite directions are detected virtually simultaneously by two detectors in the ring that localises the emitting nucleus to the line between them. This dispenses with the need for a collimator in front of the detector to confine detection of emission to a specific region, as used in SPECT imaging. If the slight difference in arrival time of the two photons can be measured, the difference in distance travelled by the two photons and the position of the original annihilation can be estimated, typically referred to as time of flight (TOF), with a resulting improvement in image quality. By collecting the emission data from all detectors for several minutes, sufficient information to reconstruct a 3D distribution of the tracer is acquired, before moving the patient to allow detection from the adjoining region. This way a whole-body tomographic image of the tracer is obtained with a resolution down to as little as 4 mm.

### 3.3.2 Attenuation Correction

The ring of detectors will count photons which are emitted from within the patient. There are several important effects that have to be accounted for. Transmitted photons will undergo attenuation; this is interaction with human tissue due to either absorption or scatter. Attenuation increases with increasing density and volume of tissue through which photons have to be transmitted. However, since annihilation results in two photons that travel along the whole line between the detectors, the attenuation factor is the same for any position along the line. So correction for the attenuation can be made by measuring tissue density using a CT scan of the same region, where the X-ray beam is attenuated in a measurable way as it transmits through the patient, allowing attenuation factors to be calculated. Visually, the correction involves ‘adding counts’ back into areas that are more attenuated, being deeper or surrounded by dense structures, and allows accurate quantitative and qualitative measurements of activity. Both attenuation-corrected and -uncorrected sets of data are made available for clinical review.

### 3.3.3 Coincidence Detection

Another consideration is coincidence detection. Simultaneous detection can occur with true, scattered, random and multiple coincidences. A true coincidence event occurs when both annihilation photons are successfully detected. Scattered

coincidences occur when one or both photons are deflected in tissue (scattered) with the result of a misplaced line of response. Random coincidences (pair of unrelated annihilation photons) produce a background effect which could result in increasing statistical noise. Multiple coincidences occur with detection of more than two simultaneous photons, preventing localisation of a single annihilation event. There are standardised methods for correcting all the image-degrading effects mentioned above.

### 3.3.4 Hybrid Scanning

A CT scan coincident with the PET scan is now standard for attenuation correction but almost as importantly is also used to localise emission and to provide anatomical information to assist in diagnosis. CT protocols can vary as attenuation correction requires a low-resolution scan whereas a clinically useful scan requires higher resolution and energy. Magnetic resonance imaging (MRI) is an alternative combination with PET with the added benefit of greater soft-tissue contrast and lack of ionising radiation. Development of PET-MR has resulted in the development of digital PET detection. Established PET technology has used detectors made up of scintillation crystals and photomultiplier tubes (PMTs) that do not function in the MR magnetic field. New digital technology replaces PMTs with silicon-based detectors that convert light from the crystals directly to a digital signal with improved sensitivity for small lesions.

### 3.3.5 Positron-Emission Tomography with MRI for Localisation and Attenuation Correction (PET/MRI)

At the most basic level, a non-contrast anatomical MRI pulse sequence (e.g. T2- or T1-weighted imaging, Dixon, short tau–inversion–recovery) can be acquired whilst PET signal is simultaneously collected at each bed position. In this case, the primary role of MRI is to replace the anatomical localisation provided by the CT component of a PET-CT study. However, substituting MRI for CT is more challenging than it might first appear. In fact as said above, CT provides electron density data necessary for attenuation correction of PET images. Indeed, for MRI to replace CT, it must also provide a measure of electron density, a capability that it does not have. Therefore, an alternative approach is necessary. For the Siemens simultaneous PET-MRI, attenuation correction is based on Dixon fat and water separation sequences. Dixon published the first paper on a simple water and fat separation in 1984. The technique he described acquires two separate images: the first, a conventional spin-echo image with water and fat signals in phase and the other acquired with the readout gradient slightly shifted, so that the water and fat signals are 180° out of phase; the signals from the two allow derivation of separate fat and water images. Attenuation correction of PET signal can be approximated by segmenting fat and water and assigning an assumed electron density to each component. However, a major limitation of this approach is in separating air from bone, as both generate no signal on Dixon images and yet have very different electron densities. Thus, accurate attenuation correction on PET-MRI remains a work in progress with a focus on improving Dixon techniques whilst also exploring alternative strategies, e.g. attenuation maps and ultrashort echo time imaging [3].

## 3.4 Standardised Uptake Values

Standardised uptake value (SUV) calculation is a method for quantification of uptake of a tracer, particularly used for FDG uptake on PET imaging [4]. In its simplest form it is the ratio of the radioactivity concentration in a region of interest with the injected activity concentration for the whole body The SUV is the ratio of the image-derived radioactivity concentration $c_{\text{img}}$ and the whole-body concentration of the injected radioactivity $c_{\text{inj}}$ $\left( \text{SUV}_{\text{max}} = \dfrac{c_{\text{img}}}{c_{\text{inj}}} \right)$.

So a uniform distribution would have an SUV of 1 and regional increased uptake is greater than 1. SUV provides a means for comparing pathology between patients, for example different types of lung cancer, and with respect to previous images, such as response to treatment in lymphoma. However, it is important to be aware of factors that can influence SUV that include:

- The time point of scanning post-PET tracer administration
- Patient size
- Plasma glucose levels
- Partial volume effects
- Placement of regions of interest

## 3.5 PET Tracers

*Production:* Positron emission typically requires neutron-deficient nuclides (i.e. the mass number is lower than the most stable isotope) [2] (Table 3.1).

Most PET tracers are produced in a cyclotron, a device designed to accelerate small charged particles (typically hydrogen or deuterium) with a spiral trajectory in a magnetic field before collision with a target. An example is the reaction of oxygen (in water target) with a proton to produce fluorine and a neutron.

Some radionuclides can be produced using a generator. A generator consists of a store of a more stable mother nuclide that decays to a short-lived daughter nuclide. Typically the nuclide is suspended on an elution column so that the daughter nuclide can be separated from the mother by flushing through with a solvent. Examples are 82 rubidium (half-life 76 s) produced from the decay of 82 strontium (half-life of 25 days). The most common tracer used in PET imaging, fluorine-18 ($^{18}$F), is produced in a cyclotron with a half-life of 110 min. $^{18}$F is commonly used to chemically label glucose by substituting a hydroxyl group. The product, fluorodeoxyglucose (FDG), is actively transported into the cells by a group of glucose transport proteins (GLUT) where it is phosphorylated intracellularly as the first step of glycolysis; this process traps FDG within the cell. Unlike glucose, FDG cannot continue in the glycolysis pathway and remains as FDG-6-phosphate. The higher the glucose metabolism of tissue, the greater the proportion of FDG trapped and therefore the higher the PET signal from that specific tissue. This can be seen physiologically with high uptake in the brain cortex and heart as well as excretion through the kidneys. Pathological processes which involve high levels of metabolism, such as malignancy (Warburg effect), inflammation or infection, will demonstrate higher tracer accumulation and activity.

*Other Tracers:* Although FDG dominates the use of PET currently, there is increasing interest in molecular imaging of other biomarkers. There are many experimental tracers and a few that are used clinically including the following (Table 3.2):

**Table 3.2** Clinical application of different tracers

| Tracer | Clinical application |
|---|---|
| $^{18}$F-NaF | Bone scan |
| $^{18}$F-FLT | DNA synthesis and proliferation |
| $^{18}$F-FMISO | Hypoxia |
| $^{68}$Ga-DOTATATE | Somatostatin receptor analogue for neuroendocrine tumours |
| $^{68}$Ga-PSMA | Prostate cancer |

**Table 3.1** Examples of common PET nuclides including half-life and production

| PET nuclide | Stable nuclide | Half-life | Production |
|---|---|---|---|
| $^{18}$F | $^{19}$F | 109.6 min | Cyclotron |
| $^{11}$C | $^{12}$C | 20.3 min | Cyclotron |
| $^{13}$N | $^{14}$N | 9.96 min | Cyclotron |
| $^{15}$O | $^{16}$O | 122 s | Cyclotron |
| $^{64}$Cu | $^{63}$Cu/$^{65}$Cu | 12.7 h | Cyclotron |
| $^{68}$Ga | $^{69}$Ga/$^{71}$Ga | 68 min | Generator/cyclotron |
| $^{82}$Rb | $^{85}$Rb | 76 s | Generator |

## 3.6 Applications of PET

PET is useful in a wide range of diseases. Although it is used heavily in clinical oncology, PET also has uses in benign and inflammatory disease. In this section we demonstrate the uses of PET in the oncological and non-oncological setting.

### 3.6.1 PET Applications in Oncology

PET has become an established tool in clinical oncology and the applications and techniques are increasing. It is typically used for [5]:

- Primary presentation, usually for characterisation, staging of disease and guiding biopsy
- Evaluating the response to treatment
- Restaging
- Radiotherapy planning

### 3.6.2 Lung Cancer

#### 3.6.2.1 Solitary Lung Nodule

Lung nodules and masses have been traditionally evaluated by using planar chest X-rays, CT and, more recently, MRI. Some radiographic parameters such as calcifications and smooth margins of the lesion may indicate a lower likelihood that a solitary nodule is malignant, although a substantial percentage of nodules remain radiographically equivocal. Accumulating data suggests that the ability of FDG-PET to distinguish between benign and malignant is good, although not perfect. Gupta et al. showed that FDG-PET is highly accurate in differentiating malignant from benign solitary nodules for sizes from 6 to 30 mm when radiographic findings are indeterminate [6]. FDG-PET has a sensitivity of 93% and specificity of 88% for detecting malignancy [7].

A recent meta-analysis and review of the most recent literature on a total of 1297 patients [8] revealed that PET/CT is a useful tool for detecting malignant pulmonary nodules qualitatively although false-negative findings can occur in pulmonary carcinoids and bronchoalveolar lung carcinoma.

Therefore, FDG-PET is clinically useful in patients with a solitary pulmonary nodule of more than 5–6 mm, especially where biopsy may be risky or where there is a low risk of malignancy based on the history and/or radiographic findings [9]. Lesions with no FDG uptake are probably benign and can be referred for radiographic imaging follow-up, if necessary, although false-negatives can occur with bronchoalveolar carcinoma. Lesions with increased uptake are more likely malignant (Fig. 3.1), although false-positive cases have been reported in cases of inflammatory and infectious diseases, such as histoplasmosis, aspergillosis and active tuberculosis.

#### 3.6.2.2 Non-small Cell Lung Cancer

FDG-PET has become an integral part in the assessment of lung cancer patients and guidelines recommend that PET-CT should be offered to all patients potentially suitable with curative intent. A significant proportion of FDG-PET imaging time is used for management of non-small cell lung carcinomas (NSCLC) and solitary lung nodules (SLN). FDG-PET/CT is more sensitive than CT alone to assess loco-regional lymph node spread and metastatic disease [10] (Fig. 3.2).

Specifically the role of PET is to characterise mediastinal lymph node staging (equivocal cases on CT, i.e. lymph nodes <1 cm), more precisely than CT, in patients who are being considered for curative treatment (Fig. 3.3). CT and MRI may have substantial limitations in depicting mediastinal lymph node metastases. Normal sized lymph nodes may prove to have metastases upon histologic examination, whereas nodal enlargement can be due to reactive hyperplasia or other non-malignant conditions. The sensitivity and specificity of determining lymph node metastases for non-small cell lung cancer by CT are 60–70% [11] and these values have not significantly changed even considering the technical improvements of CT (from conventional to multi-detector machines). Thus, in 30–40% of cases, CT scanning will erroneously suggest the presence of metastases and will miss lymph node

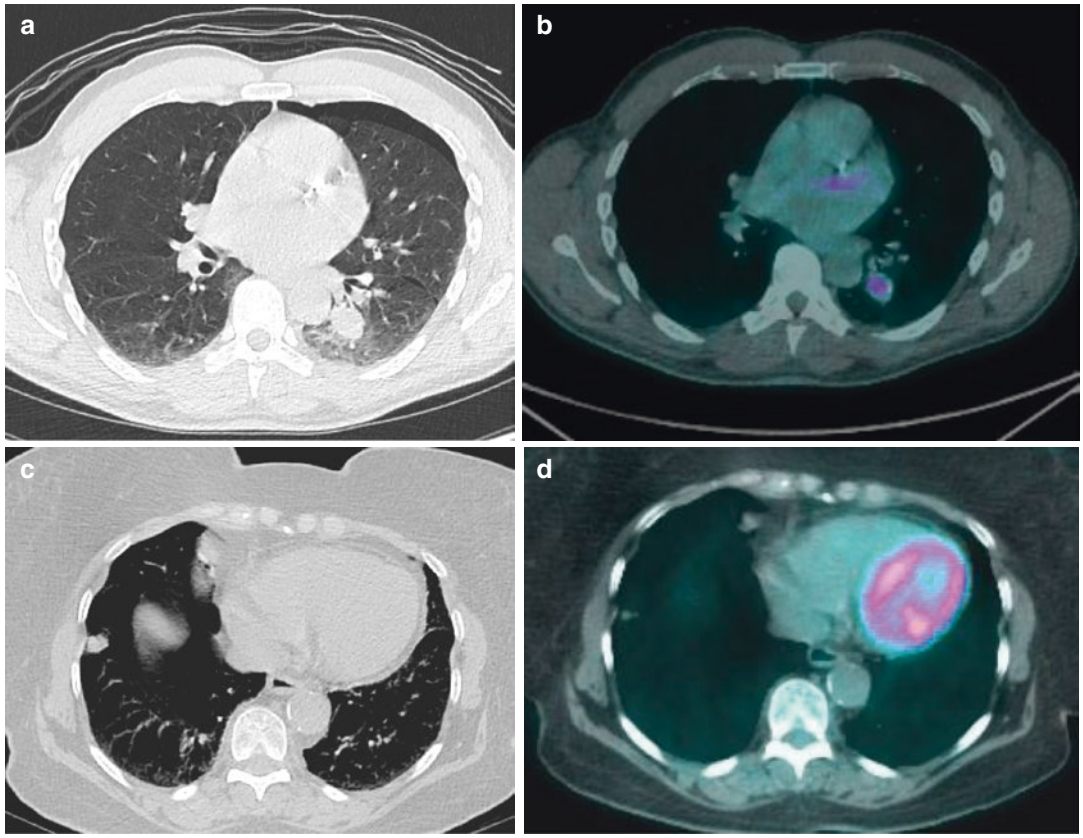


**Fig. 3.1** Two different patients: (**a**, **b**) show a left lower lobe pulmonary nodule with FDG metabolic activity, confirmed to be an adenocarcinoma on biopsy. (**c**, **d**) From a different patient with a non-FDG avid right lower lobe subpleural peripheral lesion, confirmed to be benign on subsequent follow-up

metastases in 30–40% of cases. Multiple studies have demonstrated that FDG-PET is significantly more accurate than CT in the determination of nodal status. With modern PET even small lesions (<1 cm) with an increased FDG accumulation can be detected. This represents a critical advantage of PET over CT and MRI. Several meta-analyses comparing PET and CT in the mediastinal staging of NSCLC have been performed and have calculated a mean sensitivity and specificity of 0.79 and 0.91, respectively, for PET and 0.60 and 0.77, respectively, for CT [12]. However, inflammatory mediastinal lymph nodes which accumulate FDG may occur and lead to false-positive results; thus, histopathological correlation is always recommended. The accuracy of FDG-PET in detecting mediastinal lymph node metastases is somewhat lower after induction therapy than in staging of untreated NSCLC due to inflammatory lymph nodes [13]. Therefore, for restaging after chemotherapy, it is recommended that FDG-PET should be performed after an interval of 4–8 weeks.

FDG-PET also detects distant metastases which may have been missed with conventional imaging or those which may be located in difficult review areas and/or equivocal on conventional imaging as well as occasionally indicating significant incidental findings, such as synchronous malignancies [14]. It has been shown that in about 15–20% of patients with NSCLC whole-body PET/CT detects previously unknown and unsuspected extrathoracic metastases [15] and, thus, leads to changes in therapeutic management. The most common sites of distant metastases are

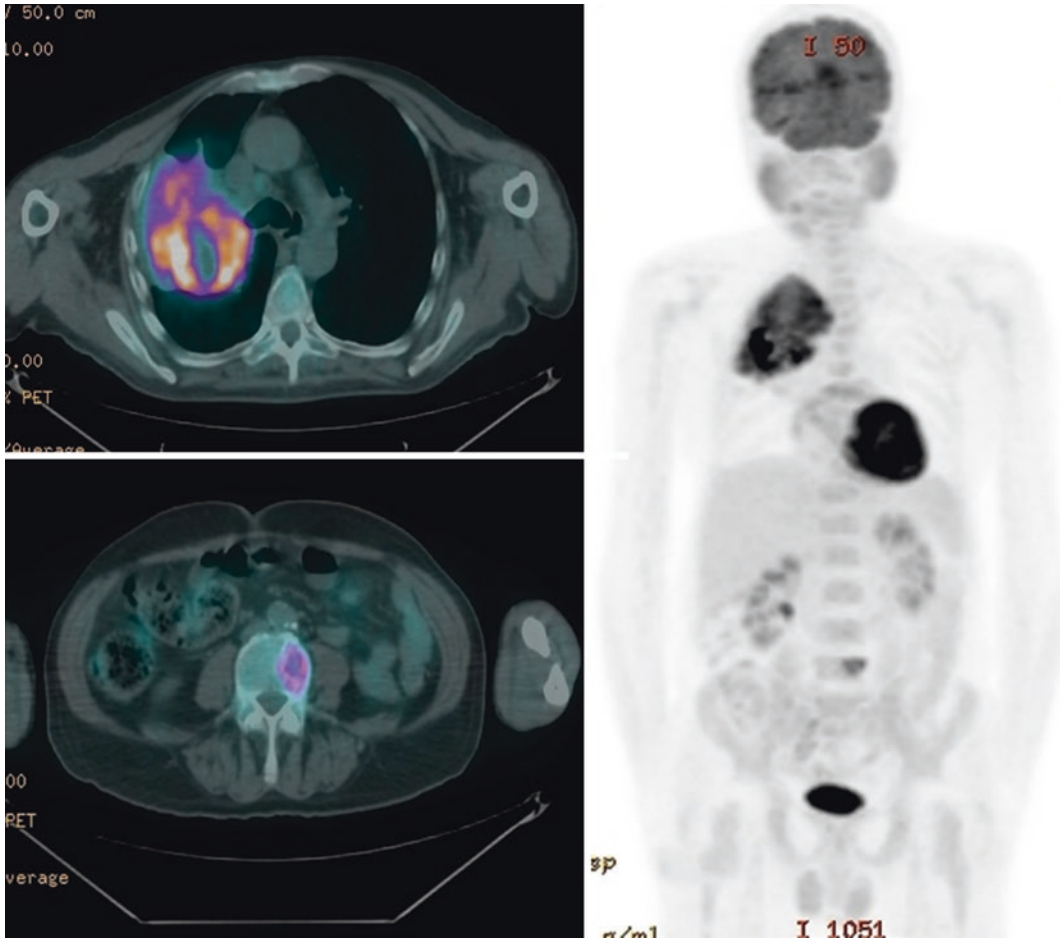


**Fig. 3.2** Fused axial FDG-PET/CT showing FDG-avid right upper lobe NSCLC. Fused axial FDG-PET/CT showing FDG-avid lytic metastasis at L4 vertebra. MIP coronal FDG-PET image demonstrating both lesions

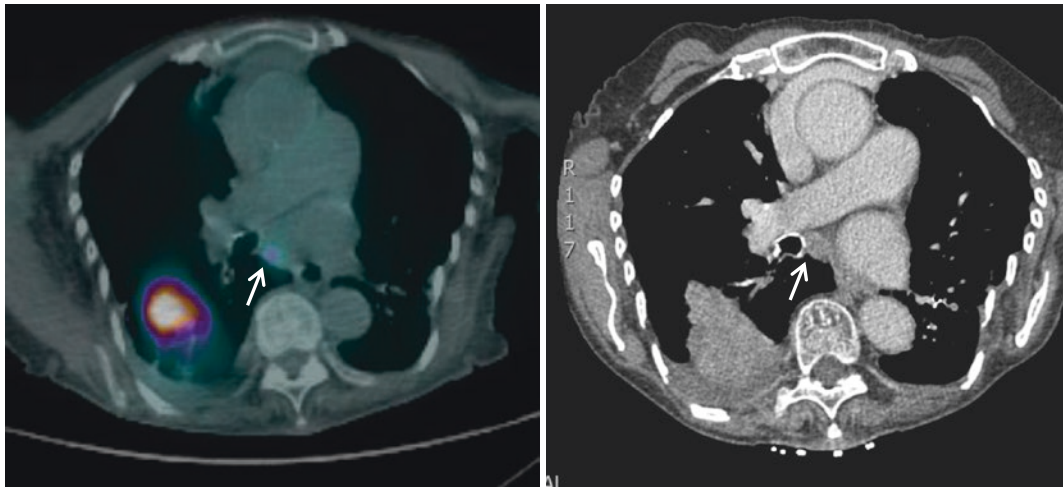

**Fig. 3.3** Right lower lobe tumour shows intense FDG uptake. On CT size borderline subcarinal node (arrow) shows FGD activity. Endoscopic bronchial ultrasound biopsy (EBUS) confirmed NSCLC on cytology

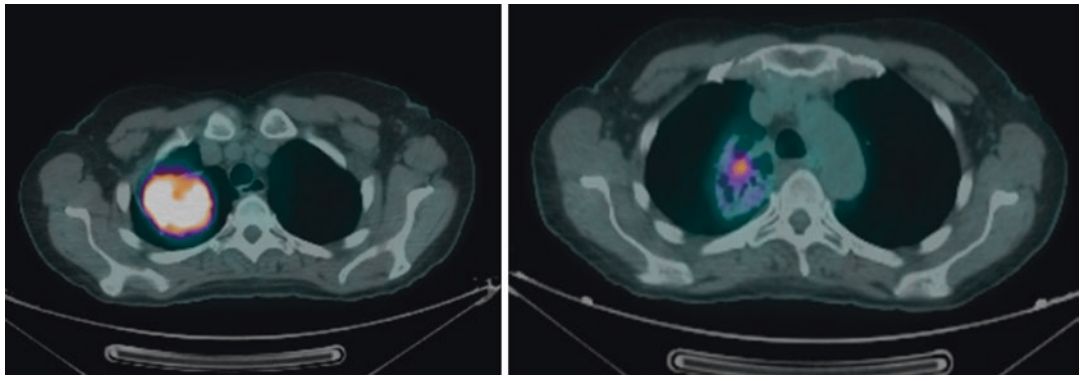

**Fig. 3.4** Pre- and post-CRT assessment scan. Right upper lobe tumour remains similar in size but significantly reduced in metabolic activity

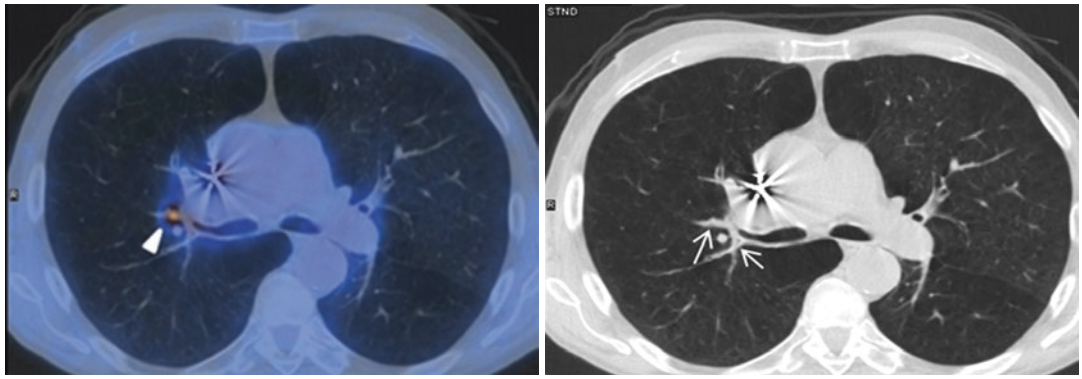

**Fig. 3.5** Previous left upper lobectomy for squamous cell carcinoma. Under surveillance for pre-invasive disease in the right lower bronchus. FDG-PET/CT shows positive uptake in the right lower bronchus despite minor CT bronchial wall thickening (arrows)

the liver, adrenal glands, bone and brain. With the exception of the brain, PET/CT is more accurate than current imaging modalities for accurate M staging of patients [16], reaching a sensitivity, specificity and accuracy of 94%, 97% and 96%, respectively, as shown in a meta-analysis of 581 patients [17].

PET is also valuable in assessing the response to treatment [18] with neoadjuvant chemoradiotherapy prior to invasive but curative surgery to ensure that invasive surgery will benefit the patient (Fig. 3.4). Following therapy (surgery and/or chemoradiotherapy) suspicion of residual or recurrent disease on conventional follow-up imaging may be challenging and equivocal due to the effects of treatment. In such circumstances PET is invaluable in assessing for recurrent disease. Guidelines recommend FDG-PET first 12 weeks after concurrent chemoradiotherapy and, in the case of radiotherapy-related changes, 3 months post-treatment.

Most recently researchers have evaluated the potential role of PET in patients with pre-invasive bronchial lesions or in assessing early recurrence at the bronchial stump in cases of previously treated patients with squamous cell cancer [19]. These precursor lesions commonly develop endobronchially or at sites of previous surgery. $^{18}$F-FDG uptake has the ability to detect invasive bronchial carcinomas at the site of or adjacent to known pre-invasive lesions and has the potential to be used as a surveillance technique for high-risk patients (Fig. 3.5).

Interestingly, even if the technical resolution of PET is still limited (i.e. 5 mm), the metabolic activity can be independent from the slice thickness used. In fact if inside a lesion (even a small one) there is high concentration of malignant cells with high metabolic rate consumption, then the FDG accumulation within these cells will be elevated regardless of their size. On a similar note there are histotypes of tumours which show elevated glucose uptake (for example squamous cell carcinoma), and others where the uptake is less conspicuous (e.g. adenocarcinoma). Understanding these different patterns of uptake helps minimise reporting errors and to provide accurate assessment of staging and follow-up scans.

#### 3.6.2.3 Future Perspectives in Lung Cancer Imaging

By combining the superior morphological resolution of contrast-enhanced CT with PET imaging it is possible to achieve a more complete structural and metabolic staging in just one exam [20]. Furthermore by analysing the kinetics of contrast or tracer uptake within tumours it is possible to obtain functional information that can be used as novel biomarkers of cancer (prognosis, angiogenesis, tissue proliferation and aggressiveness) (Fig. 3.6).

#### 3.6.2.4 Small-Cell Lung Cancer

Small-cell lung cancer (SCLC), which accounts for approximately 15–20% of new lung cancer cases, is an aggressive disease characterised by rapid growth and often disseminated by the time of diagnosis (Fig. 3.7). As such SCLC treatment is divided into two groups, localised (limited stage) and metastatic (extensive stage) disease, reflecting differences in treatment strategy and prognosis [21]. SCLC is highly sensitive to both chemotherapy and radiotherapy although patients with metastases develop resistance. Although the role of FDG-PET in SCLC is being developed, the assessment of the extent of disease, lymph

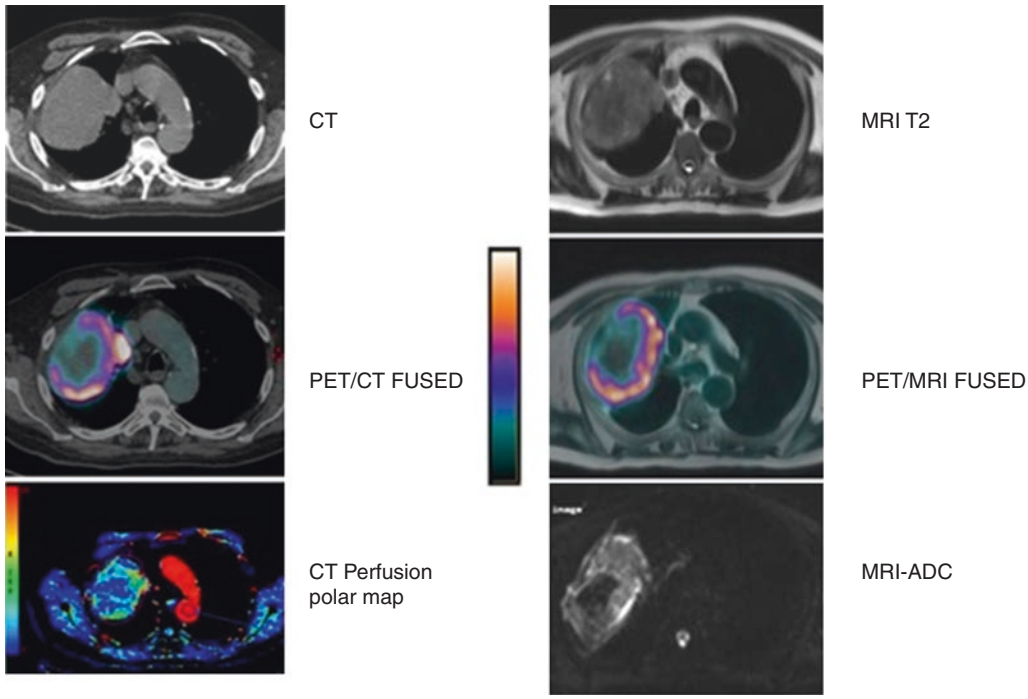


**Fig. 3.6** Different biomarkers of the same tumor: CT and MR provide anatomical information including size, blood supply, and infiltration of other structures. PET provides metabolic information and detail about heterogeneity. Perfusion provides a map of blood supply and diffusion gives information on cellularity

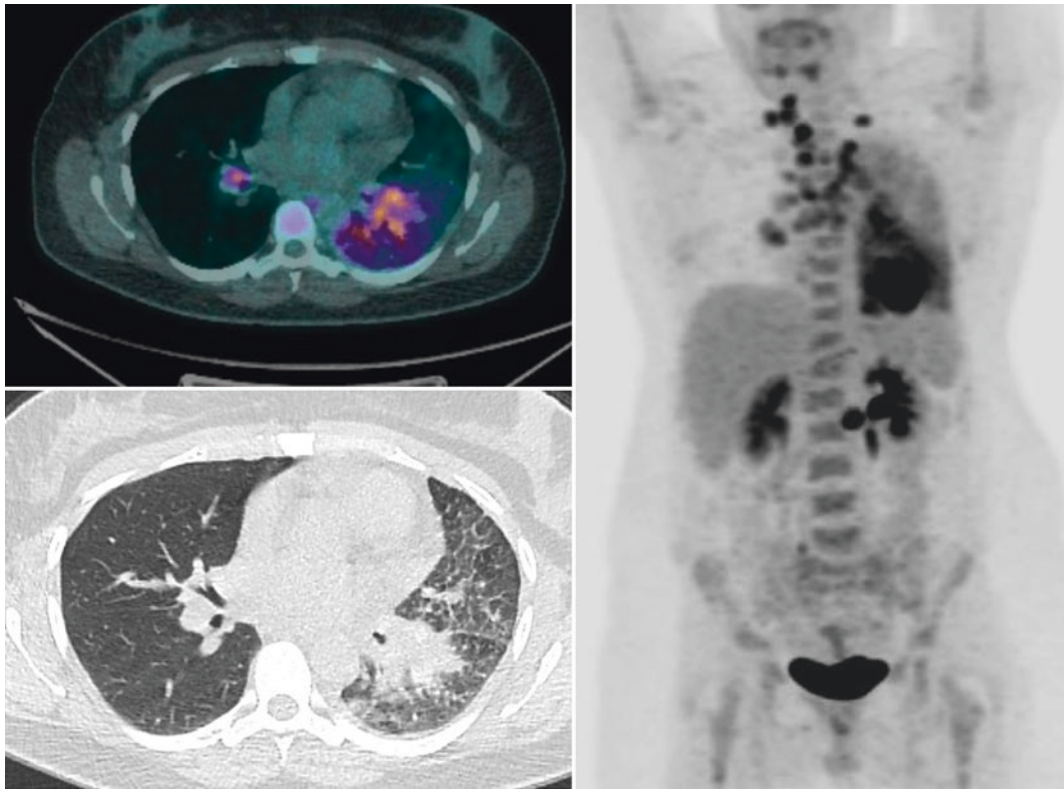

**Fig. 3.7** A large FDG-avid lung mass is seen in the perihilar left lower lobe with signs of lymphangitic spread (lymphangitic carcinomatosis) towards the periphery. There are multiple FDG-avid bilateral hilar, mediastinal and bilateral supraclavicular lymph nodes

node involvement and metastatic deposits mirrors in essence the same pathway used for NSCLC.

Overall the use of PET CT is recommended in the initial staging of patients with SCLC with localised disease who are being considered for radical therapy and/or stereotactic radiotherapy. FDG-PET can also be useful in treatment response or follow-up of suspicious findings. SCLC is often associated with paraneoplastic syndrome and FDG-PET can provide a useful tool to investigate these patients, where the potential underlying malignancy has not been found.

### 3.6.2.5 Neuroendocrine Tumours (NET) and Lung Carcinoids

Neuroendocrine tumours encompass a distinctive set of tumours which arise from cells of neural and hormonal origins, most commonly carcinoid tumours or phaeochromocytomas. Although CT remains the first-line imaging modality, PET with a tracer analogue of somatostatin is needed for characterising primary NET tumours and extent of metastases [22].

NET represent a spectrum of diseases, although the degree of differentiation and tumour aggressiveness influences the type of nuclear medicine-based imaging. Well-differentiated tumours, WHO grade G1 and G2 characterised by a low Ki67 (<20%), typically have high somatostatin receptor expression and relatively normal metabolic rate and are best imaged with somatostatin receptor tracers [23]. Scintigraphic agents such as $^{111}$In octreotide have been extensively used. Increasingly gallium-68 ($^{68}$Ga)-labelled PET somatostatin receptor (SST) agents DOTA-TATE, -TOC and -NOC are being used with the improved resolution and sensitivity afforded by PET (Fig. 3.8).

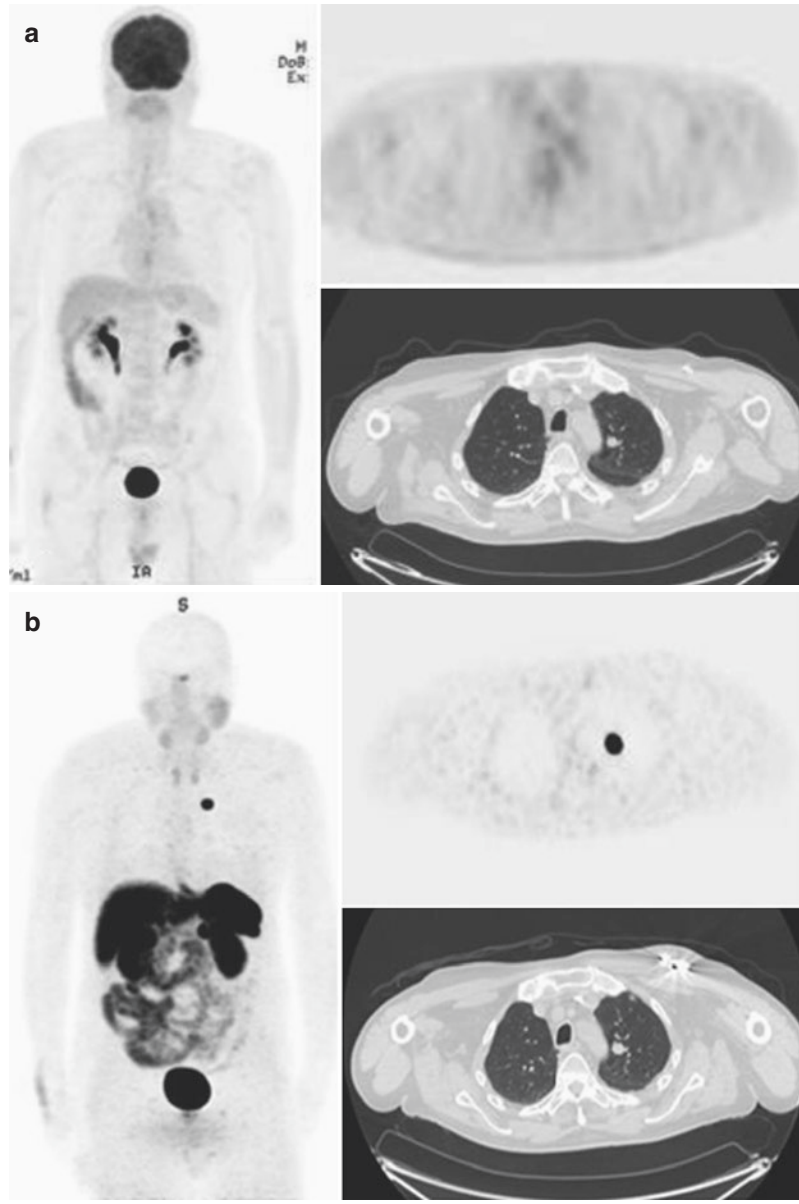


**Fig. 3.8** (**a**) Coronal FDG-PET, axial PET and axial CT showing left upper lobe nodule which shows no FDG uptake. (**b**) Coronal $^{68}$Ga-dotatate PET, axial PET and axial CT showing left upper lobe nodule shows intense uptake consistent with a carcinoid tumour

A recent review of the literature and a meta-analysis [24] reported that $^{68}$Ga-DOTATATE was more sensitive than octreotide SPECT with a sensitivity of 90.9% and specificity of 90.6%.

The results of this review also highlighted that $^{68}$Ga-DOTATATE better demonstrated disease extent (100%) than octreotide (83%) and conventional imaging (68%). Therefore treatment change impact measured by change in intended treatment before versus after $^{68}$Ga-DOTATATE scanning was high (intermodality) in 47%, moderate (intramodality) in 10%, low in 41% and not assessable in 2%. High impact included identifying candidates for potentially curative surgery, identifying nonsurgical candidates and changing type of systemic treatment. In essence $^{68}$Ga-DOTATATE PET/CT had a high clinical impact compared with conventional and octreotide imaging.

Tumours that avidly take up somatostatin receptor tracers are potentially targets for peptide receptor radionuclide therapy (PRRT) with beta radiation-emitting therapeutic agents such as lutetium-177 ($^{177}$Lu)-labelled DOTATATE. This is essentially localised radiotherapy achieved by administering a systemic agent that localises very specifically to tissue-overexpressing somatostatin receptors. The combination of diagnosis and therapy based around radionuclides and a specific ligand has been termed theranostics and has found most application with NET and tracers such as $^{123}$I and $^{131}$I MIBG and $^{68}$Ga-DOTATATE and $^{177}$Lu-DOTATATE.

Poorly differentiated neuroendocrine tumours (WHO grade G3) have increased metabolic activity, lower somatostatin receptor expression and converse imaging characteristics. These tumours are better characterised by FDG-PET.

The European Neuroendocrine Tumour Society guidelines [23] on pulmonary NET/carcinoid tumours suggest that nuclear medicine is useful as more specific than CT for assessing the tumour as well as providing whole-body nodal and metastatic staging. Somatostatin receptor tracers are useful for typical carcinoids and FDG-PET for atypical carcinoids.

## 3.7 Lymphoma

Lymphoma incorporates a heterogeneous group of diseases which arise from cells of the immune system or their precursors. Imaging with FDG tracer has become an essential tool in the assessment of this disease [25].

There is little doubt of the role of FDG-PET in the staging and follow-up of FDG-avid disease. Even in less avid tumours (indolent lymphomas/low-grade lymphomas) suspected of high-grade transformation, FDG-PET can help identify a suitable site to biopsy as well as determine the extent of high-grade disease. PET forms one of the imaging investigations for the initial staging of (FDG avid) lymphomas as well as assessing response following completion of treatment (first and subsequent treatments) as defined by the Lugano criteria [26]. Defining the response to therapy on CT or MRI can be difficult in patients who have residual abnormalities as a result of fibrosis or necrosis. FDG-PET offers the advantage of functional tissue characterisation. The 5-point Deauville criteria scale is recommended when assessing the initial staging and subsequent response to treatment in Hodgkin's (HL) and certain types of non-Hodgkin's lymphomas (NHL) using the FDG uptake in each lesion relative to liver or blood pool levels: 1 is complete and 5 is no response or progressive disease (Fig. 3.9).

## 3.8 Mesothelioma

The differentiation of benign pleural disease from malignant pleural mesothelioma (MPM) can be challenging with conventional imaging.

Malignant pleural disease often leads to pleural reaction and pleural effusion which makes the correct staging and assessment of local extension of disease difficult based on conventional imaging.

FDG-PET is playing a more central role in this cohort of patients [27]. Its use is particularly valuable to guide areas of avid disease where biopsy will be most likely positive. Accurate staging is essential when determining the most appropriate multimodality treatment options (Fig. 3.10). Hence FDG-PET which offers unique functional information is of significant value in the initial staging of patients as well as assessing the response to treatment [19].

The role of FDG-PET/CT in the staging of disease is still under consideration. However previous studies have shown that a qualitative assessment and semiquantitative measurements (using SUV) with FDG-PET can correctly identify malignancy with sensitivity of 95–97% and specificity of 78–92% [28].

In a prospective study of 29 patients [29], Erasmus et al. noted that use of FDG-PET/CT precluded surgery in 41% of patients by identifying locally advanced tumour and extrathoracic metastasis not seen on conventional imaging. PET/CT has also shown superior accuracy compared with mediastinoscopy for assessment of T4

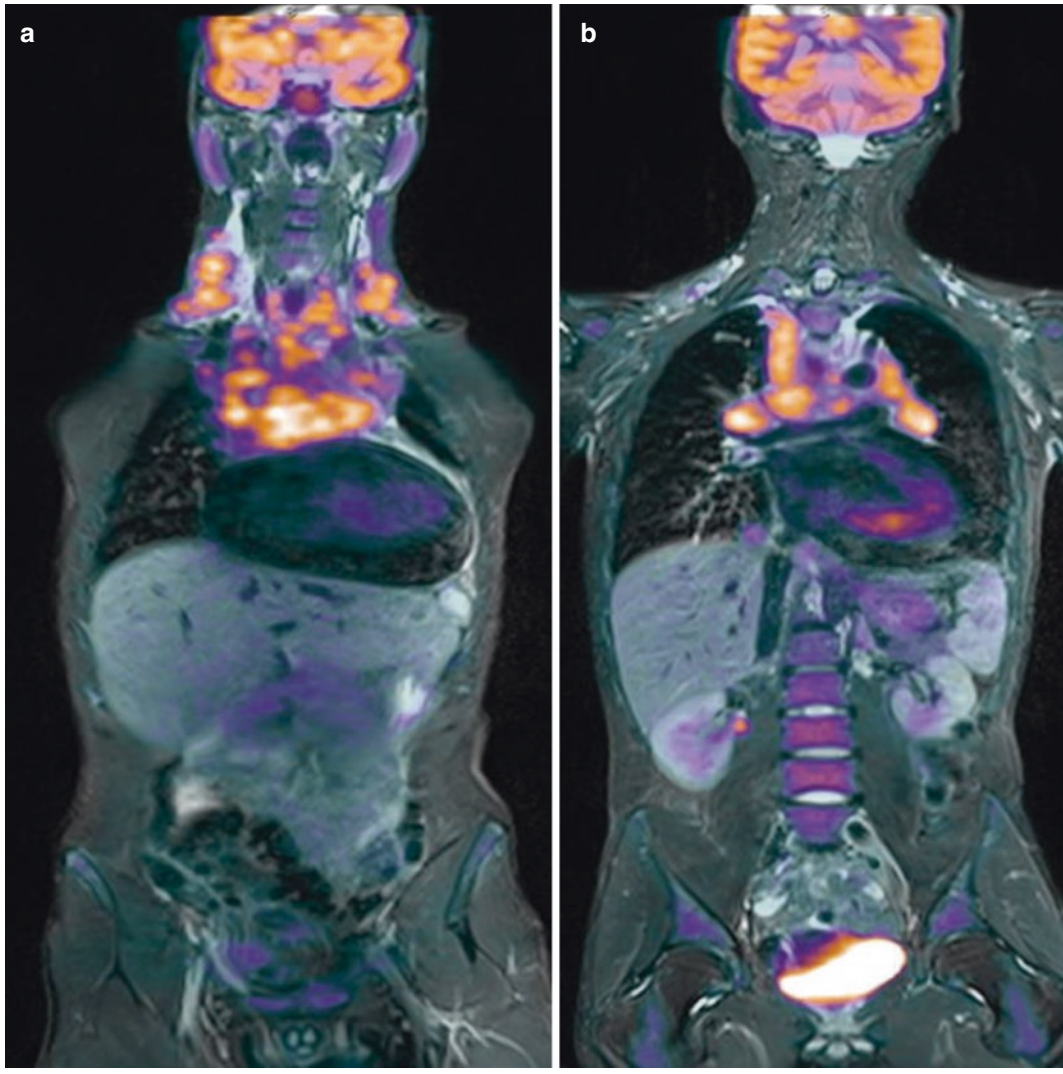


**Fig. 3.9** Young patient with lymphoma. FDG-PET/MR which demonstrates extensive supra-diaphragmatic lymphadenopathy (**a**: before treatment; **b**: interim PET). PET/MR has specific advantages on these young patients and when radiation exposure is a concern. The initial staging and assessment of treatment response in Hodgkin's lymphoma (HL) and certain types of non-Hodgkin's lymphomas (NHL) are based on Deauville five-point scale (Deauville 5 ps) criteria. 1: no uptake or no residual uptake (when used interim); 2: slight uptake, but below blood pool (mediastinum); 3: uptake above mediastinal, but below or equal to uptake in the liver; 4: uptake slightly to moderately higher than liver; 5: markedly increased uptake or any new lesion (on response evaluation). Each FDG-avid (or previously FDG-avid) lesion is rated independently

and N2/N3 categories. In 2008 Plathow et al. [30, 31] compared the accuracy of malignant pleural mesothelioma staging by CT, PET, MRI and PET/CT for patients in a predicted resectable state (stages II and III). The staging accuracy of CT, PET, MRI and PET/CT was 77%, 86%, 80% and 100%, respectively, for patients with stage II disease and 75%, 83%, 90% and 100%, respectively, for patients with stage III disease.

On the response therapy assessment front PET/CT has been shown to detect response to therapy before there is measurable morphologic

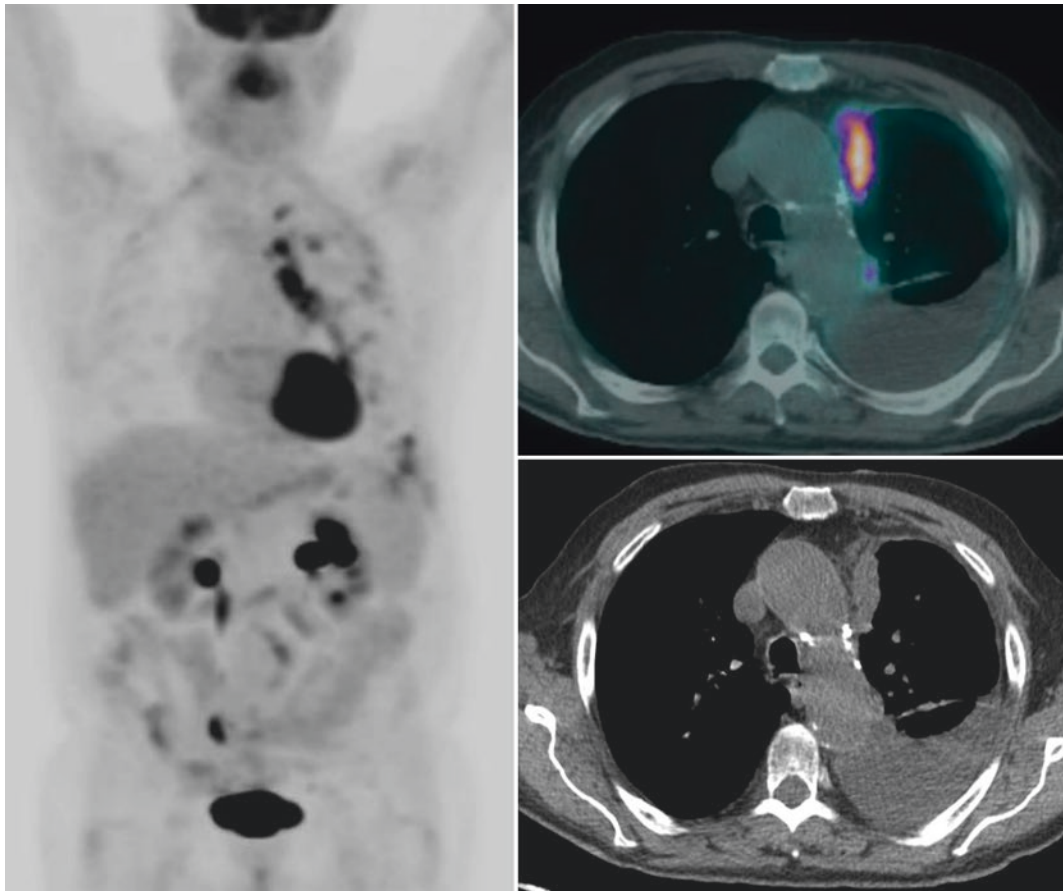

**Fig. 3.10** MIP image shows multiple hyper-metabolic foci in the left pleural surface, better demonstrated in the axial CT and fused images as focal pleural thickening

change on CT. In a preliminary study, Carretta et al. [32] observed that reduction in PET uptake in comparison with pretreatment values suggested response to chemotherapy in contrast with CT evaluation, which showed stable disease.

FDG-PET/CT offers unique functional information that complements conventional anatomic imaging of pleural tumours. This modality has proven utility in the differentiation of benign or malignant pleural thickening, aiding in the diagnosis of malignant pleural mesothelioma and benign versus malignant solitary fibrous tumour. PET/CT has gained an increasing role in the management of malignant pleural mesothelioma by assisting with staging, monitoring of treatment response and assessment of prognosis.

## 3.9 Thymoma

Although rare, thymic neoplasms are the most common primary tumours of the anterior mediastinum. It is essential to distinguish patients with high-grade tumours who may benefit from radical treatment and improved survival outcomes. PET has a role when assessing indeterminate thymic lesions [33]. Although CT and MRI are excellent at localisation of mediastinal masses,

the functional information obtained with FDG-PET is invaluable in assessment of the aggressiveness of masses but more importantly in identifying viable tumour in residual masses after chemotherapy or radiotherapy.

With FDG-PET functional imaging, the low-grade thymic tumours (WHO grades A, AB and B1) have significantly lower SUV values than the higher risk B2, B3 and C types. FDG-PET is therefore recommended for the initial staging of patients considered for surgical resection. Patients with high-grade tumours identified on PET will require preoperative biopsy; this is to identify non-surgical diseases such as lymphoma or more aggressive tumours which may not be amenable to surgical resection (Figs. 3.11 and 3.12).

Sung et al. [33] reported that low-risk thymoma has a heterogeneous uptake when compared with high-risk thymoma and thymic carcinoma, which are more likely to have homogeneous uptake. $SUV_{max}$ has been shown to be an important factor for differentiating among various histopathological subtypes of thymic tumours on $^{18}$F-FDG-PET-CT although an overlap has also been reported.

## 3.10 Oesophageal Cancer

Oesophagectomy is the treatment of choice for patients with early localised disease and accurate staging [34] is essential to identify patients with resectable disease who will benefit from surgical intervention which gives the best long-term outcome. Endoscopic ultrasonography (EUS) and CT are the conventional imaging modalities. However there is now an increase in the utility of FDG-PET (in particular when associated to EUS and CT) which allows the

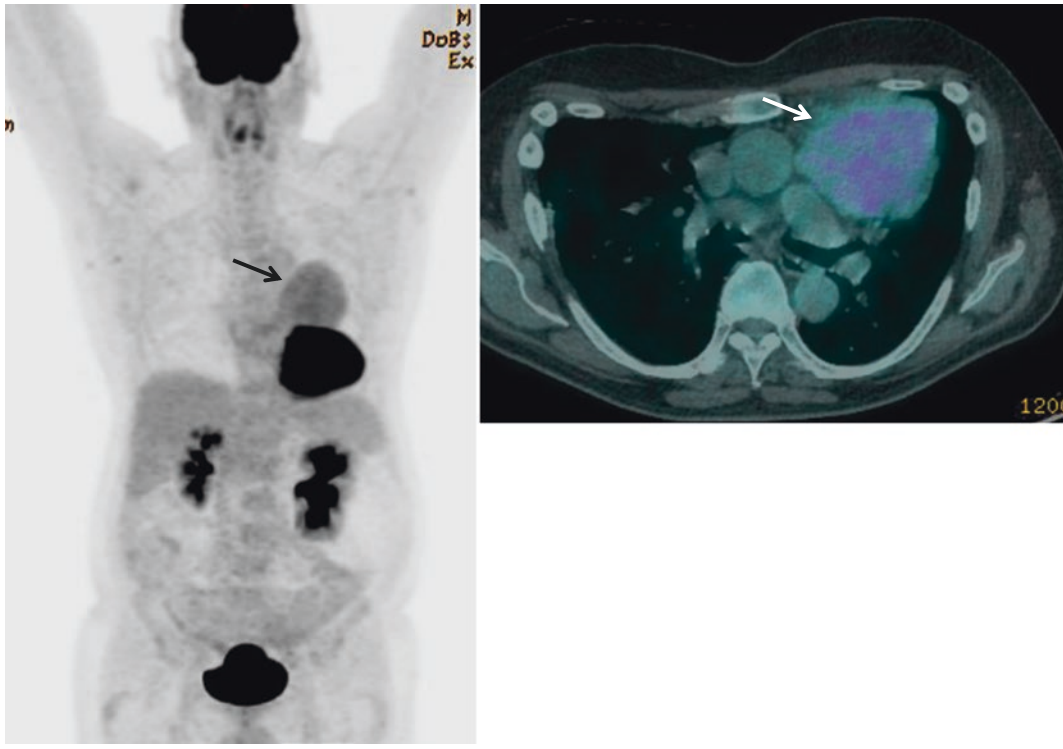

**Fig. 3.11** MIP image (right) and axial fused image (left) show mild FDG uptake in the large mediastinal lesion (arrow) confirmed to be a Thymic tumour grade 1B on histology following surgical resection

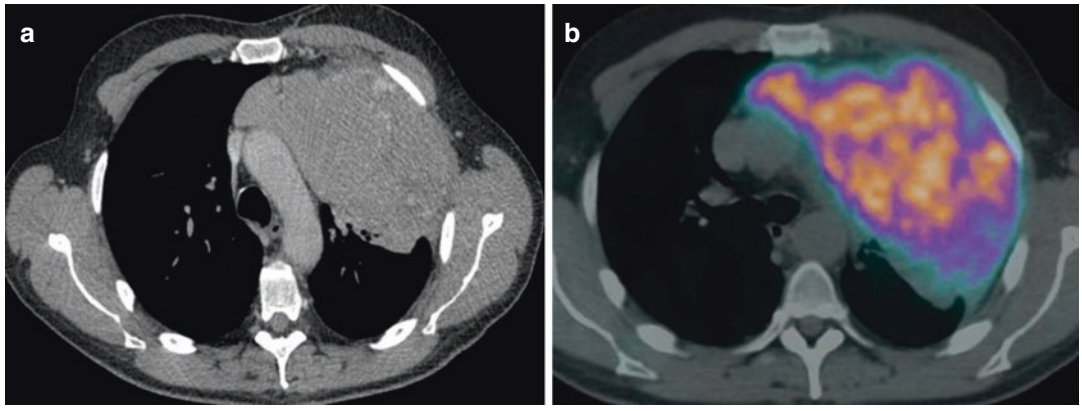


**Fig. 3.12** Axial post-contrast section (**a**) and same-level PET/CT fused image (**b**) show a large highly avid anterior mediastinal mass thymic in origin

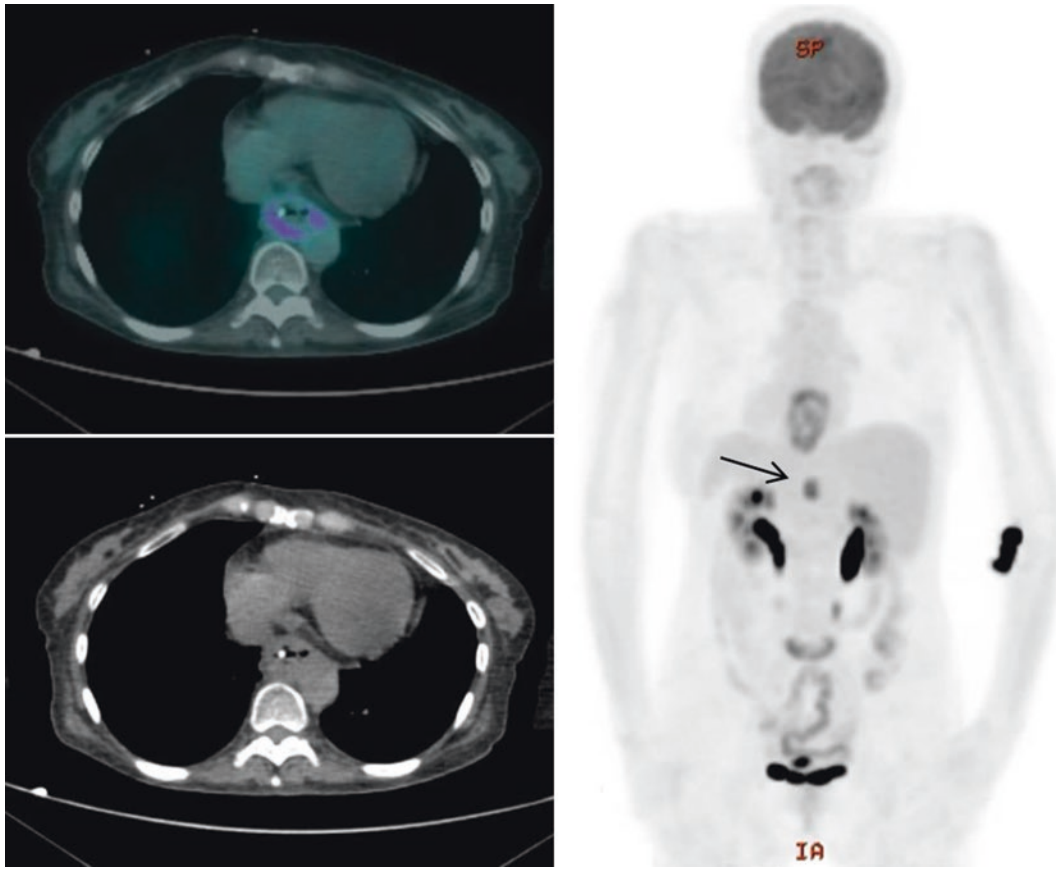


**Fig. 3.13** CT demonstrates oesophageal thickening. The hybrid study with FDG-PET demonstrates avid uptake secondary to oesophageal squamous cell carcinoma and uptake in an epigastric lymph node (arrow)

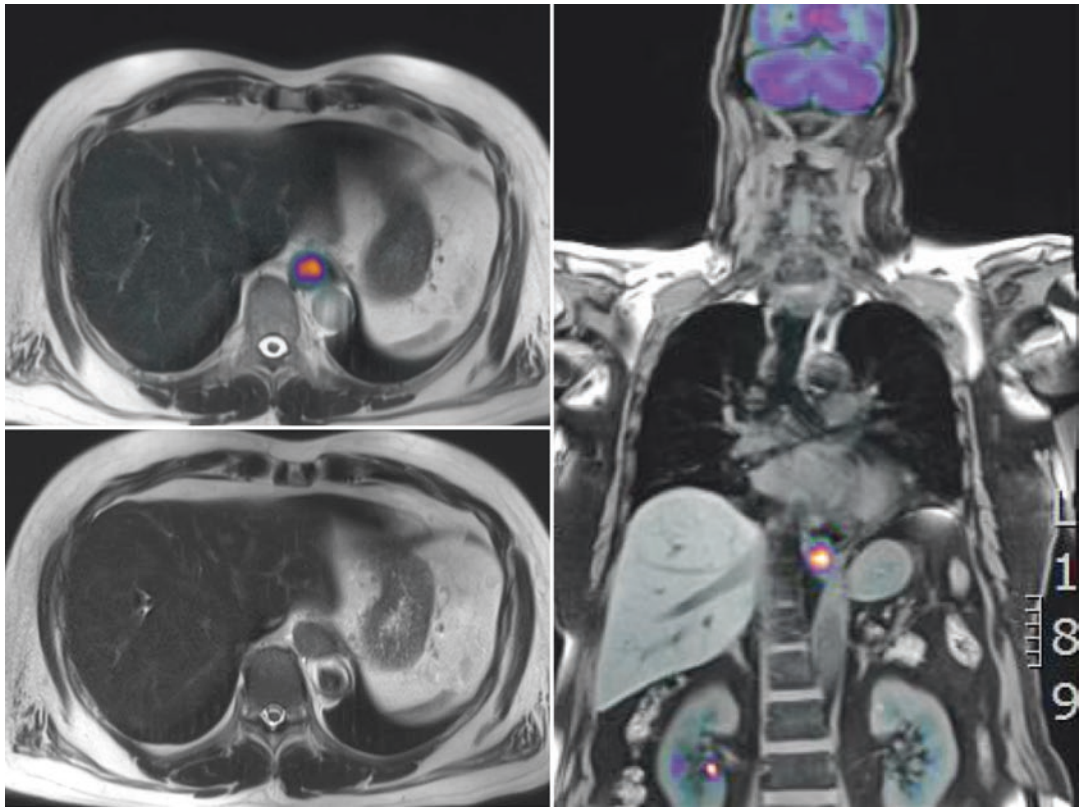

**Fig. 3.14** PET/MR study in an oesophageal cancer patient. The MRI allows a clear definition and visualization of the peri-oesophageal fat, including two tiny non-FDG-avid nodes. Coronal view allows to identify the correct extension, and hence to plan correctly the extension of radiotherapy field

detection of metastatic and nodal disease that may not have been identified with other modalities; the accuracy of the preoperative staging therefore prevents inappropriate surgery (Figs. 3.13 and 3.14).

In two meta-analyses published in 2004 and 2008, the pooled sensitivity and specificity of FDG-PET for the detection of distant metastases were 67% and 97% [35], and 71% and 93% [36], respectively. FDG-PET findings led to a significant change in patient management in about one-third of the patients in this indication, as reported by recently published data of the Australian group (ASCO Annual Meeting Proceedings Part I Journal of Clinical Oncology, 25 (2007)).

Therefore, a diagnostic strategy including EUS, CT and FDG-PET/CT allows a more accurate initial staging of oesophageal cancer. The impact on decision-making is crucial in order to discriminate patients who are candidates for surgery, or exclusive chemoradiotherapy (CRT) with curative intent, from patients with metastatic disease, for whom a local treatment is not feasible. Thus, FDG-PET/CT is recommended in non-metastatic oesophageal cancer, a condition for which its use is likely to change the therapeutic strategy.

Several studies have also suggested a predictive value of metabolic changes for assessing early response to chemoradiotherapy (CRT) and prognosis of patients with locally advanced oesophageal cancer, but their results vary according to the metabolic parameter considered. For example Cuenca et al. recently analysed a mixed population of SCC and ADK with a large majority of SCC (41 vs. 18), and reported that a decrease greater than 50% in $SUV_{max}$ 5 weeks after CRT induction was correlated with survival [37].

The conventional imaging techniques (CT, MRI and EUS) are frequently unable to differentiate between residual disease and post-therapy changes and often there may be a delay before which the therapy response can be adequately assessed. This is another scenario where functional imaging (specifically PET) can differentiate, at an earlier phase, residual disease from post-therapy change. This will avoid the delay, during which time the disease may theoretically be upstaged but also provide definitive management for the anxious patient.

## 3.11 Non-oncological Application

FDG-PET is increasingly used for non-oncological applications. It has become a valuable tool in the diagnosis, treatment response and follow-up of patients with thoracic disease and a variety of inflammatory or infective disorders [38]. In this section we focus on the non-oncological applications of PET imaging.

### 3.11.1 Tuberculosis

TB remains a widespread important health problem and in primary TB chest radiography and CT remain the mainstay of imaging diagnosis. In complex cases such as post-primary infection, extrapulmonary infection and spondylitis and poor treatment response, MR and FDG-PET-CT are useful problem-solving tools [39] (Fig. 3.15).

It has been reported that $^{18}$F-FDG-PET is able to differentiate active TB from old or inactive disease, as active tuberculoma has significantly higher $SUV_{max}$ values compared with inactive tuberculoma [40]. When a $SUV_{max}$ of 1.05 (at 60 min) was used as the cut-off, the sensitivity and specificity were 100% and 100%, respectively. The authors showed that patients with old healed TB lesions with a higher $SUV_{max}$ may be at higher risk of active TB. Further investigation is needed to confirm these results.

The evaluation of monitoring response is probably the most important clinical application of $^{18}$F-FDG-PET/CT in TB. During anti-TB treatment, some bacillus-negative tuberculomas do not decrease in size and may even increase, making it difficult for the physician to decide whether or not to modify treatment. In these cases, $^{18}$F-FDG-PET/CT imaging may help, as the changes in glycolytic activity within the inflammatory lesion, measured by $^{18}$F-FDG uptake, correlate well with the clinical markers of response. Several studies have confirmed the value of $^{18}$F-FDG-PET/CT in the follow-up and evaluation of the treatment response, especially in patients with extrapulmonary involvement and when drug resistance is prevalent. In pulmonary and extrapulmonary TB, a decrease of approxi-

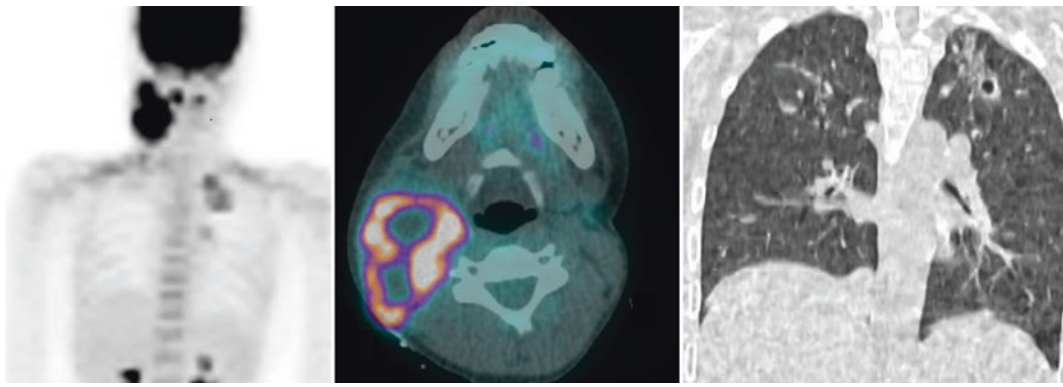

**Fig. 3.15** Coronal MIP showing FDG uptake of cavitating parenchymal changes in the left apex in addition to necrotic right cervical and lymphadenopathy. This was proven to be TB on biopsy

mately one-third in $SUV_{max}$ has been reported after 1 month of anti-TB treatment when there is a good response [41].

After 4 months of anti-TB treatment $^{18}$F-FDG-PET/CT can also evaluate the treatment response in patients with high sensitivity and specificity, using the value of 4.5 as the $SUV_{max}$ cut-off [42].

### 3.11.2 Skeletal Infection

Osteomyelitis refers to inflammation of bone secondary to infection which may be bacterial, fungal or mycobacterial in origin. Early diagnosis is essential to initiate early antimicrobial therapy and therefore prevent further tissue destruction and improve patient outcome. The diagnosis of acute osteomyelitis is made based on clinical assessment and biochemical markers of infection and imaging. There is a delay of approximately 2–3 weeks before any visible change occurs on plain radiographs. As a result functional imaging with conventional nuclear medicine scintigraphy, mainly three-phase bone scanning ($^{99}$m Technetium) or radiolabeled white blood cell imaging, has been and is currently being used which also demonstrates high sensitivity; bone scintigraphy can effectively detect osteomyelitis within 24 h of symptom onset. However the diagnosis of chronic osteomyelitis (symptoms > 6 weeks) or recurrence is difficult by physical examination and challenging by means of anatomical or conventional nuclear medicine imaging, particularly if there is pre-existing change to the osseous structures. FDG-PET is highly sensitive for detecting chronic osteomyelitis particularly within the axial skeleton [43]. Spondylodiscitis refers to infection of the intervertebral disc and adjacent vertebrae and MRI is the mainstay modality for diagnosis because of its ability to demonstrate changes in water content as well as excellent structural definition and spatial resolution. However metallic implants can produce local artefacts which decrease image quality and produce an inconclusive result. FDG-PET CT imaging is less affected by metallic artefacts and therefore patients with past spinal fixation devices can benefit from this modality as well as patients who have contraindications to MR imaging. Furthermore FDG-PET is particularly of use in the assessment of the postoperative spine; in MRI inflammatory changes can be seen long after the disappearance of the infection and certainly in this scenario FDG-PET is superior to MRI. Indeed one of the unmet clinical needs in the evaluation of skeletal infection is the assessment of response to therapy in chronic disease, to differentiate granulomatous tissue and fibrosis from active inflammation. FDG-PET has shown a central role for this assessment and particularly for patient's management (antibiotic therapy, or surgical intervention). Ito et al. on a cohort of 29 patients found that clinical management changed on 52% (15 of 29) of the patients allowing to extend the therapeutic period in some patients and to decide the biopsy sites in other patients [44] (Fig. 3.16).

### 3.11.3 Immunodeficiency

Immunocompromised patients can present with a wide range of atypical infections. The difficulty for clinicians is identifying the type of organisms and the extent of disease. There are a wide variety of atypical pulmonary infections which include fungal infections such as Aspergillosis or Coccidioidomycosis as well as mycobacterial infections [45]. Clinical, biochemical and haematological assessment is limited and anatomical imaging has a central role in identifying the cause. However this can be indeterminate particularly in patients with a background of lung disease. FDG-PET can provide a functional assessment of any suspicious areas, identifying the avidity which a biopsy would most likely yield the diagnosis (Fig. 3.17). Once the underlying disease has been identified, treatment of atypical infections involves prolonged antimicrobial therapy, the specific length being guided by clinical assessment of the patient but importantly the progression or improvement of the disease on imaging, which may be inconclusive. In this scenario of therapy assessment FDG-PET is particularly valuable; the presence of sustained disease will demonstrate avidity and therefore the

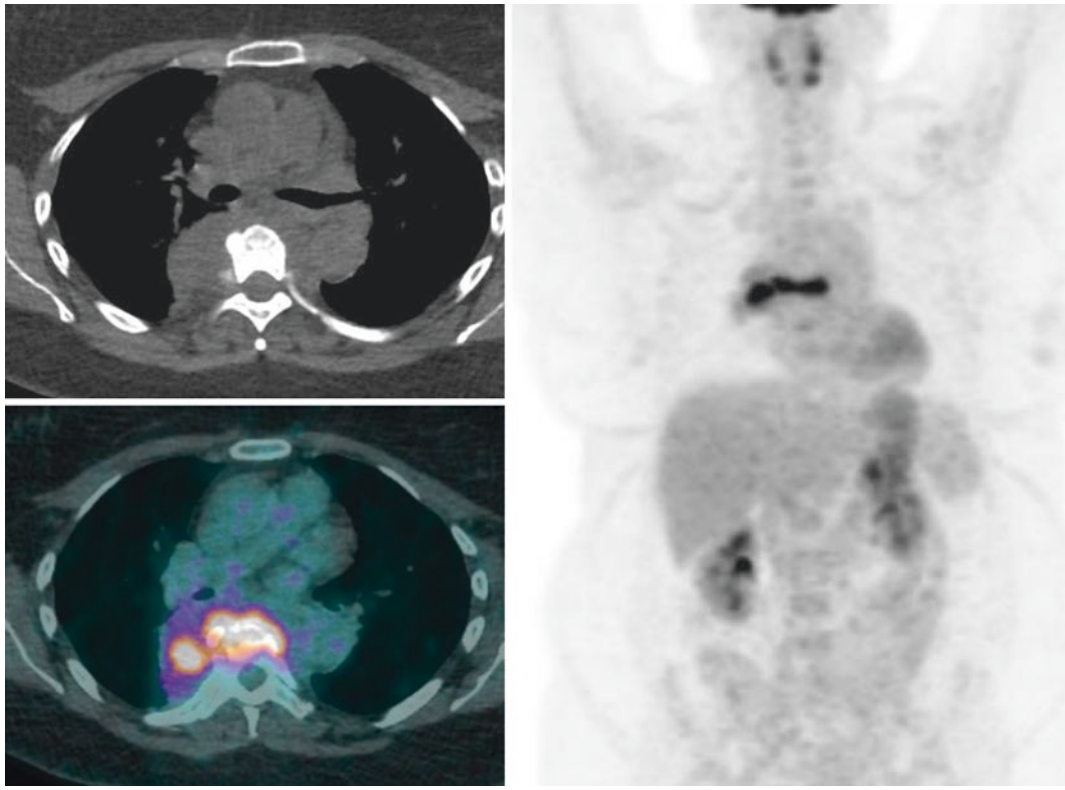

**Fig. 3.16** T6/T7 discitis with prevertebral collection extending in the right lower lobe which appears collapsed

requirement for further therapy. FDG-PET has an established role in treating complications in patients with HIV [46] or immunocompromise secondary to treatment with chemotherapy. FDG-PET can also be useful in diagnosis, response and complication monitoring in a number of rare primary specific immunodeficiency disease patients, of which common variable immune deficiency (CVID) is the most common. Patients with CVID are at higher risk of developing lymphoma or granulomatous lymphocytic interstitial lung disease. FDG-PET provides a hybrid technique that allows whole-body anatomical and metabolic assessment, with disease distribution and biopsy targeting improving diagnostic sensitivity.

## 3.12 Vasculitis

Vasculitis encompasses a large group of disorders characterized by blood vessel inflammation. There are many different methods for disease classification one of which, based on the size of vessels, divides the disease into small, medium and large vessel disease. Patients with clinical suspicion of vasculitis generally present with nonspecific symptoms and elevated inflammatory markers. In order to obtain a definitive diagnosis, patients may require vessel biopsy which is invasive and a repeat may be required if the initial biopsy is inconclusive. The pattern of changes on imaging may be suggestive and even more so on FDG-PET-CT. Early diagnosis is essential in order to initiate medical treatment early to prevent complications and possible need for surgical intervention. As a result there is an increasing role for the use of PET to aid in diagnosis of patients suspected of large-vessel vasculitis (LVV): giant-cell arteritis (GCA) and Takayasu arteritis (TA) [47]. FDG accumulates in the activated inflammatory cells due to overexpression of glucose transporters and overproduction of glycolytic enzymes. As a result, areas of inflamed vessels will demonstrate avidity and

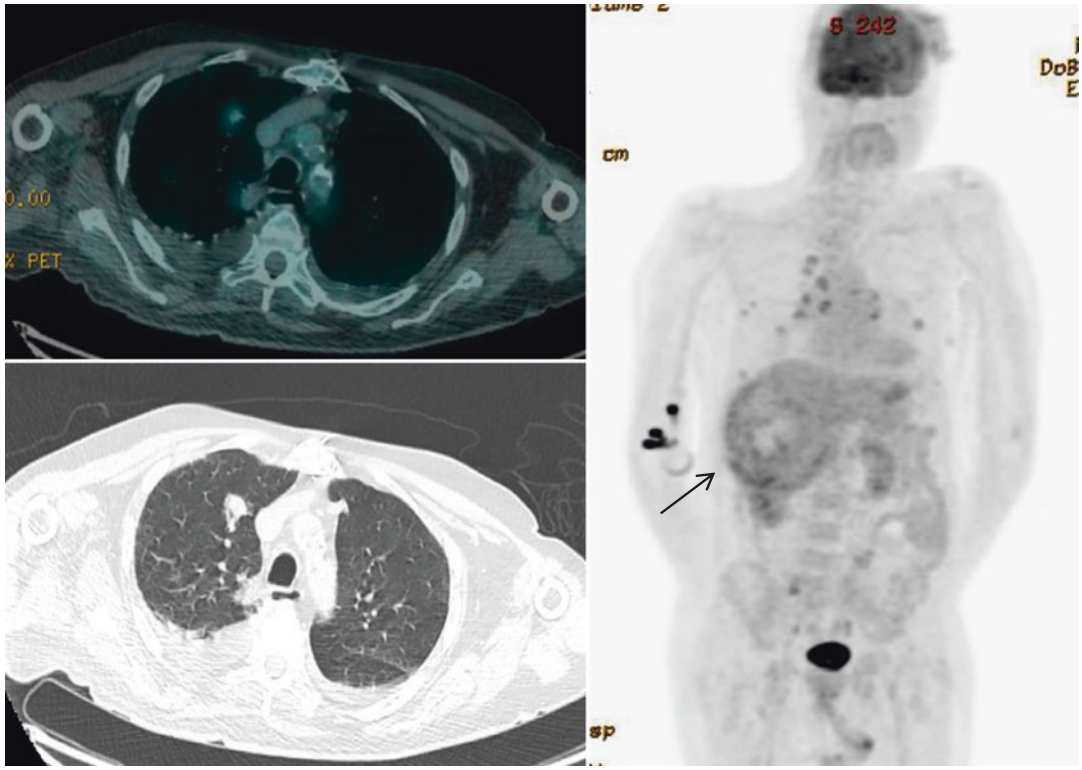


**Fig. 3.17** MIP image shows multiple hyper-metabolic foci in both lungs and an inhomogeneous appearance of the liver (arrow). Single section fused PET/CT slice and corresponding-level CT confirm the presence of several mildly FDG-avid nodules consistent with fungal infection in a patient with a large hepatic abscess

determine the extent and distribution of disease. This may also aid clinicians to identify the area which is most likely to lead to a positive biopsy (Figs. 3.18 and 3.19).

Furthermore $SUV_{max}$ values obtained from PET studies are positively associated with inflammatory markers (CRP and ESR). This supports the assumption that FDG-PET activity mirrors that of disease activity; hence FDG-PET can be conducted to monitor response to therapy [48]. As a result the use of PET CT is recommended in patients with large-vessel vasculitis where conventional investigations are inconclusive and patient treatment will be altered if ongoing inflammation is confirmed [48, 49]. Over the last years, the diagnostic accuracy and clinical relevance of FDG-PET/CT in vasculitis have been studied by several groups. Recently, two meta-analyses were published on the diagnostic performance of FDG-PET. Lee et al. included eight studies with a total of 400 patients including 230 subjects as controls for further analysis and they reported a sensitivity of 75.9% and a specificity of 93.0% [50]. In another meta-analysis, published by Soussan et al. [51] in 2015, 21 studies were included and the systematic review included 413 cases of LVV, with 127 cases of GCA, 197 cases of TA and 89 cases with LVV in which no discrimination between GCA and TA could be made because of a lack of sufficient data. The control group included 299 patients with different indications to undergo an FDG-PET scan (oncologic, infections, etc.). FDG-PET was able to detect a vascular arterial uptake in 70% (288/413) of patients with GCA/TA and 7% (22/299) of controls. Interestingly, in 87% (110 out of 127 patients) of patients suffering from GCA vascular arterial uptake was detected, which was a significantly higher detection rate compared to TA patients (58%, 114 out of 197

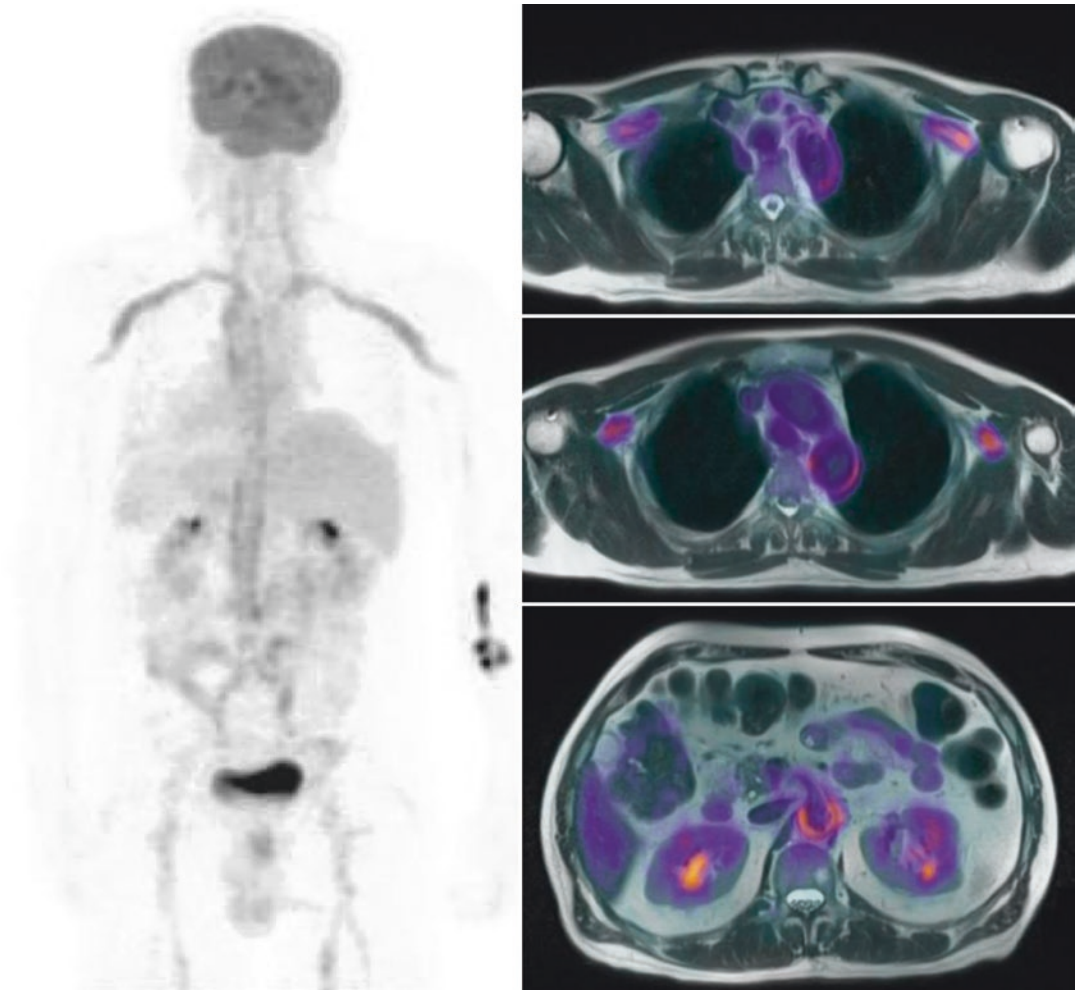

**Fig. 3.18** The FDG-PET/MR demonstrates increased tracer uptake throughout the larger arteries including the aorta, subclavian, and carotid arteries of a patient with large-vessel vasculitis

patients). Using the liver as a reference for visual analysis of the vascular FDG uptake, only moderate and high uptake (≥ the liver uptake) showed a significant higher frequency in GCA/TA patient compared to controls (84% vs. 18%, $P < 0.001$), whereas a considerably high number of 45% of the control subjects were identified with a slight uptake (<the liver uptake). This needs to be considered carefully and suggests that a slight vascular FDG uptake should most likely not to be considered as indicative of pathological changes.

In conclusion, although there is still insufficient literature for FDG-PET to be described as an evidence-based indication in vasculitis, we can conclude, on the basis of a cumulated reported accuracy (>85%) and expert opinion, that $^{18}$F-FDG-PET/CT is a valid tool for the primary evaluation of vasculitides.

## 3.13 Sarcoidosis

Sarcoidosis is a chronic multisystem granulomatous disease of unknown aetiology. The disease most commonly affects the lungs and lymph nodes but may disseminate to involve other viscera such as the liver, heart or brain. It may be

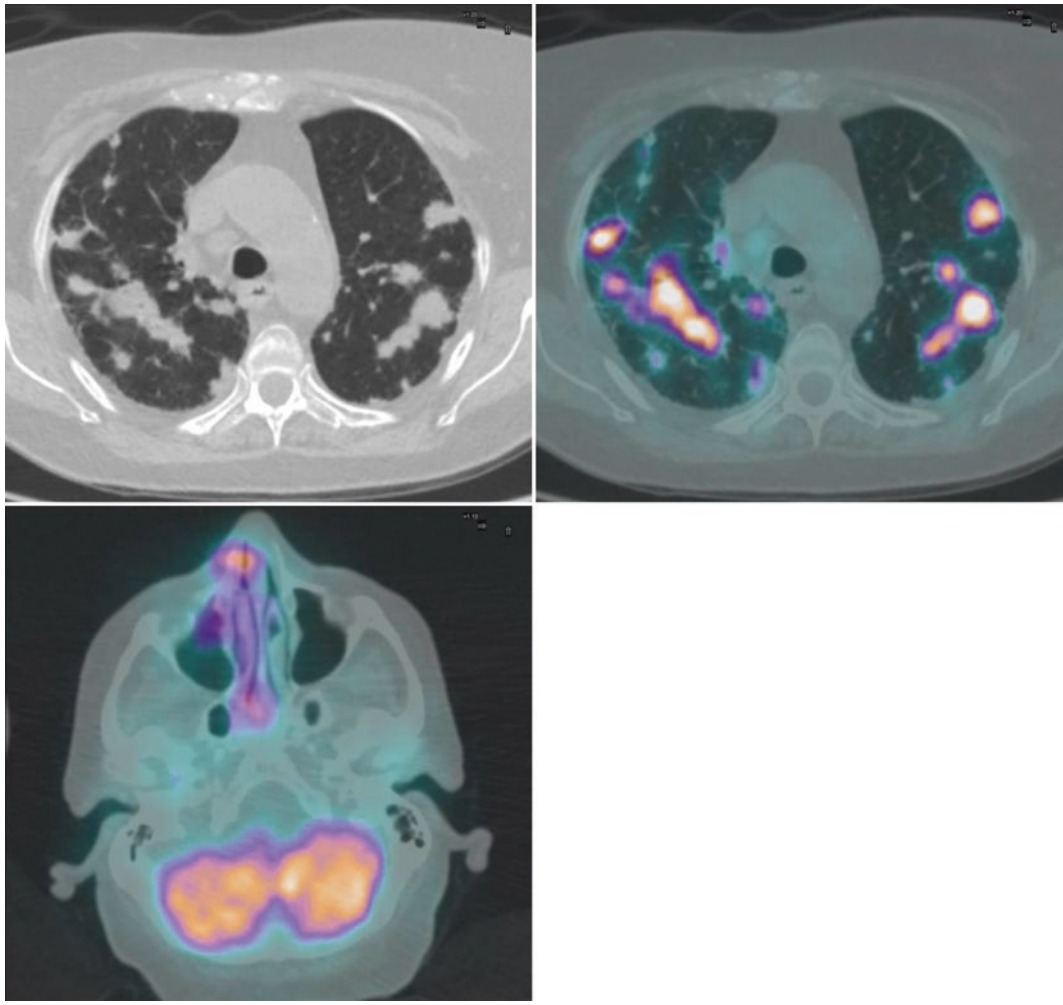

**Fig. 3.19** Axial CT and fused FDG-PET/CT showing multiple avid lung nodules. FDG uptake in the postnasal space and ethmoid sinuses. The patient had presented with query lung metastases, but the distribution of FDG-avid disease on PET/CT raised the suspicion of Wegner's granulomatosis which was subsequently proven on biopsy

asymptomatic or present with symptoms related to the organs involved. The diagnostic workup generally involves serological inflammatory marker analysis and high-resolution chest CT from which, based on the typical imaging features, the diagnosis can often be made without biopsy. Although PET is not the first-line diagnostic technique it is a valuable tool in a select group of patients who have more extensive or atypical disease and represent diagnostic uncertainty [52]. Although invasive, histological diagnosis can be made using bronchoscopy with trans-bronchial biopsy and bronchoalveolar lavage. When this provides insufficient evidence for diagnosis, PET can reveal a suitable location for biopsy to obtain a positive histological sample (Figs. 3.20 and 3.21).

Suspected cardiac sarcoidosis carries high risk of major cardiac events and detection is important for prognosis. Specific heart protocols involve carbohydrate exclusion and high-protein and -fat diets before fasting to switch the myocardium from glucose to free fatty acid metabolism and suppress physiological FDG uptake. An intravenous bolus injection of unfractionated heparin 15 min before FDG also promotes this

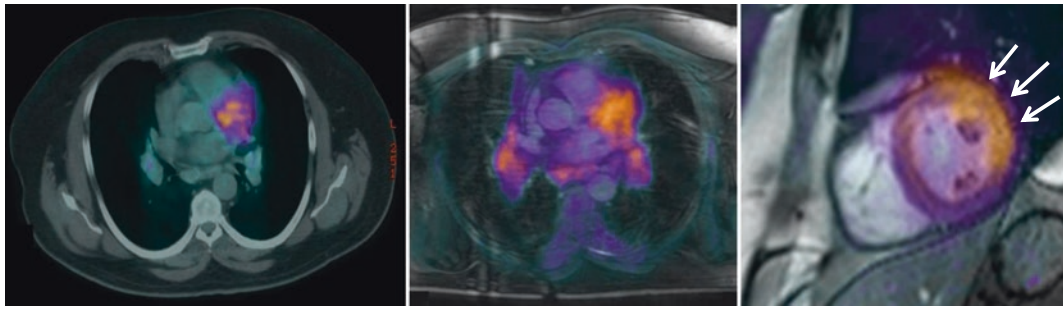

**Fig. 3.20** Sarcoidosis with bilateral hilar adenopathy. FDG-PET demonstrates avid uptake in the myocardium secondary to cardiac sarcoid, most clearly demonstrated by fused PET/MR (arrows)

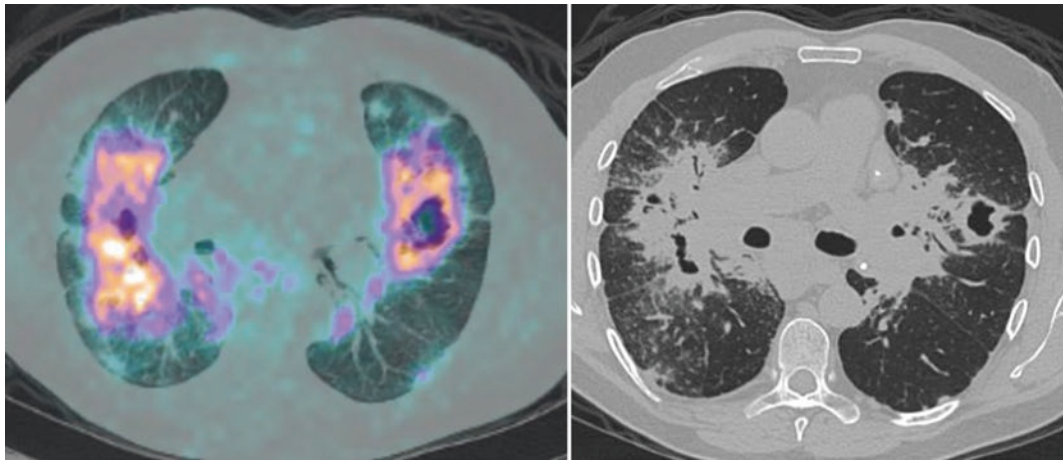

**Fig. 3.21** Increased metabolic activity in the bilateral perihilar consolidative changes and FDG-avid lymphadenopathy is compatible with sarcoidosis

effect. As a result of suppression of normal physiological myocardial uptake, true myocardial inflammation can be demonstrated, with fasting cardiac PET being as, or more, sensitive as MR for detection of myocardial imflammation. Sarcoidosis may affect lymph nodes and a variety of viscera and as such can mimic any number of differential diagnoses including infection (particularly TB), lymphoma, diffuse metastatic disease, inhalation/hypersensitivity pneumonitis, Wegener granulomatosis and local sarcoid reactions. To complicate matters further, there is an association between sarcoidosis and lymphoproliferative disease which makes accurate diagnosis a challenge for conventional imaging techniques. Following diagnosis and instigation of treatment, patients may demonstrate persistent disabling symptoms in the absence of serological signs of inflammatory activity. In this group of patients PET is recommended to assess the level of disease response [53]. This is particularly true when patients have radiographic signs of lung fibrosis. Here, the presence of avidity on PET will provide valuable information for clinicians of continued disease activity.

## 3.14 Future Developments

Hybrid imaging, and particularly PET-CT, is at the centre of a remarkable period of development. PET can be fused with both CT and MR

and therefore combine with the new techniques being developed in both modalities. This includes low-dose CT gating allowing cine imaging to match gated PET, dual-energy or spectral CT allowing better tissue characterisation and metal artefact suppression. PET developments include new tracers, for example tracers for angiogenesis and hypoxia, and faster more sensitive scanners that allow practical multi-time-point scanning and ultimately kinetics that may provide the key to improving FDG specificity.

### Conclusion

PET is at the forefront of developments in molecular imaging. New tracers, kinetic methods and combinations with other techniques all provide tools for improving imaging pathophysiology.

FDG-PET is integral to assessment in several cancers including lung and lymphoma, and is increasingly used as a problem-solving tool in other cancers, particularly for assessing response and recurrence.

Non-oncological applications of FDG-PET are increasing, particularly in infection and inflammation.

PET tracers other than FDG open the possibility for imaging biomarkers to assess different facets of pathophysiology.

**Acknowledgments** Thanks to Dr. Leon Menezes for the cardiac sarcoid case, and to Dr. Ben Thomas and Dr. Trine Hjørnevik for commenting on the physics and technical part of the manuscript.

## References

1. Cherry SR, Sorenson JA, Phelps ME. Physics in nuclear medicine. 4th ed. Amsterdam: Elsevier; 2012.
2. Conti M, Eriksson L. Physics of pure and non-pure positron emitters for PET: a review and a discussion. EJNMMI Phys. 2016;3:8.
3. Fraioli F, Punwani S. Clinical and research applications of simultaneous positron emission tomography and MRI. Br J Radiol. 2014;87(1033):20130464.
4. Kinahan PE, Fletcher JW, et al. PET/CT standardized uptake values (SUVs) in clinical practice and assessing response to therapy. Semin Ultrasound CT MR. 2010;31(6):496–505. https://doi.org/10.1053/j.sult.2010.10.001.
5. Scarsbrook A, Barrington S. Evidence-based indications for the use of PET-CT in the United Kingdom 2016. Royal college of radiologists. 2016. https://www.rcr.ac.uk/publication/evidence-based-indications-use-pet-ct-united-kingdom-2016. Accessed 3 April 2017.
6. Gupta NC, Maloof J, Gunel E. Probability of malignancy in solitary pulmonary nodules using fluorine-18-FDG and PET. J Nucl Med. 1996;37(6):943–8.
7. Inoue T, Kim EE, Komaki R, et al. Detecting recurrent or residual lung cancer with FDG-PET. J Nucl Med. 1995;36(5):788–93.
8. Ruilong Z, Daohai X, Li G, et al. Diagnostic value of 18F-FDG-PET/CT for the evaluation of solitary pulmonary nodules: a systematic review and meta-analysis. Nucl Med Commun. 2017;38(1):67–75.
9. Yilmaz F, Tastekin G. Sensitivity of (18)F-FDG PET in evaluation of solitary pulmonary nodules. Int J Clin Exp Med. 2015;8(1):45–51. eCollection 2015.
10. Boellaard R, Delgado-Bolton R, Oyen WJG, et al. FDG PET/CT: EANM procedure guidelines for tumour imaging: version 2.0. Eur J Nucl Med Mol Imaging. 2015;42:328–54. https://doi.org/10.1007/s00259-014-2961-x.
11. Novello S, Barlesi F, Califano R, Cufer T, Ekman S, Giaj Levra M, Kerr K, Popat S, Reck M, Senan S, Simo GV, Vansteenkiste J, Peters S. Metastatic non-small-cell lung cancer: ESMO Clinical Practice Guidelines. 2016. www.esmo.org/Guidelines/Lung-and-Chest-Tumours. Accessed 10 May 2017.
12. Dwamena BA, Sonnad SS, Angobaldo JO, Wahl RL. Metastases from non-small cell lung cancer: mediastinal staging in the 1990s—meta-analytic comparison of PET and CT. Radiology. 1999;213(2):530–6.
13. Akhurst T, Downey RJ, Ginsberg MS, et al. An initial experience with FDG-PET in the imaging of residual disease after induction therapy for lung. Cancer. Ann Thorac Surg. 2002;73(1):259–64.
14. Chopra A, Ford A, De Noronha R, Matthews S. Incidental findings on positron emission tomography/CT scans performed in the investigation of lung cancer. Br J Radiol. 2012;85(1015):e229–37. https://doi.org/10.1259/bjr/60606623.
15. Lee SM, Goo JM, Park CM, et al. Preoperative staging of non-small cell lung cancer: prospective comparison of PET/MR and PET/CT. Eur Radiol. 2016;26(11):3850–7.
16. Marom EM, McAdams HP, Erasmus JJ, et al. Staging non-small cell lung cancer with whole-body PET. Radiology. 1999;212(3):803–9.
17. Hellwig D, Ukena D, Paulsen F, et al. Meta-analysis of the efficacy of positron emission tomography with F-18-fluorodeoxyglucose in lung tumors. Basis for discussion of the German consensus conference on PET in oncology 2000. Pneumologie. 2001;55(8):367–77.
18. Sheikhbahaei S, Mena E, Yanamadala A, Reddy S, Solnes LB, Wachsmann J, Subramaniam RM. The

value of FDG PET/CT in treatment response assessment, follow-up, and surveillance of lung cancer. Am J Roentgenol. 2017;208:420–33. https://doi.org/10.2214/AJR.16.16532.
19. Fraioli F, Kayani I, Smith L-J, et al. Positive 18F Fluorodeoxyglucose-positron emission tomography/computer tomography predicts Preinvasive Endobronchial lesion progression to invasive cancer. Am J Respir Crit Care Med. 2016;193:576–9.
20. Weller A, O'Brien MER, Ahmed M. Mechanisms and non-mechanism based imaging biomarkers for assessing biological response to treatment in non-small cell lung cancer. Eur J Cancer. 2016;59:65–78.
21. Kalemkerian GP. Staging and imaging of small cell lung cancer. Cancer Imaging. 2011;11(1):253–8.
22. Bodei L, Sundin A, Kidd M, Prasad V, Modlin IM. The status of neuroendocrine tumor imaging: from darkness to light? Neuroendocrinology. 2015;101:1–17. https://doi.org/10.1159/000367850.
23. Caplin ME, Baudin E, Ferolla P, et al. Pulmonary neuroendocrine (carcinoid) tumors: European neuroendocrine tumor society expert consensus and recommendations for best practice for typical and atypical pulmonary carcinoids. Ann Oncol. 2015;26(8):1604–20. https://doi.org/10.1093/annonc/mdv041.
24. Deppen SA, Blume J, Bobbey A, et al. 68Ga-DOTATATE compared with 111In-DTPA-octreotide and conventional imaging for pulmonary and gastroenteropancreatic neuroendocrine tumors: a systematic review and meta-analysis. J Nucl Med. 2016;57(6):872–8.
25. Barrington SF, Mikhaeel NG, Kostakoglu L, et al. Role of imaging in the staging and response assessment of lymphoma: consensus of the international conference on malignant lymphomas imaging working group. J Clin Oncol. 2014;32(27):3048–58. https://doi.org/10.1200/JCO.2013.53.5229.
26. Cheson BD, Ansell S, Schwartz L, Gordon LI, Advani R, Jacene HA, Hoos A, Barrington SF, Armand P. Refinement of the Lugano classification response criteria for lymphoma in the era of immunomodulatory therapy. 2016. www.bloodjournal.org/content/early/.../blood-2016-05-718528. Accessed 10 May 2017.
27. Baas P, Dl F, Kerr KM, Van Schil PE, Haas RL, Peter S. Malignant pleural mesothelioma: ESMO clinical practice guidelines. Ann Oncol. 2015;26(5):v31–9. https://doi.org/10.1093/annonc/mdv199.
28. Kruse M, Sherry SJ, Paidpally V, Mercier G, Subramaniam RM. FDG PET/CT in the management of primary pleural tumors and pleural metastases. AJR Am J Roentgenol. 2013;201(2):W215–26. https://doi.org/10.2214/AJR.13.10572. Review.
29. Erasmus JJ, Truong MT, Smythe WR, et al. Integrated computed tomography-positron emission tomography in patients with potentially resectable malignant pleural mesothelioma: staging implications. J Thorac Cardiovasc Surg. 2005;129(6):1364–70.
30. Plathow C, Staab A, Schmaehl A, et al. Computed tomography, positron emission tomography, positron emission tomography/computed tomography, and magnetic resonance imaging for staging of limited pleural mesothelioma: initial results. Investig Radiol. 2008;43(10):737–44. https://doi.org/10.1097/RLI.0b013e3181817b3d.
31. Basu S, Saboury B, Torigian DA, Alavi A. Current evidence base of FDG-PET/CT imaging in the clinical management of malignant pleural mesothelioma: emerging significance of image segmentation and global disease assessment. Mol Imaging Biol. 2011;13(5):801–11. https://doi.org/10.1007/s11307-010-0426-6.
32. Carretta A, Landoni C, Melloni G, Ceresoli GL, et al. P.18-FDG positron emission tomography in the evaluation of malignant pleural diseases - a pilot study. Eur J Cardiothorac Surg. 2000;17(4):377–83.
33. Sung YM, Lee KS, Kim BT, Choi JY, Shim YM, Yi CA. 18F-FDG PET/CT of thymic epithelial tumors: usefulness for distinguishing and staging tumor subgroups. J Nucl Med. 2006;47(10):1628–34.
34. Lordick F, Mariette C, Haustermans K, Obermannová R, Arnold D. Oesophageal cancer: ESMO clinical practice guidelines for diagnosis, treatment and follow-up. Ann Oncol. 2016;27(5):v50–7. https://doi.org/10.1093/annonc/mdw329.
35. van Westreenen HL, Westerterp M, Bossuyt PM, et al. Systematic review of the staging performance of18F-fluorodeoxyglucose positron emission tomography in esophageal cancer. J Clin Oncol. 2004;22(18):3805–12. Review.
36. Van Vliet EP, Heijenbrok-Kal MH, Hunink MG, et al. Staging investigations for oesophageal cancer: a meta-analysis. Br J Cancer. 2008;98(3):547–57. https://doi.org/10.1038/sj.bjc.6604200.
37. Cuenca X, Hennequin C, Hindié E, Rivera S, et al. Evaluation of early response to concomitant chemoradiotherapy by interim 18F-FDG PET/CT imaging in patients with locally advanced oesophageal carcinomas. Eur J Nucl Med Mol Imaging. 2013;40(4):477–85. https://doi.org/10.1007/s00259-012-2325-3.
38. Love C, Tomas MB, Tronco GG, Palestro CJ. FDG PET of infection and inflammation. Radiographics. 2005;25(5):1357–68.
39. Skoura E, Zumla A, Bomanji J. Imaging in tuberculosis. Int J Infect Dis. 2015;32:87–93.
40. Kim IJ, Lee JS, Kim SJ, Kim YK. Double-phase 18F-FDG PET-CT for determination of pulmonary tuberculoma activity. Eur J Nucl Med Mol Imaging. 2008;35(4):808–14.
41. Martinez V, Castilla-Lievre MA, Guillet-Caruba C, Grenier G. (18)F-FDG PET/CT in tuberculosis: an early non-invasive marker of therapeutic response. Int J Tuberc Lung Dis. 2012;16(9):1180–5. https://doi.org/10.5588/ijtld.12.0010.
42. Sathekge M, Maes A, D'Asseler Y, Vorster M, et al. Tuberculous lymphadenitis: FDG PET and CT findings in responsive and nonresponsive disease. Eur J Nucl Med Mol Imaging. 2012;39(7):1184–90. https://doi.org/10.1007/s00259-012-2115-y.
43. Pineda C, Espinosa R, Pena A. Radiographic imaging in osteomyelitis: the role of plain radiography, computed tomography, ultrasonography, magnetic reso-

nance imaging and scintigraphy. Semin Plast Surg. 2009;23(2):80–9.
44. Ito K, Kubota K, Morooka M, Hasuo K, et al. Clinical impact of (18)F-FDG PET/CT on the management and diagnosis of infectious spondylitis. Nucl Med Commun. 2010;31(8):691–8. https://doi.org/10.1097/MNM.0b013e32833bb25d.
45. Sharma P, Mukherjee A, Karunanithi S, Bal C, Kumar R. Potential role of 18F-FDG PET/CT in patients with fungal infections. Am J Roentgenol. 2014;203:180–9.
46. Davison JM, Subramaniam RM, Surasi DS, et al. FDG PET/CT in patients with HIV. Am J Roentgenol. 2011;197:284–94.
47. Balink H, Bennink RJ, van Eck-Smit BLF, Verberne HJ. The role of 18F-FGD PET/CT in large vessel vasculitis: appropriateness of current classification criteria? Biomed Res Int. 2014;2014:687608. https://doi.org/10.1155/2014/687608.
48. Papathanasiou ND, Du Y, Menezes LJ, Almuhaideb A, Shastry M, Beynon H, Bomanji JB. 18FFludeoxyglucose PET/CT in the evaluation of large-vessel vasculitis: diagnostic performance and correlation with clinical and laboratory parameters. Br J Radiol. 2012;85(1014):e188–94.
49. Bucerius J. Monitoring Vasculitis with 18F-FDG PET. QJ Nucl Med Mol Imaging. 2016;60(3):219–35.
50. Lee YH, Choi SJ, Ji JD, Song GG. Diagnostic accuracy of 18F-FDG PET or PET/CT for large vessel vasculitis: a meta-analysis. Z Rheumatol. 2016;75(9):924–31. Review.
51. Soussan M, Nicolas P, Schramm C, Katsahian S, Pop G, Fain O, Mekinian A. Management of large-vessel vasculitis with FDG-PET: a systematic literature review and meta-analysis. Medicine (Baltimore). 2015;94(14):e622. https://doi.org/10.1097/MD.0000000000000622.
52. Prabhakar HB, Rabinowitz CB, Gibbons FK, O'Donnell WJ, Shepard J-AO, Aquino SL. Imaging features of sarcoidosis on MDCT, FDG PET, and PET/CT. Am J Roentgenol. 2008;190:S1–6.
53. Mostard RL, van Kroonenburgh MJ, Drent M. The role of the PET scan in the management of sarcoidosis. Curr Opin Pulm Med. 2013;19(5):538–44.

# MRI

4

Angelo Iannarelli, Stefano Badia, and Marco Rengo

**Abstract**

Among the modalities for chest imaging such as X-ray and computed tomography (CT), magnetic resonance imaging (MRI) has been the latest to be introduced into clinical practice.

It is emerging as a valuable alternative when radiation exposure or iodinated contrast material is contraindicated such as in the case of pediatric patients affected by cystic fibrosis or acute pulmonary embolism in pregnant women because it gives additional functional information on respiratory mechanics and regional lung perfusion.

Unlike CT and PET-TC, MRI has superior soft-tissue contrast with high spatial resolution but it is more susceptible to cardiac and respiratory motion artifacts; however recent advances in MRI techniques like diffusion-weighted, perfusion sequences and use of new contrast media have improved the diagnostic capabilities of MRI in detecting and staging lung cancer providing not only morphologic but also functional information.

Another peculiarity of this technique is considered to be the gold standard also for the evaluation of the pleural interface, characterization of complex pleural effusion, and identification of exudate and hemorrhage, as well as in the analysis of superior sulcus tumors, as it enables more accurate staging.

Unfortunately, MRI of the chest is still rarely used, except in a few centers, due to lack of consistent protocols customized to clinical needs.

**Keywords**

Magnetic resonance imaging · Chest · Pulmonary lesions · Diffusion-weighted imaging · Apparent diffusion coefficient · Cystic fibrosis · Central lung carcinoma · Pleural disease · Pulmonary embolism · Airway disease · Functional imaging

## 4.1 Advantages and Limits of Chest MRI

Magnetic resonance imaging (MRI) is considered the most fascinating and innovative imaging technique and it is emerging as a valuable alternative to chest computed tomography (CT) and chest plain film. In fact, MRI offers both

A. Iannarelli
Department of Radiological, Oncological and Pathological Sciences, University of Rome "Sapienza"—Rome, Rome, Italy

S. Badia · M. Rengo (✉)
Department of Radiological, Oncological and Pathological Sciences, University of Rome "Sapienza"—Polo Pontino, Latina, Italy
e-mail: marco.rengo@uniroma1.it


M. Anzidei, M. Anile (eds.), *Diagnostic Imaging for Thoracic Surgery*,
https://doi.org/10.1007/978-3-319-89893-3_4

morphological and functional details in a single examination, without any radiation exposure to the patient. Furthermore, in the latest 10 years MRI has enjoyed a great technological development both in the hardware and software field.

The long acquisition times and the high rate of motion artifacts have limited the spread of this technique, especially in chest imaging. However, a good accuracy is reported in the evaluation of posterior chest wall and thoracic outlet, both relative static locations, by using standard turbo-spin-echo (TSE) sequences. On the contrary, the main issue in chest imaging is the continuous motion in the anterior and lower sections, where heart pulsation and respiratory cycle movements are most prominent. Most recent advances, such as parallel imaging, have led to an increase of temporal resolution allowing to scan the entire chest in a single breath-hold sequence, with very short echo times (for example T2 half-Fourier acquisition single-shot turbo spin echo or ultra-fast turbo spin echo); this technique allows to overcome both cardiac pulsation and respiratory motion but their disadvantage is lower spatial resolution and signal-to-noise ratio (SNR).

With recent advances in gradient system and power amplifier technology, gradient-recalled echo (GRE) sequences have become fast and robust. One type of fast GRE sequence is a steady-state sequence with non-spoiled magnetization, in which longitudinal magnetization and transverse magnetization are kept constant with each cycle. Steady-state sequences have proved useful in a variety of applications, including imaging of the heart and great vessels. Furthermore, steady-state sequences allow to scan entire chest in a single apnea and may be used to image the lung parenchyma [1] (Fig. 4.1).

Other tools to avoid motion-related artifacts are pneumatic belt or compressible cushion: these devices are placed upper the chest so that the scanner can register, continuously, the thorax excursions during respiration; then the sequence, usually, starts at the end of expiration. More sophisticated techniques, called "navigator sequences," are characterized by real-time image acquisition of a small volume at the top of the diaphragm and the trigger signal is set when the diaphragm reaches the zenith, during the end of expiration. Anyway, all triggering procedures lengthen the acquisition time.

Non-Cartesian k-space sampling techniques, such as radial and spiral, are introduced to reduce also the acquisition time. Radial (or helical) k-space sampling offers robust images with less motion-related artifacts, especially in areas close to great vessels. These sequences (BLADE, PROPELLER, MultiVane) are widely used to image the upper mediastinum and the chest wall (Fig. 4.2).

MRI, thanks to high contrast resolution and multiparametric capabilities, like diffusion-weighted imaging (DWI) and dynamic contrast

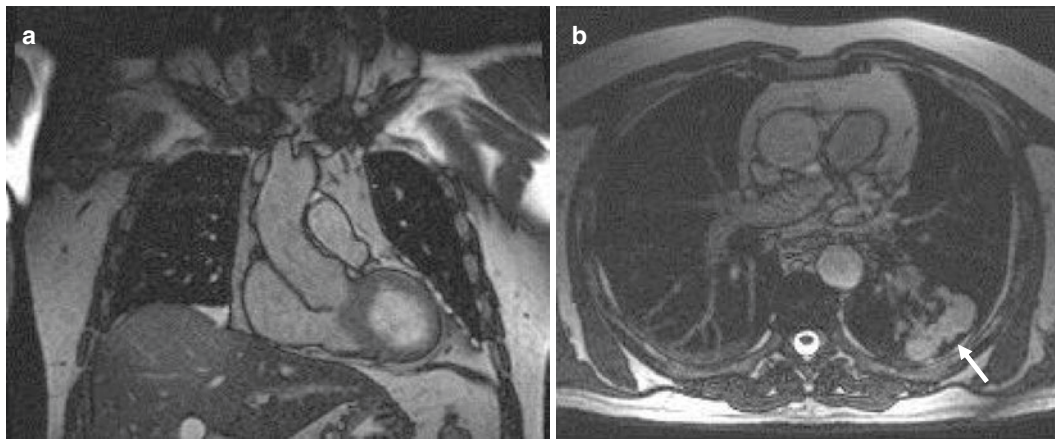


**Fig. 4.1** Balanced steady-state free precession (bSSFP) breath-hold sequences. (**a**) Coronal plane allows good representation of mediastinum; (**b**) axial plane, arrow shows a lung lesion (adenocarcinoma)

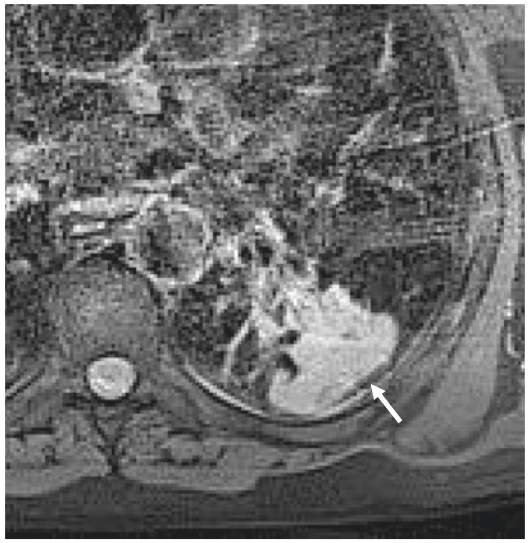

**Fig. 4.2** Axial T2 BLADE sequence, same patient before. Note the increased sharpness of the lung-pleural interface (arrow)

enhanced (DCE), has better soft tissue characterization than CT and despite the issues related with moving organs, in the next future, it is bound to have an increasingly important role for both mediastinal tumors and chest wall mass evaluation.

Another advantage of MRI is given by the possibility to obtain a perfusion analysis by using very fast gradient echo sequences, specially using centric k-space sampling.

Conversely, MRI of the lung has some limitations such as low proton density of the air and the high magnetic field inhomogeneity due to susceptibility artifacts at air-tissue interfaces. However, thanks to technical advances, chest MRI con be performed in an increasing number of clinical scenarios [2].

## 4.2 Current Applications

### 4.2.1 Mediastinal Lesions

An excellent soft-tissue contrast designates MRI as an ideal tool to evaluate mediastinal lesions [3].

MRI of the mediastinum requires dedicated effort to eliminate respiratory and cardiac motion: breath-hold sequences are mandatory in most cases and cardiac gating should be considered in certain scenarios. Breath-hold sequences should last as least as possible, up to a maximum of 20 s, to obtain patient cooperation and to avoid motion artifacts.

Fast T1- and T2-weighted sequences (fast gradient-echo and fast spin-echo imaging) are the most used sequences to image the mediastinum and allow differentiation between solid and cystic lesion (Fig. 4.3).

Periodically rotated overlapping parallel lines with enhanced reconstruction sequences (such as PROPELLER, BLADE and MultiVane) are characterized by central k-space oversampling and inherent motion correction properties that result in less motion artifacts and subtle respiratory modulations as well as increased sharpness of the lung/pleural interface.

Many authors have shown rather convincingly that normal thymus and thymic hyperplasia can be differentiated from primary thymic neoplasms and lymphoma within- and out-of-phase gradient-echo imaging. Normal thymus and thymic hyperplasia are uniformly suppressed on out-of-phase images due to the presence of interspersed microscopic fat within the nonneoplastic thymic tissue [4, 5] (Fig. 4.4).

DWI is another special tool hat unveils minute metabolic and biophysical differences between tissues. According to Gumustas, the mean apparent diffusion coefficient (ADC) for the malignant mediastinal entities could be significantly lower than that for the benign diseases [6].

### 4.2.2 Chest Wall Lesion

Thanks to high contrast resolution, MRI allows an optimal evaluation of the chest wall and thanks to the multiplanar acquisition allows a good lesion characterization [7] (Fig. 4.5).

Furthermore, as radiation-free technique, MRI allows multiple sequence acquisition during contrast medium administration so that perfusion analysis can be obtained (Fig. 4.6).

MRI showed higher accuracy to discern chest wall or diaphragm infiltration over CT, which

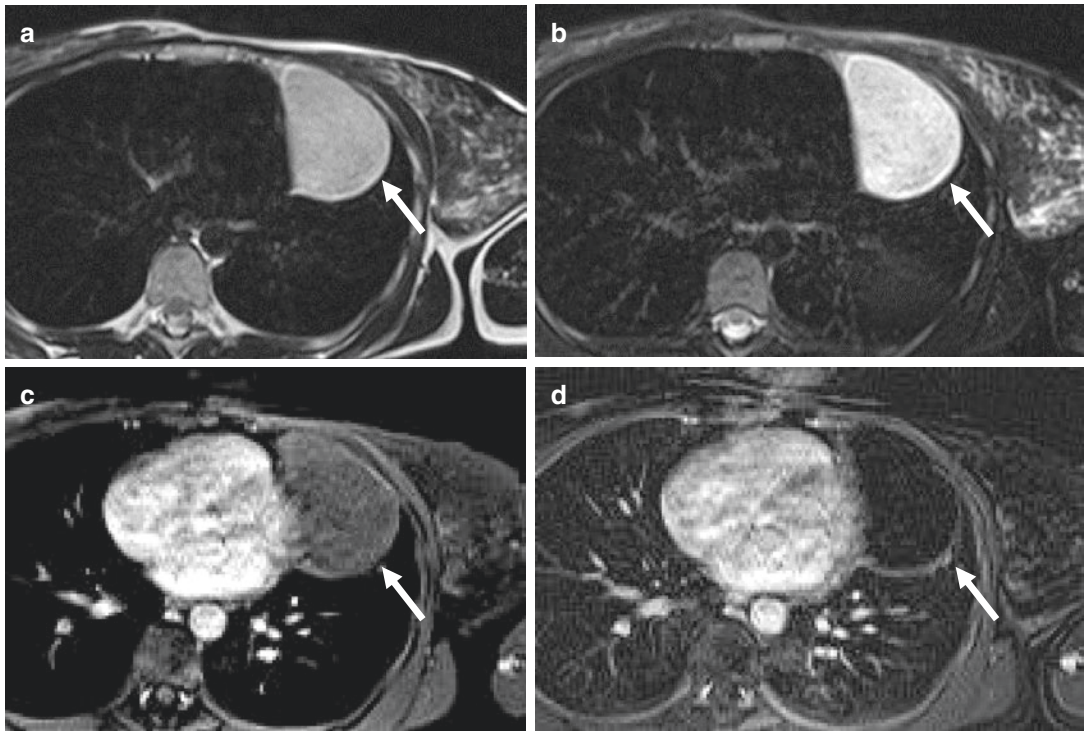


**Fig. 4.3** (**a**) Axial T2 HASTE. (**b**) Axial T2 HASTE fat-sat. (**c**) Axial T1 GRE fat-sat post-Gad. (**d**) Subtracted sequence. Arrows indicate pleuro-pericardial cyst

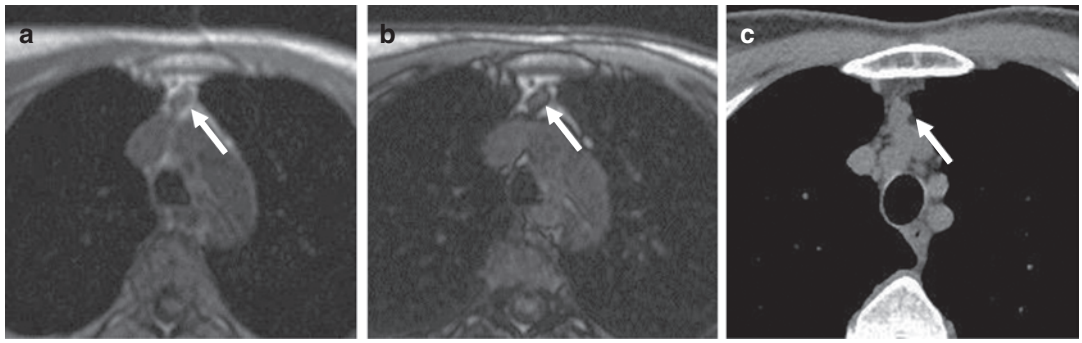


**Fig. 4.4** (**a**) Axial T1 DUEL ECHO in-phase and (**b**) out of phase. (**c**) NECT. Arrows indicate thymic lesion, intracytoplasmic lipids within the lesion suggest benign nature (thymic hyperplasia)

is important when staging and determining respectability: the combination of morphologic criteria and signal intensity could correctly diagnose infiltration of these structures in case of lung or mediastinal cancer.

Other studies, comparing CT with MRI, have confirmed that MRI is better at discerning encasement/infiltration of vessels, which is more important for parenchymal than pleural disease, but gives further strength to its use in preoperative evaluation [8].

In 1996, Falaschi et al. demonstrated the high accuracy of mild signal hyperintensity on T2-weighted images (specificity of 87%, sensitivity of 100%, and negative predictive value of 100%) in detecting malignant lesions [9].

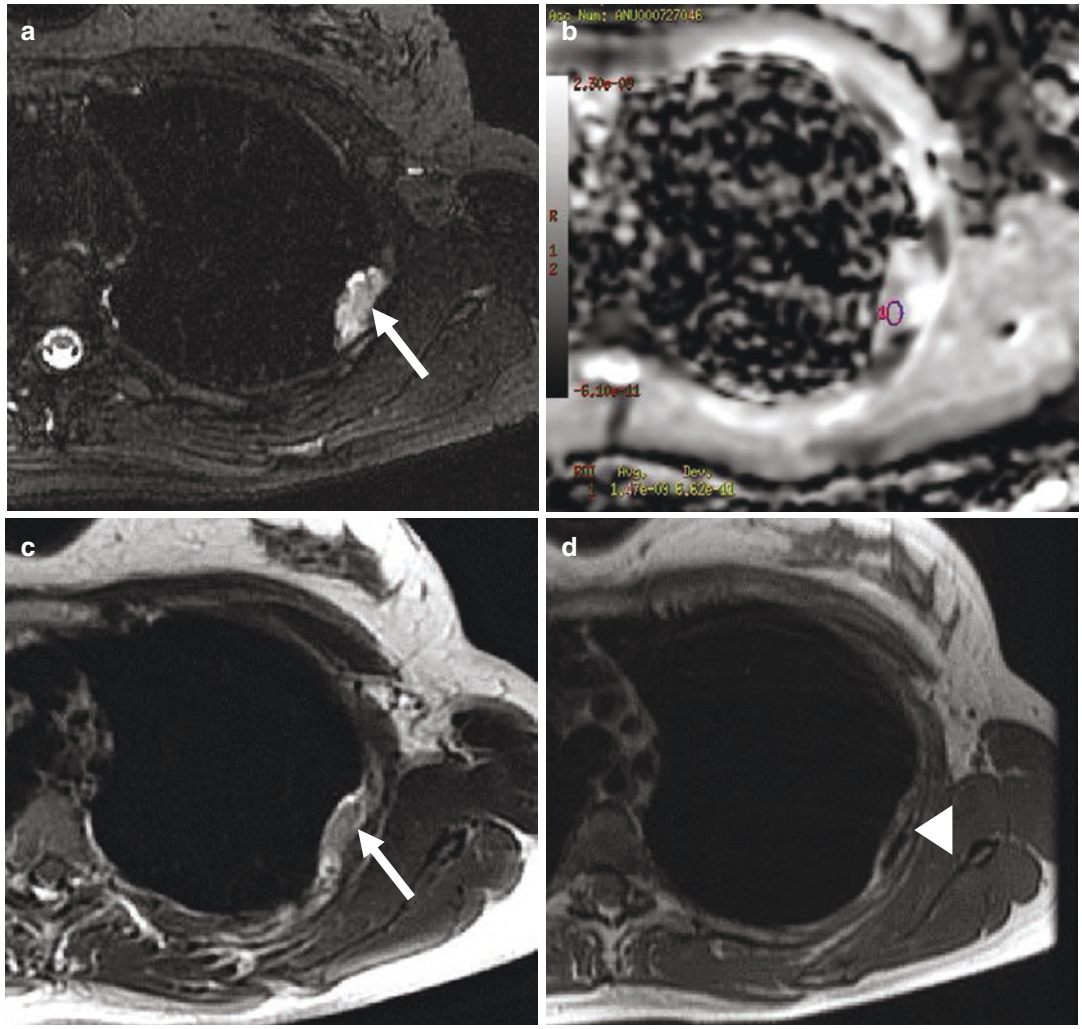


**Fig. 4.5** (**a**) Axial T2 HASTE fat-sat, arrow shows hyperintense subpleural lesion; (**b**) ADC value 1,47; (**c**) axial T2 PROPELLER; (**d**) axial T1 TSE: note periosteal reaction of the rib (arrowhead)

T1-weighted sequences are important to rule out the presence of hemoglobin-degradation products in hemorrhagic tissue, such as pleural endometriosis or blood within an expansive lesion.

Non-fat-saturated 2D multislice balanced steady-state free precession (bSSFP) sequences are often extremely useful, providing exquisite anatomic information as well as dynamic information on diaphragmatic excursion with respiration so, occasionally, relative tumor mobility can be assessed on these image acquisitions. This technique demonstrates T2/T1 weighting with high contrast and SNR and can be obtained also with fat suppression. These are typically performed as breath-hold acquisitions but can be tailored to be free breathing.

### 4.2.3 Staging N (Differences Between DWI and PET-CT)

In case of malignant lung lesion a specific accurate assessment of local disease is necessary: patients with different cancer stages need the most appropriate therapy plan to gain the best

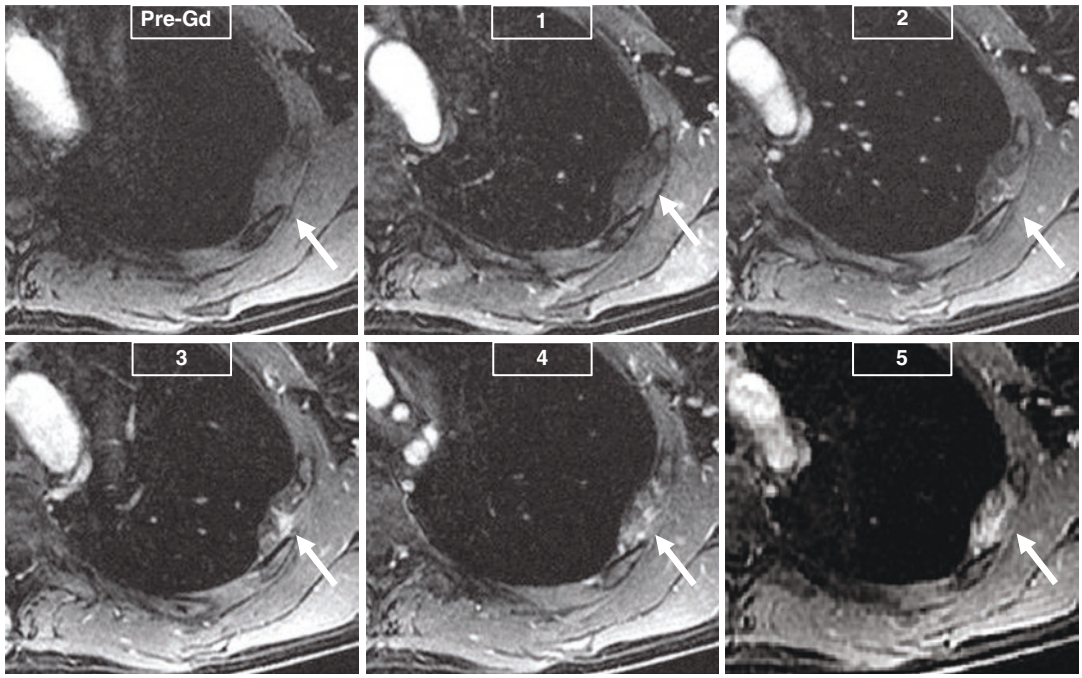


**Fig. 4.6** Perfusional study reveals slow and centripetic enhancement of the lesion. The lesion resulted in pleural hemangioma

therapeutic success. If there are no complications or contraindications most patients at first clinical tumor stage can undergo a surgery; contrariwise in case of pathological involvement of contralateral mediastinal lymph nodes neoadjuvant radiotherapy or chemotherapy is preferred.

According to RECIST 1.1 criteria, radiological staging criterion for pathological lymph nodes is the short-axis diameter (SAD): lymph nodes with SAD >1 cm are metastatic and they can be considered target lesion with an SAD ≥1.5 cm [10].

However, the size criteria are not sufficient to make the diagnosis: lymph node size changes can occur in case of an acute or a chronic respiratory disease. More than one decade ago and to nowadays the introduction of hybrid systems like positron-emission tomography/computed tomography (PET/CT) scanners changed oncologic imaging and patient management: with these metabolic information obtained by PET can be anatomically localized thanks to high-resolution multidetector CT (MDCT) scanners. However the diagnostic efficacy PET/CT is reduced in early-staging lung cancer due to limited spatial resolution and, in case of acute or chronic lung disease with lymphadenitis, we can have false positives; other limitations of PET/CT are the lack of brain staging and the exposure of patient and medical personnel to a considerable dose of radiation.

Although MRI accuracy is lower than MDCT on morphological criteria, it can be considered the only alternative of imaging technique that allows the radiologist to perform, without using ionizing radiations and in case of renal failure, a complete body study: MRI enables a better soft-tissue study with high spatial resolution, although it is limited by cardiac and respiratory artifacts; however it is now possible thanks to technical improvements, with introduction of DWI and perfusion sequences [11].

DWI is based on the diffusion properties of water molecules within tissues: these movements, classically called Brownian motions, are caused by thermal agitation and are highly influenced by cellular density, especially in tumor and tissue architecture. The apparent diffusion

coefficient (ADC), i.e., the quantification of signal intensity loss due to dispersion phase, is a parameter that refers to the specific diffusion capacity of a tissue that allows to distinguish benignant and malignant lesions. For example, in case of inflammatory lymphadenitis, an increased $^{18}$F-fluorodeoxyglucose (FDG) uptake usually showed in PET/CT without a restricted diffusion of water molecules in MRI, which justifies the difference in false-positive results between both techniques.

In a recently published study of Huellner et al. about the use of a hybrid system like PET/MR, using dedicated pulmonary MRI protocols, patients affected by lung cancer did not find advantages in thoracic staging in comparison with PET/CT; however the introduction of short inversion time inversion recovery sequences (STIR) and DWI showed an improvement on thoracic staging with a high sensitivity and specificity on pathological lymph node [12] (Figs. 4.7 and 4.8).

### 4.2.4 MRI in Pancoast Tumor

Pancoast tumor, also called as superior sulcus tumor, refers to a rare situation where a primary bronchogenic carcinoma arises in the lung apex

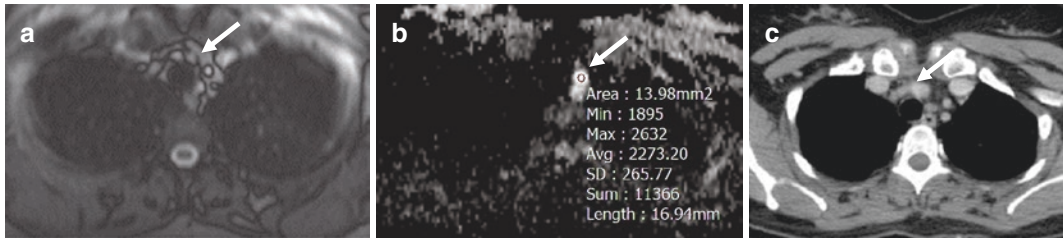


**Fig. 4.7** (**a**) Axial T1 DUEL ECHO out of phase. (**b**) ADC map with high values. (**c**) CT. Arrows indicate benign mediastinal lymph node

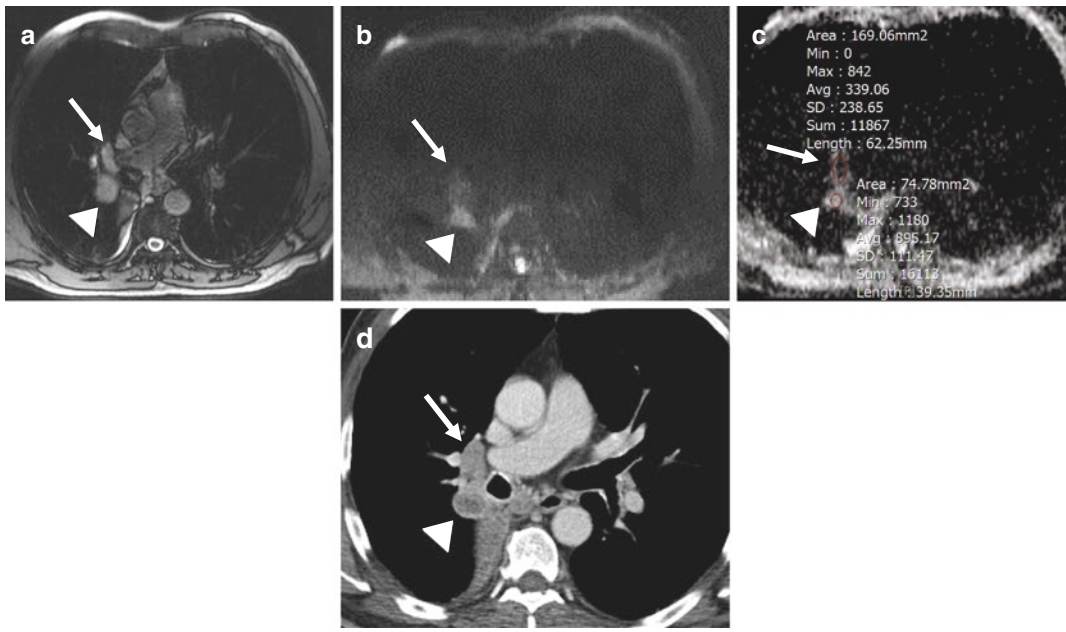


**Fig. 4.8** (**a**) Balanced steady-state free precession (bSSFP) breath-hold sequences in axial plane in patient affected by lung adenocarcinoma. (**b**) DWI b1000 shows high signal intensity of pathological lymph nodes. (**c**) ADC map with low values. (**d**) CT in axial plane. Arrow and arrowhead show pathological hilar lymph nodes

and invades the surrounding soft tissues causing a wide variety of sensorial and motor disorders of neck and arms like Pancoast syndrome (in case of the involvement of the inferior portion of the brachial plexus) with neck and medial arm pain, paresthesias, weakness, and like Horner syndrome (in case of invasion of the stellate ganglion) characterized by miosis, ptosis, enophthalmos, and anhidrosis of the affected side.

In this case MRI, due to higher soft-tissue resolution than CT, is useful for the assessment of superior sulcus tumor involvement, especially for the evaluation of its locoregional extension (particularly brachial plexus, subclavian vessels, parietal pleura, subpleural fat, neurovertebral foramina, and spinal canal).

The study of apical lung structures is based on spin-echo (SE) or TSE T1-weighted and T2-weighted image protocol and STIR sequences (using surface coils and slice thickness 3–4 mm): T1-weighted sequence images have high anatomical resolution to visualize the relationship of the subclavian vessels with other anatomical components; T2-weighted sequences with fat-signal suppression are useful for studying the brachial plexus; and STIR sequences, as reported in MR neurography, allow the study of nerve roots. DWI also guarantees the possibility to identify nodes and nervous structure involvement [13].

In this case contrast medium (CM) is useful for the assessment of vascular invasion, like subclavian vessels, and it is also helpful to differentiate posttreatment fibrosis from cancer persistence or relapse.

### 4.2.5 MRI of Chest in Radiotherapy

Stereotactic body radiotherapy (SBRT) or intensity-modulated radiotherapy (IMRT), associated with chemotherapy, can be considered a valid alternative treatment for different staging of lung cancer with a decrease of normal tissue toxicity: in case of inoperable locally advanced lung cancer the median survival average is about 21 months [14]; in case of inoperable early stage of lung cancer they can offer a high curative potential with local control rates amounting to 89% [15].

The high rating of success of radiotherapy is given not only by an adequate tight control of patient positioning during the therapy but also by an accurate gross tumor volume (GTV) definition and its vascular characteristics. Although currently the PET/TC is the most accurate imaging technique for lung cancer staging it has some limits: firstly, the spatial resolution is limited to 5 mm which makes it prone to inaccuracies in GTV definition, and secondly, dedicated PET/TC scanners for radiotherapy planning are lacking in most centers.

Nowadays the growing availability of MRI scanners, the improving of their technical evolution with the introduction of DWI sequences, the shorter examination time, their low cost-effectiveness, and the nonuse of ionizing radiation can make it a valid alternative pre-radiotherapy planning compared to PET/TC; in fact, as reported in literature by Fleckenstein et al., GTV values obtained both with PET/CT and MRI are similar. In addition, Chang et al. reported that DWI has also a great potential with respect to PET/TC to evaluate the early response of cancer to chemotherapy and radiotherapy through the early changes in ADC map and obtain information about microscopic tumoral structures, such as cell density/integrity or necrosis, without performing a biopsy with the risks that may arise [16, 17].

Another essential factor for the response to radiotherapy is the vascular characteristics that influence radiosensitivity through their effect on oxygen free radical generation: dynamic contrast enhancement MRI (DCE-MRI), as reported by Tao et al., is a useful tool for evaluation of microvascular cancerous structures improving its sensitivity to the therapy and prediction of tumor response for patients with locally advanced cancer lung [18].

### 4.2.6 Chest MRI as Alternative of Radiation-Based Techniques in Specific Group of Patients

Thanks to the lack of ionizing radiation, MRI is the preferable imaging technique in patients in which radiation exposure must be avoided, such as pregnant women, children, and patients

affected by DNA-related pathologies (such as ataxia telangiectasia).

In 1991, the Safety Committee of the Society of Magnetic Resonance Imaging stated, "MR imaging may be used in pregnant women if other non-ionizing forms of diagnostic imaging are inadequate or if diagnosis would otherwise require exposure to ionizing radiation. Pregnant patients should be informed that, to date, there has been no indication that the use of clinical MR imaging during pregnancy has produced deleterious effects" [19]. US represents the gold standard imaging technique in pregnant women but its utility in chest pathologies is limited. Chest MRI may substitute radiation-based techniques in pregnant women in suspect of pulmonary embolism, pneumonia, and pneumothorax. However, the clinicians should consider the overall performance status of the patient and the possibility of obtaining a faster diagnosis with conventional CT or plain film.

In children, the main difficulty is represented by the lack of collaboration of patient and, often, sedation is required; therefore breath-hold sequences are, almost always, not achievable. Besides, most mediastinal masses are malignant and CT is required to stage the lung parenchyma; in this scenario MRI cannot substitute CT and the two techniques are complementary. However, MRI is helpful in the diagnosis of cystic and fatty lesion and allows a good evaluation of mediastinal vascular malformation. Furthermore, MRI is very helpful in differentiation between thymic hyperplasia and neoplasm [20].

Ataxia telangiectasia (AT) is a rare autosomal recessive syndrome characterized by DNA repair disorder. If the patient's conditions are not critical, radiation exposure must be avoided in order to prevent further DNA mutations, so chest MRI could be considered in these patients [21].

## 4.3 Future Applications

Although MRI of the lung is subjected by susceptibility artifacts at air-tissue interfaces, thanks to recent technical improvements such as parallel imaging, shared echo technique, and rotating phase encoding, it can be recommended in a wide number of clinical cases offering an alternative solution to routine diagnostic challenges and an alternative radiation-free diagnostic option for young and pregnant patients [22].

### 4.3.1 MRI in Cystic Fibrosis

Cystic fibrosis (CF) is a genetic disorder that affects mostly the lungs caused by mutations in the cystic fibrosis transmembrane conductance regulator (CFTR) gene and it remains one of the most frequent lethal diseases in the Caucasian population: physiopathologically this disease is characterized by chronic airway infection that leads to a progressive lung failure since the childhood.

Recent studies in which there was a direct correlation between early onset of symptoms and lung failure demonstrated that a highly sensitive noninvasive measure of abnormal lung structure and function is essential for the improvement of clinical management and the development of new treatment strategies that may delay or even prevent irreversible lung damage for improving the quality of life of patients [23].

Forced expiratory volume in 1 s (FEV1) has been used for many years as a noninvasive monitoring and as clinical trial endpoint of lung disease in CF; however, due to its low sensitivity, in some cases of CF it can remain normal in most children with CF on current treatment regimens [24].

Nowadays imaging techniques such as chest X-ray and high-resolution CT (HRCT) have been the preferred methods for CF monitoring; however both techniques have many limitations, respectively: X-ray helps to detect only macroscopic lung alterations, such as consolidation, atelectasis, and pleural effusion; in short-term follow-up with HRCT the patients, especially youth, are exposed to high doses of radiation [25].

MRI and HRCT have the same sensitivity in the detection of morphological changes in the CF lung; however MRI is superior to HRCT for assessing functional changes such as altered pulmonary perfusion. Moreover with particular

scan protocols, including DWI, it is possible to detect bronchiectasis, bronchial wall thickening, mucus plugs, air fluid levels, consolidation, and parenchymal destruction in order to quantify the degree of severity of the disease [26, 27].

The bronchial thickening depends on bronchial size and signal: a hyperintensity on T2-weighted images represents edema caused by inflammation; enhancement of thickened bronchial wall in post-contrast T1-weighted fat-sat images refers to inflammatory activity.

Mucus plugs are recognized as a hyperintense T2 signal filling of the bronchus along its course with branching in the periphery giving a grape-like or tree-in-bud appearance. They can be differentiated from bronchial wall thickening because they do not enhance (Fig. 4.9).

### 4.3.2 Screening for Lung Cancer

A recent meta-analysis reported that CT is more accurate than MRI in the overall pulmonary nodule detection but the techniques are equally accurate in distinguishing between malignant and benign solitary pulmonary nodules [28].

In fact, MRI allows characterization of pulmonary hamartomas using chemical shift sequences, thanks to the possibility to detect fat within nodule. Diffusion-weighted MRI may be able to be used alternatively to PET/TC to distinguish malignant from benign pulmonary nodules/masses with fewer false-positive results [29].

Use of MRI in the evaluation of pulmonary nodules has thus far been limited. The reasons include limited spatial resolution, high susceptibility differences between air spaces

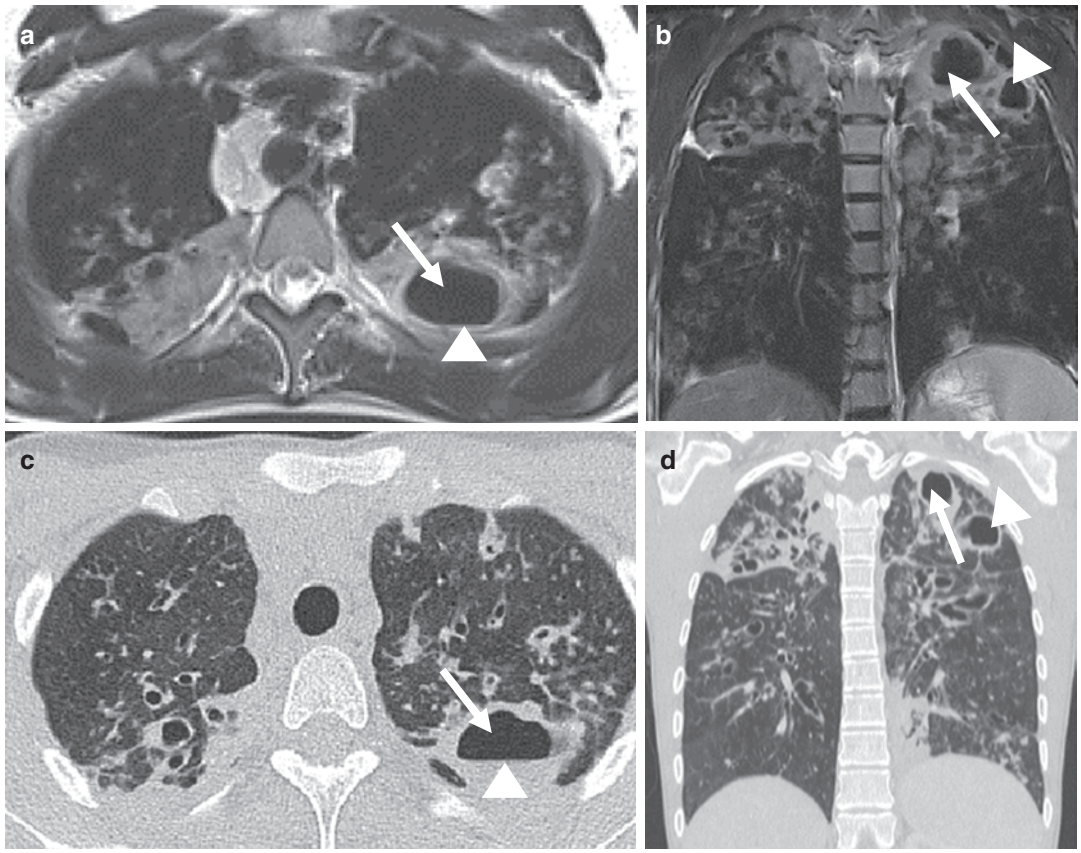


**Fig. 4.9** Balanced steady-state free precession (bSSFP) breath-hold sequences in axial plane in young patient affected by cystic fibrosis: (**a**) axial plane, (**b**) coronal plane. HRCT in the same patient: (**c**) axial plane, (**d**) coronal plane. Arrows show bronchiectasis. Arrowheads show bronchial wall thickening

and pulmonary interstitium, and presence of respiratory and cardiac motion artifacts. However, in the recent years, the availability of high-performance gradient systems, in conjunction with phased-array receiver coils and optimized imaging sequences, has made new approaches possible to MR-based pulmonary imaging. Turbo spin echo sequence shows many pulmonary nodules, including lung cancers, pulmonary metastases, and low-grade malignancies such as carcinoids and lymphomas, with low or intermediate signal intensity on T1-weighted imaging and slightly high intensity on T2-weighted imaging.

Schroeder et al. reported an axial spatial resolution of 2.4 × 1.3 mm2 using 1.5 T scanner and performing breath-hold 2D half-Fourier acquisition single-shot turbo spin echo (HASTE) sequences. To compensate the poor resolution in the z-axis (slice thickness 5 mm), the sequences should be acquired both in the axial and coronal planes [30].

HASTE MRI sequences showed sensibility of 73% for lesions smaller than 3 mm, 86.3% for lesions between 3 and 5 mm, 95.7% for lesions between 6 and 10 mm, and 100% for lesions bigger than 10 mm. A theoretical advantage of MRI is that pulmonary arteries and veins are depicted as flow voids without any apparent signal black blood inversion sequence; in CT, small pulmonary masses often have attenuation levels similar to those of blood vessels and thus are often indistinguishable from vessels of similar size.

Although MRI spatial resolution is lower than that of MDCT, the real differences in terms of accuracy in detection of lung cancer are under investigation.

Recently, Koyama et al., in a study over 200 pulmonary nodules, directly compared detection rates and capability of differentiation of malignant from benign nodules between noncontrast-enhanced multidetector CT and MRI using a 1.5 Tesla system [28].

Although the overall detection rate of thin-section MDCT was superior to that of respiratory-triggered STIR or TSE imaging, there were no significant differences in malignant nodule detection rate between the methods. Decrease in the detection rate of benign nodules without significantly missing malignant nodules may lead to lower false-positive results and less expensive screening program (Figs. 4.10 and 4.11).

### 4.3.3 Characterization of Lung Lesions: DCE, DWI, or Both?

As mentioned before, MRI and CT showed similar results in differentiating malignant from benign lung lesions [3].

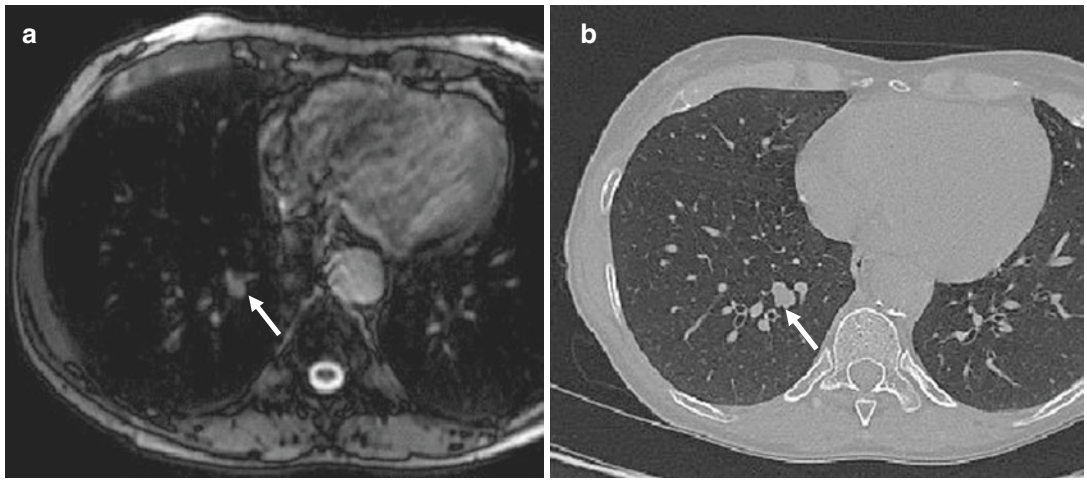


**Fig. 4.10** (**a**) Axial balanced steady-state free precession (bSSFP); (**b**) NECT. Small nodule in the right inferior lobe; diagnosis was squamocellular carcinoma (arrows)

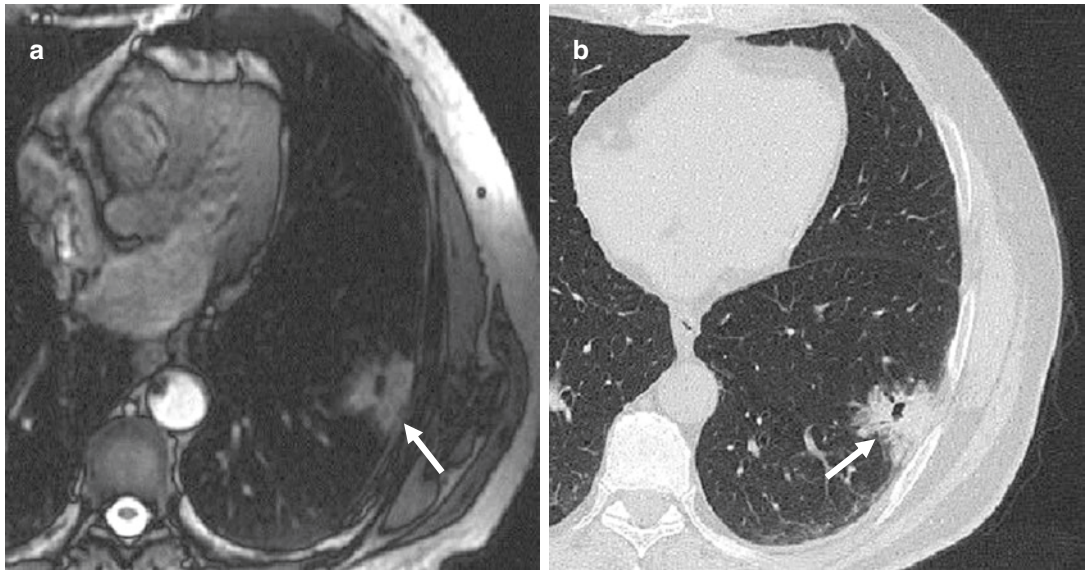


**Fig. 4.11** (**a**) Axial balanced steady-state free precession (bSSFP); (**b**) NECT. Cavitated lesion in the inferior left lobe; diagnosis was adenocarcinoma (arrows)

The lack of ionizing radiation makes MRI a safe tool for repeated dynamic evaluations of tumor perfusion. DCE-MRI with the 3D GRE sequence requires less than 30-s breath-holding for acquisition of all thorax [31]; however, field of view (FOV) may be focused on the region of interest and the single-frame length could be reduced.

Besides, a recent meta-analysis reported that there were no significant differences in diagnostic performance among dynamic CT, dynamic MRI, PET/CT, and single-photon emission tomography (SPECT) [32].

Malignant tumors are characterized by increased cellularity, larger nuclei with more abundant macromolecular proteins, a larger nuclear/cytoplasmic ratio, and less extracellular space relative to normal tissue; due of these features, the diffusion of water molecules in cancers is restricted, resulting in reduced ADC. Recently, DWI sequences have been suggested as a new method for nodule detection and/or evaluation, including subtype classification of pulmonary adenocarcinoma. Quantitative and/or qualitative sensitivities and specificities of the ADC for differentiation of malignant from benign single pulmonary nodules were 70.0–88.9% for sensitivity and 61.1–97.0% for specificity [33] (Figs. 4.12 and 4.13).

Furthermore, patients with central lung cancer frequently present with peripheral lung collapse or post-obstructive pneumonia. These findings make it difficult to differentiate central tumor from the surrounding lung consolidation; in fact an exact knowledge of the tumor extension has a fundamental importance in patients planned for radiotherapy. In a previous study conducted by Baysal et al. ADC values of central carcinoma masses were significantly lower than those of pneumonic consolidations and atelectasis [34] (Fig. 4.14).

ADC values allow differentiation between cancer tissue (lower values) and necrosis and atelectasis (higher values) and should be useful in the planning of transthoracic CT-guided biopsy [31].

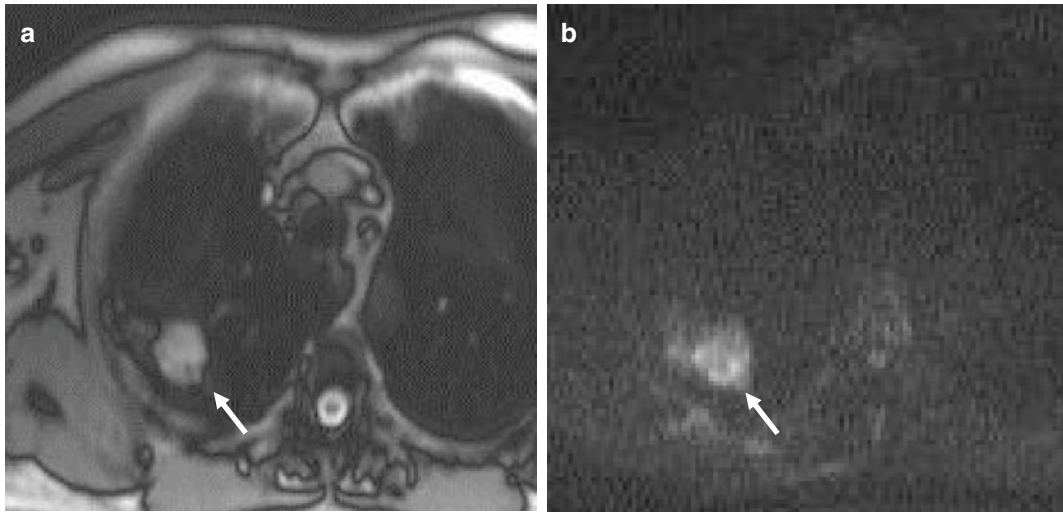


**Fig. 4.12** (**a**) Axial balanced steady-state free precession (bSSFP); (**b**) DWI b1000. The lesion resulted in adenocarcinoma (arrows)

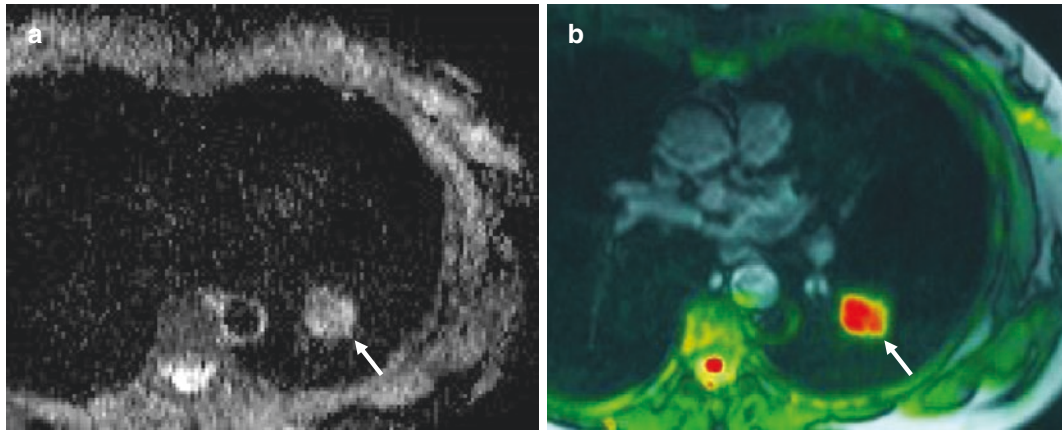


**Fig. 4.13** (**a**) ADC value was $1.18 \times 10^{-3}$. (**b**) DWI b1000 and axial balanced steady-state free precession (bSSFP) matching sequence. The lesion was adenocarcinoma (arrows)

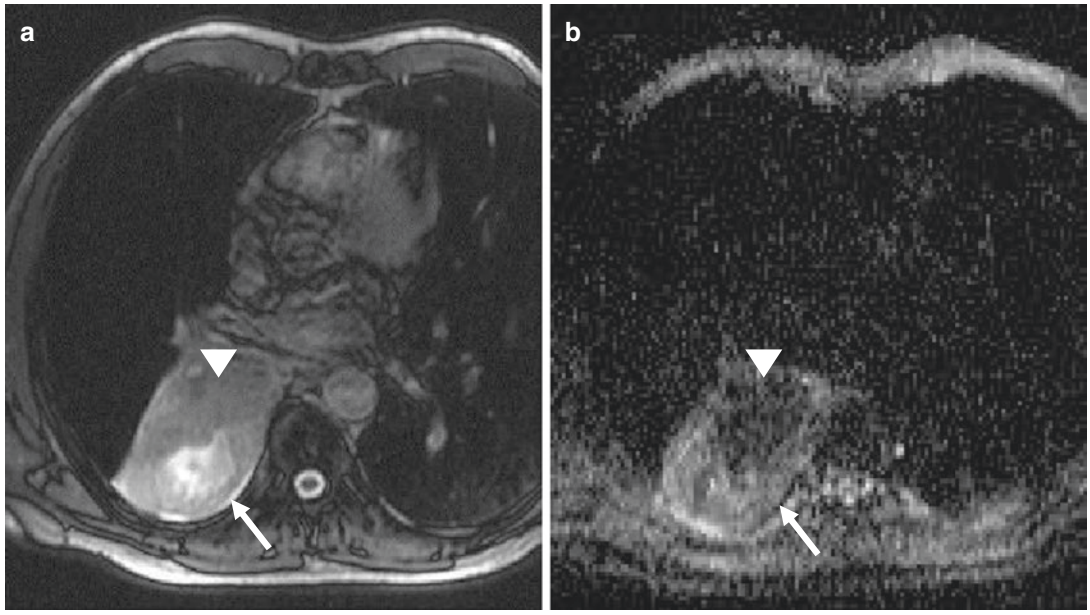


**Fig. 4.14** (**a**) Axial balanced steady-state free precession (bSSFP). (**b**) ADC map. MRI allows good differentiation between atelectasis (arrowhead) and tumor (arrow). Tumor shows lower ADC value ($0.8 \times 10^{-3}$). Surgery confirmed hilar microcytoma and large atelectasis of right inferior lobe

## References


1. Wild JM, Marshall H, Bock M, Schad LR, Jakob PM, Puderbach M, Molinari F, Van Beek EJ, Biederer J. MRI of the lung (1/3): methods. Insight Imaging. 2012;3(4):345–53.
2. Biederer J, Beer M, Hirsch W, Wild J, Fabel M, Puderbach M, Van Beek EJ. MRI of the lung (2/3). Why … when … how? Insight Imaging. 2012;3(4):355–71.
3. Puderbach M, Hintze C, Ley S, Eichinger M, Kauczor HU, Biederer J. MR imaging of the chest: a practical approach at 1.5T. Eur J Radiol. 2007;64(3):345–55.
4. Ackman JB, Wu CC. MRI of the thymus. AJR Am J Roentgenol. 2011;197(1):W15–20.
5. McInnis MC, Flores EJ, Shepard JA, Ackman JB. Pitfalls in the imaging and interpretation of benign thymic lesions: how thymic MRI can help. AJR Am J Roentgenol. 2016;206(1):W1–8.
6. Gumustas S, Inan N, Sarisoy HT, Anik Y, Arslan A, Ciftci E, Akansel G, Demirci A. Malignant versus benign mediastinal lesions: quantitative assessment with diffusion weighted MR imaging. Eur Radiol. 2011;21(11):2255–60.
7. Weber MA, Bock M, Plathow C, Wasser K, Fink C, Zuna I, Schmahl A, Berger I, Kauczor HU, Schoenberg SO. Asbestos-related pleural disease: value of dedicated magnetic resonance imaging techniques. Investig Radiol. 2004;39(9):554–64.
8. Armstrong P. Preoperative computed tomographic scanning for staging lung cancer. Thorax. 1994;49(10):941–3.
9. Falaschi F, Battolla L, Mascalchi M, Cioni R, Zampa V, Lencioni R, Antonelli A, Bartolozzi C. Usefulness of MR signal intensity in distinguishing benign from malignant pleural disease. AJR Am J Roentgenol. 1996;166(4):963–8.
10. Eisenhauer EA, Therasse P, Bogaerts J, Schwartz LH, Sargent D, Ford R, Dancey J, Arbuck S, Gwyther S, Mooney M, et al. New response evaluation criteria in solid tumours: revised RECIST guideline (version 1.1). Eur J Cancer. 2009;45(2):228–47.
11. Ohno Y, Koyama H, Nogami M, Takenaka D, Yoshikawa T, Yoshimura M, Ohbayashi C, Sugimura K. STIR turbo SE MR imaging vs. coregistered FDG-PET/CT: quantitative and qualitative assessment of N-stage in non-small-cell lung cancer patients. J Magn Reson Imaging. 2007;26(4):1071–80.
12. Huellner MW, Appenzeller P, Kuhn FP, Husmann L, Pietsch CM, Burger IA, Porto M, Delso G, von Schulthess GK, Veit-Haibach P. Whole-body non-enhanced PET/MR versus PET/CT in the staging and restaging of cancers: preliminary observations. Radiology. 2014;273(3):859–69.
13. Manenti G, Raguso M, D'Onofrio S, Altobelli S, Scarano AL, Vasili E, Simonetti G. Pancoast tumor: the role of magnetic resonance imaging. Case Rep Radiol. 2013;479120(10):31.
14. McCloskey P, Balduyck B, Van Schil PE, Faivre-Finn C, O'Brien M. Radical treatment of non-small

cell lung cancer during the last 5 years. Eur J Cancer. 2013;49(7):1555–64.
15. Palma D, Lagerwaard F, Rodrigues G, Haasbeek C, Senan S. Curative treatment of stage I non-small-cell lung cancer in patients with severe COPD: stereotactic radiotherapy outcomes and systematic review. Int J Radiat Oncol Biol Phys. 2012;82(3):1149–56.
16. Fleckenstein J, Jelden M, Kremp S, Jagoda P, Stroeder J, Khreish F, Ezziddin S, Buecker A, Rube C, Schneider GK. The impact of diffusion-weighted MRI on the definition of gross tumor volume in radiotherapy of non-small-cell lung cancer. PLoS One. 2016;11(9):e0162816.
17. Chang Q, Wu N, Ouyang H, Huang Y. Diffusion-weighted magnetic resonance imaging of lung cancer at 3.0 T: a preliminary study on monitoring diffusion changes during chemoradiation therapy. Clin Imaging. 2012;36(2):98–103.
18. Tao X, Wang L, Hui Z, Liu L, Ye F, Song Y, Tang Y, Men Y, Lambrou T, Su Z, et al. DCE-MRI perfusion and permeability parameters as predictors of tumor response to CCRT in patients with locally advanced NSCLC. Sci Rep. 2016;6:35569.
19. Shellock FG, Crues JV. MR procedures: biologic effects, safety, and patient care. Radiology. 2004;232(3):635–52.
20. Juanpere S, Canete N, Ortuno P, Martinez S, Sanchez G, Bernado L. A diagnostic approach to the mediastinal masses. Insight Imaging. 2013;4(1):29–52.
21. Montella S, Mollica C, Finocchi A, Pession A, Pietrogrande MC, Trizzino A, Ranucci G, Maglione M, Giardino G, Salvatore M, et al. Non invasive assessment of lung disease in ataxia telangiectasia by high-field magnetic resonance imaging. J Clin Immunol. 2013;33(7):1185–91.
22. Biederer J, Mirsadraee S, Beer M, Molinari F, Hintze C, Bauman G, Both M, Van Beek EJ, Wild J, Puderbach M. MRI of the lung (3/3)-current applications and future perspectives. Insight Imaging. 2012;3(4):373–86.
23. Sly PD, Brennan S, Gangell C, de Klerk N, Murray C, Mott L, Stick SM, Robinson PJ, Robertson CF, Ranganathan SC. Lung disease at diagnosis in infants with cystic fibrosis detected by newborn screening. Am J Respir Crit Care Med. 2009;180(2):146–52.
24. Sly PD, Gangell CL, Chen L, Ware RS, Ranganathan S, Mott LS, Murray CP, Stick SM. Risk factors for bronchiectasis in children with cystic fibrosis. N Engl J Med. 2013;368(21):1963–70.
25. Eichinger M, Heussel CP, Kauczor HU, Tiddens H, Puderbach M. Computed tomography and magnetic resonance imaging in cystic fibrosis lung disease. J Magn Reson Imaging. 2010;32(6):1370–8.
26. Puderbach M, Eichinger M, Gahr J, Ley S, Tuengerthal S, Schmahl A, Fink C, Plathow C, Wiebel M, Muller FM, et al. Proton MRI appearance of cystic fibrosis: comparison to CT. Eur Radiol. 2007;17(3):716–24.
27. Ciet P, Serra G, Andrinopoulou ER, Bertolo S, Ros M, Catalano C, Colagrande S, Tiddens HA, Morana G. Diffusion weighted imaging in cystic fibrosis disease: beyond morphological imaging. Eur Radiol. 2016;26(11):3830–9.
28. Koyama H, Ohno Y, Kono A, Takenaka D, Maniwa Y, Nishimura Y, Ohbayashi C, Sugimura K. Quantitative and qualitative assessment of non-contrast-enhanced pulmonary MR imaging for management of pulmonary nodules in 161 subjects. Eur Radiol. 2008;18(10):2120–31.
29. Mori T, Nomori H, Ikeda K, Kawanaka K, Shiraishi S, Katahira K, Yamashita Y. Diffusion-weighted magnetic resonance imaging for diagnosing malignant pulmonary nodules/masses: comparison with positron emission tomography. J Thorac Oncol. 2008;3(4):358–64.
30. Schroeder T, Ruehm SG, Debatin JF, Ladd ME, Barkhausen J, Goehde SC. Detection of pulmonary nodules using a 2D HASTE MR sequence: comparison with MDCT. AJR Am J Roentgenol. 2005;185(4):979–84.
31. Guimaraes MD, Marchiori E, Odisio BC, Hochhegger B, Bitencourt AG, Zurstrassen CE, Tyng CC, Gross JL, Chojniak R, Godoy MC. Functional imaging with diffusion-weighted MRI for lung biopsy planning: initial experience. World J Surg Oncol. 2014;12:203.
32. Cronin P, Dwamena BA, Kelly AM, Carlos RC. Solitary pulmonary nodules: meta-analytic comparison of cross-sectional imaging modalities for diagnosis of malignancy. Radiology. 2008;246(3):772–82.
33. Satoh S, Kitazume Y, Ohdama S, Kimula Y, Taura S, Endo Y. Can malignant and benign pulmonary nodules be differentiated with diffusion-weighted MRI? AJR Am J Roentgenol. 2008;191(2):464–70.
34. Baysal T, Mutlu DY, Yologlu S. Diffusion-weighted magnetic resonance imaging in differentiation of postobstructive consolidation from central lung carcinoma. Magn Reson Imaging. 2009;27(10):1447–54.

# Interventional Radiology

5

Claudio Pusceddu, Francesco Allegra, and Luca Saba

**Abstract**

Computed tomography (CT) and ultrasound (US) are currently considered as the the main imaging modalities in the field of interventional radiology. Because of the different characteristics of these modalities their use is different. In particular CT is widely used to obtain accurate needle-tip localization and excellent delineation of interposed vital structures but the most important draback is the lack of real-time imaging. On the other hand US is readily available, relatively inexpensive, and allows for real time imaging. Moreover, Color flow Doppler imaging can help identify the vascular nature of the mass and the adjacent vascular structures. In this chapter we will show the different Interventional Radiology Procedures by showing advantages and limits of these techniques.

**Keywords**

Computed tomography · Ultrasound · Interventional radiology

C. Pusceddu (✉)
Department of Radiology, AOB, Cagliari, Italy

F. Allegra · L. Saba
Department of Radiology, University of Cagliari, Cagliari, Italy

## 5.1 Interventional Radiology Procedures

### 5.1.1 Guidance Techniques

Computed tomography (CT) and ultrasound (US) are the main imaging modalities aimed at the field of interventional radiology, both diagnostic and therapeutic.

- **CT** provides high spatial and high contrast resolution that allows accurate needle-tip localization, excellent delineation of interposed vital structures, and target viable portion of a mass; it also allows for early detection of complications (i.e., pneumothorax) [1]. On the other hand different density between normal tissues and lesions on noncontrast CT images may not be sufficiently large; another disadvantage is the lack of real-time imaging and last, but not least, use of ionizing radiation [2].
- **US** is readily available, relatively inexpensive, and portable, and does not use ionizing radiation. It is optimal for superficial lesions and provides real-time visualization and monitoring of the needle tip. Color flow Doppler imaging can help identify the vascular nature of the mass and the adjacent vascular structures. Ultrasound-guided biopsy may not be possible when lesions are too deep or behind a


M. Anzidei, M. Anile (eds.), *Diagnostic Imaging for Thoracic Surgery*,
https://doi.org/10.1007/978-3-319-89893-3_5

reflective surface such as bone or gas-filled bowel, limited for obese patients [3].

## 5.2 Lung and Mediastinal Biopsy

Lung cancer remains the most common cancer diagnosed worldwide and represents the leading oncologic cause of death. Not all lung masses are primary, with greater than 70% of multiple lung nodules representing metastatic deposits. Also mediastinum represents a region of interest due to frequent localization of lymph nodes or masses.

### 5.2.1 General Principles

Relative contraindications to percutaneous lung biopsy include uncooperative patients, positive-pressure ventilation, severe respiratory compromise, pulmonary artery hypertension, severe interstitial lung disease, small lesions close to the diaphragm, and central lesions adjacent to large vessels or bronchi.

The platelet count, prothrombin time, international normalized ratio (INR), and activated partial thromboplastin time should be routinely checked prior to the procedure. Although local standards apply, according to recent consensus guidelines, INR should be corrected if >1.5, and transfusion should be performed for platelet counts <50,000/μL.

Clopidogrel (Plavix®) should be held for 5 days prior to the procedure. Aspirin does not need to be held, but the last dose of low-molecular-weight heparin should be held prior to the procedure [4].

### 5.2.2 Indication

The most common indication for *lung* biopsy is an indeterminate solitary pulmonary nodule, both in cases where the nodule in question is almost certainly malignant but unsuitable for resection and where it is of equivocal or likely benign nature, but also biopsy is frequently performed for solitary or multiple pulmonary nodules, masses, or consolidations when tissue is required to diagnose and further characterize potentially malignant lesions.

Another common indication is suspected lung abscess in which bronchoscopy or sputum cytology and culture have not yielded a diagnosis; additional indications include enlarging ground-glass opacities, and evaluating for local recurrence following therapy [5].

The vast majority of *pleural* biopsies are performed to evaluate for malignant diseases of the pleura, including malignant mesothelioma, metastatic disease, and lymphoma. However, many benign conditions may also involve the pleura (i.e., pleural tuberculosis) [6].

About *mediastinal* lesions: Masses and lymph node are the most common indications for biopsy.

### 5.2.3 Patient Preparation

Patient positioning should be chosen based on the location of the lesion, size of the lesion, and patient's ability to tolerate positioning. The prone position is preferred because the posterior ribs move less than the anterior ribs, posterior intercostal spaces are wider than the anterior intercostal spaces, and prone positioning prevents the patient from visualizing the needle during the procedure, which may decrease anxiety. The oblique and decubitus positions are less desirable because they are not as stable, but they can be utilized if necessary for lateral subpleural lesions.

For CT-guided procedures, preliminary 3- or 5-mm-thick contiguous axial slices are obtained to confirm the location of the target lesion and to determine the optimal entry site for the needle. The important factors in choosing an access route include avoiding chest wall vessels such as subclavian, internal mammary, intercostal, and intrapulmonary vessels. It is also important to minimize pleural transgression by performing a single pleural puncture and avoiding fissures if possible. Large bullae should also be avoided.

If biopsy is being performed for a lesion of mixed CT attenuation, biopsy should be targeted

toward the solid component of the nodule or mass. Similarly, if there is central necrosis, biopsy should be directed at the wall of the lesion [7].

### 5.2.4 Anesthesia

Adequate pleural anesthesia is a primary point of a successful biopsy, as patient's comfort and cooperation. Placement of the coaxial needle is essential for achieving pleural anesthesia and optimal trajectory for needle placement into the target lesion.

Anesthesia of the parietal pleura requires the precise placement of the needle tip in an extrapleural location immediately adjacent to and superficial to the parietal pleura while avoiding both the underlying parietal and visceral pleura, which if violated increases the risk of an early pneumothorax.

The costal and diaphragmatic parietal pleuras are innervated by the overlying intercostal nerve, which means that inadequate anesthesia is characterized by significant pain and discomfort [8]. Local analgesics are used like lidocaine 1% (most common) and bupivacaine (for longer onset and duration).

Systemic analgesia like paracetamol or opioids (fentanyl, morphine) could be used in uncollaborative patient with severe pain.

### 5.2.5 Devices and Techniques

The needle selected depends upon lesion characteristics, type/amount of tissue required, and operator preference. Biopsy needles can be divided into two groups: **aspiration needles** for retrieval of specimens for cytologic evaluation, and **core biopsy needles** for retrieval of specimens for histologic evaluation.

- **Aspiration Needle (FNAB)**: FNAB is a minimally invasive procedure that is performed using a 21-, 23-, or 25-gauge needle attached to a 10 cm 3 syringe. Aspiration needles are thin walled and flexible, and are used for obtaining specimens for cytologic or microbiologic evaluation (Fig. 5.1). However, because the needles are flexible, they can easily bend or deflect off course; such effects are magnified when using a longer needle. The needle is introduced into the lesion and moved several times, dislodging cells, which are aspirated and deposited into glass slides. Direct smears

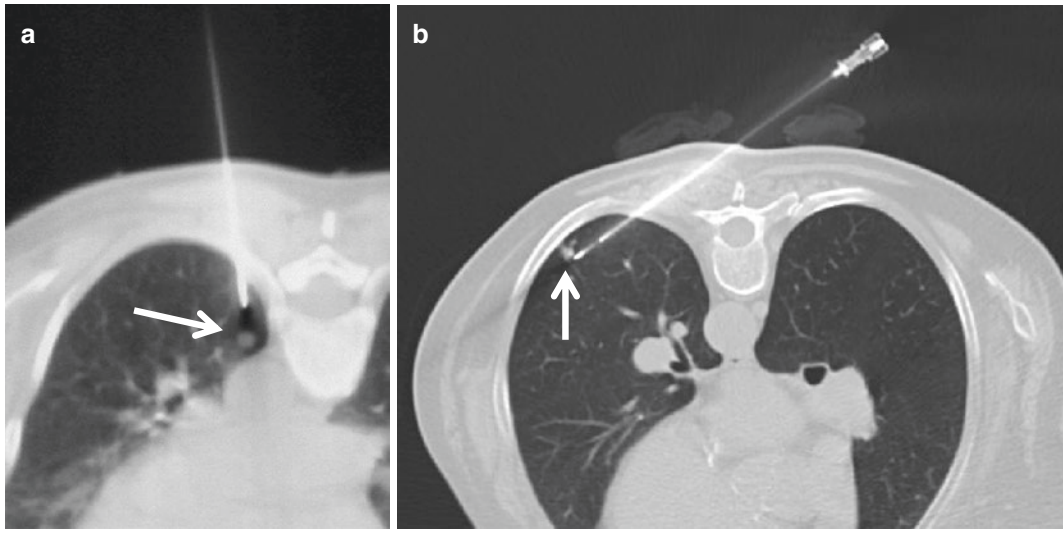


**Fig. 5.1** Axial CT images show two different cases of FNAB of 5 mm nodules (*arrows*) located in the left lung both reached with posterior approach (*arrows*)

are made manually and fixed in alcohol for staining using the Papanicolaou or hematoxylin and eosin (H&E) method and then air-dried for staining using the Diff-Quik method for conventional cytological examination. By changing the direction of the needle during aspiration, different sites in the target area can be evaluated [9]. Aspiration needles are useful for making diagnoses of epithelial carcinomas (adenocarcinoma or squamous cell carcinoma) because these diagnoses can be made on cytological analysis alone. Today, though, the diagnosis is not limited to cell type, but includes evaluation of tumor markers and analysis of tumor mutational status, which require procurement of additional tissue. In cases where cytologic sampling may have been adequate in the past, histologic sampling may be required to have sufficient tissue for analysis [10].

- **Core Needle Biopsy (CNB)**: Automated core biopsy needles are generally used to obtain tissue for histologic evaluation. The automated devices obtain higher quality and more intact core biopsy samples than obtained with manual needles (Fig. 5.2). Use of an automated biopsy device may improve results if a pathologist is not on-site at the time of biopsy because, depending on tumor type, the needle will obtain similar core samples that are free of crush injury sometimes imparted by smaller conventional needles. Currently, side-cutting biopsy guns are available in a variety of sizes, ranging from 20 gauge (the smallest) to 14 gauge (the largest). Usually, 2–4 cores of tissue are obtained from the lesion. For conventional pathological examination, the samples are fixed in formalin, routinely processed, and embedded in paraffin.

FNAB and CNB are complementary techniques for evaluating the lesion of interest; both have distinct advantages and limitations. FNAB is the preferred method in technically challenging sites such as those close to major blood vessels or neurovascular bundles. In addition, FNAB is the preferred method for obtaining material for microbiologic culture studies from lesions that are thought to be infectious.

CNB samples invariably contain more tissue than do FNAB samples, making ancillary studies possible.

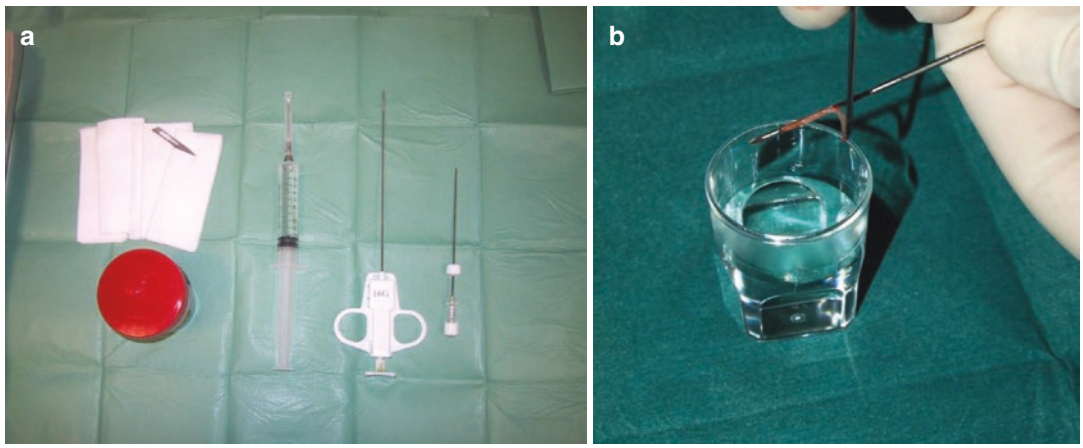


**Fig. 5.2** The pictures show the set for a lung biopsy which includes several surgical gauze, a syringe with local anesthetic, a surgical scalpel, and a biopsy needle (**a**). High-quality core biopsy sample obtained using a 16-gauge automated biopsy device (**b**)

## 5.3 CT-Biopsy Procedure

After appropriate patient positioning, a radiopaque marker is placed on the patient's skin over the area of interest. During suspended respiration, a short spiral CT scan of the region of interest is obtained, and from these images an appropriate table position and needle trajectory are chosen. The shortest straight pathway from the skin to the lesion is preferred over a longer oblique pathway, and ideally the needle should cross the pleura at a 90° angle rather than at an oblique angle. The depth from the skin entry site to the lesion is then measured.

Next, the patient is moved back into the CT gantry to the desired table position. With the use of the gantry laser light to delineate the Z-axis position, and the radiopaque skin marker to reference the *X*-axis position, the needle entry site is marked with indelible ink on the patient's skin.

The skin site is prepped and draped using sterile technique. Palpation of underlying structures to determine the contour of the ribs or the location of adjacent skeletal structures is helpful. For local anesthesia, a 27-gauge or similar needle is used to inject 1% or 2% lidocaine into the skin and subcutaneous tissues, followed by deeper infiltration of the intercostal muscles.

The biopsy needle is inserted through the dermatotomy into the subcutaneous tissues. All needle movements should be performed with patient's respiration suspended. When advancing the needle, it is important to maintain the same trajectory with each movement, as even slight deviations of the needle at the skin or within the subcutaneous tissues will produce marked deviation at a deeper level. The needle is advanced to the level of the pleura, and the needle position and angle are verified with a short-segment CT (typically obtained using a sequential technique). Next, the needle is advanced in one motion through the pleura to the prescribed depth. Afterwards, the patient may breathe quietly, and the needle should be allowed to sway to and fro with respiratory motion; the needle should not be held or fixed during respiration, as this will cause a lacerating effect on the pleura with each breath.

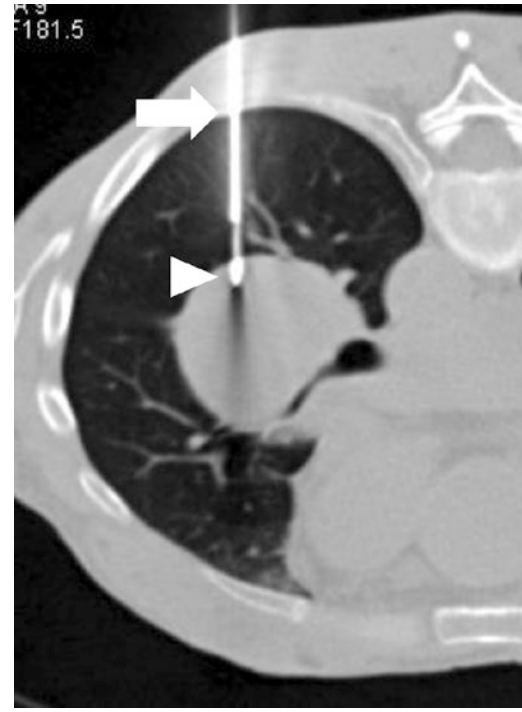


**Fig. 5.3** Axial CT image shows a central mass in the left lung. CNB was performed using a posterior approach. The needle crosses the pleura approximately at a 90° (*arrow*). The tip of the needle is in the mass ready for biopsy (*arrowhead*)

Confirmation of needle tip position must be performed before aspirating or cutting (Fig. 5.3). After needle tip position within the lesion is confirmed, a tissue sample may be obtained. If an aspiration or a cutting needle is used, the inner stylet is removed from the needle and the cannula quickly covered to block entry of air into the needle.

## 5.4 US-Guided Biopsy Procedure

Ultrasound-guided TNB is limited to regions that provide an adequate acoustic window to the lesion and is best suited for peripheral pulmonary or mediastinal masses that abut the pleura. The affected region is studied using US (usually from 1 to 5 MHz) convex probe parallel to the ribs in

the intercostal spaces. Local anesthesia is used in every case through local subcutaneous injection (10–20 mL xylocaine 2% or lidocaine).

The core biopsy needle having a size of 16-, 18-, or 20-G needle, length of 20 cm, and core length of 10, 15, or 20 mm is chosen according to the size and type of the lesion. The needle is placed into the biopsy gun and the puncture is performed using continuous visual control on the monitor.

After the puncture the needle is removed and compression is applied at the puncture site. When the tissue sample is considered sufficient, no further punctures are performed and the sample is placed in a tube containing 4% formaldehyde and is sent to the pathological department. Chest radiograph is performed after the biopsy to rule out any complications (i.e., pneumothorax). Generally all patients are observed for at least 12 h after the procedure up to 1 week to detect any complications [11].

### 5.4.1 Complications

Some complications could occur after a lung biopsy procedure. The most common complications are pneumothorax and bleeding. Although most patients can tolerate a small pneumothorax or mild hemorrhage, when performing TNB in high-risk patients with significant cardiopulmonary disease or single functional or anatomic lung, even a small pneumothorax or mild hemorrhage may cause significant respiratory compromise.

- **Pneumothorax**: PNX is the most common complication of transpulmonary biopsy (TNB). The reported incidence ranges from 0% to 61%. Factors reported to be associated with a higher incidence of pneumothorax and chest tube insertion include obstructive airway disease, increased lesion depth, decreased lesion size, a small angle of the needle with the thoracic pleura, multiple pleural punctures, fissure and bulla transgression, small and deeply situated lesions, longer procedure duration, and operator inexperience [12]. Some studies suggest no difference in pneumothorax rate between larger and smaller needles [13]. Pneumothoraces can occur during or immediately after the procedure, which is why it is important to perform a CT scan of the region following removal of the needle (Fig. 5.4) If the patient develops a pneumothorax during or after TTNB, the patient should immediately be placed biopsy-side down, and oxygen via nasal cannula or facemask should be administered at 2–4 L/min. If the biopsy needle is still within the thorax, manual aspiration of the PNX may be performed (Fig. 5.5). Aspiration of excess pleural air results in improved apposition of the visceral and parietal pleura, minimizing the need for chest tube

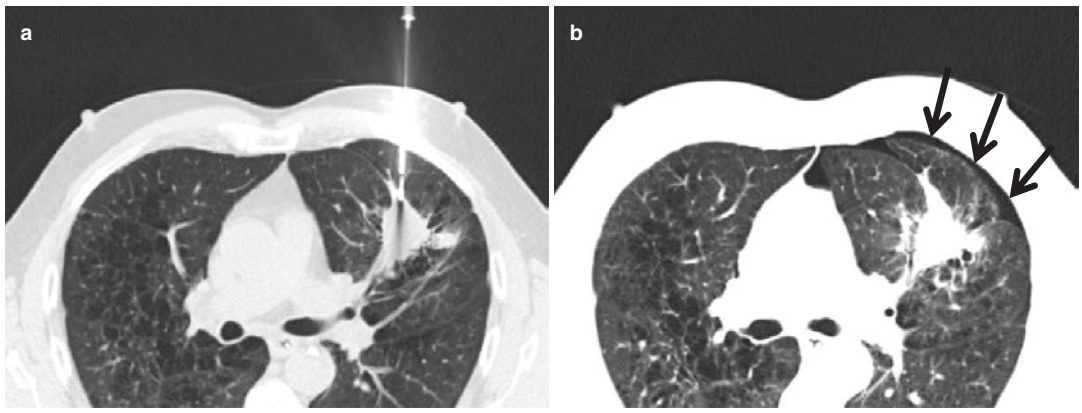


**Fig. 5.4** Axial CT images show a mass in the left lung in patient with severe emphysema. The needle is positioned for biopsy (**a**). Axial CT image shows small pneumothorax immediately after the procedure (*arrows*) (**b**)

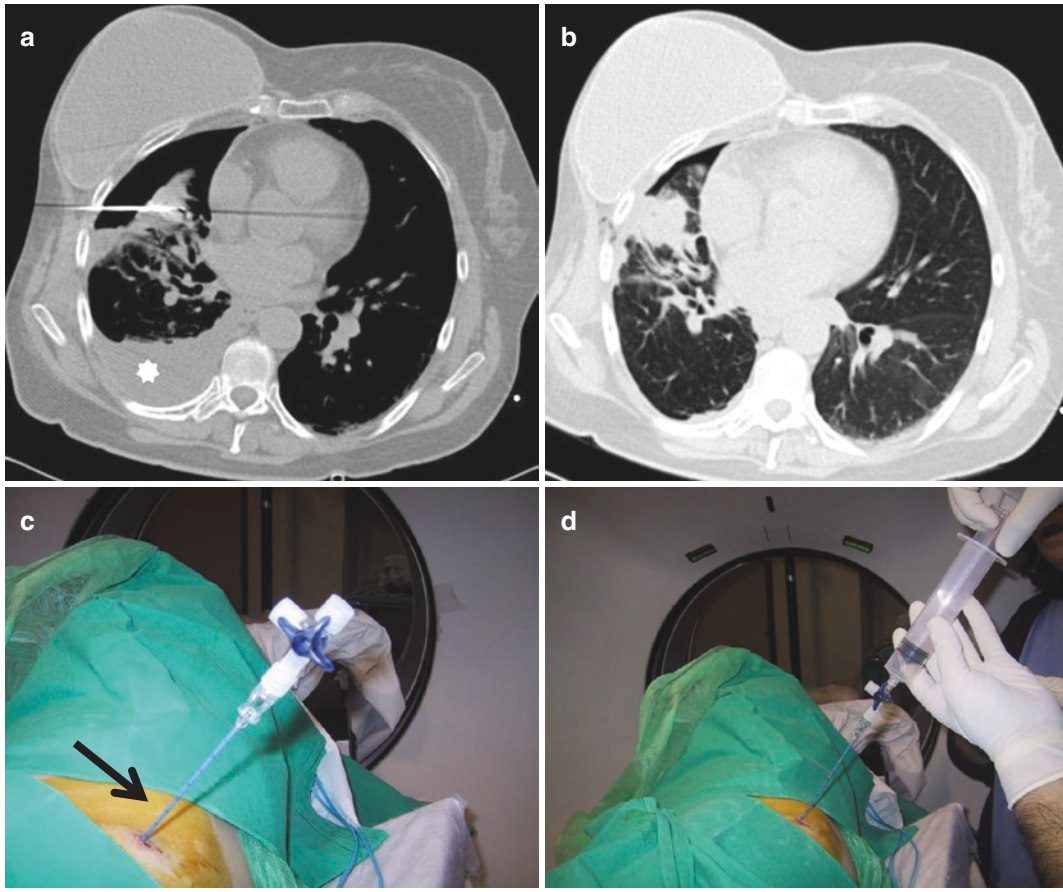


**Fig. 5.5** Axial CT image shows a pneumothorax during biopsy of the right lung metastasis (**a**) immediately drained with a catheter directly in the CT room (*arrow*) (**c**, **d**). Axial CT image after drainage of the pneumothorax and pleural effusion (*) which was already present before the biopsy (**b**)

insertion. Long-term pleural drainage may be required for a persistent air leak despite conservative management, or for a large (>20–30%) or symptomatic pneumothorax. A small-gauge drainage catheter (<16-French) can be placed in a relatively quick and safe manner using either a direct trocar method versus guide wire approach. Typically, a pneumothorax is drained via the second or third intercostal space on the medioclavicular line, and an effusion is drained via the sixth or seventh intercostal space on the midaxillary line. Once in place, the catheter can be connected to chest drainage systems such as Pleur-evac suction or to a Heimlich valve depending on the rate of air leak (techniques) [14].

- **Hemoptysis and Pulmonary Hemorrhage**: Hemorrhage, with or without hemoptysis, is the second most common complication of TNB. Although most bleeding is self-limited, hemorrhage is considered to be the most dangerous potential complication of percutaneous lung biopsy. The use of fine needles for aspiration and biopsy has reduced the incidence of significant bleeding to 0–10% with most series reporting an incidence of less than 5%. In addition, small-gauge (18–20-gauge) automated cutting needles are now widely avail-

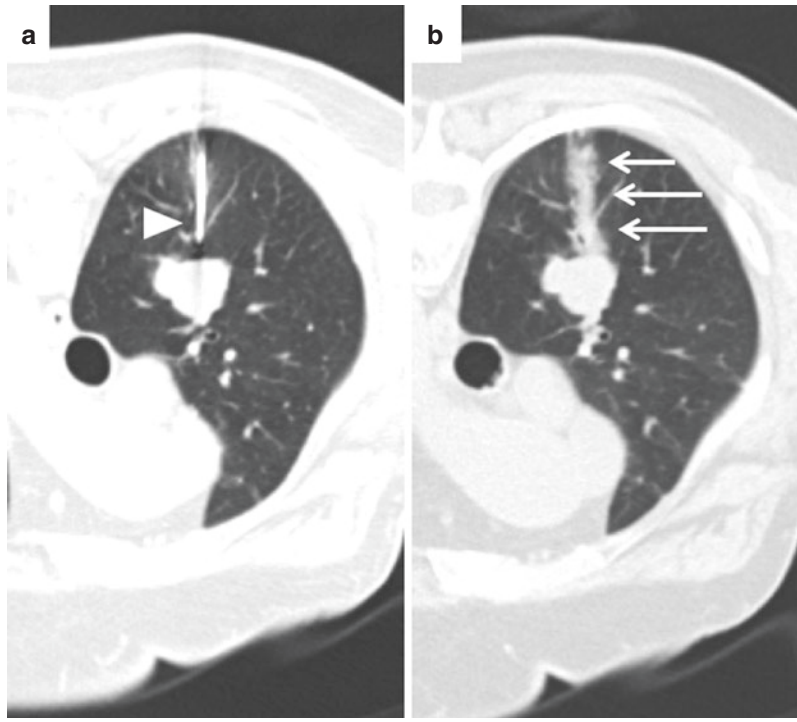


**Fig. 5.6** Axial CT image shows the needle positioned for lung biopsy (*arrowhead*) (**a**). After removing the needle a hemorrhage occurs in his trajectory (*arrows*) (**b**)

able and do not appear to be associated with a significantly increased risk of hemorrhage compared with aspirating needles, particularly when their use is confined to lesions in the peripheral third of the lung [15]. Hemorrhage is characterized by the development of perilesional or in the path airspace and ground-glass opacities on CT; sometimes it can occur also in the pathway of the needle (Fig. 5.6). Most episodes of parenchymal hemorrhage or hemoptysis will settle spontaneously. However, if the patient is hemodynamically unstable, appropriate fluid resuscitation ± blood transfusion is required. Rarely, bronchial or pulmonary transcatheter arterial embolization is required. Hemoptysis is often associated with coughing secondary to airway irritation. Severe coughing can result in pleural laceration and increases the risk of a pneumothorax. If pulmonary venous damage has occurred, the swings from negative (inspiration) to positive (coughing) intrathoracic pressure increase the risk for air embolism and Trendelenburg positioning may be added to facilitate clearance of blood and reduce the risk of an air embolus reaching the cerebral circulation [16].

- **Infection**: Rarely infection can be introduced into the lung lesion secondary to the biopsy procedure. Management: Appropriate antibiotic treatment.
- **Failure**: If insufficient tissue cores are obtained, histology can be inconclusive and thus no diagnosis is made. In this case it is necessary to repeat the percutaneous biopsy. To avoid this situation an inspection of the tissue cores at the time of the biopsy procedure is recommended in order to ensure sufficient tissue volume. To reduce the number of inadequate biopsy it is preferable to

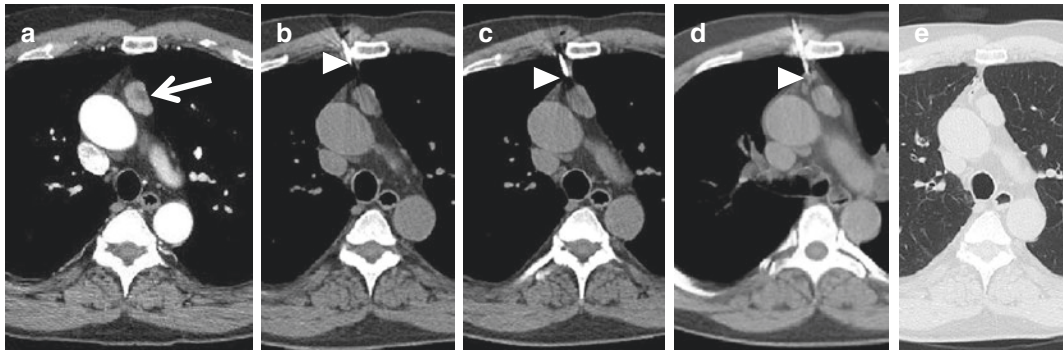


**Fig. 5.7** Axial CT image shows a mass into the anterior mediastinum on the left (*arrow*) (**a**). The needle is positioned between the sternum and right mammary vessels avoiding the lung parenchyma (*arrowheads*) (**b**–**d**). CT image acquired immediately after procedure doesn't show any sign of pneumothorax (**e**)

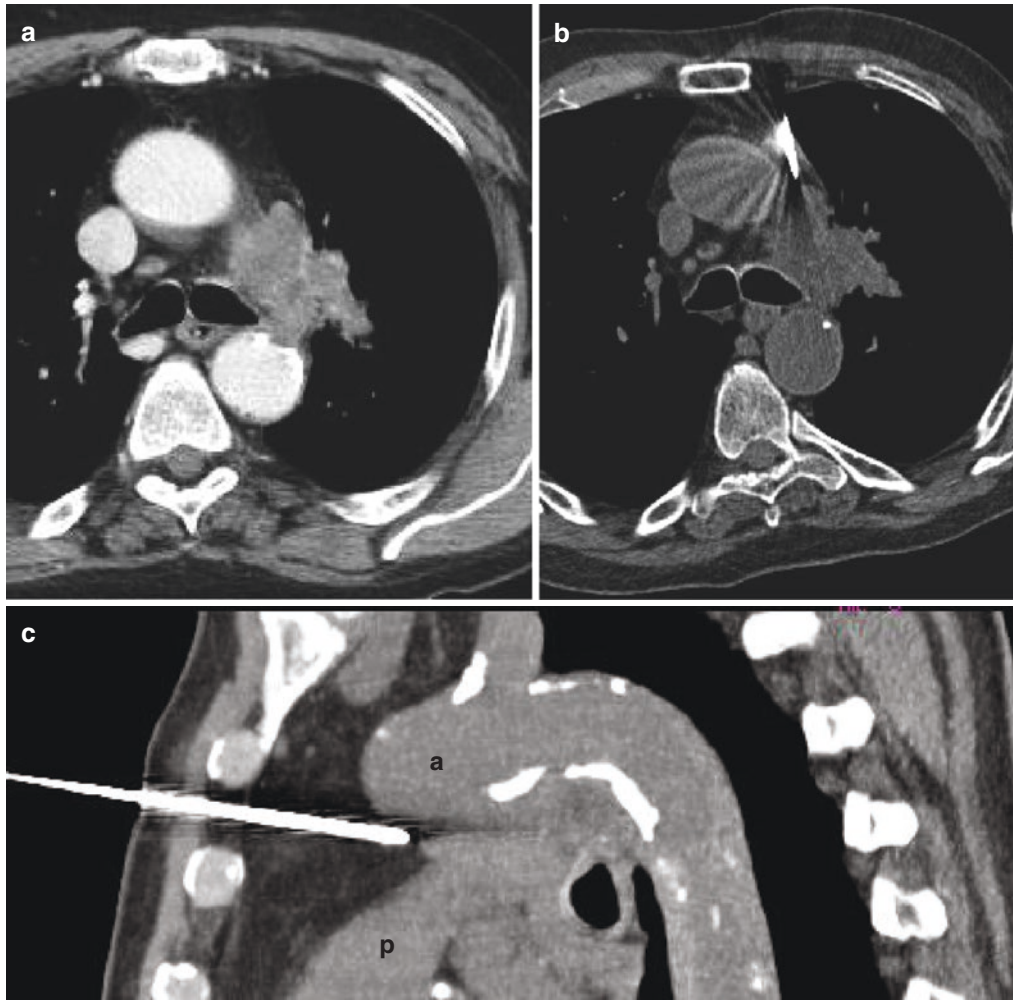


**Fig. 5.8** Axial CT image shows a metastasis of NSCLC in the aortopulmonary window (*arrow*) (**a**). The needle is inserted with parasternal approach trough the mediastinal fat (*arrowheads*) (**b**). Sagittal CT volumetric reconstruction images show the tip of the needle into the mass (m) below to the aorta (a) and above to the pulmonary artery trunk (**c**, **d**)

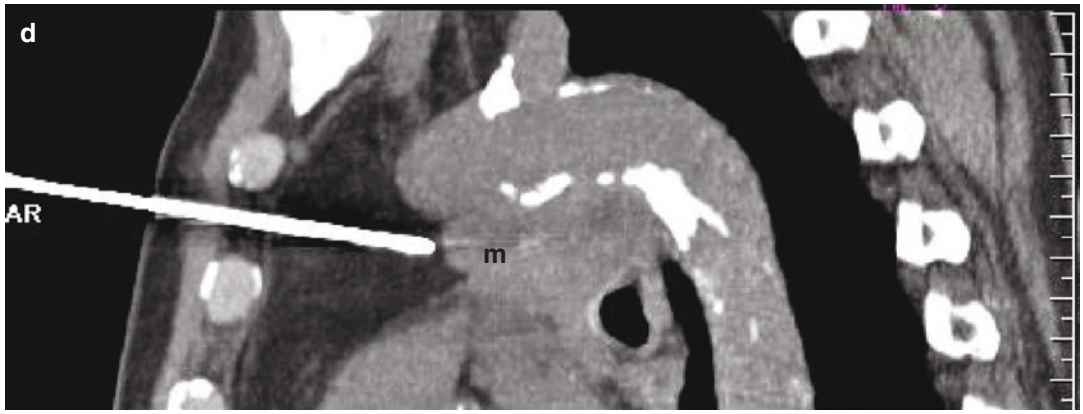


**Fig. 5.8** (continued)

acquire more than one specimen in the same session using the same cannula adequately oriented.

- **Air Embolism**: Rare complication due to puncture of a pulmonary vein with air being sucked in and embolizing to the systemic circulation via the left heart, resulting in symptoms resembling those of stroke, transient ischemic attack, seizure, or cardiopulmonary collapse. Management: Remove the biopsy needle, place the patient in the supine position, and administer 100% oxygen. Hyperbaric oxygen therapy is recommended. A diagnosis may be established by performing immediate brain or cardiac CT to search for intravascular air bubbles.

## 5.5 Mediastinum

### 5.5.1 Anatomic and Technical Considerations

#### 5.5.1.1 Parasternal Approach

A direct mediastinal approach involves placement of the biopsy needle through an extrapleural space medial to the lung to avoid traversal of the lung and the pleura. The needle can be advanced through or lateral to the sternum, through the posterior paravertebral space, through the suprasternal notch, or through the subxiphoid space.

In the parasternal approach the needle is inserted lateral to the sternum and advanced through the parasternal muscles and mediastinal fat into the target lesion (Fig. 5.7). The internal mammary blood vessels are located on either side of the sternum; the artery is usually situated lateral to the vein (Fig. 5.8).

Occasionally, the space between the lateral edge of the sternum and the internal mammary vessels may be too small to allow safe parasternal needle placement. Placing the patient in a lateral decubitus position may cause the mediastinum to shift laterally toward the dependent side, bringing the lesion or the mediastinal fat into direct contact with the parasternal chest wall and allowing the needle access to the lesion. Alternatively, saline solution ("salinoma") or diluted contrast medium can be injected to create an artificial extrapleural path for needle placement. The use of US guidance is generally limited to biopsies of large anterior mediastinal lesions [17].

#### 5.5.1.2 Paravertebral Approach

The paravertebral approach allows access to posterior mediastinal lesions and is used mostly for biopsy of subcarinal lesions from the right side. For the paravertebral approach, the patient is generally placed in the prone position; patients who are unable to lie prone may be placed in a prone oblique or lateral decubitus position. The needle is advanced immediately lateral to the vertebral

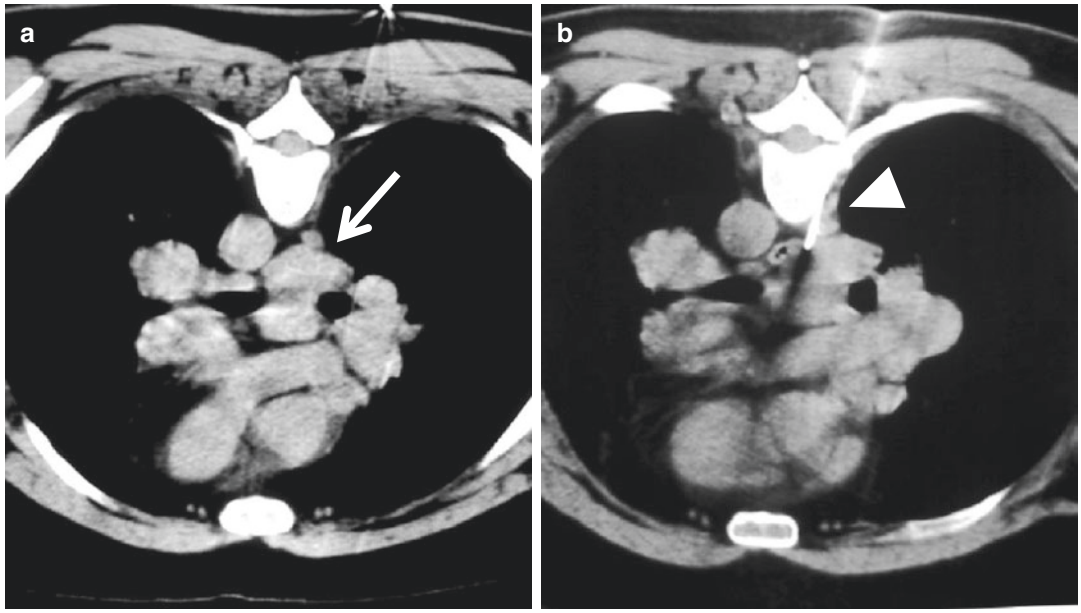


**Fig. 5.9** Axial CT image shows a mass in the subcarinal space (*arrow*) (**a**). The needle is positioned with posterior approach between the endothoracic fascia and the parietal pleura (*arrowhead*) (**b**)

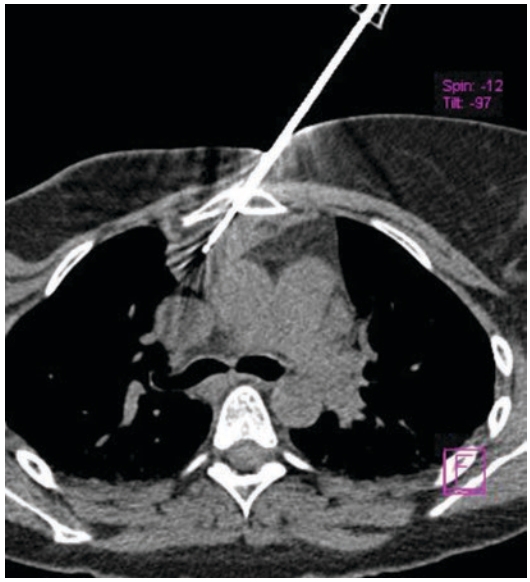


**Fig. 5.10** The axial CT image shows a retrosternal mass. The needle is positioned with trans-sternal approach with oblique pathway to get biopsy avoiding mediastinal vessels

body between the endothoracic fascia and the parietal pleura (Fig. 5.9).

In most patients, injection of 10–20 mL of saline solution is sufficient to achieve adequate mediastinal widening; however, larger volumes may be required. The injection of saline solution also displaces mediastinal structures, such as the azygos vein, esophagus, nerves, and vertebral blood vessels, from the needle's path [17].

#### 5.5.1.3 Trans-Sternal Approach

The trans-sternal approach is used for biopsy of lesions that are not safely accessible by the parasternal approach. To reach the target a cannula adequately oriented is previously positioned across the sternum. Through the cannula the biopsy needle is inserted and the sample is taken (Fig. 5.10). The entire procedure can be performed in local anesthesia but the anesthetic infiltration of the periosteum is required to avoid pain during and after biopsy. The use of a hammer can help to push the needle crossing the sternum.

There are some other techniques due to mediastinal biopsy, like the following:

- **Suprasternal Approach**
  The suprasternal approach is another alternative method for obtaining tissue samples for cytologic or histologic diagnosis of mediasti-

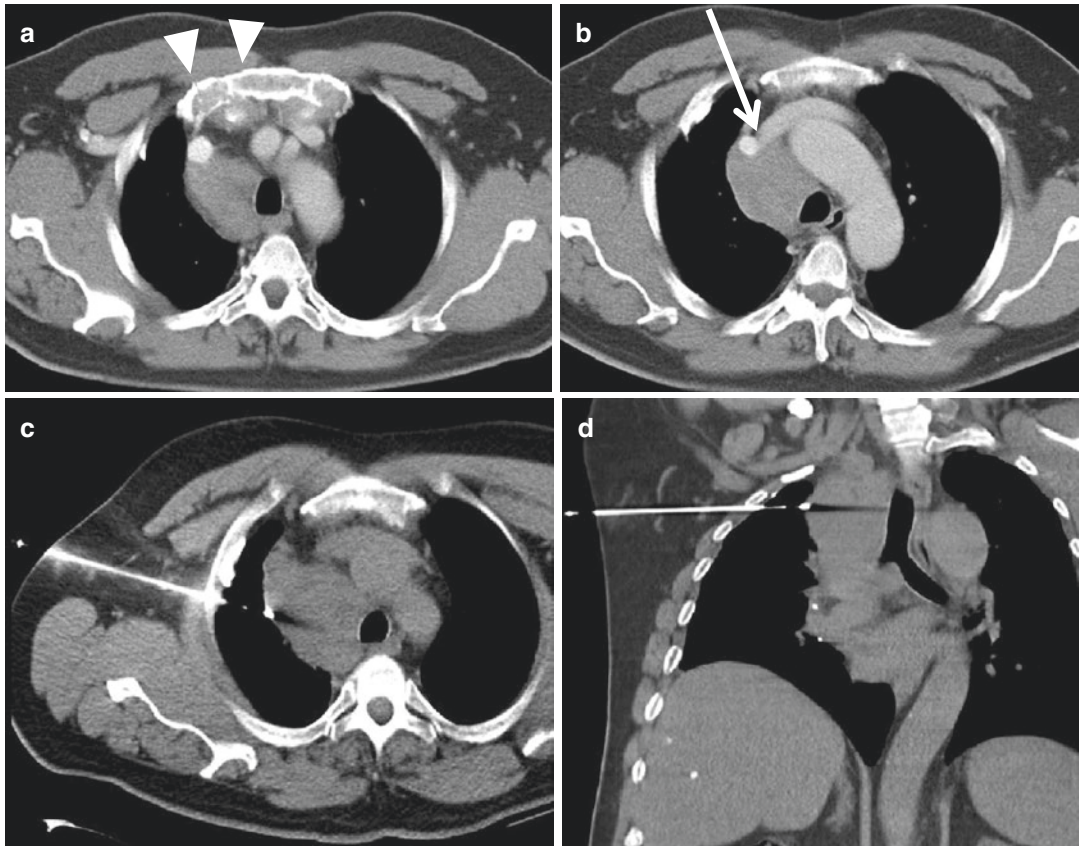


**Fig. 5.11** The interposition of the sternum (*arrowheads*) or the major vascular structures (*arrow*) (**a**) obstacles the extrapleural biopsy of the mediastinal mass (**b**). The biopsy was performed using a transpulmonary approach (**c**, **d**)

nal lesions. The use of the suprasternal approach for US- and CT-guided biopsy is taken into consideration to reach small retrosternal lesions located in the anterior and middle mediastinum. A direct mediastinal approach, which enables extrapleural needle placement, is the preferred method to avoid the risk of pneumothorax especially for patients affected by BPCO or other emphysematous conditions. Patients have to be positioned on their back with their head hyperextended. Hemorrhagic complications are rare and are due to an unaspected vascular puncture.

– **Transpulmonary Approach**
The transpulmonary approach is usually used to biopsy lesions inaccessible with an extrapleural approach (Fig. 5.11). This approach involves transgression of the lung and visceral pleura by the biopsy needle and the major limitation is the pneumothorax which is more frequent with respect to the biopsy of the lung because the needle passes the parietal and visceral pleura to reach the mediastinum. The injection of physiological saline solution in the subpleural space in the point of insertion of the needle can help to reduce the pneumothorax rate.

– **Approach Through the Pleural Space**
CT guidance is usually used to perform the mediastinum biopsy through pleural space and the needle can be advanced increasing the pleural space by injection of saline or through a preexistent pneumothorax or pleural effusion. In the preexistent pleural effusion US guidance can be used to advance the needle and to reach the target through the pleural space. In the posterior

mediastinal mass a paravertebral approach with patient prone can be used. The pleural fluid can be used as an "acoustic window" for needle placement. During mediastinal biopsy through the pleural space an inadvertently puncture of the visceral pleura can occur with consequent pneumothorax.

## 5.6 Drainage

Chest drainage procedures can be classified based on the anatomical regions of the pleural space, lung parenchyma, and mediastinum.

Placing an image-guided percutaneous chest catheter is an important alternative to surgically placed chest tubes because of the advantage of precise placement under image guidance (US or CT) and small caliber of the catheter (5–14 F versus approximately 24 F for chest tubes).

Most common indications are pleural space: pleural effusion, pneumothorax, empyema, or infection, and lung parenchyma and mediastinum: abscess.

### 5.6.1 Pleural Space

- **Pleural Effusion**: Defined as accumulation of fluid in the pleural space. Intrapleural pressure is lower than the interstitial fluid pressure of the pleural tissues, favoring flow of fluid into the pleural space. The protein and cellular concentration in this fluid is typically low because pleural fluid is effectively a filtrate. Normally, the influx of fluid into the pleural space is balanced by its removal via the lymphatic system. In certain clinical conditions, the balance between the secretion and absorption can be disturbed and fluid may accumulate in the pleural space. In disease states, the normal composition of pleural fluid is altered, which allows for diagnosis via pleural fluid analysis. Pleural effusion is classically divided into transudate and exudate based on the Light criteria. The Light criteria consist of measurement of the lactate dehydrogenase (LDH) and protein concentration in the pleural fluid and serum.
- **Pneumothorax**: PNX is an imaging finding and clinical condition in which air accumulates within the pleural space. Pneumothoraces can be either spontaneous, associated with underlying lung disease (lymphangioleiomyomatosis, blebs, etc.), or the result of traumatic injury to the chest wall, pulmonary parenchyma, or airways. Traumatic pneumothorax most often results from penetrating or blunt trauma; spontaneous pneumothorax may be divided into a primary form (rupture of an apical intrapleural bleb) and a secondary form, which is associated with underlying parenchymal lung disease.
- **Empyema**: This is a collection of purulent fluid in the pleural space. The most common cause is pneumonia. Lung abscess, bronchopleural fistula, esophageal perforation, postsurgical complications, and trauma may also result in empyema. Along with antibiotic therapy and treatment of the underlying disease process, early and complete drainage of the infected fluid is considered essential in the successful management of empyema [18].

### 5.6.2 Intervention

- **Thoracentesis**: Although the procedure can be performed at bedside without imaging guidance, it is generally recommended to use ultrasonographic guidance to avoid potential complications, most of all in pediatric patients. Once the patient is best positioned for the procedure, ultrasound can be used to determine the optimal needle trajectory to the effusion. Use of the lower frequency 3–5 MHz probe offers a wider depth of field and a more global view of the lung and the effusion [19]. There is a method for estimating the size of the pleural effusion in medical intensive care unit patients. An equation was described between the volume of the effusion and the separation distance between the lung and the outer parietal pleura as *the effusion size (cc) = 20 × separation*

*(sep) in mm*; here the separation (sep) was identified as the maximal separation distance between the parietal and visceral pleura during end expiration [20]. There are two options for positioning of the patient for the thoracentesis procedure. An upright position is traditionally preferred by many clinicians, with the patient leaning forward on a support. This allows access to the posterior approach to thoracentesis. The supine position, allowing a lateral approach to the chest cavity, may be employed in patients unable to sit up. This would be a similar position to that used for the typical placement of a chest tube. Optimally, the head of the bed should be elevated in this position to facilitate the drainage of the pleural fluid inferiorly and to accumulate the effusion closer to the location of standard needle placement [21]. Once the optimal needle puncture location is determined by using ultrasound, it is important to use a liberal amount of local anesthesia to provide maximal patient comfort during the procedure. For a simple diagnostic thoracentesis, a 20-gauge needle and syringe is generally sufficient for fluid collection. For greater volume drainage, a specific thoracentesis kit has the benefit of a plastic catheter that can be advanced over a metal trocar. Removing the metal trocar immediately as the pleural effusion is entered, while simultaneously advancing the flexible plastic catheter, will have the benefit of decreasing the risk of injury to the lung. When ready to proceed, one should advance the needle into the pleural space while simultaneously drawing back with the plunger of the syringe. Once pleural fluid is flowing into the syringe, adequate fluid (usually 20–30 cc) should be removed and sent for the usual laboratory studies [22].

- **Chest Drain Insertion**: The preferred position for drain insertion is on the bed, slightly rotated, with the arm on the side of the lesion behind the patient's head to expose the axillary area. In fact the most common position for chest tube insertion is in the midaxillary line. For apical pneumothoraces the second intercostal space in the midclavicular line is sometimes chosen but is not recommended routinely as it may be uncomfortable for the patient and may leave an unsightly scar. The majority of physicians now use smaller catheters (10–14 French) and studies have shown that these are often as effective as larger bore tubes and are more comfortable and better tolerated by the patient [23]. As a chest drain may potentially be in place for a number of days, aseptic technique is essential to avoid wound-site infection or secondary empyema. After local anesthesia the tube will be positioned and the incision for insertion of the chest drain should be similar to the diameter of the tube being inserted. If possible, the tip of the tube should be aimed apically to drain air and basally for fluid. Two sutures are usually inserted—the first to assist later closure of the wound after drain removal and the second, a stay suture, to secure the drain [24].

## 5.7 Lung and Mediastinum

**Abscess**: A lung abscess usually results from aspiration of anaerobic oropharyngeal bacteria into gravity-dependent portions of the lung, most often the posterior segments of the upper lobes and the superior segments of the lower lobes. Mediastinal abscesses are a rare and potentially fatal condition; common etiologies of mediastinal abscess include head and neck infections that descend into the mediastinum, trauma, and postsurgical. Bronchial obstruction due to malignancy, inflammation, or foreign body is also an important risk factor for development of lung abscess because it impairs effective clearing of aspirated oropharyngeal fluid.

Current first-line therapy for lung abscess is an antibiotic therapy directed at the suspected causative organisms.

### 5.7.1 Intervention

When nonresponsive to antibiotics, postural drainage, and bronchoscopic drainage, image-guided catheter drainage allows high success rate of more than 70% after 10–15 days of drainage [25]. If the abscess abuts the pleura, the catheter can be placed without lung parenchymal transgression.

It typically involves the use of 7–14 F (French) catheter for drainage and Seldinger technique. Ideally, insertion should be in the "triangle of safety," an area bordered by the lateral edge of the latissimus dorsi, the lateral border of the pectoralis major muscle, and a line superior to the horizontal level of the nipple.

Principals steps of Seldinger technique [26]:

1. Insert an introducer needle into the pleural space and confirm that either fluid or air is returned. If this does not occur, do not proceed.
2. If fluid or air is returned, the syringe is removed.
3. Insert the guide wire through the introduced needle into the pleural space.
4. The introducer needle is then removed, leaving the guide wire in position.
4. Pass the dilators sequentially over the guide wire to dilate the tract in a slight twisting action. Never use the force.
5. Remove the dilator.
6. Pass the chest tube into the pleural space over the guide wire.
7. Remove the guide wire and any tube stiffeners, leaving the chest tube in place.
8. Secure the tube in place with a suture, dress with gauze, connect the drainage system, obtain a chest radiograph to confirm the tube position, assess lung expansion, and monitor the initial drainage from the tube.

Complications:

- Hemorrhage.
- Pneumothorax, rare and usually from air introduced during procedure: This will resolve with the catheter in place.
- Lung injury can lead to bleeding into bronchial tree and aspiration into contralateral side. If bleeding appears in endotracheal tube or expectorate, place patient ipsilateral side down. Extremely rare with imaging guidance.

## 5.8 Lung and Soft-Tissue Ablation

Interventional radiology offers also some therapeutic opportunities with the use of radiofrequency ablation (RF), microwave ablation (MW), cryoablation, etc. In particular lung cancer has been the most common target of this procedures;

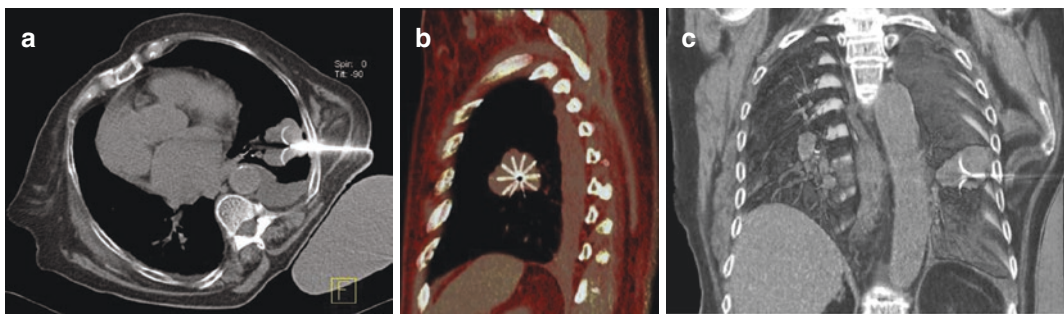


**Fig. 5.12** Axial CT image shows a NSCLC in 71-year-old man treated with RFA using an umbrella-shape device (**a**). The coronal and sagittal volumetric reconstructions show the correct central position of the device into the mass (**b**, **c**)

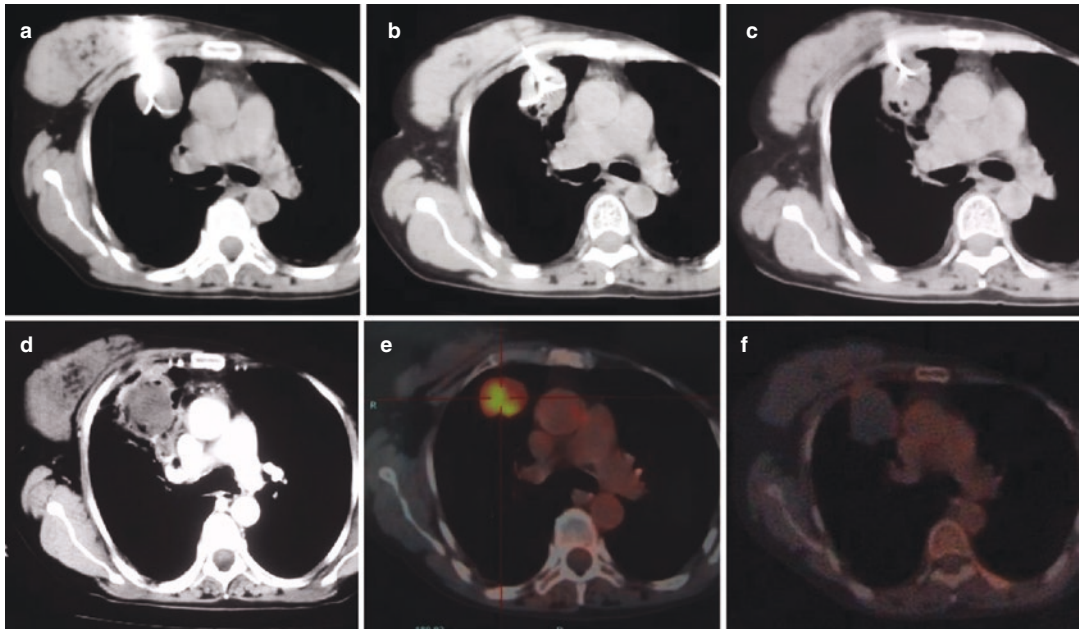


**Fig. 5.13** Successful RFA of a breast cancer lung metastasis ineligible for surgery. The RF device is positioned in three different depths (**a**–**c**). Contrast CT image acquired after ablation shows lack of contrast enhancement of the tumor (**d**). 2 months later, the follow-up PET-CT image shows complete loss of 18F-FDG avidity indicative of metabolic response to treatment (*arrow*) (**e**, **f**)

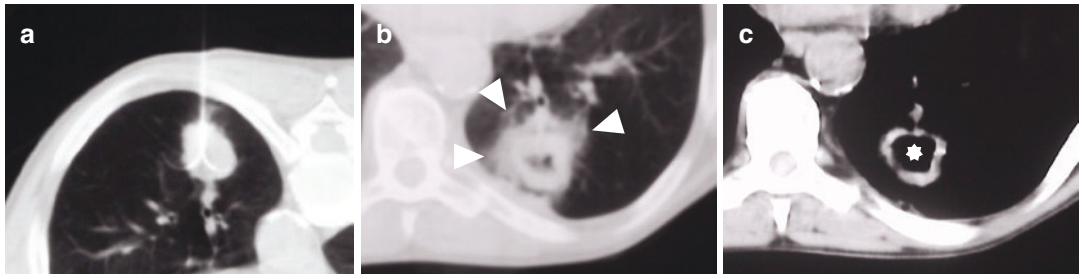


**Fig. 5.14** Patient with NSCLC on the left lung. Axial CT image shows the device positioned into the tumor with posterior approach (*arrow*) (**a**). Immediately after the treatment a ground-glass opacity is visible around the tumor (*arrowheads*) (**b**). Cavitation of the mass 1-month follow-up (*) (**c**)

actually surgical resection remains the gold standard of therapy in early-stage non-small cell lung cancer (NSCLC), being the only therapeutic option with proven long-term cure and survival, reserved for only stage I–II of the disease [27]. Thermal ablation has recently been advocated as an alternative treatment, especially in patients with early-stage disease who are not surgical candidates.

## 5.9 Radiofrequency Ablation

Radiofrequency ablation (RFA) uses a high-frequency current to heat and coagulate tissues. An alternating electrical current of usually 500 kHz with a power of up to 200 Watts is applied to the target lesion by means of an electrode. The therapeutic range for RFA is quite narrow: between 65 C and 105 C, in

which protein denaturation takes place, leading to coagulative necrosis [28]. Radiofrequency ablation is indicated in patients for whom treatment of lung cancer is expected to convey a survival benefit and/or improved quality of life [29].

RFA is usually reserved for patients with early stage I or II NSCLC, in whom a surgical resection is contraindicated. RFA can also be suitable in patients with advanced disease who responded to chemo/radiotherapies, but who have a persistent peripheral focus of disease. RFA has also been used in isolated recurrence of NSCLC in postsurgical patients in whom further surgery is contraindicated. Patients with limited peripheral lung metastases can also be suitable candidates for RFA treatment provided that the primary cancer is controlled [30]. Large tumors (usually >5 cm), proximity to major pulmonary vessels or major bronchus, hilar tumors, and more than three tumors in one lung are usually contraindicated for RFA treatment.

Virtually all cases of RFA are carried out under CT guidance, even though there have been reports of US being used if the target lesion is in contact with the parietal pleura [31]. The aim is to achieve complete ablation of the tumor along with a parenchymal margin of 0.5 cm to 1 cm. Differently from the liver the ablation of

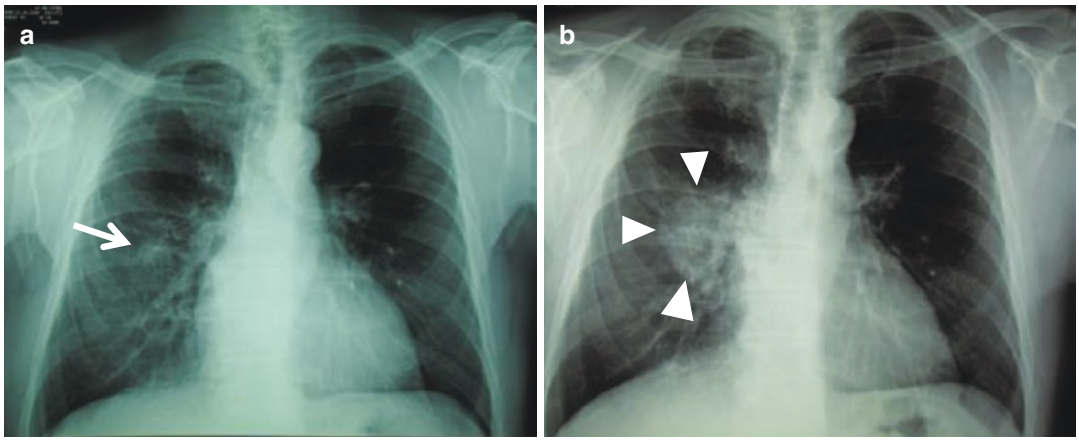


**Fig. 5.15** Patient with perihilar NSCLC of right lung treated with RFA. X-ray image shows a nodular opacity (*arrow*) (**a**). X-ray image acquired 24 h after ablation shows large ground-glass opacity which completely covers the tumor (*arrowheads*) (**b**)

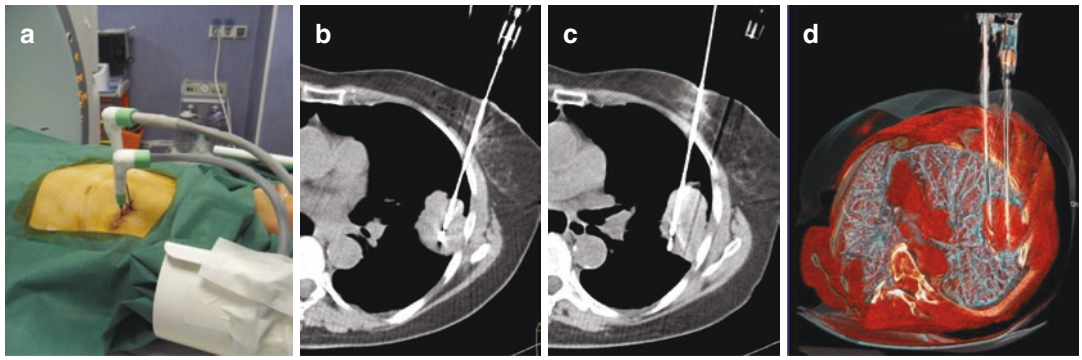


**Fig. 5.16** MWA of a NSCLC to the left lung in a 64-year-old woman not candidate for surgery. Two antennas are inserted percutaneously with CT guidance (**a**–**c**). The volumetric reconstruction shows the two antennas correctly positioned parallel into the mass (**d**)

needle track is usually not. During the procedure the use of computerized tomography reconstructions allows to see if the tumor is completely covered by the treatment (Fig. 5.12). In large tumors the multiple positioning of the RF electrode can be used to better treat the mass (Fig. 5.13a–c). Post-procedure care usually involves repeat imaging of the chest to assess the presence of any pneumothorax and a 24-h observation period [29].

RFA often induces an inflammatory reaction in the surrounding lung parenchyma, which may appear as ground-glass opacification or even consolidation on imaging. In several cases cavitation of the mass can occur (Fig. 5.14). Most centers use a 1-month follow-up CT scan as baseline, because the high-density treated area is usually larger than the initial tumor [31]. CT scans are repeated at 3 months, 6 months, and then every 6 months post-procedure.

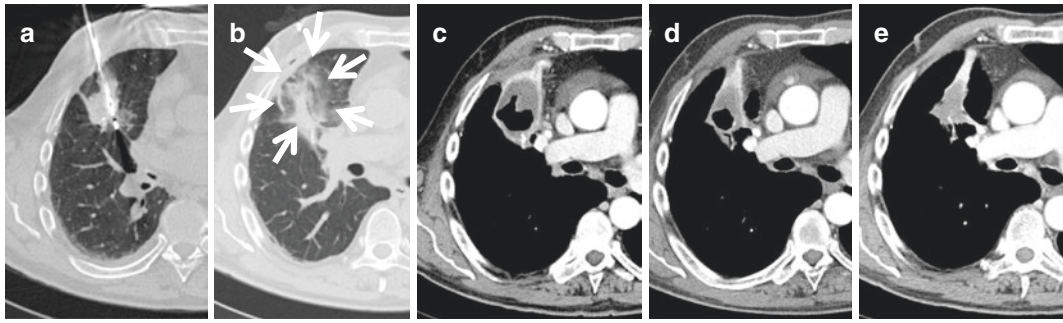


**Fig. 5.17** MWA of a NSCLC to the right lung in a 69-year-old man. Axial CT image shows the antenna positioned into the mass with anterior approach (**a**). Ground-glass opacity around the tumor immediately after ablation (*arrows*) (**b**). Progressive reduction in size of the cavitated area and no contrast enhancement at 3-, 6-, and 12-month follow-up confirm the success of the treatment (**c**–**e**)

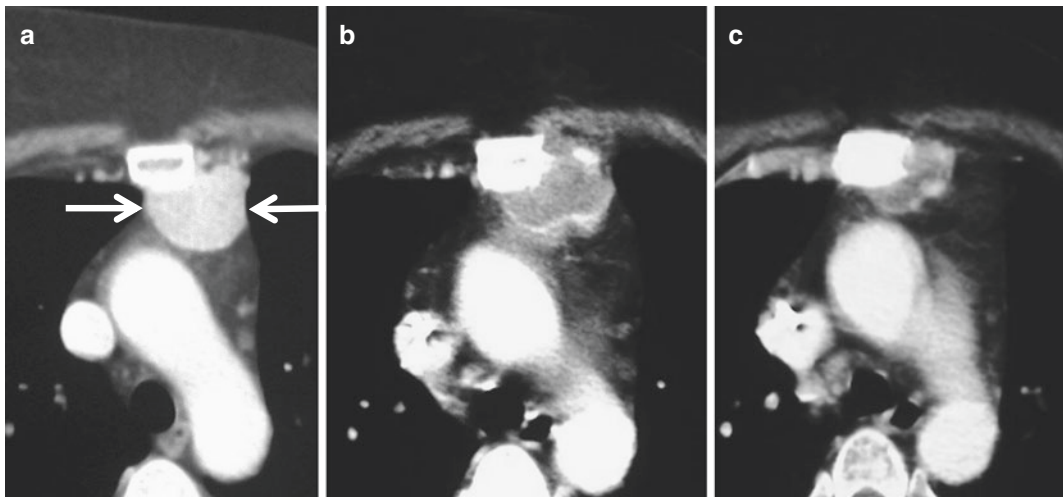


**Fig. 5.18** MWA of a breast cancer metastasis in the anterior mediastinum of a 70-year-old woman. Contrast CT image shows a 5 cm soft tissue of high density (*arrows*) (**a**). Contrast CT images show downsizing and lack of contrast enhancement of the mass at 3- and 6-month follow-up (**b**, **c**)

Sometimes PET-FDG scan is required by oncologists to check if the tumor has been completely destroyed by the ablation (Fig. 5.13f). Before discharge the patient usually acquires an X-ray of the thorax to check complications and to evaluate the treated area which appears as a large ground-glass opacity around the lesion (Fig. 5.15).

The most common complications encountered with RFA treatment are pneumothorax and pleural effusion, most of which are usually small and self-limiting. Management of this complications is the same as that in the lung biopsy.

## 5.10 Microwave Ablation

MW basically uses dielectric hysteresis to produce heat. During the application of electromagnetic waves (usually at 900–2500 MHz), the polar water molecules are forced to realign constantly with the oscillating electric field, increasing their kinetic energy and converting this energy into heat which increases tissue temperatures to cytotoxic levels. Unlike from RFA that results in heating in tissues adjacent to the electrode, in MWA direct "radiating" heating occurs in the volume of tissues around the antenna. Moreover, MWA is able to produce a larger heating zone with higher temperature and more rapidly than RF. The microwave system consists of a generator connected to an antenna through a coaxial transmission line. The delivery of electromagnetic energy from the generator to the antenna is usually via a coaxial transmission line. However, a major disadvantage is due to the fact that the smaller the cable diameter, the more the power loss and resulting cable heating. MWA is usually carried out in a similar fashion to RFA, under conscious sedation and local anesthesia and CT or US guidance.

The mean tumor diameter was 3.0 cm and the mean ablation diameter obtained was 4.0 cm. Histological analysis of the ablated specimens showed marked coagulation necrosis and complete thermocoagulation and absence of any viable tumor [32]. To control the size of coagulative necrosis we can change the coagulative performance using different power levels and different exposure times. In large masses MWA can be performed simultaneously using two coaxial antennas (connected with two generators) to obtain a major necrosis

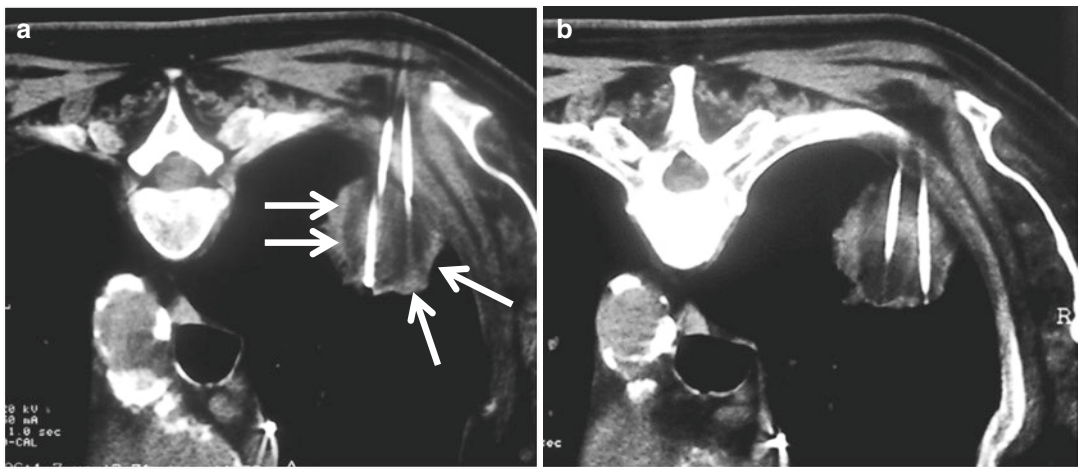


**Fig. 5.19** Cryoablation of a NSCLC of a 77-year-old man. Axial CT image shows the cryoprobes into the tumor during the freezing phase. The formation of *ice ball* appears as an ovoid, well-delimitated hypodense area around the needles into the tumor (*arrows*) (**a**, **b**)

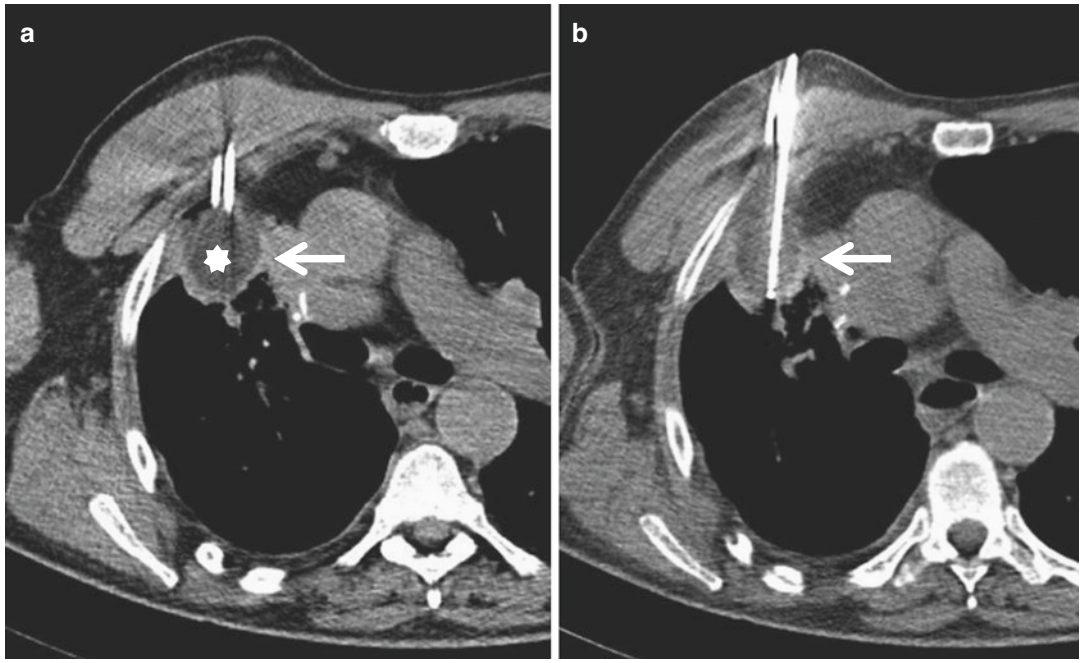


**Fig. 5.20** Cryoablation of a NSCLC in a 65-year-old man after a previous superior lobectomy. The axial CT images acquired during the freezing phase show a well-delimited ice ball (*) into the tumor in contact to the superior vena cava (*arrows*) (**a**, **b**)

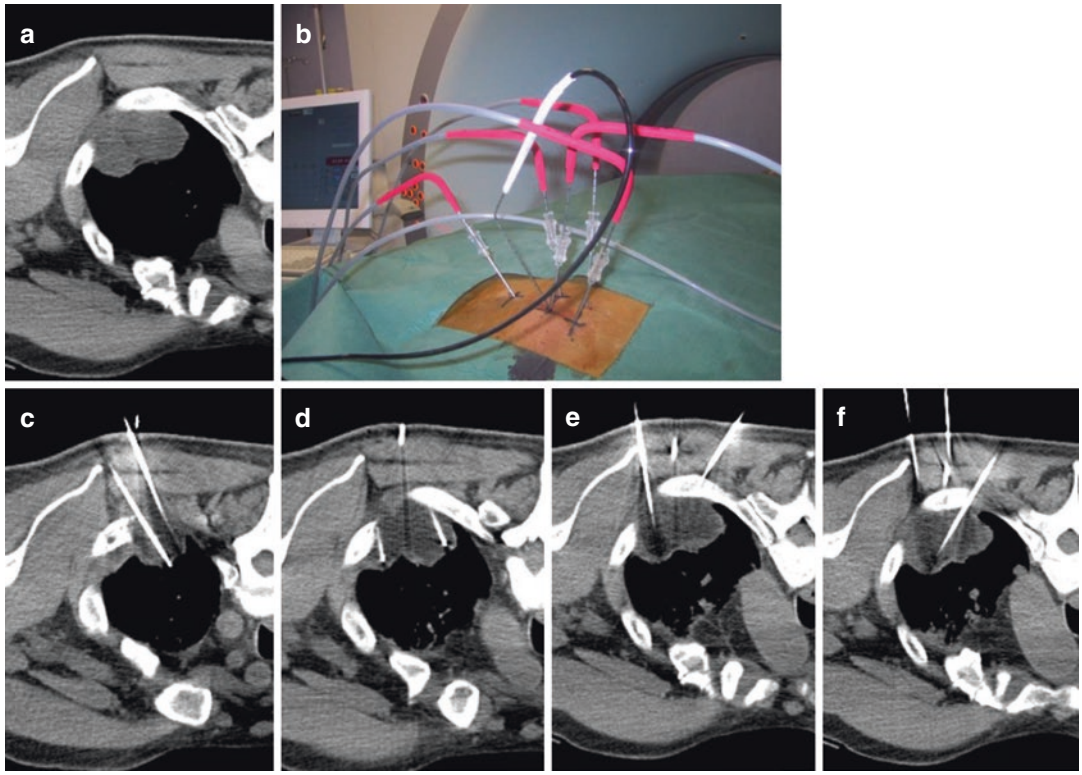


**Fig. 5.21** Axial CT image shows a 54-year-old man who presented a strong pain due to pleural and infiltration of a rib by a large metastasis of liposarcoma (**a**) treated with insertion of 5 cryoprobes and a thermosensor (**b**–**f**)

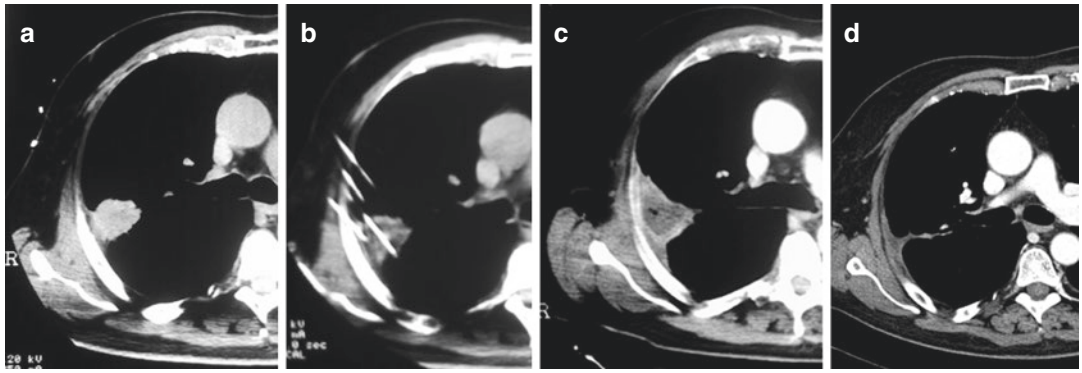


**Fig. 5.22** Successful CRA of a large colorectal lung metastasis in patient ineligible for surgery. Axial CT image shows a 3.7 cm metastasis in the right lung (**a**) treated with 4 cryoprobes (**b**). Contrast axial CT image acquired after 1 month shows lack of enhancement and initial reduction in size of the lesion (**c**) which evolved in a scar after 20-month follow-up (**d**)

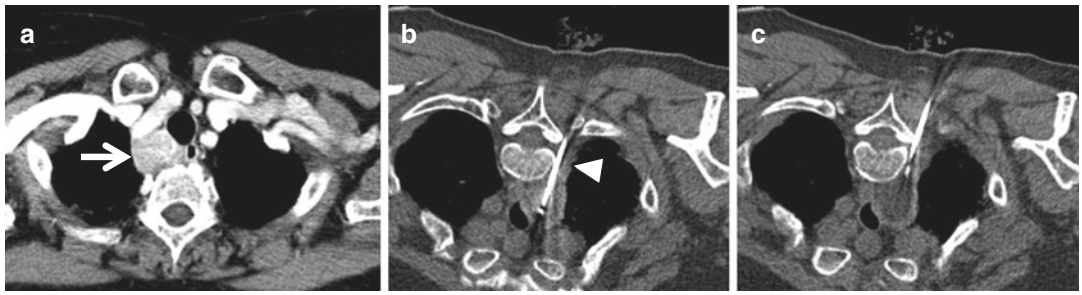


**Fig. 5.23** Contrast axial CT image shows a 64-year-old woman who presents a mediastinal metastasis of thyroid carcinoma (*arrow*) (**a**). Axial CT image shows the cryoprobe into the mass, positioned with paravertebral approach between thoracic fascia and parietal pleura (*arrowhead*) (**b**)

area in very short time (Fig. 5.16). Follow-up CT scans were performed at 1-, 3-, and 6-month interval, and the mean follow-up period was 10 months [33]. Stable or reduction in size and absence of tumor enhancement CT images are considered indicative of complete tumor necrosis. Cavitation, similar to RFA, can occur after MWA and usually does not require any intervention. The evolution consists of a slow but progressive reduction in size of the mass (Fig. 5.17). Also mediastinal tumors can be treated with MWA and the evolution of the tissue mass is similar to lung tumors (Fig. 5.18).

### 5.10.1 Complications

Hemoptysis, skin burns, pneumothorax, and infections are uncommon but possible complications which can occur after MWA of the lung. A rare but serious complication is the bronchopleural fistula after MWA which consists of a direct communication of pleural cavity and the bronchial tree. The fistula usually spontaneously closes itself but sometimes the suture of the bronchial defect is necessary.

### 5.10.2 Cryoablation

Like RFA and MWA, cryoablation is performed under image guidance, most commonly CT or US. Cryoablation uses extreme cold to cause tissue destruction. Modern cryoablation systems utilize specialized probes to deliver cycles of argon and helium gases to, respectively, freeze and thaw targeted tissues. The procedure relies upon the rapid decompression (Joule–Thomson effect) of argon and helium gases circulating

inside the probe. Depending on the distance from the needle, the effect of the ice is different. Temperatures ranging between 40° and 20° below zero result in intracellular ice formation with membrane rupture and cell death. With temperatures above 20° below zero we have resulting supercooling of the tissues without intracellular ice formation. Apoptosis is possible but inconstant and we need to repeat the cycles. Cellular damage occurs via a complex combination of cellular damage during a freezing and thawing cycle. Direct cell injury occurs via a combination of metabolic disruptions, cell dehydration, and formation of intracellular ice crystals which disrupts organelles and cell membranes and leads to cell death [34]. Cryoablation may be superior to RFA as larger ablation margins can be obtained, multiple applicators can be used, and it has been associated with less pain. Visualization of the ablation zone is another distinct advantage of cryoablation, which is seen as an "ice ball" on CT scans (Fig. 5.19) particularly useful during the treatment of tumors closed to major vascular structures (Fig. 5.20). However, for tumors adjacent to or contacting large vascular structures, such as the aorta or main pulmonary artery, a triple-freezing protocol is generally preferred to overcome sink effect of blood flow and to obtain larger ablation. Cryoablation also preserves the underlying collagenous architecture of the target tissues [35]. Cryoablation is a method which can also be used to treat lung lesions with severe pain due to pleural infiltration or involvement of the thoracic wall (Fig. 5.21). Potential risks and complications of pulmonary cryoablation are essentially those deriving from percutaneous interventional treatment such as local hematomas, pneumothorax, pleural effusion, and pulmonary bleeding. The use of thin needles to perform the ablation allows to reduce the number and severity of complications [36]. Compared to the lesions treated RFA or MWA the transformation of the lung lesion treated with cryoablation is similar. There is lack of contrast enhancement after 1 month followed by a scar evolution after a few months' follow-up (Figs. 5.22 and 5.23).

## References


1. Gupta S. Role of image-guided percutaneous needle biopsy in cancer staging. Semin Roentgenol. 2006;41:78–90.
2. Collins JM, Kriegshauser JS, Leslie KO. CT-guided biopsy of perivascular tumor encasement using simultaneous IV contrast enhancement. Am J Roentgenol. 2009;193:W283–7.
3. Ahrar K, Gupt S, editors. Percutaneous image-guided biopsy. New York: Springer; 2013.
4. Pate IJ, Davidson JC, Nikolic B, et al. Standards of practice committee, with cardiovascular and interventional radiological Society of Europe (CIRSE) endorsement. Consensus guidelines for periprocedural management of coagulation status and hemostasis risk in percutaneous image-guided interventions. J Vasc Interv Radiol. 2012;23(6):727–36.
5. Manhire A, Charig M, Clelland C, et al. Guidelines for radiologically guided lung biopsy. Thorax. 2003;58(11):920–36.
6. Khadadah ME, Muqim AT, Al-Mutairi AD, et al. Closed percutaneous pleural biopsy. A lost art in the new era. Saudi Med J. 2009;30(6):793–7.
7. Winokur RS, Pua BB, Sullivan BW, Madoff DC, FSIR. Percutaneous lung biopsy: technique, efficacy, and complications. Semin Interv Radiol. 2013;30:121–7.
8. Ahrar K, Gupta S, editors. Percutaneous image-guided biopsy. New York: Springer; 2014. Chapter 11
9. Frable WF. Fine needle aspiration biopsy techniques. In: Bibbo M, Wilbur D, editors. Comprehensive cytopathology. 3rd ed. Philadelphia: Saunders, Elsevier; 2008. p. 579–98.
10. Solomon SB, Zakowski MF, Pao W, et al. Core needle lung biopsy specimens: adequacy for EGFR and KRAS mutational analysis. AJR Am J Roentgenol. 2010;194(1):266–9.
11. Morvay Z, Szabó E, Tiszlavicz L, Furák J, Troján I, Palkó A. Thoracic core needle biopsy using ultrasound guidance. Ultrasound Q. 2001;17:113–21.
12. Moore EH, Shepard JO, McLoud TC, et al. Positional precautions in needle aspiration lung biopsy. Radiology. 1990;175:733–5.
13. Swischuk JL, Castaneda F, Patel JC, et al. Percutaneous transthoracic needle biopsy of the lung: review of 612 lesions. J Vasc Interv Radiol. 1998;9(2):347–52.
14. Aziz A, Ashizawa K, Nagaoki K, Hayashi K. High resolution CT anatomy of the pulmonary fissures. J Thorac Imaging. 2004;19:186–91.
15. Arakawa H, Nakajima Y, Kurihara H, et al. CT-guided transthoracic needle biopsy: a comparison between automated biopsy gun and fine needle aspiration. Clin Radiol. 1996;51(7):503–6.
16. Wallace AB, Suh RD. Percutaneous transthoracic needle biopsy: special considerations and techniques used in lung transplant recipients. Semin Interv Radiol. 2004;21(4):247–5.

17. Ahrar K, Gupta S, editors. Percutaneous image-guided biopsy. New York: Springer; 2014. p. 119.
18. Light RW. Parapneumonic effusions and empyema. ClinChestMed. 1985;6(1):55–62.
19. Feller-Kopman D. Ultrasound-guided thoracentesis. Chest. 2006;129(6):1709–14.
20. Balik M, Plasil P, Waldauf P, et al. Ultrasound estimation of volume of pleural fluid in mechanically ventilated patients. Intensive Care Med. 2006;32(2):318–21.
21. Nicolaou S, Talsky A, Khashoggi K, Venu V. Ultrasound-guided interventional radiology in critical care. Crit Care Med. 2007;35(supplement 5):S186–97.
22. Sikora K, Perera P, Mailhot T, Mandavia D. Ultrasound for the detection of pleural effusions and guidance of the thoracentesis procedure. ISRN Emergency Medicine. 2012;2012:676524.
23. Patz EF, Goodman PC, Erasmus JJ. Percutaneous drainage of pleural collections. J Thorac Imaging. 1998;13(2):83–92.
24. Laws D, Neville E, Duffy J, on behalf of the British Thoracic Society Pleural Disease Group, a subgroup of the British Thoracic Society Standards of Care Committee. BTS guidelines for the insertion of a chest drain. Thorax. 2003;58(Suppl II):ii53–9.
25. Ghaye B, Dondelinger RF. Image guided thoracic interventions. Eur Respir J. 2001;17:507–28.
26. Heunks L, Demoule A, Windisch W. Pulmonary emergencies. Sheffield: ERS; 2016. p. 230–9.
27. National Lung Cancer Audit – LUCADA.
28. Nikfarjam M, Muralidharan V, Christophi C. Mechanisms of focal heat destruction of liver tumors. J Surg Res. 2005;127(2):208–23.
29. Hiraki T, Gobara H, Mimura H, Toyooka S, Fujiwara H, Yasui K, et al. Radiofrequency ablation of lung cancer at Okayama University Hospital: a review of 10 years of experience. Acta Med Okayama. 2011;65(5):287.
30. Abbas G, Pennathur A, Landreneau RJ, Luketich JD. Radiofrequency and microwave ablation of lung tumors. J Surg Oncol. 2009;100(8):645–50.
31. Ambrogi MC, Fanucchi O, Cioni R, Dini P, De Liperi A, Cappelli C, et al. Longterm results of radiofrequency ablation treatment of stage I non-small cell lung cancer: a prospective intention-to-treat study. J Thorac Oncol. 2011;6(12):2044–51.
32. Simon CJ, Dupuy DE, Mayo-Smith WW. Microwave ablation: principles and applications. Radiographics. 2005;25(suppl 1):S69–83.
33. Wolf FJ, Grand DJ, Machan JT, DiPetrillo TA, Mayo-Smith WW, Dupuy DE. Microwave ablation of lung malignancies: effectiveness, CT findings, and safety in 50 patients1. Radiology. 2008;247(3):871.
34. Gage AA, Baust J. Mechanisms of tissue injury in cryosurgery. Cryobiology. 1998;37(3):171–86.
35. Wang H, Littrup PJ, Duan Y, Zhang Y, Feng H, Nie Z. Thoracic masses treated with percutaneous cryotherapy: initial experience with more than 200 procedures. Radiology. 2005;235(1):289.
36. Pusceddu C, Sotgia B, Fele RM, Melis L. CT-guided thin needles percutaneous cryoablation (PCA) in patients with primary and secondary lung tumors: a preliminary experience. Eur J Radiol. 2013;82(5):e246–53.

# 6 Normal Radiologic Anatomy and Anatomical Variants of the Chest Relevant to Thoracic Surgery

Cheng Ting Lin and Elliot K. Fishman

**Abstract**

Preoperative planning requires the careful review of imaging obtained to define anatomy and determine the optimal approach. Normal anatomy and anatomical variants can be challenging and in select cases may simulate pathology. Understanding the radiologic anatomy of the chest is essential to perform safe and successful surgery. This section focuses on the critical anatomic structures seen on imaging that every thoracic surgeon should recognize.

**Keywords**

Normal anatomy · Computed tomography · Aortic arch variants · Tracheobronchial variants · Accessory fissures · Lymph node stations · Adenopathy mimics · Chest wall anomaly · Thoracic nerves

## Abbreviations

| | |
|---|---|
| CT | Computed tomography |
| DA | Descending aorta |
| E | Esophagus |
| IASLC | International Association for the Study of Lung Cancer |
| LC | Left carotid |
| LPA | Left pulmonary artery |
| LS | Left subclavian |
| MR/MRI | Magnetic resonance/magnetic resonance imaging |
| PA | Pulmonary artery |
| RC | Right carotid |
| RLN | Recurrent laryngeal nerve |
| RPA | Right pulmonary artery |
| RS | Right subclavian |
| SVC | Superior vena cava |
| T | Trachea |
| TNM | Tumor, node, and metastasis |

C. T. Lin (✉) · E. K. Fishman
Department of Radiology and Radiological Science, Johns Hopkins University School of Medicine, Baltimore, MD, USA
e-mail: clin97@jhmi.edu; efishman@jhmi.edu


M. Anzidei, M. Anile (eds.), *Diagnostic Imaging for Thoracic Surgery*,
https://doi.org/10.1007/978-3-319-89893-3_6

**Table 6.1** Examples of thoracic anatomic variants

| | |
|---|---|
| Vascular | |
| | Right aortic arch |
| | Aberrant subclavian artery |
| | Left superior vena cava |
| Airways | |
| | Tracheal bronchus |
| | Cardiac bronchus |
| | Tracheal diverticulum |
| Lung fissures | |
| | Incomplete fissure |
| | Accessory fissure |
| | Azygos fissure |
| | Situs anomalies |
| Lymph node mimics | |
| | Pericardial recess fluid |
| | Pericardial cyst |
| | Thymic cyst |
| | Cisterna chyli |
| Bone | |
| | Cervical rib |
| | Pectus deformity |

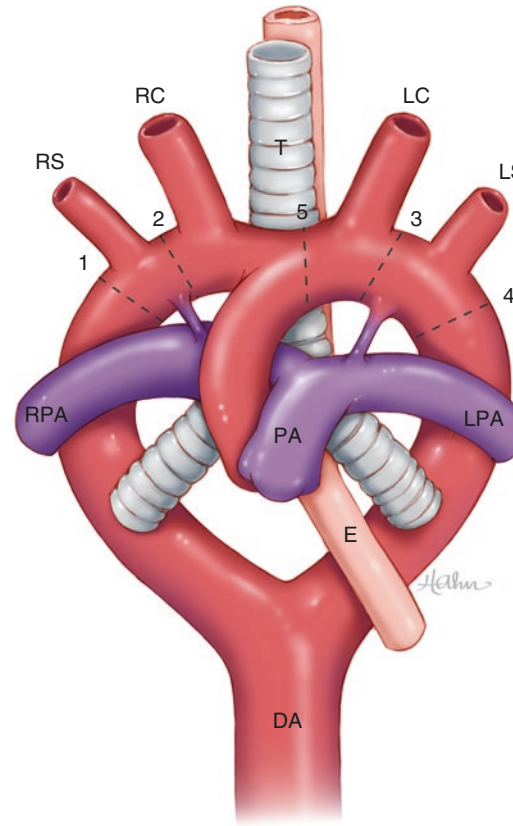


**Fig. 6.1** Illustration of Edward's hypothetical double-arch model. Regression of the right arch at location 1 or 2 results in a left arch without or with an aberrant right subclavian artery, respectively. Alternatively, obliteration of the left arch at segment 3 or 4 gives rise to a right arch with or without an aberrant left subclavian artery, respectively

## 6.1 Vascular

Aortic arch anatomy derives its basis from Edward's hypothetical double-arch model [1], depicted in Fig. 6.1. Separation of the segment between the right subclavian artery takeoff and the descending aorta results in normal anatomy. An aberrant right subclavian artery forms when there is embryological interruption between the two right-sided arch vessels.

Right-sided aortic arch is an aortic arch anomaly resulting from developmental interruption of the left aortic arch. The incidence is approximately 0.1%. Three configurations of the right-sided aortic arch have been described:

- Right aortic arch with aberrant origin of the left subclavian artery (Fig. 6.2)—persistence of the ligamentum arteriosus on the left leads to the formation of a vascular ring
- Right aortic arch with mirror-image branching of the arch vessels—typically associated with cyanotic congenital heart disease
- Right aortic arch with isolation of the left subclavian artery—least common malformation

On frontal chest radiograph, the right arch is directly visualized as a vascular silhouette causing slight leftward deviation of the trachea. The right aortic arch reaches a relatively high position along the mediastinum compared to the left aortic arch. The descending aorta is positioned on the right side. Patients with incidentally detected right arch may require additional cross-sectional imaging to evaluate for congenital heart disease or a vascular ring.

Aberrant origin of the subclavian artery originates from the distal aortic arch and generally follows a retroesophageal course. Its incidence varies from 0.5% to 2%, with a higher association with right-sided arch than left-sided arch. The anomalous subclavian artery is

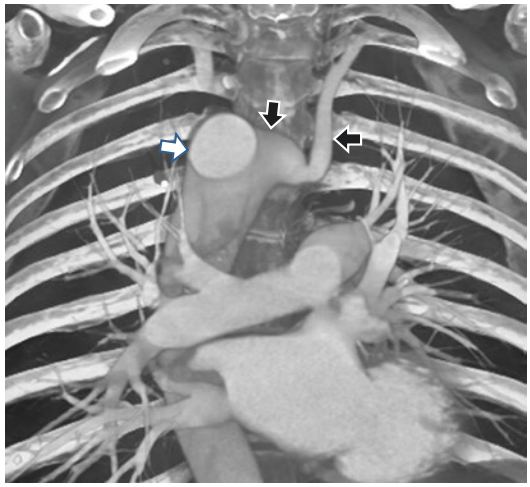

**Fig. 6.2** Volume-rendering technique image demonstrating aberrant origin of the left subclavian artery (*black arrows*) with a diverticulum of Kommerell at its origin from the right-sided aortic arch (*white arrow*). The aberrant left subclavian artery is the last branch to arise from the aortic arch and courses between the esophagus and vertebral bodies

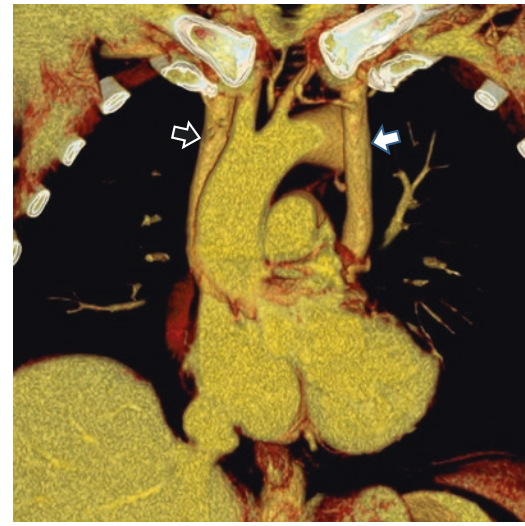

**Fig. 6.3** Volume-rendering technique image showing a persistent left SVC (*white arrow*) draining into the coronary sinus (not shown) as well as a normal right-sided SVC (*black arrow*). No bridging brachiocephalic vein is present between the two SVC

readily seen on CT or MR imaging (Fig. 6.2). Kommerell's diverticulum is an aneurysmal dilation of the most proximal portion of the aberrant subclavian artery. While most patients with this anomaly are asymptomatic, occasionally patients can develop swallowing difficulty termed dysphagia lusoria. Rare presentations include rupture or dissection of a diverticulum of Kommerell.

The persistent left superior vena cava (SVC) is a congenital venous anomaly that arises from failure of the left anterior cardinal vein to obliterate during embryological development. It occurs in ~0.4% of the general population and ~5% of those with congenital heart disease. In most cases (82–90%) of persistent left SVC, the right-sided SVC is present and decreased in caliber compared to normal. The persistent left SVC drains into a dilated coronary sinus in 92% of the cases, whereas it terminates at the left atrium in 8% of the cases resulting in a right-to-left shunt which is usually not clinically significant. Cases of persistent left SVC are typically diagnosed during line placement or incidentally during chest CT exams (Fig. 6.3). Patients are usually asymptomatic in the absence of concomitant congenital heart disease.

## 6.2 Airways

### 6.2.1 Normal Tracheobronchial Anatomy

The tracheobronchial tree divides in a predictable pattern with occasional variations [2]. The carina is normally at the level of T4–T5. The right mainstem bronchus comes off the trachea at a more vertical angle compared to the left mainstem bronchus. The bronchial segments are named per their corresponding pulmonary segments (Fig. 6.4). Visceral pleura envelopes each pulmonary lobe, except at the pulmonary hilum or when there is an incomplete interlobar fissure. The trilobed right lung is made up of the right upper, right middle, and right lower lobes. The bilobed left lung is made up of the left upper and left lower lobes.

The right upper lobe bronchus is an eparterial bronchus, meaning that it arises from the mainstem bronchus adjacent to or above the corresponding pulmonary artery. It further divides into the apical, anterior, and posterior segmental bronchi. The bronchus intermedius is the segment from the right upper lobe bronchus takeoff to the bifurcation of the right middle and right lower lobe

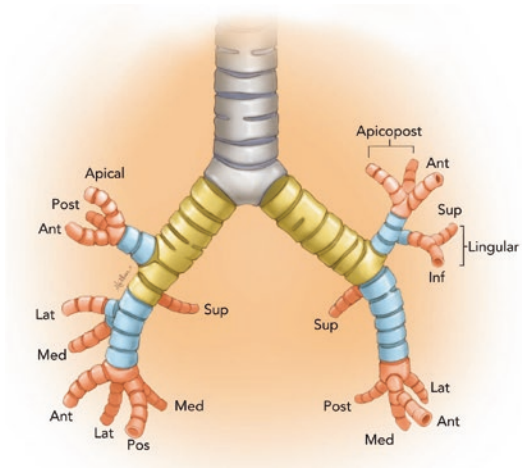


**Fig. 6.4** Illustration of the lobar and segmental bronchial anatomy

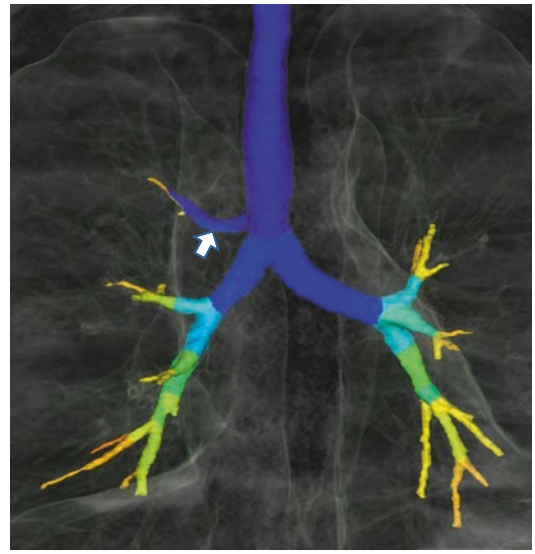

**Fig. 6.5** Virtual bronchoscopy image demonstrating a tracheal bronchus (*arrow*) supplying the right upper lobe

bronchi. The right middle lobe bronchus divides into the medial and lateral segmental bronchi. The first branch to come off the bronchus intermedius is normally the bronchus to the right lower lobe superior segment, which projects posteriorly. The remaining four basal segmental bronchi of the right lower lobe have variable division patterns.

The left upper lobe bronchus is normally hyparterial and originates below the left pulmonary artery. The upper portion of the left upper lobe (analogous to the right upper lobe) is divided into the apicoposterior and anterior segments. The lower portion of the left upper lobe (analogous to the right middle lobe) is termed the lingular lobe which is divided into the superior and inferior segments. Like its right-sided counterpart, the bronchus to the left lower lobe superior segment comes off the left lower lobe bronchus before the basal segmental branches. The anterior and medial basal segmental bronchi of the left lower lobe often share a common origin from the lobar bronchus; therefore, they could be considered as the anteromedial segmental bronchus instead.

### 6.2.2 Tracheal Bronchus

A tracheal bronchus represents a variant bronchus arising from trachea and supplying the ipsilateral upper lobe [3]. The variant mostly occurs on the right side with a prevalence of 0.1–1.3%. It can supply the entire right upper lobe (Fig. 6.5)—whereby the term "pig bronchus" or "bronchus suis" is sometimes applied—or a segment/subsegment of the right upper lobe. Tracheal bronchi are for the most part incidentally detected on CT or bronchoscopy. Adult patients with tracheal bronchus are generally asymptomatic. Recurrent pneumonia, stridor, and respiratory distress in children with tracheal bronchus have been reported. The tracheal bronchus is also susceptible to blockage during endotracheal intubation.

### 6.2.3 Cardiac Bronchus

Cardiac bronchus is an accessory bronchus originating from the inferomedial aspect of the right main bronchus or bronchus intermedius. The cardiac bronchus courses medially towards the heart (hence its name) in a direction opposite to the right upper lobe bronchus (Fig. 6.6). Its frequency ranges from 0.09% to 0.5%. Accessory cardiac bronchus can be blind-ending or terminates in vestigial parenchymal tissue. They may

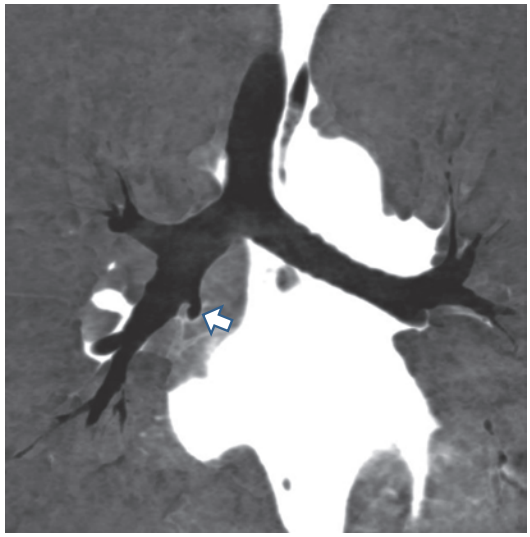

**Fig. 6.6** Minimum intensity projection image of a patient with an incidentally detected accessory cardiac bronchus (*arrow*)

be a potential reservoir for infectious material which can lead to pneumonia or hemoptysis. Patients with recurrent pneumonia due to an accessory cardiac bronchus may benefit from surgical treatment.

### 6.2.4 Tracheal Diverticulum

Tracheal diverticulum is a paratracheal air cyst with a narrow, often imperceptible, connecting stalk [4]. It occurs in approximately 1% of the general population. The tracheal diverticulum is most commonly located in the thoracic inlet at the right posterolateral aspect of the trachea (Fig. 6.7). Tracheal diverticulum can be acquired in the setting of chronic cough (e.g., chronic obstructive pulmonary disease) secondary to increased intraluminal pressure and resulting herniation of membrane. Thin-section CT is helpful for distinguishing tracheal diverticulum from pneumomediastinum and apical blebs or bullae. Although it is typically a benign incidental finding, symptomatic cases have been reported and attributed to infected secretions within the diverticula.

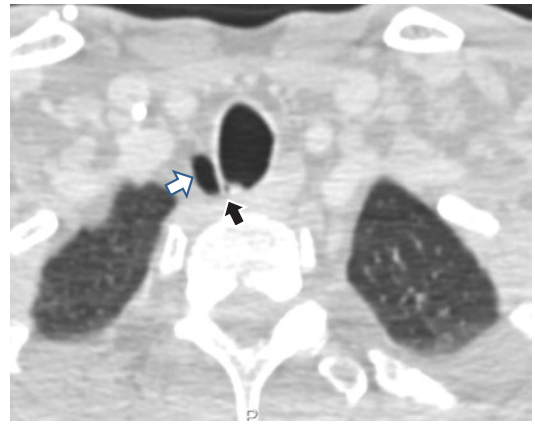

**Fig. 6.7** Axial CT image in lung window showing a tracheal diverticulum (*white arrow*) with a small thin connection (*black arrow*) to the posterolateral aspect of the trachea

## 6.3 Fissures

### 6.3.1 Normal and Variant Pulmonary Fissures

Lung fissures are made up of two layers of visceral pleura that form the boundaries of lobar anatomy [5]. Incomplete fissures are common and do not extend all the way to the mediastinum or hilum, allowing pulmonary infections and tumors to cross fissures. On frontal chest radiograph, only the minor (horizontal) fissure separating the right upper and middle lobes can be visualized. The lateral chest radiography shows the major (oblique) fissure extending from the anterior diaphragm to the third–fifth thoracic vertebrae, separating the upper and lower lobes on the left and upper lobe from the middle/lower lobes on the right.

Accessory fissures are common developmental variants in patients with otherwise normal pulmonary anatomy [6], as shown in Fig. 6.8. Accessory fissures are generally incomplete. Common accessory fissures include the left minor fissure, inferior accessory fissure, and superior accessory fissure. A left minor fissure divides the lingular lobe from the left upper lobe proper. The inferior accessory fissure extends in

a cranial direction from the diaphragmatic pleura. The superior accessory fissure lies between the superior and basal segments of the lower lobe.

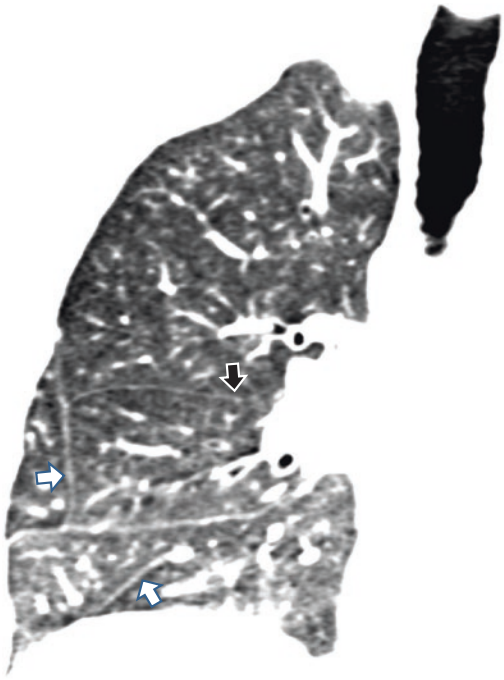

**Fig. 6.8** Coronal CT image showing two accessory fissures (*white arrows*) and an incomplete right minor fissure (*black arrow*)

### 6.3.2 Azygos Fissure

The azygos fissure is the result of embryological migration of the posterior cardinal vein—precursor to the azygos vein—into the upper lobe, typically on the right. The portion of the lung bordered laterally by the azygos fissure is called the azygos lobe (Fig. 6.9a). This anatomic variant occurs in 0.5–1% of the population. Unlike other fissures, the azygos fissure contains a total of four layers of pleura—two layers each of visceral and parietal pleura. The azygos lobe represents partial separation of a normal upper lobe rather than a supernumerary lobe. Unawareness of its presence can lead to technical difficulties during video-assisted thoracic sympathectomy. Displacement of the azygos vein from the azygos fissure to the mediastinum can occur during thoracic surgery, resulting in an "empty azygos fissure" (Fig. 6.9b).

### 6.3.3 Situs Anomalies

Thoracic situs can be grouped into three categories: situs solitus (normal), situs ambiguous (heterotaxy), and situs inversus totalis [7]. Heterotaxy syndromes are abnormal embryological arrangement of the thoracoabdominal viscera, classically divided into bilateral right-sidedness (asplenia)

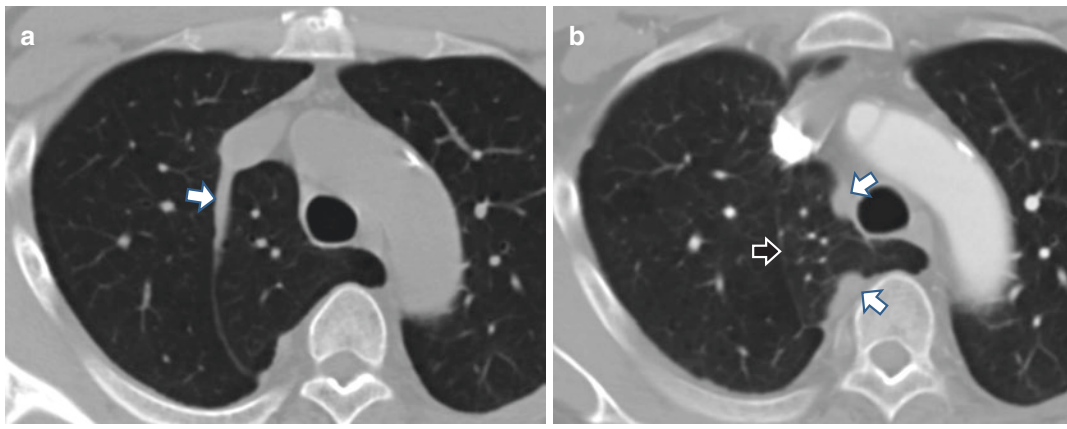


**Fig. 6.9** An azygos fissure containing the azygos vein (*arrow*) was identified on preoperative CT (**a**). CT exam performed after video-assisted thoracic surgery shows that the azygos vein (*white arrows*) has migrated from the azygos fissure to the medial mediastinum, resulting in an empty azygos fissure (*black arrow*) (**b**)

and bilateral left-sidedness (polysplenia). Bronchial anatomy is a reliable indicator of thoracic situs. The typically left-sided trilobed lung is associated with an eparterial bronchus and a minor fissure, while the bilobed lung is associated with a hyparterial bronchus and no minor fissure (Fig. 6.10).

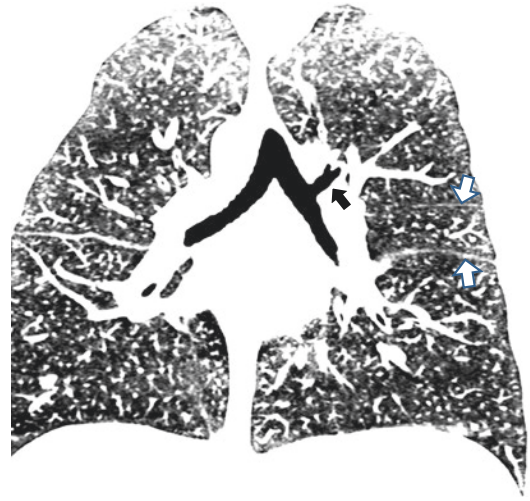

**Fig. 6.10** Coronal CT image of a patient with two left-sided fissures (*white arrows*) and one right-sided fissure, representing trilobed left lung and bilobed right lung, respectively. Also note the eparterial bronchus on the left side (*black arrow*) which is typically found on the right. Findings are consistent with situs inversus totalis

## 6.4 Lymph Nodes

### 6.4.1 Nodal Station Map

Accurate staging of thoracic nodes requires use of the International Association for the Study of Lung Cancer (IASLC) lymph node map [8]. This nodal classification system is an essential component of the 7th edition of the tumor, node, and metastasis (TNM) classification of lung cancer published in 2009. Each of the 14 lymph node stations is bounded anatomically by structures best identified on thoracic CT scans (Fig. 6.11).

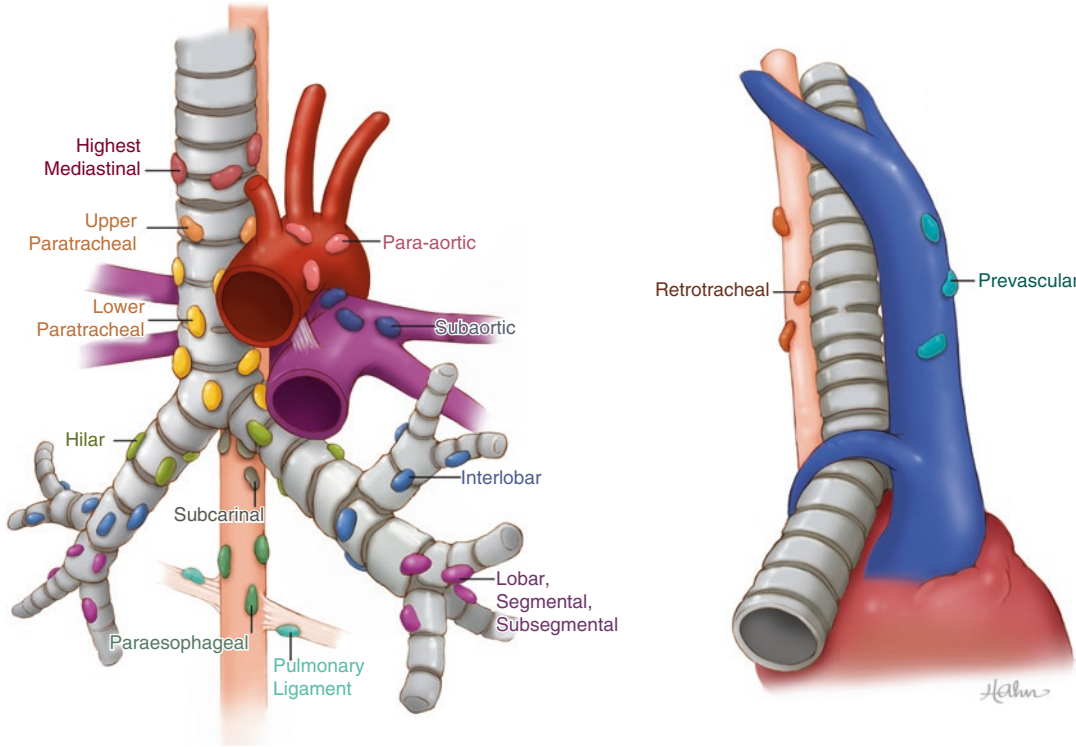


**Fig. 6.11** Illustration of the IASLC lymph node map

Level 1 (supraclavicular) nodes are just above the level of the clavicles. Superior mediastinal nodes consist of the level 2 (right and left upper paratracheal), 3 (prevascular or retrotracheal), and 4 (right and left lower paratracheal) nodes. Level 5 (subaortic) and 6 (para-aortic) nodes are aortic nodes due to their proximity to the aorta. Level 7 (subcarinal), 8 (paraesophageal), and 9 (pulmonary ligament) nodes occupy the inferior mediastinum. N1 nodes by the 7th edition TNM classification consist of level 10 (hilar), 11 (interlobar), 12 (lobar), 13 (segmental), and 14 (subsegmental) nodes.

### 6.4.2 Mimics of Adenopathy

Pericardial recess fluid is a common mimicker of mediastinal adenopathy [9]. The visceral pericardium adheres to the heart and great vessels, forming recesses and sinuses where fluid can accumulate (Fig. 6.12a). Pericardial recesses arise from pericardial cavity proper, transverse sinus, or oblique sinus. Pericardial cavity proper gives rise to the bilateral pulmonic vein and postcaval recesses. The transverse sinus lies posterior to ascending aorta and main pulmonary artery, giving rise to the superior aortic, inferior aortic, and bilateral pulmonic recesses. The oblique sinus is located between the left atrium and the esophagus, and gives rise to the posterior pericardial recess. On CT/MR imaging, pericardial recess fluid measures fluid attenuation, does not demonstrate contrast enhancement, is crescentic or lenticular in shape, and communicates with other pericardial recesses.

Pericardial cyst is a benign cystic lesion adherent to the pericardium [10]. It is considered a developmental defect due to the persistence of a blind-ending parietal pericardial recess. Pericardial cysts are found at the right cardiophrenic angle in 80% of the cases, but can appear anywhere along the pericardium. Cross-sectional imaging typically shows a well-circumscribed unilocular mass with homogeneous fluid density (Fig. 6.12b), without internal septations or enhancement. Its walls are rarely calcified. Most pericardial cysts are asymptomatic and can be monitored, whereas cyst aspiration or resection should be considered for symptomatic cases (e.g., chest pain or cough).

Thymic cysts are rare anterior mediastinal masses derived from the thymus. The congenital form may develop from a patent thymopharyngeal duct. An acquired thymic cyst can form because of an inflammatory process. They present on imaging as unilocular or multilocular well-circumscribed cystic structures (Fig. 6.12c). Internal soft-tissue attenuation on CT may be due to proteinaceous debris or hemorrhage.

The cisterna chyli is a dilated lymphatic sac located anterior to the L1–L2 vertebrae [11, 12]. It represents the confluence of the thoracic duct and abdominal lymphatic channels. The cisterna chyli is identified on CT by a retrocrural ovoid structure with fluid attenuation (mean of 4–5 Hounsfield units) and no contrast enhancement. Continuity with the thoracic duct is considered diagnostic (Fig. 6.12d). While the cisterna chyli is a part of normal anatomy, it can potentially be misdiagnosed as an enlarged retrocrural lymph node.

## 6.5 Bones

### 6.5.1 Chest Wall Anatomy

The osseous components of the chest wall consist of the sternum, 12 pairs of ribs, and thoracic vertebrae [13]. During inspiration, the sternum moves forward and the ribs elevate. The upper seven ribs are called true ribs because they directly articulate with the sternum, while the eighth through tenth ribs are called false ribs as their cartilage is joined together forming the costal arch. The two lowermost ribs lack any attachment to the sternum. The intercostal spaces, the zone between ribs, are held together by the internal and external intercostal muscles. The intercostal neurovascular bundle runs along the caudal groove of the ribs. Caution is warranted in avoid injury to these structures during thoracoscopy and other thoracic procedures that use intercostal space access.

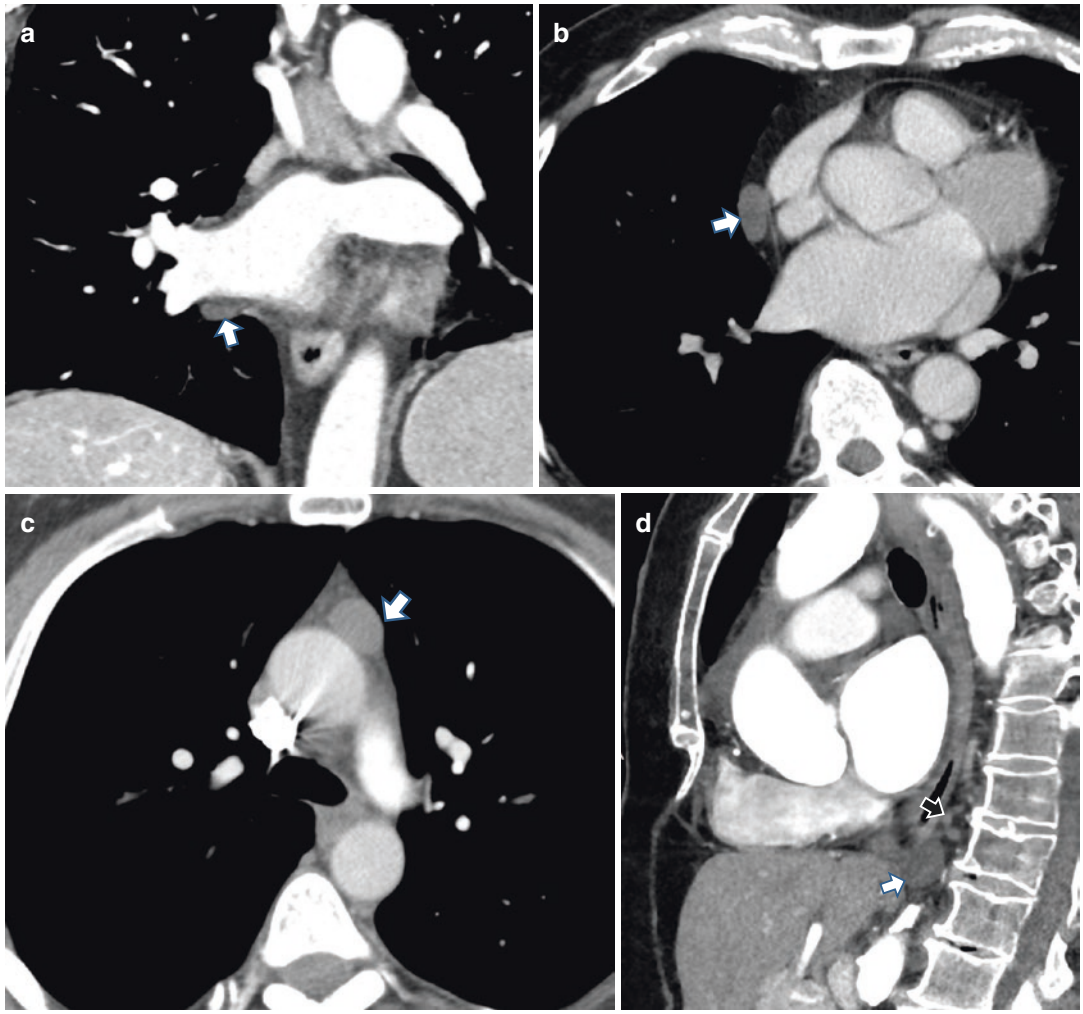


**Fig. 6.12** Mimics of adenopathy. Coronal CT demonstrating an oval fluid density below the right inferior pulmonary vein (*arrow*) consistent with pulmonary venous recess fluid (**a**). Axial CT showing a right pericardial fluid attenuation lesion (*arrow*) compatible with pericardial cyst (**b**). Anterior mediastinal well-circumscribed density with soft-tissue attenuation (*arrow*), which was resected and identified as a thymic cyst on pathology (**c**). Low-attenuation oval lesion at the level of the aortic hiatus (*white arrow*) with communication with the thoracic duct (*black arrow*), characteristic for a cisterna chyli (**d**)

### 6.5.2 Cervical Rib

Cervical ribs are accessory ribs that articulate with the transverse process of the seventh cervical vertebrae [14, 15]. Its incidence in the general population is about 0.5%. Cervical ribs can be identified on chest radiograph as supernumerary ribs above the true ribs. Angiography with CT or MR is indicated to establish the anatomic relationship of the anomalous rib and adjacent vascular structure (Fig. 6.13). While most patients with cervical ribs are asymptomatic, thoracic outlet syndrome develops in a small percentage of cases due to compression of the subclavian vessels or brachial plexus. Symptoms of this syndrome include pain, weakness, decreased pulses, or swelling of the affected upper extremity.

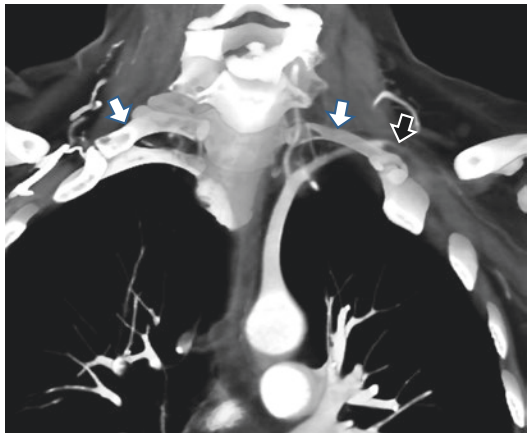

**Fig. 6.13** Coronal thick-slice maximum intensity projection image revealing bilateral cervical ribs (*arrows*), on the left causing occlusion of the subclavian artery (*arrowhead*). The cervical ribs articulate with bony processes protruding from the first ribs

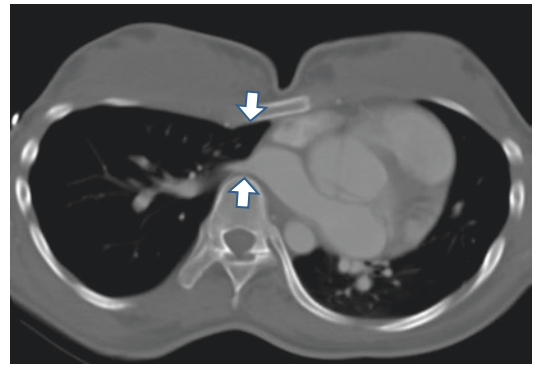

**Fig. 6.14** Axial CT image of a patient with Marfan syndrome. The anteroposterior distance between the sternum and the vertebral body is markedly decreased (*arrow*), diagnostic for pectus excavatum. Note the leftward displacement of the heart

### 6.5.3 Pectus Excavatum

Pectus excavatum (funnel chest) is the most common congenital deformity of the chest wall, occurring in approximately 1 in 700 births [16]. Abnormal growth and orientation of the lower costochondral cartilage are generally thought to be the etiology of pectus excavatum. The inferior sternum is depressed into a concave shape causing the ribs to protrude anteriorly. Pectus excavatum is readily diagnosed on lateral chest radiograph. Cross-sectional imaging demonstrates the severity of sternal depression and associated cardiac displacement (Fig. 6.14). Haller et al. developed the "pectus index" which is calculated by dividing the transverse diameter of the chest wall by the anteroposterior distance. He found that patients with pectus excavatum requiring surgery had an index >3.25, whereas normal control patients had a mean index of 2.56.

## 6.6 Thoracic Nerves

The brachial plexus comprises an arrangement of the C5–T1 nerves, responsible for sensorimotor innervation to the ipsilateral shoulder and upper extremity [17]. It travels alongside the subclavian artery and passes through the interscalene triangle—a space bordered by the anterior scalene muscle, the middle scalene muscle, and the first rib (Fig. 6.15). Due to its proximity to the lung apex, the brachial plexus is susceptible to invasion by superior sulcus tumor, also known as Pancoast tumor. Limited involvement of the brachial plexus may be amenable to surgical resection, whereas extensive tumor invasion of the brachial plexus remains a contraindication to surgery. The extent of brachial nerve and vascular involvement is best assessed using MRI techniques.

The phrenic nerve forms from the C3–C5 nerve roots and courses inferiorly to innervate the diaphragms. The paired phrenic nerves are located along the anterolateral mediastinum and pericardium, run parallel to pericardiophrenic arteries and veins, and arborize at the diaphragmatic surface (Fig. 6.15). Injury to the phrenic nerve is not uncommon due to invasive tumor or after cardiac surgery. Direct visualization of phrenic nerve injury is generally not possible with cross-sectional imaging. Chest fluoroscopy is an appropriate examination for establishing the diagnosis of diaphragmatic paralysis.

Awareness of the course of the recurrent laryngeal nerve (RLN) is important as damage to this nerve can occur anywhere along its course and lead to vocal cord paralysis. The right vagus nerve runs posterolateral to the common carotid arteries before giving off the right RLN, which

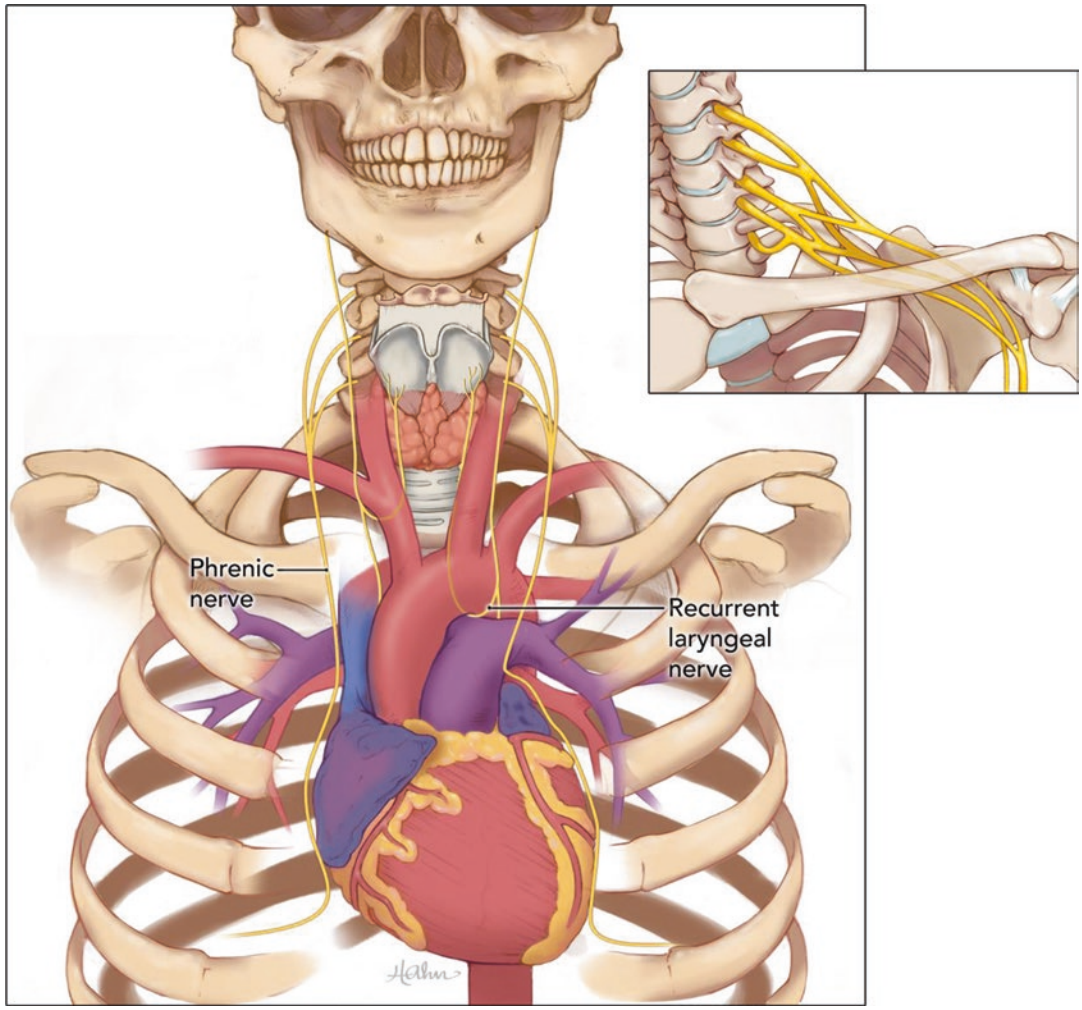


**Fig. 6.15** Illustration of the phrenic nerves, recurrent laryngeal nerves (RLNs), and brachial plexus (insert). Note the path of the left RLN between the aortic arch and pulmonary artery, while the right RLN courses under the right subclavian artery. Phrenic nerves follow the lateral borders of the cardiomediastinal structures. The C5–T1 nerve roots form the branching network called the brachial plexus, coursing between the scalene muscles and under the clavicle

then travels posterior to the subclavian artery before moving to the larynx. The left RLN branches off from the vagus nerve at the aortopulmonary window and courses under the aortic arch posterior to the ligamentum arteriosum before ascending to the larynx. Therefore, in patients presenting with hoarseness concerning for vocal cord dysfunction, CT imaging should extend inferiorly to include the mediastinum.

## References

1. Davies M, Guest PJ. Developmental abnormalities of the great vessels of the thorax and their embryological basis. Br J Radiol. 2003;76:491–502.
2. Wooten C, Patel S, Cassidy L, et al. Variations of the tracheobronchial tree: anatomical and clinical significance. Clin Anat. 2014;27:1223–33.
3. Ghaye B, Szapiro D, Fanchamps JM, Dondelinger RF. Congenital bronchial abnormalities revisited. Radiographics. 2001;21:105–19.

4. Soto-Hurtado EJ, Penuela-Ruiz L, Rivera-Sanchez I, Torres-Jimenez J. Tracheal diverticulum: a review of the literature. Lung. 2006;184:303–7.
5. Aziz A, Ashizawa K, Nagaoki K, Hayashi K. High resolution CT anatomy of the pulmonary fissures. J Thorac Imaging. 2004;19:186–91.
6. Yildiz A, Golpinar F, Calikoglu M, Duce MN, Ozer C, Apaydin FD. HRCT evaluation of the accessory fissures of the lung. Eur J Radiol. 2004;49:245–9.
7. Applegate KE, Goske MJ, Pierce G, Murphy D. Situs revisited: imaging of the heterotaxy syndrome. Radiographics. 1999;19:837–52; discussion 53–4.
8. Jawad H, Sirajuddin A, Chung JH. Review of the international association for the study of lung cancer lymph node classification system: localization of lymph node stations on CT imaging. Clin Chest Med. 2013;34:353–63.
9. Truong MT, Erasmus JJ, Gladish GW, et al. Anatomy of pericardial recesses on multidetector CT: implications for oncologic imaging. AJR Am J Roentgenol. 2003;181:1109–13.
10. Jeung MY, Gasser B, Gangi A, et al. Imaging of cystic masses of the mediastinum. Radiographics. 2002;22:S79–93.
11. Kiyonaga M, Mori H, Matsumoto S, Yamada Y, Sai M, Okada F. Thoracic duct and cisterna chyli: evaluation with multidetector row CT. Br J Radiol. 2012;85:1052–8.
12. Feuerlein S, Kreuzer G, Schmidt SA, et al. The cisterna chyli: prevalence, characteristics and predisposing factors. Eur Radiol. 2009;19:73–8.
13. Restrepo CS, Martinez S, Lemos DF, et al. Imaging appearances of the sternum and sternoclavicular joints. Radiographics. 2009;29:839–59.
14. Kurihara Y, Yakushiji YK, Matsumoto J, Ishikawa T, Hirata K. The ribs: anatomic and radiologic considerations. Radiographics. 1999;19:105–19; quiz 51–2.
15. Guttentag AR, Salwen JK. Keep your eyes on the ribs: the spectrum of normal variants and diseases that involve the ribs. Radiographics. 1999;19:1125–42.
16. Jeung MY, Gangi A, Gasser B, et al. Imaging of chest wall disorders. Radiographics. 1999;19:617–37.
17. Aquino SL, Duncan GR, Hayman LA. Nerves of the thorax: atlas of normal and pathologic findings. Radiographics. 2001;21:1275–81.

# Pulmonary Nodules: Detection and Risk Evaluation

7

Fabrizio Andrani, Roberto Scipione, Andrea Porfiri, and Michele Anzidei

**Abstract**

Pulmonary nodules can be defined as round/irregular opacities no larger than 3 cm and may represent an incidental finding during CT exams (prevalence of 8–51% in different studies). Incidental and undetermined solid non-calcific pulmonary nodules have a relatively low malignancy rate; nevertheless, their evaluation is a matter of great interest in clinical management, since it is based on the detection of subjects with malignant lesions that can have potentially complete benefits from surgical treatment, or on the avoidance of invasive procedures in patients with benign lesions. In fact, several options are available in the management of an undetermined incidental pulmonary nodule, and the most appropriate choice depends on a careful evaluation of patient's risk factors and of the characteristics of the nodule.

This chapter provides a brief review of all the main features of pulmonary nodules that need to be analyzed in order to establish a potential malignant nature (dimension, morphology and position, density, growth); following that, it illustrates a practical guide for the management of both single and multiple pulmonary nodules, depending on their dimension and patient's risk factors. Finally, the main malignant causes of multiple pulmonary nodules are described.

**Keywords**

Pulmonary nodules · Lung cancer · CT · Incidental nodule · Risk assessment · Guidelines

## 7.1 Pulmonary Nodules: Detection and Risk Evaluation

A pulmonary nodule can be defined as a well-delimited sphere of abnormal tissue, or as a round/irregular opacity no larger than 3 cm on its maximum diameter [1]. Pulmonary nodules can represent incidental findings during CT scans made for other reasons (i.e., cardiac-CT), with no relationship to other underlying known pathologies, with a prevalence of 8–51% in different studies. Incidental solid non-calcific pulmonary nodules are often more than one and present a maximum diameter <10 mm in 96% of cases, and <5 mm in 72% of cases. However, their malignancy rate is relatively low (1–12% in various studies) [2].

F. Andrani · R. Scipione (✉) · A. Porfiri · M. Anzidei
Department of Radiological, Oncological and Pathological Sciences, Policlinico Umberto I, Sapienza University of Rome, Rome, Italy
e-mail: roberto.scipione@uniroma1.it; michele.anzidei@uniroma1.it


M. Anzidei, M. Anile (eds.), *Diagnostic Imaging for Thoracic Surgery*, https://doi.org/10.1007/978-3-319-89893-3_7

It is clear then that the evaluation of undetermined small incidental nodules is a matter of great interest in clinical management, since it is based on the detection of subjects with malignant lesions that can have potentially complete benefits from surgical treatment, or on the avoidance of invasive procedures in patients with benign lesions.

### 7.1.1 Incidental Pulmonary Nodule Detection

Generally all CT scans of the chest in adults should be reconstructed and visualized with contiguous thin slice (typically 1.0 mm, at most 1.5 mm) to allow an accurate detection and characterization of small pulmonary nodules. Also off-axis series (coronal and sagittal) should be routinely acquired; this improves the radiologist investigation, enabling for example the distinction between nodules and scars or pleural thickenings. Furthermore, It has been widely demonstrated that maximum intensity projection (MIP) systems determine a statistically significant improvement in the detection of small pulmonary nodules (<5 mm), compared to simple 1-mm- or 5-mm-thick axial images without MIP implementation (Fig. 7.1) [3].

### 7.1.2 Undetermined Pulmonary Nodule Risk Evaluation

With the adequate techniques and precautions, as exposed in the previous paragraph, the detection of an incidental pulmonary nodule is often easy, also for less experienced radiologists. The real problem is this: "What to do after identification of a parenchymal nodule?"

There are several options in the management of an undetermined pulmonary nodule:

- To ignore the finding

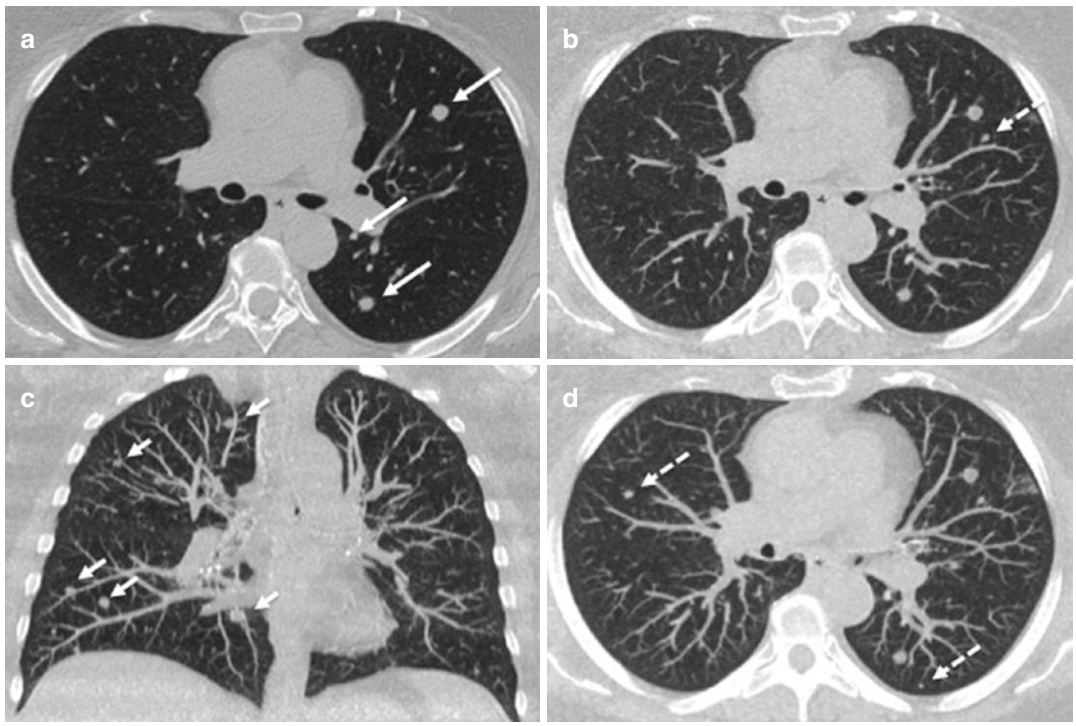


**Fig. 7.1** Maximum intensity projection (MIP) technique increases pulmonary nodule identification: (**a**) 1 mm standard axial image; (**b**) 5 mm axial image without MIP system; (**c**) 10 mm coronal MIP reconstruction; (**d**) 10 mm axial MIP reconstruction

- To plan a CT exam follow-up
- To suggest a contrast-enhanced CT or PET-CT study
- To perform a biopsy of the detected lesion (FNAB or core biopsy)
- To consider surgical intervention (open surgery or VATS)

The most appropriate choice among these options depends on a careful evaluation of patient's risk factors and characteristics of the nodule.

Patient's **risk factors** for pulmonary malignancy include age, genetic predisposition (sex, race, and personal or family history of tumors), environmental factors (in particular tobacco smoke but also other carcinogen exposure), as well as some chronic pulmonary diseases such as emphysema and fibrosis [4].

#### 7.1.2.1 Cigarette Smoking History

The association between tobacco smoke and lung tumor is clear since the 1960s. Cigarette smoking history, that is 30 pack-years or more, is considered in fact the major risk factor for pulmonary cancer, with an increased incidence of 10–35 times in smokers compared to non-smokers. This is true in particular for small-cell or squamous cell carcinomas while the association between cigarette smoke and development of adenocarcinoma is weaker and not clearly defined. It should be always remembered that also second-hand smoke is a proved risk factor, although less relevant. Quitting smoking for at least 15 years removes the smoke-related risk.

#### 7.1.2.2 Age, Sex, and Race

Lung tumor incidence is very low in individuals younger than 35 years, while increases progressively with age, in particular after 40 years, reaching the maximum incidence around the sixth decade.

Some studies detected also a mild increased risk of lung tumor in female compared to male, probably due, partly, to a lower educational level and lower body mass index (BMI) that were associated with an increased risk of cancer.

For what concerning race, the incidence of lung tumor is significantly higher in black men and native Hawaiian men, compared to white men.

#### 7.1.2.3 Family History of Lung Tumors

A first-degree relative with lung cancer is a known risk factor for lung tumor development. Family history of lung tumors is estimated to increase the relative risk between 1.5 and 1.8 points for both smoking and nonsmoking individuals.

#### 7.1.2.4 Chronic Pulmonary Disease

Several studies demonstrated that some chronic pulmonary diseases such as emphysema and idiopathic pulmonary fibrosis (IPF) represent independent risk factors for lung cancer development, respectively. Moreover increasing severity of centrilobular emphysema coincides with increasing risk of malignancy and patients with combined pulmonary fibrosis and emphysema (CPFE) have a higher risk of lung cancer development compared with those with emphysema alone.

#### 7.1.2.5 Other Carcinogen Exposure

Risk factors for lung malignancy include also exposure to other inhaled carcinogens different from tobacco smoke, such as asbestos, uranium, or radon.

The **characteristics of the detected nodule** that need to be analyzed in order to establish a potential malignant nature are the following:

#### 7.1.2.6 Dimension

Size of the nodule represents a dominant factor in patient management. This is because it has been largely demonstrated that the probability of a pulmonary nodule to develop malignant features progressively increases with its dimension:

– Nodules within 4 mm of diameter have a <1% risk to develop malignancy or to progress to a potentially lethal cancer.
– Nodules >8 mm present a >25% risk to be malignant.

Moreover, malignant nodules show a more rapid growth in smokers, compared to those in patients with no smoke status.

#### 7.1.2.7 Morphology–Shape–Position

A pulmonary nodule with ovoid or polygonal shape adjacent to pleural surface or in a peripheral location is likely to be a benign lesion (Fig. 7.2a).

Conversely a nodule with irregular margins and not closely adjacent to pleural surface, in particular those located in the upper right lobe, is more likely to be a lung tumor.

Nodules with regular margins, in fact, have 20–30% probability of being malignant (Fig. 7.2a), while this value increases to 33–100% in case of lesions with lobulated/irregular or spiculated margins (Fig. 7.2b) [5].

Likewise, superior lobe location is associated with a greater chance of malignancy, in particular for lesion in right lung, with an odds ratio up to around 2.0 (Fig. 7.2b). Furthermore squamous cell carcinomas (Fig. 7.3) and small-cell lung cancer (Fig. 7.4) are generally located in hilar or peri-hilar position while adenocarcinomas (Fig. 7.5) and metastases tend to affect more peripheral areas.

#### 7.1.2.8 Density

Depending on the density, a pulmonary nodule can be classified as solid, pure ground glass (Fig. 7.6a), or part solid (Fig. 7.6b), in case of a solid component within the ground-glass opacity. Sub-solid nodules, that include pure ground-glass and part-solid nodules, can represent a bronchioloalveolar carcinoma, an adenocarcinoma, an atypical adenomatous hyperplasia, an infection, or a focal area of fibrosis.

Malignancy prevalence varies according to the composition of the nodule: for partially solid nodules it is 63%, for pure ground-glass nodules it is 18%, and for completely solid nodules it is only 7% [6].

#### 7.1.2.9 Growth Rate

Increasing in size over time represents a clear sign of malignancy.

Lung malignancies have a wide range of growth rates depending on histology and density pattern. Volume doubling time (VDT), that corresponds to a 26% increase in diameter, for solid nodules is well established and is approximately 149 days (100–400 days) (Fig. 7.7) while VDT for sub-solid nodules is generally longer, with an average value of 813 days for pure ground-glass nodules

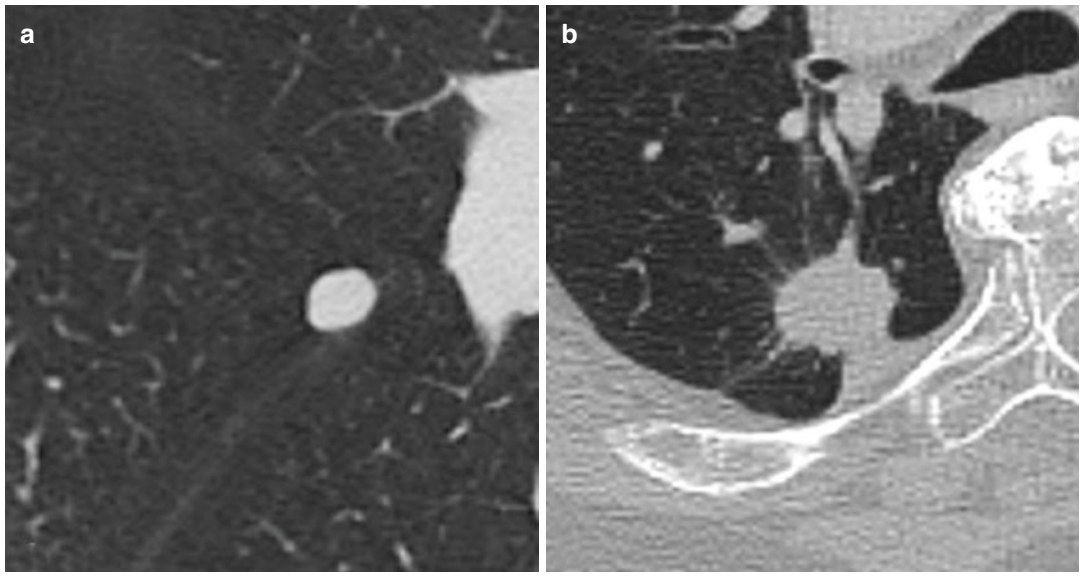


**Fig. 7.2** (**a**) Solid nodule adjacent to pleura, with ovoid shape and regular margins, located in the medium lobe, of benign nature. (**b**) Solid nodule adjacent to pleura, with irregular margins and pleural attraction, of malign nature

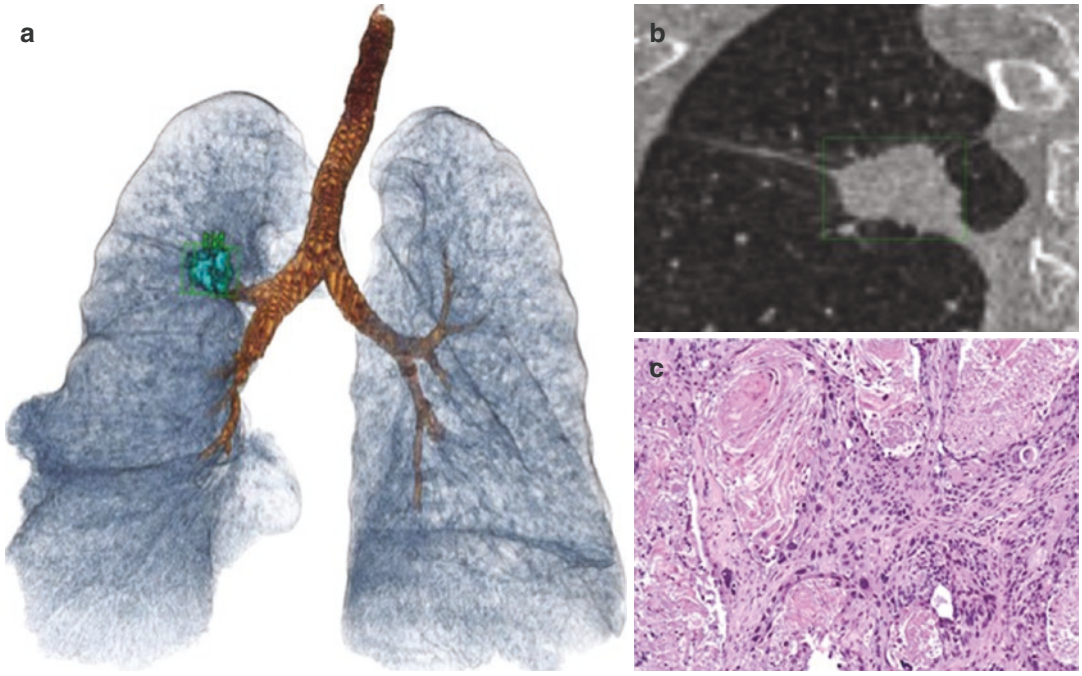


**Fig. 7.3** (**a**) 3D reconstruction, (**b**) coronal CT scan, and (**c**) histological section of a squamous cell carcinoma in perihilar position

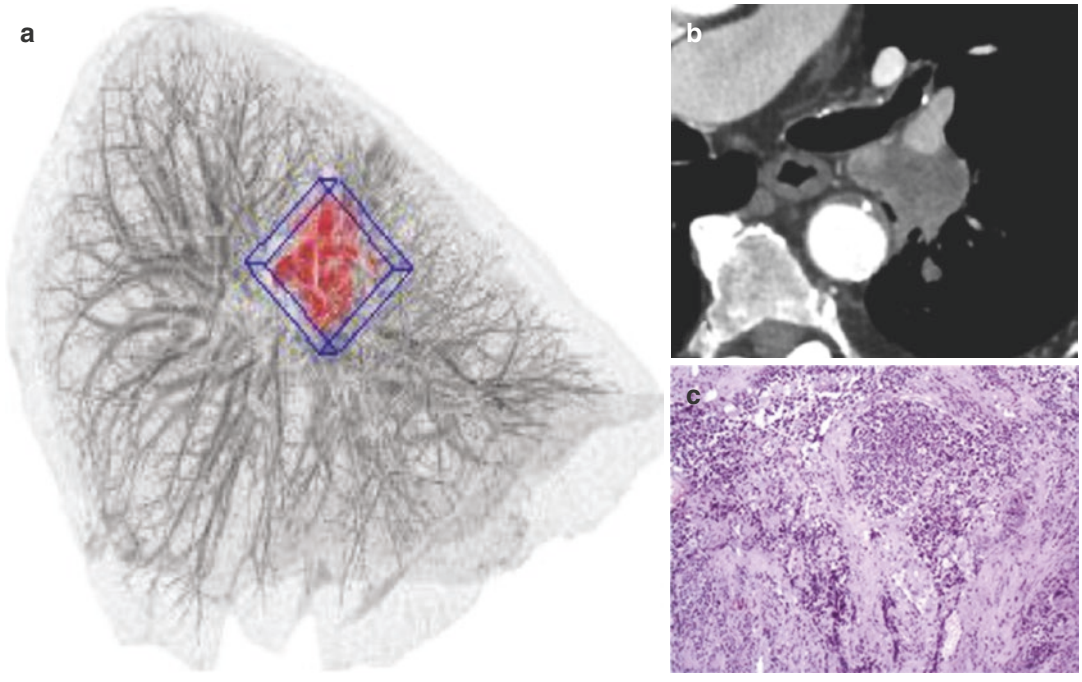


**Fig. 7.4** (**a**) 3D reconstruction, (**b**) coronal CT scan, and (**c**) histological section of a small-cell lung cancer in left hilar location

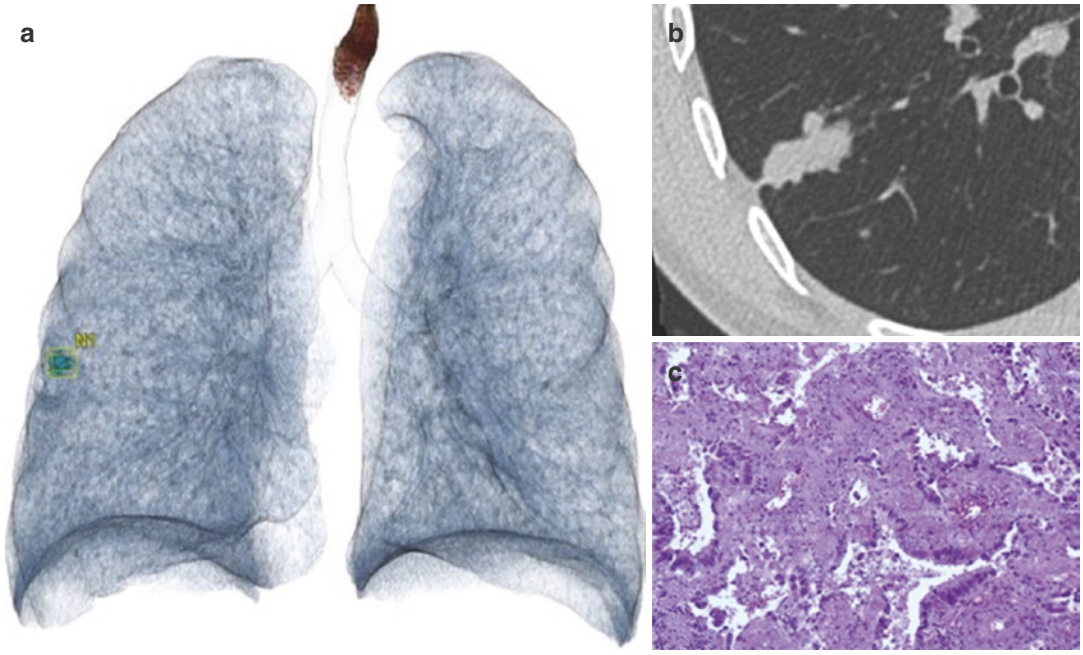


**Fig. 7.5** (**a**) 3D reconstruction, (**b**) coronal CT scan, and (**c**) histological section of an adenocarcinoma which traditionally arises peripherally

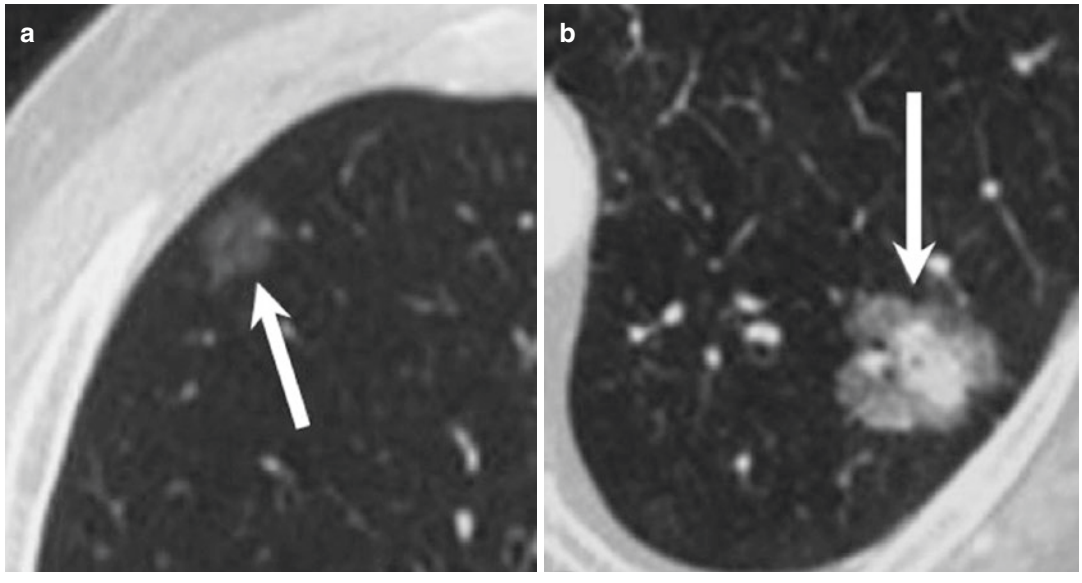


**Fig. 7.6** (**a**) Pure ground-glass nodule; (**b**) part-solid nodule with central solid component and peripheral ground-glass area

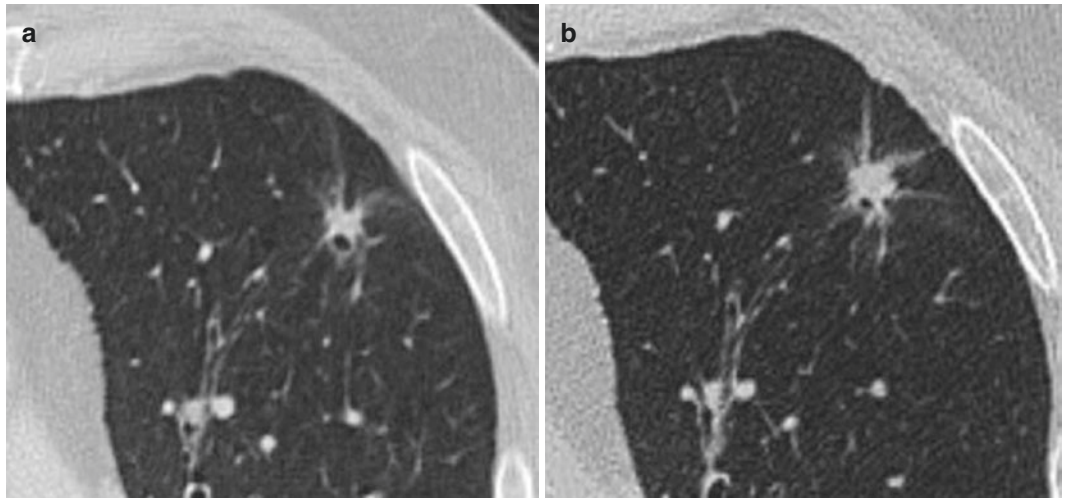


**Fig. 7.7** Solid nodule. (**a**) Nodule observed at first exam; (**b**) 10-month-control CT, showing the same nodule with clearly detectable growth

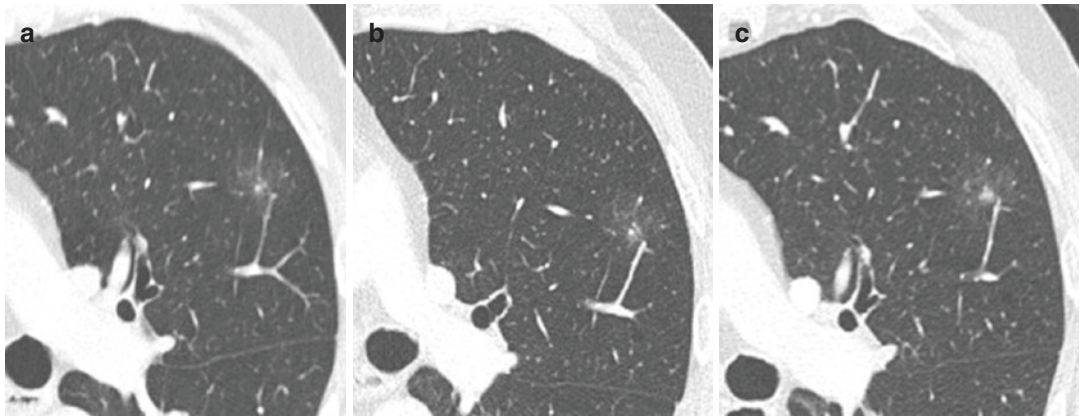


**Fig. 7.8** Sub-solid nodule with slow growth. (**a**) Nodule observed at first exam; (**b**) 6-month follow-up and (**c**) 12-month control, with slow growth observation. Diagnostic deepening with needle biopsy identified it as a nodule of atypical adenomatous hyperplasia with small aggregates of bronchioloalveolar carcinoma cells

(Fig. 7.8) and an intermediate value for part-solid nodules, approximately 457 days (Fig. 7.9) [7].

Growth rate is obviously another dominant factor in patient management determining the time of the first follow-up and the also the total length of follow-up. This is because follow-up intervals must be planned with the aim to minimize the number of examinations and, as the same time, to reduce the chance of a possible tumor to advance in stage prior to diagnosis, considering also the radiologist ability to detect small changes of nodule size.

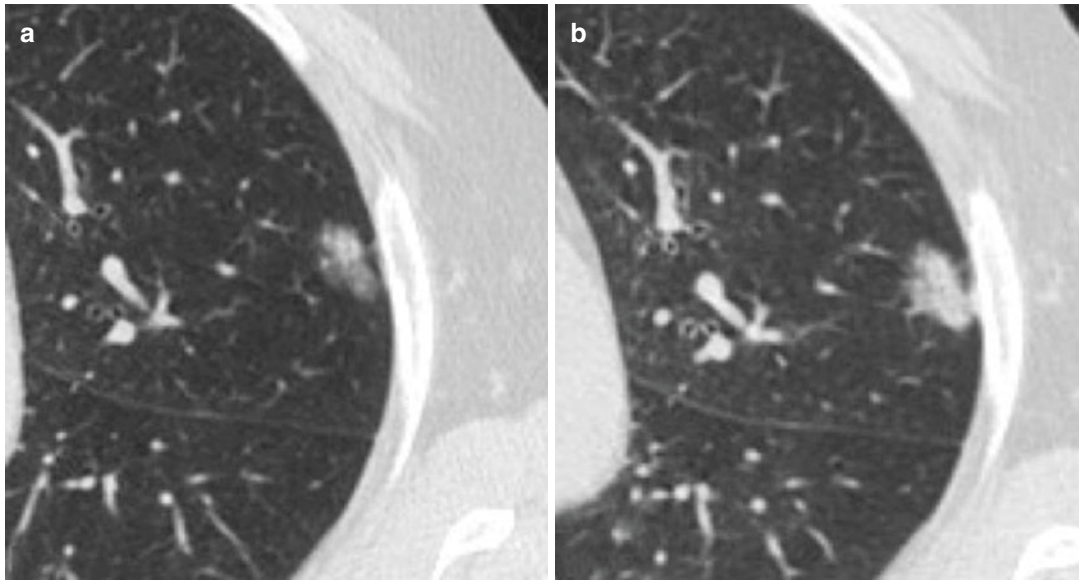


**Fig. 7.9** Mixed nodule. (**a**) First control; (**b**) 20-month revaluation: growth of total diameters and of the solid component. This patient underwent surgery, with final histological results of adenocarcinoma

## 7.2 Pulmonary Nodule Management

### 7.2.1 Guidelines in the Management of a Single Pulmonary Nodule

First guidelines on undetermined pulmonary nodules required a close follow-up for each nodule, repeating CT examination at 3, 6, 12, 18, and 24 months, irrespectively of the dimensions of the lesion and individual risk factors. This management program had several disadvantages, such as the increase of unnecessary CT exams, and then an excessive increase in ionizing radiation exposure and in overall clinical costs, with a contextual loss of credibility from the radiologist. At present, most recent recommendations for pulmonary nodule are based on patient's risk factors and characteristics of the nodule, with particular attention on nodule density (solid nodule vs. sub-solid nodule) and its dimensions. Likewise more attention is given also to patient radiation exposure during follow-up examinations.

In particular Fleischner Society recently published new guidelines [8], improving the previous indications published in 2005. These new guidelines, in consideration of several recent screening trials for lung cancer and increased knowledge on lung tumor histology and biological behavior, make some substantial changes on undetermined nodule management. In particular, for solid nodules, the minimum size for routine follow-up has been increased from 4 to 6 mm, and fewer CT follow-ups are recommended in case of nodule stability. Furthermore, for subsolid nodules, because of their higher volume doubling time value, a longer period is recommended before the first follow-up, and the total length of follow-up has been extended to 5 years.

Also the American College of Chest Physicians (ACCP) Guidelines (updated in 2013) based their recommendations on nodule size and the pretest probability of malignancy [9].

#### 7.2.1.1 Fleischner Society Guidelines for Solid Pulmonary Nodules

As mentioned, volume doubling time for malignant solid nodules is approximately 149 days

**Table 7.1** Fleischner Society 2017 Guidelines for follow-up of patients with solid solitary pulmonary nodule and **low risk** of malignancy; patients who have little or no history of smoking and no other risk factors are considered of low risk [8]

| | Low-risk patients | |
|---|---|---|
| Nodule dimension | Management | Comments |
| <6 mm | No follow-up required | Nodules <6 mm do not require routine follow-up, but certain patients at high risk with suspicious nodule morphology, upper lobe location, or both may warrant 12-month follow-up (recommendation 1A). |
| 6–8 mm | CT follow-up at 6–12 months, then consider CT at 18–24 months | |
| >8 mm | Consider CT, PET/CT, or tissue sampling at 3 months | |

**Table 7.2** Fleischner Society 2017 Guidelines for follow-up of patients with solid solitary pulmonary nodule and **high risk** of malignancy; patients with a history of smoking or other exposures or risk factors are considered of high risk [8]

| | High-risk patients | |
|---|---|---|
| Nodule dimension | Management | Comments |
| <6 mm | Optional CT at 12 months | Nodules <6 mm do not require routine follow-up, but certain patients at high risk with suspicious nodule morphology, upper lobe location, or both may warrant 12-month follow-up (recommendation 1A). |
| 6–8 mm | CT at 6–12 months, then CT at 18–24 months | |
| >8 mm | Consider CT, PET/CT, or tissue sampling at 3 months | |

while a morphological stability over a period of 2 years is an indicator of benignity. In this case the lesion does not require additional diagnostic studies; conversely the growth in size of the nodule needs a histological diagnosis, if not specifically contraindicated.

In patients with overall **low risk**, CT imaging follow-up should be performed depending on the dimension of the detected nodule (Table 7.1). For nodules <6 mm no follow-up should be performed; nodules between 6 and 8 mm require a CT follow-up at 6–12 months, and then a further CT at 18–24 months can be considered, while for nodules >8 mm a PET/CT, tissue sampling, or CT follow-up at 3 months are recommended.

Conversely, in patients with overall **high risk**, follow-up should be more frequent and prolonged over time (Table 7.2). In patients with a nodule <6 mm a CT follow-up at 12 months must be considered; nodules between 6 and 8 mm require CT follow-up at 6–12 months and 18–24 months, while for nodules >8 mm a PET/CT, tissue sampling, or CT follow-up at 3 months are recommended.

PET/CT examination is helpful in the management of pulmonary nodules reducing the need of puncture of non-enhancing solid nodules, with high sensitivity and specificity for solid pulmonary nodules between 1 and 3 cm in diameter. Nevertheless, it must be taken into consideration that active inflammation (i.e., active tuberculosis, histoplasmosis, rheumatoid nodules) may cause false positive on PET/CT scans because of their high glucose metabolism (Fig. 7.10) and that, likewise, low-grade malignant tumors, such as carcinoid or low-grade adenocarcinoma, may result as false negatives due to their low glucose metabolism.

#### 7.2.1.2 American College of Chest Physicians Guidelines for Solid Pulmonary Nodules

According to malignancy risk factors, pulmonary nodules **>8 mm** follow these recommendations:

- Low probability (<5%): CT follow-up at 3 to 6, 9 to 12, and 18 to 24 months, using thin sections and noncontrast, low-dose techniques.
- Intermediate probability (5–65%): functional imaging is needed, preferably with PET.
- High probability (>65%): Additional exams are not required; only biopsy should be performed before surgery (open or VATS) [10].

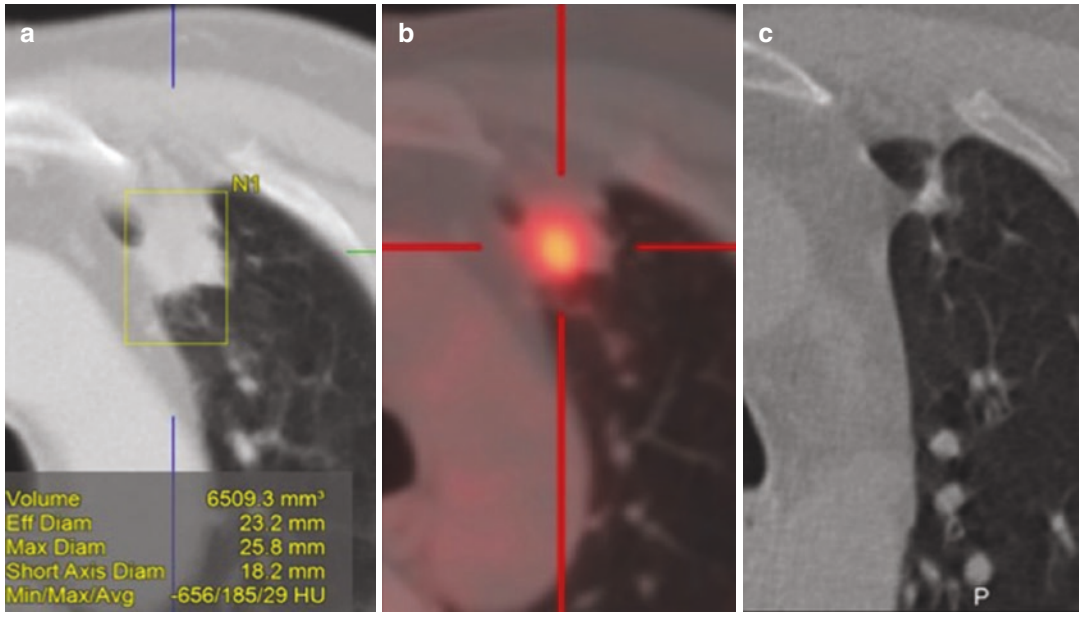


**Fig. 7.10** (**a**) Axial CT scan of a subpleural solid nodule in the upper left lobe with irregular margin; (**b**) PET/CT scan showing FDG uptake of the nodule; (**c**) CT follow-up after antibiotic therapy demonstrating the benign nature of lesion

Conversely, pulmonary nodules **≤8 mm** follow these recommendations:

- Nodules <4 mm need not be followed.
- Nodules 4–6 mm should be reevaluated at 12 months (no additional follow-up if unchanged).
- Nodules 6–8 mm should be reevaluated sometime at 6–12 months, and then again at 18–24 months.

#### 7.2.1.3 Particular Cases in the Management of Undetermined Incidental Pulmonary Nodules

- *Patients with known or suspected malignancy:* In case of patients with a malignant tumor that may induce pulmonary metastasis, follow-up should be planned according to the protocol of the interested neoplasia.
- *Young patients:* In <35-year-old patients, lung carcinoma is a rare finding, while radiation exposure has a heavy impact, with considerable risks. Therefore, unless a known primary neoplasia is present, the exposure to multiple CT during the follow-up of small incidental nodules should be avoided. In young patients, a single low-dose CT should be considered, 6–12 months after the first exam.
- *Patients with fever of unknown origin:* In some cases, such as patients with neutropenic fever, a pulmonary nodule can represent an active infection. Therefore, in these cases, a short-time follow-up or the possibility of a different intervention should be considered [4].

#### 7.2.1.4 Fleischner Society Guidelines for Sub-solid Pulmonary Nodules

It is known that tumors with sub-solid aspect have generally a long VDT and that a 2-year follow-up does not exclude the risk of malignancy. However, the aggressiveness of these lesions is uncertain and may not be significant during patient's life. Non-solid nodules can also have different evolution; for example, mixed nodules present greater malignancy prevalence, while small "pure" ground-glass nodules can even spontaneously regress because of their possible inflammatory nature [11].

**Table 7.3** Fleischner Society 2017 Guidelines for follow-up of patients with sub-solid solitary pulmonary nodule [8]

| | Pure ground glass | |
|---|---|---|
| Nodule dimension | Management | Comments |
| <6 mm | No follow-up required | In certain suspicious nodules <6 mm, consider follow-up at 2 and 4 years. If solid component(s) or growth develops, consider resection (recommendations 3A and 4A). |
| >6 mm | CT at 6–12 months to confirm persistence, then CT every 2 years until 5 years | |
| | **Part solid** | |
| **Nodule dimension** | **Management** | **Comments** |
| <6 mm | No follow-up required | Persistent part-solid nodules with solid components >6 mm should be considered highly suspicious (recommendations 4A–4C) |
| >6 mm | CT at 3–6 months to confirm persistence. If unchanged and solid component remains <6 mm, annual CT should be performed for 5 years. | |

For this reason Fleischner Society recommendations present some differences for pure ground-glass or part-solid lesion management (Table 7.3).

#### 7.2.1.5 American College of Chest Physicians Guidelines for Sub-solid Pulmonary Nodules

In case of **pure ground-glass** (nonsolid) morphology, ACCP suggests annual surveillance with noncontrast thin-section chest CT for at least 3 years only for those nodules larger than **5 mm**, while lesions <5 mm don't need further evaluation (Grade 2C).

They remark also that early follow-up at 3 months may be indicated for nonsolid nodules measuring more than 10 mm.

In case of **part-solid** (>50% ground-glass) appearance, ACCP suggests CT surveillance at approximately 3, 12, and 24 months, followed by annual CT surveillance for an additional 1–3 years, for nodules measuring less than **8 mm** (Grade 2C). Conversely lesions larger than 8 mm in diameter need reevaluation with chest CT at 3 months followed by further investigations with PET, nonsurgical biopsy, and/or surgical resection in case of nodule persistence (Grade 2C).

### 7.2.2 Guidelines in the Management of a Multiple Pulmonary Nodules

Multiple pulmonary nodules are focal areas of abnormal tissue, with approximately spherical morphology, whose dimensions range between a few millimeters and 3 cm.

According to Fleischner Society 2017 Guidelines, as in single-nodule evaluation, also multiple nodules require a clinical management mainly depending on dimension, density, and patient-related factors; when addressing multiple nodules, clinical decision should be guided by the most suspicious nodule (Tables 7.4 and 7.5) (Fig. 7.11) [8].

**Table 7.4** Fleischner Society 2017 Recommendations for management of incidentally detected multiple pulmonary nodules with **solid** density [8]

| Multiple solid nodules in low-risk patient | | |
|---|---|---|
| Nodule dimension | Management | Comments |
| <6 mm | No routine follow-up is required | Use most suspicious nodule as guide to management. Follow-up intervals may vary according to size and risk (recommendation 2A) |
| ≥6 mm | CT follow-up at 3–6 months; then consider CT at 18–24 months | |
| **Multiple solid nodules in high risk patient** | | |
| **Nodule dimension** | **Management** | **Comments** |
| <6 mm | Optional CT at 12 months | Use most suspicious nodule as guide to management. Follow-up intervals may vary according to size and risk (recommendation 2A) |
| ≥6 mm | CT follow-up at 3–6 months, then at 18–24 months | |

The anatomic distribution of multiple pulmonary nodules is generally one of the most important factors in differential diagnosis; considering anatomical architecture of secondary pulmonary lobule, three main location patterns have been described [12]:

**Table 7.5** Fleischner Society 2017 Recommendations for management of incidentally detected multiple pulmonary nodules with **sub-solid** density

| Multiple sub-solid nodules | | |
|---|---|---|
| Nodule dimension | Management | Comments |
| <6 mm | CT follow-up at 3–6 months; consider CT at 2 and 4 years, if stable[a] | Multiple <6 mm pure ground-glass nodules are usually benign, but consider follow-up in selected patients at high risk at 2 and 4 years (recommendation 5A) |
| ≥6 mm | CT follow-up at 3–6 months. Subsequent management based on the most suspicious nodule(s) | |

[a]Multiple <6 mm pure ground-glass nodules are usually benign, but follow-up at 2 and 4 years should be considered in selected patients at high risk [8]

- **Perilymphatic** distribution (Fig. 7.12a), where nodules predominantly occur in relation to pulmonary lymphatics, involving the peri-hilar-peribronchovascular interstitium, interlobular septa, and subpleural regions: It may be associated with different conditions, such as sarcoidosis, silicosis, CWP and other pneumoconiosis, lymphangitic spread of carcinoma or lymphoma, and lymphoproliferative diseases.
- **Centrilobular** distribution (Fig. 7.12b), where nodules are usually separated from pleural surface, fissures, and interlobular septa by a distance of at least several millimeters: These structures are typically spared, as opposed to the other two distribution patterns. Centrilobular nodules may present solid and with homogeneous density or ill-defined sub-solid density (ground-glass opacity), and their dimensions may range from a few millimeters to about 1 cm. Nodules limited to the centrilobular regions can reflect the presence of either interstitial or airspace abnormalities; in particular, they are typically seen in hypersensitivity pneumonitis, respiratory bronchiolitis in smokers, and infectious airway diseases

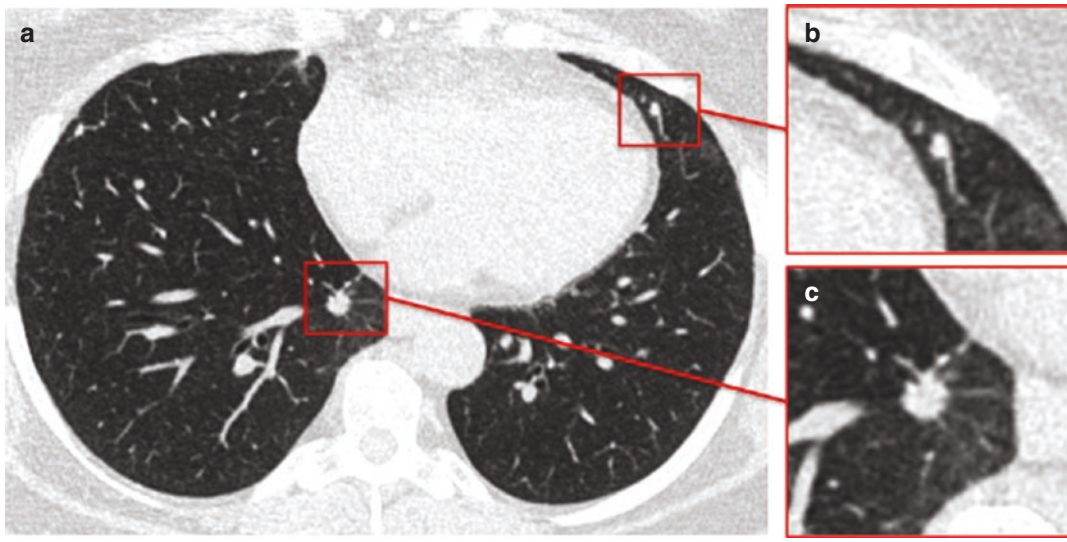


**Fig. 7.11** (**a**) Axial CT scan showing multiple lung nodules with different size and margins in the some patient. (**b**) 5 mm solid nodule with regular margin and (**c**) 9 mm solid nodule with irregular margins: management should be guided by the most suspicious nodule

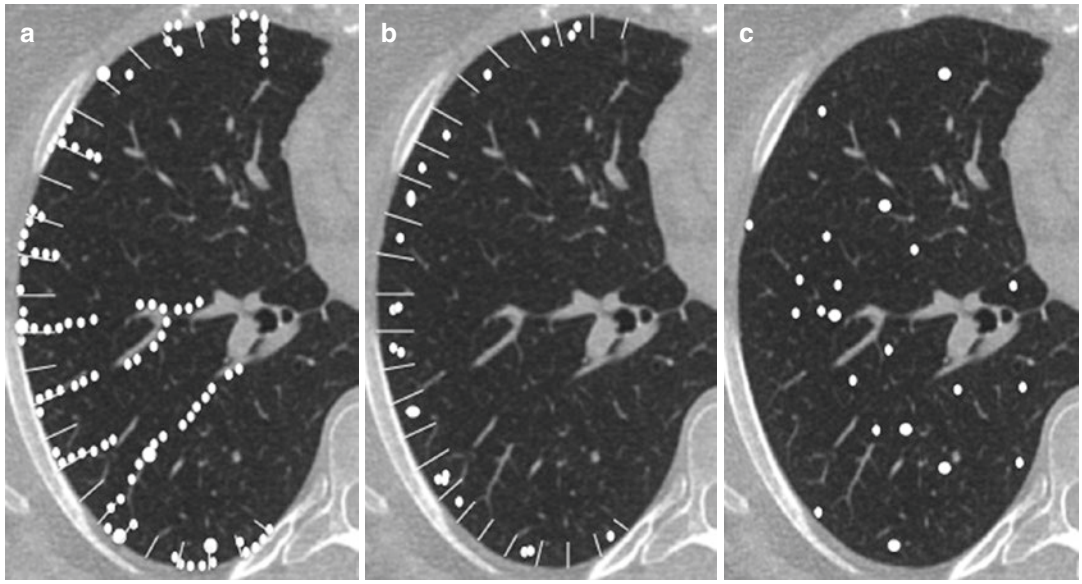


**Fig. 7.12** Schematic representation of nodular pattern distribution: (**a**) Perilymphatic distribution, where nodules predominantly occur in relation to pleural surfaces, interlobular septa, and peribronchovascular interstitium. (**b**) Centrilobular distribution where nodules spare the pleural surface, fissures, and interlobular septa. (**c**) Random distribution, nodules are variously distributed in relation to structures of the secondary lobule and lung

(endobronchial spread of tuberculosis or nontuberculous mycobacteria, bronchopneumonia); even if uncommonly, they may be seen in bronchioloalveolar carcinoma, pulmonary edema, and vasculitis.

- **Random** distribution (Fig. 7.12c), where nodules are variously distributed in relation to structures of the secondary lobule and lung: As with a lymphatic distribution, nodules can be seen in relation to the pleural surfaces, small vessels, and interlobular septa but do not appear to have a consistent or predominant relationship to any of these. On HRCT, a uniform distribution of nodules throughout the lung, without any respect for anatomical structures, is most typical. Lung involvement tends to be bilateral and symmetrical. An upper or a lower lobe predominance in size and number of nodules may be seen. Random distribution is commonly seen in patients with military tuberculosis, military fungal infections, and hematogenous metastasis.

Although these features may overlap in most cases, HRCT allows to evaluate the predominant pattern of nodule distribution. Once this pattern is assessed, the overall distribution of nodules (i.e., lobe location) and symmetry should be considered for differential diagnosis [12].

It appears clear, then, that multiple pulmonary nodules can be an expression of a wide range of pathologies; only malignant causes will be examined in depth in the following paragraphs.

### 7.2.3 Metastases

A really high percentage of multiple lung lesions have a metastatic nature (84–98%) [13]. Pulmonary metastases are relatively common and result from hematogenous or lymphatic spread of tumors from different origins; the most common are testicle, ovary, kidney, and breast, or other variable locations for melanomas and sarcomas.

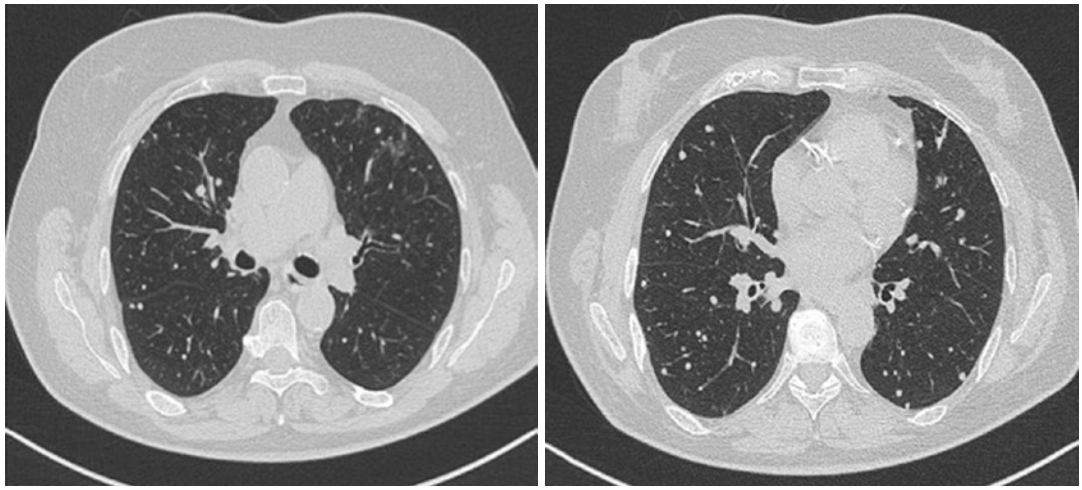

**Fig. 7.13** "Miliary" pulmonary metastases from medullary thyroid carcinoma

Commonly, hematogenous metastases lack the specific relationship to lobular structures and interlobular septa that are mostly seen in patients who have lymphatic involvement and appear as multiple, circumscribed, and round nodules with typical soft-tissue attenuation, with various dimension, and with random distribution, although they are often located in the most peripheral regions of the lung. It is not uncommon for some nodules to be seen in relation to small branches of pulmonary arteries (*feeding vessel sign)*, suggesting the modality of the dissemination. Detection of pulmonary nodules and assessment of their relationship to vascular structure are improved with the use of maximum intensity projection (MIP) technique.

Some tumors, such as melanoma, thyroid medullary tumor, and renal cell carcinoma are associated with metastasis with a typical ***miliary*** pattern, with countless millimetric nodules (Fig. 7.13).

"***Cannonball***" metastases are large (even greater than 10 cm), well-circumscribed, round pulmonary lesions that usually come from sarcoma, colorectal carcinoma, renal carcinoma, and melanoma (Fig. 7.14).

Metastatic nodules can also ***cavitate***, as typically occurs in squamous cell carcinoma of the head and neck, of the uterine cervix, and of the bladder, or in case of gastric adenocarcinoma or sarcoma (Fig. 7.15).

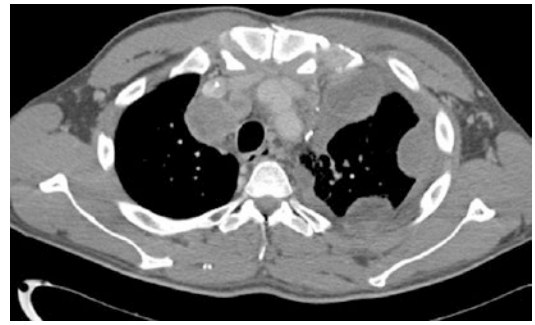

**Fig. 7.14** Large "cannonball" metastases from sarcoma

Sometimes metastases may contain ***calcifications***, as in the case of osteosarcoma, chondrosarcoma, papillary thyroid carcinoma, mucinous carcinoma of the gastrointestinal tract, breast cancer, and ovary carcinoma (Fig. 7.16); otherwise, calcifications may appear as a consequence of antiproliferative treatments.

In other cases, metastasis may show a "***lepidic growth***" pattern, meaning that they can spread throughout preexistent anatomical structures without destroying the alveolar architecture, then generating pneumonia-like areas of parenchymal consolidation, sometimes with air bronchogram sign within, or multiple semisolid nodules in the airspaces, often with peripheral halo. This behavior, which is typical of bronchioloalveolar carcinoma, can also be shown by other types of

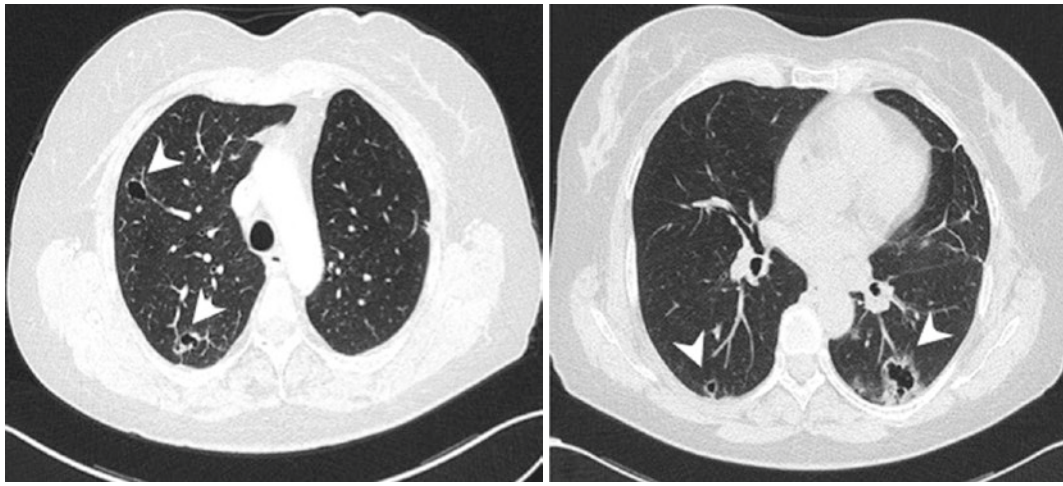

**Fig. 7.15** Cavitary pulmonary metastases from cervical cancer (*arrows*)

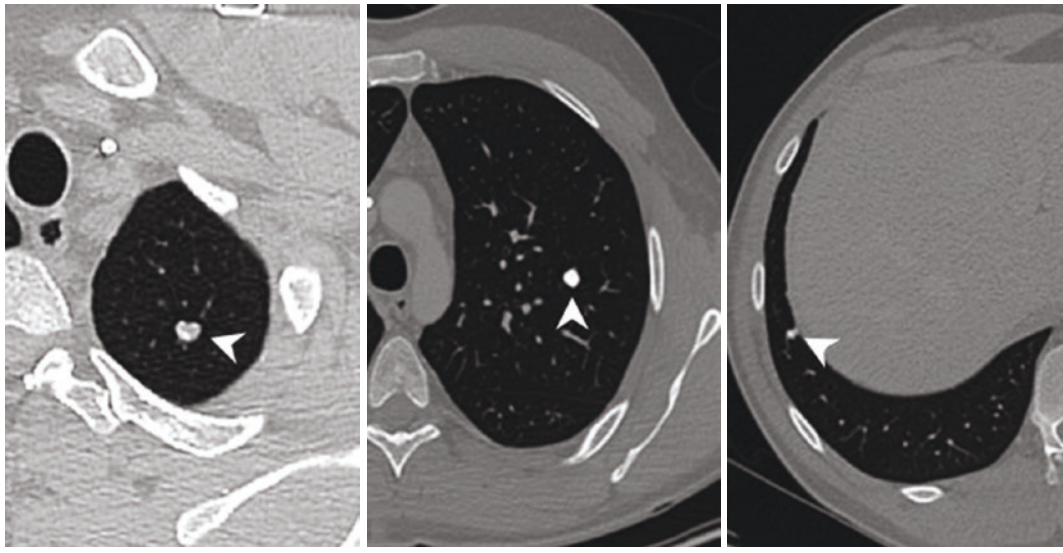

**Fig. 7.16** "Calcified" metastases from osteosarcoma (*arrows*)

adenocarcinoma, especially from gastric or colorectal origin.

Moreover, some metastases may present a peripheral sub-solid zone as a result of hemorrhagic phenomena (Fig. 7.17); this appearance is defined as "***halo sign***" and is commonly associated with hypervascular tumors such as choriocarcinoma or angiosarcoma.

Contrary to what happens with hematogenous metastases, patients with lymphatic metastases do not present discrete tumor nodules, but rather a widespread interstitial infiltration with reticular or reticulo-nodular pattern, determining a typical condition of **pulmonary lymphangitic carcinomatosis (PLC)** (Fig. 7.18). PLC usually results from hematogenous spread to the lung, with subsequent interstitial and lymphatic invasion, but can also occur because of direct lymphatic spread of tumor from mediastinal and hilar lymph nodes. However, the first process seems the most likely, since hilar lymphadenopathy is visible in only 50% of patients with PLC.

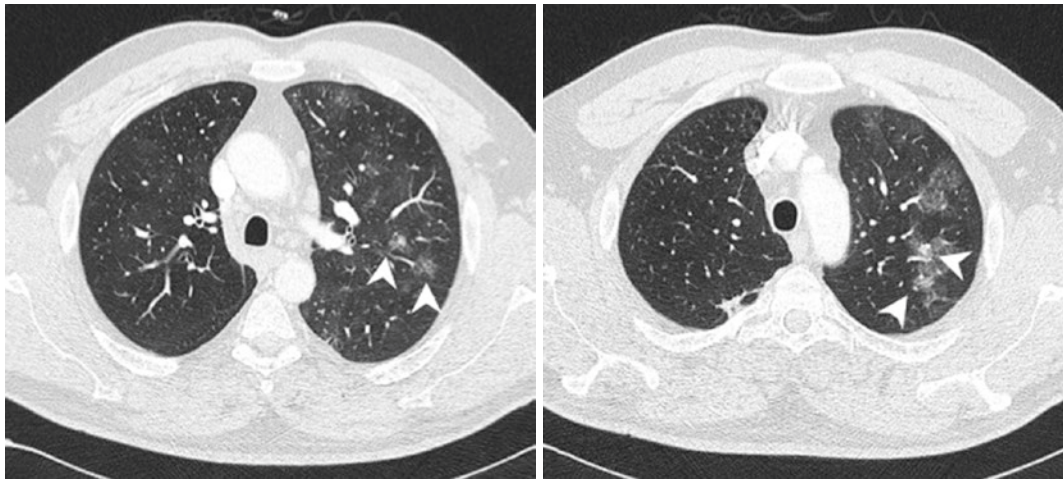

**Fig. 7.17** "Hemorrhagic" metastases from melanoma (*arrows*)

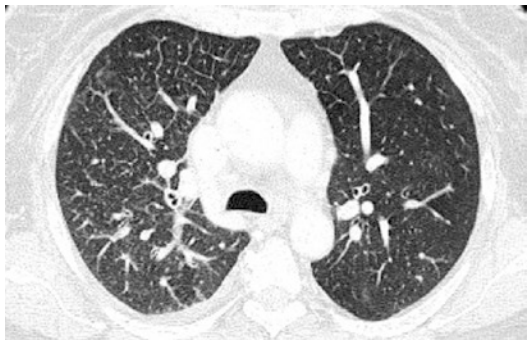

**Fig. 7.18** Pulmonary lymphangitic carcinomatosis (PLC) with reticulo-nodular interstitial infiltration pattern

This condition is commonly determined by primitive tumors from lung, stomach, breast, pancreas, prostate, cervix, or thyroid, and in patients with metastatic adenocarcinoma from an unknown primary site.

CT exam may highlight a smooth or nodular thickening of the peribronchovascular interstitium around bronchi and vessels in peri-hilar regions of the lung, and smooth or nodular thickening of interlobular septa and subpleural interstitium, sometimes with pleural carcinomatosis and fissure thickening; peribronchovascular and subpleural nodules are typically not as profuse as in patients with sarcoidosis; normal architecture of secondary pulmonary lobule remains preserved despite the presence of these findings. In patients with lymphangitic carcinomatosis, lung involvement may be unilateral, patchy, bilateral, or symmetric; the abnormalities often present a central or peri-hilar predominance and they may predominate in the upper or lower lobes or may be diffuse.

In a patient with known tumor history and symptoms of dyspnea, typical PLC findings at CT are usually considered diagnostic, and lung biopsy is usually not required in clinical practice. On the other hand, in patients without a known neoplasm, HRTC may be helpful in directing lung biopsy to the most productive sites, as PLC is often focal. Also, because transbronchial biopsy is usually positive in PLC, typical HRCT findings can also serve to suggest this as the most appropriate procedure.

### 7.2.4 Adenocarcinoma In Situ, Minimally Invasive Adenocarcinoma, and Invasive Adenocarcinoma of Lung

According to IASLC classification of 2011, adenocarcinoma in situ (**AIS**), minimally invasive adenocarcinoma (**MIA**), and invasive adenocarcinoma of lung represent new classification entities which now replaces the defunct term **bronchoalveolar carcinoma (BAC)** [14].

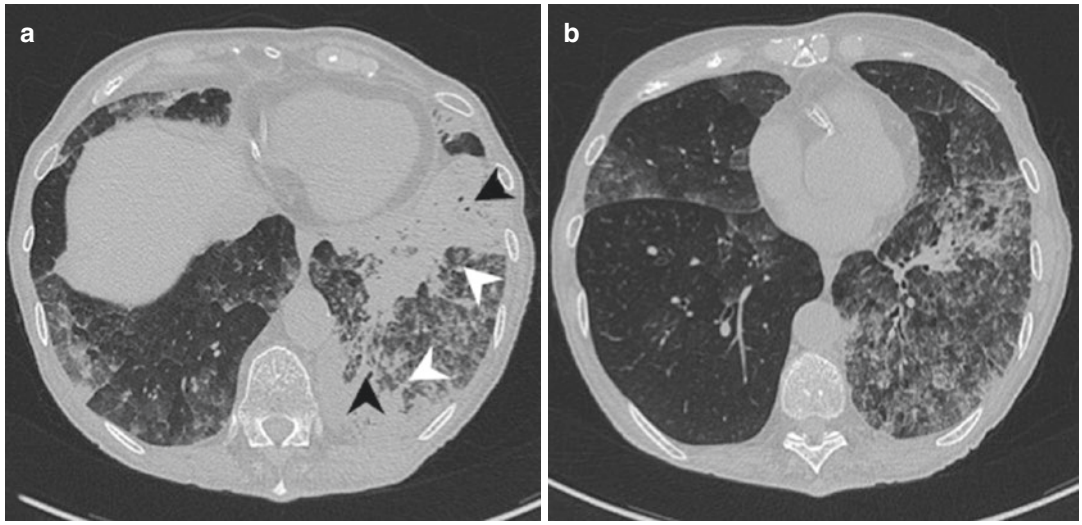


**Fig. 7.19** Invasive adenocarcinoma of lung. (**a**) Segmental areas of parenchymal consolidation (*white arrows*) with air bronchogram sign (*black arrows*); (**b**) diffuse interstitial spread of invasive adenocarcinoma in left lower lobe

This histotype has a peculiar growth pattern, since it spreads along preexisting structures and maintains alveolar architecture intact (lepidic growth). At CT, AIS and MIA can appear as single, peripheral, sub-solid pulmonary nodule (≤3 cm) while invasive adenocarcinoma as segmental or lobar areas of parenchymal consolidation, or as a diffuse pulmonary disease (Fig. 7.19).

The latter form may appear as multiple pulmonary nodules with various degrees of border definition and solid or semisolid density, whose sizes typically range from 1 mm to 3 cm (Fig. 7.20), often associated with halo sign. Commonly, the predominant nodule distribution is centrilobular, indicating endobronchial spread of tumor, or bronchocentric, due to lymphatic spread.

Alternative presentations of the diffuse form include multiple areas of parenchymal consolidation, with possible air bronchogram sign, air-filled cystic spaces or pseudocavitations, and patchy or multifocal ground-glass opacity with or without interlobular septal thickening (crazy paving). Areas of consolidation or ground-glass opacity can represent the intra-alveolar tumor growth or the presence of mucin and fluid produced by the tumor. Since fluid and mucus have a low attenuation, if CT is performed with contrast infusion, contrast-enhanced pulmonary vessels appear denser than the surrounding opacified lung, a condition known as the *CT angiogram sign*. However, this sign shows only limited value in differential diagnosis, because it depends on the volume and concentration of contrast injected and has also been observed in other diseases, such as bacterial pneumonia, lipoid pneumonia, pulmonary lymphoma, pulmonary infarction, and pulmonary edema. Moreover, when considering a pulmonary consolidation, the peripheral localization or the coexistence of nodules should raise the suspect for diffuse adenocarcinoma.

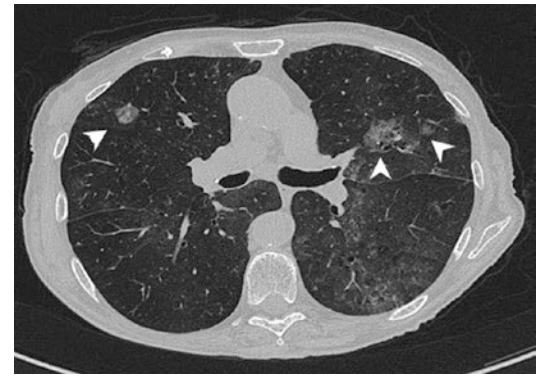

**Fig. 7.20** Multiple and bilateral sub-solid nodules from invasive adenocarcinoma of lung (*arrows*)

However, on the basis of imaging appearance alone, it may be impossible to differentiate a pulmonary adenocarcinoma from an alveolar metastasis; in these cases, the evaluation of other basic aspects is necessary, such as the presence of

an extrapulmonary tumor, or the detection of mediastinal or thoracic lymphadenopathies, in nontypical sites for lung tumors.

### 7.2.5 Multiple Primitive Pulmonary Tumors

A non-negligible percentage of newly diagnosed lung tumors (about 8%) occur in patients with a history of previous neoplasia.

The cases of multiple primitive pulmonary tumors are increasing because of the improvement in diagnosis and surveillance tools (CT and PET) and the increasing of overall patients' survival.

Multiple primitive pulmonary tumors can be either synchronous or metachronous and they are difficult to distinguish from metastatic lesions, because of the sharing of analogue histological characteristics and the difficulty in the evaluation of lesions occurring in areas of previous radiotherapy, with unavoidable modifications in tissue organization [15].

The distinction between multiple primitive pulmonary tumors (synchronous or metachronous) and intrapulmonary metastasis is currently based on established clinicopathological criteria [16, 17]. The expectation is that new promising molecular and genomic methods might contribute to a clear and effective differentiation, especially for a correct treatment choice, which is surgical in case of a second primary lung cancer, in the first instance.

### 7.2.6 Pulmonary Lymphoma

The term pulmonary lymphoma indicates the involvement of lung parenchyma as part of a systemic lymphomatous disease. This occurrence can be the result of two different processes, so that it is possible to define the following:

– *Secondary lung lymphoma*: It is the most common type, involving about 4% of patients with NHL, and it is determined by the hematogenous dissemination of the disease (HL and NHL) or the direct invasion of pulmonary parenchyma from hilar or mediastinal lymph nodes. It is considered as the progression of a known hematologic disorder, originating from mediastinum or other extra-thoracic locations.
– *Primary lung lymphoma*: More rarely seen, it only accounts for 3–4% of lymphomas with extranodal location and for 0.5–1% of all lung tumors. It is characterized by the involvement of pulmonary parenchyma without any detectable extrapulmonary manifestation. In clinical practice, lymphoma involving the lung can be considered *primary pulmonary lymphoma* if there is no history of lymphoma, mediastinal lymph node enlargement is invisible on chest radiographs, it is unassociated with extra-thoracic disease, and there is no evidence of extra-thoracic dissemination for at least 3 months after the initial diagnosis. The category of primary lung lymphomas includes three distinct disease entities: low-grade pulmonary B-cell lymphoma, high-grade pulmonary B-cell lymphoma, and lymphomatoid granulomatosis [18].

Possible radiological appearances of lung lymphoma include bilateral multiple pulmonary nodules, sometimes with bronchocentric distribution, widespread opacities with reticulonodular pattern, or consolidation areas, sometimes with cavitations or with air bronchogram sign. Pleural thickening or effusion can be associated with these findings (Fig. 7.21).

### 7.2.7 Kaposi Sarcoma

Prior to the use of highly active antiretroviral therapy (HAART), 10–25% of patients with AIDS developed Kaposi sarcoma, a low-medium-grade mesenchymal tumor involving the lymphovascular system. However, even after the introduction of this form of treatment, Kaposi sarcoma remains the most common cancer identified in patients with HIV/AIDS. Approximately one-third of all patients with Kaposi sarcoma show a pulmonary location, which can appear with either a nodular or an interstitial pattern. CT exam identifies bilateral nodules with hazy and irregular margins, with typical "flame-like" morphology. These lesions do not show any cavitations nor calcifications, and often have a symmetrical bronchocentric

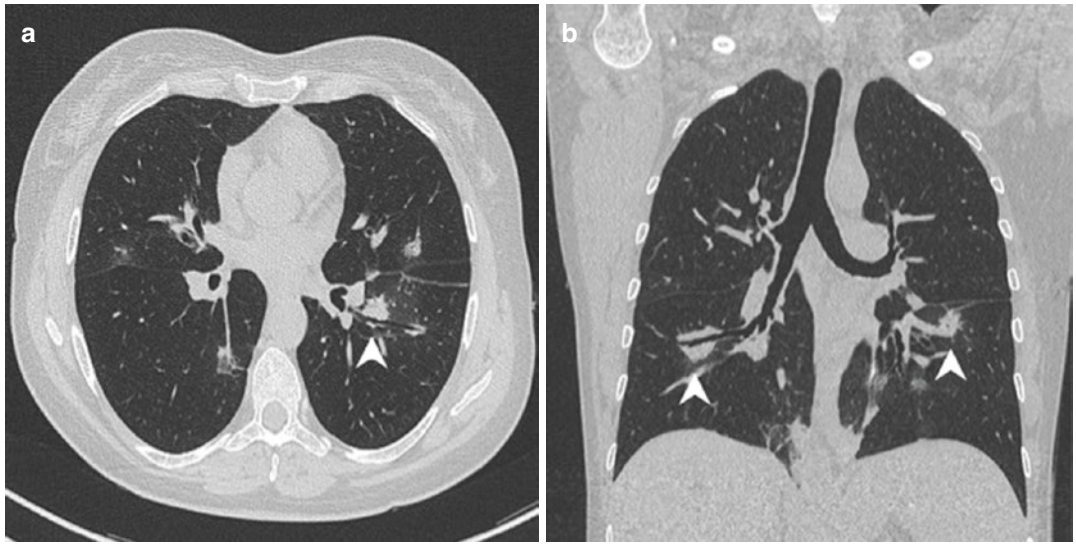


**Fig. 7.21** Bilateral multiple pulmonary nodules with "bronchocentric" distribution from lung lymphoma (*arrows*)

location, usually in para-hilar and basal regions; surrounding irregular sub-solid areas, thickening of interlobular septa, pleural effusion, and lymphadenopathies can all be associated.

## References


1. Hansell DM. Fleischner Society: glossary of terms for thoracic imaging. Radiology. 2008;246(3):697–722.
2. Wahidi MM. Evidence for the treatment of patients with pulmonary nodules: when is it lung cancer?: ACCP evidence-based clinical practice guidelines (2nd edition). Chest. 2007;132(3 Suppl):94S–107S.
3. Valencia R. Value of axial and coronal maximum intensity projection (MIP) images in the detection of pulmonary nodules by multislice spiral CT: comparison with axial 1-mm and 5-mm slices. Eur Radiol. 2006;16(2):325–32.
4. MacMahon H. Guidelines for management of small pulmonary nodules detected on CT scans: a statement from the Fleischner Society. Radiology. 2005;237(2):395–400.
5. Edey AJ, Hansell DM. Incidentally detected small pulmonary nodules on CT. Clin Radiol. 2009;64(9):872–84.
6. Henschke CI. CT screening for lung cancer: frequency and significance of part-solid and nonsolid nodules. AJR Am J Roentgenol. 2002;178(5):1053–7.
7. Hasegawa M. Growth rate of small lung cancers detected on mass CT screening. Br J Radiol. 2000;73(876):1252–9.
8. MacMahon H, Naidich DP, Goo JM, et al. Guidelines for Management of Incidental Pulmonary Nodules Detected on CT images: from the Fleischner Society 2017. Radiology. 2017;23:161659.
9. Gould MK, Donington J, Lynch WR, et al. Evaluation of individuals with pulmonary nodules: when is it lung cancer? Chest. 2013;143(5 suppl):e93S–e120S.
10. Gould MK. Evaluation of patients with pulmonary nodules: when is it lung cancer?: ACCP evidence-based clinical practice guidelines (2nd edition). Chest. 2007;132(3 Suppl):108S–30S.
11. Oh JY. Clinical significance of a solitary ground-glass opacity (GGO) lesion of the lung detected by chest CT. Lung Cancer. 2007;55(1):67–73.
12. Cancellieri A, Dalpiaz G, et al. Diffuse lung disease, clinical features, pathology, HRCT. New York: Springer; 2004.
13. Seo JB, Im JG, Goo JM, Chung MJ, Kim MY. Atypical pulmonary metastases: spectrum of radiologic findings. Radiographics. 2001;21(2):403–17.
14. Travis WD, et al. State of the art: concise review. International Association for the Study of Lung Cancer/American Thoracic Society/European Respiratory Society International Multidisciplinary Classification of Lung Adenocarcinoma. J Thorac Oncol. 2011;6(2):244–85.
15. Loukeri AA, et al. Metachronous and synchronous primary lung cancers: diagnostic aspects, surgical treatment, and prognosis. Clin Lung Cancer. 2015;16(1):15–23.
16. Martini N, Melamed MR. Multiple primary lung cancers. J Thorac Cardiovasc Surg. 1975;70:606–12.
17. Antakli T, Schaefer RF, Rutherford JE, et al. Second primary lung cancer. Ann Thorac Surg. 1995;59:863–7.
18. Cadranel J, Wislez M, et al. Primary pulmonary lymphoma. Eur Respir J. 2002;20(3):750–62.

# Staging of Non-small Cell Lung Cancer

8

Gregor Sommer and Mark N. Wiese

**Abstract**

The process of lung cancer staging is getting increasingly complex and requires distinct input from specialized physicians of radiology, nuclear medicine, thoracic surgery, and pathology. Also after the advent of the revised 8th edition of the TNM classification, noninvasive imaging with CT and $^{18}$F-FDG-PET, supplemented by MRI, continues to provide the initial basis for clinical staging by determining the anatomic extent of the disease and thus plays a pivotal role in the diagnosis and management of NSCLC. In cases without distant metastatic disease, pretherapeutic mediastinal staging with invasive methods (mediastinoscopy or endoscopic procedures) is mandatory to determine the most appropriate treatment strategy if imaging findings are positive or in certain scenarios that come along with a high risk of false-negative imaging results. The most important limitation inherent to the current TNM staging system is its purely anatomic character that provides insufficient information related to the many different sorts of novel targeted therapies. This translates also to imaging-derived staging of NSCLC in radiology and nuclear medicine, where—besides higher anatomic resolution and image quality—the most important remaining challenge is to gather more "functional" information and generate a more comprehensive picture of the disease by noninvasive staging methods.

**Keywords**

Non-small cell lung cancer · Neoplasm staging
TNM classification · Positron-emission tomography · Computed tomography
Magnetic resonance imaging · Mediastinoscopy
Endoscopic ultrasonography

## 8.1 Development and Evaluation of T, N, and M Descriptors

Lung cancer is the most common cancer worldwide accounting for nearly 13% of all newly diagnosed cancers in 2012 [1]. With almost 20% of all cancer-related deaths it is also the most common cause of death from cancer despite substantial improvements in diagnosis, therapy, and prevention in the last decades. Non-small cell lung cancer (NSCLC) is by far the most often occurring type of lung cancer with a proportion of 83.4% [2].

G. Sommer (✉)
Clinic of Radiology and Nuclear Medicine, University Hospital Basel, University of Basel, Basel, Switzerland
e-mail: gregor.sommer@usb.ch

M. N. Wiese
Clinic of Thoracic Surgery, University Hospital Basel, University of Basel, Basel, Switzerland
e-mail: mark.wiese@usb.ch


M. Anzidei, M. Anile (eds.), *Diagnostic Imaging for Thoracic Surgery*,
https://doi.org/10.1007/978-3-319-89893-3_8

Staging of cancer describes the diagnostic process of gathering all pieces of information relevant to define the extent of the disease of an individual patient. Correct staging is crucial both for defining the prognosis of the patient and for selecting the most appropriate therapy. Imaging has developed as an important contributor to this assessment at initial diagnosis, as well as during post-interventional follow-up. As for most solid tumors, staging of NSCLC follows the TNM (tumor, node, metastasis) formula, which has initially been proposed by Denoix in 1946 [3] and has been accepted shortly after by the Union Internationale Contre le Cancer (UICC) and the American Joint Committee on Cancer (AJCC) as the official system for coding the anatomic extent of the disease.

Although staging is most commonly performed in the context of the initial diagnosis, it can also take place at other significant points of time in the history of a cancer patient. Thus, along with the TNM formula, it's important to record in which context the tumor stage has been defined. For this purpose, prefixes are applied to distinguish between the clinical stage (cTNM), the pathological stage (pTNM), post-therapeutic stages (yc/ypTNM), tumor stages at the time of progression or recurrence (rTNM), and the stage at autopsy (aTNM).

Table 8.1 summarizes the TNM descriptors for lung cancer as applied in the 8th edition of the TNM system [5] that came into effect on January 1st 2017. As the 7th edition [6], the 8th edition of the TNM classification applies to all histopathological subtypes of NSCLC, to small-cell carcinoma and to atypical carcinoids.

The T descriptor denotes the extent of the primary tumor by describing its morphological features like size and location, rates the involvement of adjacent anatomic structures, and reports the presence of separate tumor nodules in the lung. As compared to the T descriptors in the 7th edition, the T categories in the 8th edition were further refined by introducing two new size cut points at 1 and 4 cm. This refinement was made also with respect to the increasing numbers of screening detected cancers. Also, a new category for minimally invasive adenocarcinoma (T1(mi)) was added. Moreover, tumors between 5 and 7 cm in size were

**Table 8.1** T, N, and M descriptors for the 8th edition of TNM classification for lung cancer

| Descriptor | Definition | |
|---|---|---|
| T: Primary tumor | | |
| T*x* | | Primary tumor cannot be assessed or tumor proven by presence of malignant cells in sputum or bronchial washings but not visualized by imaging or bronchoscopy |
| T0 | | No evidence of primary tumor |
| Tis | | Carcinoma in situ |
| T1 | | Tumor ≤3 cm in greatest dimension, surrounded by lung or visceral pleura, without invasion more proximal than the lobar bronchus |
| | **T1(mi)** | **Minimally invasive adenocarcinoma**[a] |
| | **T1a** | **Tumor ≤1 cm in greatest dimension**[b] |
| | **T1b** | **Tumor >1 cm but ≤2 cm in greatest dimension**[b] |
| | **T1c** | **Tumor >2 cm but ≤3 cm in greatest dimension**[b] |
| **T2** | | Tumor >3 cm **but ≤5 cm** or with any of the following features[c]:<br>– **Involves main bronchus regardless of distance from the carina but without involvement of the carina**<br>– Invades visceral pleura<br>– **Associated with atelectasis or obstructive pneumonitis that extends to the hilar region, involving part or all of the lung** |
| | **T2a** | **Tumor >3 cm but ≤4 cm in greatest dimension** |
| | **T2b** | **Tumor >4 cm but ≤5 cm in greatest dimension** |
| **T3** | | **Tumor >5 cm but ≤7 cm in greatest dimension** or associated separate tumor nodule(s) in the same lobe as the primary tumor or directly invades any of the following structures: chest wall (including the parietal pleura and superior sulcus tumors), phrenic nerve, parietal pericardium |
| **T4** | | Tumor >7 cm in greatest dimension or associated with separate tumor nodule(s) in a different ipsilateral lobe than that of the primary tumor or invades any of the following structures: **diaphragm**, mediastinum, heart, great vessels, trachea, recurrent laryngeal nerve, esophagus, vertebral body, and carina |

**Table 8.1** (continued)

| Descriptor | Definition | |
|---|---|---|
| N: Regional lymph node involvement | | |
| N*x* | | Regional lymph nodes cannot be assessed |
| N0 | | No regional lymph node metastasis |
| N1 | | Metastasis in ipsilateral peribronchial and/or ipsilateral hilar lymph nodes and intrapulmonary nodes, including involvement by direct extension |
| N2 | | Metastasis in ipsilateral mediastinal and/or subcarinal lymph node(s) |
| N3 | | Metastasis in contralateral mediastinal, contralateral hilar, ipsilateral or contralateral scalene, or supraclavicular lymph node(s) |
| M: Distant metastasis | | |
| M0 | | No distant metastasis |
| M1 | | Distant metastasis present |
| | M1a | Separate tumor nodule(s) in a contralateral lobe; tumor with pleural or pericardial nodule(s) or malignant pleural or pericardial effusion[d] |
| | **M1b** | **Single extrathoracic metastasis[e]** |
| | **M1c** | **Multiple extrathoracic metastases in one or more organs** |

Changes to the 7th edition are in bold
Reprinted from [4] with permission from Elsevier
[a]Solitary adenocarcinoma, ≤3 cm with a predominately lepidic pattern and ≤5 mm invasion in any one focus
[b]The uncommon superficial spreading tumor of any size with its invasive component limited to the bronchial wall, which may extend proximal to the main bronchus, is also classified as T1a
[c]T2 tumors with these features are classified as T2a if ≤4 cm in greatest dimension or if size cannot be determined, and T2b if >4 cm but ≤5 cm in greatest dimension
[d]Most pleural (pericardial) effusions with lung cancer are due to tumor. In a few patients, however, multiple microscopic examinations of pleural (pericardial) fluid are negative for tumor and the fluid is nonbloody and not an exudate. When these elements and clinical judgment dictate that the effusion is not related to the tumor, the effusion should be excluded as a staging descriptor
[e]This includes involvement of a single distant (nonregional) lymph node

adjusted in terms of prognosis (now classified as T3 instead of T2b), and some reassignments were made concerning tumor invasion to the diaphragm (now classified as T4) and the main bronchus within 2 cm of the carina (now classified as T2).

The N descriptor reports about the absence, presence, and location of locoregional lymph node metastases, which strongly affects the extensiveness of therapy and the prognosis of the patient. For this reason, N staging may be regarded as the most important component of intrathoracic staging. N staging is based on a standardized lymph node map (Fig. 8.1) that assigns any thoracic lymph node to a defined anatomic zone. The different stations and zones can be separated following clear anatomic landmarks assessable on cross-sectional imaging (see also Sect. 8.2.1). This lymph node map has been officially released by the International Association for the Study of Lung Cancer (IASCL) along with the 7th edition of the TNM classification [7] and is a combination and further development of the two previously used maps proposed by Mountain and Dresler [8] and the Japan Lung Cancer Society [9]. Using this map, N stage is defined by the most remote metastatic lymph node with respect to the location of the primary tumor. N descriptors of the 8th edition are unchanged compared to the 7th edition. However, a subclassification based on the number of involved nodes in N1 and N2 stations has been proposed for testing to enable potential refinements in future revisions (not contained in Table 8.1).

The M category finally describes the absence, presence, and location of distant metastases. Here, the 8th edition introduced a new M category to distinguish the rare but prognostically favorable cases with one single extrathoracic metastasis (new M1b) from those with multiple extrathoracic metastases (new M1c). The category M1a, as before, describes intrathoracic metastases in the contralateral lung, pleura, or pericardium.

As for other tumors, optional descriptors of prognostic relevance as listed in Table 8.2 may be used along with the TNM descriptors in the classification. These include the grade of differentiation (G); the absence or presence of perineural, lymphatic, or vascular invasion (Pn, L, and V); and the completeness of surgical tumor resection (R).

It is important to be aware that the T, N, and M classifiers describe the extent of disease only in respect to anatomic criteria. The key role of a

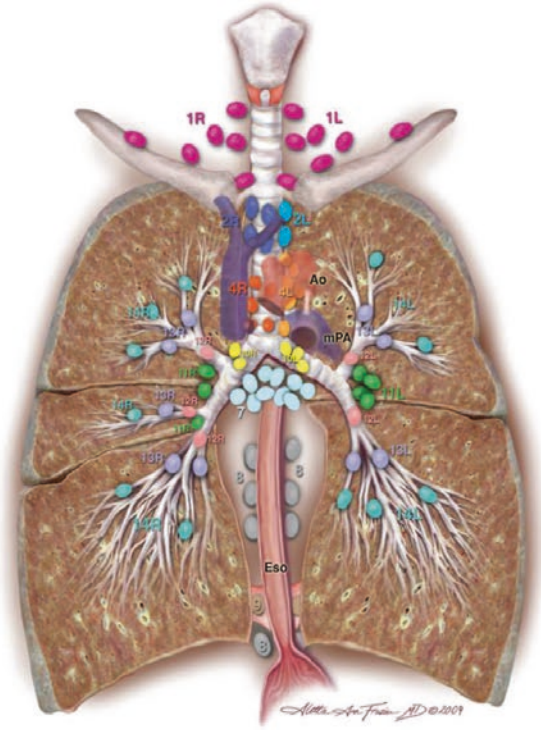


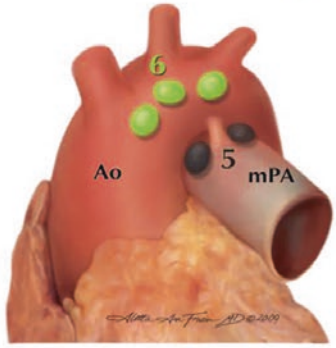


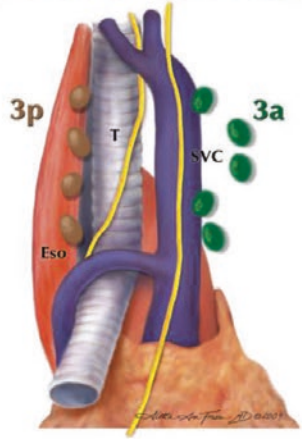


*Supraclavicular zone*
- 1 Low cervical, supraclavicular, and sternal notch nodes

SUPERIOR MEDIASTINAL NODES

*Upper zone*
- 2R Upper Paratracheal (right)
- 2L Upper Paratracheal (left)
- 3a Prevascular
- 3p Retrotracheal
- 4R Lower Paratracheal (right)
- 4L Lower Paratracheal (left)

AORTIC NODES

*AP zone*
- 5 Subaortic
- 6 Para-aortic (ascending aorta or phrenic)

INFERIOR MEDIASTINAL NODES

*Subcarinal zone*
- 7 Subcarinal

*Lower zone*
- 8 Paraesophageal (below carina)
- 9 Pulmonary ligament

N1 NODES

*Hilar/Interlobar zone*
- 10 Hilar
- 11 Interlobar

*Peripheral zone*
- 12 Lobar
- 13 Segmental
- 14 Subsegmental

**Fig. 8.1** The International Association for the Study of Lung Cancer (IASLC) lymph node map, including the proposed grouping of lymph node stations into "zones" for the purposes of prognostic analyses. Reprinted from [7] with permission from Elsevier

classification system for cancer, however, is to translate this anatomic information into prognostic information. For this purpose, so-called prognostic groups are derived from the anatomic TNM descriptors. These prognostic groups are also referred to as the UICC tumor stages and form the core element of the TNM classification system. It is obvious that TNM descriptors and stage groupings need to be continuously adapted to the ever-changing conditions in lung cancer diagnosis and therapy. The stage groupings of the 8th edition of the TNM classification are shown in Table 8.3. Changes from the 7th edition include the introduction of several new subcategories for stage IA (subdivided into IA1–3), stage III (new category IIIC), and stage IV (subdivided into IVA and IVB). In addition, some of the TNM groups have been relocated into a different stage, which are T1 N1 M0 (former IIA, now IIB), T2a N1 M0 (former IIA, now IIB), and T3 N2 M0 (former IIIA, now IIIB). An overview on the effect of the refined stage grouping in terms of overall survival is given in Fig. 8.2.

**Table 8.2** Optional descriptors of prognostic relevance to be used with the TNM classification [5]

| Optional TNM descriptors | | |
|---|---|---|
| G | | Grade of differentiation |
| | G1 | Well differentiated |
| | G2 | Moderately differentiated |
| | G3 | Poorly differentiated |
| | G4 | Undifferentiated |
| Pn | | Perineural invasion |
| | Pn0 | No perineural invasion |
| | Pn1 | Perineural invasion |
| L | | Lymphatic invasion |
| | L0 | No lymphatic invasion |
| | L1 | Lymphatic invasion |
| V | | Vascular invasion |
| | V0 | No venous invasion |
| | V1 | Microscopic venous invasion |
| | V2 | Macroscopic venous invasion |
| R | | Completeness of resection |
| | R0 | No residual tumor |
| | R1 | Microscopic residual tumor |
| | R2 | Macroscopic residual tumor |

The UICC published its first edition of the TNM Classification of Malignant Tumors in 1958. It has been revised seven times until the proposals for the 8th edition of the TNM classification were published in 2015 and 2016 [4, 10, 11]. By consensus between the UICC and the AJCC, efforts were made from the beginning to avoid publication of different classifications. Editions 2–6 of the UICC manual on the TNM Classification of Malignant Tumors were based on a continuously growing database of patients

**Table 8.3** Definition of UICC stages from the TNM descriptors according to the 8th edition of the TNM staging system for NSCLC [4]

| UICC stage | TNM Descriptors | | | |
|---|---|---|---|---|
| Occult carcinoma | T*x* N0 M0 | | | |
| 0 | Tis N0 M0 | | | |
| IA1 | T1(mi) N0 M0<br>T1a N0 M0 | | | |
| IA2 | T1b N0 M0 | | | |
| IA3 | T1c N0 M0 | | | |
| IB | T2a N0 M0 | | | |
| IIA | T2b N0 M0 | | | |
| IIB | T3 N0 M0 | T1a-c N1 M0<br>T2a-b N1 M0 | | |
| IIIA | T4 N0 M0 | T3 N1 M0<br>T4 N1 M0 | T1a-c N2 M0<br>T2a-b N2 M0 | |
| IIIB | | | T3 N2 M0<br>T4 N2 M0 | T1a-c N3 M0<br>T2a-b N3 M0 |
| IIIC | | | | T3 N3 M0<br>T4 N3 M0 |
| IVA | M1a-b (any T, any N) | | | |
| IVB | M1c (any T, any N) | | | |

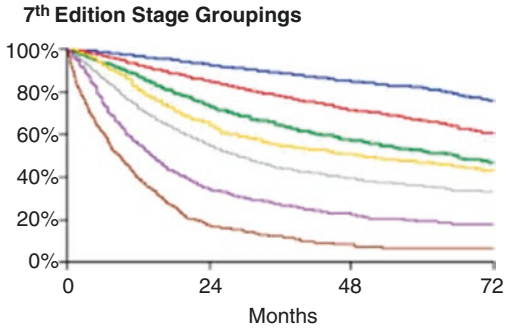


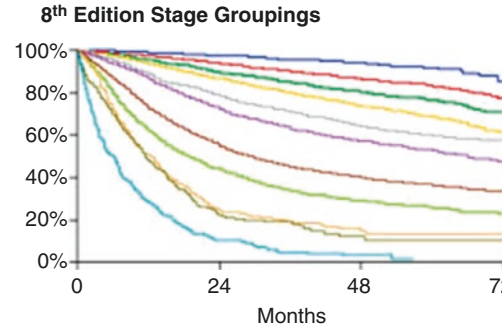


| 7th Ed. | Events / N | MST | 24 Month | 60 Month |
|---|---|---|---|---|
| IA | 1119 / 6303 | NR | 93% | 82% |
| IB | 768 / 2492 | NR | 85% | 66% |
| IIA | 424 / 1008 | 66.0 | 74% | 52% |
| IIB | 382 / 824 | 49.0 | 64% | 47% |
| IIIA | 2139 / 3344 | 29.0 | 55% | 36% |
| IIIB | 2101 / 2624 | 14.1 | 34% | 19% |
| IV | 664 / 882 | 8.8 | 17% | 6% |

| Proposed 8th Ed. | Events / N | MST | 24 Month | 60 Month |
|---|---|---|---|---|
| IA1 | 68 / 781 | NR | 97% | 92% |
| IA2 | 505 / 3105 | NR | 94% | 83% |
| IA3 | 546 / 2417 | NR | 90% | 77% |
| IB | 560 / 1928 | NR | 87% | 68% |
| IIA | 215 / 585 | NR | 79% | 60% |
| IIB | 605 / 1453 | 66.0 | 72% | 53% |
| IIIA | 2052 / 3200 | 29.3 | 55% | 36% |
| IIIB | 1551 / 2140 | 19.0 | 44% | 26% |
| IIIC | 831 / 986 | 12.6 | 24% | 13% |
| IVA | 336 / 484 | 11.5 | 23% | 10% |
| IVB | 328 / 398 | 6.0 | 10% | 0% |

**Fig. 8.2** Overall survival by clinical stage according to the 7th edition and the proposed 8th edition groupings using the entire database available for the 8th edition. MST, median survival time. Survival is weighted by type of database submission: registry versus other. Reprinted from [4], with permission from Elsevier

**Table 8.4** Comparison of the databases used for the 6th, 7th, and 8th editions of the TNM classification for lung cancer [13, 14]

| | TNM 6 | TNM 7 | TNM 8 |
|---|---|---|---|
| Evaluation period | 1975–1988 | 1990–2000 | 1999–2010 |
| Number of patients | 5319 | 100,869 | 94,708 |
| Number of institutions/databases | Mainly single center | 45 | 35 |
| Origin | US only | 58% Europe<br>21% North America<br>12% Asia<br>9% Australia | 49% Europe<br>5% North America<br>44% Asia<br>2% Australia |

that was essentially collected and managed by Dr. Clifton Mountain at the University of Texas, MD Anderson Cancer Center, with contributions from the United States National Cancer Institute Cooperative Lung Cancer Study Group. By the time of the editions 5 and 6 (which were of identical content) in 1997 and 2002, this database included 5319 patients, 4351 of them originating from MD Anderson. Despite its considerable size, the fact of using a patient database stemming predominantly from a single institution to create an "international" staging classification was subject to increasing criticism at that time. In consequence, the 7th edition of the TNM classification for lung cancer enacted in January 2010 was the first to be developed under the roof of the IASCL, which was founded in 1974 as the only global organization dedicated to the study of lung cancer. To overcome the limitations of the 6th edition, the IASCL lung cancer staging project

[12] with its subcommittees for T, N, and M components, stage grouping, validation, SCLC, carcinoids, visceral pleura invasion, lymph node map, and nonanatomic prognostic factors established and evaluated an international database to include patients treated in different healthcare systems and a broad spectrum of therapeutic modalities (Table 8.4). This broad international concept was followed also for the 8th edition. Its new database included 94,708 cases of lung cancer diagnosed between 1999 and 2010 at 35 institutions in 16 countries, treated with all sorts of therapeutic procedures [15].

## 8.2 Radiologic Diagnosis

### 8.2.1 Computed Tomography (CT)

Computed tomography is the most commonly applied imaging examination in patients with suspected lung cancer. It is used either in the first instance in cases of various suspected pulmonary pathologies or as the second-line modality following an abnormal chest X-ray. It also has an emerging role as a screening test for individuals at high risk.

CT scans for staging purposes, i.e., examinations of patients with proven or at least strongly suspected lung cancer, should be performed after intravenous injection of an iodine-based contrast agent. The scan range should cover the entire chest from the supraclavicular areas to the upper abdomen to allow for the assessment of the liver and adrenal glands. A section thickness of less than 1.5 mm with contiguous or overlapping slices is recommended [16]. Images should be reconstructed using soft-tissue and lung reconstruction kernels. Multiplanar reconstruction is essential to determine the size of tumor (Fig. 8.3), differentiate between nodules and scars, and describe the extent of the tumor with respect to anatomical landmarks, e.g., its distance to the pleural surface or to the carina. Additional thin-section maximum intensity projection (MIP) reconstruction is considered helpful for the detection of smaller pulmonary nodules.

#### 8.2.1.1 Tumor Detection

The primary task of CT in lung cancer management is to detect any lesion suspicious for lung cancer and describe its exact location. In this context, CT serves as an essential guide to biopsy, either by CT-guided needle biopsy, bronchoscopy, or surgery. The reported performance of low-dose CT applied for detection of lung cancer in the framework of two large lung cancer screening trials is summarized in Table 8.5.

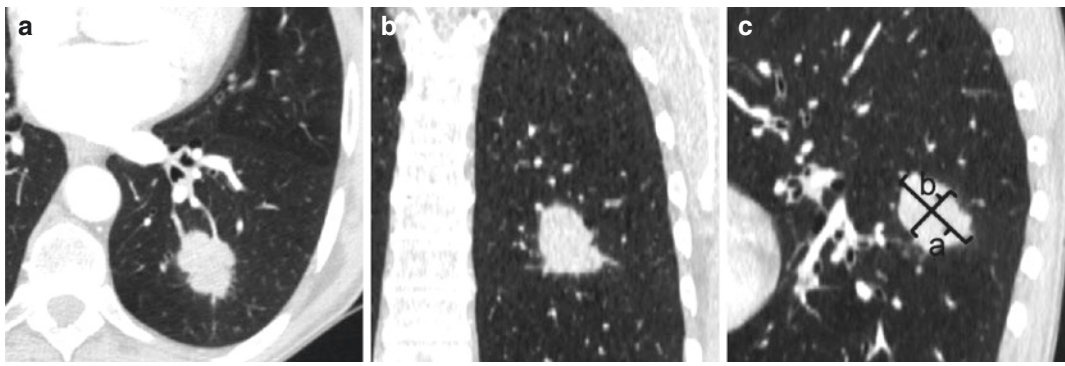


**Fig. 8.3** CT of a pulmonary adenocarcinoma in the left lower lobe superior segment. Reformats in three dimensions (**a**: axial, **b**: coronal, **c**: sagittal) are necessary to determine the size of the tumor and describe its exact location for biopsy. Note that size measurements for the management of incidentally detected pulmonary nodules and tumor staging are different: While the first is determined by the average of long- and short-axis diameters on the image that reveals the greatest dimensions ((*a* + *b*)/2 rounded to the nearest whole millimeter) [16], the latter is determined by the longest diameter of the tumor in three dimensions (**b**). For part-solid nodules, the maximum diameters of both the solid component (→T stage) and the entire lesion should be reported [17]

**Table 8.5** Performance of low-dose CT for detection of lung cancer in the framework of lung cancer screening

| | NLST | | NELSON | |
|---|---|---|---|---|
| | Value (%) | 95% CI (%) | Value (%) | 95% CI (%) |
| Sensitivity | 93.8 | 90.6–96.3 | 84.6 | 79.6–89.2 |
| Specificity | 73.4 | 72.8–73.9 | 98.6 | 98.5–98.8 |
| PPV | 52.9[a] | 48.4–57.4[a] | 40.4 | 35.9–44.7 |
| NPV | 99.9 | 99.86–99.94 | 99.8 | 99.8–99.9 |

*NLST* National Lung Screening Trial [18]; *NELSON* NEderlands Leuvens Longkanker Screenings ONderzoek [19]; *PPV* Positive predictive value; *NPV* Negative predictive value
[a]PPV for any positive finding that led to a biopsy procedure

#### 8.2.1.2 T Staging

CT has the highest spatial resolution among all imaging modalities for measuring tumor size. It is therefore the method of choice to analyze the extent of the disease using the size cutoffs of the TNM classification as a reference. This applies particularly to the assessment of the earlier T stages (T1a–T2b). For staging purposes, the longest dimension of the tumor in the three axes must be reported (Fig. 8.3). For part-solid lesions, T stage is determined based on the solid component of the lesion [17], but the size of the non-solid component should be reported as well. Volumetric assessment may increase the measurement accuracy in the context of screening, assessment of incidentally found unspecified pulmonary nodules, and therapy monitoring. Staging of locally advanced lung cancer (T3 and T4) may be challenging with CT alone, as it can describe some, but not all, of the features that characterize these stages. Consequently, the reliability of CT for predicting T3/T4 disease is relatively poor [20]. Typical features that are evident on CT are, for instance, the presence of satellite nodules, crossing of the tumor through fissures (Fig. 8.4), tumor infiltration to the main bronchus or the carina (Fig. 8.5), and an involvement of bones, evident as lytic or sclerotic changes (Fig. 8.6). The presence of atelectasis, pneumonia, and carcinomatous lymphangitis may be seen as well. An exact differentiation between such changes and the tumor, however, can be difficult even on contrast-enhanced scans, and FDG uptake in PET may serve as a helpful guide in this context. Regarding invasion of vascular structures or organs, the integrity of the fatty layers around the vessel or organ is a strong indicator in terms of resectability. On the other hand, the absence of such layers must not be taken as a proof of vascular infiltration, unless the entire circumference of the vessel is enclosed by the tumor (Fig. 8.7) or there is evidence of endovascular tumor growth. Another difficult diagnosis is invasion of the pleura outside the fissures. Here, only a visible penetration *through* the pleural surface with signs of infiltration of adjacent structures (e.g., ribs, mediastinal fat) may be counted as infiltration, while simple contact of the tumor with the pleura or pleural effusion does not prove pleural invasion. In cases of doubt, particularly concerning a suspected infiltration of the chest wall and mediastinum on CT, MRI is a potential modality to provide more clarity (see below). The reported accuracy of CT for T staging is 68% overall [21] and varies from 43% in T3 tumors to 81% in T1 and T2 tumors and 88% in T4 tumors [22].

#### 8.2.1.3 N Staging

Lymph node involvement in NSCLC is assessed and documented based on the IASCL lymph node map displayed above (Fig. 8.1). Notably, N stage is only determined by the anatomic extent, i.e., by the fact whether or not an anatomic zone is affected, but not by the number or size of the affected lymph nodes in each station. Dedicated manuals are available on how to make the assignment of a suspicious node to one of the 14 lymph node stations and 7 anatomic zones using anatomic landmarks on CT [23]. An important such landmark is, for instance, the left lateral wall of the trachea that—instead of the anatomic midline—separates the right from the left mediastinal zones. While CT is very exact in assigning individual lymph nodes to a particular station or zone, its accuracy to differentiate benign from malignant lymph nodes is limited: The

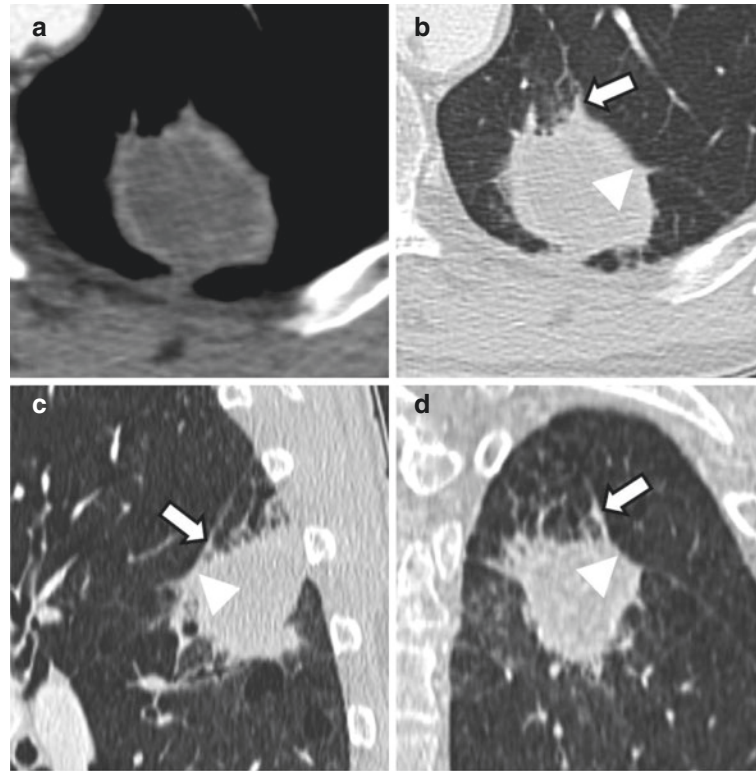


**Fig. 8.4** Adeno carcinoma of the left lower lobe superior segment with evident invasion of the visceral pleura on CT. (**a**) Soft-tissue window, transverse section; (**b**–**d**) lung window in transverse (**b**), sagittal (**c**), and coronal view (**d**). The tumor has a maximum diameter of 44 mm and shows retraction (*arrowheads*) and thickening (*arrows*) of the adjacent fissure as signs of visceral pleura invasion. The combination of both features finally classifies the tumor as stage T2b

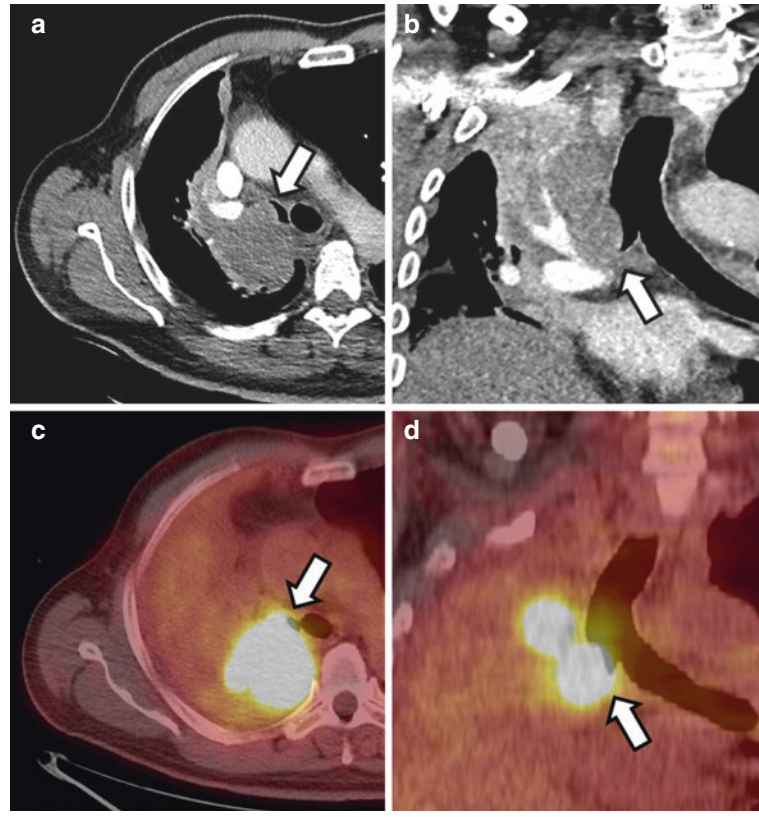


**Fig. 8.5** Infiltration of the main bronchus in a 58-year-old man with pulmonary squamous cell carcinoma stage cT3 cN2 cM1b. (**a**, **b**) Contrast-enhanced CT; (**c**, **d**) FDG-PET/CT with non-enhanced CT acquired 2 days after the initial CT exam. A hypermetabolic mass (*arrows*) is noted invading the right main bronchus with a remaining distance of less than 2 cm to the carina. Note that the distance threshold of 2 cm separating the stages T2 and T3 in the 7th edition is not included anymore in the 8th edition of the TNM classification

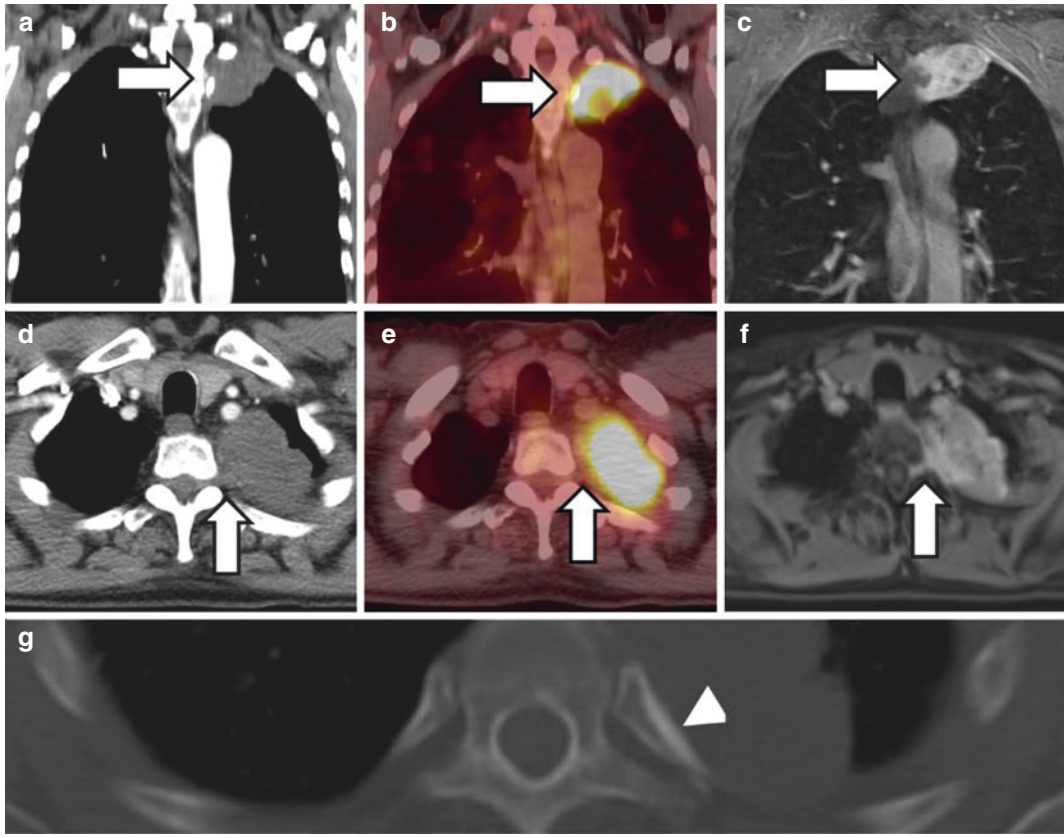


**Fig. 8.6** NSCLC of the left upper lobe apicoposterior segment with infiltration of the paravertebral space and adjacent neuroforamina Th2 and Th3. Evidently, the process of tumor invasion (*arrows*) is much better visualized with MRI (fat-suppressed T1-weighted gradient echo post-contrast, **c** and **f**) as compared to contrast-enhanced CT (**a**, **d**) and FDG-PET/CT (**b**, **e**). Note, however, the presence of a sclerotic periosteal reaction at the head of the third rib on the left side as a sign of tumor invasion in CT (*arrowhead* in **g**)

reported sensitivity and specificity for detecting mediastinal lymph node metastases with CT alone do not exceed 51% and 81%, respectively [24]. This limitation mainly originates from the fact that the key CT feature for malignancy is size: Usually, a short-axis diameter of 10 mm is taken as the cut-off value to differentiate benign from malignant lymph nodes [24]. It is well known, however, that microscopic lymph node metastases may be present also in lymph nodes of normal size, while on the other hand lymph node enlargement may be caused by inflammation, as well. Thus, the use of size cutoffs on CT leads to approximately 40% false-positive diagnoses (benign nodes >1 cm) and 20% false-negative diagnoses (malignant lymph nodes <1 cm) [25–27].

#### 8.2.1.4 M Staging

M staging is a very important issue also in NSCLC, as the presence of distant metastases strongly limits the available treatment options and thus significantly lowers the prognosis of the patient. About 40% of the NSCLC patients do have a distant metastasis at the time of initial diagnosis [28]. In approximately 90% of these patients, the disease manifests itself through specific symptoms of metastatic spread, particularly in cases of bone or brain metastases. CT as the number one imaging modality in emergency radiology plays a pivotal role in these cases. The situation is different in cases without clinical evidence of metastatic disease at the time of initial diagnosis. Here, the focus is on the exclusion of

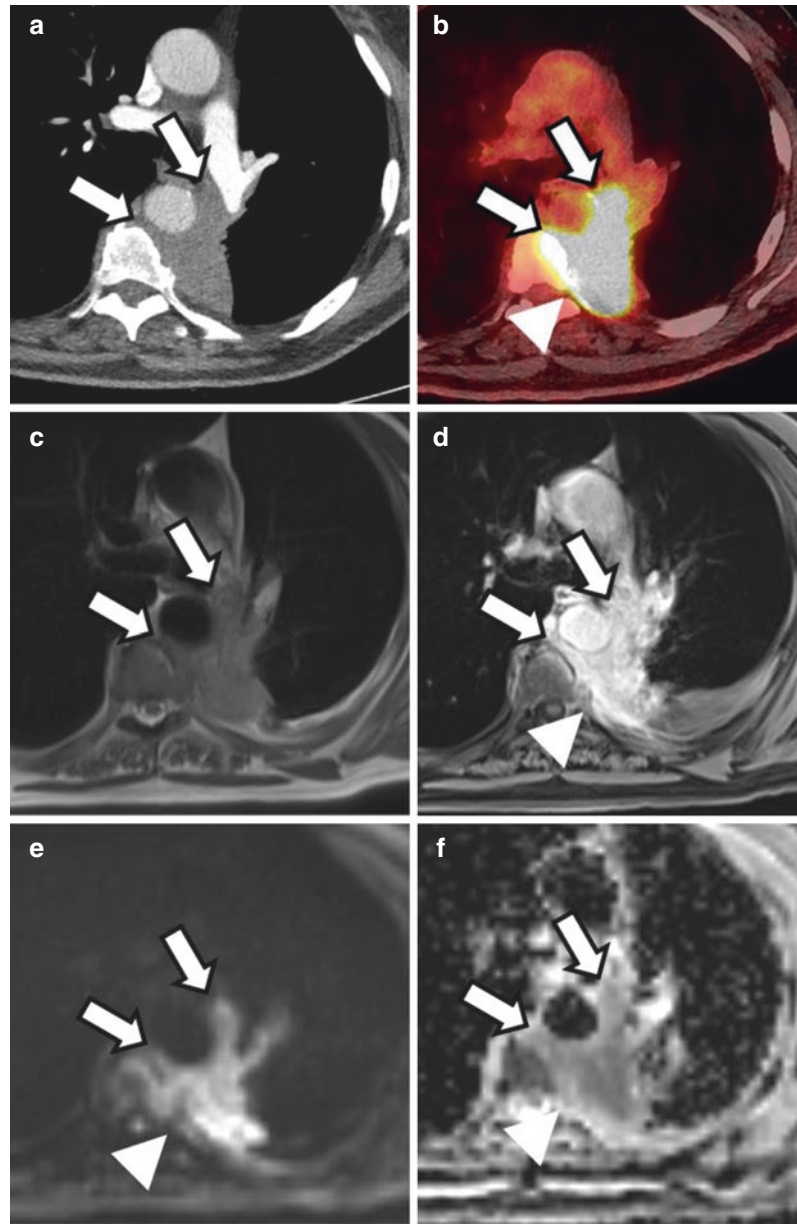


**Fig. 8.7** Assessment of mediastinal invasion from NSCLC with CT (**a**), FDG-PET/CT (**b**), and MRI (**c**–**f**), including T2-weighted fast spin-echo (**c**), contrast-enhanced fat-suppressed T1-weighted gradient echo (**d**), diffusion-weighted MRI with *b*-value = 800 s/mm$^2$ (**e**), and ADC map (**f**). A centrally located, strongly hypermetabolic tumor is seen in the left lower lobe extending towards the mediastinum, surrounding half of the circumference of the thoracic aorta (*arrows*). In addition, osseous infiltration of the adjacent rib and vertebral body is noted in PET and MRI (*arrowhead*)

metastases in order to assign the patient to a curative treatment strategy. As for primary tumor detection, the sensitivity and negative predictive value of CT to detect or rule out tumor nodules in the contralateral lung (M1a metastatic disease) are unsurpassed by other modalities. The diagnostic value of CT for the detection of pleural metastases can be limited by the presence of pleural effusion. The sensitivity and specificity of CT for the detection of metastases to the bone, liver, and adrenals are reasonable, but inferior to combined FDG-PET/CT (see below). The pooled sensitivity and specificity for the detection of brain metastases with contrast-enhanced CT are reported as 73% (95% CI, 60–83%) and 85% (95% CI, 72–92%), respectively [24]. This is less compared with MRI, but accepted as a method to exclude brain metastases if MRI is not available.

### 8.2.2 $^{18}$F-Fluorodeoxyglucose-Positron-Emission Tomography/Computed Tomography (FDG-PET/CT)

Positron-emission tomography (PET) is a nuclear imaging modality used to detect and localize radioactive $\beta^+$ decay. In comparison to scintigraphy and single-photon-emission computed tomography (SPECT), PET has a higher spatial resolution (≈5 mm) and detection efficiency. PET works with numerous tracers that are marked with $\beta^+$ emitters. By far the most important one is $^{18}$F-2-fluor-2-deoxy-D-glucose ($^{18}$F-FDG), which is an analogue of D-glucose and, as such, mimics the glucose uptake into the cells. Like D-glucose, FDG is taken up into the cells via the glucose transporter molecules (GLUT) and becomes phosphorylated inside the cell by the enzyme hexokinase. The phosphorylated FDG, unlike D-glucose, cannot be processed further and thus accumulates inside the cell, while it decays with a half-life time of 110 min. The known pharmacokinetics allow expressing the FDG uptake in each voxel as quantitative numbers using the standardized uptake value (SUV), thereby enabling a quantitative assessment of the metabolic activity of tissues and particularly malignant tumors. A general SUV cutoff that characterizes malignancy does not exist, as the intensity of FDG uptake depends on several factors such as tumor histology, volume of vital tumor cells, movement of the target lesion during the acquisition, and physiological uptake of the adjacent background [29]. Having been developed and applied historically as separate techniques, PET and CT have been integrated more than a decade ago into one modality, named PET/CT. The particular strength of PET/CT is the synergetic effect of a functional imaging method (PET) that offers a high sensitivity for the detection of malignant tissue and a morphology-based imaging method (CT) highly accurate in describing the anatomic location and extent of affected structures. In consequence, FDG-PET/CT is the most powerful noninvasive examination tool for staging of NSCLC available today [30]. PET is not developed or sold as a stand-alone technology anymore, and only rarely used as such. Nevertheless, much data on the accuracy of FDG-PET for staging of NSCLC is still considered valid and provides parts of the basis of the current guidelines.

Patient preparation and data acquisition for FDG-PET follow standardized examination protocols as published in the procedure guidelines of the European Association for Nuclear Medicine (EANM) [29]. The imaging agent $^{18}$F-FDG is administered intravenously in a predefined dose that is adapted to the patient's body weight. Patients must respect a fasting period of at least 6 h before administration. Eventually, images are acquired after a resting period of 60 min after the injection of the radiopharmaceutical. For lung cancer, an extended torso scan ranging from the top of the skull to the mid-thigh is recommended. The patient's arms must be elevated during the procedure. Along with the PET, a CT scan of the chest and upper abdomen should be performed as described in 8.2.1 if no recent chest CT exam of sufficient quality is available. Otherwise a non-contrast-enhanced low-dose CT protocol for attenuation correction and anatomic reference is considered sufficient.

#### 8.2.2.1 Tumor Detection

The role of FDG-PET/CT in the context of tumor detection is that of a tool for stratification of pulmonary nodules with intermediate probability of malignancy. As such, FDG-PET/CT has been shown to decrease the number of futile invasive biopsies and thoracotomies [31]. Due to the high sensitivity of FDG-PET, a negative FDG-PET result can rule out malignancy reliably in the majority of pulmonary lesions. Exceptions to this rule are nodules smaller than 10 mm and non-solid solitary pulmonary nodules, which should be followed up by CT in a structured program [16]. A final diagnosis of cancer is not possible based on a positive FDG-PET result alone due to the limited specificity of the exam (82% according to [32]). An invasive histopathological or cytological proof of malignancy is therefore mandatory in any PET-positive finding. False-positive findings in FDG-PET are known to occur

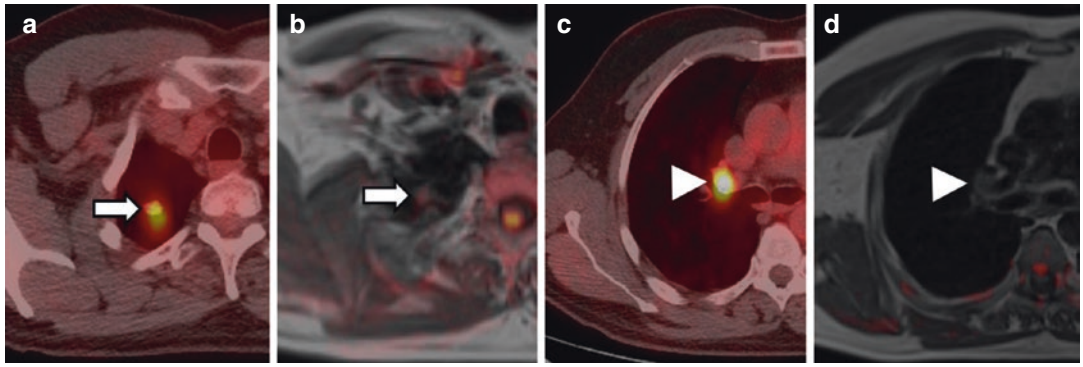


**Fig. 8.8** False-positive findings in FDG-PET/CT in a patient with primary tuberculosis. (**a**, **c**) FDG-PET/CT; (**b**, **d**) hybrid images from diffusion-weighted MRI ($b = 800$ s/mm$^2$) and T1-weighted fast spin-echo MRI. The PET/CT was rated false positive for malignancy (T1a N1, UICC IIA (TNM 7)) due to high FDG uptake in both the primary lesion (**a**) and in a right hilar lymph node (**c**). On the MRI exam (performed in the same patient within the framework of a prospective trial) only slightly restricted diffusion is noted within the primary lesion (**b**) and no suspicious lymphadenopathy is seen (**d**). Figure adapted from [33], with permission

particularly in the presence of infectious, inflammatory, or granulomatous diseases (Fig. 8.8).

#### 8.2.2.2 T Staging

FDG-PET/CT is a better overall predictor for T stage than FDG-PET or CT alone. The reported staging accuracy across all T stages is 82% for PET/CT versus 55% for PET alone and 68% for CT alone (pooled average over eight studies published between 2003 and 2007 [20]). As for CT, the staging accuracy of FDG-PET/CT depends on the tumor stage and is worst for T3 (45%), followed by stages T1/T2 (81%) and T4 (83%) [22]. Regarding the prognostically most relevant identification of T3 and T4 disease, varying sensitivities and specificities can be found in literature. These range from 38% to 90% and from 40% to 90%, respectively, for the detection of parietal pleural or chest wall invasion, and from 40% to 84% and from 57% to 94%, respectively, for mediastinal tumor invasion [21]. While PET can reliably differentiate tumor from atelectasis (which is commonly FDG negative), it has limited capability to differentiate tumor from pneumonia and carcinomatous lymphangitis. Other assets of hybrid FDG-PET/CT for T staging are to detect or rule out secondary tumor nodules in the ipsilateral lung (stages T3 and T4) and identify tumor invasion into vessels, organs, or bones by increased metabolism (Figs. 8.6 and 8.7).

#### 8.2.2.3 N Staging

N staging is the particular strength of FDG-PET, as the mechanism of highlighting the tumor tissue by its increased glucose metabolism allows identifying cancer infiltration also in normal sized lymph nodes (Fig. 8.9). This leads to a significantly higher sensitivity of FDG-PET (77%) compared to CT (55%) with also slightly higher specificity of 86% (CT 81%) [24]. An even higher increase in sensitivity and specificity results from the combination of both modalities with numbers of 80–90% sensitivity and 85–95% specificity for hybrid FDG-PET/CT [20]. FDG-PET/CT, in particular, allows ruling out metastatic spread to locoregional lymph nodes with a very high negative predictive value of 88–95% [27] and thus helps avoiding invasive staging procedures. Limitations of FDG-PET/CT for N staging are known, however, for three particular scenarios [20]: The first is in patients with suspected N1 disease (central tumor or positive N1 lymph node in PET/CT and otherwise normal mediastinum). In these patients, who have an intermediate suspicion of N2 and N3 involvement, the false-negative rate of FDG-PET/CT for N2 and N3 disease is around 30%. The second scenario refers to cases

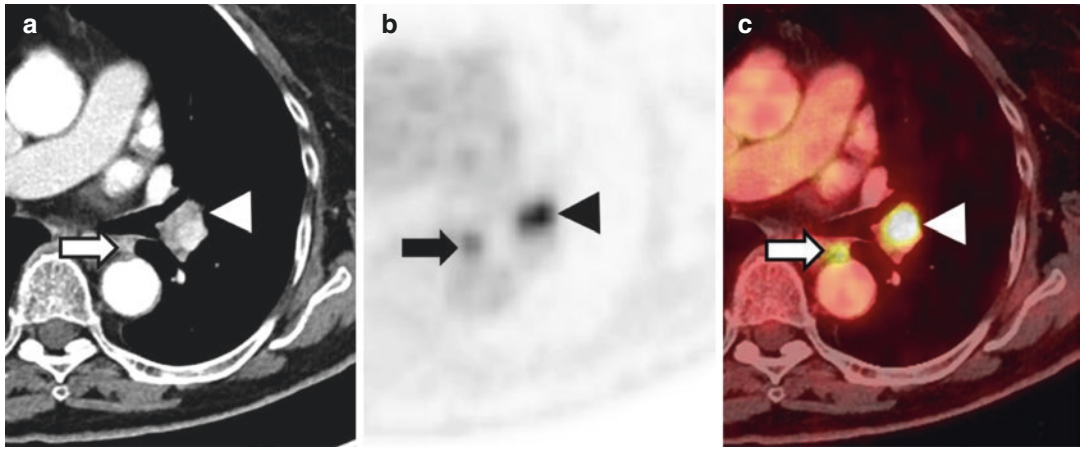


**Fig. 8.9** High sensitivity of FDG-PET demonstrated in a case of adenocarcinoma originating from the left lower lobe with N2 disease involving lymph nodes at the left hilum (visibly enlarged at CT, *arrowhead*) and a normal sized node in the left mediastinum hardly visible on CT (*arrow*). (**a**) contrast-enhanced CT, (**b**) FDG-PET, (**c**) hybrid FDG-PET/CT

where the size of the primary tumor is larger than >3 cm and the NPV for mediastinal lymph node involvement goes down to 85–89%. The third scenario is that of a central tumor with negative appearance in FDG-PET. Here, the reported false-negative rate for assessment of lymph node involvement with FDG-PET/CT is as high as 21.6%. All patients who are affected by one of the three scenarios mentioned are recommended to undergo invasive staging of the mediastinum. In any case, patients who have a positive finding on FDG-PET/CT that is suspicious for a lymph node metastasis need to have this finding confirmed by tissue sampling. This is due to the considerable number of false positives occurring in FDG-PET from infection or inflammation that limit the positive predictive value of FDG-PET and PET/CT to 75% and 63%, respectively [24].

#### 8.2.2.4 M Staging

The most common locations for extrathoracic metastatic spread are the brain, bone, liver, and adrenal glands. FDG-PET/CT is considered the superior imaging technology for detecting these metastases on a whole-body level and it has been shown that PET scanning discloses previously unsuspected metastases in 6–37% of cases [24]. As for the T and N stages, the particular strength of FDG-PET/CT is its high negative predictive value that allows ruling out metastatic disease with high accuracy, thereby reducing the number of futile treatment trials [31]. An exception from this rule applies particularly to scans of the brain, where the sensitivity of FDG-PET is limited by the high background FDG uptake of the brain and consequently MRI or contrast-enhanced CT is preferred (Fig. 8.10). Regarding the detection of bone metastases, FDG-PET is reported to have an excellent performance with specificity, sensitivity, NPV, PPV, and accuracy all above 90%, surpassing also radionuclide bone scanning [34, 35]. Adrenal masses are a relatively common finding occurring in approximately 5% of patients without known malignancy [36] and the vast majority of these lesions are known to be benign adenomas. The prevalence of adrenal metastases from NSCLC increases with the intrathoracic extent of the tumor [37]. Accuracy values as high as 100% have been reported for FDG-PET to detect these adrenal metastases. False negatives, however, may occur in small lesions, and false positives have also rarely been described. MRI, especially with chemical shift and contrast-enhanced techniques, may be useful in case of uncertainty (Figs. 8.11 and 8.12). The prevalence of benign liver lesions, mainly cysts and hemangiomas, in the general population is even higher than that of adrenal masses and reaches 15% in large-scale

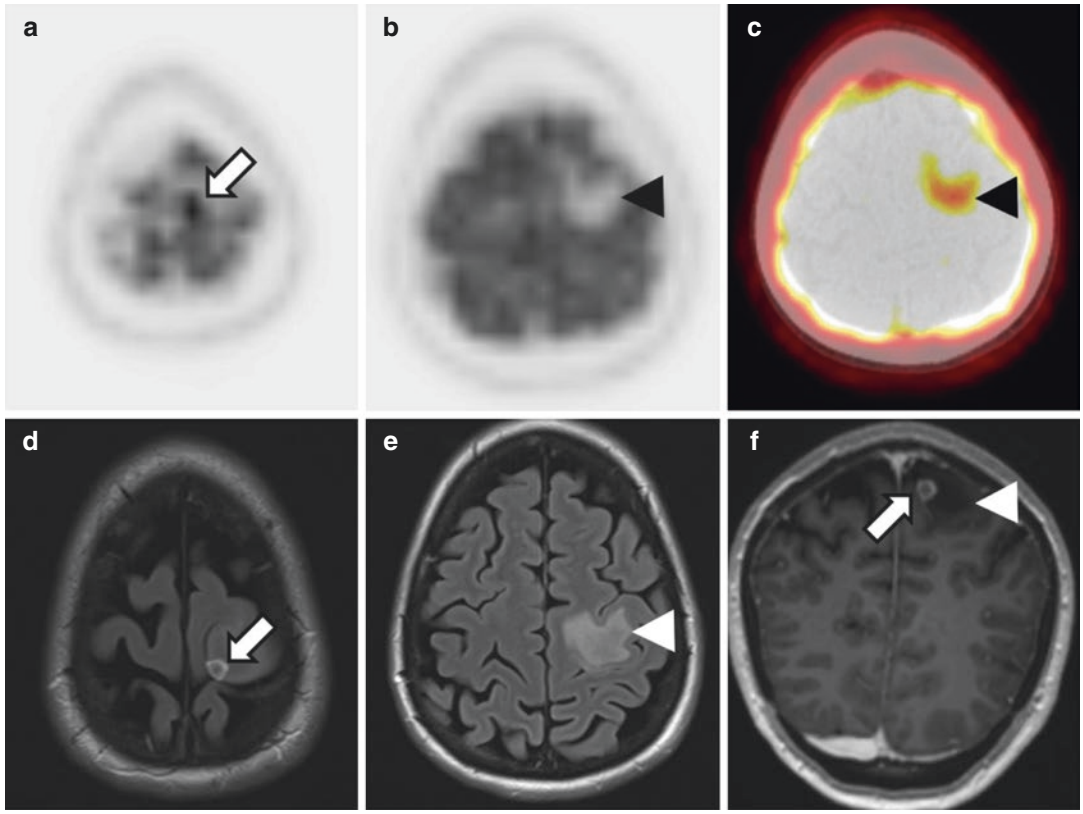


**Fig. 8.10** Brain metastasis detected in a 43-year-old woman with NSCLC (not otherwise specified) stage UICC IV. (**a**, **b**) FDG-PET; (**c**) hybrid PET/CT image; (**d**, **e**) T2-weighted fluid-attenuated inversion recovery (FLAIR), (**f**) T1w gradient-echo post-Gd. The presence of this small brain metastasis in the cortex of the left precentral gyrus (*arrows*) becomes mainly evident through the effect of its surrounding edema (*arrowheads*). The lesion itself is hardly visible on FDG-PET (**a**), due to the physiologic FDG uptake of the surrounding cortex. In contrast, MRI (**d**, **f**) provides a much better differentiation of the lesion against the background both using T2-weighted and contrast-enhanced techniques

ultrasound studies [38]. In contrast, the frequency of liver metastases in asymptomatic patients with NSCLC is reported to be only 3% [39]. FDG-PET can detect liver metastases from NSCLC with a very high accuracy of 92–100% and only few false positives [40]. The further characterization of any unclear FDG-negative liver lesions remains the domain of ultrasound, contrast-enhanced CT, and MRI.

According to the guidelines of the American College of Chest Physicians (ACCP) and the European Society of Thoracic Surgery (ESTS), FDG-PET is recommended as the imaging modality of choice to evaluate for metastases in patients with a normal clinical evaluation and no suspicious extrathoracic abnormalities on chest CT being considered for treatment with curative intent. It is not indicated for patients already classified as non-curative by CT or other imaging. In patients with an imaging finding suggestive of a metastasis, further evaluation of the abnormality with tissue sampling is recommended to pathologically confirm the clinical stage prior to choosing treatment [24].

### 8.2.3 Magnetic Resonance Imaging

Magnetic resonance imaging (MRI) is a method for cross-sectional imaging that is available in clinical routine since the 1980s. Methodically, it is based on the fact that the magnetic properties of protons,

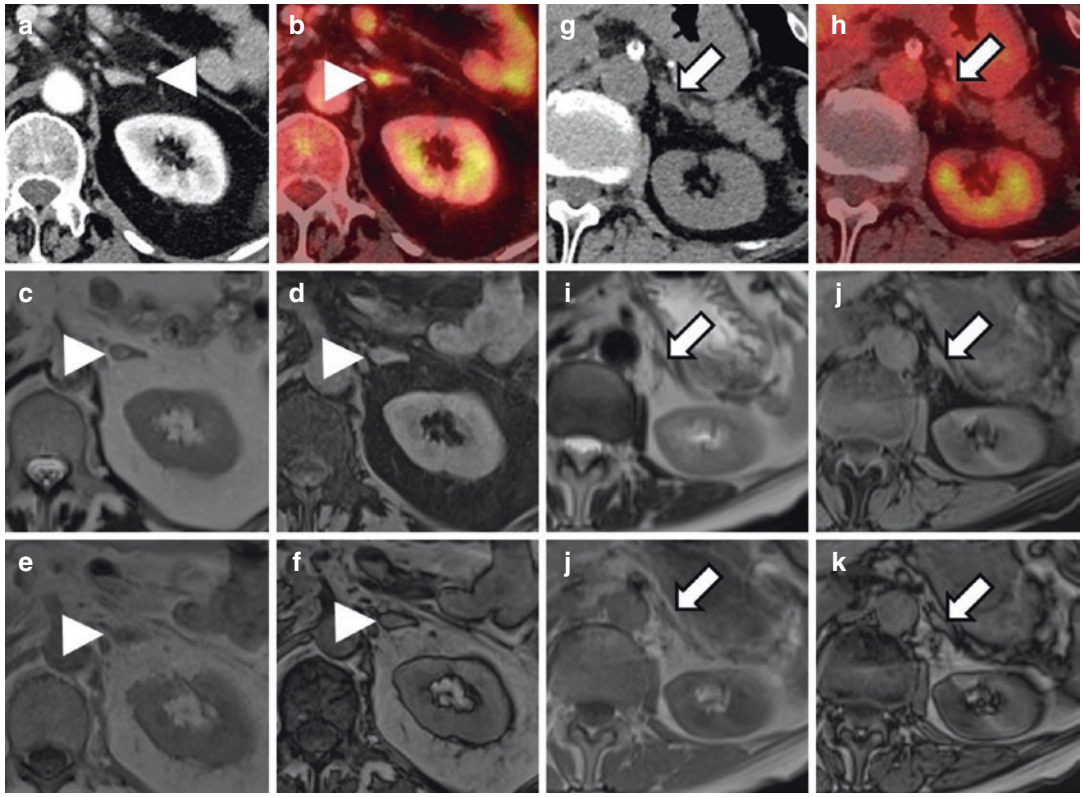


**Fig. 8.11** True- and false-positive findings of small adrenal lesions in FDG-PET/CT and MRI. (**a**–**f**) Adrenal metastasis in a patient with pulmonary adenocarcinoma stage T1b N1. The lesion is too small to be noticed on contrast-enhanced CT (**b**), but identified by its increased uptake of FDG ($SUV_{max}$ = 5.0) in PET (**a**). MRI confirms the finding showing a hyperintense lesion in T2-weighted fast spin echo (**c**) with slightly less contrast enhancement compared to the surrounding adrenal tissue in fat-suppressed T1-weighted gradient-echo post-contrast (**d**) and no signal drop in opposed-phase (**e**) compared to in-phase gradient echo (**f**). (**g**–**l**) Nodular thickening of the left adrenal of another patient with stage T2a N2 pulmonary adenocarcinoma in CT (**g**) showing faint uptake ($SUV_{max}$ = 3.1) of FDG in PET (**h**). MRI, however, showed an entirely normal signal behavior of the left adrenal (**i**–**l**, sequences as described in **c**–**f**), ruling out adrenal metastasis in this patient

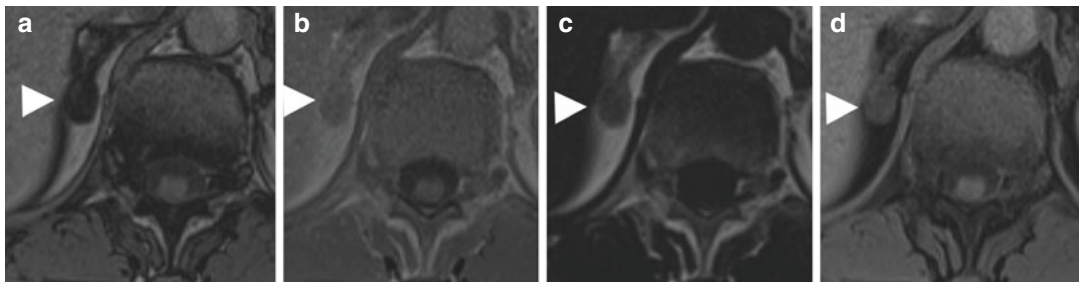


**Fig. 8.12** Typical signal characteristics of an adrenal adenoma (*arrowheads*) in T1-weighted Dixon MRI at 1.5 T field strength: (**a**) Opposed-phase image (echo time = 2.4 ms); (**b**) in-phase image (echo time = 4.8 ms); (**c**) fat image (after Dixon reconstruction); (**d**) water image (after Dixon reconstruction). As adrenal adenomas contain fat in a microscopic distribution (i.e., the size of fat deposits is far below the voxel resolution of the MRI), this fat is not seen macroscopically (dark appearance of the adenoma in (**c**)), but can only be identified indirectly by chemical shift effects that cause a drop of >20% in signal intensity in the opposed-phase image (**a**) compared to the in-phase image (**b**)

which are bound to water or other molecules in human tissue, vary depending on their physical and biochemical environment. Static and variable magnetic fields are used to interact with this magnetization and display its spatial distribution in the body. The particular strength of MRI is its ability to generate different sorts of contrast for tissue characterization, such as T1 weighting, T2 weighting, diffusion-weighted MRI (DW-MRI), or contrast enhancement from intravenously administered, gadolinium-based contrast agents. The various MRI methods may be applied either alone (within a protocol including T1-weighted, T2-weighted, diffusion-weighted, and contrast-enhanced sequences), or in combination with FDG-PET within hybrid FDG-PET/MRI approaches. The first is widely available at least in larger hospitals and is described below. Hybrid PET/MR, which still has limited clinical availability, is further discussed in the Sect. 8.4 at the end of this chapter.

#### 8.2.3.1 Tumor Detection

As the sensitivity of MRI for the detection of pulmonary nodules is considerably lower than that of CT, it is not an accepted method to rule out pulmonary malignancy in patients with clinically suspected cancer. Nevertheless, there is some discussion about a potential role of MRI as a tool for lung cancer screening where the repetitive radiation exposure associated with CT is an issue [41].

#### 8.2.3.2 T Staging

The accuracy of MRI for T staging has already been investigated in studies from the early 1990s [42]. These reported a comparable sensitivity and specificity of MRI (56% and 80%) and CT (63% and 84%) in distinguishing T3–T4 tumors from T1–T2 tumors using standard MRI sequences such as T2 and T1 weighting. MRI was found, in particular, to be significantly more accurate than CT in the diagnosis of mediastinal invasion (Figs. 8.6 and 8.7), whereas no significant differences were found between the two techniques for diagnosis of bronchial involvement or chest wall invasion. These results have been corroborated also in a recent randomized study of 263 patients comparing post hoc co-registered whole-body FDG-PET/MRI and FDG-PET/CT [43]. According to the current guidelines [24], MRI should not be performed routinely for staging of the mediastinum, but is considered useful when there is concern about involvement of the superior sulcus or the brachial plexus.

#### 8.2.3.3 N Staging

The additional benefit of morphologic MRI protocols over CT for nodal staging is generally limited, as both methods basically rely on size and shape as the main imaging criteria. Interesting additional options have been provided by two research groups from Japan [44, 45], who described their methods based on short TI inversion recovery (STIR) turbo spin-echo sequences to be superior to FDG-PET/CT for N staging of lung cancer (91.4% vs. 80.7% accuracy as reported by [44]). Another very promising MRI technique is diffusion-weighted MRI (DW-MRI), which has been adapted to whole-body oncologic imaging by Takahara in 2004 [46] and identifies cancer metastases by their dense microstructure that restricts the diffusion of water molecules (Fig. 8.13). The most recent meta-analysis on the diagnostic performance of FDG-PET/CT and DW-MRI for detection of mediastinal nodal metastasis in NSCLC based on 43 studies found no significant difference between the two modalities [47]. The pooled sensitivity and specificity for FDG-PET/CT were 65% (95% CI: 63–67%) and 93% (93–94%), respectively, whereas the corresponding values of DW-MRI were 72% (68–76%) and 97% (96–98%), respectively. Despite these positive results, a general recommendation for using STIR or DW-MRI routinely for staging of NSCLC has not yet been made, as data from large prospective studies comparing their value with that of FDG-PET are still missing [20].

#### 8.2.3.4 M Staging

The most important role of MRI for M staging of NSCLC staging is the detection or exclusion of brain metastases (Fig. 8.11), where MRI represents the standard of reference for clinical staging. The overall prevalence of brain metastases in clinically asymptomatic patients with NSCLC is very low, with 3% on average [24], but increases to >20% in

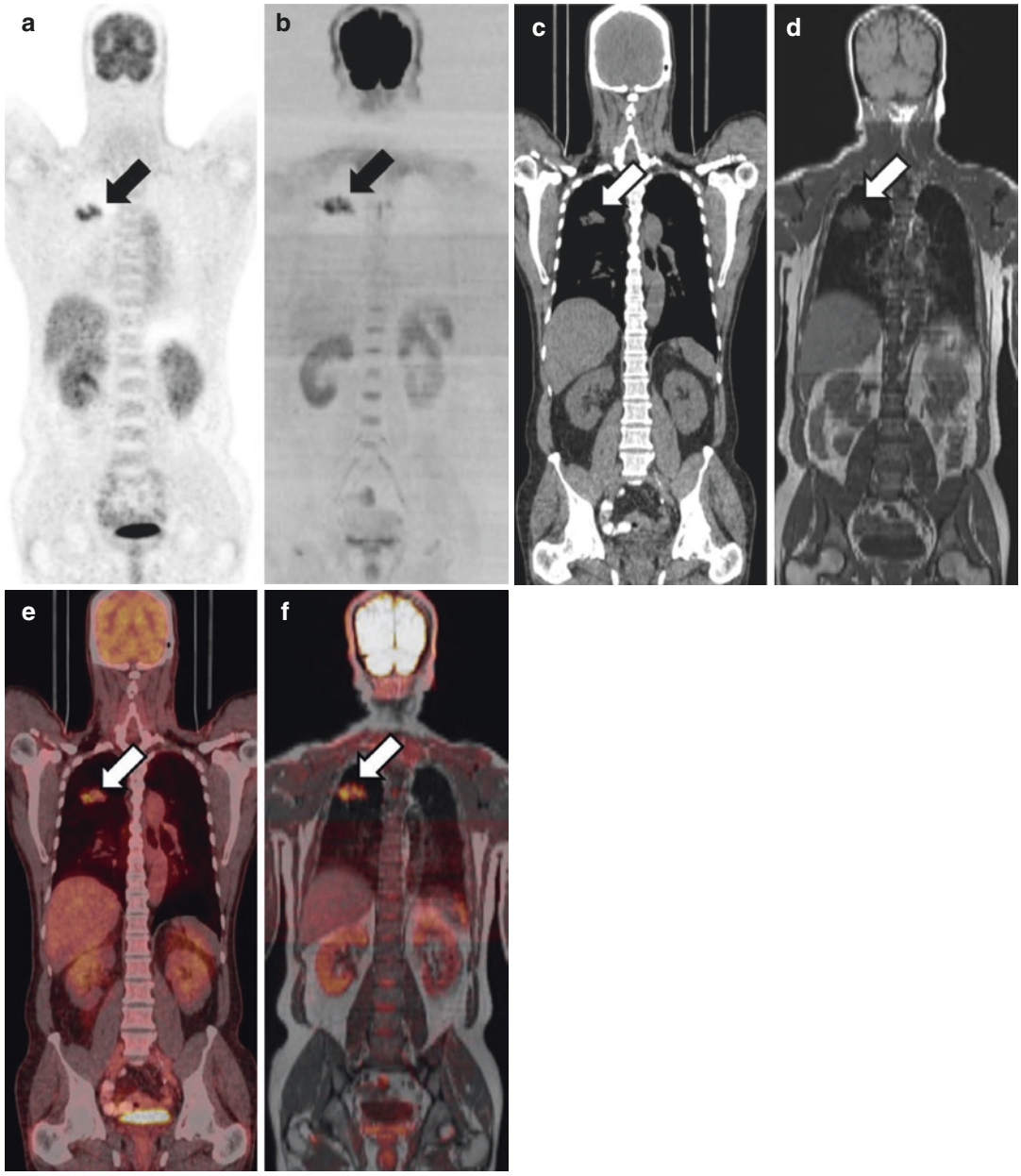


**Fig. 8.13** Side-by-side comparison of FDG-PET/CT (right) and whole-body MRI (left) in a patient with pulmonary squamous cell carcinoma stage T2a N0 M0 showing comparable image contrast of the tumor in the right upper lobe with both methods. (**a**) FDG-PET; (**b**) diffusion-weighted MRI ($b$ = 800 s/mm$^2$); (**c**) CT (soft-tissue window); (**d**) T1w fast spin-echo MRI; (**e**, **f**) hybrid images after fusion of **a/c**, and **b/d**, respectively. MRI data were acquired as 2D slices in transverse orientation

stage III and IV diseases [48] or with primary tumor size >3 cm [49]. As shown already in studies from the 1990s [50], MRI is able to detect more and smaller lesions than contrast-enhanced CT in the preoperative setting. However, it has not yet been proven that this technical advantage translates into a significant effect on patient survival. The current guidelines recommend performing routine imaging of the brain with MRI in clinically symptomatic patients and in patients with clinical stage III or IV NSCLC, even if they have a negative clinical evaluation [24]. The guidelines give no general recommendation to use MRI to detect or exclude metastases from NSCLC outside the brain, due to the good performance of FDG-PET/CT in these areas. In particular, there is no recommendation to use whole-body MRI techniques, such as DW-MRI (Fig. 8.13) for M staging, despite some promising results that have been presented recently (98.6% reported accuracy of assessment of distant metastatic spread with DW-MRI according to [44]). MRI is accepted, nevertheless, as a problem-solving tool to characterize unclear lesions in the liver and help with the differential diagnosis of suspicious adrenal lesions (Figs. 8.11 and 8.12).

### 8.2.4 Bone Scintigraphy

Bone scintigraphy, also known as bone scan, is a traditional method of nuclear medicine used to detect and display pathologic alterations of bone metabolism. It uses γ-emitting substances like $^{99m}$Tc-methyl-diphosphonate (MDP) that are adsorbed to the surface of bone in places of increased bone matrix turnover after intravenous injection. Images are acquired 2–4 h after injection of the radiotracer as 2-dimensional anterior and posterior projection

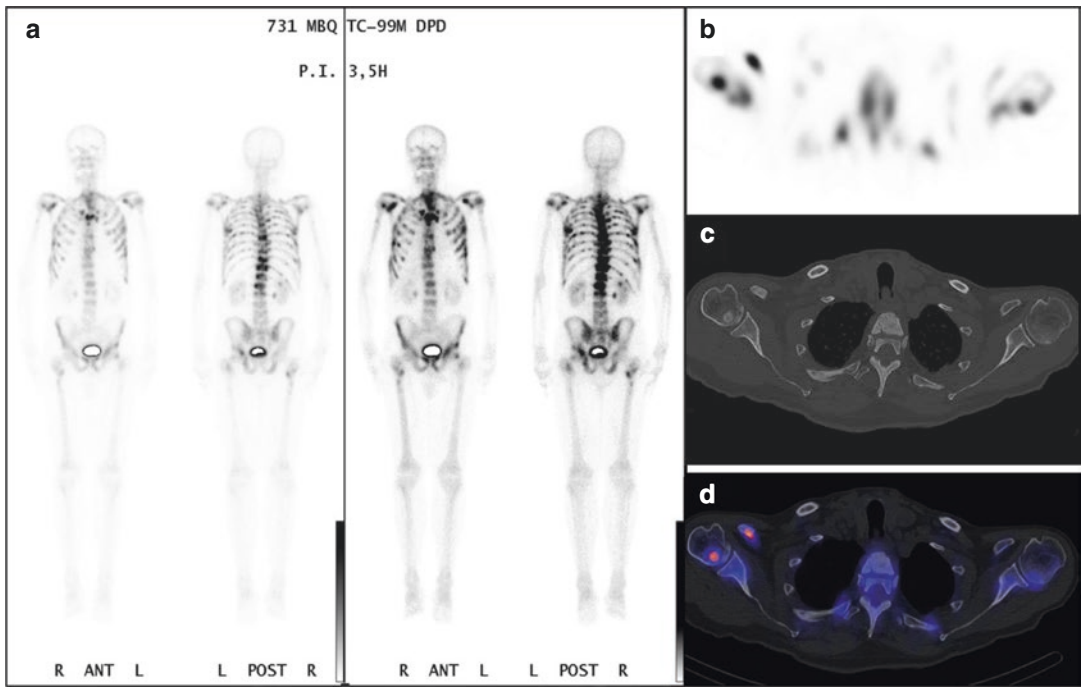


**Fig. 8.14** Bone scan performed in a 72-year-old patient with pulmonary adenocarcinoma stage cT2a cN3 cM1b with evidence of bone metastases. (**a**) Planar scintigraphy in anterior and posterior projection with two different window/level settings; (**b**) SPECT, transverse image orientation; (**c**) CT, bone window; (**d**) hybrid SPECT/CT. Though the mechanism of tracer accumulation is per se unspecific, the pattern of distribution mostly allows identifying metastatic disease already on planar scintigraphy (**a**). Combined SPECT/CT (**b**–**d**) is used to differentiate metastatic from degenerative disease more specifically and to evaluate pathologic fractures

views (Fig. 8.14), supplemented by focal planar projection images or 3-dimensional SPECT acquisitions in particularly suspicious areas [51]. Bone scintigraphy has a relatively high diagnostic sensitivity for bone metastases from NSCLC of 92.5% [35], but is very sensitive to degenerative, traumatic, and inflammatory changes of the skeleton, as well. Due to this lack in specificity, bone scintigraphy only has a moderate accuracy of 72.5% for skeletal M staging that is significantly inferior to the 93.5% of FDG-PET [35]. In consequence, bone scintigraphy is not recommended anymore for evaluation of bone metastases in patients with NSCLC since the era of FDG-PET/CT. Nevertheless, it may still be used in combination with a thoracoabdominal CT in institutions where PET is not available.

## 8.3 Correlation with Surgical Staging

Pretherapeutic mediastinal staging has a central role in determining the most appropriate treatment strategy in cases of NSCLC without metastatic disease. Even if imaging findings are positive, microscopic confirmation of malignancy and histopathological type are required in all cases. In cases of doubt, the 8th edition of the Union for International Cancer Control (UICC) TNM staging system should be adopted to accurately determine tumor stage. The majority of cases of UICC stage IIA to IIIA NSCLC with N1 lymph node involvement are resectable. However, curative surgery is not possible for stage IIIB disease. In recent years, it has become clear that N2 staging is complex. Therefore, in such cases, differentiation should be improved by using the Robinson classification [52] in addition to TNM staging. Single-level stage IIIA-N2 NSCLC is suitable for surgery, either initially or after neoadjuvant therapy, while cases of multilevel N2-IIIA disease should preferentially undergo neoadjuvant therapy before surgery. However, bulky-N2 stage disease is considered inoperable. In the following, a short review of the currently available invasive procedures for mediastinal staging is provided. Table 8.6 provides an overview on their sensitivity, specificity, NPV, and PPV in comparison to CT, PET, and PET/CT. The current ESTS guidelines for primary mediastinal staging of NSCLC are referenced at the end of this subchapter.

### 8.3.1 Mediastinoscopy

Due to its high sensitivity and specificity, mediastinoscopy and especially video-assisted mediastinoscopy (VMS) are considered to be the gold standard technique for invasive mediastinal lymph node staging/diagnosis. Several factors can influence mediastinoscopy results. Not every lymph node localization that is important for staging can be reached by standard mediastinoscopy methods (Table 8.7). Lymph nodes in the aortopulmonary window (APW; station 5) and anterior mediastinal (station 6), posterior subcarinal (station 7), and inferior mediastinal (stations 8 and 9), hilar (station 10), and lobar/intralobar (stations 11–14) areas cannot be accessed by standard mediasti-

**Table 8.6** Performance of different locoregional staging techniques (adapted from [53])

| | Sensitivity (%) | Specificity (%) | NPV (%) | PPV (%) |
|---|---|---|---|---|
| CT | 57 | 82 | 83 | 56 |
| PET | 84 | 89 | 93 | 79 |
| Combined PET/CT [20, 27] | 80–90 | 85–95 | 88–95 | 83–93 |
| Mediastinoscopy (standard) | 81 | 100 | 91 | 100 |
| Mediastinoscopy (incl. ECM/VAMLA) [54] | 96 | 100 | 100 | 100 |
| Blind TBNA | 76 | 96 | 71 | 100 |
| EBUS-TBNA [55] | 88 | 100 | 85 | 100 |
| EUS-FNA | 88 | 91 | 77 | 98 |
| Combined EBUS-TBNA/EUS-FNA [54, 56] | 86–88 | 99–100 | 83 | 99 |

*NPV* Negative predictive value; *PPV* Positive predictive value; *TBNA* Transbronchial needle aspiration; *EBUS* Endobronchial ultrasound; *EUS* Endoscopic ultrasound; *FNA* Fine-needle aspiration

**Table 8.7** Accessibility of mediastinal lymph node stations to different invasive procedures

| Procedure | Accessible lymph node stations |
|---|---|
| Mediastinoscopy | Stations 1–4, 7 (anterior mediastinal) |
| Extended cervical mediastinoscopy (ECM) | Stations 5, 6 (para-aortic) |
| Video-assisted mediastinoscopic lymphadenectomy (VAMLA) | Stations 7, 8 |
| Chamberlain procedure (anterior mediastinotomy) | Station 5 (aortopulmonary window) |
| Endobronchial ultrasound (EBUS)-guided needle aspiration | Stations 2R/2L, 4R/4L, 7, and 10 |
| Endoscopic ultrasound (EUS)-guided needle aspiration | Stations 4L, 7–9 |
| Video-assisted thoracoscopic surgery (VATS) | Ipsilateral mediastinal nodes |

noscopy. Limitations to access to relevant lymph node stations may impact the number of false-negative results with this technique and its sensitivity.

The sensitivity of standard mediastinoscopy is 81% (range 40–97%) while its specificity and PPV are both 100% and the NPV is 91% (Table 8.6). The number of accessible lymph node stations has been increased by enhancements of the standard mediastinoscopy technique, including extended cervical mediastinoscopy (ECM: can access stations 5 and 6), and video-assisted mediastinoscopic lymphadenectomy (VAMLA: can access stations 7 and 8). These enhancements have resulted in a sensitivity of 96% as well as a specificity of 100%, with almost unchanged morbidity and mortality [54].

### 8.3.2 Endoscopic Techniques

Endoscopic techniques are minimally invasive and provide histological or cytological confirmation of nodal involvement. By the combination of endoscopic ultrasound (EUS) and endobronchial ultrasound (EBUS) with PET/CT imaging, similar results can be achieved as for mediastinoscopy. The benefits of an endosonographic diagnosis are based on its low morbidity and mortality, which have been shown to be 2% and 0.08%, respectively, with mediastinoscopy [57]. Furthermore, these techniques are less costly than VMS.

Transbronchial needle aspiration (TBNA) has been shown to be a safe procedure and is useful in patients with enlarged mediastinal lymph nodes. However, this so-called blind or unguided technique has a moderate yield and is reliant on the experience of the investigator. Furthermore, the results of TBNA depend on the size of the lymph node (>15–20 mm short axis on CT scan). Although TBNA is mostly used to obtain subcarinal lymph node biopsies, it may also be used to obtain paratracheal lymph node biopsies. Paratracheal lymph nodes may sometimes be harder to access because of the difficulty of sufficiently angulating the bronchoscope and the needle. In an overview, TNBA had a sensitivity of 78% (range 14–100%) and a false-negative rate of 29% in cN2 disease [24]. Similar sensitivity and false-negative rates were reported in another overview by Lardinois [53] (Table 8.6). This high false-negative rate has limited the use of conventional TBNA for complete mediastinal lymph node staging. Conventional TBNA is useful if it leads to proof of N3 disease, but too often does not exclude N3 disease in cases of proven N2 disease.

The accuracy of TBNA can be improved by the use of endoscopic ultrasonography guidance techniques like EBUS-guided TBNA (EBUS-TBNA) or EUS-guided fine-needle aspiration (EUS-FNA) either alone or in combination. A recent meta-analysis of EUS-FNA alone, EBUS-TBNA alone, and EUS/EBUS combined has reported a pooled sensitivity and specificity of 86% and 100%, respectively, for mediastinal staging of lung cancer [56]. EBUS can be used to access lymph node stations 2R/2L, 4R/4L, 7, and 10 (hilar lymph nodes) as shown in Table 8.7. EUS particularly visualizes superior mediastinal lymph nodes in station 4L and inferior mediastinal nodes in stations 7, 8, and 9. Thus, EUS-FNA complements other techniques, as it can visualize lymph nodes (i.e., in stations 8 and 9) that are not

accessible by EBUS-TBNA or mediastinoscopy. Lymph node stations 5 and 6 can be well visualized by EUS but are rarely sampled without traversing the pulmonary artery/aorta. Lymph node stations 5 and 6 are predominantly affected by left upper lobe tumors and the surgical staging method of choice for such nodes is video-assisted thoracoscopic surgery (VATS).

### 8.3.3 Current Guidelines for Primary Mediastinal Staging

The current guidelines for primary mediastinal staging of NSCLC provided by the European Society of Thoracic Surgeons (ESTS) [20] are visualized in Fig. 8.15. Endosonography is recommended over surgical staging as the initial procedure for mediastinal nodal staging in patients with suspected or proven NSCLC with abnormal mediastinal and/or hilar nodes at CT, PET, or PET/CT. The combination of EBUS-TBNA and EUS-FNA is preferred over either test alone. Endoscopic needle techniques have sensitivities of approximately 90% when used in combination with ultrasound (EUS, EBUS). In direct comparison with surgical staging, they have emerged as the best first diagnostic tools to obtain tissue. However, in cases where the clinical suspicion of mediastinal lymph node involvement remains high after a negative result using a needle technique, surgical staging like mediastinoscopy or video-assisted thoracoscopic surgery (VATS) should be performed. In particular, patients with small mediastinal lymph nodes without FDG

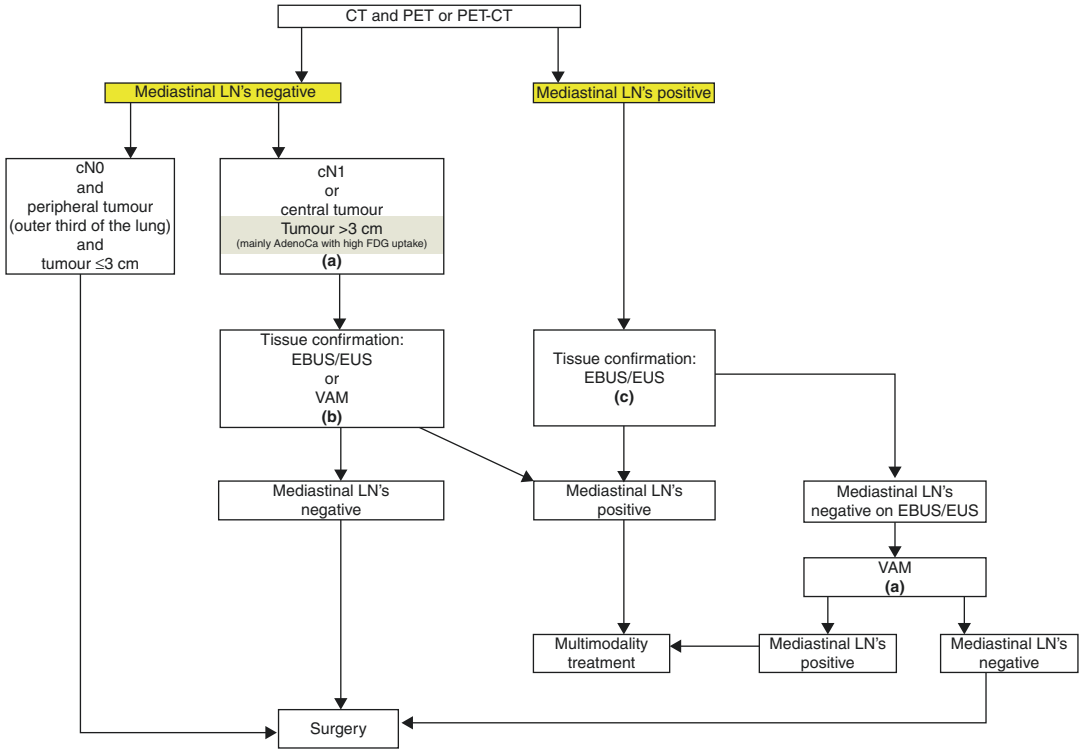


**(a)** : In tumours > 3 cm (mainly in adenocarcinoma with high FDG uptake) invasive staging should be considered
**(b)** : Depending on local expertise to adhere to minimal requirements for staging
**(c)** : Endoscopic techniques are minimally invasive and are the first choice if local expertise with EBUS/EUS needle aspiration is available
**(d)** : Due to its higher NPV, in case of PET positive or CT enlarged mediastinal LN's, videoassisted mediastinoscopy (VAM) with nodal dissection or biopsy remain indicated when endoscopic staging is negative. Nodal dissection has an increased accuracy over biopsy

**Fig. 8.15** Revised ESTS guidelines for primary mediastinal staging. Reprinted from [20] with permission from Oxford University Press

uptake present a 6–30% risk of having mediastinal metastases in the following cases:

- Enlarged or FDG-avid hilar lymph nodes, or small and FDG-avid hilar lymph nodes
- Non-FDG-avid lung tumor (i.e., pulmonary carcinoid, pulmonary adenocarcinoma in situ)
- Lung tumor >3 cm (mainly in the case of adenocarcinoma with high FDG uptake) without any lymph node involvement at CT or PET

In these cases, mediastinal staging should be performed for accurate mediastinal nodal assessment in order to allocate patients appropriately for therapy with curative intent.

Mediastinal lymph node metastases are present in less than 6% of patients with small peripheral tumors that present with neither enlarged nor FDG-avid hilar or mediastinal lymph nodes [58]. It is therefore suggested in the guidelines that for patients with a peripheral clinical stage IA tumor (i.e., negative nodal involvement by FDG-PET/CT) no invasive preoperative evaluation of the mediastinal nodes is required.

For patients with a left upper lobe tumor in whom invasive mediastinal staging is indicated (as defined in previous recommendations), it is suggested that invasive assessment of the APW nodes be performed (via Chamberlain procedure, VATS, or extended cervical mediastinoscopy) if other mediastinal node stations are found to be uninvolved [24]. N1 nodes are usually resected with the primary tumor, if complete surgical resection is undertaken.

Since the effectiveness of endoscopic (EUS/EBUS) and mediastinoscopic techniques relies heavily on the experience of the examiner/operator, the choice between these techniques for use in mediastinal staging should be based on available expertise. Moreover, the surgical staging techniques (e.g., VMS, VATS, or Chamberlain procedure) should be considered as complementary more than competing methods. To ensure the most accurate staging in treatment centers, all noninvasive imaging techniques and invasive surgical and minimally invasive needle-based endoscopic staging techniques should be available.

Due to the low negative predictive value of EBUS or EUS in the event of negative results it is necessary to subsequently conduct a mediastinoscopic lymph node biopsy. In the case of a low probability of a targeted diagnosis by endoscopy initially, a mediastinoscopical approach should be conducted primarily, in order to avoid double examinations. This is especially important for clinical stages with central tumors, including stage cN2 or cN3 disease. In the case of a positive PET/CT result, a confirmatory mediastinoscopy should always be performed. However, if the initial PET/CT is negative, a rate of 20% of false-negative results should be considered. Due to the low probability of positive results with EBUS/EUS when staging central tumors, mediastinoscopy should be conducted right away in these cases.

## 8.4 Limitations and Perspectives

Despite the most recent adaptation to the TNM staging system for non-small cell lung cancer, there are still a considerable number of limitations inherent to the current system. An important source of error lies in the data itself. Even though former limitations of an oligocentric database from a single country have been overcome, the gathering of suitable data for each revision remains challenging. This is particularly because treatment recommendations, as indirectly implicated in the TNM classification, should be derived whenever possible from properly conducted clinical trials.

The prognostic discriminatory power of any staging system is intimately connected to the level of sophistication of its underlying database, which, in turn, is determined by the structure of the previous staging classification and the therapeutic concepts available at the time. The backward compatibility of a redefined staging system to its predecessors is generally limited, depending on the extent of changes that have been applied. As a consequence of the aforesaid, a newly revised staging classification will be of limited help for any decision on treatment strategies that have not contributed to its underlying

database, a situation that currently applies to the different sorts of novel targeted therapies, in particular.

Another important limitation of the TNM staging system is that the information used for staging is purely anatomic and as such does not capture any prognostic information that is unrelated to the anatomic extent of the disease. This applies to all sorts of parameters obtained from blood samples and other laboratory tests, such as tumor markers, as well as clinical factors, such as performance status and comorbidities. Many selection criteria for modern therapy approaches, such as tumor type or genetic patterns, are therefore not covered by the TNM system. This gap between the TNM system and therapy decisions is getting even larger with the continuously increasing number of novel treatment options.

The ever-growing richness of detail of modern staging classifications also represents a challenge for the available imaging technologies in radiology and nuclear medicine. Remaining challenges are in particular the limited accuracy in the evaluation of mediastinal and chest wall infiltration for T staging, the decreased NPV of FDG-PET-negative lymph nodes in specific high-risk subgroups, and the generally low PPV of FDG-PET/CT for N staging [59]. Apart from higher anatomic resolution and image quality, the technical development of diagnostic imaging strongly focusses on the inclusion of "functional" image information, as well as on "molecular" and hybrid—morphologic and functional—imaging technologies. The most prominent examples for this development are CT perfusion [60], dual-energy CT [61], and hybrid FDG-PET/MRI [62, 63], where promising initial results have been published in recent years. The technical equipment required to perform these examinations, however, is still quite novel to clinical radiology and not yet available in every hospital. In consequence, the existing data on the staging performance of CT perfusion, dual-energy CT, and hybrid FDG-PET/MRI is scattered, mostly stemming from only a few different sites and obtained in limited numbers of patients. A much broader investigation of these methods in prospective interdisciplinary multicenter trials is required to tackle the persisting challenges for imaging-derived staging of NSCLC.

## References


1. World Health Organization. International Agency for Research on Cancer. GLOBOCAN 2012: Estimated Cancer Incidence, Mortality and Prevalence Worldwide in 2012. Lung Cancer. http://globocan.iarc.fr/Pages/fact_sheets_cancer.aspx. Accessed 7 May 2017.
2. U.S. National Institutes of Health. National Cancer Institute: SEER Cancer Statistics Review, 1975–2012. http://seer.cancer.gov/csr/1975_2012/browse_csr.php?sectionSEL=15&pageSEL=sect_15_table.28.html. Accessed 7 May 2017.
3. Denoix P. Enquête permanente dans les centres anticancéreux. Bull Inst Natl Hyg. 1946;1:70–5.
4. Goldstraw P, Chansky K, Crowley J, et al. International Association for the Study of Lung Cancer Staging and Prognostic Factors Committee, Advisory Boards, and Participating Institutions.; International Association for the Study of Lung Cancer Staging and Prognostic Factors Committee Advisory Boards and Participating Institutions. The IASLC Lung Cancer Staging Project: Proposals for Revision of the TNM Stage Groupings in the Forthcoming (Eighth) Edition of the TNM Classification for Lung Cancer. J Thorac Oncol. 2016;11(1):39–51.
5. Birley JD, Gospodarowicz M, Wittekind C, editors. TNM classification of malignant tumours. 8th ed. Oxford: Wiley-Blackwell; 2016.
6. Sobin L, Gospodarowicz M, Wittekind C, editors. TNM classification of malignant tumours. 7th ed. Oxford: Wiley-Blackwell; 2009.
7. Rusch VW, Asamura H, Watanabe H, et al. The IASLC lung cancer staging project: a proposal for a new international lymph node map in the forthcoming eventh edition of the TNM classification for ung cancer. J Thorac Oncol. 2009;4(5):568–77.
8. Mountain CF, Dresler CM. Regional lymph node classification for lung cancer staging. Chest. 1997;111(6):1718–23.
9. The Japan Lung Cancer Society. Classification of lung cancer. Tokyo: Kanehara & Co; 2000.
10. Rami-Porta R, Bolejack V, Crowley J, et al. IASLC Staging and Prognostic Factors Committee, Advisory Boards and Participating Institutions. The IASLC Lung Cancer Staging Project: Proposals for the Revisions of the T Descriptors in the Forthcoming Eighth Edition of the TNM Classification for Lung Cancer. J Thorac Oncol. 2015;10(7):990–1003.
11. Eberhardt WE, Mitchell A, Crowley J, Kondo H, Kim YT, Turrisi A 3rd, Goldstraw P, Rami-Porta R, International Association for Study of Lung Cancer Staging and Prognostic Factors Committee, Advisory Board Members, and Participating Institutions. The

IASLC Lung Cancer Staging Project: Proposals for the Revision of the M Descriptors in the Forthcoming Eighth Edition of the TNM Classification of Lung Cancer. J Thorac Oncol. 2015;10(11):1515–22.
12. Goldstraw P, Crowley J, IASCL International Lung Cancer Staging Project. The IASCL international project on lung cancer. J Thorac Oncol. 2006;1:208–86.
13. Nair A, Klusmann MJ, Kirupa H, Jogeesvaran H, Grubnic S, Green SJ, Vlahos I. Revisions to the TNM. Staging of non–small cell lung cancer: rationale, clinicoradiologic implications, and persistent limitations. Radiographics. 2011;31:215–38.
14. Rami-Porta R, Asamura H, Goldstraw P. Predicting the prognosis of lung cancer: the evolution of tumor, node and metastasis in the molecular age—challenges and opportunities. Transl Lung Cancer Res. 2015;4(4):415–23.
15. Rami-Porta R, Bolejack V, Giroux DJ, Chansky K, Crowley J, Asamura H, Goldstraw P, International Association for the Study of Lung Cancer Staging and Prognostic Factors Committee, Advisory Board Members and Participating Institutions. The IASLC lung cancer staging project: the new database to inform the eighth edition of the TNM classification of lung cancer. J Thorac Oncol. 2014;9(11):1618–24.
16. MacMahon H, Naidich DP, Goo JM, et al. Guidelines for management of incidental pulmonary nodules detected on CT images: from the Fleischner Society 2017. Radiology. 2017;23:161659. https://doi.org/10.1148/radiol.2017161659.
17. Travis WD, Asamura H, Bankier AA, et al. International Association for the Study of Lung Cancer Staging and Prognostic Factors Committee and Advisory Board Members. The IASLC Lung Cancer Staging Project: Proposals for Coding T Categories for Subsolid Nodules and Assessment of Tumor Size in Part-Solid Tumors in the Forthcoming Eighth Edition of the TNM Classification of Lung Cancer. J Thorac Oncol. 2016;11(8):1204–23.
18. The National Lung Screening Trial Research Team. Results of initial low-dose computed tomographic screening for lung cancer. N Engl J Med. 2013;368:1980–91.
19. Horeweg N, Scholten ET, de Jong PA, et al. Detection of lung cancer through low-dose CT screening (NELSON): a prespecified analysis of screening test performance and interval cancers. Lancet Oncol. 2014;15:1342–50.
20. De Leyn P, Dooms C, Kuzdzal J, et al. Revised ESTS guidelines for preoperative mediastinal lymph node staging for non-small-cell lung cancer. Eur J Cardiothorac Surg. 2014;45(5):787–98.
21. De Wever W, Stroobants S, Coolen J, Verschakelen JA. Integrated PET/CT in staging non-small cell lung cancer: tech-nical aspects and clinical integration. Eur Respir J. 2009;33:201–12.
22. Pauls S, Buck AK, Hohl K, et al. Improved non-invasive T- staging in non-small cell lung cancer by integrated 18F-FDG PET/CT. Nuklearmedizin. 2007;46:9–14.
23. El-Sherief AH, Lau CT, Wu CC, Drake RL, Abbott GF, Rice TW. International Association for the Study of Lung Cancer (IASLC) lymph node map: radiologic review with CT illustration. Radiographics. 2014;34:1680–91.
24. Silvestri GA, Gonzalez AV, Jantz MA, Margolis ML, Gould MK, Tanoue LT, Harris LJ, Detterbeck FC. Methods for staging non-small cell lung cancer: diagnosis and management of lung cancer, 3rd ed: American College of Chest Physicians evidence-based clinical practice guidelines. Chest. 2013;143(5 Suppl):e211S–50S.
25. Gould MK, Kuschner WG, Rydzak CE, et al. Test erformance of positron emission tomography and computed tomography for mediastinal staging in patients with nonsmall-cell lung cancer: a meta-analysis. Ann Intern Med. 2003;39:879–92.
26. Dwamena BA, Sonnad SS, Angobaldo JO, Wahl RL. Metastases from non-small cell lung cancer: mediastinal staging in the 1990s–meta-analytic comparison of PET and CT. Radiology. 1999;213:530–6.
27. Toloza EM, Harpole L, McCrory DC. Noninvasive staging of non-small-cell lung cancer: a review of the current evidence. Chest. 2003;123(1 Suppl):137S–46S.
28. National Institute for Health and Clinical Excellence (NICE). NICE updates guidance on the diagnosis and treatment of lung cancer. https://www.nice.org.uk/guidance/cg121/chapter/1-Guidance#diagnosis-and-staging. Accessed 22 June 2017.
29. Boellaard R, Delgado-Bolton R, Oyen WJ, et al. European Association of Nuclear Medicine (EANM). FDG PET/CT: EANM procedure guidelines for tumour imaging: version 2.0. Eur J Nucl Med Mol Imaging. 2015;42(2):328–54.
30. Lardinois D, Weder W, Hany TF, et al. Staging of non-small-cell lung cancer with integrated positron-emission tomography and computed tomography. N Engl J Med. 2003;348:2500–7.
31. Madsen PH, Holdgaard PC, Christensen JB, et al. Clinical utility of F-18 FDG PET-CT in the initial evaluation of lung cancer. Eur J Nucl Med Mol Imaging. 2016;43:2084.
32. Fletcher JW, Kymes SM, Gould M, et al. A comparison of the diagnostic accuracy of 18F-FDG PET and CT in the characterization of solitary pulmonary nodules. J Nucl Med. 2008;49:179–85.
33. Sommer G, Wiese M, Winter L, Lenz C, Klarhöfer M, Forrer F, Lardinois D, Bremerich J. Preoperative staging of non-small-cell lung cancer: comparison of whole-body diffusion-weighted magnetic resonance imaging and 18F-fluorodeoxyglucose-positron emission tomography/computed tomography. Eur Radiol. 2012;22(12):2859–67.
34. Stroobants SG, D'Hoore I, Dooms C, et al. Additional value of whole-body fluorodeoxyglucose positron emission tomography in the detection of distant

metastases of non-small-cell lung cancer. Clin Lung Cancer. 2003;4:242–7.
35. Hsia TC, Shen YY, Yen RF, Kao CH, Changlai SP. Comparing whole body 18 F-2-deoxyglucose positron emission tomography and technetium-99m methylene diophosphate bone scan to detect bone metastases in patients with non-small cell lung cancer. Neoplasma. 2002;49(4):267–71.
36. Song JH, Chaudhry FS, Mayo-Smith WW. The incidental adrenal mass on CT: prevalence of adrenal disease in 1,049 consecutive adrenal masses in patients with no known malignancy. AJR Am J Roentgenol. 2008;190(5):1163–8.
37. Eggesbø HB, Hansen G. Clinical impact of adrenal expansive lesions in bronchial carcinoma. Acta Radiol. 1996;37(3 Pt 1):343–7.
38. Kaltenbach TE-M, Engler P, Kratzer W, et al. Prevalence of benign focal liver lesions: ultrasound investigation of 45,319 hospital patients. Abdominal Radiology. 2016;41:25–32.
39. Hillers TK, Sauve MD, Guyatt GH. Analysis of published studies on the detection of extrathoracic metastases in patients presumed to have operable non-small cell lung cancer. Thorax. 1994;49(1):14–9.
40. Hustinx R, Paulus P, Jacquet N, Jerusalem G, Bury T, Rigo P. Clinical evaluation of whole-body 18 F-fluorodeoxyglucose positron emission tomography in the detection of liver metastases. Ann Oncol. 1998;9(4):397–401.
41. Sommer G, Tremper J, Koenigkam-Santos M, et al. Lung nodule detection in a high-risk population: comparison of magnetic resonance imaging and low-dose computed tomography. Eur J Radiol. 2014;83(3):600–5.
42. Webb WR, Gatsonis C, Zerhouni EA, et al. CT and MR imaging in staging non-small cell bronchogenic carcinoma: report of the radiologic diagnostic oncology group. Radiology. 1991;178:705–13.
43. Yi CA, Lee KS, Lee HY, et al. Coregistered whole body magnetic resonance imaging-positron emission tomography (MRI-PET) versus PET-computed tomography plus brain MRI in staging resectable lung cancer: comparisons of clinical effectiveness in a randomized trial. Cancer. 2013;119:1784–91.
44. Ohno Y, Koyama H, Yoshikawa T, et al. Three-way comparison of whole-body MR, Coregistered whole-body FDG PET/MR, and integrated whole-body FDG PET/CT imaging: TNM and stage assessment capability for non-small cell lung cancer patients. Radiology. 2015;275:849–61.
45. Morikawa M, Demura Y, Ishizaki T, et al. The effectiveness of 18F-FDG PET/CT combined with STIR MRI for diagnosing nodal involvement in the thorax. J Nucl Med. 2009;50:81–7.
46. Takahara T, Imai Y, Yamashita T, et al. Diffusion weighted whole body imaging with background body signal suppression (DWIBS): technical improvement using free breathing, STIR and high resolution 3D display. Radiat Med. 2004;22:275–82.
47. Shen G, Lan Y, Zhang K, Ren P, Jia Z. Comparison of 18F-FDG PET/CT and DWI for detection of mediastinal nodal metastasis in non-small cell lung cancer: a meta-analysis. PLoS One. 2017;12(3):e0173104.
48. Hochstenbag MM, Twijnstra A, Hofman P, Wouters EF, ten Velde GP. MR-imaging of the brain of neurologic asymptomatic patients with large cell or adenocarcinoma of the lung. Does it influence prognosis and treatment? Lung Cancer. 2003;42(2):189–93.
49. Earnest F IV, Ryu JH, Miller GM, et al. Suspected non small cell lung cancer: incidence of occult brain and skeletal metastases and effectiveness of imaging for detection—pilot study. Radiology. 1999;211(1):137–45.
50. Yokoi K, Kamiya N, Matsuguma H, et al. Detection of brain metastasis in potentially operable non-small cell lung cancer: a comparison of CT and MRI. Chest. 1999;115(3):714–9.
51. Van den Wyngaert T, Strobel K, Kampen WU, et al. The EANM practice guidelines for bone scintigraphy. Eur J Nucl Med Mol Imaging. 2016;43:1723–38.
52. Robinson LA, Wagner H Jr, Ruckdeschel JC, American College of Chest Physicians. Treatment of stage IIIA non-small cell lung cancer. Chest. 2003;123(1 Suppl):202S–20S.
53. Lardinois D. Pre- and intra-operative mediastinal staging in non-small-cell lung cancer. Swiss Med Wkly. 2011;141:w13168.
54. Zielinski M, Szlubowski A, Kołodziej M, Orzechowski S, Laczynska E, Pankowski J, Jakubiak M, Obrochta A. Comparison of endobronchial ultrasound and/or endoesophageal ultrasound with transcervical extended mediastinal lymphadenectomy for staging and restaging of non-small-cell lung cancer. J Thorac Oncol. 2013;8(5):630–6.
55. Um SW, Kim HK, Jung SH, et al. Endobronchial ultrasound versus mediastinoscopy for mediastinal nodal staging of non-small-cell lung cancer. J Thorac Oncol. 2015;10(2):331–7.
56. Zhang R, Ying K, Shi L, Zhang L, Zhou L. Combined endobronchial and endoscopic ultrasound-guided fine needle aspiration for mediastinal lymph node staging of lung cancer: a meta-analysis. Eur J Cancer. 2013;49(8):1860–7.
57. Van Schill PE, et al. Surgical treatment of early-stage non-small-cell lung cancer. EJC Suppl. 2013;11(2):110–22.
58. Tournoy KG, Keller SM, Annema JT. Mediastinal staging of lung cancer: novel concepts. Lancet Oncol. 2012;13:e221–9.
59. Sommer G, Stieltjes B. Magnetic resonance imaging for staging of non-small-cell lung cancer—technical advances and unmet needs. J Thorac Dis. 2015;7(7):1098–102.

60. Ippolito D, Capraro C, Guerra L, De Ponti E, Messa C, Sironi S. Feasibility of perfusion CT technique integrated into conventional $^{18}$FDG/PET-CT studies in lung cancer patients: clinical staging and functional information in a single study. Eur J Nucl Med Mol Imaging. 2013;40(2):156–65.
61. Sudarski S, Hagelstein C, Weis M, Schoenberg SO, Apfaltrer P. Dual-energy snap-shot perfusion CT in suspect pulmonary nodules and masses and for lung cancer staging. Eur J Radiol. 2015;84(12):2393–400.
62. Schwenzer NF, Schraml C, Müller M, et al. Pulmonary lesion assessment: comparison of whole-body hybrid MR/PET and PET/CT imaging—pilot study. Radiology. 2012;264:551–8.
63. Heusch P, Buchbender C, Köhler J, et al. Thoracic staging in lung cancer: prospective comparison of 18F-FDG PET/MR imaging and 18F-FDG PET/CT. J Nucl Med. 2014;55:373–8.

# Staging of Small-Cell Lung Cancer

9

Girish S. Shroff, Neda Kalhor, Reza J. Mehran, Patricia M. de Groot, and Brett W. Carter

**Abstract**

Small-cell lung cancer (SCLC) is the most common and most aggressive pulmonary neuroendocrine malignancy. SCLCs account for approximately 13% of all lung cancers and are characterized by rapid growth, early development of metastatic disease, dramatic initial response to chemotherapy and radiation therapy, and frequent association with paraneoplastic syndromes. Computed tomography (CT) and positron-emission tomography (PET)/CT are the imaging modalities routinely used in the evaluation of patients with SCLC. On imaging, SCLC usually manifests as a large centrally located lung mass or as mediastinal or mediastinal and hilar lymphadenopathy. Most patients have metastatic disease at presentation. Historically, the Veterans Administration Lung Study Group (VALG) staging system has been used to stage SCLC. More recently, it has been recommended by the International Association for the Study of Lung Cancer (IASLC) that the tumor, node, metastasis (TNM) staging system replace the VALG staging system. Despite characteristic responsiveness to initial therapy, disease invariably recurs and the overall prognosis remains poor.

**Keywords**

Small-cell lung cancer (SCLC) · Neuroendocrine malignancy · (TNM) staging system · Computed tomography (CT) · Positron-emission tomography/computed tomography (PET/CT)

## 9.1 Introduction and Clinical Features

Lung cancer is typically divided into non-small cell lung cancer (NSCLC) and small-cell lung cancer (SCLC). SCLC is an aggressive high-grade malignancy that is characterized by rapid growth, early development of metastatic disease, dramatic initial response to chemotherapy and radiation therapy, and frequent association with paraneoplastic syndromes. Among all histologic types of lung cancer, SCLC and squamous cell carcinoma have the highest correlation with ciga-

G. S. Shroff (✉) · P. M. de Groot · B. W. Carter
Department of Diagnostic Radiology, MD Anderson Cancer Center, Houston, TX, USA
e-mail: GShroff@mdanderson.org; pdegroot@mdanderson.org; bcarter2@mdanderson.org

N. Kalhor
Department of Pathology, MD Anderson Cancer Center, Houston, TX, USA
e-mail: nkalhor@mdanderson.org

R. J. Mehran
Department of Thoracic and Cardiovascular Surgery, MD Anderson Cancer Center, Houston, TX, USA
e-mail: rjmehran@mdanderson.org


M. Anzidei, M. Anile (eds.), *Diagnostic Imaging for Thoracic Surgery*, https://doi.org/10.1007/978-3-319-89893-3_9

rette smoking; approximately 90–95% of patients with SCLC are either current or past smokers [1]. The risk of developing SCLC increases with both the number of cigarettes smoked each day and the duration of smoking [1].

Analysis of the United States National Cancer Institute's Surveillance, Epidemiologic, and End Results (SEER) database from 1973 to 2002 showed that the percentage of SCLC among all cases of lung cancer in the United States peaked in 1986 at approximately 17% and decreased gradually over the next decade and a half to approximately 13% [2]. The proportion of women with SCLC increased during that same period from 28% in 1973 to 50% in 2002 [2]. The slight decrease in overall incidence of SCLC from 1986 to 2002 may be explained by several factors including (1) the decreased percentage of smokers, particularly among men; (2) the change in cigarette composition (e.g., decreased tar and nicotine); and (3) a change in the pathologic criteria for SCLC whereby some cases previously classified as SCLC are now classified as large-cell neuroendocrine carcinoma [2]. Currently, SCLC accounts for approximately 13% of all lung cancers in the United States [3]. Despite modest but statistically significant improvement in 2- and 5-year survival in the SEER study period from 1973 to 2002, outcomes and prognosis remain poor [2]. Median survival ranges from 10 to 18 months in limited-stage (LS) disease and from 7 to 12 months in extensive-stage (ES) disease [4, 5]. Up to 37% of patients with LS-SCLC survive 2 years and 7–18% survive 5 years [4, 6, 7]. ES-SCLC portends a much worse prognosis with 2- and 5-year survival rates of 4% and 1–2%, respectively [4, 5].

Most patients with SCLC are symptomatic at presentation; the majority demonstrate short symptom duration (usually less than 3 months), an indication of rapid tumor progression [8]. Presenting symptoms of SCLC may be constitutional, pulmonary/thoracic, related to extrathoracic metastatic spread, or due to paraneoplastic syndromes [9]. In one series, fatigue (occurring in 79%) was the most common symptom among SCLC patients; decreased activity, cough, decreased appetite, dyspnea, pain, and weight loss were also common, though each occurred in at least half of the patients [10]. Hemoptysis occurred in 14% [10]. Symptoms referable to regional tumor extension to the mediastinum include hoarseness and dysphagia. Hoarseness is a manifestation of vocal cord paralysis and usually represents recurrent laryngeal nerve involvement by tumor although lesions anywhere along the course of the vagus nerve can produce this symptom [11]. Dysphagia can be due to extrinsic compression of the esophagus by tumor/lymphadenopathy or due to direct invasion of the esophagus [11]. Involvement of the superior vena cava (SVC) can result in SVC obstruction/SVC syndrome; in one review, 9% of SCLC patients had signs or symptoms of SVC obstruction (e.g., collateral venous circulation, upper hemibody edema, increased jugular venous pressure, dyspnea, peripheral cyanosis, and confusion) [12]. Approximately 70–80% of patients have overt metastatic disease at presentation and involvement of liver, adrenal glands, and bone is frequently encountered. Hepatic and adrenal metastases are typically asymptomatic; skeletal metastases may manifest as osteolytic lesions, often without bone pain [9]. Vertebral involvement can lead to acute or subacute neurologic deficits, particularly in cases of spinal cord compression (by tumor or a collapsed vertebra) or when spinal cord vasculature is obstructed [11]. In a review of 432 patients with SCLC by Seute et al. 18% were found to have brain metastases at diagnosis though in approximately one-third of cases, the brain metastases did not cause symptoms [13]. When symptomatic, brain metastases may manifest with seizures, alteration in mental status, or ataxia. The 2-year cumulative risk of brain metastases was 49% for patients with LS-SCLC and 65% for patients with ES-SCLC [13].

Paraneoplastic syndromes are more commonly associated with SCLC than with other histological types of lung cancer [14]. Paraneoplastic syndromes are typically the result of either ectopic production of hormones by cancer cells or immune-mediated tissue destruction caused by neural antigen expression

from cancer cells [15]. The most common paraneoplastic syndrome associated with SCLC is the syndrome of inappropriate antidiuretic hormone (SIADH), also referred to as hyponatremia of malignancy [15]. SIADH, which occurs in 15% of patients with SCLC, results from the ectopic production of arginine vasopressin (AVP, also known as antidiuretic hormone or ADH) from tumor cells [15]. Symptoms associated with SIADH/hyponatremia of malignancy include nausea, vomiting, lethargy, and seizures. Cushing syndrome, related to the production of adrenocorticotropic hormone (ACTH), is the second most common paraneoplastic syndrome associated with SCLC, occurring in 5% of patients [15]. In terms of antibody-mediated (neurologic) paraneoplastic syndromes associated with SCLC, Lambert-Eaton myasthenic syndrome (LEMS) is most common, seen in 1–3% of patients at presentation [15]. Features of LEMS include slowly progressive proximal muscle weakness, characteristically worse in the lower extremities, and fatigue. Clinical symptoms of paraneoplastic syndromes frequently precede the diagnosis of SCLC by months to years [13, 15]. Treatment is aimed at the underlying lung cancer; in cases of clearly identifiable serum antibodies, immunosuppression is an alternate option.

## 9.2 Histological Features

SCLC is a malignant epithelial tumor composed of small round, oval, or spindle-shaped cells with scant cytoplasm, ill-defined cell borders, fine granular nuclear chromatin that is uniformly distributed (yielding a "salt and pepper" appearance), and absent or inconspicuous nucleoli [16]. Cells have a high nuclear/cytoplasmic ratio and nuclear molding is a prominent feature [16]. Mitotic count is high and necrosis is typically extensive [16].

SCLC is defined by light microscopy and the most important stain is a high-quality hematoxylin and eosin (H&E) stain (Fig. 9.1) [17]. Most cases are diagnosed by H&E alone; in difficult cases, immunohistochemical stains can be used to help differentiate SCLC from other tumors [17]. Immunohistochemical stains used in the diagnosis of SCLC include a pancytokeratin antibody such as AE1/AE3 (which helps demonstrate cell lineage, i.e., the tumor is a carcinoma rather than a lymphoma, melanoma, or sarcoma); neuroendocrine markers such as CD56, chromogranin, and synaptophysin; TTF-1 (thyroid transcription factor-1, which helps determine the primary site of malignancy); and Ki-67 (a marker for cellular proliferation; SCLCs show a high proliferation rate by Ki-67, averaging 80–100%) [17–19].

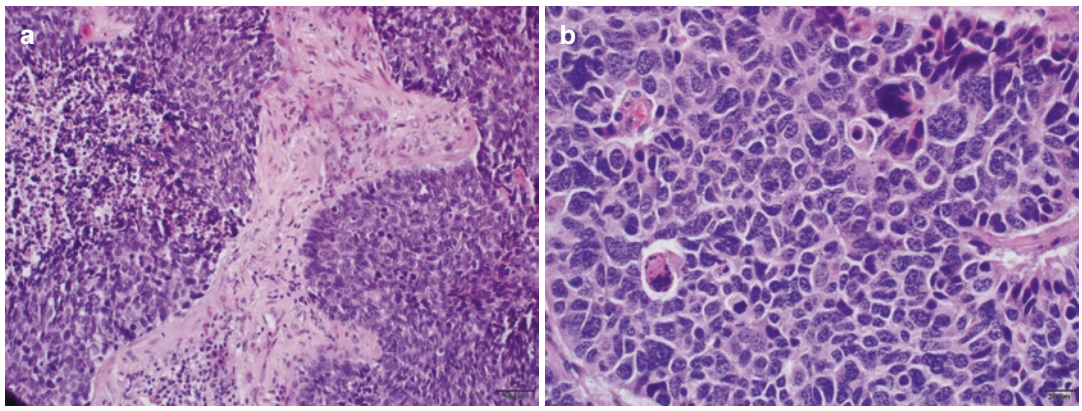


**Fig. 9.1** Microscopic features of SCLC. (**a**) High-power photomicrograph (original magnification, ×20; hematoxylin-eosin stain) and (**b**) high-power photomicrograph (original magnification, ×40; hematoxylin-eosin stain) showing tumor composed of predominantly small- to medium-sized malignant cells with high nuclear:cytoplasmic ratio, numerous mitotic figures and apoptotic cells, and abundant necrosis. Nuclear molding, a characteristic but nonspecific feature, can be seen. The chromatin within the nuclei of these neoplastic cells is fine, and prominent nucleoli are not seen

Histologic classification of SCLC has undergone numerous changes over the last half century. SCLC was subdivided by the World Health Organization (WHO) in 1962 into oat cell (roundish to oval cells with sparse cytoplasm and naked nuclei) and polygonal forms [20]. In the first official WHO lung cancer classification (published in 1967), SCLC was subdivided based on morphology into four groups: lymphocyte-like (synonymous with oat cell), polygonal, fusiform, and others [21]. In the 1981 revision, the lymphocyte-like designation was replaced by the term oat cell and the remaining three subtypes were included in an intermediate category. In 1988, a consensus report by the pathology committee of the International Association for the Study of Lung Cancer (IASLC) recommended the following classification: (1) small-cell carcinoma (i.e., all SCLC tumors that have no non-small cell elements; most of the tumors previously categorized as oat cell and intermediate subtypes); (2) mixed small-cell/large-cell carcinoma (i.e., a small-cell carcinoma that contains a subpopulation of cells resembling large-cell lung carcinomas); and (3) combined small-cell carcinomas (i.e., SCLC admixed with areas of differentiated squamous cell or adenocarcinoma). Subsequent revisions to the WHO classification of lung tumors have resulted in further changes—previous classifications and terms such as oat cell carcinoma, intermediate cell type, mixed small-cell/large-cell carcinoma, and others (e.g., small-cell anaplastic carcinoma and undifferentiated small-cell carcinoma) are now considered obsolete and are no longer recognized. The WHO now recognizes two types of SCLC: pure SCLC and combined SCLC [14]. If SCLC has a pure histology, it is classified as SCLC [17]. Combined SCLC is defined as SCLC combined with a non-small cell lung cancer (NSCLC) component such as adenocarcinoma, squamous cell carcinoma, large-cell carcinoma, spindle cell carcinoma, or giant-cell carcinoma [16]. The diagnosis of combined SCLC is accompanied by a description of the NSCLC component or components [18]. To make the diagnosis of combined SCLC/large-cell carcinoma, the tumor should be composed of at least 10% large or giant cells; for other combined SCLCs, there is no percentage requirement for diagnosis [18].

SCLCs, like the other neuroendocrine tumors of the lung, arise from Kulchitsky cells that are normally present in the bronchial mucosa. The neuroendocrine family of lung tumors is comprised of SCLC, large-cell neuroendocrine carcinoma (LCNEC), and typical and atypical carcinoid tumors; these tumors share morphological, ultrastructural, immunohistochemical, and molecular characteristics [14]. Despite being grouped together, there are major differences among the pulmonary neuroendocrine tumors. SCLC and LCNEC are high-grade tumors, atypical carcinoids are intermediate-grade tumors, and typical carcinoids are low-grade tumors. SCLC and LCNEC patients are older, have a worse prognosis, and have a stronger association with smoking than patients with carcinoid tumors [22]. SCLC and LCNEC have higher mitotic rates and more necrosis than carcinoid tumors [22]. SCLC and LCNEC may show combinations with other histologic types of lung cancer. Carcinoid tumors have very few genetic abnormalities compared with the high-grade pulmonary neuroendocrine tumors [22].

Macroscopically, SCLCs are typically tan-white, soft, friable masses with extensive necrosis [16]. Nodal involvement is frequent. In the lung, tumor commonly spreads along bronchi in a submucosal and circumferential manner and frequently involves lymphatics [16].

## 9.3 Imaging of SCLC

### 9.3.1 Computed Tomography (CT)

The majority (90–95%) of SCLCs are located centrally and arise from the lobar or main stem bronchi [23]. On CT, SCLCs most commonly manifest either as (1) a large centrally located lung mass or as (2) mediastinal or mediastinal and hilar lymphadenopathy (Fig. 9.2) [24, 25]. A noncontiguous parenchymal lesion (i.e., a parenchymal lesion not contiguous with hilar/mediastinal adenopathy) was seen in 41% of cases in one review [25]. The absence of visualization of a primary lung tumor

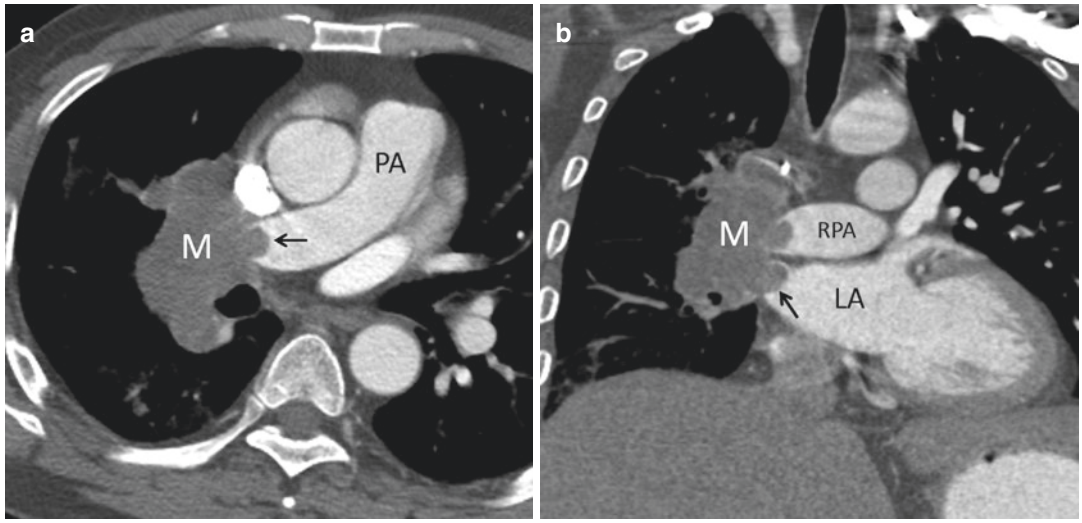


**Fig. 9.2** SCLC with invasion of the pulmonary artery and left atrium. (**a**) Contrast-enhanced axial CT shows a right hilar mass (M) invading the right pulmonary artery (arrow). (**b**) Coronal reformation also depicts invasion of the left atrium (arrow). *LA* Left atrium; *PA* Pulmonary artery; *RPA* Right pulmonary artery

even in the presence of bulky lymphadenopathy is not uncommon however. Narrowing of the tracheobronchial tree (either secondary to extrinsic compression or endobronchial growth) and/or displacement of the tracheobronchial tree are frequent findings, occurring in approximately two-thirds of cases [25, 26]. As a result of their central location and propensity to narrow the tracheobronchial tree, SCLCs can result in post-obstructive atelectasis of either a lobe or an entire lung; atelectasis of at least a lobe is found in 30% of cases (Fig. 9.3) [25]. SCLCs may narrow or displace major vessels (present in approximately two-thirds of cases) (Fig. 9.4) [25]. The thin-walled low-pressure venous system is prone to obstruction/invasion by tumor. SVC obstruction, for instance, occurs in up to 9% of cases and manifests with narrowing or obliteration of the SVC by tumor; obstruction of the SVC is accompanied by the development of collateral venous return to the heart from the upper half of the body, most commonly through the azygous venous system (Fig. 9.5). Atypical imaging presentations of SCLC include lymphangitic carcinomatosis (visualized as smooth and/or nodular thickening of bronchovascular bundles and interlobular septa), replacement of an entire lobe by tumor (Fig. 9.6), and consolidation [27]. Metastatic disease to serosal surfaces (i.e., the pleura and pericardium) may manifest as an effusion and/or smooth or nodular thickening (Fig. 9.7). Importantly, the absence of serosal thickening in the presence of an effusion does not exclude metastatic disease. Other common sites of metastatic disease, e.g., lungs, liver,

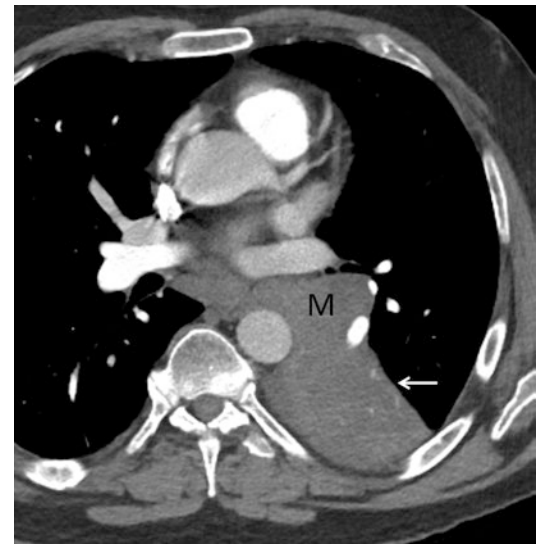


**Fig. 9.3** SCLC resulting in lobar atelectasis. Contrast-enhanced axial CT shows a left infrahilar SCLC (M) and associated post-obstructive atelectasis of the left lower lobe (arrow)

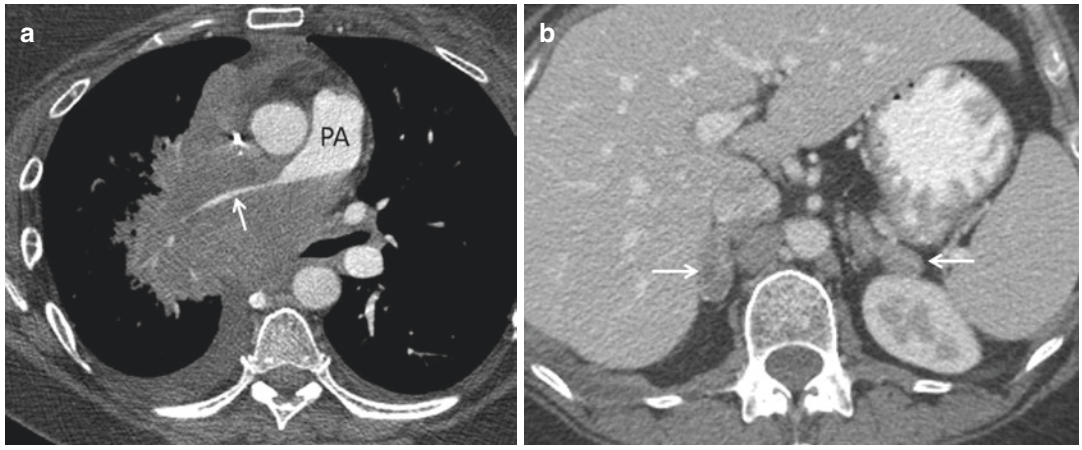


**Fig. 9.4** SCLC with mediastinal invasion and adrenal metastases. (**a**) Contrast-enhanced axial CT at the level of the pulmonary artery (PA) shows a large right hilar mass invading the mediastinum and causing slit-like narrowing of the right pulmonary artery (arrow). (**b**) Contrast-enhanced axial CT of the abdomen demonstrates bilateral adrenal metastases (arrows)

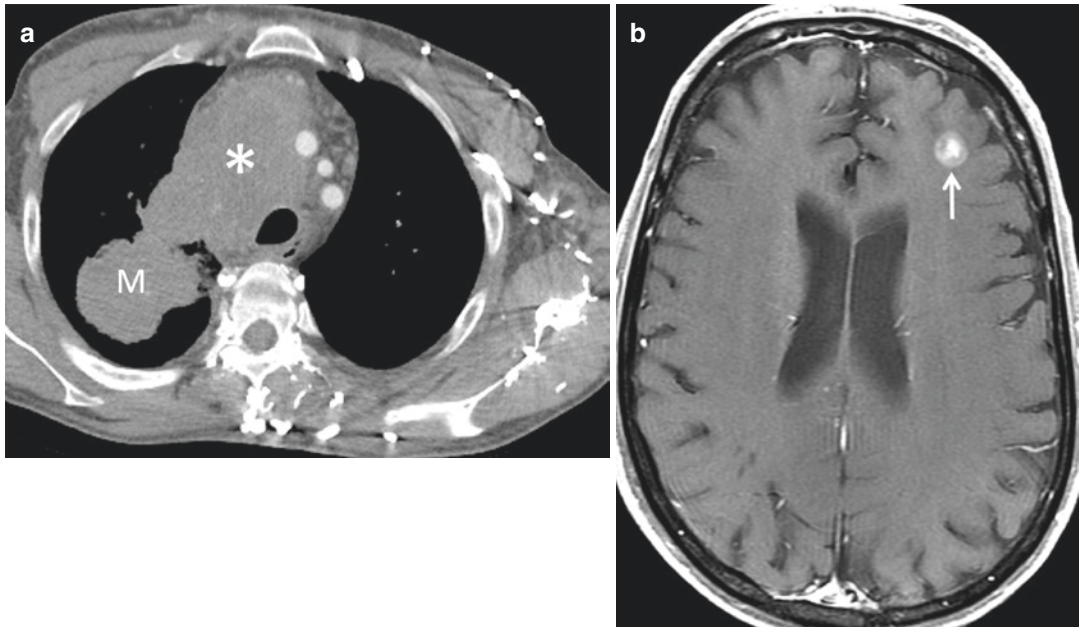


**Fig. 9.5** SCLC resulting in superior vena cava syndrome and brain metastasis in a 53-year-old man who presented with facial and neck swelling. (**a**) Contrast-enhanced axial CT shows a right upper lobe mass (M) and bulky mediastinal lymphadenopathy (*) related to SCLC. Lymphadenopathy has obliterated the SVC. Note the extensive collateral venous circulation that has developed in order to return blood to the right heart. (**b**) T1-weighted post-contrast MR imaging of the brain shows a metastasis in the left frontal lobe (arrow) for which the patient was asymptomatic

adrenal glands, and skeleton, are also readily evaluated on CT (Fig. 9.8).

In a minority (5–10%) of cases, SCLC may present as a solitary pulmonary nodule without lymphadenopathy (Fig. 9.9) [18]. SCLCs that present as a solitary pulmonary nodule have a nonspecific appearance. They are usually homogeneous in attenuation, and round or lobulated, and

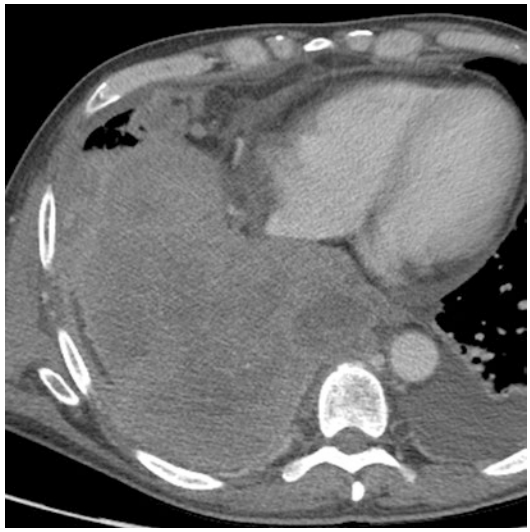

**Fig. 9.6** Replacement of a lobe by SCLC. Contrast-enhanced axial CT shows a large tumor replacing the right lower lobe and most of the middle lobe

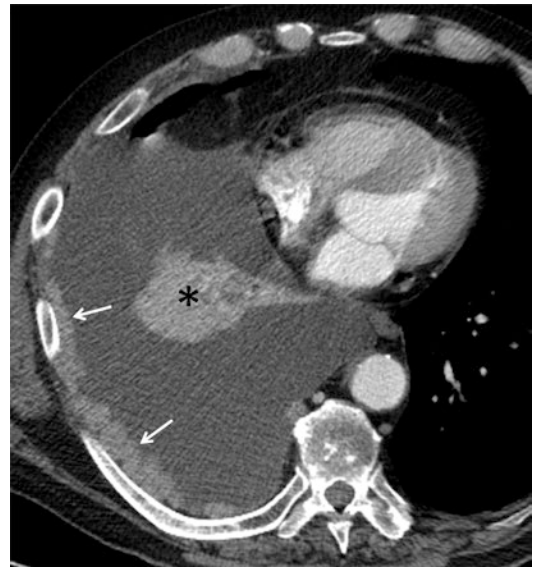

**Fig. 9.7** Pleural metastatic disease. Contrast-enhanced axial CT shows a large right pleural effusion and lobular pleural thickening (arrows), consistent with pleural metastatic disease. Note the atelectatic right lower lobe (asterisk)

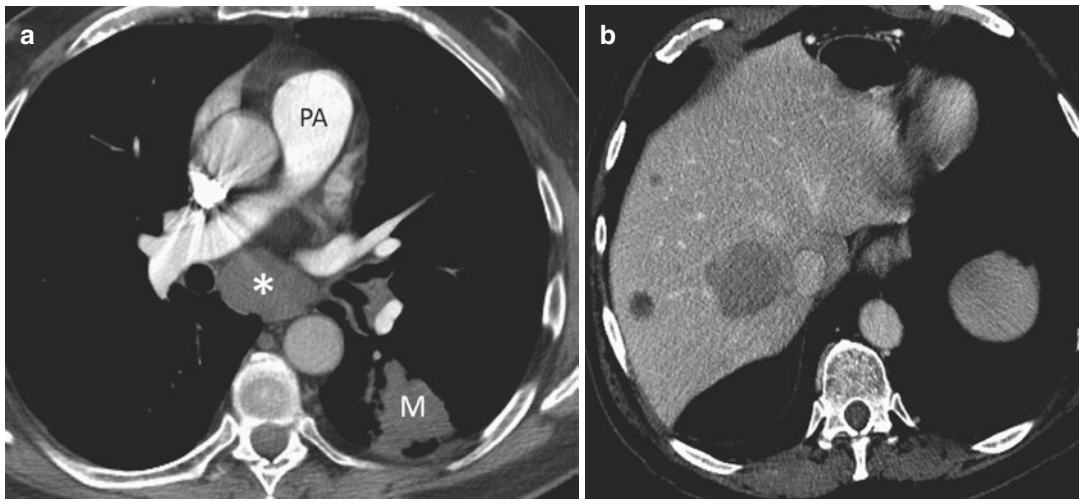


**Fig. 9.8** SCLC with lymph node and hepatic metastases. (**a**) Contrast-enhanced axial CT at the level of the pulmonary artery (PA) shows the left lower lobe primary tumor (M) and subcarinal lymph node metastasis (asterisk). (**b**) Contrast-enhanced axial CT of the upper abdomen shows several low-attenuation hepatic lesions, consistent with metastases

have well-defined margins [28]. In some instances, tumor margins may be ill defined with either spiculation (corresponding to vascular, lymphatic, or alveolar invasion) or ground-glass opacity (corresponding to edema, hemorrhage, or intra-alveolar invasion) [28].

### 9.3.2 Positron-Emission Tomography/Computed Tomography (PET/CT)

$^{18}$F-fluorodeoxyglucose ($^{18}$F-FDG) PET/CT combines functional information with anatomic infor-

mation and is an important examination in the evaluation of patients with SCLC [24]. FDG PET/CT plays a role in staging and restaging, guiding of therapy, and suggesting prognosis [24]. Because of the high metabolic activity of SCLC (Fig. 9.10), staging accuracy is better with PET/CT than with conventional imaging [29–31] and PET/CT is superior to PET alone [31]. In their review of 14 studies comparing pretreatment FDG PET to conventional staging procedures in patients with SCLC, Kalemkerian and Gadgeel found that 18% of patients diagnosed with limited disease by conventional imaging were upstaged to extensive disease by FDG PET (Fig. 9.11) [32]. Along similar lines, 11% of patients diagnosed with extensive disease by conventional imaging were downstaged to limited disease based on PET results [32]. PET was more sensitive and specific at most sites of metastatic disease but was inferior to MRI or CT in the detection of brain metastases [32].

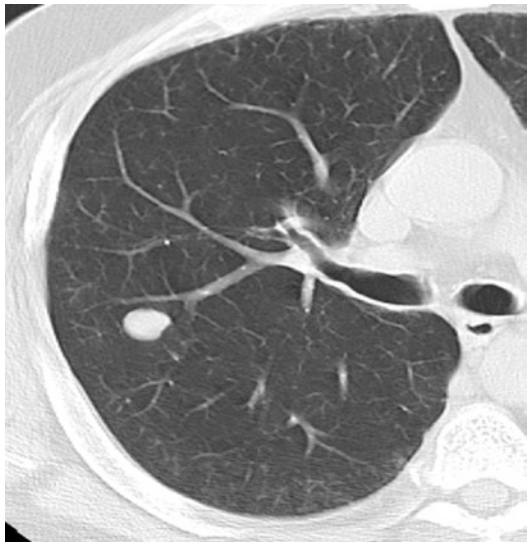

**Fig. 9.9** SCLC presenting as a solitary pulmonary nodule. Contrast-enhanced axial CT performed to evaluate a pulmonary nodule detected on chest radiography confirms a solitary nodule in the right upper lobe. There was no lymphadenopathy. The patient underwent right upper lobectomy and was treated with adjuvant chemotherapy and prophylactic cranial irradiation

Several studies have evaluated changes in the initial management of SCLC patients based on PET; in their review of these studies, Kalemkerian and Gadgeel found that PET findings led to a change in initial management in 28% of patients—of patients who had a change in management, 32% had a change in the general treatment plan as a result of change in overall stage and 68% had changes in the extent of the radiation field [32]. In terms of restaging after therapy, studies have shown that 20–57% of patients had more disease while 14–38% had less disease on PET than with CT alone [33–36].

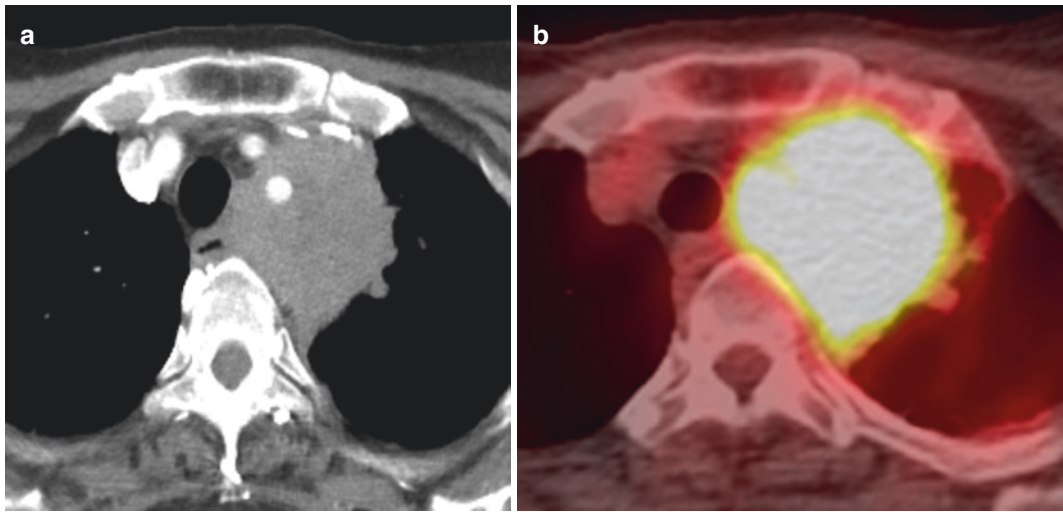


**Fig. 9.10** Mediastinal SCLC with characteristic increased FDG uptake. (**a**) Contrast-enhanced axial CT shows a large soft-tissue mass in the left mediastinum. (**b**) Fused axial PET/CT image shows intense FDG uptake with maximum SUV of 14. Because of its high metabolic activity, SCLC typically demonstrates intense FDG uptake on PET/CT

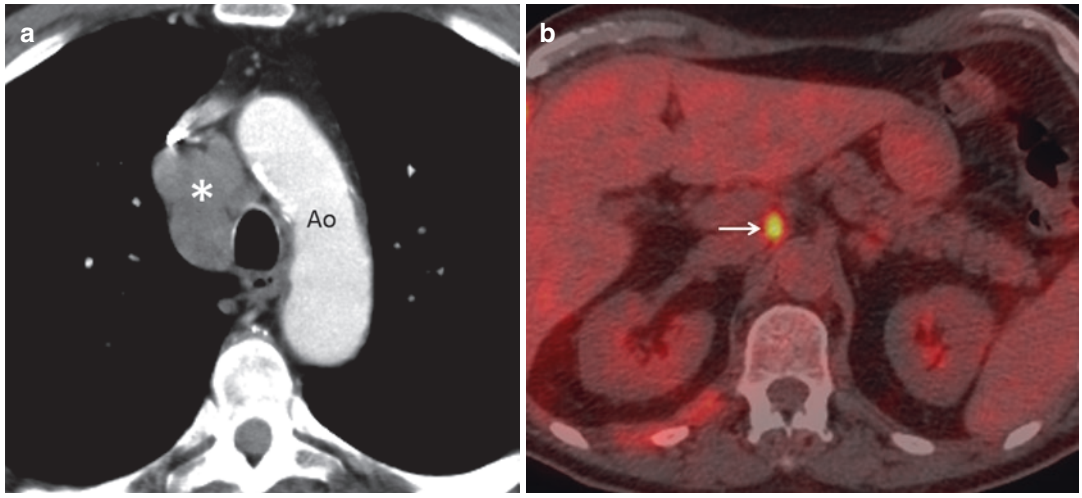


**Fig. 9.11** Improved staging accuracy with PET/CT. (**a**) Contrast-enhanced axial CT at the level of the aortic arch (Ao) shows right paratracheal lymphadenopathy (asterisk), proven to represent SCLC. The abdominal CT did not reveal any evidence of metastatic disease. (**b**) Fused PET/CT image reveals an FDG-avid lymph node in the right retroperitoneum (arrow), proven to represent distant metastasis. Staging accuracy is better with PET/CT than with conventional imaging alone

PET imaging provides prognostic information in both staging and restaging of SCLC. In a review by Chong et al., $SUV_{max}$ (maximum standard uptake value) of SCLC before treatment showed a negative correlation with survival time; an $SUV_{max}$ of greater than 13.7 suggested a short survival time [37]. In a review by Pandit et al., patients with a positive FDG PET scan after initial therapy were found to have a significantly worse prognosis than those with a negative study; furthermore, a high $SUV_{max}$ was associated with poor survival [38].

## 9.4 Magnetic Resonance (MR) Imaging

Thoracic MR imaging is not routinely performed to evaluate patients with SCLC. However, it can be valuable in certain situations, such as the suspected invasion of mediastinal or vascular structures in a patient in whom intravenous contrast is contraindicated (e.g., in cases of renal failure or allergy) [24]. Brain MR imaging is the imaging modality of choice for the evaluation of intracranial metastatic disease; due to the high incidence of brain metastases in SCLC, routine imaging of the brain is warranted in the staging of the tumor [39]. Spinal MR imaging is the modality of choice in the evaluation of suspected cord compression.

### 9.4.1 Differential Diagnosis

The differential diagnosis of SCLC, especially in cases of ES-SCLC, primarily includes other malignancies such as NSCLC, metastatic disease from another primary malignancy (such as breast cancer, sarcoma, or melanoma), and lymphoma. Other neuroendocrine neoplasms (e.g., of lung or alternate primary site) may also be considered. In the case of a solitary pulmonary nodule, the differential diagnosis is broad and includes other malignancies (primary or metastatic), benign lung tumors, and nonmalignant etiologies such as infection (e.g., bacterial or fungal pneumonia) or inflammation (e.g., nonnecrotizing granulomatous inflammation and granulomatosis with polyangiitis).

### 9.4.2 Staging

Historically, the TNM staging system was not used in the staging of SCLC since the TNM system relies on surgical confirmation for accuracy

and patients with SCLC rarely present with localized disease amenable to surgical resection [40, 41]. SCLC has instead been traditionally staged using a two-stage system that was introduced by the Veterans Administration Lung Study Group (VALG) in 1957. In the VALG staging system, patients are classified as having either LS-SCLC or ES-SCLC. LS-SCLC was originally defined as tumor involvement limited to one hemithorax that could be treated within a tolerable single radiotherapy port; ipsilateral supraclavicular lymph nodes could be classified as LS-SCLC if they could be included in the radiation port. ES-SCLC was defined as a disease that could not be classified as LS-SCLC and included malignant pleural or pericardial effusions and contralateral hilar and contralateral supraclavicular lymph nodes. Due to a lack of uniformity and controversy in the handling of patients with ipsilateral pleural effusion and of patients with contralateral mediastinal or contralateral supraclavicular lymph node metastases, the IASLC modified the VALG staging system in 1989 [42]. LS-SCLC was redefined as disease restricted to one hemithorax with regional lymph node metastases, including hilar, ipsilateral, and contralateral mediastinal, and ipsilateral and contralateral supraclavicular lymph nodes; an ipsilateral pleural effusion (independent of positive or negative cytology) was also included as LS-SCLC given that no extrathoracic metastases were detected [42]. ES-SCLC was defined as disease at sites beyond the definition of LS-SCLC. In practice, clinicians typically classify contralateral mediastinal and ipsilateral supraclavicular lymph node involvement as LS-SCLC. Controversy still exists with regard to the classification of contralateral supraclavicular or contralateral hilar lymph node involvement; treatment is usually based on the ability to include the area in a tolerable radiotherapy port [32].

In 2007, the IASLC, based on a retrospective analysis of over 8000 patients diagnosed with SCLC between 1990 and 2000, recommended that the (at the time forthcoming) 7th edition of the AJCC/UICC (American Joint Committee on Cancer/Union for International Cancer Control) TNM staging system replace the VALG staging system for SCLC [41]. They found that in patients without hematogenous metastases, both the T and N descriptors were discriminatory for overall survival; clinical stage groupings I–IV were also predictive of overall survival [32, 41]. An updated (8th) edition of the TNM staging system has recently been published based upon an analysis of a new database of patients that were diagnosed with lung cancer (including over 5000 with SCLC) between 1999 and 2010; analysis has again confirmed the prognostic value of TNM staging in patients with SCLC and continued usage of the TNM system in SCLC is recommended [43]. Minor changes to some of the TNM descriptors and TNM stage categories have been introduced in the 8th edition. Using the 8th edition of the TNM system, limited disease corresponds to T(any), N(any), M0 except T3–4 due to multiple lung nodules that do not fit in a tolerable radiation field while extensive disease corresponds to T(any), N(any), M1a/b/c or T3–4 due to multiple lung nodules. The M1b category represents oligometastatic disease in which there is a single metastatic deposit in one distant organ while M1c represents multiple metastases in one or more distant sites.

### 9.4.3 Treatment Guidelines

Systemic chemotherapy is the mainstay of treatment in all patients with SCLC. Combination therapy with etoposide plus a platinum-based agent (e.g., cisplatin or carboplatin) is the recommended standard chemotherapy regimen [44]. In ES-SCLC, chemotherapy alone is the recommended treatment although radiotherapy may be used for palliation of symptoms (for

example, in cases of SVC syndrome, obstructive atelectasis, painful bone metastases, and spinal cord compression) [44]. In patients with ES-SCLC and brain metastases, chemotherapy is given before or after whole-brain radiotherapy depending on the presence or absence of neurologic symptoms—if asymptomatic, chemotherapy is given first; if symptomatic, whole-brain radiotherapy is administered before chemotherapy unless immediate systemic therapy is required [44]. Patients with LS-SCLC, regardless of the visible extent of tumor, also receive chemotherapy because of the high likelihood of micrometastatic disease and because of the high initial response rate to cytotoxic therapy [32]. The addition of thoracic radiotherapy to chemotherapy in patients with LS-SCLC results in a 25–30% reduction in local failure and a 5–7% improvement in 2-year survival when compared with chemotherapy alone [45, 46]. LS-SCLC is therefore treated with a combination of chemotherapy and early concurrent thoracic radiotherapy, administered with cycle 1 or 2 of chemotherapy. Although SCLC is highly responsive to initial chemotherapy, approximately 80% of patients with LS-SCLC and almost all patients with ES-SCLC develop recurrent or progressive disease (Fig. 9.12) [24]. Second-line therapy may provide palliation and the likelihood of response is dependent on the time from initial therapy to relapse; for instance, if the interval between initial therapy and relapse is less than 3 months, response rates are <10% whereas if the interval is greater than 3 months, response rates are approximately 25% [44, 47].

Due to the high risk of the development of brain metastases, prophylactic cranial irradiation (PCI) is recommended in patients with LS-SCLC and ES-SCLC who have a good response to initial therapy [44]. In patients with LS-SCLC, PCI decreases the incidence of brain metastases and increases overall survival [48, 49]. In terms of patients with ES-SCLC, a study published in 2007 concluded that PCI decreases brain metastases and increases overall survival [50]. A recent Japanese trial, however, showed that PCI did not result in longer overall survival compared with observation in patients with extensive disease [51]. PCI is not administered concurrently with systemic chemotherapy due to the increased risk of neurotoxicity [44].

Surgery may be considered in SCLC patients with clinical stage I (T1–2, N0) disease. Patients with higher T- or N-stage disease do not benefit from surgery [52]. When surgery is being considered, occult lymph node metastasis should be excluded by pathologic mediastinal staging which may include mediastinoscopy, endoscopy (bronchoscopy or esophagoscopy) with ultrasound-guided fine-needle aspiration (FNA) procedures, thoracoscopy, or a combination of these procedures [53]. After confirmation that mediastinal lymph nodes are uninvolved, complete resection (preferably a lobectomy with either mediastinal lymph node dissection or sampling) is performed [44]. Patients without lymph node metastases are treated with postoperative chemotherapy whereas patients with nodal metastases are treated with postoperative concurrent chemotherapy and mediastinal radiotherapy [44].

**Conclusions**

SCLC is the most aggressive pulmonary neuroendocrine malignancy and is characterized by rapid growth and early development of metastatic disease. On CT, SCLC usually manifests as a large central lung mass or as mediastinal or mediastinal and hilar lymphadenopathy. Although SCLC has traditionally been staged using the modified VALG staging system, utilization of the TNM system is now recommended. Systemic chemotherapy is the mainstay of treatment in all patients with SCLC. Despite characteristic responsiveness to initial therapy, disease invariably recurs and the prognosis remains poor.

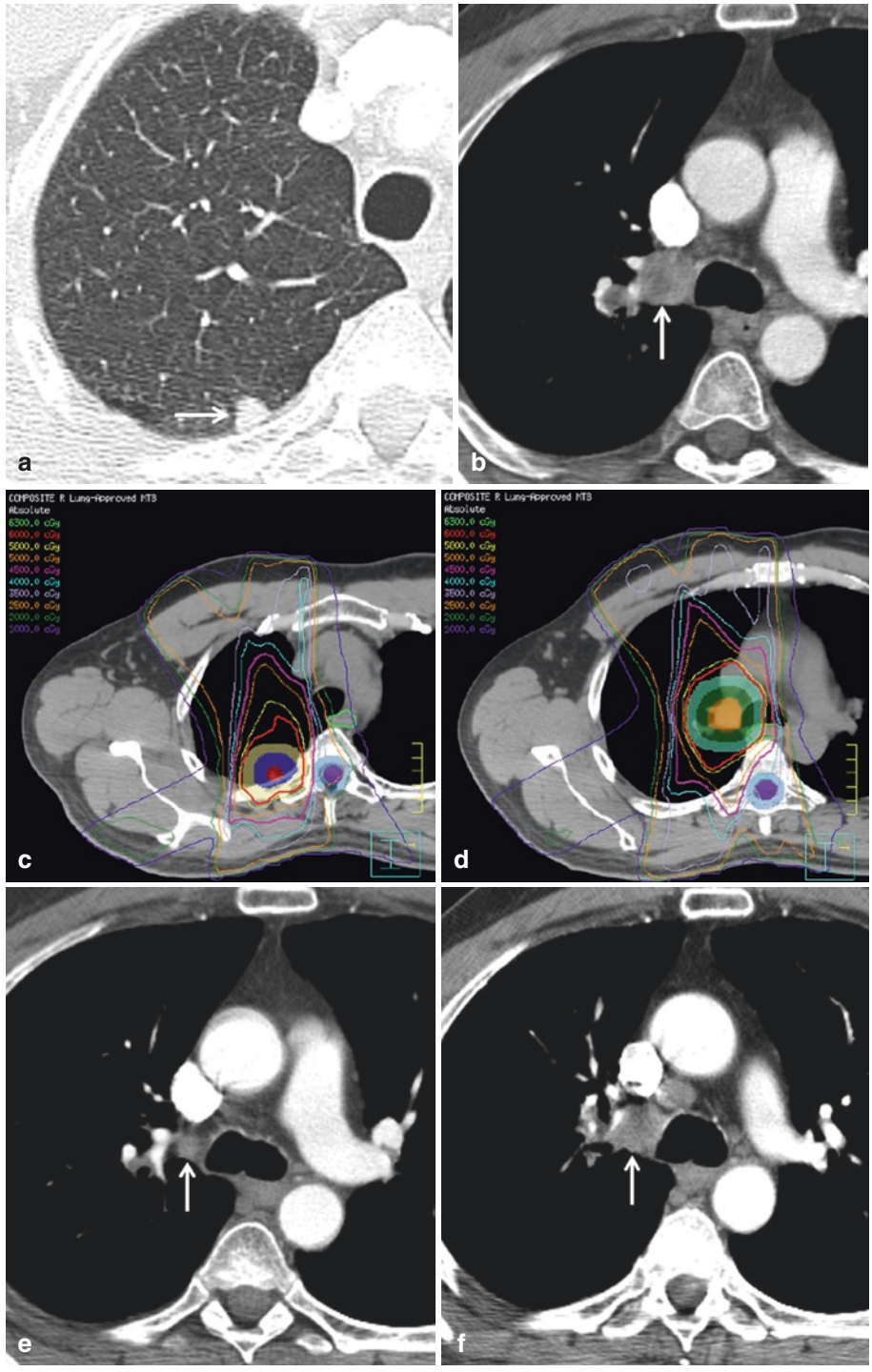


**Fig. 9.12** Recurrent SCLC. Axial CTs in lung (**a**) and soft-tissue (**b**) windows show the right upper lobe primary tumor (arrow in **a**) and a right hilar lymph node metastasis (arrow in **b**). Images from the radiation treatment plan (**c**, **d**) show targeting of both lesions for treatment with radiation. (**e**) CT after radiation shows decrease in the treated lymph node metastasis (arrow). The primary tumor (not shown) has also decreased in size. (**f**) CT performed 8 months later shows recurrence of the lymph node metastasis (arrow) and a new right paratracheal lymph node metastasis

## References


1. Brownson RC, Chang JC, Davis JR. Gender and histologic type variations in smoking-related risk of lung cancer. Epidemiology. 1992;3:61–4.
2. Govindan R, Page N, Morgensztern D, et al. Changing epidemiology of small-cell lung cancer in the United States over the last 30 years: analysis of the surveillance, epidemiologic, and end results database. J Clin Oncol. 2006;24:4539–44.
3. American Cancer Society: Cancer Facts and Figures (2017) https://www.cancer.org/content/dam/cancer-org/research/cancer-facts-and-statistics/annual-cancer-facts-and-figures/2017/cancer-facts-and-figures-2017.pdf. Accessed 27 Mar 2017.
4. Albain KS, Crowley JJ, Livingston RB. Long-term survival and toxicity in small cell lung cancer. Expanded Southwest Oncology Group experience. Chest. 1991;99:1425–32.
5. Lassen U, Osterlind K, Hansen M, et al. Long-term survival in small-cell lung cancer: posttreatment characteristics in patients surviving 5 to 18+ years--an analysis of 1,714 consecutive patients. J Clin Oncol. 1995;13:1215–20.
6. Osterlind K, Hansen HH, Hansen M, et al. Long-term disease-free survival in small-cell carcinoma of the lung: a study of clinical determinants. J Clin Oncol. 1986;4:1307–13.
7. Tai P, Tonita J, Yu E, et al. Twenty-year follow-up study of long-term survival of limited-stage small-cell lung cancer and overview of prognostic and treatment factors. Int J Radiat Oncol Biol Phys. 2003;56:626–33.
8. Watson WL, Berg JW. Oat cell lung cancer. Cancer. 1962;15:759–68.
9. Pietanza MC, Krug LM, Wu AJ, et al. Small cell and neuroendocrine tumors of the lung. In: DeVita VT, Lawrence TS, Rosenberg SA, editors. Devita, Hellman, and Rosenberg's cancer: principles & practice of oncology. 10th ed. Philadelphia: Wolters Kluwer; 2015. p. 536–57.
10. Hollen PJ, Gralla RJ, Kris MG, et al. Quality of life assessment in individuals with lung cancer: testing the lung cancer symptom scale (LCSS). Eur J Cancer. 1993;29A(Suppl 1):S51–8.
11. Cohen MH, Matthews MJ. Small cell bronchogenic carcinoma: a distinct clinicopathologic entity. Semin Oncol. 1978;5:234–43.
12. Sculier JP, Evans WK, Feld R, et al. Superior vena caval obstruction syndrome in small cell lung cancer. Cancer. 1986;57:847–51.
13. Seute T, Leffers P, ten Velde GP, et al. Neurologic disorders in 432 consecutive patients with small cell lung carcinoma. Cancer. 2004;100:801–6.
14. Travis WD, Brambilla E, Burke AP, Marx A, Nicholson AG, editors. WHO classification of tumours of the lung, pleura, thymus and heart. Lyon: IARC Press; 2015.
15. Gandhi L, Johnson BE. Paraneoplastic syndromes associated with small cell lung cancer. J Natl Compr Cancer Netw. 2006;4:631–8.
16. Travis WD, Brambilla E, Muller-Hermelink HK, Harris CC, editors. WHO classification of tumours pathology and genetics of tumours of the lung, pleura, thymus and heart. Lyon: IARC Press; 2004.
17. Travis WD. Update on small cell carcinoma and its differentiation from squamous cell carcinoma and other non-small cell carcinomas. Mod Pathol. 2012;25(Suppl 1):S18–30.
18. Travis WD. Advances in neuroendocrine lung tumors. Ann Oncol. 2010;21(Suppl 7):vii65–71.
19. Kim KW, Krajewski KM, Jagannathan JP, et al. Cancer of unknown primary sites: what radiologists need to know and what oncologists want to know. AJR Am J Roentgenol. 2013;200:484–92.
20. Kreyberg L. Histological lung cancer types. A morphological and biological correlation. Acta Pathol Microbiol Scand Suppl. 1962;157:1–92.
21. Hirsch FR, Matthews MJ, Aisner S, et al. Histopathologic classification of small cell lung cancer. Changing concepts and terminology. Cancer. 1988;62:973–7.
22. Travis WD, Brambilla E, Nicholson AG, et al. The 2015 World Health Organization classification of lung tumors: impact of genetic, clinical and radiologic advances since the 2004 classification. J Thorac Oncol. 2015;10:1243–60.
23. Rosado-de-Christenson ML, Templeton PA, Moran CA. Bronchogenic carcinoma: radiologic-pathologic correlation. Radiographics. 1994;14:429–46.
24. Carter BW, Glisson BS, Truong MT, et al. Small cell lung carcinoma: staging, imaging, and treatment considerations. Radiographics. 2014;34:1707–21.
25. Pearlberg JL, Sandler MA, Lewis JW Jr, et al. Small-cell bronchogenic carcinoma: CT evaluation. AJR Am J Roentgenol. 1988;150:265–8.
26. Whitley NO, Fuks JZ, McCrea ES, et al. Computed tomography of the chest in small cell lung cancer: potential new prognostic signs. AJR Am J Roentgenol. 1984;142:885–92.
27. Kazawa N, Kitaichi M, Hiraoka M, et al. Small cell lung carcinoma: eight types of extension and spread on computed tomography. J Comput Assist Tomogr. 2006;30:653–61.
28. Yabuuchi H, Murayama S, Sakai S, et al. Resected peripheral small cell carcinoma of the lung: computed tomographic-histologic correlation. J Thorac Imaging. 1999;14:105–8.
29. Podoloff DA, Ball DW, Ben-Josef E, et al. NCCN task force: clinical utility of PET in a variety of tumor types. J Natl Compr Cancer Netw. 2009;7(Suppl 2):S1–26.
30. Bradley JD, Dehdashti F, Mintun MA, et al. Positron emission tomography in limited-stage small-cell lung cancer: a prospective study. J Clin Oncol. 2004;22:3248–54.
31. Fischer BM, Mortensen J, Langer SW, et al. A prospective study of PET/CT in initial staging of small-cell lung cancer: comparison with CT, bone scintigraphy and bone marrow analysis. Ann Oncol. 2007;18:338–45.

32. Kalemkerian GP, Gadgeel SM. Modern staging of small cell lung cancer. J Natl Compr Cancer Netw. 2013;11:99–104.
33. Schumacher T, Brink I, Mix M, et al. FDG-PET imaging for the staging and follow-up of small cell lung cancer. Eur J Nucl Med. 2001;28:483–8.
34. Kamel EM, Zwahlen D, Wyss MT, et al. Whole-body 18F-FDG PET improves the management of patients with small cell lung cancer. J Nucl Med. 2003;44:1911–7.
35. Blum R, MacManus MP, Rischin D, et al. Impact of positron emission tomography on the management of patients with small cell lung cancer: preliminary experience. Am J Clin Oncol. 2004;27:164–71.
36. Arslan N, Tuncel M, Kuzhan O, et al. Evaluation of outcome prediction and disease extension by quantitative 2-deoxy-2-[18F] fluoro-D-glucose with positron emission tomography in patients with small cell lung cancer. Ann Nucl Med. 2011;25:406–13.
37. Chong S, Lee KS, Kim BT, et al. Integrated PET/CT of pulmonary neuroendocrine tumors: diagnostic and prognostic implications. AJR Am J Roentgenol. 2007;188:1223–31.
38. Pandit N, Gonen M, Krug L, et al. Prognostic value of [18F]FDG-PET imaging in small cell lung cancer. Eur J Nucl Med Mol Imaging. 2003;30:78–84.
39. Ravenel JG, Rosenzweig KE, Kirsch J, et al. ACR appropriateness criteria non-invasive clinical staging of bronchogenic carcinoma. J Am Coll Radiol. 2014;11:849–56.
40. Jackman DM, Johnson BE. Small-cell lung cancer. Lancet. 2005;366:1385–96.
41. Shepherd FA, Crowley J, Van Houtte P, et al. The International Association for the Study of Lung Cancer lung cancer staging project: proposals regarding the clinical staging of small cell lung cancer in the forthcoming (seventh) edition of the tumor, node, metastasis classification for lung cancer. J Thorac Oncol. 2007;2:1067–77.
42. Stahel RA, Ginsberg R, Havemann K, et al. Staging and prognostic factors in small cell lung cancer: a consensus report. Lung Cancer. 1989;5:119–26.
43. Nicholson AG, Chansky K, Crowley J, et al. The International Association for the Study of Lung Cancer Lung Cancer Staging Project: Proposals for the Revision of the Clinical and Pathologic Staging of Small Cell Lung Cancer in the Forthcoming Eighth Edition of the TNM Classification for Lung Cancer. J Thorac Oncol. 2016;11:300–11.
44. NCCN Clinical Practice Guidelines in Oncology, Small Cell Lung Cancer, Version 3.2017-February 23, 2017. NCCN.org. Accessed 21 April 2017.
45. Pignon JP, Arriagada R, Ihde DC, et al. A meta-analysis of thoracic radiotherapy for small-cell lung cancer. N Engl J Med. 1992;327:1618–24.
46. Warde P, Payne D. Does thoracic irradiation improve survival and local control in limited-stage small-cell carcinoma of the lung? A meta-analysis. J Clin Oncol. 1992;10:890–5.
47. Owonikoko TK, Behera M, Chen Z, et al. A systematic analysis of efficacy of second-line chemotherapy in sensitive and refractory small-cell lung cancer. J Thorac Oncol. 2012;7:866–72.
48. Arriagada R, Le Chevalier T, Rivière A, et al. Patterns of failure after prophylactic cranial irradiation in small-cell lung cancer: analysis of 505 randomized patients. Ann Oncol. 2002;13:748–54.
49. Aupérin A, Arriagada R, Pignon JP, et al. Prophylactic cranial irradiation for patients with small-cell lung cancer in complete remission. Prophylactic Cranial Irradiation Overview Collaborative Group. N Engl J Med. 1999;341:476–84.
50. Slotman B, Faivre-Finn C, Kramer G, et al. Prophylactic cranial irradiation in extensive small-cell lung cancer. N Engl J Med. 2007;357:664–72.
51. Takahashi T, Yamanaka T, Seto T, et al. Prophylactic cranial irradiation versus observation in patients with extensive-disease small-cell lung cancer: a multicentre, randomised, open-label, phase 3 trial. Lancet Oncol. 2017;18(5):663–71.
52. Lad T, Piantadosi S, Thomas P, et al. A prospective randomized trial to determine the benefit of surgical resection of residual disease following response of small cell lung cancer to combination chemotherapy. Chest. 1994;106(6 Suppl):320S–3S.
53. Schneider BJ, Saxena A, Downey RJ. Surgery for early-stage small cell lung cancer. J Natl Compr Cancer Netw. 2011;9:1132–9.

# Staging of Malignant Pleural Mesothelioma

10

Patricia M. de Groot, Girish S. Shroff, Carol C. Wu, David R. Rice, and Brett W. Carter

**Abstract**

Primary malignancy of the pleura is rare and usually has a poor prognosis. Malignant pleural mesothelioma is linked to occupational and environmental exposures with a latency period of 2–6 decades. Patients usually present late in the course of the disease with chest pain, dyspnea, and weight loss. Outcomes are related to both the histological subtype of the tumor and staging at presentation. Computed tomography (CT) is the imaging modality most commonly used for preliminary noninvasive clinical staging. Magnetic resonance (MR) imaging, particularly dynamic sequences, is useful in evaluating chest wall, diaphragm, and mediastinal invasion. It can be helpful when CT findings are equivocal to distinguish resectable from unresectable disease. Positron-emission tomography (PET)/CT is performed in patients being considered for surgical resection, as it may identify nodal and/or distant metastases not seen on CT. PET/CT may also have a role in evaluation of response to treatment and detection of recurrent disease. The 8th edition of the TNM staging system is in effect as of January 1, 2018.

**Keywords**

Malignant pleural mesothelioma · Epithelioid mesothelioma · Sarcomatoid mesothelioma Staging

## 10.1 Introduction

Malignant pleural mesothelioma (MPM) is an aggressive primary malignancy of the pleura with a generally poor prognosis. A few cases of pleural mesothelioma were reported in the 1930s and 1940s but the tumor was uncommon until the second half of the twentieth century [1]. Studies in the 1960s identified the association between MPM and industrial exposure to silicate asbestos fibers in occupations such as asbestos mining and construction-related fields [2, 3]. All types of asbestos, amphibole and serpentine, are classified as group I carcinogens by the International

P. M. de Groot · G. S. Shroff
C. C. Wu B. W. Carter (✉)
Department of Diagnostic Radiology, The University of Texas MD Anderson Cancer Center, Houston, TX, USA
e-mail: pdegroot@mdanderson.org; GShroff@mdanderson.org; ccwu1@mdanderson.org; BCarter2@mdanderson.org

D. R. Rice
Department of Thoracic and Cardiovascular Surgery, The University of Texas MD Anderson Cancer Center, Houston, TX, USA
e-mail: drice@mdanderson.org


M. Anzidei, M. Anile (eds.), *Diagnostic Imaging for Thoracic Surgery*, https://doi.org/10.1007/978-3-319-89893-3_10

Agency for Research on Cancer [4]. The most commonly used commercial asbestos is the serpentine type, chrysotile [5]. Another cohort of patients with MPM have environmental exposure to erionite, an aluminosilicate zeolite mineral which is also a group I carcinogen found in homes and buildings made of local stone in central Anatolia in Turkey. Erionite deposits are also located in the western United States [6].

Since the early 1970s, more than 60 countries have enacted legislation restricting the use of asbestos, but the long latency period between exposure and malignancy (20–60 years) ensures that the incidence of mesothelioma continues to increase in a number of industrialized countries [5]. Documented age standardized annual incidence per million is highest in Australia (29), the United Kingdom (29), and Italy (24) [7]. The World Health Organization's current estimate of worldwide asbestos exposure is 125 million individuals [8]. Russia and China are the foremost producers of asbestos in the twenty-first century and the largest markets are in China, India, Russia, Thailand, and Brazil, but data regarding mesothelioma incidence from these regions is incomplete [5, 9].

Symptoms of MPM are often insidious and nonspecific, including cough, dyspnea, and chest pain. Consequently, the malignancy is often advanced at the time of diagnosis. Prognosis depends on the histological type of tumor, patient performance status, and extent of disease. Accurate staging is required to determine whether patients may be candidates for potentially curative treatment alternatives such as extrapleural pneumonectomy or pleurectomy/decortication versus palliative options including limited pleural resection, pleurodesis, or isolated radiation therapy. Multimodality therapy with surgery, chemotherapy, and radiation therapy prolongs survival.

## 10.2 Evaluation and Staging of MPM

Malignant pleural mesothelioma arises from the mesothelial cells of the thoracic parietal pleura and has three major subtypes with implications for prognosis. The epithelioid variety of mesothelioma accounts for 60% of cases and has better outcomes, while the biphasic (20–35%) and sarcomatoid types (10–15%) have comparatively decreased survival. The biphasic or mixed tumor can arise because mesothelial cells are able to display both epithelioid and mesenchymal features [1]. By definition, the biphasic tumor must contain ≥10% each of epithelioid and sarcomatoid elements [10]. Desmoplastic mesothelioma is a subtype of the sarcomatoid lineage [11].

A stratification scheme for patients with the epithelioid variant of MPM using nuclear atypia and mitotic counts has been proposed based on the results of multivariate analysis. A preliminary study showed that grade I cases of epithelioid MPM with lower atypia and mitotic counts had a median overall survival of 28 months, while grade II patient had median survival of 14 months, and grade III patients had only 5 months' median survival. Further work is needed to validate this stratification method [11].

Pleural biopsy is necessary to establish the diagnosis of MPM and provide tissue for immunohistochemical analysis. Thoracentesis for cytologic analysis, and pleural biopsy, preferably via thoracoscopy, is recommended by the National Comprehensive Cancer Network as part of the first-line evaluation for pleural thickening or recurrent pleural effusions [12].

The risk of tumor track seeding from fine-needle aspiration, biopsy, thoracentesis, placement of drainage catheters, and/or thoracoscopy is known to be increased in mesothelioma, unlike secondary tumors affecting the pleura (Fig. 10.1). Track seeding in pleural mesothelioma has been reported in 4% of image-guided core-needle biopsies and in 22% in surgical biopsies [13]. For this reason, a number of investigators have explored the efficacy of prophylactic radiotherapy following chest intervention, with good results [14, 15].

## 10.3 TNM Classification

The 8th edition of the TNM staging system for MPM is implemented as of January 1, 2018, by the American Joint Committee on Cancer (AJCC)/Union for International Cancer Control (UICC). Recommendations for the 8th

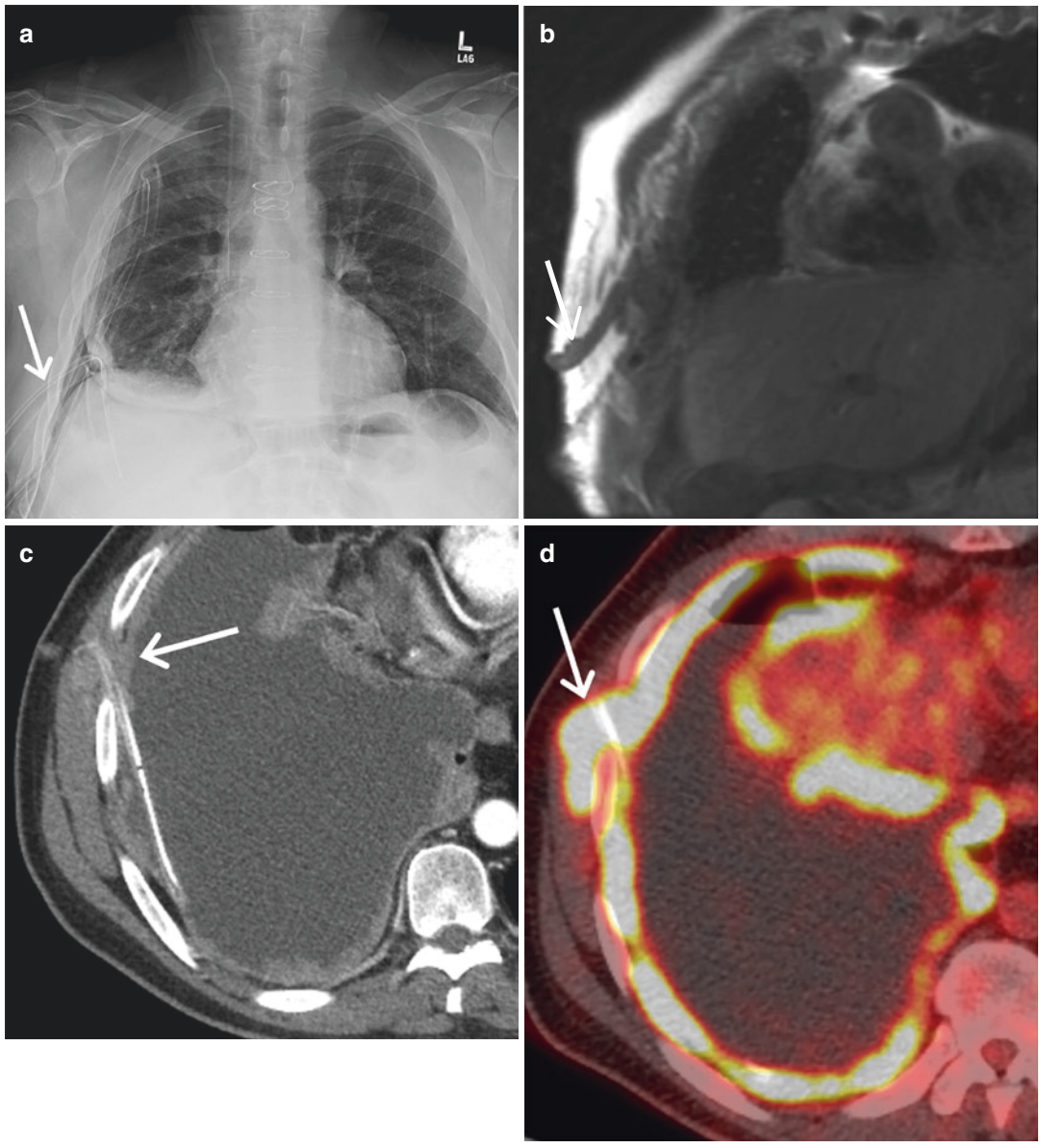


**Fig. 10.1** Tract seeding in malignant pleural mesothelioma. (**a**) Frontal radiograph of the chest shows two chest tubes entering the right thorax (arrow). (**b**) Coronal T1-weighted MRI of the right thorax in the same patient demonstrates hypointense tubular-shaped soft tissue (arrow) within the subcutaneous fat corresponding to metastatic seeding of the chest tube tracts. (**c**) Axial contrast-enhanced CT in narrow windows in another patient demonstrates a tunneled pleural catheter within a malignant right pleural effusion (arrow). A small soft-tissue nodule is present within the subcutaneous fat. (**d**) Axial fused FDG PET/CT image of the second patient shows intense FDG activity in the chest wall outside the thoracic rib cage (arrow) compatible with metastatic seeding

edition are the result of an international collaboration and analysis of case databases under the auspices of the International Association for the Study of Lung Cancer (IASLC) [16].

### 10.3.1 T Descriptor

The T component of staging for mesothelioma is based entirely upon the location of tumor tissue

and anatomic site of invasion; unlike the staging of other malignancies, measurements are not used. Nevertheless, unidimensional measurements of pleural thickness obtained for some cases in the study suggest that quantitative measures of disease burden may have prognostic value. Further work is planned to assess whether this limited preliminary data may add independent information to the staging system in the future [17, 18].

The T descriptor is categorized as follows:

| | |
|---|---|
| Tx | Primary tumor cannot be assessed |
| T0 | No evidence of primary tumor |
| T1 | Tumor of the ipsilateral pleura (parietal, visceral, mediastinal, diaphragmatic) |
| T2 | Tumor involving all ipsilateral pleural surfaces, plus at least one of the following: |
| | Invasion of the diaphragm |
| | Extension into lung parenchyma |
| T3 | Tumor involving all ipsilateral pleural surfaces, plus at least one of the following: |
| | Involvement of the endothoracic fascia |
| | Invasion of mediastinal fat |
| | Solitary, resectable focus of chest wall invasion |
| | Involvement of the pericardium without transmural invasion |
| T4 | Tumor involving all ipsilateral pleural surfaces, plus at least one of the following: |
| | Multifocal chest wall invasion, with or without rib destruction |
| | Direct transdiaphragmatic extension into the peritoneum |
| | Direct extension to the contralateral pleura |
| | Direct invasion of mediastinal organs |
| | Direct invasion of the spine |
| | Transmural involvement of the pericardium, with or without pericardial effusion |

Changes to the 8th edition include the collapsing of T1a and T1b into a single T1 category. T3 describes locally advanced but potentially resectable tumor. T4 tumors are technically not resectable [17].

### 10.3.2 N Descriptor

The N component of the MPM staging system was originally based on the N staging for lung cancer. However, lymphatic drainage of the pleura is distinct from that of the lung [10]. The 8th edition is the first evidence-based system for nodal staging of mesothelioma. Lymph node metastases occur in 35–50% of mesothelioma patients who undergo surgical resection; an autopsy series found nodal disease in 76%. Nodal metastases can decrease long-term survival by up to 50% [19].

The N descriptor is categorized as follows:

| | |
|---|---|
| Nx | Regional lymph nodes cannot be assessed |
| N0 | No regional lymph node metastases |
| N1 | Metastases of ipsilateral lymph nodes: |
| | Bronchopulmonary |
| | Hilar |
| | Mediastinal |
| | Internal mammary |
| | Peridiaphragmatic/pericardial |
| | Intercostal |
| N2 | Metastases of contralateral lymph nodes: |
| | Bronchopulmonary |
| | Hilar |
| | Mediastinal |
| | Metastases of ipsilateral *or* contralateral supraclavicular lymph nodes |

Changes from the previous edition include the categorization of all ipsilateral intrathoracic nodal diseases as N1. Supraclavicular nodes, whether ipsilateral or contralateral, constitute N2 disease, as do contralateral intrathoracic node metastases. Survival data shows greater correlation with the degree of nodal disease than with the location of nodes [19]. N2 disease generally carries a poor prognosis and may preclude surgical resection except in centers with significant expertise in MPM [12].

### 10.3.3 M Descriptor

The M component of the staging system is binary: distant metastases are present or absent. While mesothelioma is locally invasive, metastases are a late manifestation of disease.

The M descriptor is categorized as follows:

| | |
|---|---|
| M0 | No distant metastases |
| M1 | Distant metastases are present: |
| | Contralateral pleura |
| | Contralateral lung |
| | Peritoneum/abdomen |
| | Extrathoracic lymph node (excepting supraclavicular) |
| | Bone |
| | Liver |
| | Brain |
| | Other site |

Initial results of the IASLC Mesothelioma Staging Project suggest that multiplicity of metastatic lesions may have an effect on prognosis and further research on this question may inform future editions of the TNM classification [18].

**Stage groupings for 8th edition TNM Staging of Malignant Pleural Mesothelioma**

| | N0 | N1 | N2 |
|---|---|---|---|
| T1 | IA | II | IIIB |
| T2 | IB | II | IIIB |
| T3 | IB | IIIA | IIIB |
| T4 | IIIB | IIIB | IIIB |
| M1 | IV | IV | IV |

#### 10.3.3.1 Imaging Evaluation

Given the nonspecific nature of presenting symptoms, patients with undiagnosed mesothelioma may have a chest radiograph as the first imaging examination. Radiographic findings of MPM may include pleural effusion (30–80%), a pleural rind (60%), crowding of the ipsilateral ribs and volume loss, lymphadenopathy, and pulmonary nodules [10]. These radiographic findings are themselves not specific; they can also be seen in metastatic carcinomas, particularly adenocarcinomas, and in lymphoma. The presence of bilateral calcified pleural plaques supports remote asbestos exposure. An abnormal chest radiograph should prompt further evaluation: the initial assessment of pleural thickening and/or recurrent pleural effusion should include a chest CT with contrast [12].

Computed tomography (CT) is the most widely used modality in evaluation and staging of mesothelioma [5, 10]. Contrast-enhanced study is preferred. Concurrent or subsequent abdominal scanning is indicated when considering possible curative resection [12]. Magnetic resonance (MR) imaging and positron-emission tomography (PET)/CT with $^{18}$F-fluorodeoxyglucose (FDG) are useful in select patients.

CT findings of MPM include thickening of the unilateral pleural surfaces greater than 1 cm in width, with or without concurrent pleural effusion. Circumferential thickening and nodular or mass-like pleural soft tissue favor malignancy [20]. The disease often extends into the fissures. While mesothelioma may occur on either side, the right thorax is more often involved. Pleural thickening in MPM can cause entrapment of the lung and volume loss in the thorax. The mediastinum will shift toward the side of disease and the ipsilateral hemidiaphragm is elevated. The intercostal spaces decrease in width as the disease fibroses (Fig. 10.2).

Calcified pleural plaques from asbestos exposure are seen in up to 20% of mesothelioma patients [21]. These interrupted linear pleural calcifications must be distinguished from the linear opacities along the pleural surface that occur following talc pleurodesis; the talc lines are usually less dense than calcification and they also exhibit inflammation-related FDG avidity on PET/CT, unlike pleural plaques. It must also be differentiated from pleural mesothelioma that exhibits osteocartilaginous differentiation, which manifests as intratumoral foci of ossification with variable size [10] (Fig. 10.3).

Chest wall invasion by mesothelioma is considered T3 disease when solitary, but T4 disease when multifocal. Imaging findings of chest wall involvement include obliteration of extrapleural

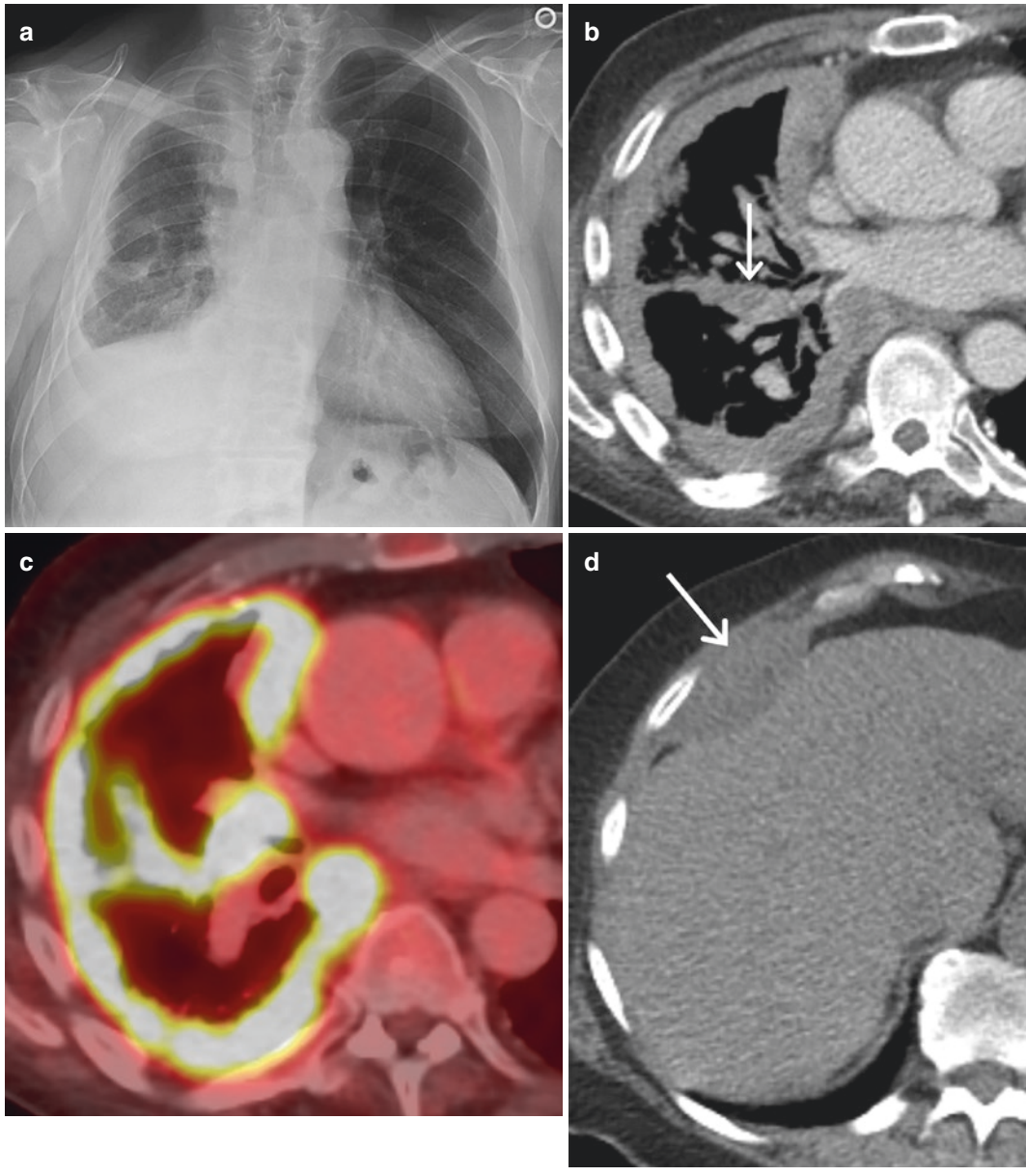


**Fig 10.2** Malignant pleural mesothelioma. (**a**) Frontal radiograph of a 76-year-old man demonstrates a pleural thickening in the right hemithorax with crowding of the ipsilateral ribs. Some dependent pleural fluid is also present. (**b**) Axial contrast-enhanced CT image in narrow windows shows circumferential pleural thickening and nodularity in the right hemithorax involving all pleural surfaces. Disease also extends along the major fissure (arrow). (**c**) Axial fused FDG PET/CT image of the same patient demonstrates intense metabolic activity in the pleural thickening. This is the most typical presentation of mesothelioma. (**d**) Axial contrast-enhanced CT image in narrow windows demonstrates a focal nodule arising from the right pleural surface in a 67-year-old man (arrow). (**e**) Axial fused FDG PET/CT image of the second patient shows intense FDG activity within the nodule. No other areas of disease were found. Limited disease at presentation has a better prognosis

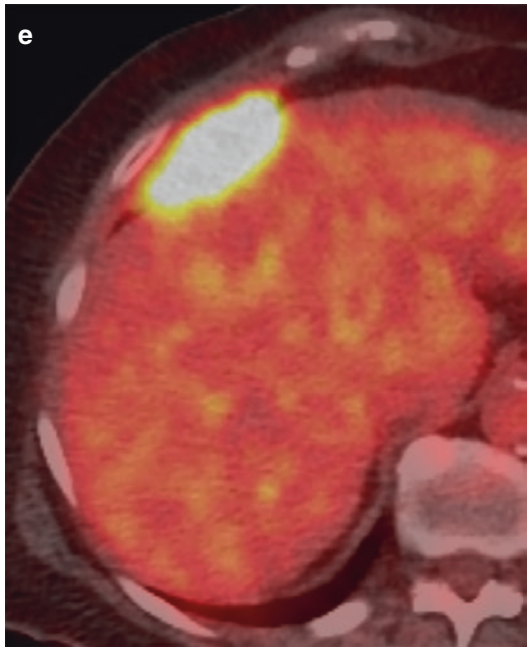


**Fig. 10.2** (continued)

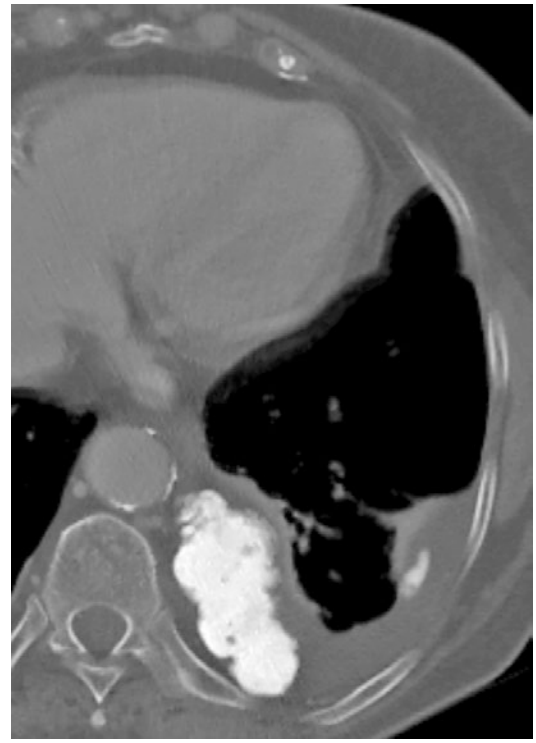

**Fig. 10.3** Mesothelioma with osteocartilaginous differentiation. Axial CT image with bone algorithm demonstrates extensive high-density material within nodular pleural disease in the left thorax. The findings represent pleural mesothelioma with osteocartilaginous differentiation, a rare variant

fat planes between the pleura and the intercostal muscles and bone displacement or destruction. In some cases the tumor exhibits gross extension through the intercostal spaces [21]. Direct mediastinal invasion obliterates the fat planes of the mediastinum, consistent with T3 tumor. Tracheal and/or esophageal invasion is suspected when they are more than 50% surrounded by tumor; both indicate T4 disease. Involvement of the pericardium may be nontransmural, T3, or transmural, T4. The preservation of subjacent epicardial fat is an indicator that the disease has not traversed the pericardium (Fig. 10.4). Findings of more extensive pericardial involvement include effusion, nodularity, and infiltrative soft tissue [10].

The accepted CT size criterion for malignant nodal involvement is ≥10 mm short axis for lymph nodes in the mediastinum or hila. There is no minimum size for nodes seen in the internal mammary, extrapleural, or retrocrural spaces; when present, they are considered positive [10]. Patterns of lymphatic drainage from the pleura and diaphragm are important for assessment of nodal disease. The anterior pleura and the anterior and lateral diaphragm are drained by internal mammary and anterior diaphragmatic lymph nodes. The posterior pleura is drained by extrapleural lymph nodes, while the posterior diaphragm is drained by para-aortic and mediastinal nodes [22]. The chest wall drains to the ipsilateral axillary and retropectoral lymph nodes [23].

Pulmonary metastases constitute one of the features of unresectable T4 disease and may be seen as discrete parenchymal nodules or lymphangitic carcinomatosis with thickening and nodularity of the interlobular septae [10]. Extrathoracic metastases can be seen in the liver, bones, brain, peritoneum and abdomen, and distant lymph nodes [18].

MR imaging can be a useful tool in evaluating features that may distinguish between resectable and unresectable disease. In particular, the excellent spatial resolution of MRI for soft tissues and the availability of dynamic sequences allow more

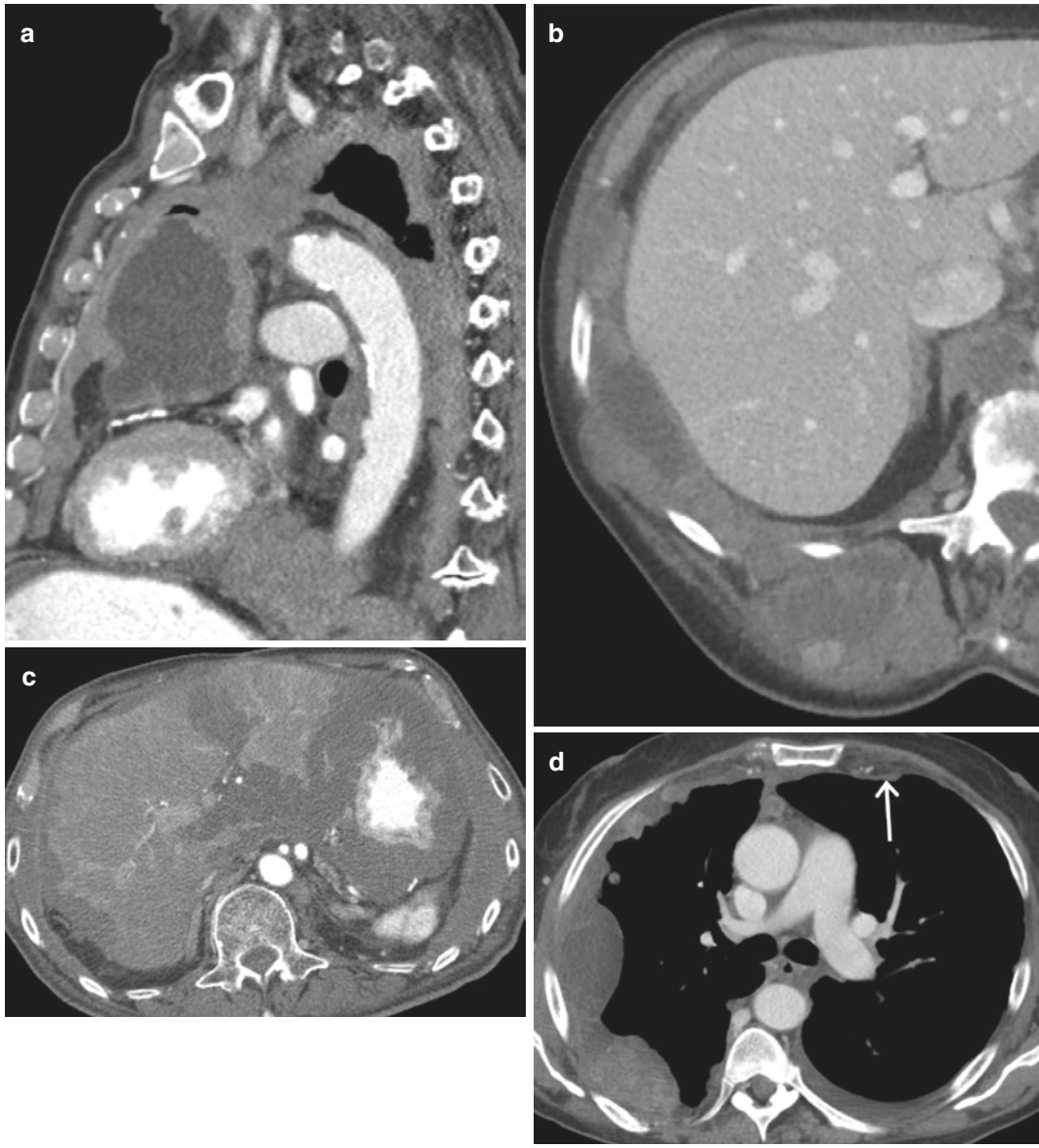


**Fig. 10.4** Malignant pleural mesothelioma, extent of disease. (**a**) Sagittal contrast-enhanced CT demonstrates a fluid collection with mural nodularity in the prevascular mediastinum. It invades the pericardium (arrowhead) without transmural extension. The pericardial fat around the atherosclerotic left anterior descending coronary artery is seen without compromise. This constitutes T3 disease. (**b**) Axial contrast-enhanced CT in narrow windows in another patient shows multiple foci of chest wall invasion (arrows), compatible with T4 disease. (**c**) Axial contrast-enhanced CT in narrow windows demonstrates extensive invasion of the upper abdomen in a patient with T4 unresectable disease. There is extension of disease along both pleural reflections (asterisks), in addition to invasive disease along the liver capsule (arrowheads) and a circumferential rind around the gastric body (arrows). (**d**) Axial contrast-enhanced CT of a patient with left thoracic mesothelioma shows thickening of the contralateral anterior pleural surface (arrow), a feature of T4 disease

definitive assessment of chest wall, diaphragm, and mediastinal, including pericardial, invasion. It is utilized where CT findings are equivocal or iodinated contrast material is contraindicated (Fig. 10.5). Pleural mesothelioma is mildly to moderately hyperintense to muscle on T1- and T2-weighted

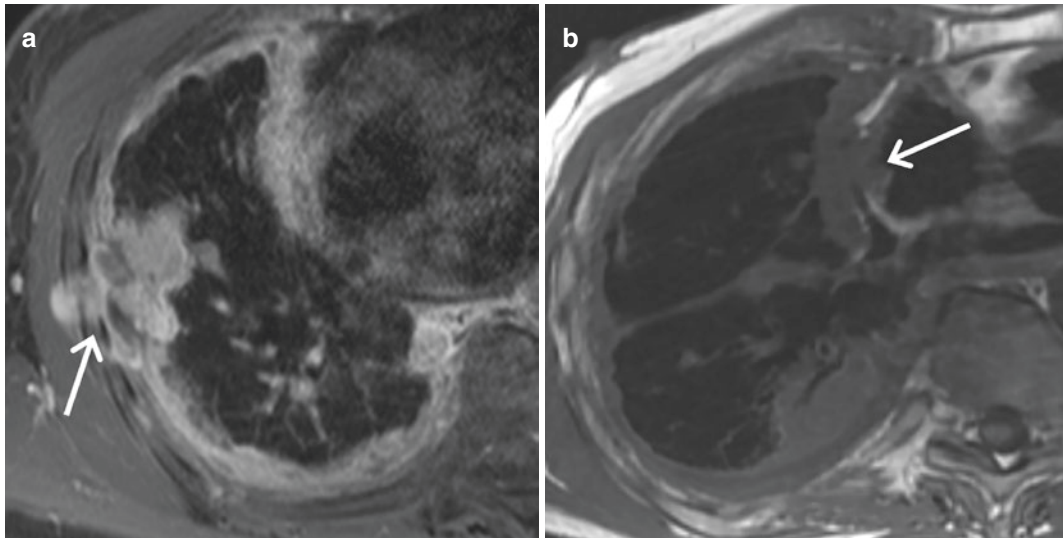


**Fig. 10.5** MRI of mesothelioma. (**a**) Axial contrast-enhanced fat-suppressed T1-weighted MRI shows focal invasion of the right chest wall by pleural disease (arrow), consistent with T3 disease. (**b**) Axial T1-weighted MRI image of the thorax shows invasion of the right atrium (arrow), a descriptor of unresectable T4 disease

sequences. It exhibits intense enhancement following intravenous administration of gadolinium contrast [10]. Accuracy of MR in determining chest wall invasion (69%) and invasion of the diaphragm (82%) exceeds that of CT (46% and 55%, respectively) [24]. Diffusion-weighted MR imaging (DWI) and apparent diffusion coefficient (ADC) calculation have been shown to correlate with histologic subtypes of MPM. Epithelioid mesothelioma has a higher ADC value than sarcomatoid and biphasic mesothelioma, with a cutoff value of $1.31 \times 10^{-3}$ mm$^2$/s [25].

FDG PET/CT is performed in patients considered for surgical resection [12]. It is demonstrated to be more accurate for MPM staging than chest CT, thoracic MRI, or PET alone. It should be undertaken prior to attempts at pleurodesis, as inflammatory uptake related to the procedure can persist for years and may confound image interpretation. PET/CT is useful for identifying nodal disease and distant metastases; it localizes metastatic disease not identified on diagnostic CT in 10% of patients [26] (Fig. 10.6). The degree of FDG avidity exhibited by MPM has been associated with median time to progression; more metabolically active tumors have shorter progression-free survival. This suggests

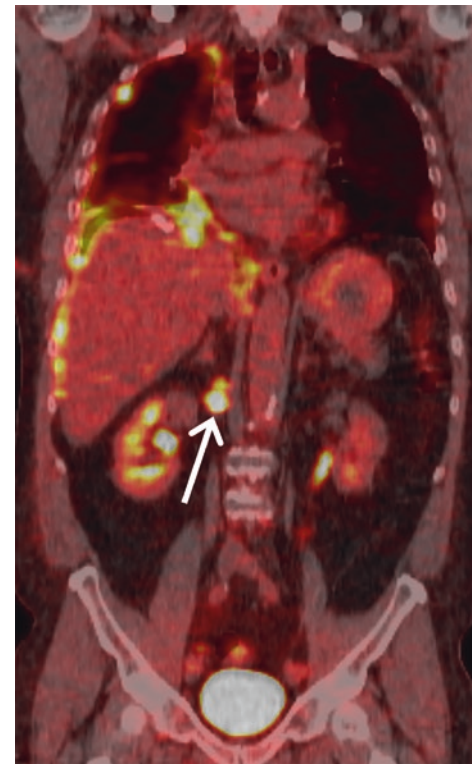

**Fig. 10.6** PET/CT of metastatic mesothelioma. Coronal fused FDG PET/CT image reveals metastatic abdominal nodal disease (arrow), which constitutes M1 disease. Curative resection is not possible

that PET/CT may be useful for patient stratification and evaluation of response to treatment. It also helps detect recurrent disease, especially in patients with extensive and complex treatment-related CT findings [10] (Fig. 10.7).

#### 10.3.3.2 Clinical and Surgical Staging

It is fairly common for clinical staging of the T descriptor to be upstaged on pathologic determination, with 56% of T1 cases, 51% of T2 cases, and 39% of T3 cases in the IASLC database receiving a higher final pathologic stage. In particular, microscopic invasion of the chest wall and pericardium and other T3 or T4 factors can be occult on imaging studies. It is rare for a stage to be downgraded [17]. Since anatomic and metabolic imaging studies may not be sufficient for complete staging of MPM, potential candidates for curative resection also undergo surgical staging to assess for disease that is not evident on imaging.

If suggested by imaging studies, patients with MPM may undergo laparoscopy to exclude peritoneal disease under the diaphragm. Video-assisted thoracoscopic surgery (VATS) should be considered if contralateral disease is suspected [12]. Either of these findings, if present, would constitute unresectable T4 disease.

Those patients who are candidates for surgery having stage I through III disease and epithelioid histology should undergo mediastinoscopy or endobronchial ultrasound fine-needle aspiration (EBUS-FNA) of mediastinal lymph nodes for definitive nodal staging. These patients will also have pulmonary function testing (PFTs), including DLCO, and a cardiac stress test, to assess cardiopulmonary reserve and ability to withstand the morbidity of extrapleural pneumonectomy or pleurectomy/decortication.

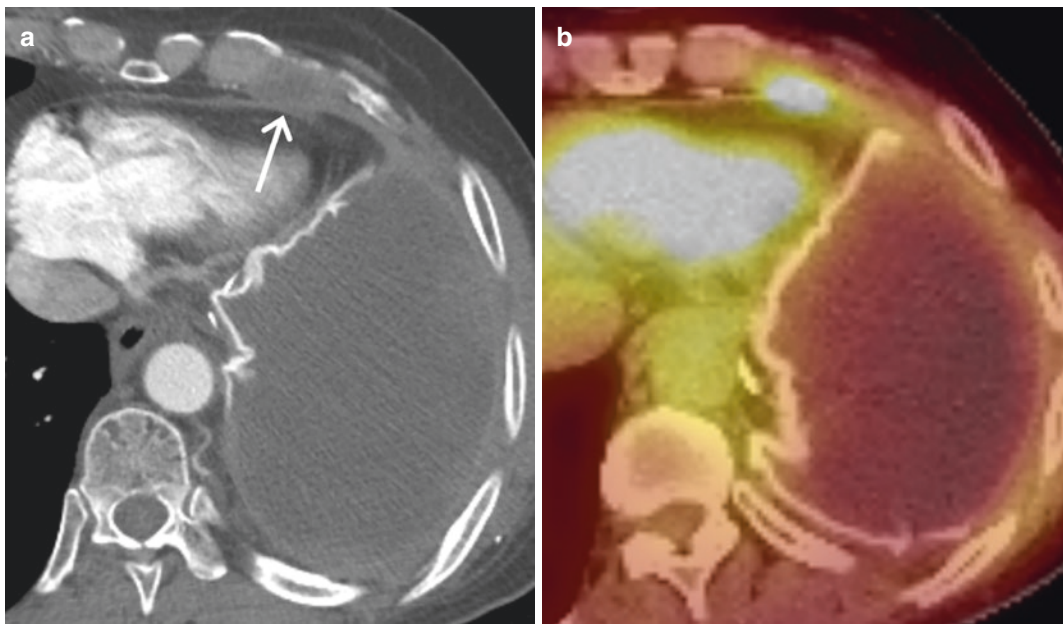


**Fig. 10.7** Recurrent malignant pleural mesothelioma. (**a**) Axial contrast-enhanced CT in narrow windows shows new nodular soft tissue (arrow) along the anterior right rib cage status post-extrapleural pneumonectomy for malignant pleural mesothelioma. (**b**) Axial fused FDG PET/CT image demonstrates intense metabolic activity of the anterior soft tissue, confirming the presence of recurrent disease

**Conclusion**

Imaging studies, including CT, MRI, and PET/CT, have an important role in staging MPM and selecting patients for appropriate therapy to improve patient management and survival outcomes. Surgical staging with mediastinoscopy, EBUS, VATS, and/or laparotomy is complementary and may be indicated for complete staging prior to resection with curative intent. Patients with early-stage disease and epithelioid histology have improved survival.

## References


1. Mark EJ, Kradin RL. Pathological recognition of diffuse malignant mesothelioma of the pleura: the significance of the historical perspective as regards this signal tumor. Semin Diagn Pathol. 2006;23(1):25–34.
2. Wagner JC, Sleggs CA, Marchand P. Diffuse pleural mesotheliomas and asbestos exposure in Northwestern Cape Province. Br J Ind Med. 1960;17:260–71.
3. Newhouse ML, Thompson H. Mesothelioma of pleura and peritoneum following exposure to asbestos in the London area. Br J Ind Med. 1965;22(4):261–9.
4. IARC. Monographs on evaluation of carcinogenic risk to humans: World Health Organization Press; 2012. http://monographs.iarc.fr/ENG/Monographs/vol100C/index.php. Accessed 28 July 2017
5. Prazakova S, Thomas PS, Sandrini A, Yates DH. Asbestos and the lung in the 21st century: an update. Clin Respir J. 2014;8(1):1–10.
6. Carbone M, Baris YI, Bertino P, et al. Erionite exposure in North Dakota and Turkish villages with mesothelioma. Proc Natl Acad Sci U S A. 2011;108(33):13618–23.
7. Robinson BM. Malignant pleural mesothelioma: an epidemiological perspective. Ann Cardiothorac Surg. 2012;1(4):491–6.
8. World Health Organization. Asbestos: elimination of asbestos-related diseases: World Health Organization Media Centre; 2017. http://www.who.int/mediacentre/factsheets/fs343/en/. Accessed 06 Sept 2017
9. Schuz J, Schonfeld SJ, Kromhout H, et al. A retrospective cohort study of cancer mortality in employees of a Russian chrysotile asbestos mine and mills: study rationale and key features. Cancer Epidemiol. 2013;37(4):440–5.
10. Nickell LT Jr, Lichtenberger JP 3rd, Khorashadi L, Abbott GF, Carter BW. Multimodality imaging for characterization, classification, and staging of malignant pleural mesothelioma. Radiographics. 2014;34(6):1692–706.
11. Galateau-Salle F, Churg A, Roggli V, Travis WD. The 2015 World Health Organization classification of tumors of the Pleura: advances since the 2004 classification. J Thorac Oncol. 2016;11(2):142–54.
12. NCCN. Malignant pleural mesothelioma *NCCN Evidence Blocks*. NCCN.org: NCCN; 2017.
13. Agarwal PP, Seely JM, Matzinger FR, et al. Pleural mesothelioma: sensitivity and incidence of needle track seeding after image-guided biopsy versus surgical biopsy. Radiology. 2006;241(2):589–94.
14. Boutin C, Rey F, Viallat JR. Prevention of malignant seeding after invasive diagnostic procedures in patients with pleural mesothelioma. A randomized trial of local radiotherapy. Chest. 1995;108(3):754–8.
15. West SD, Foord T, Davies RJ. Needle-track metastases and prophylactic radiotherapy for mesothelioma. Respir Med. 2006;100(6):1037–40.
16. Pass H, Giroux D, Kennedy C, et al. The IASLC Mesothelioma Staging Project: improving staging of a rare disease through international participation. J Thorac Oncol. 2016;11(12):2082–8.
17. Nowak AK, Chansky K, Rice DC, et al. The IASLC Mesothelioma Staging Project: Proposals for revisions of the T descriptors in the forthcoming eighth edition of the TNM Classification for Pleural Mesothelioma. J Thorac Oncol. 2016;11(12):2089–99.
18. Rusch VW, Chansky K, Kindler HL, et al. The IASLC Mesothelioma Staging Project: Proposals for the M Descriptors and for Revision of the TNM Stage Groupings in the Forthcoming (Eighth) Edition of the TNM Classification for Mesothelioma. J Thorac Oncol. 2016;11(12):2112–9.
19. Rice D, Chansky K, Nowak A, et al. The IASLC Mesothelioma Staging Project: Proposals for Revisions of the N Descriptors in the Forthcoming Eighth Edition of the TNM Classification for Pleural Mesothelioma. J Thorac Oncol. 2016;11(12):2100–11.
20. Leung AN, Muller NL, Miller RR. CT in differential diagnosis of diffuse pleural disease. AJR Am J Roentgenol. 1990;154(3):487–92.
21. Wang ZJ, Reddy GP, Gotway MB, et al. Malignant pleural mesothelioma: evaluation with CT, MR imaging, and PET. Radiographics. 2004;24(1):105–19.
22. Sharma A, Fidias P, Hayman LA, Loomis SL, Taber KH, Aquino SL. Patterns of lymphadenopathy in thoracic malignancies. Radiographics. 2004;24(2):419–34.
23. Kim SB, Varkey B, Choi H. Diagnosis of malignant pleural mesothelioma by axillary lymph node biopsy. Chest. 1987;91(2):279–81.
24. Heelan RT, Rusch VW, Begg CB, Panicek DM, Caravelli JF, Eisen C. Staging of malignant pleural mesothelioma: comparison of CT and MR imaging. AJR Am J Roentgenol. 1999;172(4):1039–47.
25. Gill RR, Umeoka S, Mamata H, et al. Diffusion-weighted MRI of malignant pleural mesothelioma: prelimiary assessment of apparent diffusion coefficient in histologic subtypes. AJR Am J Roentgenol. 2010;19592:W125–30.
26. Rusch VW. Extrapleural pneumonectomy and extended pleurectomy/decortication for malignant pleural mesothelioma: the Memorial Sloan-Kettering Cancer Center approach. Ann Cardiothorac Surg. 2012;1(4):523–31.

# 11 Imaging of Nonneoplastic Lung Diseases Requiring a Surgical Management

S. Piciucchi and A. Carloni

**Abstract**

There are several nonneoplastic disorders affecting the chest requiring a surgical treatment.

The recommendations for surgery depend on the severity of the respiratory symptoms or on the risk of further development of neoplasm.

These disorders, either congenital or acquired, include parenchymal, pleural, and airway diseases.

**Keywords**

Congenital tracheal stenosis · Bronchial atresia
Bronchopulmonary foregut malformation
Congenital lung hyperinflation (CLH)
Congenital pulmonary and airway malformations (CPAM) · Pulmonary sequestration
Pulmonary aspergillosis · Tuberculosis
Pneumothorax · Lung abscess · Empyema

## 11.1 Introduction

Lung abnormalities requiring a surgical approach represent a heterogenic group of congenital and acquired entities. Their recommendations for surgical treatment are related to a direct impairment of the respiratory function or to an increased risk of neoplastic degeneration particularly for some specific congenital abnormalities.

Congenital diseases are developmental disorders with radiologic and clinical findings that may range from a complete absence of symptoms (in that cases diagnosis is usually based on incidental findings report) to a severe impairment of the respiratory function which requires an immediate surgical treatment.

On the other hand, acquired abnormalities are usually consequence of chronic infectious or noninfectious diseases.

### 11.1.1 Embryological Development of the Lung

The onset of congenital disorders is strictly related to the different embryological steps of maturation [1].

In the prenatal period, the lung passes through five distinct phases of maturation: embryonic, pseudoglandular, canalicular, saccular, and alveolar.

S. Piciucchi (✉)
U.O. Radiologia, G.B. Morgagni Hospital, Forlì, Italy

Azienda USL Romagna, Forlì, Italy

A. Carloni
U.O. Radiologia, Santa Maria Hospital, Viale Tristano di Joannuccio, Terni, Italy


M. Anzidei, M. Anile (eds.), *Diagnostic Imaging for Thoracic Surgery*,
https://doi.org/10.1007/978-3-319-89893-3_11

Firstly, during the embryonic phase, which lasts about 7 weeks, the diverticulum of the foregut reaches the maturation.

After that, this diverticulum elongates and forms the parenchymal bud.

By the 28th day, the latter divides into two bronchial branches that enlarge and form the primary bronchi.

The pseudoglandular phase (weeks 7–16) is represented by the maturation of the airways.

The canalicular phase (weeks 17–26) includes the following events: tubular widening, differentiation of the cuboidal epithelium into type I and type II cells, and beginning of the surfactant production.

The saccular stage (weeks 27–40) includes the growth of the pulmonary parenchyma, thinning of the connective tissue between the airspaces, and further maturation of the surfactant system. These are the most important steps toward independent life.

At birth, although already functional, the lung is structurally still in an immature condition, because alveoli are practically missing.

During the first 1–3 years of postnatal life, the alveoli are formed through a multiplication process that greatly and progressively increases the gas exchange surface area, reaching the complete maturation of the gas exchange unit of the lung [1–3].

## 11.2 Congenital Airway Abnormalities

### 1. Congenital Tracheal Stenosis

Congenital tracheal stenosis represents a rare disorder characterized by a focal or diffuse narrowing of the tracheal cartilage rings. Approximately 50% of the overall congenital tracheal stenoses are of focal subtype, 30% generalized, and 20% funnel shaped [4–6].

### 2. Bronchial atresia

The bronchial atresia derives from the focal obliteration of a segmental or, more rarely, subsegmental bronchus. The consequence is the absence of communication of this branch with the central airways [7].

At the present, two are the main embryogenic theories regarding the bronchial atresia.

Firstly, it may be a consequence of an obliterated connection between the bronchial bud and the primitive bronchial cells.

Secondly, it can be the result of a focal ischemia due to the interruption of the bronchial arterial supply, with a final result of focal bronchial disconnection.

The consequence of this atresia is that the bronchi, distally to the stenosis, progressively develop a bronchocele with mucus impaction.

CT scan is the most precise modality to demonstrate either presence or features of bronchial atresia.

It can be visualized as a round or an ovoidal shape bronchus in the site of the atresia with a mosaic attenuation distally to the obliterated branch (Fig. 11.1).

If the patient has a good compliance, expiratory scan will confirm the focal air trapping.

Bronchial atresia has been described in association with other complex congenital pulmonary anomalies, such as extralobar pulmonary sequestration (in 100% of cases), intralobar sequestrations (82% of cases), CPAMs (70% of cases), and congenital lobar hyperinflation (50% of cases) [7–9].

### 3. Bronchopulmonary foregut malformations

These entities derive from an abnormal budding of the embryonic foregut and tracheobronchial tree.

They include foregut, bronchogenic, enteric, and neuroenteric cysts.

Bronchogenic cysts are the most frequent malformations originating from the ventral foregut. They can be subcarinal, representing approximately two-thirds of cases (Fig. 11.2), and intraparenchymal (one-third) [10–12].

These cysts are lined by ciliated columnar or cuboidal epithelium and filled by mucus. They can also develop an air fluid level, in case of infection (the incidence of infection is about 20% of patients).

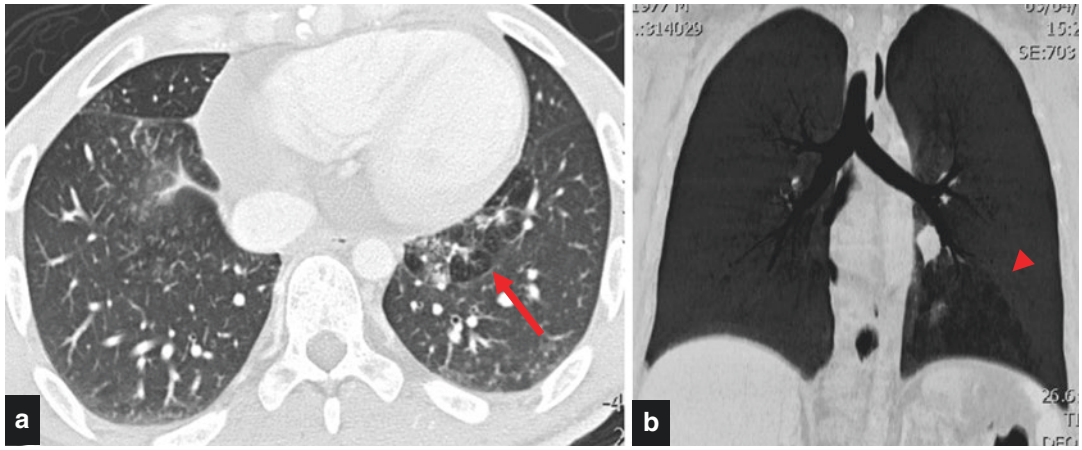


**Fig. 11.1** CT scan (**a**: axial; **b**: MinIP reconstruction) shows a mosaic attenuation in the left lower lobe (red arrow and arrowhead), with focal hypodensity related to a hyperinflation. Moreover, some mucus plugs are present in the context of the hypodensity. This finding is suggestive of bronchial atresia

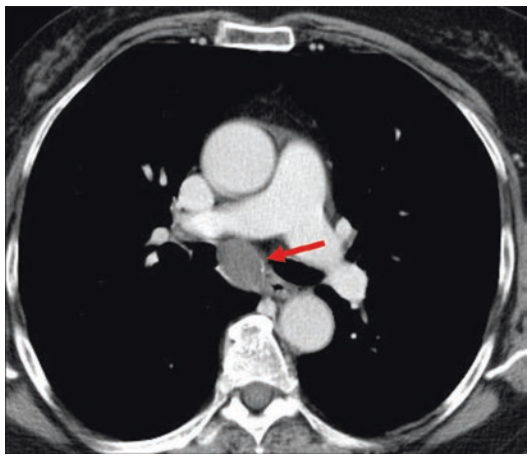

**Fig. 11.2** Hypodense ovoidal bronchogenic cyst (red arrow) in the subcarinal region

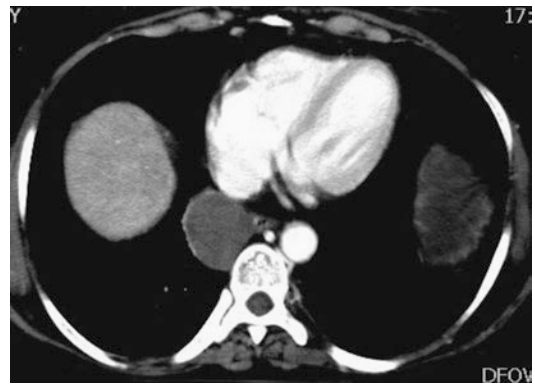

**Fig. 11.3** CT scan shows a rounded hypodense lesion which is strictly adjacent with esophagus; the finding is suggestive of duplication cyst

Symptoms include cough, wheezing, stridor, and dyspnea and are usually related to the effect of the compression on the tracheal or bronchial wall.

The differential diagnosis includes esophageal duplication cyst (Figs. 11.3 and 11.4), neuroenteric cyst, and CPAM [10–12].

In infants and children, the chest X-rays can be the first step of diagnosis, because of the fluid density. However, CT scan with contrast medium shows the highest sensitivity and spatial resolution with identification of all the structures with whom the cysts are in contact. This allows a precise plan for surgery [13–15].

## 11.3 Acquired Airway Abnormalities

1. **Tracheal stenosis**

The most common causes of tracheal stenosis are granulomatosis with polyangiitis and consequence of tracheotomy [16, 17].

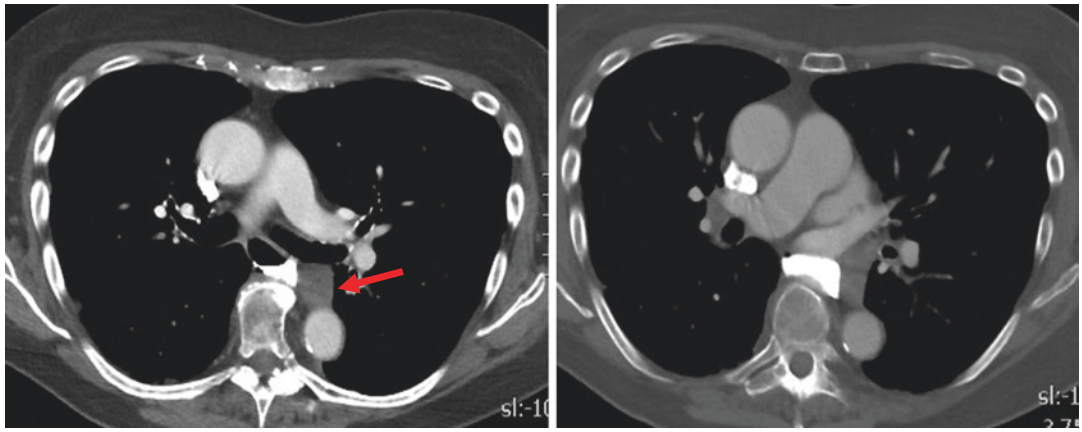

**Fig. 11.4** CT scan obtained after oral administration of iodinated hydrosoluble contrast medium. The lumen of the esophagus is hyperattenuated and closely adjacent with a duplication cyst on the left side of the wall (red arrow)

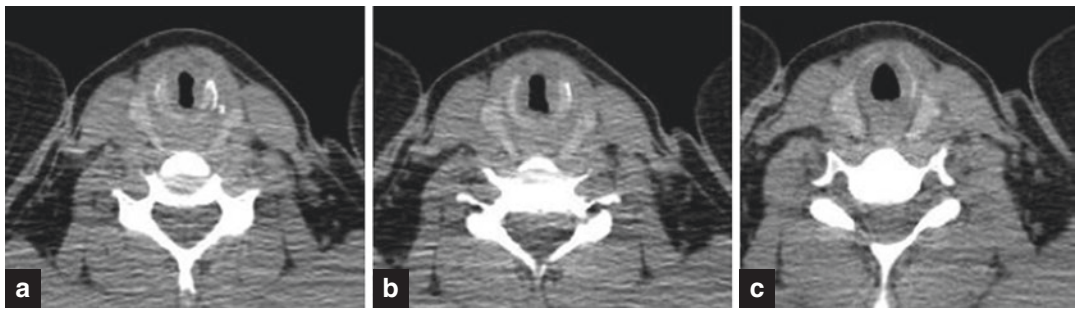


**Fig. 11.5** CT scan in a patient affected by vasculitis with polyangiitis shows a moderate mucosal thickening which causes a mild stenosis of the infraglottic tract with initial involvement of the proximal tract of the trachea. In Fig. 11.5 (**a**) there is a moderate stenosis that shows a mild improvement in (**b**) after the first bolus of cyclophosphamide and a further improvement in (**c**)

Granulomatosis with polyangiitis can give an involvement of the airways in 55% of cases, typically as a late complication. Long-term mucosal inflammation with subsequent fibrosis can cause subglottic stenosis that can be refractory to the immunosuppressive treatment (Fig. 11.5).

With regard to the post-tracheotomy stenosis, tracheostomy can facilitate a bacterial colonization through the wound. Subsequently, the removal of the tracheostomy induces a repair for secondary scar tissue healing with a possible dense scar with stenosis.

Another form of tracheal stenosis is represented by the cuff-induced stenosis, represented by the sequelae of the high-pressure cuffs of ventilation tubes. This kind of damage results in a circular necrosis of the tracheal mucosa with consequent stenosis. When the parietal damage is deeper, the injury induces the formation of granulation tissue and, later, a sandglass stenosis [16, 17].

## 2. Tracheomalacia

Malacia of the trachea is a change in shape of the lumen, with a consequent obstruction of the airflow [5].

It is the consequence of an altered wall due to a change in the elastic components.

It can also be caused by acquired conditions, like chronic inflammation (prolonged intubation, severe tracheobronchitis) or external compression (vascular, cardiac, mass).

The dynamic form of tracheomalacia can induce almost the complete obstruction of the flow during the normal breathing (Fig. 11.6).

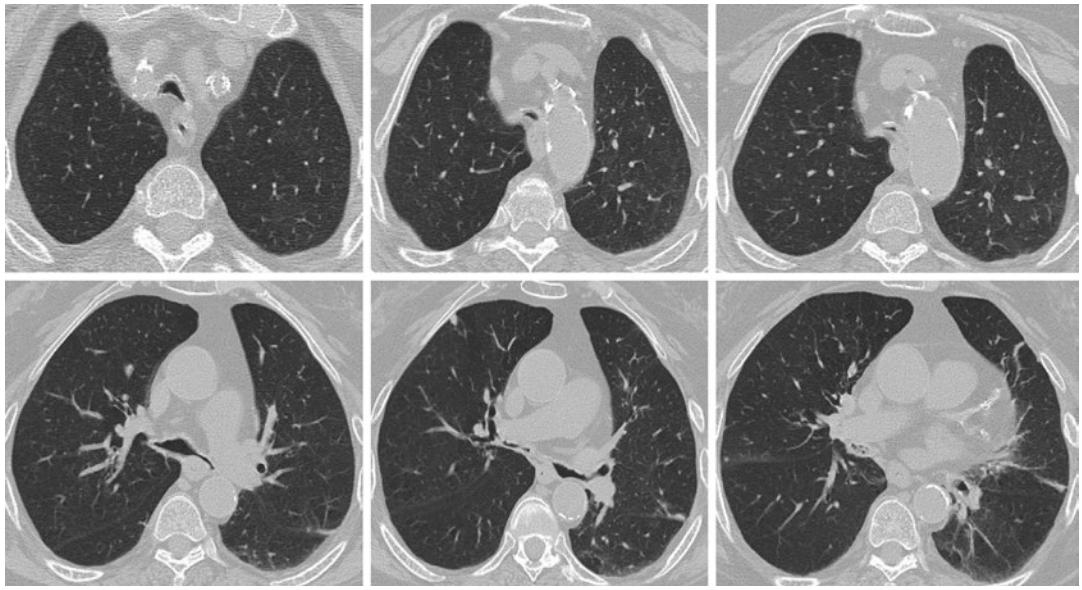

**Fig. 11.6** Severe collapse of the tracheal lumen, of the left main bronchus, and of the origin of the right inferior lobe. Bilateral mucus plugging is also present. Findings are suggestive of tracheomalacia

The clinical presentation is characterized by dyspnea, cough, and recurrent respiratory infections. Surgery is recommended in selected cases, particularly: COPD, mass, and congenital forms [5, 17, 18].

3. **Bronchopleural fistula (BPF)**

BPF is a fistulous communication between the bronchial branches and the pleural space, with severe inflammatory consequences like empyema or necrotizing pneumonias.

It can be peripheral or central, depending on the site of the communication. The fistulous tract can be central or peripheral.

The central BPF connects the trachea with the pleura. In the peripheral BPF, the connection is between the pleura and the bronchi distal to the segmental bronchi.

The most common causes are represented by invasive procedures, particularly pneumonectomy, with an incidence ranging from 2 to 20% and lobectomies with an incidence of 0.5–3%.

Moreover, other conditions can underline the occurrence of BPF: infections, rheumatoid arthritis, TB, granulomatosis with polyangiitis, and sarcoid. CT scan represents the first step in diagnosis of BPF allowing the identification of the fistulous tract and of the possible complications like abscesses and empyema. Besides the axial images, multiplanar reconstructions and virtual endoscopy may be useful, in the planning of the repair procedure [19–21].

## 11.4 Congenital Parenchymal Abnormalities

1. **Congenital Lung Hyperinflation**

Formerly named "congenital lobar emphysema," congenital lung hyperinflation (CLH) is characterized by the hyperinflation and the distension of one or multiple pulmonary lobes. It is classified into two distinct types based on the alveolar number at the histologic analysis.

The "hypoalveolar type" CLH has a smaller number of alveoli than in normal subjects.

The "polyalveolar type" CLH has 3–5 times increase in the number of alveoli in the affected

segment of the lung. Patients with the polyalveolar form of CLH may present symptoms later in the course of life compared with those affected by the hypoalveolar form [7, 22, 23].

CLH is mainly located in the left upper lobe, followed in incidence by the middle lobe (Fig. 11.7). Respiratory distress can occur in the first 6 months of life. However, the severity of the symptoms depends on the amount of parenchymal involvement.

Diagnosis of CLH is generally performed during the prenatal ultrasound. Fetal US shows in fact a hyperechoic mass of the left upper lobe.

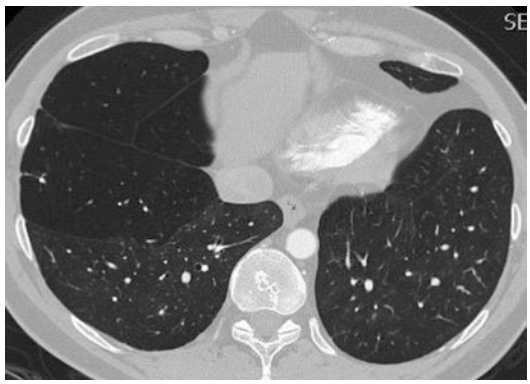

**Fig. 11.7** Extensive hypoattenuation of the middle and right upper lobe related to hyperinflation and distension. The findings are suggestive of congenital lung hyperinflation

The fetal MR shows a homogeneous mass characterized by an increase of T2 signal.

In the chest X-rays, the CLH typically shows time-related changes of morphology after the birth. Indeed, in the first 2 h of life, CLH is still an opacity with water density related to the fluid retention by the fetal lung. As the fluid is drained, the affected lobe becomes hyperlucent.

CT scan may be helpful in identification of the extension of the disease.

Surgical lobectomy is the main indication for this entity. Furthermore, it becomes urgent in cases of large lesions [7, 23].

## 2. Congenital Pulmonary and Airway malformations

Formerly named as "congenital cystic adenomatoid malformations," congenital pulmonary and airway malformations (CPAMs) derive from an early anomalous development of the airways, due to an overgrowth of the primary bronchioles (Fig. 11.8).

CPAM was first described by Stocker and colleagues [24] and subsequently renamed and reclassified into five types (0–4) by the same author [25].

The CPAM type 0 is the consequence of a marked dysgenesis of the acinus or of the large airways that involves the whole parenchyma and it is not compatible with life.

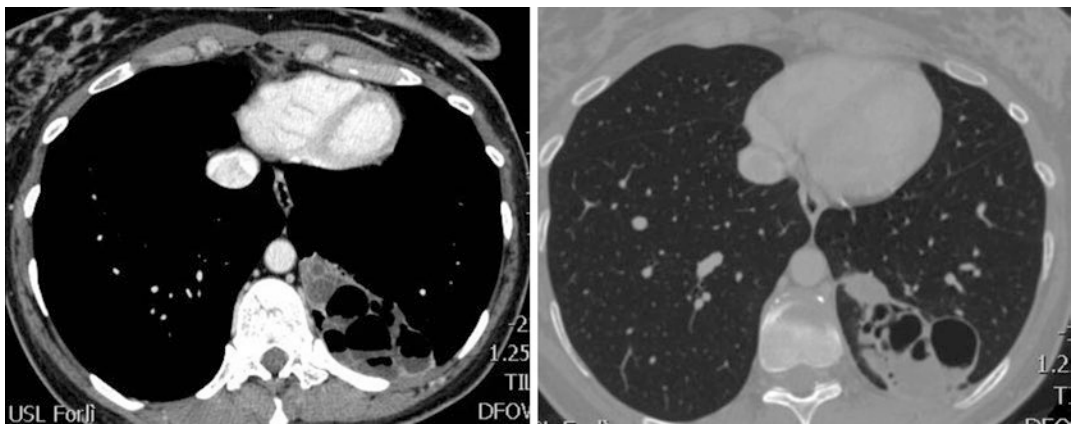

**Fig. 11.8** Loculated lesion in the left lower lobe, characterized by multiple cysts, most of them with air fluid levels. They measure from few mm to 2cm in size. These findings are suggestive of type 2 CPAM

The CPAM type 1 consists of unique or multiple cysts that are bigger than 2 cm in size. The epithelium of this cyst may be bronchiolar or bronchial.

The CPAM type 2 is characterized by single or multiple cysts with size ranging from 0.5 to 2 cm.

The CPAM type 3 is characterized by multiple microcystic lesions, with cysts measuring less than 5mm.These lesions derive from the distal bronchiolar tract.

Finally, the CPAM type 4 is a lesion with acinar origin. Even though symptoms include respiratory distress, CPAM may also remain completely asymptomatic and can be discovered in adulthood. Nowadays, prenatal diagnosis can easily identify the presence of CPAMs.

### 3. Pulmonary sequestration

The pulmonary sequestration is represented by an anomalous portion of parenchyma that doesn't have any connection with the tracheobronchial tree and receives the arterial supply by the systemic arteries originating from subclavian, celiac, and intercostal splenic and rarely from coronary arteries [22].

The pulmonary sequestration has been subclassified into intralobar or extralobar, based on the pleural layers and venous drainage.

The intrapulmonary sequestration (about 75% of cases) drains into the pulmonary veins of the same side and doesn't show its own pleural investment.

On the other hand, the extralobar sequestration (about 25% of cases) has its pleural layer and a systemic venous drainage (azygous, portal veins, or subclavian vein).

A first diagnostic suspicion can derive from the mass-like effect that the sequestration shows in the chest radiograph.

Then, a CT angiography clearly demonstrates the consolidate lesion with systemic arterial supply. The venous phase can also visualize if the sequestration has a pulmonary or systemic drainage (Fig. 11.9).

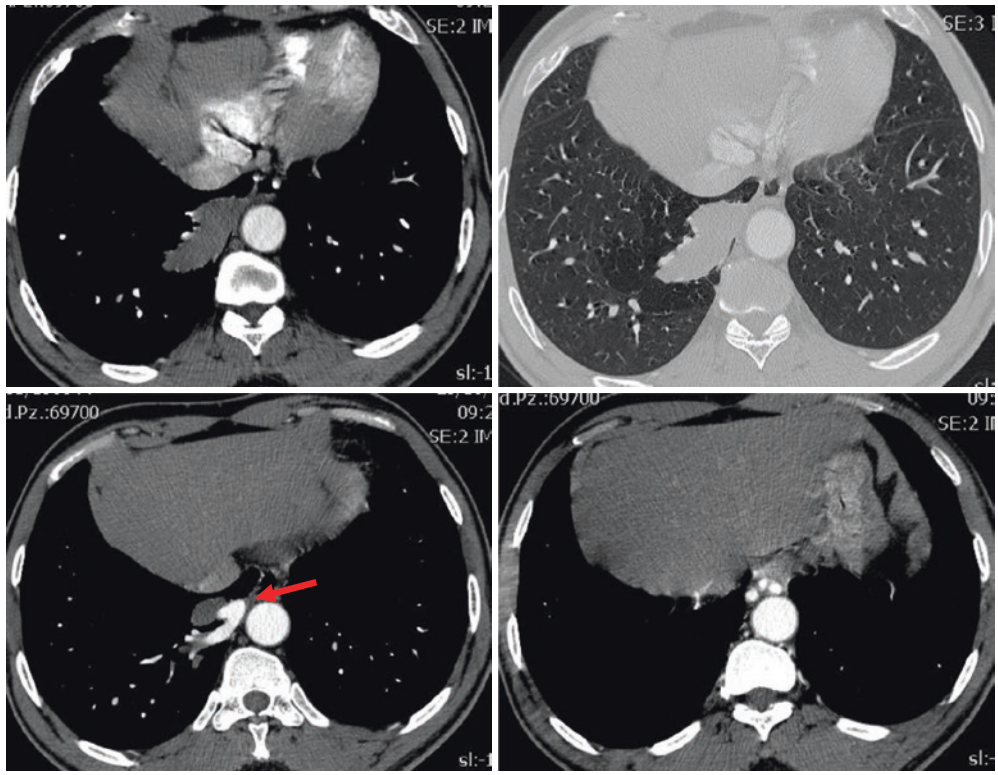

**Fig. 11.9** CT scan of an intralobar sequestration. The consolidated lesion in right lower lobe is surrounded by mosaic attenuation and is supplied by a recurrent artery arising from the celiac artery

The pulmonary sequestration may develop several infectious complications. For this reason, the surgical resection is recommended [7, 22].

## 11.5 Acquired Parenchymal Abnormalities

The acquired nonneoplastic diseases for which there is indication for surgical resection, include chronic pulmonary aspergillosis, drug-resistant-tuberculosis, and pulmonary abscesses.

1. **Chronic Pulmonary Aspergillosis**

Chronic pulmonary aspergillosis (CPA) is represented by a chronic cavitary pulmonary aspergillosis and, less commonly, by the aspergillus nodule or a single aspergilloma. In all these cases, the patients are usually immunocompetent, with a prior or coexistent underlying pulmonary disease.

Recently the European Consensus has published the new guidelines for management of the several manifestations of CPA.

In all the above-cited forms, diagnosis requires CT scan with findings highly confident with CPA and evidence of aspergillus directly or through serological dosage [26, 27].

(1a) **Single Aspergilloma**. It represents a late form of disease and is represented by a fungal ball into a preexistent pulmonary cavity (tubercular cavity, NTB lesions, ABPA, honeycombing, rheumatoid nodules, silicosis, fibrotic sarcoid) (Fig. 11.10). Besides the parenchymal lesions, pleural cavities can be involved, such as in case of chronic pneumothorax. In the cavity, a mat of fungal growth starts the colonization. It is characterized by an ovoidal, solid intracavitary lesion, partially surrounded by air in the upper portion, creating the air crescent sign that is mobile in the prone position. The fungal balls don't have enhancement after contrast medium. Wherever the fungus colonization occurs in the pleural space, it can give empyema.

(1b) **Chronic Cavitary Pulmonary Aspergillosis (CCPA).** This entity was formerly named "complex aspergilloma" and is characterized by multiple cavities containing aspergillomas. If these lesions are left untreated, they may increase and coalesce. A possible evolution of these lesions is represented by chronic

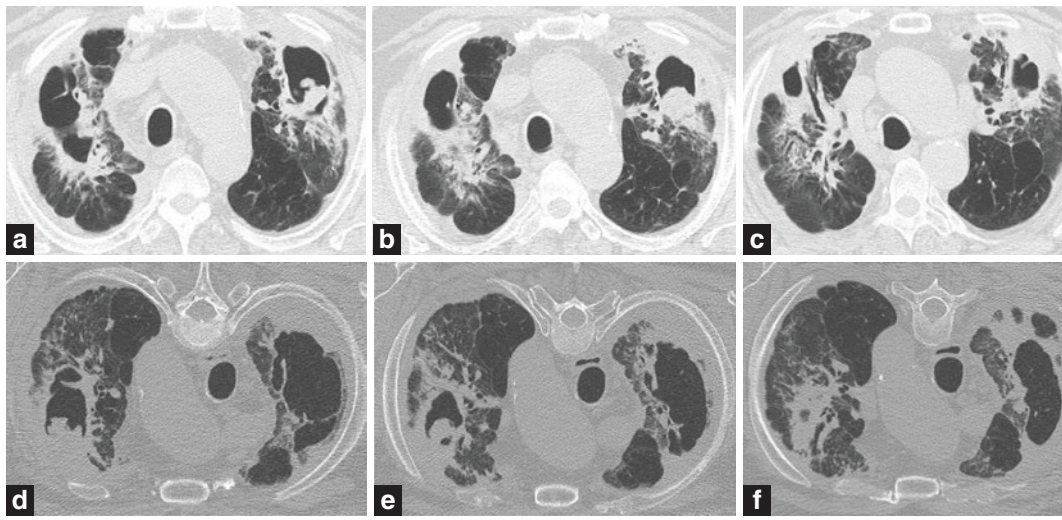


**Fig. 11.10** Big cavitary lesions in both upper lobes in a severe parenchymal distortion caused by Langerhans cell histiocytosis. The images (**a**, **b**, **c**) are in supine position, whereas the images (**d**, **e**, **f**) are in prone position. In the cavity of left upper lobe, amorphous material is present and its mobile with the prone position

fibrosing pulmonary aspergillosis (CFPA) that is a fibrotic mass surrounding multiple cavitary lesions. CCPA usually destroys at least two lobes. In the presence of extensive CCPA and CFPA multiple bronchiectasis can be present. Moreover, some pseudoaneurysm may coexist, being cause sometimes of severe hemoptysis.

(1c) **Aspergillus Nodule.** These nodular lesions are commonly less than 3 cm in size and can mimic neoplastic lesions or other chronic infections like tuberculomas or cryptococcal nodules.

(1d) **Subacute Invasive Aspergillosis (SAIA).** This form was formerly named as semi-invasive aspergillosis. SAIA is commonly seen in moderately immunocompromised patients (diabetes mellitus, malnutrition, alcoholism).

Besides the medical treatment with antifungal drugs, surgical procedures remain indicated as definitive treatment of aspergilloma.

Moreover, surgery is recommended in all cases of hemoptysis following a catheter embolization of the bronchial arteries. Procedures include bullectomy, segmentectomy, sublobar resection, wedge resection, lobectomy, pleurectomy, and pneumonectomy.

2. **Drug-Resistant Tuberculosis**

Surgical procedures can be advocated in those cases of tuberculosis which have resistance to the medical treatment [27–30]. The rationale that supports surgery is that resecting active TB lesions dramatically reduces the overall bacilli in the lung and removes the sites of resistance to therapy.

Candidates to the surgery should have the following criteria: localized disease, adequate pulmonary reserve, and persistent positive sputum smears or cultures despite treatment. Tseng et al. [29] demonstrated that, even though around 50% of patients undergoing VATS therapeutic resection were converted to thoracotomy, patients with medically failed pulmonary TB could benefit from VATS before complicated and irreversible parenchymal damage occurred (Fig. 11.11).

In those patients with contraindications for resections, the collapse thoracoplasty represents a second choice [27–30].

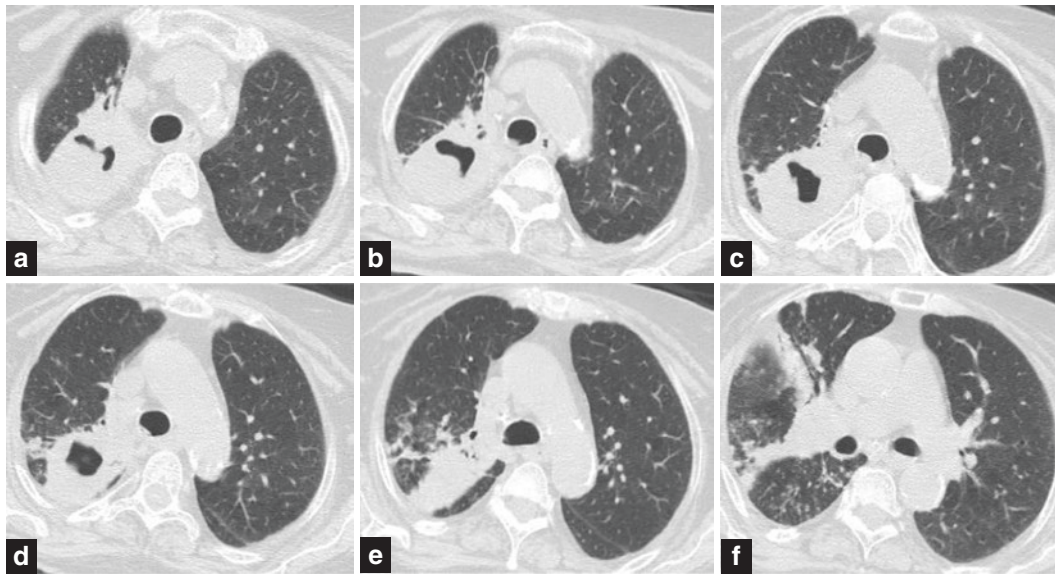


**Fig. 11.11** Cavitary lesion with thickened wall is present in the right upper lobe (**a**–**d**). Multiple centrilobular nodules with tree-in-bud are present in the right upper lobe, middle lobe, and apical segment of right lower lobe (**e**–**f**). These findings are related to tubercular cavitation with endobronchial spread

3. **Lung abscess**

The abscess is defined by a circumscribed area of debris inside the parenchyma. The natural history of the abscess is the progression to the cavitary lesion, and the formation of the bronchopulmonary fistula with consequent formation of the air-fluid level [31–33]. The abscess can be primary when it derives from the aspiration from the oropharyngeal tract or secondary when it is the consequence of a preexisting condition such as congenital malformations (sequestration), bronchial branch obstructions (bronchogenic neoplasms, adenopathies, or foreign bodies), bronchiectasis, cystic fibrosis, emphysema, infarcts, traumatic contusion, and hematogenic dissemination of the infection (sepsis, endocarditis, infection of central lines, Lemierre's syndrome). Histologically, the abscess is characterized by numerous neutrophilic granulocytes and bacteria. The abscess sometimes can be difficult to differentiate from the empyema. However, it is a rounded lesion in the CT scan and it's surrounded by a consolidated and/or necrotic parenchyma. It tends to form an acute angle with the pleural surface in contrast with the loculated empyema, in which the angle is obtuse. In children the abscesses tend to drain spontaneously. In adults, the first approach is the medical therapy as well.

However, the surgical removal or percutaneous drainage is required in a percentage ranging from 11 to 21% [31–33].

## 11.6 Acquired Pleural Abnormalities

1. **Pneumothorax**

Pneumothorax is represented by the presence of gas in the pleural space. Spontaneous pneumothorax is divided into primary (PSP) and secondary (SSP), based on the presence (secondary type) or absence (primary type) of parenchymal abnormalities in the underlying portion of the lung [34–42].

It can be visualized in the upright position on the chest X-ray as a radiolucent space, usually in the apical portion of the affected hemithorax (Fig. 11.12).

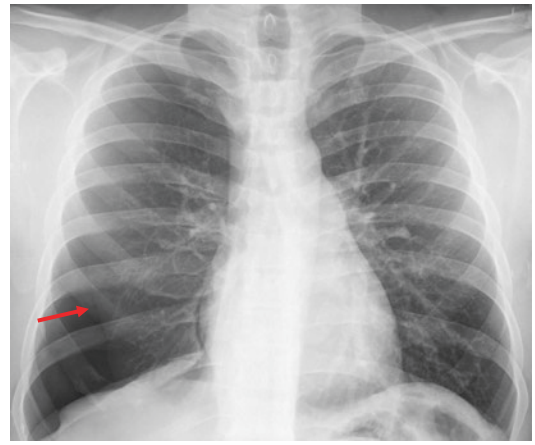

**Fig. 11.12** Chest X-rays show right pneumothorax with a mild contralateral shift of mediastinum

When the radiograph is obtained in the supine position, the air collection is localized anteriorly creating a sharp margin of the hemidiaphragm, with the so-called deep sulcus sign. A relevant complication of the pneumothorax is represented by the tension-pneumothorax, in which mediastinum shows a contralateral shift and there is a concomitant depression of the hemidiaphragm ipsilateral to the pneumothorax, due to the increased pressure in the pleural space. This entity represents an emergency and requires urgent placement of the chest tube.

The most important risk factor for PSP is tobacco smoking, with an increase of the risk of about ninefold in women and 22-fold in men [39–42].

Moreover, height and low mass index have been described as associated to an increased incidence of pneumothorax.

On the other hand, SSP can occur as a complication of preexisting abnormalities: chronic obstructive pulmonary disease, cystic fibrosis [39], cystic diseases (Birt-Hogg-Dubè; LAM, Langerhans cell histiocytosis) [39, 40], pleuroparenchymal fibroelastosis [41], lung malignancy (primary or metastatic), and necrotizing pneumonia [42] (Fig. 11.13).

The management of persistent or recurrent PSP continues to be debated. However, there is a

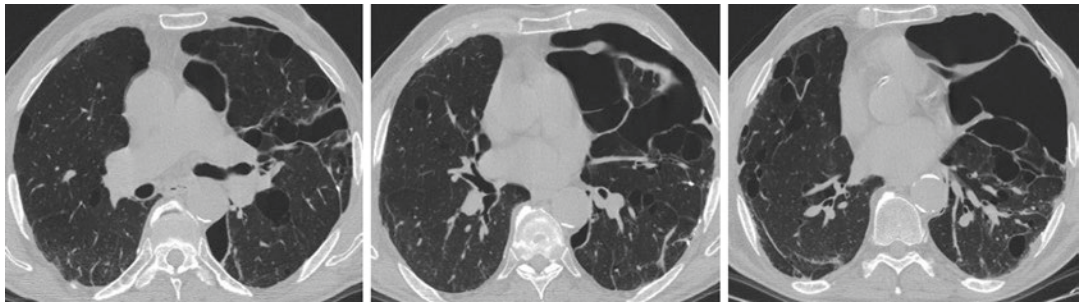

**Fig. 11.13** CT scan shows bilateral cysts, with regular morphology and variable sizes. These findings are suggestive of Birt-Hogg-Dubé. Moreover, in the left hemithorax a chronic pneumothorax which is present also in the fissure. Multiple sediments are present in the pleural space

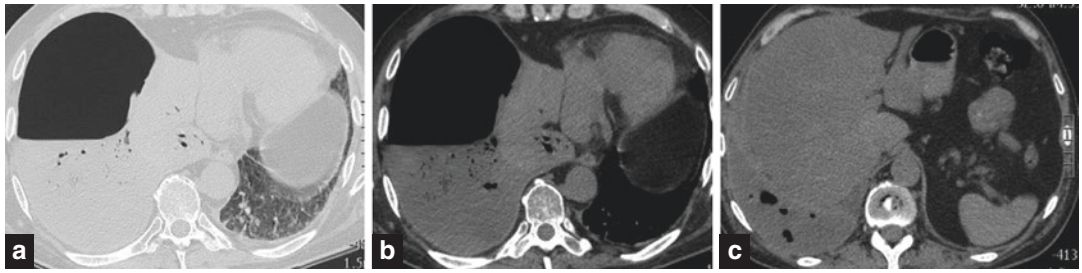


**Fig. 11.14** CT scan with lung window (**a**) and mediastinal window (**b**, **c**) shows a significant amount of pleural effusion in the right hemithorax. This effusion has several spots in the pleural fluid and an air fluid level that are suggestive of hydropneumothorax, resembling an empyema

general agreement that the definitive-surgical treatment should be considered for those patients with second episode of PSP; persisting air leak >3–5 days; hemopneumothorax; bilateral pneumothorax; and professional risk [42].

2. **Empyema**

The empyema occurs when the infection spreads into the pleural space.

The first consequence is that pleural effusion can be loculated or not.

In most cases, CT scan is not required. Ultrasound can in fact well identify the amount and the features (sedimentations, fibrosis) of the empyema. 3.5–5.0 MHz sector transducer probes show an acceptable spatial resolution at low depth to better study the pleural space.

Whenever it's required, it should be performed with a delay from the contrast medium administration of about 60 s, to allow the best enhancement of the pleural surface. In the early phase (so-called exudative), the empyema shows only a moderate pleural fluid related to the increased permeability of the pleura. No significant thickening of the parietal and visceral pleural is seen. In the fibrinopurulent phase, a significant thickening of the pleural layers occurs. Parietal and visceral pleura are separated by loculated fluid that creates the "split pleura" sign. In the last phase, the empyema develops fibrosis in the pleural space with a marked thickening of the pleura. Air fluid level is often observed [43]. Thoracoscopy for drainage of the purulent fluid is recommended in these cases.

## References

1. Keslar P, Newman B, Oh KS. Radiographic manifestation of anomalies of the lung. Radiol Clin North Am. 1991;29:255–70.
2. Skandalakis JE, Gray SW, Symbas P. The trachea and the lung. In: Skandalakis JE, Gray SW, editors.

Embryology for surgeons. 3rd ed. Baltimore, MD: Williams & Wilkins; 1994. p. 414–50.
3. Kluth D, Fiegel H. The embryology of the foregut. Semin Pediatr Surg. 2003;12:3–9.
4. Wailoo M, Emery JL. Structure of the membranous trachea in children. Acta Anat. 1980;106:254–61.
5. Beasley SW, Qi BQU t. J Pediatr Child Health. 1998;34:209–10.
6. Cox WL, Shaw RR. Congenital chondromalacia of the trachea. J Thorac Cardiovasc Surg. 1965;49: 1033–9.
7. Lee EY, Dorkin H, Vargas SO. Congenital pulmonary malformations in pediatric patients: review and update on etiology, classification, and imaging findings. Radiol Clin North Am. 2011;49(5):921–48.
8. Berrocal T, Madrid C, Novo S, et al. Congenital anomalies of the tracheobronchial tree, lung, and mediastinum: embryology, radiology, and pathology. Radiographics. 2004:24.
9. Riedlinger WF, Vargas SO, Jennings RW, et al. Bronchial atresia is common to extralobar sequestration, intralobar sequestration, congenital cystic adenomatoid malformation, and lobar emphysema. Pediatr Dev Pathol. 2006;9(5):361–73.
10. Bronchogenic cyst: imaging features with clinical and histopathologic correlation. Radiology. 2000;56:441–6.
11. Kim KW, Kim WS, Cheon JE, et al. Complex bronchopulmonary foregut malformation: extralobar pulmonary sequestration associated with a duplication cyst of mixed bronchogenic and esophageal type. Pediatr Radiol. 2001;3:265–8.
12. Nuchtern JG, Harberg FJ. Congenital lung cysts. Semin Pediatr Surg. 1994;3:233–43.
13. Ashizawa K, Okimoto T, Shirafuji T, Kusano H, Ayabe H, Hayashi K. Anterior mediastinal bronchogenic cysts: demonstration of complicating malignancy by CT and MRI. Br J Radiol. 2001;74:959–61.
14. Hantous-Zannad S, Charrada L, Mestiri I, et al. Radiological and clinical aspects of bronchogenic lung cysts: 4 case reports. Rev Pneumol Clin. 2000;56:249–54.
15. Winters WD, Effmann EL. Congenital masses of the lung: prenatal and postnatal imaging evaluation. J Thorac Imaging. 2001;16:196–206.
16. Cooper JD, Grillo HC. The evolution of tracheal injury due to ventilatory assistance through cuffed tubes: a pathologic study. Ann Surg. 1969;169:334–48.
17. Stoelben E, Koryllos A, Beckers F, Ludwig C. Benign stenosis of the trachea. Thorac Surg Clin. 2014;24:59–65.
18. Kudela O, Kocova E, Sedlak V, Koblizek V, Novotna B, Balzek M. Dynamic CT in diagnostics of tracheomalacia. Eur Respir J. 2015;46(Suppl 59)
19. Gaur P, Dunne R, Colson YL, Gill RR. Bronchopleural fistula and the role of contemporary imaging. J Thorac Cardiovasc Surg. 2014;148:341–7.
20. Sirbu H, Busch T, Aleksic I, Schreiner W, Oster O, Dalichau H. Bronchopleural fistula in the surgery of non-small cell lung cancer: incidence, risk factors, and management. Ann Thorac Cardiovasc Surg. 2001;7:330–6.
21. Cerfolio RJ. The incidence, etiology, and prevention of postresectional bronchopleural fistula. Semin Thorac Cardiovasc Surg. 2001;13:3–7.
22. Lee EY, Boiselle PM, Cleveland RH. Multidetector CT evaluation of congenital lung anomalies. Radiology. 2008;247(3):632–48.
23. Cleveland RH, Weber B. Retained fetal lung liquid in congenital lobar emphysema: a possible predictor of polyalveolar lobe. Pediatr Radiol. 1993;23(4):291–5.
24. Stocker JT. Congenital pulmonary airway malformation: a new name for and an expanded classification of congenital cystic adenomatoid malformation of the lung. Histopathology. 2002;41(Suppl 2):424–30.
25. Stocker JT, Madewell JE, Drake RM. Congenital cystic adenomatoid malformation of the lung. Classification and morphologic spectrum. Hum Pathol. 1977;8:155–71.
26. Denning WA, Cadranel J, Beigelman-Aubry C, et al. Chronic pulmonary aspergillosis: rationale and clinical guidelines for diagnosis and management. Eur Respir J. 2016;47(1):45–68.
27. Shiraishi Y, Katsuragi N, Kita H, et al. Aggressive surgical treatment of multidrug-resistant tuberculosis. J Thorac Cardiovasc Surg. 2009;138:1180–4.
28. Man MA, Nicolau D. Surgical treatment to increase the success rate of multidrug-resistant tuberculosis. Eur J Cardiothorac Surg. 2012;42:e9–12.
29. Tseng YL, Chang JM, Liu YS, et al.. The Role of Video-Assisted Thoracoscopic Therapeutic Resection for Medically Failed Pulmonary Tuberculosis. Medicine 2016; 95
30. World Health Organization. The role of surgery in the treatment of pulmonary TB and multidrug- and extensively drug-resistant TB: World Health Organization; 2014.
31. Seo H, Cha SI, Shin KM. Focal necrotizing pneumonia is a distinct entity from lung abscess. Respirology. 2013;18:1095–100.
32. Kuhajda I, Zarogoulidis K, Tsirgogianni K, Tsavlis D, Kioumis I, Kosmidis C, Tsakiridis K, Mpakas A, Zarogoulidis P, Zissimopoulos A, Baloukas D, Kuhajda D. Lung abscess-etiology, diagnostic and treatment options. Ann Transl Med. 2015;13:183.
33. Erasmus J, Page McAdams H, Rossi S, Kelly M. Percutaneous management of intrapulmonary air and fluid collections. Radiol Clin North Am. 2000;38:385–93.
34. Tschopp JM, Bintcliffe O, Astoul P, Canalis E, Driesen P, Janssen J, Krasnik M, Maskell N, Van Schil P, Tonia T, Waller DA, Marquette CH, Cardillo G. ERS task force statement: diagnosis and treatment of primary spontaneous pneumothorax. Eur Respir J. 2015;46:321–35.
35. Withers JN, Fishback ME, Kiehl PV, et al. Spontaneous pneumothorax. Suggested etiology and comparison of treatment methods. Am J Surg. 1964;108:772–6.

36. Marquette CH, Marx A, Leroy S, et al. Simplified stepwise management of primary spontaneous pneumothorax: a pilot study. Eur Respir J. 2006;27: 470–6.
37. Bense L, Eklund G, Wiman LG. Smoking and the increased risk of contracting spontaneous pneumothorax. Chest. 1987;92:1009–12.
38. Flume PA, Strange C, Ye X, et al. Pneumothorax in cystic fibrosis. Chest. 2005;128:720–8.
39. Gupta N, Vassallo R, Wikenheiser-Brokamp KA, McCormack FX. Diffuse cystic lung disease. Part I. Am J Respir Crit Care Med. 2015;191:1354–66.
40. Gupta N, Vassallo R, Wikenheiser-Brokamp KA, McCormack FX. Diffuse cystic lung disease. Part II. Am J Respir Crit Care Med. 2015;192:17–29.
41. Kokosi MA, Nicholson AG, Hansell DM, Wells AU. Rare idiopathic interstitial pneumonias: LIP and PPFE and rare histologic patterns of interstitial pneumonias: AFOP and BPIP. Respirology. 2016;21:600–14.
42. Noppen M, De Keukeleire T. Pneumothorax. Respiration. 2008;76:121–7.
43. Reynolds JH, McDonald G, Alton H, Gordon SB. Pneumonia in the immunocompetent patient. Br J Radiol. 2010;(996):998–1009.

# Lung and Airway Surgical Procedures

12

Marco Anile, Sara Mantovani, Massimiliano Bassi, Carolina Carillo, Daniele Diso, and Federico Venuta

**Abstract**

Notwithstanding that some basilar technical and oncological concepts are still valid, thoracic incisions and surgical techniques to cure lung and airway diseases have been progressively modified during the years. Minimally invasive surgery is by now considered the preferred approach in early stages of lung cancer. The improvement of perioperative patient's management and of technology has allowed performing more and more difficult and extended procedures with good results in terms of early and long-term survival. Finally, surgery represents a valid option for very selected emphysema patients.

**Keywords**

Thoracic incisions · Pulmonary resections · Extended resections

## 12.1 Introduction

Although it is not possible to identify a specific event that marks the birth of thoracic surgery, it is in second half of the nineteenth century, after the safety demonstration of ether anesthesia, that physicians in different countries began to explore the possibility to solve chest diseases with surgery. During the years, a number of personalities have contributed to create and develop surgical techniques that we actually use; of course the improvement of technology and of intraoperative patient's management has determined changes into the modalities of surgical procedures, even if the concepts of management of pleural cavity, appropriate manipulation of pulmonary parenchyma, isolation and dissection of hilar elements, control of mediastinal structures, and management of intraoperative and perioperative complications still remain stable and are of paramount importance.

In this chapter we initially present the several incisions to open the chest cavity and subsequently we describe the most frequent surgical procedures to perform pulmonary resections.

## 12.2 Thoracic Incisions

Although several incisions have been developed to enter the thorax, the basilar concept is that the incision should be performed to easily and safely expose the hilum of the lung that represents the site of the most challenging part of the surgery during standard pulmonary resections. For many years only two ways to

M. Anile (✉) · S. Mantovani · M. Bassi
C. Carillo · D. Diso · F. Venuta
Department of Thoracic Surgery, Policlinico Umberto I, University of Rome Sapienza, Rome, Italy
e-mail: marco.anile@uniroma1.it


M. Anzidei, M. Anile (eds.), *Diagnostic Imaging for Thoracic Surgery*,
https://doi.org/10.1007/978-3-319-89893-3_12

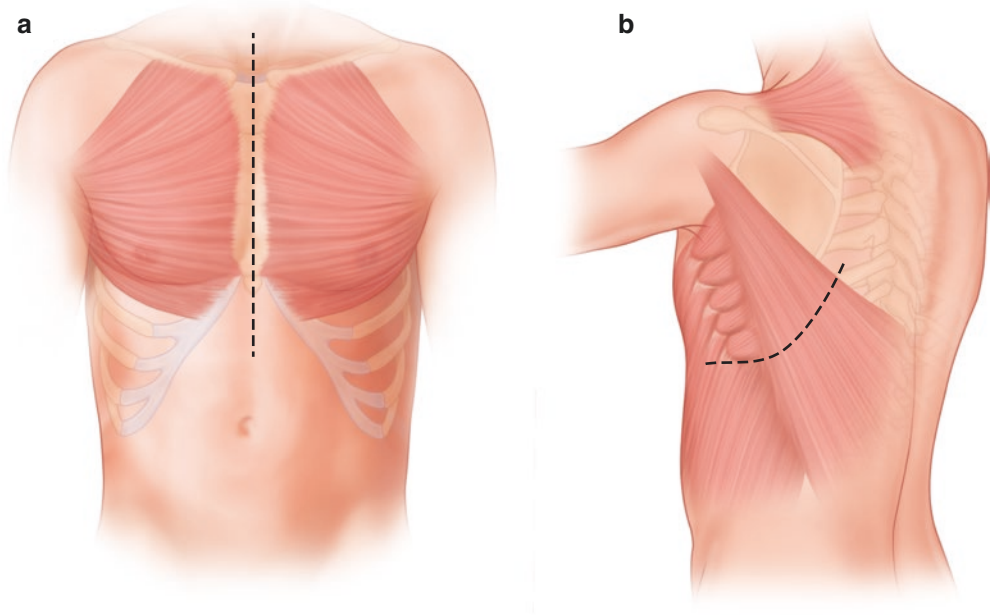


**Fig. 12.1** Standard incisions. (**a**) Median sternotomy and (**b**) posterolateral thoracotomy

open the chest were routinely used: posterolateral thoracotomy and median sternotomy [1] (Fig. 12.1). Other less invasive approaches were rarely performed, as minithoracotomy in the auscultatory triangle with no muscle incision, and only recently smaller incisions have gained a renewed interest also thanks to the rapid shifting of thoracic surgeons towards videothoracoscopic or robotic surgery. Actually, the muscle-sparing lateral thoracotomy (10–12 cm) at fifth intercostal space is the most performed incision (Fig. 12.2); this approach assures that only the serratus muscle is incised preserving the latissimus dorsi muscle with a minor traumatic impact on chest wall (Fig. 12.3) and shoulder mobility and with a strong reduction of thoracic pain with respect to the classical posterolateral thoracotomy. Video-assisted thoracoscopic surgery (VATS) and robotic assisted thoracoscopic surgery (RATS) are usually performed through two/three small incisions (1 cm) and one minithoracotomy (3–5 cm) is used to remove the specimen (Fig. 12.4). Recently [2], a variant of VATS has been proposed called uniportal VATS (with only one access of 3–5 cm) allowing to perform, in skilled surgeons, all thoracic procedures (Fig. 12.5).

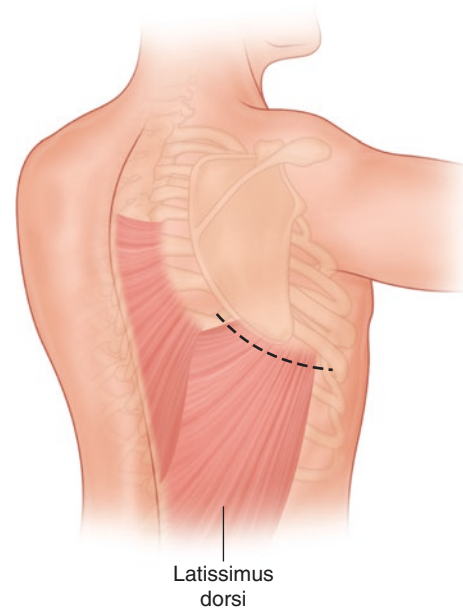


**Fig. 12.2** Lateral muscle-sparing incision

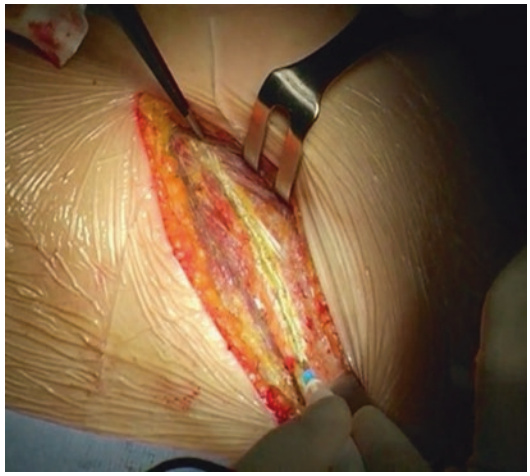

**Fig. 12.3** Lateral incision photograph

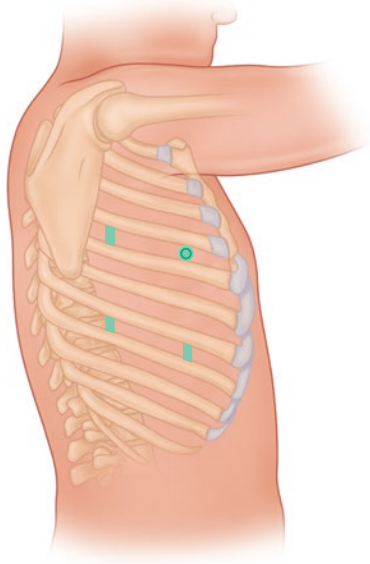

**Fig. 12.4** VATS accesses

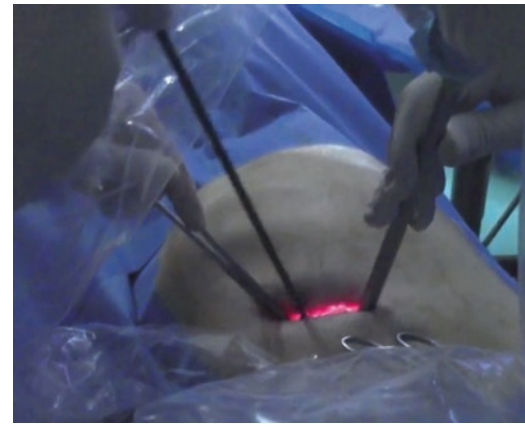

**Fig. 12.5** Uniportal VATS

### 12.2.1 Standard Resections for Lung Cancer

The gold standard treatment for lung cancer is the removal of the tumor and complete hilar and mediastinal lymphadenectomy. Due to oncological reasons, anatomical resections (Fig. 12.6) as well as segmentectomy, lobectomy, and pneumonectomy have to be preferred with respect to isolated wedge resection. Functional criteria and performance status also play a fundamental role on the decision of what kind of surgical procedure has to be performed. Historically until 1960s, pneumonectomy has been the best treatment for lung cancer patients and also actually it is an option in selected patients; however less invalidating procedures as lobectomy and, in case of smaller cancers, segmentectomy are now considered the first choice.

Standard lobectomy consists of the removal of the pulmonary lobe where cancer is localized. After the complete mobilization of lung (lysing the pleural adhesions if they are present), the elements of pulmonary hilum (pulmonary vein, branches of pulmonary artery, and lobar bronchus) are dissected and isolated. If the interlobar fissure is not fully visible it must be prepared and completed in order to separate lobes and identify the interlobar branches of pulmonary artery. Usually mechanical staplers with vascular and parenchymal load are used to cut and suture the structures, even if sometimes in case of direct infiltration of hilum elements hand-sewing sutures are still necessary.

As different independent segments regarding bronchial, vascular, and lymphatic drainage constitute every lobe, the segmentectomy is a valid and oncologically correct option in small nodules. Although the dissection of segmental elements follows the same rules of the lobectomy, the identification of segmental parenchymal limits is a crucial point of this procedure;

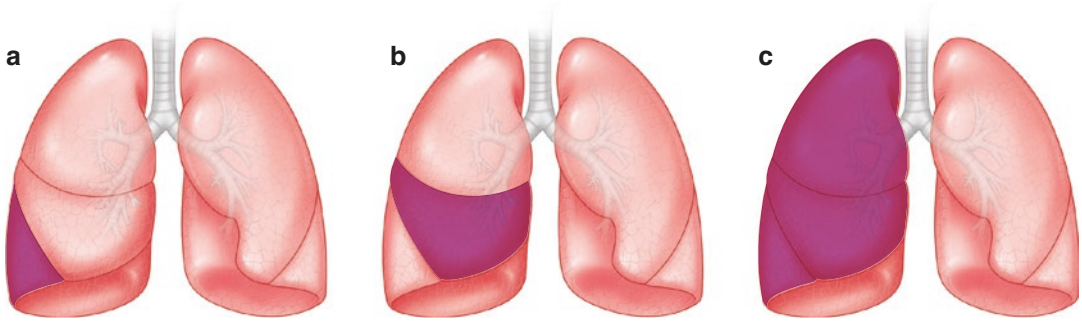


**Fig. 12.6** Standard resections

in fact, after the isolation and the clamping of the segmental bronchus, the lung is reinflated showing the non-ventilated zone that must be removed.

Notwithstanding the relevant functional impact in particular for cardiac consequences, pneumonectomy still represents an option in case of lung cancer and rather sometimes it is the only possibility to achieve a complete resection. In case of pulmonary masses involving proximally the hilum or all lobes with invasion of interlobar fissures, the removal of entire lung is necessary with sometimes also intrapericardial isolation of vessels.

Wedge resection is considered a nonanatomical resection usually performed in patients with poor cardiorespiratory reserve and low performance status (Fig. 12.7a). The rationale is the removal of the tumor with free margins of pulmonary parenchyma (at least 1 cm) using mechanical staplers. Being a nonanatomical procedure, the incidence of local recurrence is obviously higher with respect to other resections, and this occurrence is more frequent when the staple line is too close to the cancer.

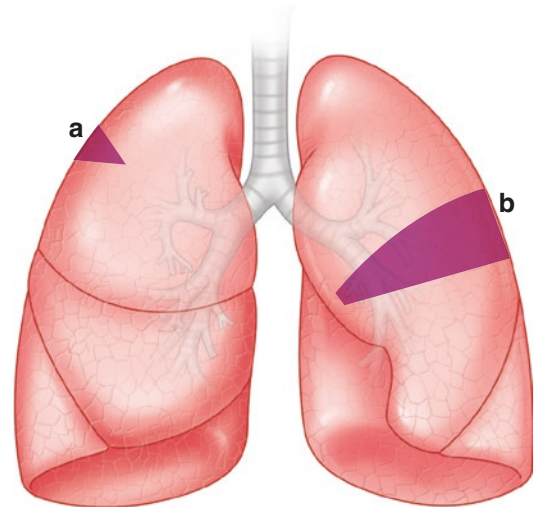


**Fig. 12.7** (**a**) Wedge. (**b**) Sleeve

### 12.2.2 Sleeve Resections (Fig. 12.7b)

In order to avoid pneumonectomy, that by some surgeons is indicated as a disease itself (in particular the right pneumonectomy) because of its cardiac consequences, in patients who functionally cannot withstand it, bronchial reconstruction alone or associated to pulmonary artery reconstruction is a feasible and safe procedure [3, 4]. The main indication is a tumor arising from the origin of lobar bronchus and/or at the origin of lobar branches of pulmonary artery; sometimes the indication is due to a metastatic lymph node (N1) infiltrating from outside the lobar bronchus.

Different techniques for bronchial reconstruction have been described: some authors prefer to perform the anastomosis with interrupted stitches of 4/0 monofilament absorbable material, whereas others favor the use of running suture. The vascular anastomosis is generally performed in running suture with 5/0 monofilament nonadsorbable material. Of paramount importance during the bronchial

and vascular anastomosis is the absence of tension; to achieve it complete mobilization of lung with extensive division of pulmonary ligament and also the opening of pericardium is mandatory.

The protection of bronchial anastomosis with tissue interposition is still a matter of discussion in the thoracic surgeons' arena. Favorable authors stress the concept that wrapping of the bronchial anastomosis with vital tissue may help the anastomosis healing and prevent dehiscence; furthermore when pulmonary artery reconstruction is associated, this tissue separates the two sutures with minor risk of fistula [5].

In rare cases, when only the pulmonary artery reconstruction is necessary and the resected portion is too long to safely perform an end-to-end suture, the interposition of a conduit is required.

### 12.2.3 Extended Resections for Lung Cancer

Also in case of more aggressive forms of lung cancer invading several structures in the thorax as well as chest wall, superior vena cava, carina, and spine, surgery (alone or associated to chemotherapy and/or radiotherapy) can play a fundamental role in the treatment.

The infiltration of chest wall is not considered a contraindication to surgery and, in the absence of lymph node metastasis, it is staged as T3N0, stage IIB. The resection of portion of chest wall not always requires a reconstruction; in fact, posterior defects of less than three ribs are covered by muscles and by scapula. When it is needed to remove at least three ribs or in case of anterolateral defects the reconstruction with several materials is mandatory to protect the pleural cavity and to stabilize the chest wall (Fig. 12.8). Several types of prostheses are available made in different components [polytetrafluoroethylene (PTFE), Goretex]; furthermore it is possible to insert metallic bars to substitute the resected ribs to make the chest wall more rigid.

Superior vena cava (SVC) may be directly involved by a cancer arising from right upper lobe or by metastatic mediastinal lymph nodes

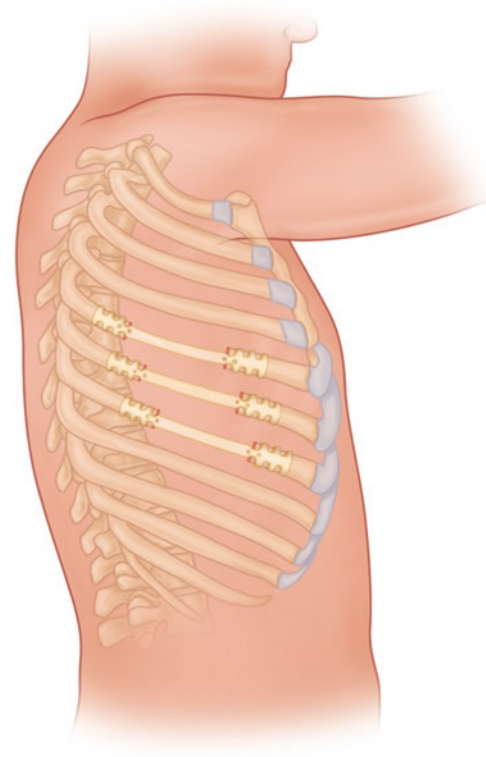

**Fig. 12.8** Rib reconstruction

(stations 2 and 4), with the staging ranging from IIIA (T4N0-1) to IIIB (T4N2). The type of reconstruction is related to the grade of vascular invasion varying from a direct suture after tangential clamping of SVC in case of involvement minor than 50% to pericardial patch reconstruction until complete substitution of a cylinder of SVC with prostheses or pericardial tubes in case of circumferential invasion [6, 7].

The involvement of carina by lung cancer represents a challenge for surgeons and anesthesiologists. Often the procedure required is a pneumonectomy with reimplantation of remnant main bronchus to the trachea (carinal pneumonectomy); however rarely, in case of endobronchial tumors invading the proximal portion of main bronchus or the tracheobronchial angle, it is possible to avoid pneumonectomy and remove only the portion of involved

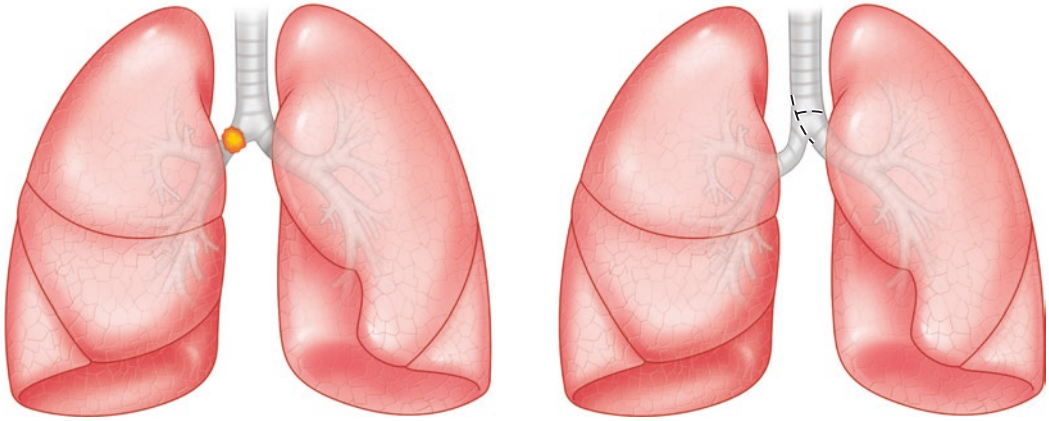

**Fig. 12.9** Carina reconstruction

airway restoring the carina (Fig. 12.9). These are very complex procedures with high rate of complications principally related to dehiscence of bronchial anastomosis.

For many years the direct infiltration of spine has been considered a contraindication for lung cancer resection. However some centers where multidisciplinary teams (thoracic surgeons, orthopedics, neurosurgeons) were present have gained experience in this field with relevant results in terms of long-term survival and functionality [8].

## 12.3 Surgery for Emphysema

Emphysema is an anatomic alteration of the lung characterized by abnormal and permanent enlargement of airspaces distal to the terminal bronchiole not associated to pulmonary fibrosis. From a radiological point of view, it is possible to distinguish two entities of emphysema: homogenous and heterogeneous. This morphological difference influences the surgical treatment: lung transplantation is usually considered for the homogenous condition (described in another chapter), whereas for heterogeneous emphysema two different surgical procedures may be performed, bullectomy and lung volume reduction surgery (LVRS).

Bullectomy is usually recommended for symptomatic patients (dyspnea, thoracic pain, chest oppression) having large and space-occupying bullae compressing normal lung parenchyma. The rationale is to reduce the ventilatory dead space and to ameliorate the function of normal parenchyma. Even if thoracotomy has been used in the past, actually the most preferred approach is the VATS and the resection of bulla is performed with mechanical staplers often wrapped with bovine pericardial strips to reinforce the staple line and prevent prolonged air leaks [9].

LVRS is a procedure reserved to patients with a form of heterogeneous emphysema localized at upper lobes. The rationale derives from the concept that in severe emphysematous patients the thorax is distended and the diaphragms are flattened; this circumstance determines the loss of physiologic circumferential pull on the small airways that could be restored by downsizing the lung. In very selected patients LVRS is accomplished removing altered and nonfunctioning pulmonary zone with the re-expansion of functioning parenchyma and remodeling of diaphragms with a clinical improvement. Historically LVRS was considered as a bilateral procedure and, consequently, performed by median sternotomy [10]. However, as several studies showed that LVRS benefits were more prolonged in case of staged operations, now the unilateral staged VATS approach is preferred; the portion of lung parenchyma removed is shaped semilunar and is accomplished with reinforced mechanical staplers.

## References


1. Fry WA. Thoracic incisions. Chest Surg Clin North Am. 1995;5:177–88.
2. Anile M, Diso D, Mantovani S, et al. Uniportal video assisted thoracoscopic lobectomy: going directly form open surgery to a single port approach. J Thorac Dis. 2014;6(Suppl 6):S641–3.
3. Rendina EA, Venuta F, Ciriaco P, et al. Bronchovascular sleeve resection. Technique, perioperative management, prevention and treatment of complications. J Thorac Cardiovasc Surg. 1993;106:73–9.
4. Venuta F, Ciccone AM, Anile M, et al. Reconstruction of the pulmonary artery for lung cancer: long-term results. J Thorac Cardiovasc Surg. 2009;138:185–91.
5. Rendina EA, Venuta F, De Giacomo T, et al. Sleeve resection and prosthetic reconstruction of the pulmonary artery for lung cancer. Ann Thorac Surg. 1999;68:995–1002.
6. Sekine Y, Suzuki H, Saitoh Y, et al. Prosthetic reconstruction of the superior vena cava for malignant disease: surgical techniques and outcomes. Ann Thorac Surg. 2010;90:223–8.
7. D'Andrilli A, Ibrahim M, Venuta F, et al. Glutaraldehyde preserved autologous pericardium for patch reconstruction of the pulmonary artery and superior vena cava. Ann Thorac Surg. 2005;80:357–8.
8. Schirren J, Dönges T, Melzer M, et al. En bloc resection of non-small-cell lung cancer invading the spine. Eur J Cardiothorac Surg. 2011;40:647–54.
9. Cooper JD. Technique to reduce air leaks after resection of emphysematous lung. Ann Thorac Surg. 1994;57:1038–9.
10. Cooper JD, Trulock EP, Triantafillou AN, et al. Bilateral pneumectomy (volume reduction) for chronic obstructive pulmonary disease. J Thorac Cardiovasc Surg. 1995;109:106–19.

# Imaging and Staging of Thymic Tumors

13

Benjamin Peters, Charlotte De Fré, Annemie Snoeckx, and Robin Peters

**Abstract**

The thymus is a primary lymphoid organ located in the upper prevascular mediastinum. A number of masses arise in relation to the thymus. Accurate knowledge of anatomy and imaging features is essential for the differentiation between non-tumoral thymic pathology and malignant thymic tumors. In general, a benign hyperplasia of the thymus occurs in children and young adults, while in adults thymoma is the most common tumor. Furthermore imaging is of great importance in the preoperative staging and (oncological) follow-up. Computed tomography (CT) is the imaging modality of choice to assess the mediastinal structures, including the thymus. Medical imaging is essential to further characterize those lesions that warrant further workup. Surgery is the gold standard for the treatment of thymoma with the aim of complete resection. We provide an overview of thymic masses with typically imaging features: thymic hyperplasia, thymic cyst, thymolipoma, thymoma, thymic carcinoma, and thymic carcinoid. Lymphoma will be discussed in *Chapter 15: Imaging of Non-thymic Mediastinal Tumors*.

**Keywords**

Prevascular mediastinum · Thymus · Thymic hyperplasia · Thymic cyst · Thymolipoma Thymoma · Thymic carcinoma · Thymic carcinoid · Staging thymic epithelial tumors Imaging

## 13.1 Introduction

The thymus is a primary lymphoid organ that functions as the initial site of T-cell maturation. It plays a crucial role in childhood immunity. The thymus is a soft-tissue organ usually containing two lateral lobes in the prevascular mediastinum. Each lobe is composed of multiple lobules, which contain small follicles. A follicle has a cortical and a medullary portion. The cortex contains mainly thymocytes, hematopoietic progenitor cells, or T cells. The medulla is composed of epithelial cells, which are essential for T-cell maturation [1, 2]. At birth, the thymus weights 10–15 g. The thymus reaches maximal size in puberty and weights between 10 and 50 g. After puberty it will gradually involute by fatty replacement. In adulthood, the thymus weights around 5–10 g [3].

B. Peters (✉) · A. Snoeckx
Department of Radiology, Antwerp University Hospital (UZA), Edegem, Belgium

C. De Fré
University of Antwerp, Edegem, Belgium

R. Peters
Department of Radiology, AZ Sint-Maria Halle, Halle, Belgium


M. Anzidei, M. Anile (eds.), *Diagnostic Imaging for Thoracic Surgery*,
https://doi.org/10.1007/978-3-319-89893-3_13

## 13.2 Embryology of the Thymus

The development of the thymus begins in the sixth gestational week and the thymus emerges from the third and fourth branchial pouches. During the seventh gestational week, the thymopharyngeal ducts are formed and migrate to the prevascular mediastinum. Thymus-related pathology can appear anywhere along the path of the thymopharyngeal duct: superior vena cava, brachiocephalic vessels, aorta, and even in the posterior mediastinum and dermis. Knowledge of this pathway is important in distinguishing ectopic thymic tissue and thymic malignancies in unusual locations from other entities [4, 5].

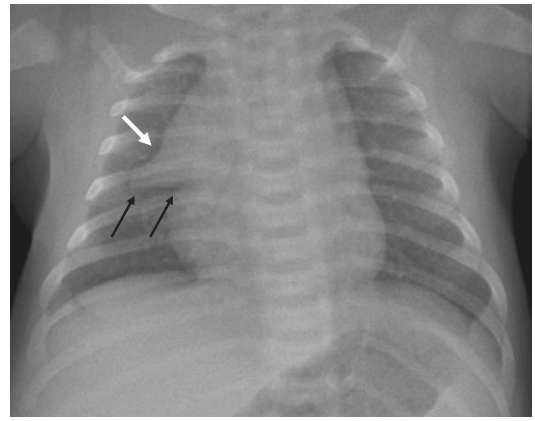

**Fig. 13.1** AP radiograph of the chest shows a normal thymus with the thymic sail (black arrow) and thymic wave sign (white arrow)

## 13.3 Thymus Anatomy and Normal Imaging Features

The thymus is anatomically located in the anterior mediastinum. The international thymic malignancy interest group (ITMIG) and the international association for the study of lung cancer group (IASLC) recently made a new classification of mediastinal compartments subdividing the mediastinum in a prevascular, visceral, and paravertebral compartment based on cross-sectional anatomic boundaries. This classification should be adopted as the new standard [6]. The thymus is located posteriorly from the sternum and overlies the pericardium, aortic arch, innominate vein, and trachea. Regarding the superior and inferior extension the thymus can reach up to the thyroid gland all the way down to the diaphragm. Morphology is variable. The thymus is usually triangular shaped, but can also be uni-lobed, trilobed, X-shaped, or inverted V-shaped [7]. Its shape, size, and attenuation change with age.

During the neonatal and childhood period, the normal thymus is seen on chest radiograph as a relatively large density with smooth borders and silhouetting the mediastinal borders. In 3–15% of children, the normal thymus can be seen as a triangular-shaped density, right sided and superior of the heart also known as the thymic sail sign (Fig. 13.1) [8, 9]. The thymic wave sign is created by the indentation of the anterior ribs on the lateral margin of the thymus (Fig. 13.1) [10]. The thymus will gradually decrease in size between 3 and 8 years and become invisible on chest radiograph.

Suprasternal ultrasound in infants will show a homogeneous finely granular echotexture with some echogenic strands with smooth well-defined margins. The thymus is mildly hypoechoic relative to thyroid gland [7].

On CT, the normal thymus usually fills the prevascular mediastinum. In children, it has a soft-tissue attenuation similar to muscle (density of 30 Hounsfield units). The attenuation decreases with age due to fatty infiltration after puberty and the thymus is usually indistinguishable from mediastinal fat in patients 40 years and older [11]. The normal thymus is a plastic organ, which will have no mass effect on mediastinal structures.

On magnetic resonance imaging (MRI), the normal thymus shows intermediate signal on T1- and T2-weighted images in children. Signal intensity on T1- and T2-weighted images (WI) will increase after puberty and in older patients.

## 13.4 Thymic Tumor Mimics

### 13.4.1 Thymic Hyperplasia

Thymic hyperplasia is a benign condition of abnormal growth of the thymus. Histologically, it can be divided into two subtypes: true thymic hyperplasia and lymphoid hyperplasia [12].

True thymic hyperplasia or rebound hyperplasia can occur when the patient recovers from a recent serious stress event. Typical examples of bodily stress inducing thymic atrophy and rebound hyperplasia are severe pneumonia, prolonged chemotherapy, corticosteroids, radiation, severe burns, hyperthyroidism, sarcoidosis, or red blood cell aplasia [13]. During a serious stress period, the thymus can atrophy and lose up to 40% of its volume depending on the duration and severity of the stress. During recovery, the thymus can grow back to its normal size and sometimes enlarges to 50% above its original volume (Fig. 13.2) [3]. Rebound hyperplasia usually occurs within 9 months but it may develop up to 5 years after initial stress [7, 14].

Lymphoid hyperplasia, also known as follicular hyperplasia, is characterized by an increased number of follicles and germinal cells in the thymic medulla. Lymphoid hyperplasia is commonly associated with myasthenia gravis, occurring in up to 65% of patients. Lymphoid hyperplasia is also associated with a variety of autoimmune disorders such as systemic lupus erythematosus, sarcoidosis, scleroderma, and Graves' disease [15].

On imaging, both true and lymphoid hyperplasia can present with a symmetrical enlargement of the thymus. Most authors consider that both conditions cannot be distinguished on imaging alone [15]. On the other hand Araki et al. concluded in a study of 31 patients that the attenuation on CT of lymphoid hyperplasia was significantly higher than in true hyperplasia with a threshold of 41.2 Hounsfield units [16]. Nevertheless, the main goal of imaging is to differentiate thymic hyperplasia from thymic tumors. Although differentiation on CT can sometimes be challenging, thymic hyperplasia will have no mass effect on mediastinal structures whereas malignancies will displace or invade mediastinal structures. MRI, especially chemical shift imaging, is also useful in the differentiation. Normal thymus or thymic hyperplasia will show a homogeneous decrease in signal on opposed-phase images compared to the in-phase images due to fatty infiltration. Thymic tumors will show no decrease in signal on chemical shift imaging. Another useful imaging biomarker is diffusion-weighted imaging (DWI). Normal thymus and thymic hyperplasia will show facilitated diffusion, whereas thymic malignancies will show restricted diffusion [11, 15, 17].

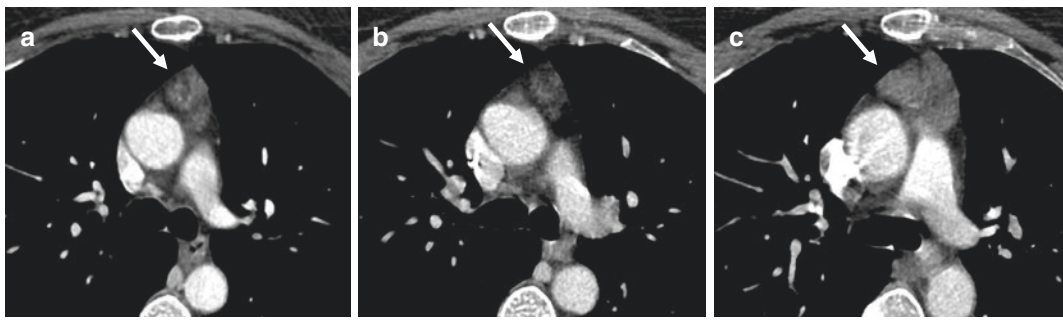


**Fig. 13.2** Follow-up CE CT of a 27 year old patient with testicular seminoma. (**a**) Baseline thymus in the prevascular mediastinum. (**b**) Follow-up CT 4 months after initation of chemotherapy. It shows a a clear volume reduction of the thymus. (**c**) Follow-up CT 1 year and a half after cessation of chemotherapy shows an enlargement of the thymus, larger then the initial volume

### 13.4.2 Thymic Cyst

Thymic cysts are well-circumscribed, usually round lesions lined with epithelium and containing fluid. They are divided into congenital and acquired cysts. Congenital cysts are derived from an embryonic remnant of the thymopharyngeal duct. Most congenital cysts are asymptomatic and diagnosed in the first two decades of life. They are usually located in the prevascular mediastinum, but can be located anywhere along the pathway of the thymopharyngeal duct, which extends from the upper neck to the prevascular mediastinum. On CT, congenital thymic cysts are usually unilocular thin walled with a clear fluid content (Fig. 13.3). An uncomplicated simple cyst has typical signal characteristics on MR imaging with a low signal on T1-WI, a high signal on T2-WI, and no contrast enhancement. Some thymic cysts show increased attenuation on CT when superimposed hemorrhage or infection occurs (Fig. 13.4) [3, 11, 18].

Acquired thymic cysts are associated with inflammatory disease, radiotherapy, or chemotherapy. Some neoplasms can mimic complicated cysts such as thymoma, thymic carcinoma, Hodgkin's lymphoma, and seminoma. Acquired cysts are usually multilocular with internal septa and gelatinous fluid. They typically have a thick, fibrous wall [19].

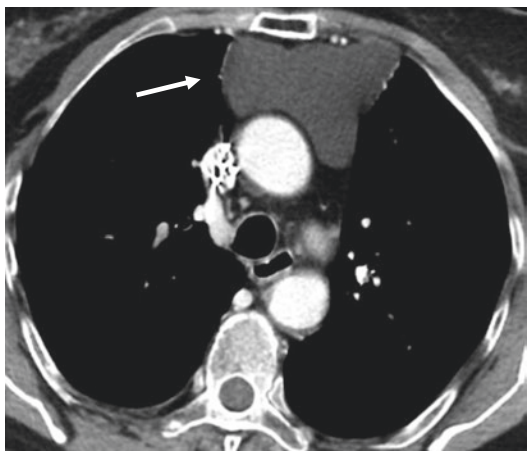

**Fig. 13.3** CE CT of the chest shows a well defined, hypodense structure in the prevascular mediastinum, without compression of the mediastinal structures

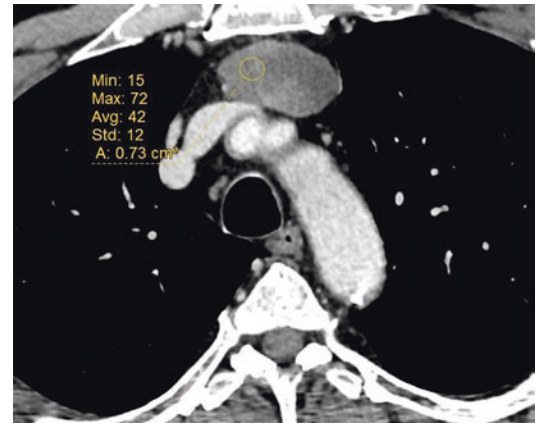


**Fig. 13.4** CE CT of the chest shows a well-defined cystic mass, with mixed fluid density content (maximal avarage of 42 HU) in the prevascular mediastinum, compatible with haemorrhagic cyst

Thymic cysts should be differentiated from other cystic prevascular mediastinal masses such as brachial cleft cysts, teratoma, dermoid cyst, or lymphangioma.

### 13.4.3 Thymolipoma

Thymolipoma is a rare, benign mass of thymic origin which is usually asymptomatic. It is a benign tumor composed of mature adipose tissue mixed with thymus tissue. The prevalence of thymolipoma is 2–9% of thymic tumors 15. CT will show a large encapsulated mass with primary fat density and strands of soft-tissue attenuation in the prevascular mediastinum (Fig. 13.5). There is usually no compression or invasion of adjacent structures. On MRI, thymolipomas have typically fat and soft tissue characteristics. No treatment is needed for this entity. Thymolipoma should be differentiated from mediastinal lipoma and extremely rare liposarcoma [35, 36].

## 13.5 Thymic Tumors

### 13.5.1 Thymoma

Thymoma is typically a slow-growing tumor derived from the epithelial cells of the thymus. It

is the most common primary prevascular mediastinal tumor, accounting for 20% of primary mediastinal neoplasms in adults. The peak prevalence is during the fifth and sixth decades. There is no gender predilection [20]. Thymomas are usually asymptomatic, although larger lesions can cause symptoms related to compression: chest pain, cough, dyspnea, dysphagia, or superior vena cava syndrome. 33–50% of patients with thymoma are associated with myasthenia gravis, whereas 10–20% of patients with myasthenia gravis have a thymoma [15, 21, 22].

The Masaoka staging system is currently the most commonly accepted staging system for thymomas. It was first proposed in 1981 by Masaoka et al. and has been modified since. It subdivides thymomas in four groups (Table 13.1) [23, 24]. For further discussion on staging thymoma see Sect. 13.6.

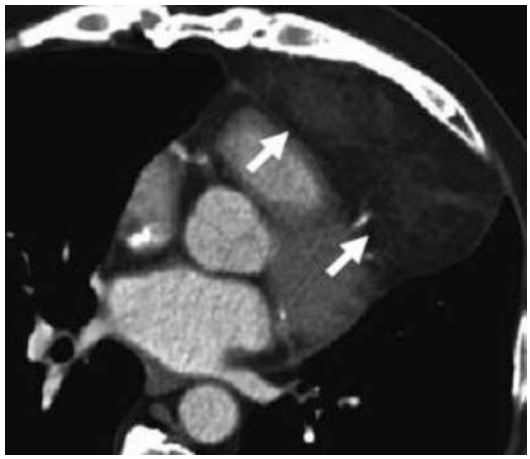

**Fig. 13.5** CE CT of the chest shows a large lesion with predominant fat attenuation containing small regions of inhomogeneous soft tissue density

There has been great debate in the literature on how to classify thymomas; recent literature opts that all thymomas should be considered malignant [25]. The WHO classification subdivides thymic epithelial tumors into six groups (Table 13.2), which is based on histologic features [26, 27]. Only in 3.2% of patients thymoma will disseminate to lymph nodes or distant metastases. Of all nodal metastases, 90% is located in the prevascular mediastinum [28, 29]. Pleural metastases or "drop metastases" manifest as one or more pleural nodules or masses. They can be smooth, nodular, or diffuse and are usually ipsilateral to the mediastinal tumor. Pleural metastases are usually ipsilateral to the primary prevascular mediastinal tumor. Associated pleural effusion is uncommon, even in extensive pleural metastases [30].

On radiograph, thymomas are best depicted on the lateral view (Fig. 13.6). Small thymomas are occult on radiograph (Fig. 13.7). Larger lesions usually appear as a well-demarcated smooth or lobulated mass in the prevascular mediastinum. Frontal chest radiograph typically shows a unilateral mass. Depending on the

**Table 13.2** WHO classification of thymomas

| WHO classification | Histological classification |
|---|---|
| A | Medullary or spindle cell thymoma |
| AB | Mixed thymoma |
| B1 | Lymphocyte-rich; lymphocytic; predominantly; organoid; predominantly cortical thymoma |
| B2 | Cortical thymoma |
| B3 | Well-differentiated thymic carcinoma; epithelial thymoma; typical thymoma; squamoid thymoma |
| C | Heterogenous thymic carcinoma |

**Table 13.1** Modified Masaoka clinical staging of thymoma according to Masaoka et al.

| Stage | Definition | TNM |
|---|---|---|
| I | Macroscopically and microscopically completely encapsulated | T1 |
| IIA | Microscopic transcapsular invasion | T2 |
| IIB | Macroscopic invasion into surrounding fatty tissue or grossly adherent to but not through mediastinal pleura or pericardium | T2 |
| III | Macroscopic invasion into adjacent organs (i.e., pericardium, great vessels, or lung) | T3 |
| IVA | Pleural or pericardial dissemination | T4 |
| IVB | Lymphogenous or hematogenous metastasis | T4 |

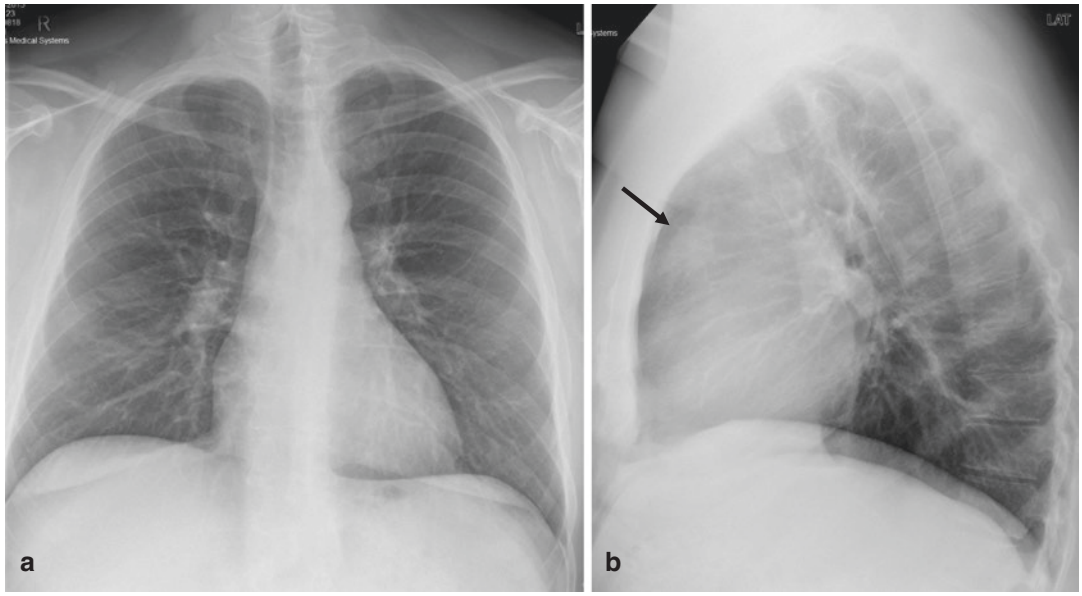


**Fig. 13.6** Anterior posterior (**a**) and lateral (**b**) view of the chest shows a small lesion in the prevascular mediastinum, only depicted on the lateral view (black arrow)

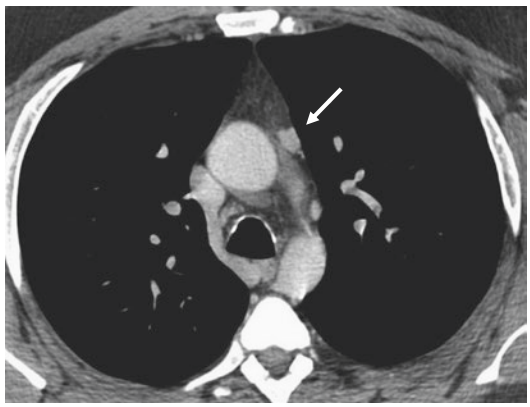

**Fig. 13.7** CE CT of the chest shows a small thymoma (white arrow) in the prevascular mediastinum, which was occult on standard radiograph

location, thymomas can obscure the right or left heart border (Fig. 13.8). On CT thymomas are well-circumscribed, heterogeneous masses with soft-tissue attenuation. Thymomas are round or lobulated, displacing the normal thymus. Large lesions can contain cystic areas, hemorrhage, or necrotic areas displacing mediastinal structures (Fig. 13.9a, b). On MRI, thymomas are isointense to muscle on T1-WI and have a relatively high signal intensity on T2-WI. Cystic areas have variable intensity on T1-WI depending on the content of the cyst, with a clear hyperintense signal intensity on T2-WI. Thymomas usually show restricted diffusion on DWI and ADC map and can help in differentiating normal/hyperplastic thymus from thymoma (Fig. 13.10). No study has currently proven the usefulness of DWI and ADC values in the differentiation of histological classifications, but might be useful in the future [3, 11, 15, 17].

The treatment options for thymomas are mainly based on the stage of the cancer. The gold standard in the treatment of thymomas is surgery with the aim of complete resection. Usually the surgeon will approach the mediastinum through a median sternotomy. If the tumor is located in a hemithorax, the surgeon can use a lateral thoracotomy. Video-assisted thoracoscopy can be used for small tumors. No other treatment is necessary for stage I. Thymomas are usually sensitive for irradiation. For incompletely resected or invasive thymoma, adjuvant radiotherapy can be applied. Neoadjuvant radiotherapy can be used to reduce the size of inoperable thymomas to achieve complete surgical

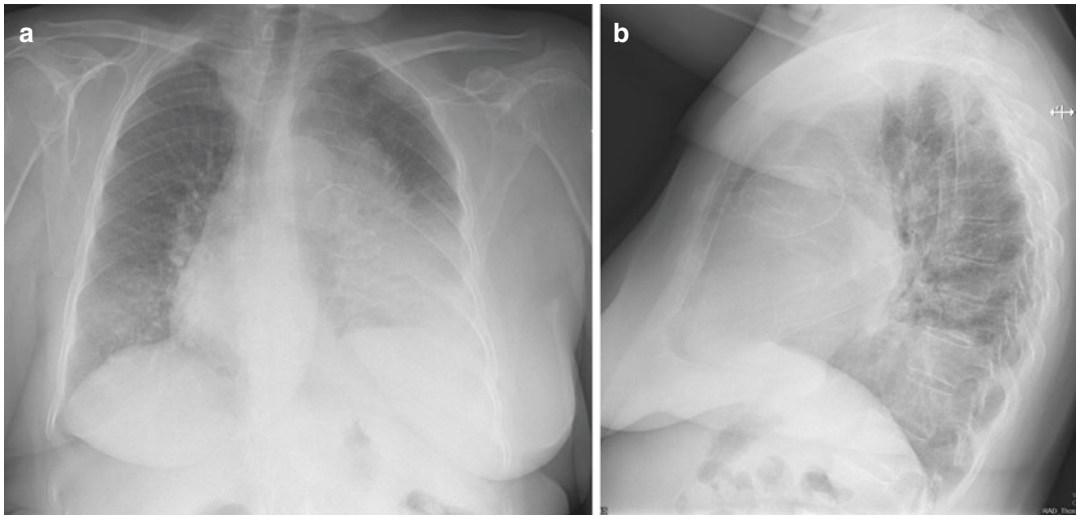


**Fig. 13.8** Anterior posterior (**a**) and lateral (**b**) view of the chest. Large mass in the prevascular mediastinum, obscuring the left heart border and containing calcifications

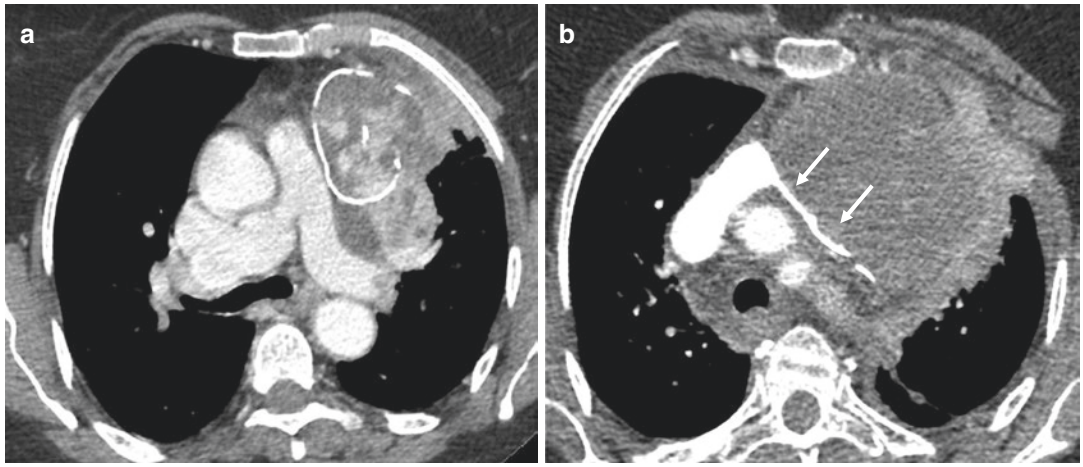


**Fig. 13.9** (**a**) CE CT of the same patient of Fig. 13.8 shows a heterogenous mass in the prevascular mediastinum containing calcifications and heterogeneous enhancement. (**b**) CE CT of the chest shows a patient with a large thymoma causing compression on the brachiocephalic vein (white arrows)

resectability. Chemotherapy can be adopted in patients with inoperable disease after local treatment. Patients with unresectable stage III and stage IV thymomas may benefit from a multimodality approach including surgical debulking, radiotherapy, and chemotherapy [31].

Thymomas are slow-growing tumors. The 5-year survival rates can be estimated based on the tumor stage and are generally considered to be approximately 60–100% for stage I–II and 46–88% for stage III disease. For stage IV cancers the survival rate is less than 24–70% [32].

### 13.5.2 Thymic carcinoma

Thymic carcinoma is an aggressive tumor arising from the thymic epithelial cells. It accounts for 20% of thymic epithelial tumors [17]. Thymic carcinoma is an aggressive tumor, usually invading

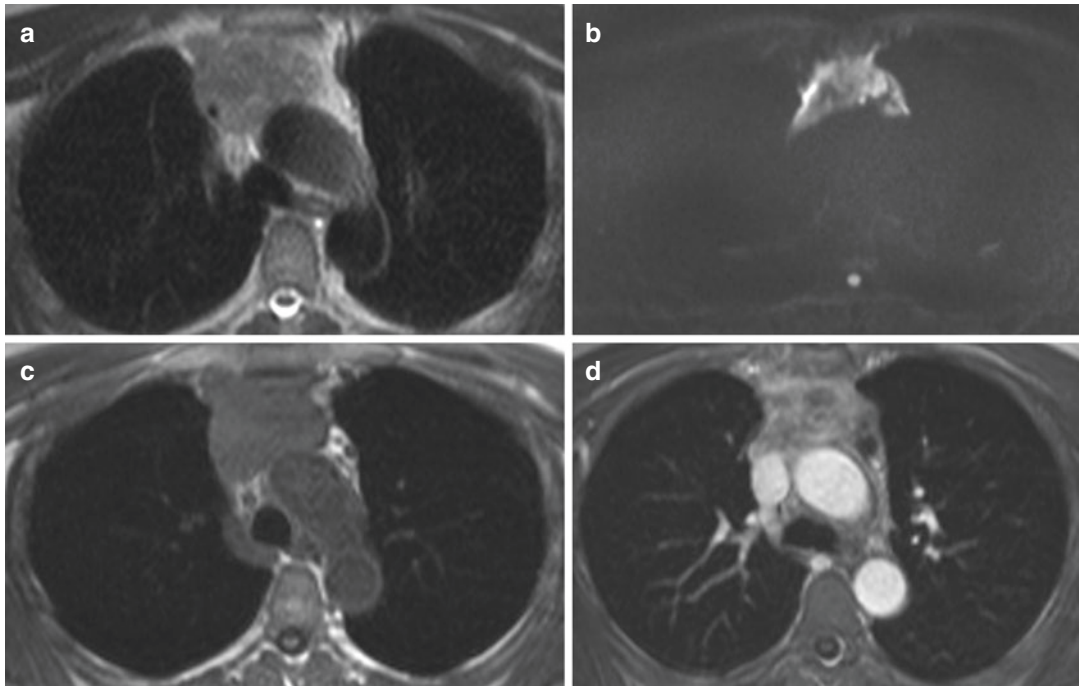


**Fig. 13.10** MR of the prevascular mediastinum shows a well demarcated isointense to slightly hyperintense lesion on T2-WI (**a**) in the prevascular mediastinum. The lesions shows diffusion restriction on DWI (**b**). The lesions is homogeneous isointense on T1-WI (**c**) and has a vivid, slight heterogeneous enhancement (**d**). APO showed a thymoma type B3

adjacent structures. Patients often present with atypical symptoms such as chest pain, dyspnea, cough, fever, weight loss, and superior vena cava syndrome. The mean age at presentation is 50 years. At the time of diagnosis, 50–60% of patients present with distant metastases [11]. Thymic carcinomas are treated with surgery and radiotherapy. They have a high recurrence rate and a poor prognosis with a 5-year survival rate of 30%. The differential between thymoma and thymic carcinoma is made on histology. On imaging, thymic carcinoma cannot reliably be distinguished from thymoma. Lymphadenopathy or distant metastasis favors thymic carcinoma [33].

On chest radiographs, a thymic carcinoma is usually a large, lobulated mass in the prevascular mediastinum with irregular margins (Fig. 13.11). CT will demonstrate a large, heterogeneous mass in the prevascular mediastinum. Thymic carcinoma can show features of necrotic areas, intralesional hemorrhage, and calcifications [3, 15]. It has usually multilobulated, poorly defined margins with invasion of adjacent structures

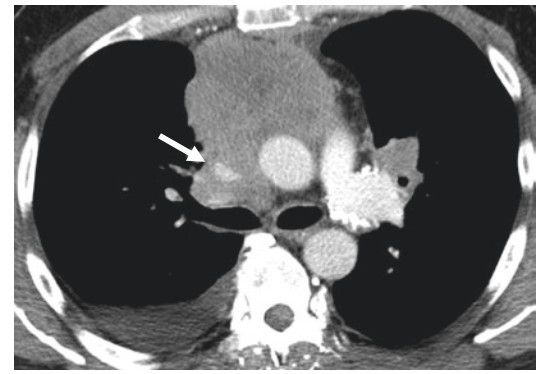

**Fig. 13.11** CE CT of the chest shows a mass with irregular margins in the prevascular medistinal, with encasement of the vena cava superior (white arrow). Note the associated pleural fluid and the left hilair enlarged lymph node

such as the pleura, pericardium, or other mediastinal structures. Associated pleural or pericardial effusion is common (Fig. 13.12) [34]. Most patients have enlarged lymph nodes and distant metastases at presentation. 70% of mediastinal

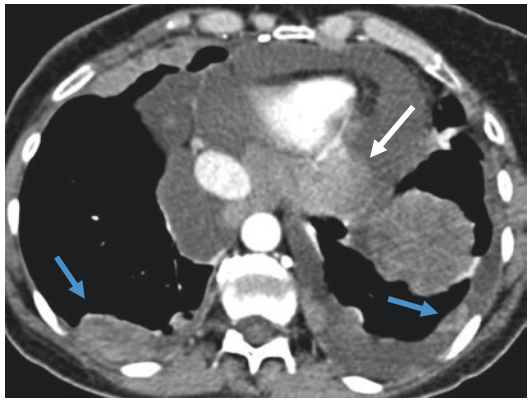

**Fig. 13.12** A folluw-up CE CT of the chest of a thymic carcinoma shows pericardial (white arrow) and multiple pleural metastasis (blue arrow), in association with pericardial and pleural fluid

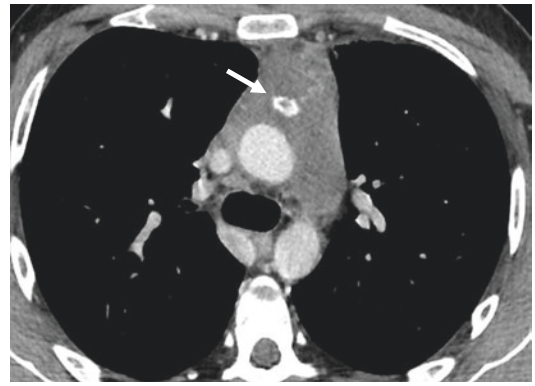

**Fig. 13.13** CE CT of the chest shows a diffuse mass in the prevascular medistinal with central calcification (white arrow). The mediastinal fat planes are obliterated, suggesting diffuse mediastinal invasion. APO showed a thymic carcinoïd

lymphadenopathy are located in the prevascular mediastinum[28].

### 13.5.3 Thymic Carcinoid or Thymic Neuroendocrine Tumors

Thymic carcinoid or thymic neuroendocrine tumor is a primary thymic tumor originating from glandular endocrine-hormone-producing cells of the thymus. They represent 2–5% of all thymic tumors [35, 36]. In contrast to carcinoid tumors in other locations, thymic carcinoids are highly aggressive and malignant in 80% of cases [37]. They are more common in men than women with a male-to-female ratio of 3:1. Thymic carcinoid tumors are hormone-secreting tumors and 50% of patients present with hormonal abnormalities. 25–40% of patients present with Cushing syndrome, related to an excess secretion of adrenocorticotrophic hormone. More uncommon clinical presentations are acromegaly (caused by excess of growth hormone-releasing hormone) and hyponatremia (caused by syndrome of inappropriate antidiuretic hormone secretion). Associated clinical symptoms of carcinoid syndrome are very rare [38, 39]. Thymic carcinoids are usually large and locally aggressive tumors. Symptoms are frequently related to mediastinal invasion or mass effect. Patients can present with chest pain, cough, dyspnea, hoarseness, and superior vena cava syndrome [39]. In up to 25% of patients thymic carcinoid is related to multiple endocrine neoplasia (MEN) type 1. Lymph node invasion is present at the time of diagnosis in 50% of cases and distant metastases in 20–40% [40–42].

Features of thymic carcinoid on imaging are similar to those of thymoma in thymic carcinoma. On radiograph they are usually large lesions with lobulated, irregular margins located in the prevascular mediastinum. On CT, they show irregular margins with central necrosis, hemorrhage, and fine calcifications (Fig. 13.13). At the time of diagnosis there is often local invasion in the pleura, pericardium, or mediastinal structures. When lymph node metastases are present, in 90% of cases they are located in the prevascular mediastinum. Bone metastases are usually osteoblastic. Imaging cannot reliably differentiate invasive thymic epithelial tumors from carcinoids [11, 15, 28].

## 13.6 Staging of Thymic Epithelial Tumors

An official stage classification system has not yet been established by the American Joint Committee on Cancer (AJCC) and the Union for International Cancer Control (UICC). The current, most widely

**Table 13.3** Proposed TNM classification according to the ITMIG and the IASLC

| TNM | Classification | Definition |
|---|---|---|
| | *T-primary tumor* | |
| Tx | | Primary tumor cannot be assessed |
| T0 | | No evidence of primary tumor |
| T1 | | Completely encapsulated tumor |
| | T1a | Tumor with no mediastinal pleura involvement |
| | T1b | Tumor with direct invasion of mediastinal pleura |
| T2 | | Tumor with direct invasion of the pericardium |
| T3 | | Tumor with direct invasion into lung, brachiocephalic vein, superior vena cava, phrenic valve, chest wall, or extrapericardial pulmonary artery/vein |
| T4 | | Tumor with invasion into aorta, arch vessels, intrapericardial pulmonary artery, myocardium, trachea, esophagus |
| | *N-regional lymph nodes* | |
| NX | | Regional lymph nodes cannot be assessed |
| N0 | | No nodal involvement |
| N1 | | Anterior nodes |
| N2 | | Deep intrathoracic or cervical nodes |
| | *M-distant metastasis* | |
| M0 | | No metastatic pleural, pericardial, or distant sites |
| M1 | | |
| | M1a<br>M1b | Separate pleural or pericardial nodule(s)<br>Pulmonary intraparenchymal nodule or distant organ metastasis |

used staging system is the Masaoka classification (Table 13.1), which is based on the data of only 91 patients. It has been modification by Koga, based on 76 patients [23, 24]. This classification system is a good prognostic predictor for thymomas; unfortunately it is not an accurate prognostic predictor for thymic carcinoma and thymic neuroendocrine tumors.

The ITMIG and the IASLC have recently reported a new classification system as a proposal for the new TNM classification of malignant tumors. This new system is a tumor, node, metastasis (TNM)-based system and can be used for all epithelial thymic malignancies (Table 13.3).

The local extent of the tumor (T component) is mainly a pathologic staging and divided into four categories (Table 13.3). Absence of surrounding fat planes on imaging suggests local invasion in the mediastinal fat. More extensive local invasion (T3-T4) can be depicted on CT or MRI and should be reported on [43–46].

The lymph node involvement is divided into three groups, depending on the location of the nodal involvement. N0 is defined as the absence of tumor cells in regional lymph nodes. N1 is tumor cells involved in the anterior, perithymic lymph nodes and N2 is defined as tumor involvement in deep intrathoracic or cervical nodes (Table 13.3). Lymph node involvement in more distant regions is considered a metastasis (M1 group) [43–46].

The M component is divided into M0 and M1. The M0 group includes no metastasis to the pleura, pericardium, or distant sites. M1 is subdivided into M1a, which includes metastasis to the pleura or pericardium, exclusive of primary tumor involvement. M1b is metastasis to the lung parenchyma or to distant organs (Table 13.3) [43–46].

## References

1. Rezzani R, Nardo L, Favero G, Peroni M, Rodella LF. Thymus and aging: morphological, radiological, and functional overview. Age (Omaha). 2014;36(1):313–51. https://doi.org/10.1007/s11357-013-9564-5.
2. Suster S, Rosai J. Histology of the normal thymus. Am J Surg Pathol. 1990;14(3):284–303. http://www.ncbi.nlm.nih.gov/pubmed/2407143.
3. Peters R, Peters O, Braak S, Verschakelen J. Pictorial essay. Pathology of the thymus on CT-imaging. J Belgian Soc Radiol. 2012;95(5):281. https://doi.org/10.5334/jbr-btr.648.
4. Lele SM, Lele MS, Anderson VM. The thymus in infancy and childhood. Embryologic, anatomic, and pathologic considerations. Chest Surg Clin N Am.

2001;11(2):233–53. http://www.ncbi.nlm.nih.gov/pubmed/11413754.
5. Safieddine N, Keshavjee S. Anatomy of the thymus gland. Thorac Surg Clin. 2011;21(2):191–5. https://doi.org/10.1016/j.thorsurg.2010.12.011.
6. Carter BW, Benveniste MF, Madan R, et al. ITMIG Classification of mediastinal compartments and multidisciplinary approach to mediastinal masses. Radiographics. 2017;37(2). https://doi.org/10.1148/rg.2017160095.
7. Nasseri F, Eftekhari F. Clinical and radiologic review of the normal and abnormal thymus: pearls and pitfalls. Radiographics. 2010;30(2):413–28. https://doi.org/10.1148/rg.302095131.
8. Walter E, Willich E, Webb WR. The thymus : diagnostic imaging, functions, and pathologic anatomy. Berlin, Heidelberg: Springer; 1992.
9. TAUSEND ME, STERN WZ. Thymic patterns in the newborn. Am J Roentgenol Radium Ther Nucl Med. 1965;95:125–30. http://www.ncbi.nlm.nih.gov/pubmed/14344350.
10. Mulvey RB. The Thymic "Wave" Sign. Radiology. 1963;81(5):834–8. https://doi.org/10.1148/81.5.834.
11. Takahashi K, Al-Janabi NJ. Computed tomography and magnetic resonance imaging of mediastinal tumors. J Magn Reson Imaging. 2010;32(6):1325–39. https://doi.org/10.1002/jmri.22377.
12. Lee YM, Koh MT, Omar A, Majid A. Hyperplasia of thymic gland. Singapore Med J. 1996;37(3):288–90. http://www.ncbi.nlm.nih.gov/pubmed/8942232.
13. Hansell DM. Imaging of Diseases of the Chest: Mosby; 2010.
14. Chertoff J, Barth RA, Dickerman JD. Rebound thymic hyperplasia five years after chemotherapy for Wilms' tumor. Pediatr Radiol. 1991;21(8):596–7. http://www.ncbi.nlm.nih.gov/pubmed/1667681.
15. Nishino M, Ashiku SK, Kocher ON, Thurer RL, Boiselle PM, Hatabu H. The Thymus: A Comprehensive Review. Radiographics. 2006;26(2):335–48. https://doi.org/10.1148/rg.262045213.
16. Araki T, Sholl LM, Gerbaudo VH, Hatabu H, Nishino M. Imaging Characteristics of Pathologically Proven Thymic Hyperplasia: Identifying Features That Can Differentiate True From Lymphoid Hyperplasia. Am J Roentgenol. 2014;202(3):471–8. https://doi.org/10.2214/AJR.13.11210.
17. Priola AM, Priola SM. Imaging of thymus in myasthenia gravis: From thymic hyperplasia to thymic tumor. Clin Radiol. 2014;69(5):e230–45. https://doi.org/10.1016/j.crad.2014.01.005.
18. Brown LR, Aughenbaugh GL. Masses of the anterior mediastinum: CT and MR imaging. AJR Am J Roentgenol. 1991;157(6):1171–80. https://doi.org/10.2214/ajr.157.6.1950860.
19. Kornstein MJ, DeBlois GG. Pathology of the thymus and mediastinum. W.B. Saunders; 1995.
20. Santana L, Givica A, Camacho C. Best Cases from the AFIP. Radiographics. 2002;22(Suppl 1):S95–S102. https://doi.org/10.1148/radiographics.22.suppl_1.g02oc12s95.
21. Lewis JE, Wick MR, Scheithauer BW, Bernatz PE, Taylor WF. Thymoma. A clinicopathologic review. Cancer. 1987;60(11):2727–43. http://www.ncbi.nlm.nih.gov/pubmed/3677008.
22. Lee H-S, Kim ST, Lee J, et al. A single institutional experience of thymic epithelial tumours over 11 years: clinical features and outcome and implications for future management. Br J Cancer. 2007;97(1):22–8. https://doi.org/10.1038/sj.bjc.6603833.
23. Masaoka A, Monden Y, Nakahara K, Tanioka T. Follow-up study of thymomas with special reference to their clinical stages. Cancer. 1981;48(11):2485–92. http://www.ncbi.nlm.nih.gov/pubmed/7296496.
24. Koga K, Matsuno Y, Noguchi M, et al. A review of 79 thymomas: modification of staging system and reappraisal of conventional division into invasive and noninvasive thymoma. Pathol Int. 1994;44(5):359–67. http://www.ncbi.nlm.nih.gov/pubmed/8044305.
25. Marx A, Ströbel P, Badve SS, et al. ITMIG Consensus Statement on the Use of the WHO Histological Classification of Thymoma and Thymic Carcinoma: Refined Definitions, Histological Criteria, and Reporting. J Thorac Oncol. 2014;9(5):596–611. https://doi.org/10.1097/JTO.0000000000000154.
26. Rosai J, Sobin LH. Histological typing of tumours of the thymus. Berlin, Heidelberg: Springer; 1999. https://doi.org/10.1007/978-3-642-60157-6.
27. Okumura M, Miyoshi S, Fujii Y, et al. Clinical and functional significance of WHO classification on human thymic epithelial neoplasms: a study of 146 consecutive tumors. Am J Surg Pathol. 2001;25(1):103–10. http://www.ncbi.nlm.nih.gov/pubmed/11145244.
28. Kondo K, Monden Y. Lymphogenous and hematogenous metastasis of thymic epithelial tumors. Ann Thorac Surg. 2003;76(6):1859–64. https://www.ncbi.nlm.nih.gov/pubmed/14667600
29. Kondo K. Tumor-Node Metastasis Staging System for Thymic Epithelial Tumors. J Thorac Oncol. 2010;5(10):S352–6. https://doi.org/10.1097/JTO.0b013e3181f20f3b.
30. Benveniste MFK, Rosado-de-Christenson ML, Sabloff BS, Moran CA, Swisher SG, Marom EM. Role of Imaging in the Diagnosis, Staging, and Treatment of Thymoma. Radiographics. 2011;31(7):1847–61. https://doi.org/10.1148/rg.317115505.
31. Tomaszek S, Wigle DA, Keshavjee S, Fischer S. Thymomas: review of current clinical practice. Ann Thorac Surg. 2009;87(6):1973–80. https://doi.org/10.1016/j.athoracsur.2008.12.095.
32. Safieddine N, Liu G, Cuningham K, et al. Prognostic factors for cure, recurrence and long-term survival after surgical resection of thymoma. J Thorac Oncol. 2014;9(7):1018–22. https://doi.org/10.1097/JTO.0000000000000215.
33. Marom EM. Advances in thymoma imaging. J Thorac Imaging. 2013;28(2):69–83. https://doi.org/10.1097/RTI.0b013e31828609a0.
34. Lee JD, Choe KO, Kim SJ, Kim GE, Im JG, Lee JT. CT findings in primary thymic carcinoma.

J Comput Assist Tomogr. 15(3):429–33. http://www.ncbi.nlm.nih.gov/pubmed/2026804.
35. Chaer R, Massad MG, Evans A, Snow NJ, Geha AS. Primary neuroendocrine tumors of the thymus. Ann Thorac Surg. 2002;74(5):1733–40. http://www.ncbi.nlm.nih.gov/pubmed/12440652.
36. Goto K, Kodama T, Matsuno Y, et al. Clinicopathologic and DNA cytometric analysis of carcinoid tumors of the thymus. Mod Pathol. 2001;14(10):985–94. https://doi.org/10.1038/modpathol.3880423.
37. Gaude GS, Hattiholi V, Malur PR, Hattiholi J. Primary neuroendocrine carcinoma of the thymus. Niger Med J. 2013;54(1):68–71. https://doi.org/10.4103/0300-1652.108904.
38. Ahn S, Lee JJ, Ha SY, Sung CO, Kim J, Han J. Clinicopathological analysis of 21 thymic neuroendocrine tumors. Korean J Pathol. 2012;46(3):221–5. https://doi.org/10.4132/KoreanJPathol.2012.46.3.221.
39. Moran MDCA, Suster MDS. Neuroendocrine Carcinomas (Carcinoid Tumor) of the Thymus. Am J Clin Pathol. 2000;114(1):100–10. https://doi.org/10.1309/3PDN-PMT5-EQTM-H0CD.
40. Teh BT, McArdle J, Chan SP, et al. Clinicopathologic studies of thymic carcinoids in multiple endocrine neoplasia type 1. Medicine (Baltimore). 1997;76(1):21–9. http://www.ncbi.nlm.nih.gov/pubmed/9064485.
41. Gibril F, Chen Y-J, Schrump DS, et al. Prospective Study of Thymic Carcinoids in Patients with Multiple Endocrine Neoplasia Type 1. *J Clin Endocrinol Metab*. 2003;88(3):1066–81. https://doi.org/10.1210/jc.2002-021314.
42. Venkatesh S, Samaan NA. Carcinoid tumors of the thymus. *West J Med*. 1990;152(1):72–4. http://www.ncbi.nlm.nih.gov/pubmed/2309479.
43. Kondo K, Van Schil P, Detterbeck FC, et al. The IASLC/ITMIG Thymic Epithelial Tumors Staging Project: Proposals for the N and M Components for the Forthcoming (8th) Edition of the TNM Classification of Malignant Tumors. J Thorac Oncol. 2014;9(9):S81–7. https://doi.org/10.1097/JTO.0000000000000291.
44. Nicholson AG, Detterbeck FC, Marino M, et al. The IASLC/ITMIG Thymic Epithelial Tumors Staging Project: Proposals for the T component for the Forthcoming (8th) Edition of the TNM Classification of Malignant Tumors. J Thorac Oncol. 2014;9(9):S73–80. https://doi.org/10.1097/JTO.0000000000000303.
45. Detterbeck FC, Stratton K, Giroux D, et al. The IASLC/ITMIG Thymic Epithelial Tumors Staging Project: proposal for an evidence-based stage classification system for the forthcoming (8th) edition of the TNM Classification of Malignant Tumors. J Thorac Oncol. 2014;9(9):S65–72. https://doi.org/10.1097/JTO.0000000000000290.
46. Bhora FY, Chen DJ, Detterbeck FC, et al. The ITMIG/IASLC Thymic Epithelial Tumors Staging Project: a proposed lymph node map for thymic epithelial tumors in the forthcoming 8th edition of the TNM Classification of Malignant Tumors. J Thorac Oncol. 2014;9(9):S88–96. https://doi.org/10.1097/JTO.0000000000000293.

# Imaging of Non-thymic Anterior Mediastinal Tumors

14

Roy A. Raad

**Abstract**

The mediastinum contains a variety of vital structures and organs, including the thymus, lymph nodes, adipose tissues, vascular structures, nerves, and esophagus, all of which can give rise to various masses and other nonneoplastic abnormalities. Imaging is the integral part of the workup for mediastinal tumors, specifically chest computed tomography (CT) and in equivocal cases magnetic resonance imaging (MRI), leading in many cases to a confident presumptive diagnosis, even without necessitating biopsy, surgery, or other confirmatory testing.

In this chapter, we focus on discussing the clinical manifestations, diagnosis, and treatment of non-thymic tumors, specifically germ cell tumors, lymphoma, and mesenchymal tumors. Although this is discussed in prior chapters, we start by discussing a generalized structured imaging approach that radiologists can use when evaluating anterior mediastinal tumors in general, aided by useful clinical and laboratory information when made available. Thymic benign and malignant tumors are discussed in detail in other chapters.

**Keywords**

Anterior mediastinum · Chest CT · Chest MR FDG PET/CT · Lymphoma · Seminoma Teratoma · Nonseminomatous germ cell tumor · Mesenchymal tumor

## Abbreviations

| | |
|---|---|
| AFP | Alpha-fetoprotein |
| CBC | Complete blood count |
| CT | Computed tomography |
| ESR | Erythrocyte sedimentation rate |
| FDG | Fluorodeoxyglucose |
| GCT | Germ cell tumor |
| HL | Hodgkin's lymphoma |
| HU | Hounsfield units |
| LBCL | Large B-cell lymphoma |
| LDH | Lactate dehydrogenase |
| MRI | Magnetic resonance imaging |
| PET/CT | Positron-emission tomography/computed tomography |
| SVC | Superior vena cava |
| β-hCG | Beta-human chorionic gonadotropin |

R. A. Raad
Department of Radiology, New York University School of Medicine, New York, NY, USA

Department of Radiology, St. George Hospital University Medical Center, Beirut, Lebanon
e-mail: roy.raad@med.nyu.edu


M. Anzidei, M. Anile (eds.), *Diagnostic Imaging for Thoracic Surgery*,
https://doi.org/10.1007/978-3-319-89893-3_14

## 14.1 Introduction

Variable statistics exist in the medical literature regarding the true incidence of anterior mediastinal masses, due to a number of reasons, such as variations in the clinical and radiological classification schemes, as well as variation in the nomenclature of particular tumors. For instance, the traditional classification schemes used in radiologic practice are based on the lateral chest radiograph, as devised by Felson [1], which divides the mediastinum into anterior, middle, and posterior compartments. More recently in 2014, the International Thymic Malignancy Interest Group (ITMIG) introduced and adopted a new classification scheme of the mediastinal compartments based on cross-sectional imaging, after modifying an original model developed by the Japanese Association for Research on the Thymus (JART), reclassifying the mediastinum into prevascular, visceral, and paravertebral compartments [2]. According to the updated classification system, the prevascular compartment (previously known as the anterior mediastinum) is bordered by the thoracic inlet superiorly, the diaphragm inferiorly, the sternum anteriorly, the parietal mediastinal pleura laterally, and the anterior aspect of the pericardium posteriorly [3]. Its major contents include the thymus, fat, lymph nodes, and left innominate vein.

Despite these challenges, the most widely reported incidence for anterior mediastinal masses includes thymic malignancies in 35% of cases, lymphoma in 25% of cases, thyroid and other endocrine tumors in 15% of cases, malignant germ cell tumors in 10% of cases, and benign thymic lesions in 5% of cases (Table 14.1).

**Table 14.1** Anterior mediastinal masses

| Mass | Incidence (%) |
|---|---|
| Thymic malignancies | 35 |
| Lymphoma | 25 |
| Thyroid/other endocrine tumors | 15 |
| Malignant germ cell tumors | 10 |
| Benign thymic lesions | 10 |
| Mesenchymal tumors | 5 |

## 14.2 General Approach to Mediastinal Masses

### 14.2.1 Clinical Approach

When evaluating mediastinal masses on any imaging modality, the first and foremost piece of information that the radiologist must make use of is all the clinical and laboratory details pertaining to the patient. Although this may be challenging in the private practice setting, it has become easily accessible nowadays at most academic centers with the increasing abundance of full access to electronic medical records that are readily available for the radiologist at the time of interpretation. In addition, a discussion between the radiologist and the clinician regarding the case in question should be encouraged whenever possible.

Basic demographic information such as patient age and gender may prove to be helpful in narrowing down the differential diagnoses. For instance, in both men and women older than 40 years of age, thyroid goiter and thymic malignancies account for more than two-thirds of anterior mediastinal masses, whereas lymphoma is the most common anterior mediastinal tumor in women between the ages of 10 and 39 [4]. Other relevant clinical information that should be evaluated includes the presence, severity, and duration of symptoms pertaining to the mediastinal structures, such as dyspnea, dysphagia, chest pain, hoarseness, or changes in voice, hemoptysis, palpable abnormalities, as well as "B symptoms" of lymphoma (fever, night sweats, weight loss). Relevant laboratory studies that should be assessed include lactate dehydrogenase (LDH), alpha-fetoprotein (AFP), and beta-human chorionic gonadotropin (β-hCG) levels. For example, in a young patient presenting with an anterior mediastinal mass, the presumptive diagnosis of lymphoma can be made with increased confidence if associated with "B" symptoms and elevated LDH levels. As another example, in a male aged 10–39 years presenting with an anterior mediastinal mass, the presumptive diagnosis of a malignant germ cell tumor can be suggested, in the presence of rapidly progressive symptoms

and elevated β-hCG and AFP levels. Attention should also be directed to the presence and details of preexisting medical conditions, such as myasthenia gravis, which is most commonly associated with thymomas, along with other less common conditions such as pure red cell aplasia and hypogammaglobulinemia [5].

### 14.2.2 Radiologic Approach

Close attention to details of the imaging appearance of mediastinal masses is of paramount importance, given that imaging is the most vital component in the workup of mediastinal masses, suggesting a certain diagnosis or guiding further investigations and confirmatory testing. Moreover, some mediastinal masses demonstrate a highly characteristic imaging appearance that leads to a presumptive diagnosis with high certainty without the need for biopsy or other confirmatory testing (Table 14.2). Other mediastinal masses demonstrate imaging findings that are suggestive of a certain diagnosis in a particular clinical context.

In all patients with mediastinal masses, the radiologist should describe the exact location, margins (well circumscribed vs. poorly circumscribed), shape (oval, round, or saccular), internal contents (fat, fluid, soft tissue or calcification), and organ of origin (if any) of the mass in question. For instance, an intrinsically high-attenuation anterior mediastinal mass, which enhances avidly following the administration of iodinated intravenous contrast and is continuous with the thyroid gland on a chest CT, can be reliably diagnosed as a thyroid goiter. On the other hand, a heterogeneous mass containing fat, soft tissue, and calcification can be diagnosed as a benign teratoma with a very high level of confidence. The presence of ancillary findings should also be assessed, such as lung metastases (which would suggest an aggressive tumor such as a malignant germ cell tumor), pleural and pericardial implants (suggestive of metastatic thymic tumor), or additional discrete intrathoracic lymph nodes (which would heighten the confidence level for the diagnosis of lymphoma).

Chest CT is the mainstay of imaging modality for evaluation of mediastinal masses, for evaluation of the above-described imaging characteristics, among others. The role of chest radiography is limited, usually limited to the incidental detection of the mere presence of a mediastinal mass, obtained as a routine imaging study or for evaluation of any symptoms. Chest MRI is usually indicated for evaluation of equivocal CT findings, mainly for better delineation of internal contents of the mass (cystic vs. enhancing soft-tissue components). 18-F-fluorodeoxyglucose (FDG) positron-emission tomography/computed tomography (PET/CT) is not usually indicated for evaluation of mediastinal masses, except in the setting of suspected or known lymphoma, for purposes of staging or guiding potential sites of biopsy.

**Table 14.2** Anterior mediastinal masses with characteristic imaging findings

| Mass | Imaging findings |
|---|---|
| Thyroid goiter | Hyperattenuating/enhancing mass connected to thyroid |
| Teratoma | Heterogeneous mass containing calcifications, fat, fluid, and soft-tissue components |
| Thymic cyst/cystic thymoma | Well-circumscribed fluid-attenuation mass near thymic bed |
| Pericardial cyst | Well-circumscribed fluid-attenuation mass at cardiophrenic angle |
| Invasive thymoma | Homogeneous or heterogeneous mass with subpleural or pericardial implants |
| Lipoma | Homogeneous fat-attenuation mass |

## 14.3 Germ Cell Tumors

By definition, germ cell tumors (GCTs) are said to be "extragonadal" in patients with no primary malignancy identified in the testes or ovaries. The location of extragonadal germ cell tumors varies with age; however they usually arise in midline structures in all age groups. The anterior mediastinum is the most common location in adults, followed by the retroperitoneum, pineal, and suprasellar regions, whereas the anterior

mediastinum is very rare in the pediatric population, in which sacrococcygeal and intracranial germ cell tumors are more common. In general, extragonadal (including mediastinal) germ cell tumors are classified as seminomas (also termed as dysgerminomas in females and germinomas in children), nonseminomatous GCTs (nondysgerminomas in females and nongerminomas in children), and mature or immature teratomas. The main distinction between seminomas and nonseminomatous GCTs is significant because of important differences in terms of prognosis and treatment. Subtypes of nonseminomatous GCTs include yolk cell tumors, choriocarcinomas, and embryonal carcinomas. Germ cell tumors (including both benign teratomas and malignant germ cell tumors) comprise around 20% of anterior mediastinal masses [4, 6].

### 14.3.1 Mature Teratomas

*Clinical manifestations*—By definition, mature teratomas of the mediastinum contain well-differentiated histologic components derived from at least two out of the three germinal cell layers (ectoderm, mesoderm, and endoderm). They are considered benign (as opposed to mature teratomas of the testes) and slow growing, and hence tend to be diagnosed incidentally while patients are still asymptomatic. When present, symptoms are typically secondary to compression and obstruction of adjacent mediastinal structures, and include chest pain, cough, postobstructive pneumonia [7], and in rare cases expectoration of hair (trichoptysis) [8].

*Diagnosis*—Most mature mediastinal teratomas are initially detected on chest radiography, whether obtained as a routine study or for evaluation of symptoms. Calcifications within the mass are present in 26% of cases, and in rare cases there is visualization of a tooth or well-formed bone within the mass (Fig. 14.1), which is further suggestive of the diagnosis. Chest CT, and in equivocal cases chest MRI, is very useful for accurate localization of the mass, determining its spatial relation to the adjacent thoracic structures, and for definitive delineation of internal components. Most mediastinal teratomas are composed of fat (typically between −40 and −120 Hounsfield units (HU) on chest CT), fluid (between 0 and 20 HU), soft tissue (greater than 20 HU), and/or calcifications (Fig. 14.1). The presence of a fat-fluid level is highly specific for teratomas; however this finding is much less common[9].

*Treatment*—Surgical resection is the main treatment modality for mature teratomas, and is curative in almost all cases [10]. Surgical approach is usually through a median sternotomy or posterolateral thoracotomy depending on the mass location, although thoracoscopic resection may be performed in a few select cases, especially in smaller masses [11]. In cases where radical resection cannot be performed without compromising neighboring vital mediastinal structures, subtotal resection may be performed for relieving compressive symptoms, followed by observation—the use of postoperative chemotherapy or radiation therapy in this setting has not demonstrated clear benefit, especially that these tumors are relatively insensitive to both chemotherapy and radiation therapy [7, 11].

### 14.3.2 Immature Teratomas

Along the same continuum of mature teratomas, immature teratomas contain mature elements of all three germinal layers, mixed with immature tissue. Imaging appearance is identical to that of mature teratomas in most cases, although there may be foci of hemorrhage or necrosis within the mass in some cases. Standardized treatment of these tumors is controversial, due to the lack of randomized controlled trials, partly due to rarity

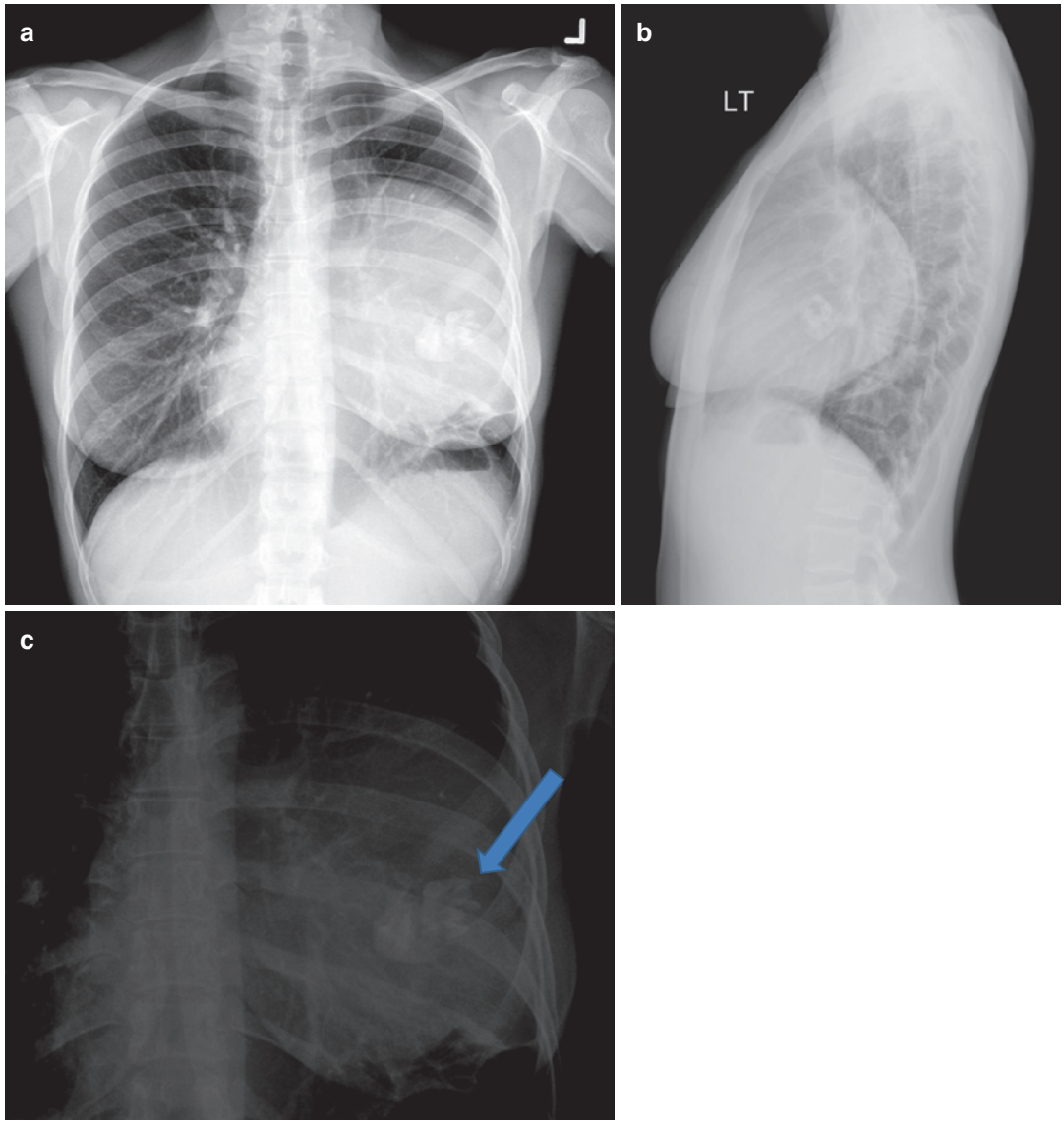


**Fig. 14.1** *24-year-old female presenting with chest pain and hemoptysis.* PA (**a**) and lateral (**b**) chest radiographs demonstrate a large anterior mediastinal mass containing calcifications. (**c**) Magnified view of the PA chest radiograph identifies a "toothlike" appearance of the calcification (blue arrow). Axial (**d**) and coronal (**e**) chest CT demonstrates fat and soft-tissue attenuation within the large anterior mediastinal mass and confirms the presence of a tooth within it. Note the secondary mass effect and narrowing of the left pulmonary artery and left mainstem bronchus. Subsequent surgical resection confirmed the diagnosis of benign mature cystic teratoma

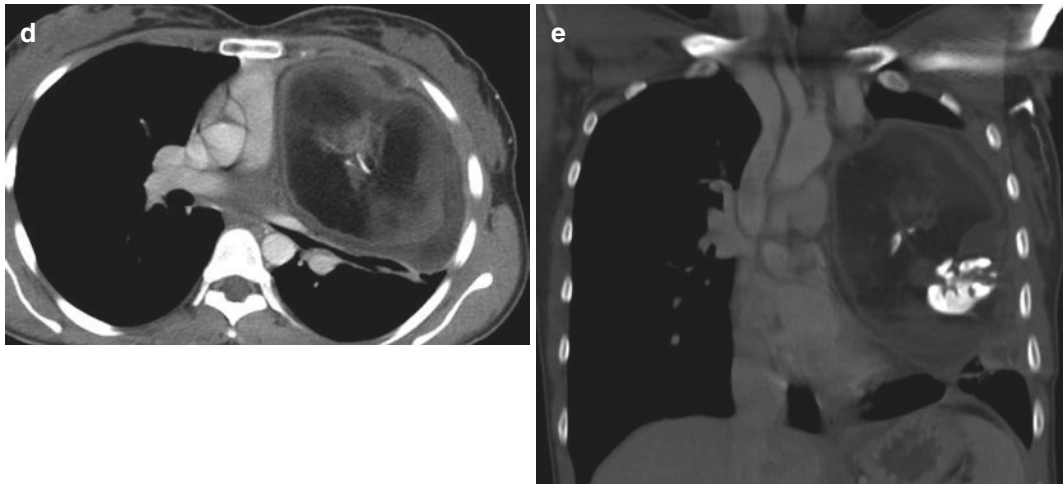


**Fig. 14.1** (continued)

of this condition. The most common approach is however preoperative chemotherapy followed by radical resection. Although adults with primary immature mediastinal teratomas usually have a poor prognosis, long-term survival has been reported in patients treated with preoperative chemotherapy and aggressive surgical resection [12]. Malignant transformation of immature teratomas is also possible [13]. On the other hand, immature mediastinal teratomas in children behave as benign tumors, in a similar manner to mature teratomas.

### 14.3.3 Mediastinal Seminomas

*Clinical manifestation*—Mediastinal seminomas account for one-third of mediastinal malignant GCTs, predominantly occurring in men between 20 and 40 years old [14, 15]. Despite the fact that testicular seminomas are unlikely to spread to the mediastinum in the absence of retroperitoneal adenopathy [16], it is advised that all men with suspected mediastinal seminoma should undergo a testicular ultrasound for exclusion of a testicular mass. Furthermore, mediastinal dysgerminomas, the female counterpart to seminomas, are rare in women with histologically normal ovaries. Most patients (75%) are asymptomatic at the time of presentation; however presenting symptoms may include chest pain, dyspnea, cough, weight loss, and superior vena cava (SVC) syndrome [17].

*Diagnosis*—Serum AFP levels must be normal since seminomas do not produce AFP, and serum β-hCG levels may be elevated up to 1000 international units (IU)/L [17]; abnormal AFP levels or elevation of β-hCG levels >1000 IU/L indicates the presence of coexisting nonseminomatous components. On chest radiograph, mediastinal seminomas manifest as bulky anterior mediastinal masses with usually well-defined borders [18], and radiographically detectable calcification may be seen in a minority of cases [19]. Cross-sectional imaging appearance on chest CT or MRI is not highly specific, although mediastinal seminomas typically present as a well-circumscribed anterior mediastinal mass, demonstrating homogeneous density and low-level homogeneous enhancement following intravenous contrast administration [20]. Foci of central necrosis and hemorrhage within the tumor may be present (Fig. 14.2). Most patients present with metastatic disease at the initial presentation, most commonly to intrathoracic lymph nodes, and less commonly to lungs, liver, and/or bones [17].

*Treatment and Prognosis*—In general, seminomas are extremely sensitive to both cisplatin-based chemotherapy and radiation therapy. Treatment recommendations are mainly established via small

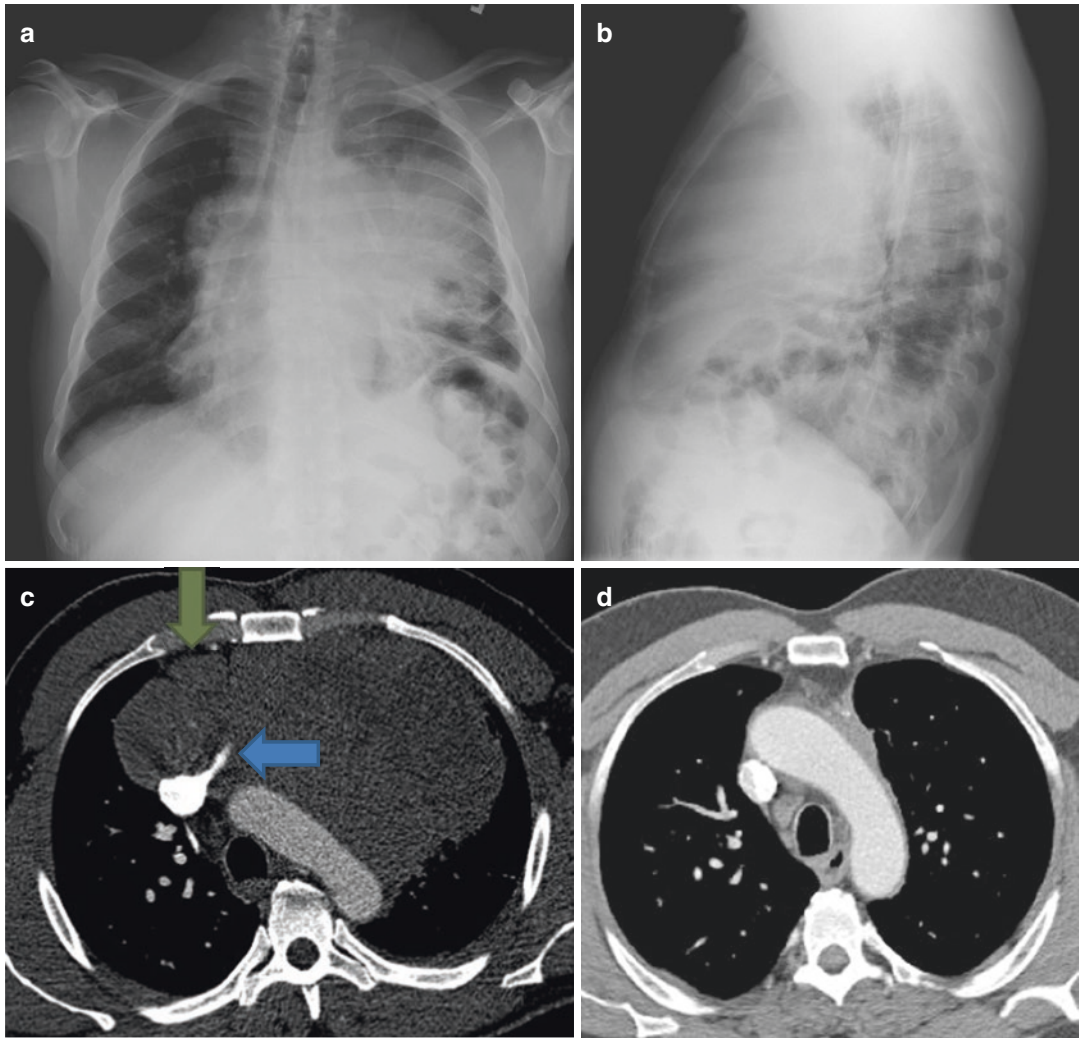


**Fig. 14.2** *44-year-old male presenting with tachycardia and shortness of breath.* PA (**a**) and lateral (**b**) chest radiographs demonstrate a large anterior mediastinal mass on both sides of midline. (**c**) Axial images of a contrast-enhanced chest CT at the time of presentation demonstrate a large slightly heterogeneous anterior mediastinal mass, containing areas of necrosis anteriorly. Note the significant mass effect and narrowing of the adjacent structures such as the left innominate vein (blue arrow). Additional small discrete mediastinal lymph nodes were also identified (green arrow). No imaging evidence of lung or other distant metastases at the time of diagnosis. CT-guided biopsy of the mass revealed seminoma. (**d**) Follow-up chest CT 2 years later following chemotherapy demonstrates near-complete resolution of the mass

case series and retrospective reviews rather than randomized clinical trials. Most clinical institutions favor chemotherapy over radiation therapy, due to reduced concerns for toxicity and reduced risk of cardiovascular complications and secondary radiation-induced malignancies, especially since most patients are young adults (20–40 years old). In patients where radiation therapy is used as an alternative strategy for patients with localized disease in the mediastinum (who are not appropriate chemotherapy candidates for instance), careful treatment planning is essential to avoid toxicities, and the radiation fields should include the mediastinum and bilateral supraclavicular regions. In general, surgery plays no role in the initial management of these tumors, due to the typical initial

presentation of bulky and/or metastatic disease [17]. Around 90% of patients treated with chemotherapy have an excellent prognosis with a long-term disease-free survival [17]. Patients treated with radiation therapy are also cured; however the recurrence rate is high, and the 5-year disease-free survival rate is only up to 67% [21].

### 14.3.4 Mediastinal Nonseminomatous Germ Cell Tumors

*Clinical manifestations*—Among the mediastinal nonseminomatous GCTs, yolk sac tumor is the most common subtype, whereas choriocarcinoma and embryonal carcinoma are less frequently encountered in the mediastinum. They occur more commonly in men than women, usually between the ages of 20 and 40 years. Most patients present with symptoms at the time of diagnosis, including fever, chills, weight loss, and SVC syndrome. In addition, patients with mediastinal nonseminomatous GCTs have a high incidence of developing various hematologic disorders, such as acute megakaryoblastic and myelogenous leukemia, myelodysplasia, and malignant histiocytosis, with the incidence reaching 6% in one series [22]. The exact reason of this increased incidence is not known; however it may be related to the presence of hematopoietic precursor cells arising within the components of the GCT [23].

*Diagnosis*—Serum AFP levels are elevated in most patients, whereas β-hCG levels are elevated in a minority of patients. In those with combined elevation of serum AFP and β-hCG levels, the diagnosis of a nonseminomatous GCT can be made even without tissue diagnosis at some institutions. Moreover, serum AFP and β-hCG levels can be used for monitoring response to therapy and detecting tumor recurrence. On chest radiograph, nonseminomatous GCTs manifest as a bulky anterior mediastinal mass (Fig. 14.3a, b), commonly exerting mass effect on adjacent mediastinal structures. Contrast-enhanced chest CT typically demonstrates a large heterogeneous anterior mediastinal mass frequently containing extensive areas of central necrosis and hemorrhage (Fig. 14.3c), as well as enhancing lobular papillary-like peripheral projections in some cases [18, 20]. Chest CT should also be queried for ancillary findings, such as lung nodules, mediastinal and hilar lymphadenopathy, and pleural and pericardial effusions [24], which would raise concern for metastatic disease. Follow-up chest CT is useful in documenting favorable response to chemotherapy or disease progression (Fig. 14.3d, e).

*Treatment and prognosis*—Since most patients present with metastatic disease, the usual treatment approach consists of initial chemotherapy followed by surgical resection of any residual masses. Cisplatin, etoposide, and ifosfamide (VIP) regimen is preferred to the bleomycin, etoposide, and cisplatin (BEP) regimen at many institutions [25], especially that most patients end up undergoing thoracic surgery, which can provoke bleomycin-induced pneumonitis. Most patients have residual masses at the conclusion of chemotherapy, requiring surgical resection, even in the presence of rising tumor markers, since the alternative of salvage chemotherapy offers dismal results usually [17]. Surgery is usually aggressive and complex necessitating performance by an experienced thoracic surgeon with these tumors. Mediastinal nonseminomatous GCTs have a distinctly worse prognosis than seminomas or teratomas, with a 5-year overall survival rate of 40-45% [17], in patients treated with this combined modality approach.

## 14.4 Mediastinal Lymphoma

Lymphoma accounts for around 25% of anterior mediastinal masses. The two most common subtypes of primary mediastinal lymphomas are Hodgkin's lymphoma (13%) and large B-cell lymphoma (12%), both of which will be the focus of the discussion.

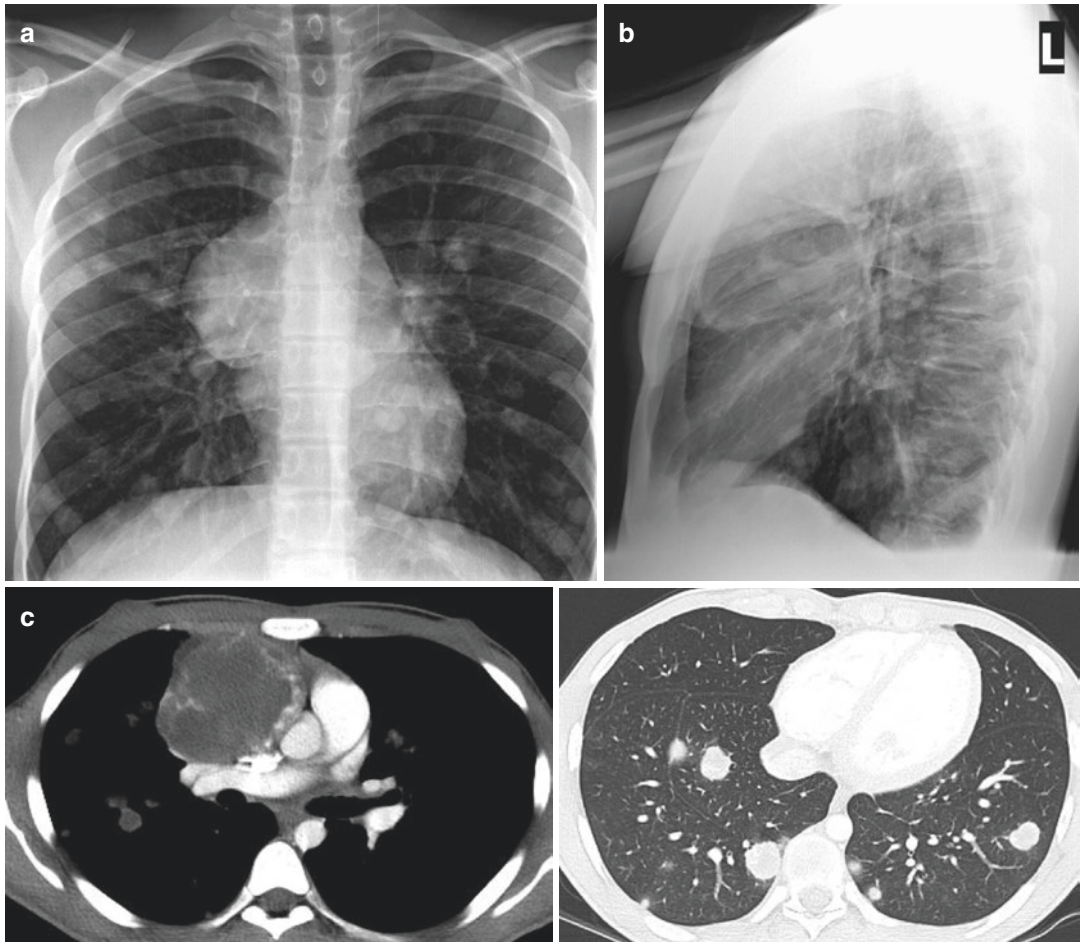


**Fig. 14.3** *16-year-old with metastatic choriocarcinoma presenting with weight loss and night sweats, as well as markedly elevated AFP and b-hCG levels.* PA (**a**) and (**b**) lateral chest radiographs demonstrate a large anterior mediastinal mass and bilateral lung nodules. (**c**) Axial contrast-enhanced chest CT demonstrates a large heterogeneous anterior mediastinal containing large foci of central necrosis and peripheral enhancing papillary-like projections. Bilateral lung nodules were also seen, consistent with lung metastases. Patient was treated with chemotherapy, resulting in favorable response in the anterior mediastinal mass and marked response in the lung metastases on follow-up chest CT (**d**), coupled with normalization of AFP and b-hCG levels. This was followed by surgical resection of the residual anterior mediastinal mass (**e**)

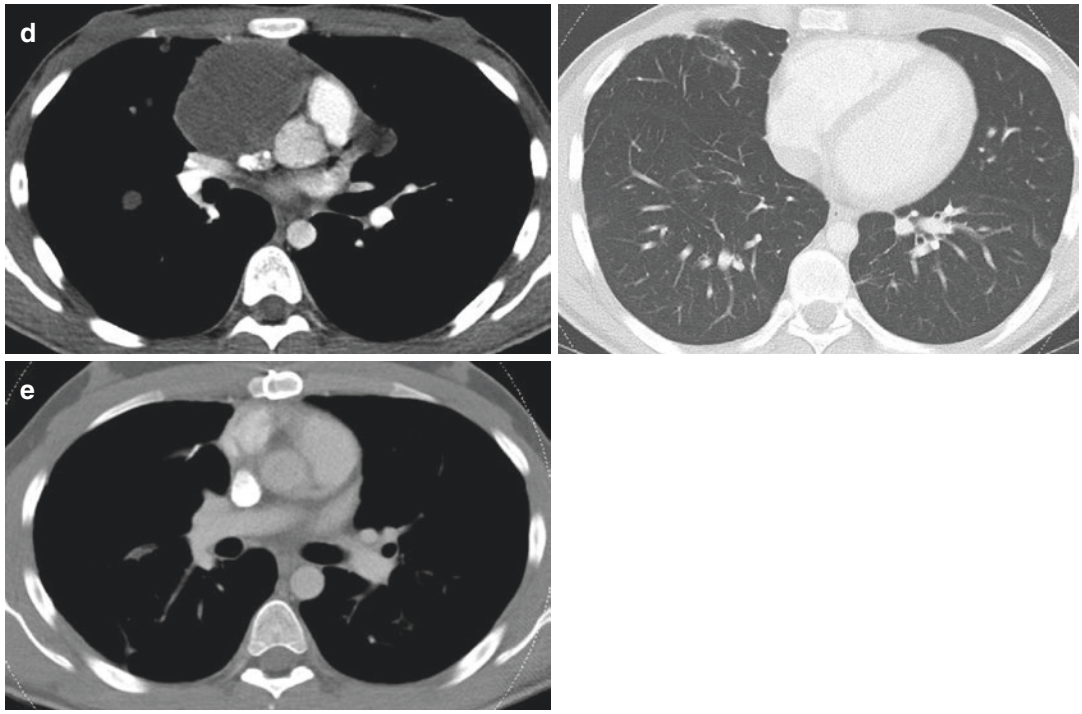


**Fig. 14.3** (continued)

### 14.4.1 Mediastinal Hodgkin's Lymphoma

*Clinical manifestations*—Primary classic Hodgkin's lymphoma (HL) is relatively rare, with the nodular sclerosis subtype being the most common subtype in more than 95% of cases [26]. Typically affecting young women, 30–50% patients are asymptomatic at the time of presentation, with the condition diagnosed incidentally by imaging for other reasons. Around 30% of patients develop B-symptoms such as fever, night sweats, and weight loss, whereas 10-15% present with generalized pruritus [26]. Although symptoms related to extrinsic compression of the mediastinal structures may occur, it is unusual in the setting of classic HL, where the nodal mass tends to displace the adjacent structures without significant compromise even in patients with bulky disease.

*Diagnosis*—Laboratory abnormalities in patients with classic HL include abnormal complete blood count (CBC) such as leukocytosis, leukopenia, or anemia. Erythrocyte sedimentation rate (ESR) and LDH are usually elevated and may correlate with the presence of bulky disease [26]; however neither is specific for the diagnosis of HL. Chest radiographs usually demonstrate a smoothly marginated or lobulated anterior mediastinal mass, or mediastinal widening [27]. On chest CT, patients may demonstrate a solitary bulky anterior mediastinal mass with lobulated contour, or multiple discrete lymph nodes that may be confluent (Fig. 14.4). Masses usually demonstrate mild-to-moderate enhancement following IV contrast administration, with occasionally cystic spaces and necrosis [28]. The most common region involved in the anterior mediastinum is the prevascular compartment [27]. In some patients, there may be additional mediastinal, hilar, axillary, supraclavicular, or internal mammary chain lymph nodes. Following the definitive diagnosis of HL by histologic sampling, most patients undergo FDG PET/CT for initial staging, which usually demonstrates intense FDG uptake within the anterior mediastinal mass

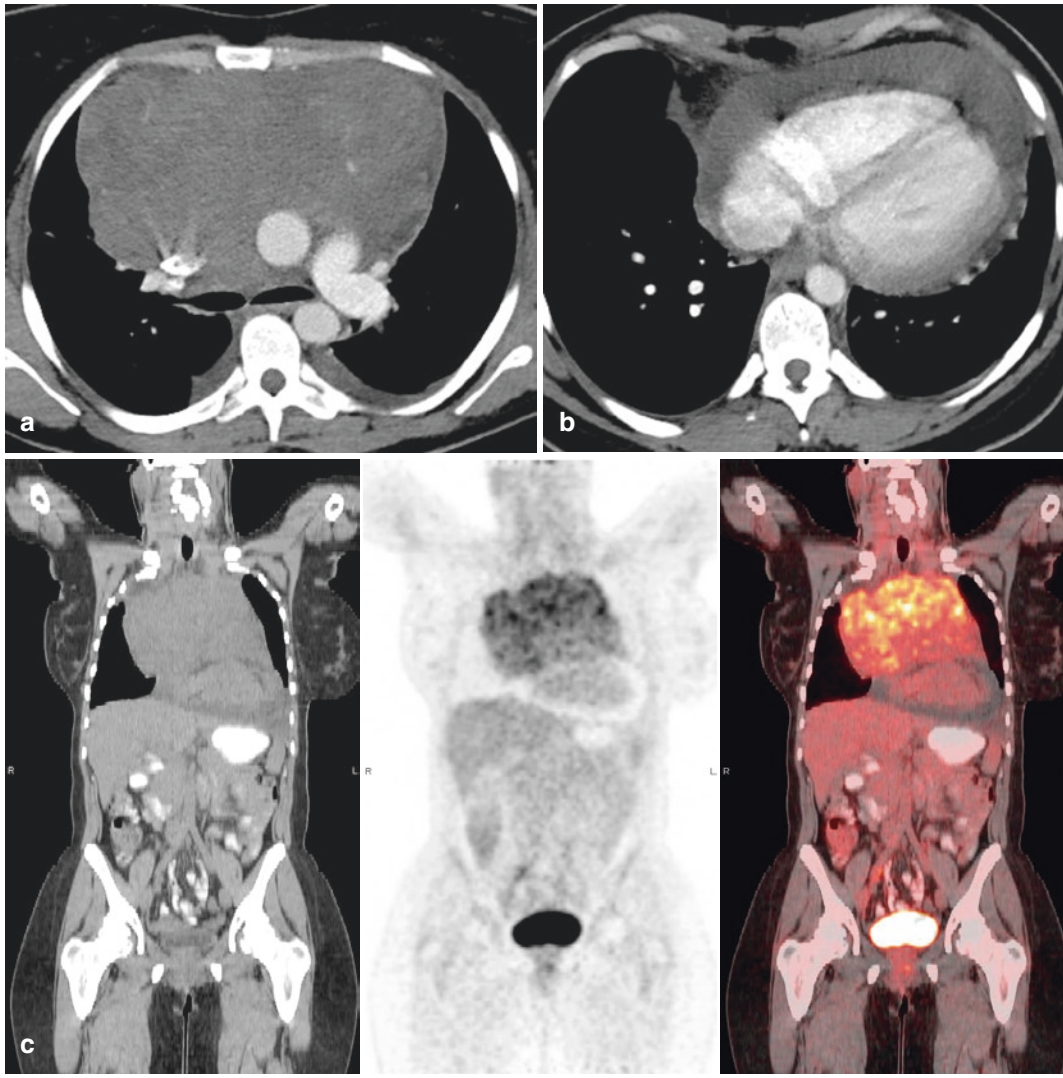


**Fig. 14.4** *34-year-old female with classic Hodgkin's lymphoma.* Axial chest CT (**a**, **b**) demonstrating a bulky heterogeneous anterior mediastinal mass with lobulated contours. Note the presence of pleural and pericardial effusions. CT-guided biopsy of the mass confirmed Hodgkin's lymphoma. Initial staging of FDG-PET/CT (**c**) revealed intense uptake within the mass (SUV 11.1), with no additional hypermetabolic lymph nodes

(Fig. 14.4), with standardized uptake values (SUVs) greater than 10 correlating with higher grade of lymphoma [29]. FDG PET/CT also helps detect additional sites of lymphoma above or below the diaphragm with higher sensitivity compared to CT [30], and is also an excellent modality for monitoring treatment response [31], as well as detection of lymphoma relapse [32]. Bulky mediastinal disease is defined by the presence of a mass measuring >10 cm.

*Treatment and prognosis*—Patients with mediastinal HL are usually categorized as either stage I (single lymph node group or thymus involvement) or stage II (two or more lymph node groups on the same side of the diaphragm), according to the Costwolds modified Ann Arbor classification [33]. Poor prognostic or "unfavorable" factors include bulky mediastinal disease, presence of B-symptoms, and elevated ESR [26]. In general, patients without bulky disease are treated with

concurrent chemotherapy and radiation therapy of the involved site(s), with an excellent prognosis, including a 10-year survival rate of 95% for patients with stage I or II disease and no unfavorable factors [34]. On the other hand, patients with bulky mediastinal disease are also treated with concurrent chemotherapy and radiation therapy, with however more cycles of the chemotherapy regimen compared to the non-bulky disease patients. These patients, especially in the presence of unfavorable factors, tend to have a worse prognosis and a relapse rate of 15% [34].

### 14.4.2 Mediastinal Large B-Cell Lymphoma

*Clinical manifestations*—Primary mediastinal large B-cell lymphoma (LBCL) is a clinically aggressive subtype of lymphoma thought to arise from B cells of thymic origin, predominantly affecting females with a median age of 30–40 years old at the time diagnosis [35]. Most cases manifest as a locally invasive anterior mediastinal mass, with patients often presenting with signs of airway compromise or SVC syndrome. In one series, SVC syndrome was present in 57% of patients, whereas 80% of patients had some degree of mass effect on the SVC by the anterior mediastinal mass [36]. Prompt clinical recognition of SVC syndrome is of paramount importance since prompt management is critical, as will be discussed in the "treatment" section below. Shortness of breath is the most common symptom, with other more specific signs including facial swelling and redness, which may be exacerbated by lying down or bending forward. Other oncologic emergencies with which patients with mediastinal LBCL may present include tumor lysis syndrome and pericardial tamponade. Systemic B symptoms, pleural or pericardial effusions, may be present in up to 50% of the cases [37].

*Diagnosis*—The majority of mediastinal LBCL patients present with elevated serum LDH levels [37]. Chest radiograph demonstrates the presence of a large mediastinal mass; however this is no longer obtained frequently, as most patients present with worrisome signs and symptoms as described above, leading to acquisition of a chest CT directly. Findings on chest CT are not very specific, and include a large anterior mediastinal mass, with additional discrete intrathoracic lymph nodes, vascular encasement, pleural or pericardial effusion, and in a few cases invasion into the adjacent chest wall, lung parenchyma, or overlying skin [38]. In addition, signs of SVC syndrome can be easily recognized on CT, including encasement and/or narrowing of the SVC, venous collaterals in the chest wall anteriorly or posteriorly, or "hot quadrate" sign in the liver (Fig. 14.5c). Almost all patients with mediastinal LBCL demonstrate intense uptake on FDG PET/CT (Fig. 14.5a, b), rendering it an excellent modality for staging and for evaluation of residual viable lymphoma following completion of therapy.

*Treatment and prognosis*—The optimal treatment strategy for patients with primary mediastinal LBCL is controversial. For management purposes, patients are classified as having limited-stage disease (can be contained with one radiation field) or advanced-stage disease, which includes disease that cannot be contained with one radiation field, bulky disease (>10 cm) or associated pleural/pericardial effusion. For both stages, the usual regimen involves induction chemoimmunotherapy, such as rituximab, cyclophosphamide, doxorubicin, vincristine, and prednisone (R-CHOP), with advanced-disease patients requiring more cycles than those with limited disease [39]. The decision of following this with radiation therapy of the involved field is more controversial and depends on many factors, such as patient and tumor characteristics, choice of the chemoimmunotherapy agents, and whether disease is confined to the chest [40]. Monitoring of treatment response is best achieved by FDG PET/CT, which should be obtained 6–8 weeks following completion of chemotherapy and 12 weeks following completion of radiation therapy [41], unless there is clinical suspicion of progression earlier, in order to avoid false-positive results related to the therapy itself. Recent studies report cure rates similar to patients with diffuse LBCL treated with aggressive therapy, with

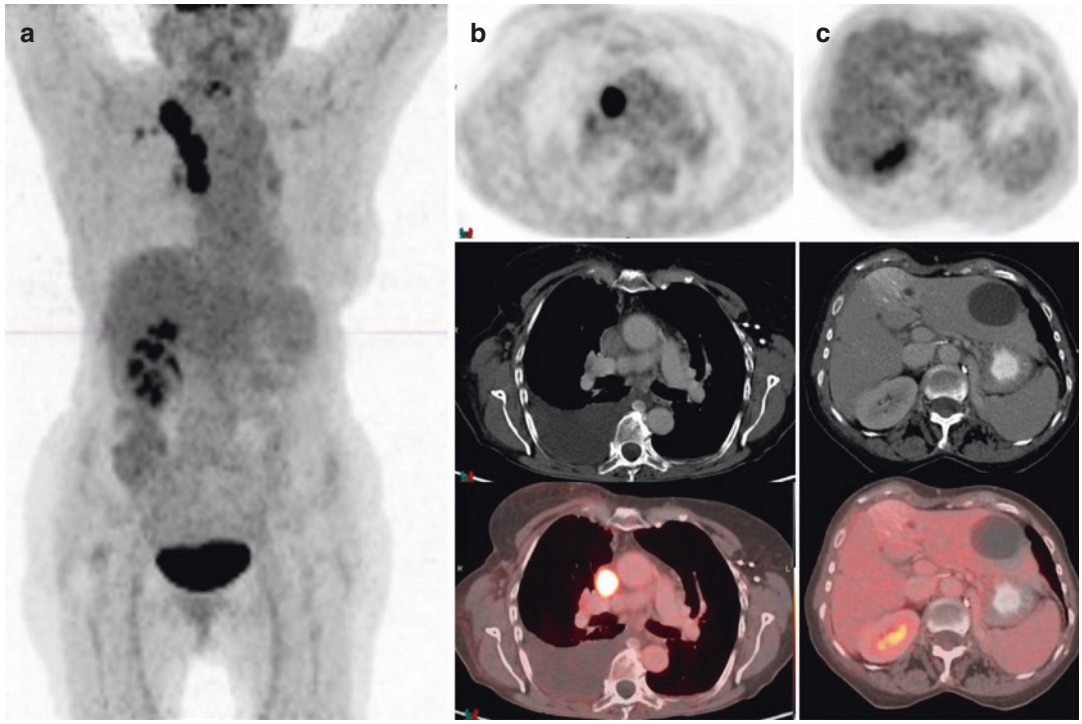


**Fig. 14.5** *35-year-old female with newly diagnosed mediastinal LBCL.* (**a**) MIP and (**b**) axial PET, CT, and fusion images demonstrating a large anterior mediastinal mass completely invading the SVC. Note the presence of an additional hypermetabolic right hilar lymph node and a right pleural effusion. (**c**) Images through the liver demonstrating a "hot quadrate" sign. Findings consistent with SVC syndrome

overall survival rates up to 72% [35]. However, in patients with relapse or disease progression, salvage therapy is rarely curative.

## 14.5 Mediastinal Mesenchymal Tumors

Mesenchymal tumors of the mediastinum are rare, comprising around 5% of mediastinal tumors [42], with a higher prevalence and malignant potential in children. This group of neoplasms consists of tumors of various origins, such as those originating from muscle, adipose tissue, lymphatics, blood vessels, skeletal tissue, and fibrous tissue, including both benign and malignant tumors (Table 14.3). For the purposes of our discussion, we briefly discuss mediastinal lipoma, rhabdomyosarcoma, and chondrosarcoma as examples of mesenchymal tumors.

### 14.5.1 Mediastinal Lipoma

Lipomas are rare in the mediastinum, accounting for less than 2% of all mediastinal masses, predominantly located in the anterior mediastinum [43]. They tend to grow in areas of minimal or absent resistance such as the right paratracheal space. Almost all patients are asymptomatic at presentation, and most lipomas are detected incidentally on imaging studies obtained for other purposes. Chest radiograph may demonstrate the incidental anterior mediastinal mass or simply thickening of the right paratracheal stripe. On chest CT, mediastinal lipomas demonstrate the characteristic appearance of a well-circumscribed mass with homogenous fat attenuation (Fig. 14.6). Chest MRI is rarely needed for the diagnosis given the characteristic appearance on CT. Surgical resection may be performed for relief of compression on adjacent mediastinal structures, and is often curable. Inhomogeneous fat attenuation or

**Table 14.3** Primary mesenchymal tumors of the mediastinum

| Tissue of origin | Benign tumor | Malignant tumor |
|---|---|---|
| Muscle | Leiomyoma | Leiomyosarcoma |
| | Rhabdomyoma | Rhabdomyosarcoma |
| Fibroblastic | Fibromatosis | Fibrosarcoma |
| | | Malignant fibrous histiocytoma (MFH) |
| Lymphatic | Lymphangioma | |
| Adipose | Lipoma | Liposarcoma |
| | Lipoblastoma | |
| Skeletal | Chondroma | Chondrosarcoma |
| | | Osteosarcoma |
| Blood vessels | Hemangioma | Hemangioendothelioma |
| | | Angiosarcoma |

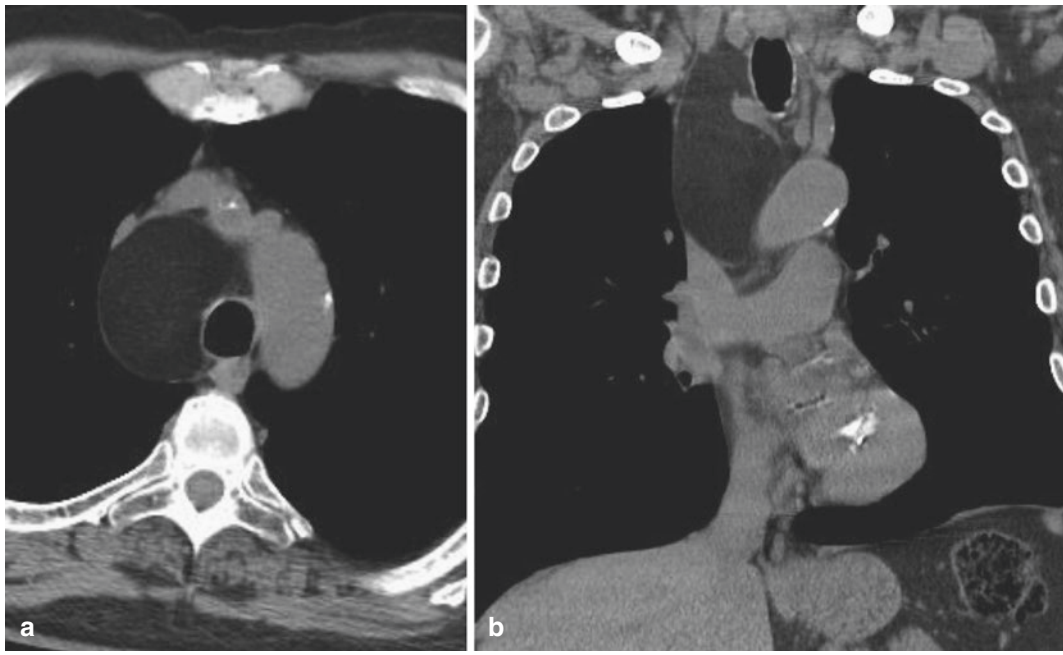


**Fig. 14.6** *86-year-old male with an incidental anterior mediastinal mass.* Axial (**a**) and coronal (**b**) nonenhanced chest CT images demonstrating a well-circumscribed right paratracheal mass with homogeneous fat attenuation, consistent with a lipoma

presence of any soft tissue or nonfat density on chest CT or MRI should raise the suspicion for a liposarcoma, which is usually treated with resection followed by radiation therapy.

### 14.5.2 Mediastinal Rhabdomyosarcoma

Rhabdomyosarcomas may present at any age, and however are much more common in children during the first decade of life [42]. Mediastinal location is rare, accounting for less than 2% of childhood rhabdomyosarcomas [43]. Rhabdomyosarcomas include pleomorphic, alveolar, and embryonal subtypes. Initial radiologic evaluation should include radiography followed by CT or MRI of the affected area. Chest CT may also be part of the metastatic workup, in addition to bone marrow aspiration and/or radionuclide bone scans. The role of FDG PET/CT for initial staging is not clear [44]. Most tumors are bulky and heterogeneous at the time of presentation

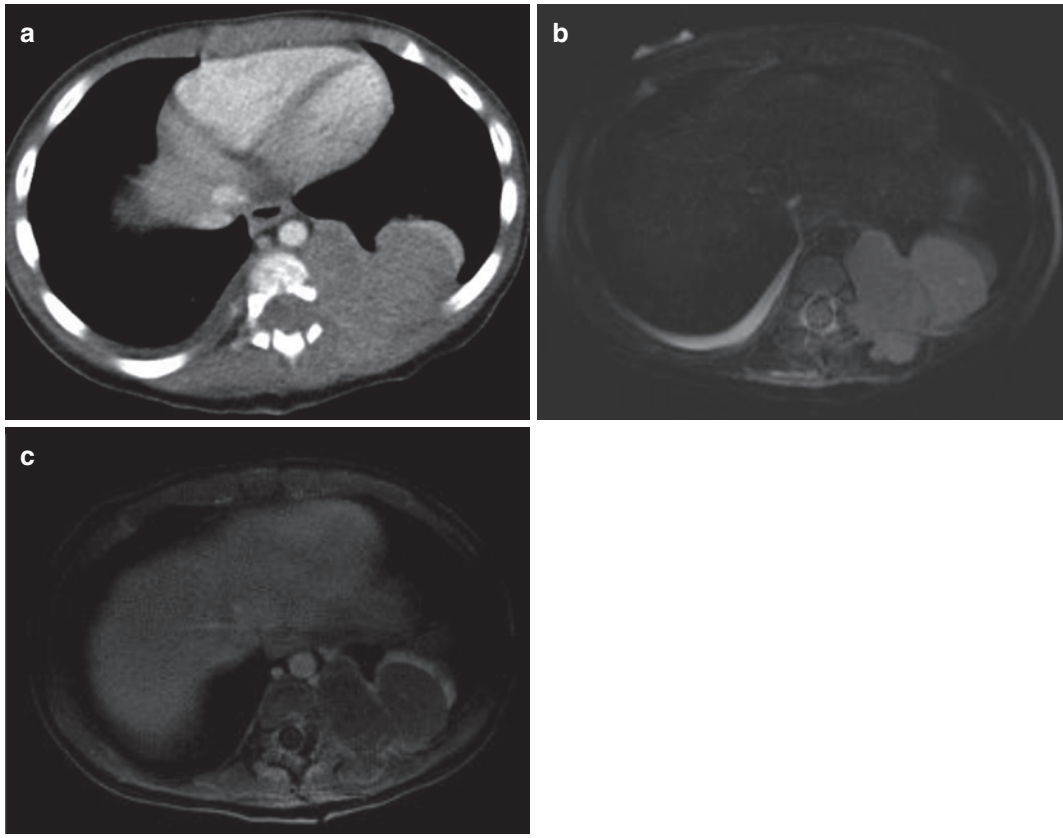


**Fig. 14.7** 6-year-old boy with posterior mediastinal rhabdomyosarcoma. Axial CT (**a**), T2 fat-saturation MR (**b**), and T1 post-contrast (**c**) images of the chest demonstrating a large infiltrative mildly enhancing mass in the posterior mediastinum extending into the adjacent neural foramina and into the posterior chest wall. Partial resection and biopsy revealed rhabdomyosarcoma

(Fig. 14.7). Treatment of rhabdomyosarcomas has evolved significantly over the past decades, with cure rates up to 70% using combined modality therapy [45]. These improved outcomes have been largely due to development of large international cooperative groups, such as the Soft Tissue Sarcoma Committee of the Children's Oncology Group (COG). Modern therapy for these tumors includes chemotherapy for local control and metastatic disease, followed by surgery if feasible, and radiation therapy for longer term control especially for sites of micrometastatic disease.

### 14.5.3 Mediastinal Chondrosarcoma

Chondrosarcomas are the third most common primary bone tumor after myeloma and osteosarcoma [46]. Extraosseous chondrosarcomas represent 2% of all soft-tissue sarcomas, most often arising from the chest wall [47]. The exact incidence of primary mediastinal chondrosarcoma is unknown due to scarce data in the literature, with a reported incidence of just 0.5 in 1 million [48]. Imaging appearance on chest CT is nonspecific, demonstrating a heterogeneous mass with cystic components and calcifications in some cases (Fig. 14.8). The few case reports in the literature describe masses arising from the sternum, cartilaginous portions of the ribs, and thyroid cartilage [47]. In general, chondrosarcomas are resistant to chemotherapy and radiation therapy, especially the low- to intermediate-grade tumors, which comprise around 90% of cases [49]. Therefore, surgery is the mainstay of treatment, with radiation therapy reportedly used in a few mediastinal chondrosarcomas, especially in high-grade tumors.

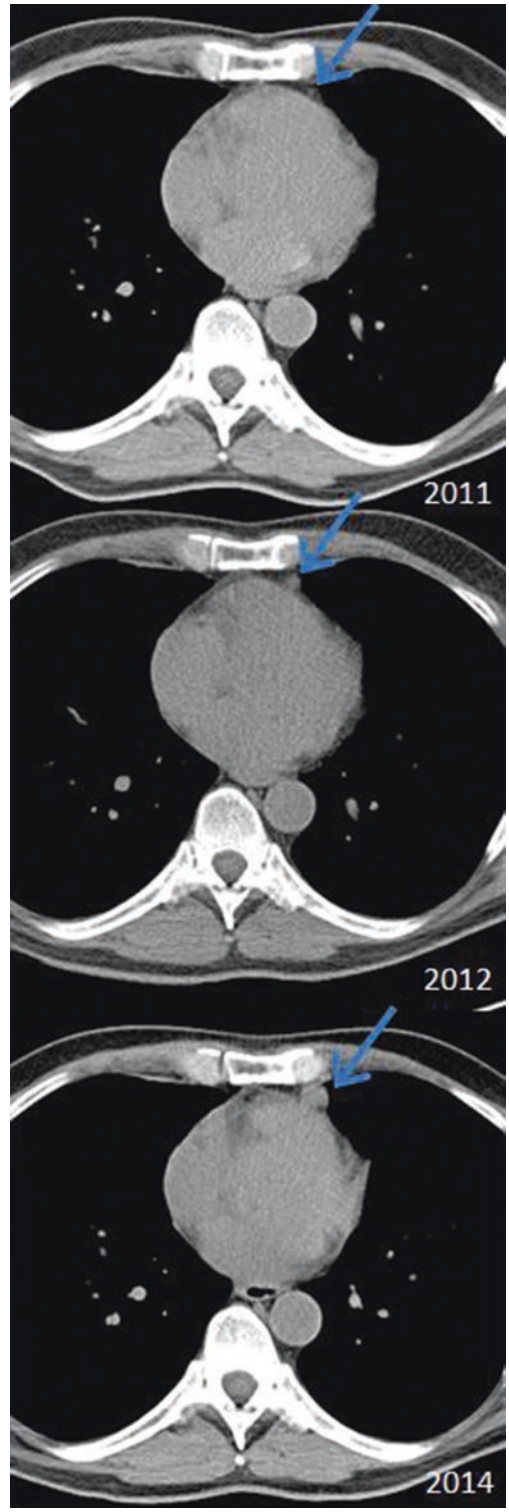


**Fig. 14.8** 67-year-old male with a history of anterior mediastinal chondrosarcoma treated with resection and radiation therapy. Axial CT images obtained over the course of 3 years demonstrating a small anterior mediastinal soft-tissue nodule progressively enlarging. Patient underwent subsequent resection, histopathology revealing recurrent chondrosarcoma

## References


1. Felson B. Chest roentgenology. Philadelphia, PA: Saunders; 1973.
2. Carter BW, Tomiyama N, Bhora FY, et al. A modern definition of mediastinal compartments. J Thorac Oncol. 2014;9:S97–101.
3. Carter BW, Benveniste MF, Madan R, et al. ITMIG Classification of mediastinal compartments and multidisciplinary approach to mediastinal masses. Radiographics. 2017;37:413–36.
4. Carter BW, Marom EM, Detterbeck FC. Approaching the patient with an anterior mediastinal mass: a guide for clinicians. J Thorac Oncol. 2014;9:S102–9.
5. Osserman KE, Genkins G. Studies in myasthenia gravis: review of a twenty-year experience in over 1200 patients. Mt Sinai J Med. 1971;38:497–537.
6. Davis RD Jr, Oldham HN Jr, Sabiston DC Jr. Primary cysts and neoplasms of the mediastinum: recent changes in clinical presentation, methods of diagnosis, management, and results. Ann Thorac Surg. 1987;44:229–37.
7. Lewis BD, Hurt RD, Payne WS, et al. Benign teratomas of the mediastinum. J Thorac Cardiovasc Surg. 1983;86:727–31.
8. Adebonojo SA, Nicola ML. Teratoid tumors of the mediastinum. Am Surg. 1976;42:361–5.
9. Moeller KH, Rosado-de-Christenson ML, Templeton PA. Mediastinal mature teratoma: imaging features. AJR Am J Roentgenol. 1997;169:985–90.
10. Takeda S, Miyoshi S, Ohta M, et al. Primary germ cell tumors in the mediastinum: a 50-year experience at a single Japanese institution. Cancer. 2003;97:367–76.
11. Feo CF, Chironi G, Porcu A, et al. Videothoracoscopic removal of a mediastinal teratoma. Am Surg. 1997;63:459–61.
12. Arai K, Ohta S, Suzuki M, et al. Primary immature mediastinal teratoma in adulthood. Eur J Surg Oncol. 1997;23:64–7.
13. Donadio AC, Motzer RJ, Bajorin DF, et al. Chemotherapy for teratoma with malignant transformation. J Clin Oncol. 2003;21:4285–91.
14. Moran CA, Suster S, Przygodzki RM, et al. Primary germ cell tumors of the mediastinum: II. Mediastinal seminomas--a clinicopathologic and immunohistochemical study of 120 cases. Cancer. 1997;80:691–8.
15. Dulmet EM, Macchiarini P, Suc B, et al. Germ cell tumors of the mediastinum. a 30-year experience. Cancer. 1993;72:1894–901.
16. Bohle A, Studer UE, Sonntag RW, et al. Primary or secondary extragonadal germ cell tumors? J Urol. 1986;135:939–43.
17. Bokemeyer C, Nichols CR, Droz JP, et al. Extragonadal germ cell tumors of the mediastinum and retroperitoneum: results from an international analysis. J Clin Oncol. 2002;20:1864–73.
18. Strollo DC, Rosado-de-Christenson ML. Primary mediastinal malignant germ cell neoplasms: imaging features. Chest Surg Clin N Am. 2002;12:645–58.
19. Shin MS, Ho KJ. Computed tomography of primary mediastinal seminomas. J Comput Assist Tomogr. 1983;7:990–4.
20. Rosado-de-Christenson ML, Templeton PA, Moran CA. From the archives of the AFIP. Mediastinal germ cell tumors: radiologic and pathologic correlation. Radiographics. 1992;12:1013–30.
21. Hainsworth JD, Greco FA. Extragonadal germ cell tumors and unrecognized germ cell tumors. Semin Oncol. 1992;19:119–27.
22. Hartmann JT, Nichols CR, Droz JP, et al. Hematologic disorders associated with primary mediastinal nonseminomatous germ cell tumors. J Natl Cancer Inst. 2000;92:54–61.
23. Orazi A, Neiman RS, Ulbright TM, et al. Hematopoietic precursor cells within the yolk sac tumor component are the source of secondary hematopoietic malignancies in patients with mediastinal germ cell tumors. Cancer. 1993;71:3873–81.
24. Nichols CR. Mediastinal germ cell tumors. Clinical features and biologic correlates. Chest. 1991;99:472–9.
25. Fizazi K, Culine S, Droz JP, et al. Primary mediastinal nonseminomatous germ cell tumors: results of modern therapy including cisplatin-based chemotherapy. J Clin Oncol. 1998;16:725–32.
26. Pina-Oviedo S, Moran CA. Primary mediastinal classical Hodgkin lymphoma. Adv Anat Pathol. 2016;23:285–309.
27. Strollo DC. Rosado de Christenson ML, and Jett JR Primary mediastinal tumors. Part 1: Tumors of the anterior mediastinum. Chest. 1997;112:511–22.
28. Shahrzad M, Le TS, Silva M, et al. Anterior mediastinal masses. AJR Am J Roentgenol. 2014;203:W128–38.
29. Itti E, Meignan M, Berriolo-Riedinger A, et al. An international confirmatory study of the prognostic value of early PET/CT in diffuse large B-cell lymphoma: comparison between Deauville criteria and DeltaSUVmax. Eur J Nucl Med Mol Imaging. 2013;40:1312–20.
30. Schaefer NG, Hany TF, Taverna C, et al. Non-Hodgkin lymphoma and Hodgkin disease: coregistered FDG PET and CT at staging and restaging--do we need contrast-enhanced CT? Radiology. 2004;232:823–9.
31. Hutchings M, Barrington SF. PET/CT for therapy response assessment in lymphoma. J Nucl Med. 2009;50(Suppl 1):21S–30S.
32. Zinzani PL, Stefoni V, Tani M, et al. Role of [18F] fluorodeoxyglucose positron emission tomography scan in the follow-up of lymphoma. J Clin Oncol. 2009;27:1781–7.
33. Lister TA, Crowther D, Sutcliffe SB, et al. Report of a committee convened to discuss the evaluation and staging of patients with Hodgkin's disease: Cotswolds meeting. J Clin Oncol. 1989;7:1630–6.
34. Diehl V, Thomas RK, Re D, Part II. Hodgkin's lymphoma--diagnosis and treatment. Lancet Oncol. 2004;5:19–26.
35. Nguyen LN, Ha CS, Hess M, et al. The outcome of combined-modality treatments for stage I and II primary

large B-cell lymphoma of the mediastinum. Int J Radiat Oncol Biol Phys. 2000;47:1281–5.
36. Jacobson JO, Aisenberg AC, Lamarre L, et al. Mediastinal large cell lymphoma. An uncommon subset of adult lymphoma curable with combined modality therapy. Cancer. 1988;62:1893–8.
37. Savage KJ, Al-Rajhi N, Voss N, et al. Favorable outcome of primary mediastinal large B-cell lymphoma in a single institution: the British Columbia experience. Ann Oncol. 2006;17:123–30.
38. Tateishi U, Muller NL, Johkoh T, et al. Primary mediastinal lymphoma: characteristic features of the various histological subtypes on CT. J Comput Assist Tomogr. 2004;28:782–9.
39. Hamlin PA, Portlock CS, Straus DJ, et al. Primary mediastinal large B-cell lymphoma: optimal therapy and prognostic factor analysis in 141 consecutive patients treated at Memorial Sloan Kettering from 1980 to 1999. Br J Haematol. 2005;130:691–9.
40. Rieger M, Osterborg A, Pettengell R, et al. Primary mediastinal B-cell lymphoma treated with CHOP-like chemotherapy with or without rituximab: results of the Mabthera International Trial Group study. Ann Oncol. 2011;22:664–70.
41. Juweid ME, Stroobants S, Hoekstra OS, et al. Use of positron emission tomography for response assessment of lymphoma: consensus of the Imaging Subcommittee of International Harmonization Project in Lymphoma. J Clin Oncol. 2007;25:571–8.
42. Lee KH, Song KS, Kwon Y, et al. Mesenchymal tumours of the thorax: CT findings and pathological features. Clin Radiol. 2003;58:934–44.
43. Macchiarini P, Ostertag H. Uncommon primary mediastinal tumours. Lancet Oncol. 2004;5:107–18.
44. McCarville MB, Christie R, Daw NC, et al. PET/CT in the evaluation of childhood sarcomas. AJR Am J Roentgenol. 2005;184:1293–304.
45. Raney RB, Walterhouse DO, Meza JL, et al. Results of the Intergroup Rhabdomyosarcoma Study Group D9602 protocol, using vincristine and dactinomycin with or without cyclophosphamide and radiation therapy, for newly diagnosed patients with low-risk embryonal rhabdomyosarcoma: a report from the Soft Tissue Sarcoma Committee of the Children's Oncology Group. J Clin Oncol. 2011;29:1312–8.
46. Dorfman HD, Czerniak B. Bone cancers. Cancer. 1995;75:203–10.
47. Ostergaard ML, Petersen RH, Kalhauge A. A chondrosarcoma in the anterior mediastinum mimicking a thymoma. Acta Radiol Open. 2015;4:2058460115595659.
48. Widhe B, Bauer HC, Scandinavian Sarcoma G. Surgical treatment is decisive for outcome in chondrosarcoma of the chest wall: a population-based Scandinavian Sarcoma Group study of 106 patients. J Thorac Cardiovasc Surg. 2009;137:610–4.
49. Angelini A, Guerra G, Mavrogenis AF, et al. Clinical outcome of central conventional chondrosarcoma. J Surg Oncol. 2012;106:929–37.

# Mediastinal Non-neoplastic Conditions

15

Beatrice Sacconi, Giada Valente, and Mariaelena Occhipinti

**Abstract**

Mediastinum can be interested by a variety of neoplastic and non-neoplastic conditions, mostly affecting the anterior mediastinum. Mediastinal disease can be suspected at conventional radiography and further investigated at CT and MRI. This chapter is focused on non-neoplastic conditions; congenital diseases are discussed in the first part, such as oesophageal duplication cysts, bronchogenic, thymic and pericardial cysts and other less common entities. In the second part of the chapter we focus on acquired conditions, such as infectious/inflammatory, vascular and iatrogenic diseases.

**Keywords**

Mediastinum · Mediastinal non-neoplastic conditions · Mediastinal congenital cysts · Fibrosing mediastinitis · Thymic hyperplasia

B. Sacconi · G. Valente
Department of Radiological, Oncological and Anatomopatological Sciences, Sapienza—University of Rome, Policlinico Umberto I, Rome, Italy

M. Occhipinti (✉)
Department of Clinical and Experimental Medicine, University of Florence, Florence, Italy

## 15.1 Mediastinal Non-neoplastic Conditions

Mediastinum can be interested by a variety of neoplastic and non-neoplastic conditions, mostly affecting the anterior mediastinum. Mediastinal disease can be suspected at conventional radiography, based on distortion of mediastinal lines. Anterior mediastinal abnormalities can be identified when the hilum overlay sign is present and the posterior mediastinal lines are maintained. A middle mediastinal abnormality can be suggested by a widening of the right paratracheal stripe and convexity relative to the aortopulmonary window reflection. Obliteration of the azygo-oesophageal recess can be observed in case of abnormalities of the middle or posterior mediastinum. Paravertebral masses can alter the paraspinal lines. The analysis of the mediastinal reflections at conventional radiography helps to localise an abnormality; identifying the involved mediastinal compartment helps in the differential diagnosis [1]. However, computed tomography (CT) is the main technique to be used. CT supports the diagnosis due to its ability to differentiate specific attenuation of air, fat, water and calcium. High-resolution multiplanar reconstructions permit to evaluate the relationships of the lesions with the adjacent structures, especially with the pericardium, heart cavities and vessels [2]. Magnetic resonance imaging (MRI) has high contrast resolution and can provide further information about the location and the extent of the disease; in addi-



M. Anzidei, M. Anile (eds.), *Diagnostic Imaging for Thoracic Surgery*,
https://doi.org/10.1007/978-3-319-89893-3_15

tion it can characterise the tissue showing the cystic or solid nature of the abnormality, or can provide information in patients with contraindications to CT contrast media [1].

This chapter is focused on non-neoplastic conditions; among them, infectious and inflammatory reactive diseases, congenital and acquired cysts and other less common conditions are discussed.

## 15.2 Congenital Disease

Among congenital conditions, a large variety of cysts can occur; bronchogenic cysts account for up to 50% of the cases, followed by oesophageal, thymic and pericardial cysts. Bronchogenic cysts (Fig. 15.1) are rare congenital malformations of the bronchial tree accounting for only 5–10% of paediatric mediastinal masses.

They are commonly located in the middle mediastinum (65–90%) and do not usually communicate with the bronchial tree, containing fluid rather than air. At X-ray the cysts usually appear as soft-tissue density rounded structures. CT usually shows well-circumscribed spherical masses of variable attenuation with variable fluid composition; thus different CT attenuations can be observed depending on the amount of proteinaceous content [3]; for the same reasons, the cysts demonstrate high signal on T2-weighted sequences and variable signal intensity on T1-weighted sequences [4]. Oesophageal duplication cysts are a type of congenital foregut duplication cyst, commonly lined by gastric epithelium, and thus prone to infection, perforation and haemorrhage. They appear as well-defined thick-walled fluid-filled structures noted along the oesophagus. Bronchogenic and oesophageal duplication cysts can be differentiated based on location (bronchogenic cysts are more commonly located in the subcarinal region, whereas the oesophageal duplication cysts are located along the oesophagus), shape (the oesophageal ones are commonly tubular rather than spherical) and wall thickness (thin-walled bronchogenic cyst vs. thick-walled thin-walled oesophageal cyst) [5]. Thymic cysts account for approximately 1-3% of all anterior mediastinal masses [6]; 50% of congenital thymic cysts are incidentally found during the first two decades of life, whereas acquired cysts usually occur much later. They usually appear as unilocular or multilocular cystic masses with well-defined walls, frequently lobulated; they may show increased CT attenuation if haemorrhage or infection occurs. Calcifications are uncommon. MR signal characteristics are similar to those of simple cyst [7]. Pericardial cysts (Fig. 15.2) are uncommon benign congenital cysts of the anterior and middle mediastinum, usually asymptomatic and incidentally discovered. Only occasionally patients may present with chest pain and dyspnoea.

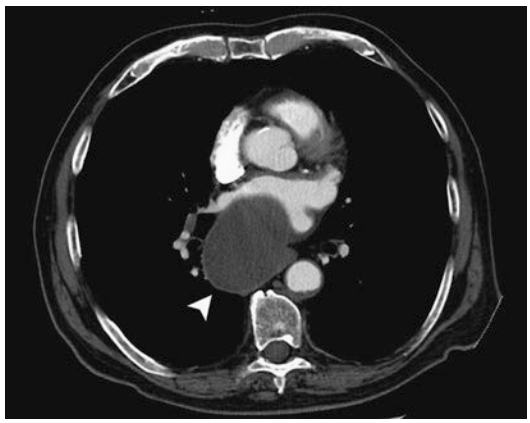

**Fig. 15.1** Axial enhanced CT image depicting a smoothly marginated and homogenous soft-tissue mass (*arrowhead*) consistent with a congenital bronchogenic cyst in a 80 years-old male

The right cardio-phrenic angle is the commonest location. At CT they appear as a well-defined, non-enhancing, fluid-filled rounded mass next to the pericardium. MR signal characteristics are those of simple fluid; even though internal septations can be observed [8].

Other uncommon types of cysts include lymphangiomas, mesothelial cysts, thoracic duct cysts and parasitic cysts, especially caused by Echinococcus granulosus. Lymphangioma is a

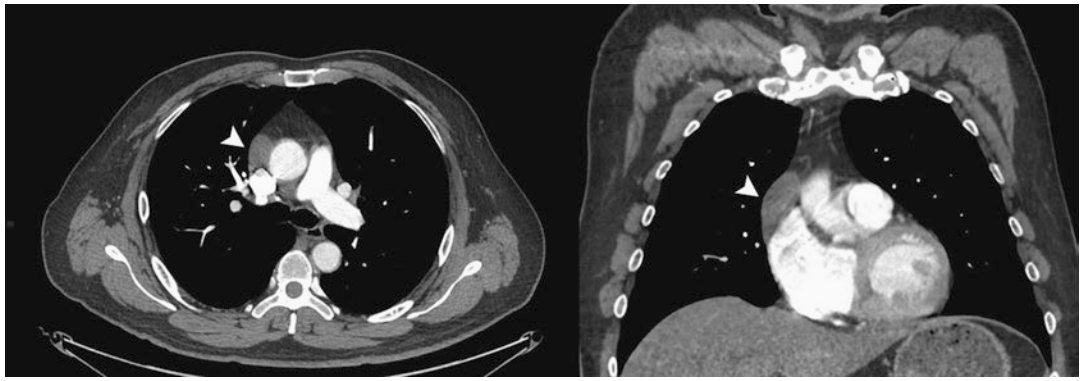

**Fig. 15.2** Axial and coronal enhanced CT images showing a congenital pericardial cyst (*arrowhead*) in a 60 years-old male

rare benign lymphatic condition, usually involving the neck or the axillary regions, and less commonly the mediastinum. In extremely rare cases pancreatic pseudocysts can extend into the mediastinum through the aortic or oesophageal hiatus, appearing as thin-walled cysts in continuity with peripancreatic fluid collections. Other non-neoplastic conditions of the mediastinum include fatty masses, Castleman disease and hamartomatous lesions. With reference to fatty lesions (excluding neoplasms, such as lipomas or thymolipomas), excessive epicardic fat (Fig. 15.3) can be observed and mimic cardiomegaly or other mediastinal masses [2].

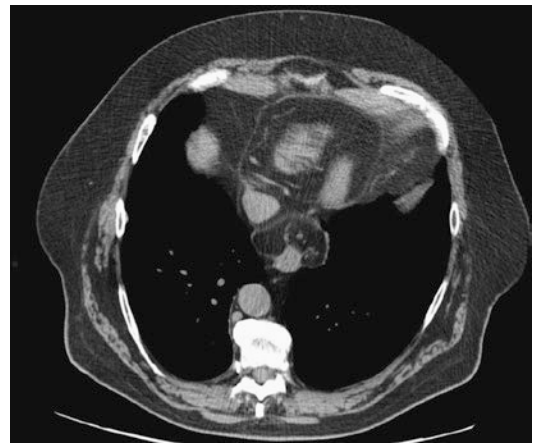

**Fig. 15.3** Axial CT image showing a mediastinal lipomatosis in a 56 years-old obese woman

Among other congenital mediastinum diseases, diaphragmatic hernias can be mentioned. In these cases, diaphragmatic hernias are defined as congenital defects in the diaphragm, whereas acquired hernias can be traumatic or iatrogenic in their origin. There are two main types of congenital diaphragmatic hernias: Bochdalek hernia (most common, located posteriorly, usually present in childhood) and Morgagni hernia (smaller, anterior, usually presenting later) [9].

As mentioned above, Bochdalek hernias (Fig. 15.4) occur posteriorly, due to a defect in the pleuroperitoneal membrane closure during pregnancy.

Large hernias, usually left sided, typically present in infancy. In adults, incidentally discovered posterior hernias are rare and usually small and right-sided hernias (68%). On chest radiograms, the hernia may appear as a lung base soft-tissue opacity lesion, located posteriorly on lateral images; CT usually shows fat above the diaphragm; the defect is well demonstrated on coronal and sagittal reconstructions [10]. Morgagni hernias (Fig. 15.5) are characterised by herniation through the foramen of Morgagni; in comparison to Bochdalek hernias, Morgagni hernias are anterior, more frequently right sided

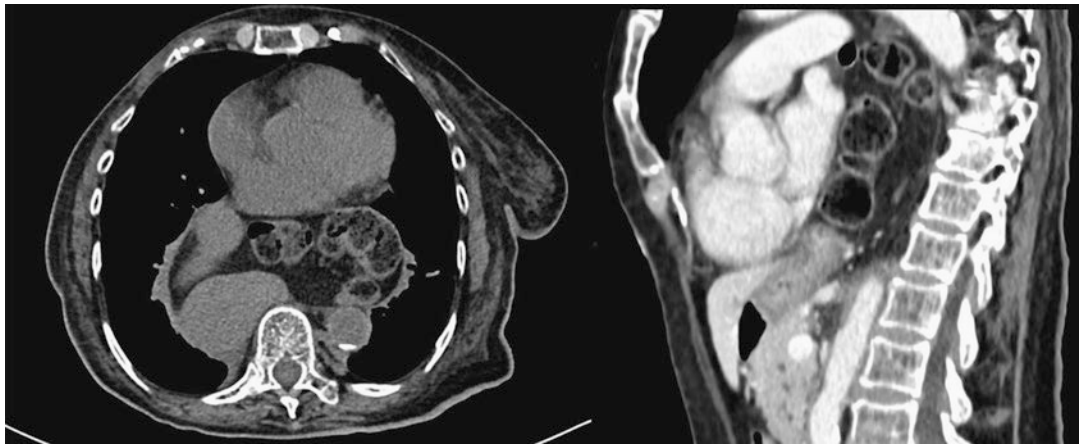

**Fig. 15.4** Axial and sagittal CT images depicting acquired Bochdalek hernia of the diaphragm in a 86 years-old male

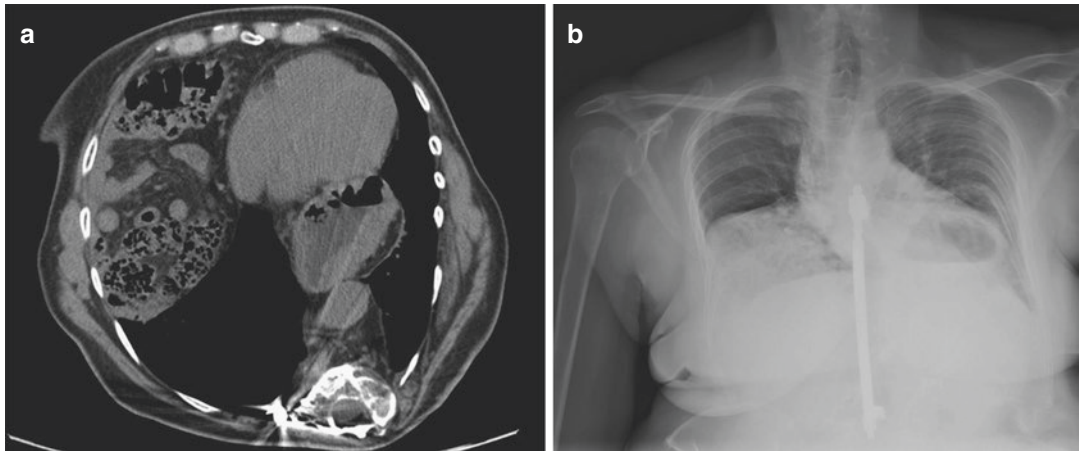


**Fig. 15.5** (**a**) Axial unenhanced CT image showing hiatal hernia and anterior right diaphragmatic hernia with small and large bowel contents in the right hemithorax in a 62 years-old woman. (**b**) Chest X-ray in a postero-anterior view depicting right Morgagni hernia

(~90%), smaller, usually asymptomatic and at low risk of prolapse [11].

## 15.3 Acquired Disease

*Infective/Inflammatory disease:* Infective acute mediastinitis can be caused by aerobic and anaerobic bacteria, frequently as a sequelae of oesophageal perforation or thoracic surgery. Fibrosing inflammation can be alternatively caused by fungal organisms, such as Aspergillus, Histoplasma and Cryptococcus, or by other species, such as micobacterias, Nocardia or Actinomyces. The lesions are histologically characterised by fibrous tissue, chronic inflammatory cells and granulomatous reaction (Fig. 15.6).

Symptoms include fever, pain, dysphagia and dyspnoea caused by massive pleural effusion or pneumothorax. Chest X-ray usually shows

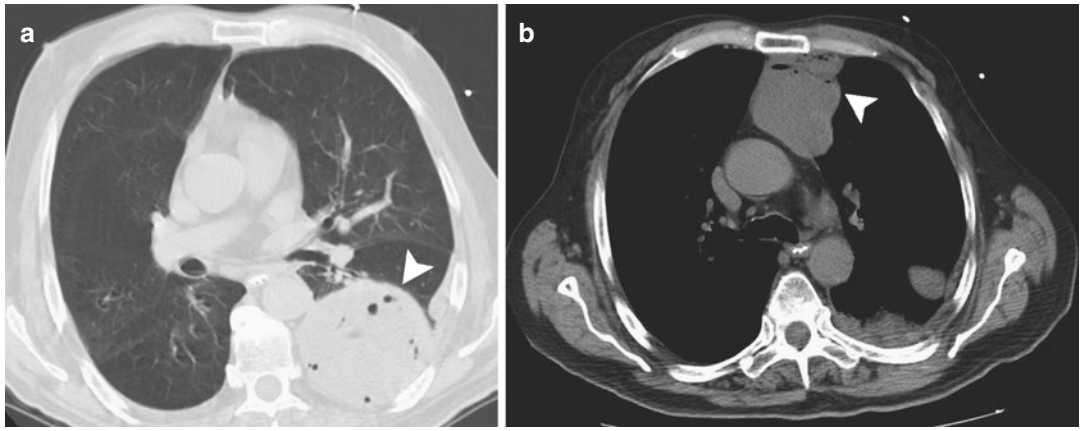


**Fig. 15.6** (**a**) Axial CT image (lung window) depicting a lung abscess in the left lower lobe (*arrowhead*) in a male patient of 80 years old. (**b**) Axial CT image (mediastinal window) showing a coexisting anterior mediastinal abscess (*arrowhead*) with an air-fluid level

mediastinal widening with ill-defined borders, determined by the amount of fibrous tissue, and pleural effusion [12]. Mycobacterium tuberculosis can be the cause of a fibrosing mediastinitis.

Chest X-ray can be a non-specific widening of the mediastinum or distortion and obliteration of normally recognisable mediastinal interfaces, often with mediastinal or hilar calcification. CT and MRI typically show involvement of the middle mediastinum, with a focal pattern (mediastinal or hilar mass) or a diffuse pattern (infiltrative tissue obliterating normal mediastinal fat planes and encasing the adjacent structures). The involvement of mediastinum can also be secondary to the spine infection (Pott disease) (Fig. 15.7) [13].

In many cases, a specific infectious agent is not identified; a potential cause can be recognised in an abnormal fibrous response secondary to rupture of a granulomatous lymphadenitis. Other cases have been related to sarcoidosis, rheumatic fever, drugs or trauma. The most frequent symptoms include dyspnoea, cough, thoracic pain, haemoptysis and dysphagia, in some cases with a self-limited course, in others with a progressive one. An asymmetric widening of the mediastinum or the presence of a lobulated mass can be detected at chest X-ray. CT can show narrowing in the bronchi and trachea and detect involvement of arteries and veins [12]. Among the mentioned inflammatory diseases of mediastinum, sarcoidosis must be further discussed; mediastinum is usually involved in stage I and stage II diseases according to the sarcoidosis staging at chest X-ray. The most common manifestation is bilateral hilar and mediastinal lymphadenopathies; classically the distribution is of bilateral hilar and right paratracheal nodal enlargement, known as the Garland triad. Lymphadenopathies can calcify, with punctuate, amorphous or eggshell patterns. At CT, sarcoidosis is often termed the "great mimicker", due to its large range of HRCT presentations; however CT is especially useful in defining as nodal enlargement in patients with normal chest X-rays (stage 0) or in identifying parenchymal involvement in those with apparently nodal involvement only [14]. Lymph nodes, especially if calcified, can also be observed in other pathologies, such as other granulomatous or occupational diseases such as silicosis and pneumoconiosis.

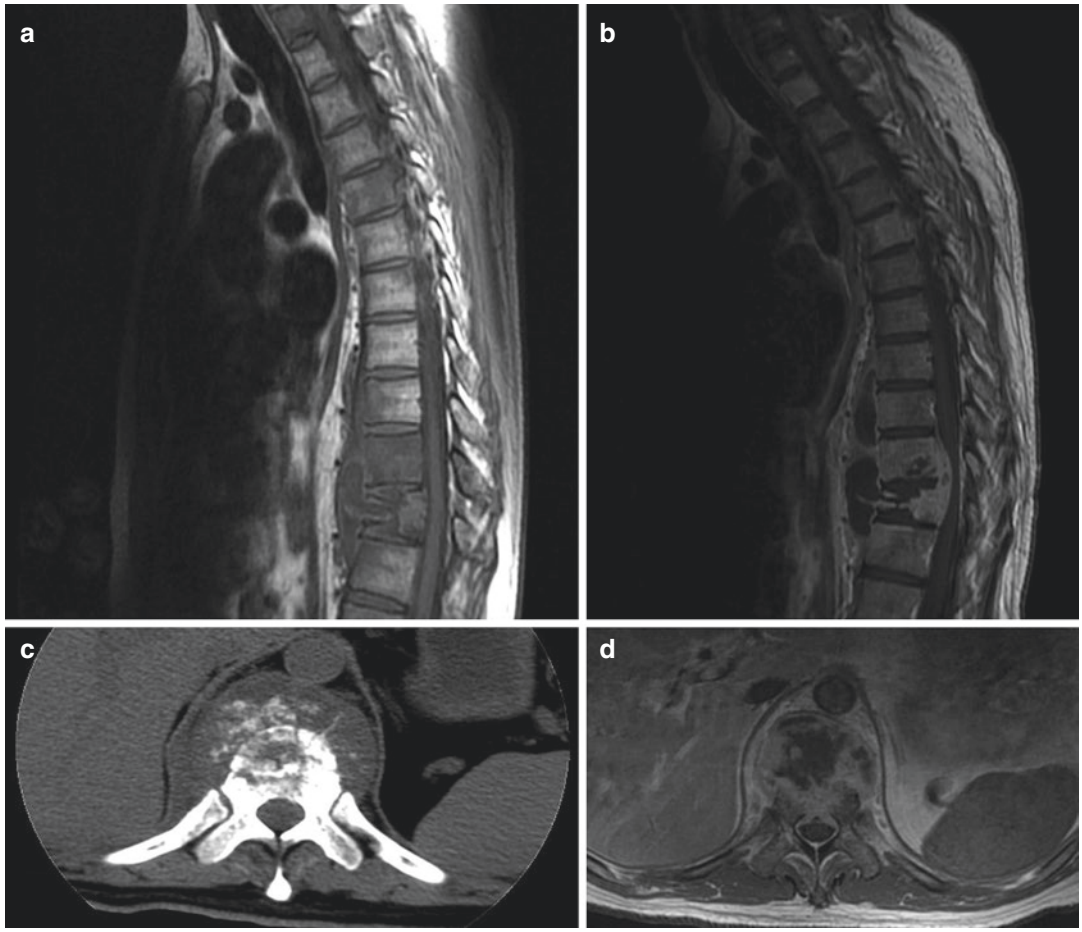


**Fig. 15.7** (**a**) Pott disease localised at the level of T11–12 vertebral bodies in a sagittal sequence T1-weighted pre- and post-contrast. (**b**)—MRI 3T showing paradiscal involvement and infection spreading to prevertebral space. (**c**) Axial CT image showing the fragmentary bone pattern and involvement of adjacent soft tissues. (**d**) Axial T1-weighted image depicting irregularity of both the endplate and anterior aspect of the vertebral body

*Benign disease:* Among pathologic conditions involving the mediastinum, thyroid and parathyroid diseases have to be considered. Mediastinal goitre represents the extension of a thyroid goitre in the mediastinum, usually appearing as lobulated inhomogeneous masses with cystic portions and calcifications. Less commonly, ectopic thyroid tissue without any connection to the thyroid in the neck can be observed. Parathyroid adenomas can be in ectopic locations, the mediastinum being the most frequent one [2]. Other pathologic conditions involve the thymus; true thymic hyperplasia is defined as enlargement of the gland, which maintains its normal shape. It is usually observed in patients undergoing chemotherapy. On the other hand, thymic lymphoid hyperplasia is usually associated with autoimmune diseases, appearing as an enlarged gland or as a mass. Other acquired conditions regard traumatic injuries, such as haematomas or diaphragmatic hernias. In comparison with the congenital hernias (discussed in a previous paragraph), traumatic hernias usually involve the left hemidiaphragm and stomach and colon are the most frequently herniated viscera. The site of the diaphragmatic rupture appears as

a segmental non-recognition of the diaphragm or a focal diaphragmatic thickening. Some radiological signs can be observed, such as the collar sign (a constriction of the herniated viscera through the site of the diaphragmatic tear) or the dependent viscera sign (the herniated viscera fall posteriorly when the patient lies supine during CT scan) [2]. Among other acquired diseases, tracheal diverticulum (Fig. 15.8) needs to be mentioned; the acquired form is usually related to prolonged increased intraluminal pressure in case of chronic cough. It is typically located in the right posterolateral tracheal wall and must be differentiated from laryngocoele and Zenker's diverticulum [15].

Enlargement of the mediastinal shape can be observed in case of oesophageal varices (Fig. 15.9) and medullary haematopoiesis [1].

*Vascular disease:* Aortic dissection (Fig. 15.10) can be a potential cause of mediastinal abnormality, representing the most common form of the acute aortic syndrome. Most aortic dissections are seen in elderly hypertensive patients, whereas in a few patients underlying connective tissue disorders may be present (such as Marfan or Ehlers-Danlos syndrome).

Contrast-enhanced coronal (Fig. 15.10a) axial (Fig. 15.10b) and sagittal (Fig. 15.10c) CT images demonstrate an intimal flap that separates the two channels in the ascending and descending aorta diagnostic of a Stanford type A and B dissection.

The patients present with chest pain; depending on the extent of dissection and branches occlusion, organ ischaemia may also be present (including abdominal organ or limb ischaemia, ischaemic or embolic stroke, paraplegia, or collapse and death in case of coronary artery involvement). Imaging is essential in depicting the extent of the dissection and for classification (according to Stanford classification) [16]. Chest radiography may show several findings, including widened mediastinum (according to some authors, more than 8 cm at the level of the aortic knob) [17], double or irregular aortic contour and displacement of atherosclerotic calcification [18]. CT is the investigation of choice, being able to diagnose and classify the dissection and to identify distal complications; it should ideally be performed ECG-gated to eliminate pulsation artefact. CT images can show the intimal flap and the presence of a double lumen;

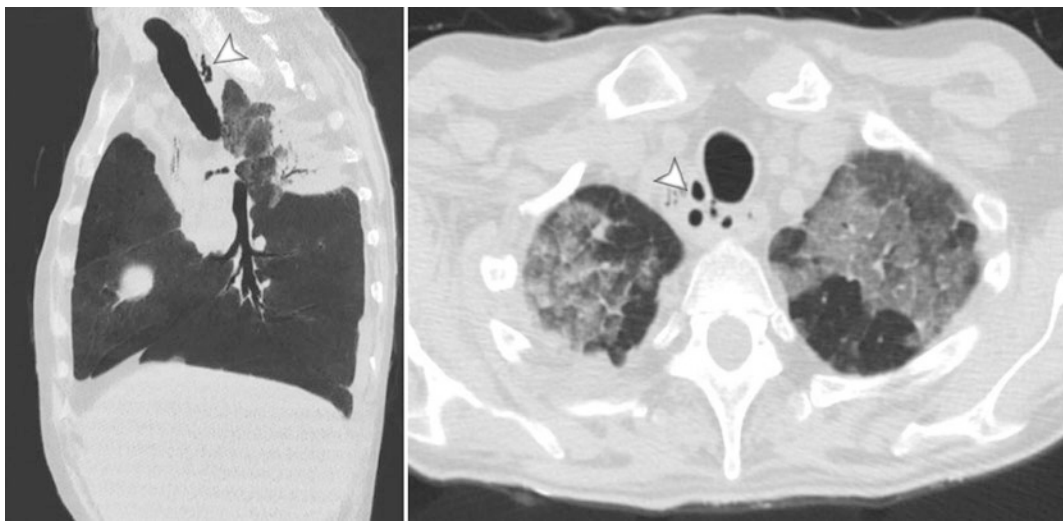

**Fig. 15.8** Sagittal reconstruction Minip and Axial scan CT without contrast depicting congenital tracheal diverticulum to the right (*arrowhead*) in a male patient with bilateral pneumonia

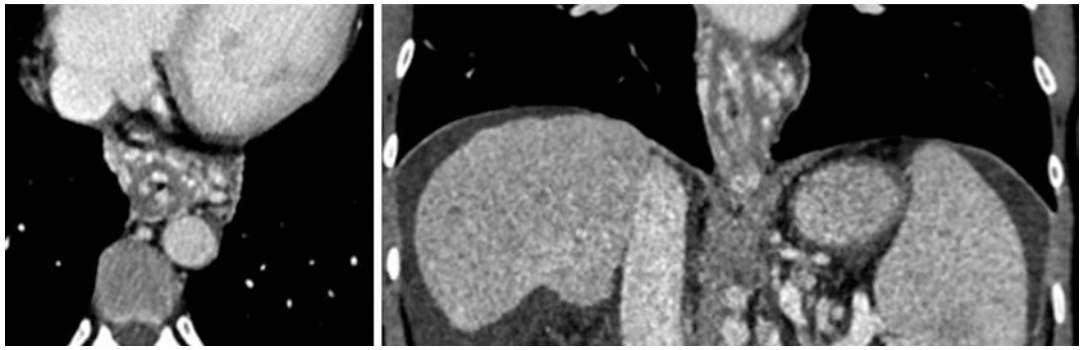

**Fig. 15.9** Axial and coronal enhanced CT images showing large and enhancing intra and paraesophageal varices in a patient with cirrhosis alcohol-related

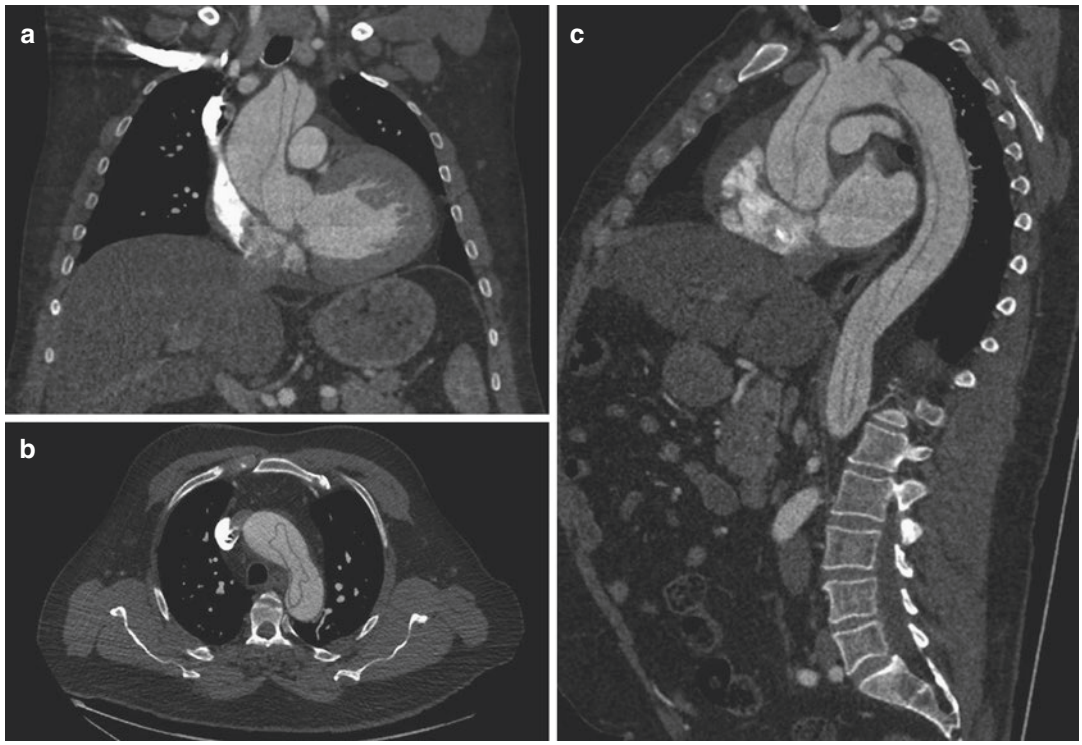


**Fig. 15.10** Contrast-enhanced coronal (**a**) axial (**b**) and sagittal (**c**) CT images demonstrates an intimal flap that separates the two channels in the ascending and descending aorta diagnostic of a Stanford type A and B dissection

an important part of the assessment of aortic dissection is to differentiate the true lumen and the false lumen, especially when no clear continuation of one lumen with normal artery is present. In this case the true lumen is usually the smaller one, with outer wall calcifications, whereas the false lumen is the larger one, beak sign often of lower contrast density due to delayed opacification [19]. Although magnetic resonance angiography is usually reserved to follow-up

examinations, rapid non-contrast imaging techniques may have a role in the acute diagnosis in patients with reduced renal function [20]. The differential on chest X-ray is that of a dilated thoracic aorta, including mediastinal mass and pulmonary mass abutting the aorta; on CT, aortic dissections have to be differentiated from pseudodissections, intramural haematoma and penetrating atherosclerotic ulcer. Vascular abnormalities can also involve the posterior mediastinum, such as aneurysms of the descendent aorta or azygos continuation [1].

*Iatrogenic disease:* Mediastinal abnormalities can be the result of diagnostic or therapeutic procedures; mediastinal haematoma can be observed after mediastinoscopy or cardiac surgery (Fig. 15.11).

Widening of the mediastinum can be observed in colon interposition for oesophageal replacement (Fig. 15.12).

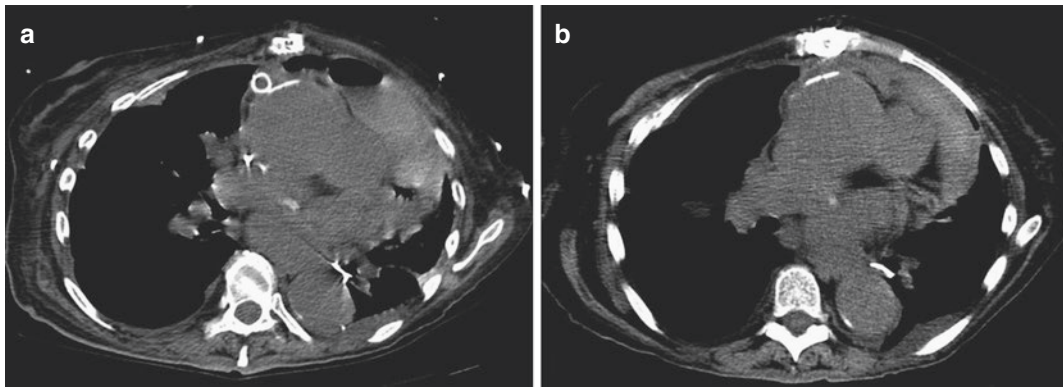


**Fig. 15.11** (**a**) Axial enhanced CT image showing a wide mediastinal hematoma in a patient who has undergone a cardiac valve replacement. (**b**) The patient performs follow-up with Axial CT scan depicting hematoma reduction

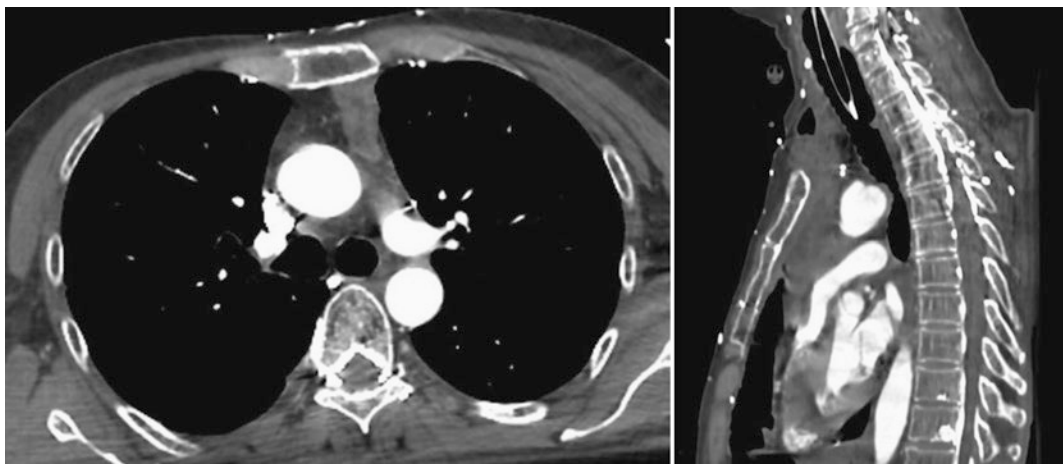

**Fig. 15.12** Axial and sagittal enhanced CT images showing retrosternal colic interposition in a patient undergoing esophageal resection for caustic ingestion

## References


1. Whitten CR, Khan S, Munneke GJ, Grubnic S. A diagnostic approach to mediastinal abnormalities. Whitten RadioGraphics. 2007;27:657–71.
2. Juanpere S, Cañete N, Ortuño P, Martínez S, Sanchez G, Bernado L. A diagnostic approach to the mediastinal masses. Insights Imaging. 2013;4(1):29–52.
3. McAdams HP, Kirejczyk WM, Rosado-de-Christenson ML, et al. Bronchogenic cyst: imaging features with clinical and histopathologic correlation. Radiology. 2000;217(2):441–6.
4. Lyon RD, Mcadams HP. Mediastinal bronchogenic cyst: demonstration of a fluid-fluid level at MR imaging. Radiology. 1993;186(2):427–8.
5. Callahan MJ, Taylor GA. CT of the pediatric esophagus. Am J Roentgenol. 2003;181(5):1391–6.
6. Brown LR, Aughenbaugh GL. Masses of the anterior mediastinum: CT and MR imaging. AJR Am J Roentgenol. 1991;157(6):1171–80.
7. Jeung MY, Gasser B, Gangi A, Bogorin A, Charneau D, Wihlm JM, Dietemann JL, Roy C. Imaging of cystic masses of the mediastinum. Radiographics. 22(Suppl 1):S79–93.
8. Wang ZJ, Reddy GP, Gotway MB, et al. CT and MR imaging of pericardial disease. Radiographics. 2003;23(Suppl 1):S167–80.
9. Taylor GA, Atalabi OM, Estroff JA. Imaging of congenital diaphragmatic hernias. Pediatr Radiol. 2009;39(1):1–16.
10. Temizöz O, Gençhellaç H, Yekeler E, et al. Prevalence and MDCT characteristics of asymptomatic Bochdalek hernia in adult population. Diagn Interv Radiol. 2010;16(1):52–5.
11. Gray H, Vogl W, et al. Gray's atlas of anatomy: Churchill Livingstone; 2008. ISBN:044306721X
12. Saldana MJ, editor. Pathology of the mediastinum (chapter). Pathology of pulmonary disease. Philadelphia: J.B. Lippincott Company; 1994.
13. Rossi SE, McAdams HP, Rosado-de-Christenson ML, Franks TJ, Galvin JR. Fibrosing mediastinitis. Radiographics. 2001;21(3):737–57.
14. Miller BH, Rosado-de-christenson ML, Mcadams HP, et al. Thoracic sarcoidosis: radiologic–pathologic correlation. Radiographics. 1995;15(2):421–37.
15. Higuchi T, Takahashi N, Shiotani M, et al. Characteristics and CT features of subcarinal air collections/main bronchial diverticula. Eur Radiol. 2010;20(1):95–9.
16. Sebastià C, Pallisa E, Quiroga S, et al. Aortic dissection: diagnosis and follow-up with helical CT. Radiographics. 19(1):45–60.
17. Lai V, Tsang WK, Chan WC, et al. Diagnostic accuracy of mediastinal width measurement on posteroanterior and anteroposterior chest radiographs in the depiction of acute nontraumatic thoracic aortic dissection. Emerg Radiol. 2012;19(4):309–15.
18. de Lacey G, Morley S, et al. The chest X-Ray: a survival guide. London: Saunders Ltd.; 2008. ISBN:0702030465
19. Lepage MA, Quint LE, Sonnad SS, et al. Aortic dissection: CT features that distinguish true lumen from false lumen. Am J Roentgenol. 2001;177(1):207–11.
20. Pereles FS, Mccarthy RM, Baskaran V, et al. Thoracic aortic dissection and aneurysm: evaluation with nonenhanced true FISP MR angiography in less than 4 minutes. Radiology. 2002;223(1):270–4.

# Imaging and Staging of Esophageal Cancers

16

Tae Jung Kim

**Abstract**

Esophageal cancer is one of the leading causes of cancer-related deaths worldwide, and the 5-year survival rate remains less than 20% in the United States. Surgical resection is currently the best treatment option for patients without distant metastases or locally advanced disease. Therefore, accurate staging of newly diagnosed can result in the most appropriate therapies being offered to patients who may potentially benefit. Currently, computed tomography (CT) and positron-emission tomography (PET)/CT are commonly used for the evaluation of distant metastases. Endoscopic ultrasound is the best modality for evaluation of tumor invasion depth and regional lymph node involvement. It is important to be familiar with staging system and particularly with multimodality approach for clinical staging because each modality has its own strengths and drawbacks for TNM staging. In this chapter, the 8th edition of TNM staging system for esophageal cancer and the diagnostic findings of esophageal cancer at CT, PET/CT, and endoscopic ultrasound are discussed in detail.

**Keywords**

Esophagus · Esophageal cancer · Staging
Imaging modality · Computed tomography
Positron emission tomography (PET)/CT
Endoscopic ultrasound

## Abbreviations

| | |
|---|---|
| AJCC | American Joint Committee on Cancer |
| CT | Computed tomography |
| EUS | Endoscopic ultrasound |
| MPR | Multiplanar reformation |
| PET | Positron emission tomography |
| PET/CT | Positron emission tomography/CT |
| UICC | Union for International Cancer Control |
| WECC | World Esophageal Cancer Consortium |

## 16.1 Anatomy of the Esophagus

1. Esophageal division in cancer staging

The esophagus is a muscular tube approximately 25 cm in length that connects the pharynx to the stomach. For the staging of esophageal cancers, the esophagus is divided into four parts: the cervical, upper thoracic, mid-thoracic, and lower thoracic esophagus (Fig. 16.1). The cervical esophagus begins at the lower border of the cricoid cartilage at the level of the sixth cervical

T. J. Kim
Department of Radiology, Samsung Medical Center, Seoul, Republic of Korea


M. Anzidei, M. Anile (eds.), *Diagnostic Imaging for Thoracic Surgery*,
https://doi.org/10.1007/978-3-319-89893-3_16

vertebra and ends at the thoracic inlet (a segment 15–20 cm from the incisors on esophagoscopy). The upper thoracic esophagus extends from the thoracic inlet to the azygos vein, which corresponds to the segment 20–25 cm from the incisors. The mid-thoracic esophagus is located between the azygos vein and the inferior pulmonary vein, which corresponds to the segment 25–30 cm from the incisors. The lower thoracic esophagus is the approximately 10 cm segment between the inferior pulmonary vein and the esophagogastric junction, which is approximately 40 cm from the incisors (Fig. 16.1).

The assessment of cancer location is critical in esophageal cancer staging. The definition of the cancer location has changed from the upper edge of the cancer (American Joint Committee on Cancer (AJCC) 7th edition) to the epicenter (8th edition) [1] (Fig. 16.2). In addition, the esophagogastric junction has been redefined in the 8th edition of AJCC esophageal cancer staging: adenocarcinomas with epicenters within 2 cm of the esophagogastric junction are staged as esophageal adenocarcinomas, and adenocarcinomas outside this region are staged as gastric adenocarcinomas, even if the esophagogastric junction is involved [1].

## 2. Architecture of the esophageal wall

The esophagus has four concentric layers, including the mucosa, submucosa, muscularis propria, and adventitia. Contrary to the gastrointestinal tract, the esophagus has no serosa, which enables the early spread of esophageal cancers into adjacent structures. The proximal third of the esophagus consists primarily of striated muscle. Smooth muscle predominates in the distal third. The middle third consists of a mixture of inner circular and outer longitudinal muscles.

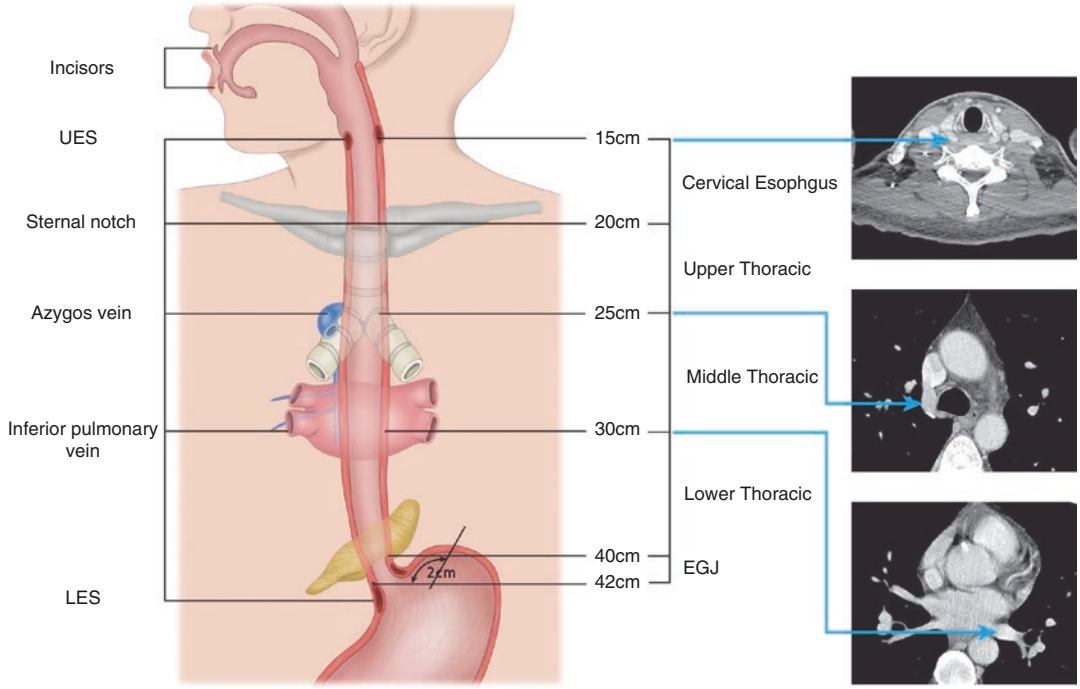


**Fig. 16.1** Division for esophageal cancer staging. Drawing and axial CT images show the location of esophageal cancer described in the 8th edition of the TNM staging system. Location of the tumor is defined by cancer epicenter. Adenocarcinomas with epicenters within 2 cm of the esophagogastric junction are staged as esophageal adenocarcinomas, and adenocarcinomas outside this region are staged as gastric adenocarcinomas, even if the esophagogastric junction is involved. *UES* upper esophageal sphincter, *LES* lower esophageal sphincter, *EGJ* esophagogastric junction

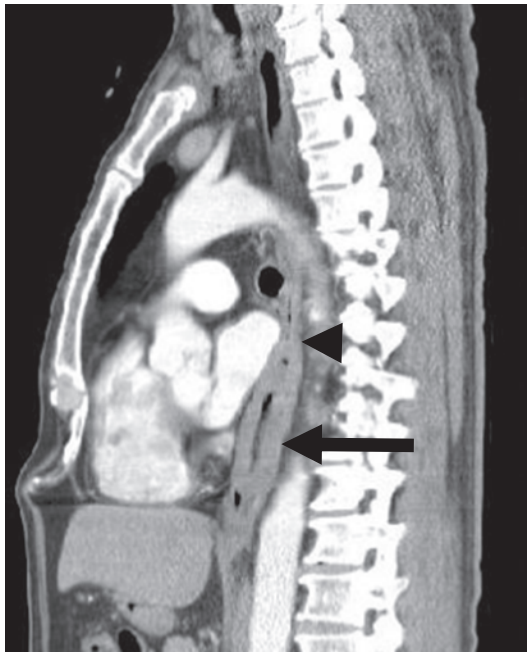

**Fig. 16.2** Location of the primary tumor. The definition of the cancer location has changed from the upper edge of the cancer (arrowhead, AJCC 7th edition) to the epicenter (arrow, AJCC 8th edition). Sagittal CT image shows diffuse wall thickening of the mid- to lower thoracic esophagus. Location of the cancer primary site is defined as lower thoracic tumor by the epicenter (arrow)

The cervical esophagus is supplied by the inferior thyroidal artery. The thoracic esophagus is supplied by the bronchial artery and the esophageal branches of the descending thoracic aorta. The lower esophagus is supplied by the ascending branches of the left phrenic and left gastric arteries. The arterial supply develops an abundant submucosal plexus; therefore, esophageal infarction is rare when compared with the gastrointestinal tract. Venous blood from the esophagus drains into a submucosal plexus, which drains into the periesophageal venous plexus. The esophageal veins arise from the plexus and drain into the adjacent azygos, hemiazygos, bronchial, and left gastric veins. The esophagus has an extensive lymphatic plexus originating from the mucosa and muscle layers. The lymphatic flow drains upward into the upper two-thirds of the esophagus and downward into the lower third, but there is a bidirectional flow at the level of the carina due to the abundant lymphatic plexus. This lymphatic flow enables cervical lymph node metastasis from lower thoracic esophageal cancers, and intra-abdominal lymph node metastasis from upper thoracic esophageal cancers [2]. The esophagus receives nerve fibers from both the sympathetic and parasympathetic nervous systems. The parasympathetic fibers are supplied via the recurrent laryngeal branches from the right and left vagus nerves. The sympathetic fibers (both efferent and afferent) are supplied through the sympathetic trunks.

## 3. Normal radiologic anatomy of the esophagus

Normal esophageal wall thickness is typically less than 3 mm on computed tomography (CT) when the esophagus is properly distended. An esophageal wall thickness greater than 5 mm should be considered abnormal [3, 4]. The esophageal lumen is usually collapsed, but a small amount of air may normally be seen. The outer esophageal wall can be delineated by periesophageal fat and the adjacent airway, but normal fat tissue may not be seen between the posterior wall of the airway and the esophagus, especially in chronically debilitated or very thin patients.

The azygoesophageal recess is located lateral or posterior to the esophagus and anterior to the spine. It extends from the anterior turn of the azygos vein to the aortic hiatus. The configuration of the azygoesophageal recess is normally a smooth arc convex to the left. Because the right lung extends into the recess, pathology in this region, such as esophageal cancer, esophageal varix, or subcarinal lymphadenopathy, can often be detected radiographically and typically manifests as increased opacity and/or as a contour abnormality [5]. The left side of the esophagus contacts the descending thoracic aorta. The triangular fat space is located between the esophagus, descending thoracic aorta, and spine (Fig. 16.3). The mid-thoracic esophagus is located posteriorly to the carina and there may be little fat between the esophagus and the carina. At this level, the thoracic duct, azygos and hemiazygos veins, and right intercostal artery pass between the esophagus and the vertebral body.

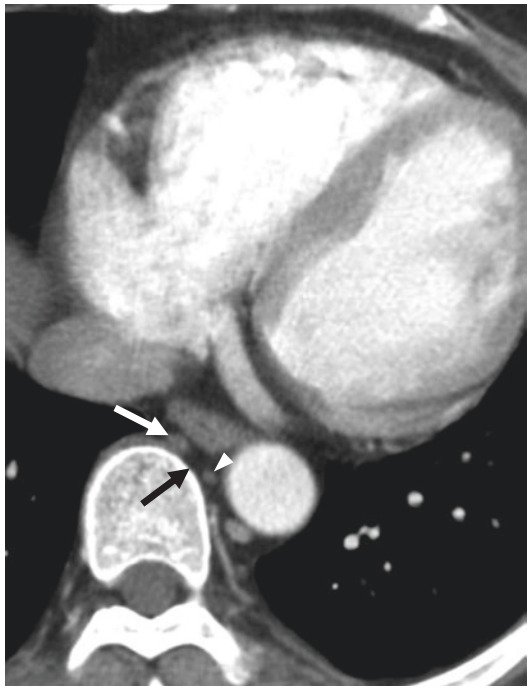

**Fig. 16.3** Triangular fat space adjacent to the normal esophagus. Triangular fat space (black arrow) is located between esophagus, aorta, and spine. Thoracic duct (arrowhead) is noted between the azygos vein (white arrow) and descending thoracic aorta

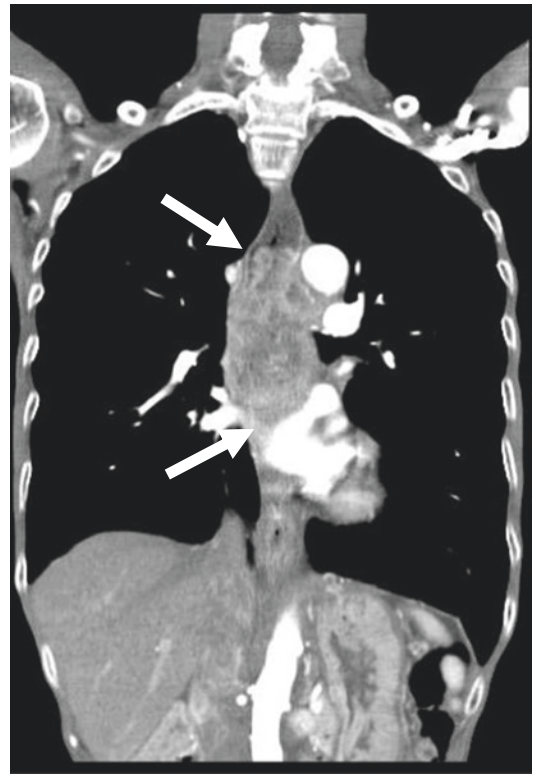

**Fig. 16.4** Advantage of multiplanar reformation (MPR) CT images in esophageal cancer staging. Coronal MPR CT clearly shows the longitudinal extent of esophageal cancer (arrows)

## 16.2 Imaging Modalities for Esophageal Cancer Staging

1. Computed tomography

CT is the mainstay for the pretreatment staging of esophageal cancer, assessment of treatment response, and postoperative surveillance. As many patients with esophageal cancer present with an advanced stage, one of the important goals of imaging studies for esophageal cancers is the identification of tumor invasion of mediastinal structures or distant metastases, as affected patients may not be suitable for curative surgical resection.

Compared with esophagoscopy, CT can provide anatomical information on the outside of the esophageal lumen as well as the inside. With the advent of three-dimensional imaging techniques, CT has become more valuable in the evaluation of T staging of esophageal cancers. Multiplanar reformation (MPR) images can provide information on the longitudinal extent of esophageal cancers (Figs. 16.4 and 16.5). CT esophagography with air insufflation or multiphasic CT scans has been reported to be useful for the evaluation of esophageal lesions [6, 7].

2. Positron-emission tomography/CT (PET/CT)

PET/CT has become a useful imaging modality for the initial staging and treatment assessment of esophageal cancers. PET/CT is useful for the detection of esophageal primary tumors, but is more valuable for the detection of lymph node or distant metastasis in initial staging. Recently, PET/CT has been more widely applied

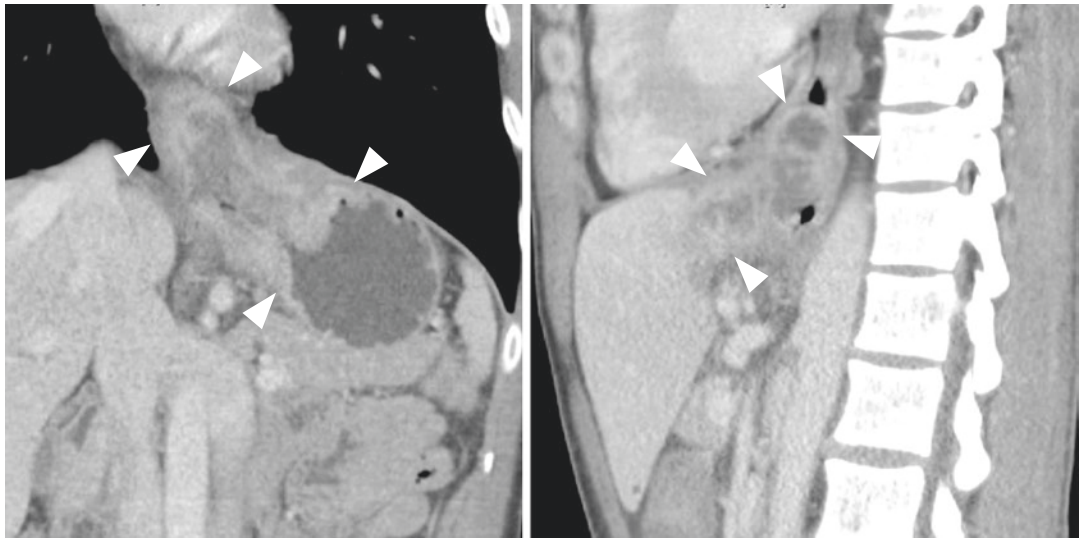

**Fig. 16.5** Esophageal cancer with involvement of the esophagogastric junction. Coronal (**a**) and sagittal (**b**) CT images clearly show tumor involvement of the lower thoracic esophagus and esophagogastric junction (arrowheads). MPR images are useful in evaluating cancers involving esophagogastric junction, which is difficult to evaluate with axial images alone

in restaging, such as the assessment of neoadjuvant chemotherapy or radiation therapy, and the detection of interval metastasis during or after neoadjuvant treatments [8–10].

3. Esophagoscopy and endoscopic ultrasound

Endoscopy is the initial diagnostic modality for patients with symptoms such as dysphagia, foreign-body sensation, heartburn, and chest pain. Esophagoscopy is essential for the diagnosis of endoluminal diseases and endoscopic biopsy, and replaced the barium esophagography. Compared with conventional esophagoscopy, endoscopic ultrasound (EUS) provides additional information on lesions outside the lumen, and is now applied for primary tumor (T staging) and regional lymph node evaluation (N staging) of esophageal cancers, and for EUS-guided aspiration biopsy. As the esophageal wall is visualized as five alternating layers of different echogenicities, EUS is currently considered to be the most accurate imaging modality for T staging in patients with esophageal cancers [11–14] (Fig. 16.6). Limitations of EUS include interobserver variation due to differences in experience

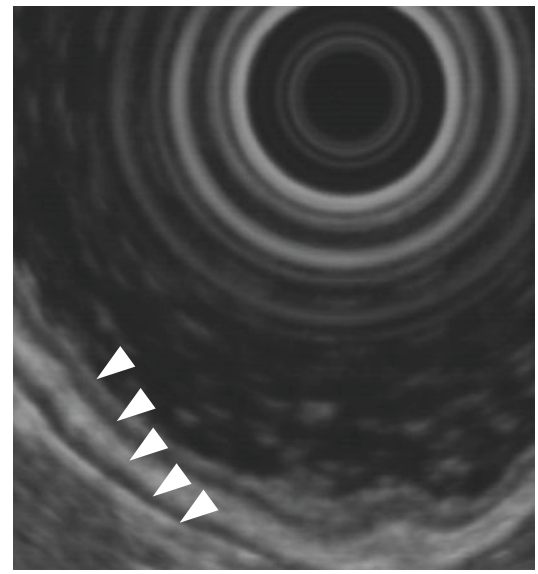

**Fig. 16.6** Normal esophageal wall on endoscopic ultrasound. Endoscopic ultrasound image shows the normal esophageal wall, with alternating hyper- and hypoechoic layers (arrowheads). The first layer is hyperechoic and represents the interface between balloon and superficial mucosa. The second layer is hypoechoic and represents the lamina propria and muscularis mucosae. The third layer is hyperechoic and represents the submucosa. The fourth layer is hypoechoic and represents the muscularis propria. The fifth layer is hyperechoic and represents the interface between the adventitia and surrounding tissues

levels among operators and limited evaluation of stenotic tumors, which may prevent the passage of the endoscope and evaluation of the entire tumor and distal esophagus [15].

## 16.3 Malignant Tumors of the Esophagus

The principal histologic types of esophageal cancer are squamous cell carcinoma and adenocarcinoma. Squamous cell carcinoma can occur in any part of the esophagus, as squamous cells line the entire esophagus; however, it typically arises in the upper two-thirds of the esophagus. Adenocarcinoma typically arises from the intestinal metaplasia (Barrett's esophagus) that develops as a result of gastroesophageal reflux disease; thus, it is common in the lower third of the distal esophagus, including the esophagogastric junction [16]. Rare malignant tumors of the esophagus include malignant gastrointestinal stromal tumor, small-cell carcinoma, malignant melanoma, lymphoma, and leiomyosarcoma.

1. Staging of esophageal cancers

The TNM classification system maintained by the AJCC and the Union for International Cancer Control (UICC) is used for esophageal cancer. The depth of invasion by the primary tumor defines T staging. N staging is defined by the number of regional lymph node metastases, and is harmonized with stomach cancer staging. M staging is divided into M0 and M1 according to the presence or absence of distant metastasis. The staging system for cancer in the esophagus and esophagogastric junction was recently revised in the 8th edition of the AJCC/UICC staging manual in 2017 [1]. The 8th edition of TNM staging provides separate classifications for the clinical (cTNM), pathologic (pTNM), and postneoadjuvant pathologic (ypTNM) stage groups. The 8th edition subcategorized pT1 as pT1a and pT1b for the subgrouping of pathologic stage I adenocarcinoma and squamous cell carcinoma. A new, simplified regional lymph node map for the esophagus was introduced. The undifferentiated histologic grade (G4) was removed, and the anatomic location was eliminated as a category of pT2N0M0 squamous cell carcinoma. The esophagogastric junction was redefined (Fig. 16.1). Similar to malignant tumors in other organs, precise pretreatment staging using multimodality assessment determines the stage-specific treatment, which is critical for the prediction of patient prognosis [8, 17].

2. T staging

T staging of esophageal cancer has become important, according to the widespread use of stage-specific treatments. T1 diseases are subcategorized as T1a (mucosa) and T1b (submucosa) diseases, producing stage subgroups IA and IB for squamous cell carcinoma and IA and IC for adenocarcinoma. In T2 squamous cell carcinoma, anatomic location was removed as a staging category. T4 diseases are subdivided into resectable T4a (invasion of the pleura, pericardium, diaphragm, or peritoneum) and unresectable T4b (invasion of the aorta, vertebral body, azygos vein, and left main bronchus) diseases [1]. For superficial T1a cancer, endoscopic tumor ablation (e.g., endoscopic mucosal resection or endoscopic submucosal dissection) is preferred [18].

1. CT

Asymmetric thickening of the esophageal wall is the primary finding of esophageal cancer, but is nonspecific. CT is limited to determination of the exact depth of tumor penetration into the esophageal wall compared with EUS [19, 20]. T1 tumors are frequently not identified on CT and may show mild wall thickening or enhancement (Figs. 16.7 and 16.8). T2 tumors usually show discrete wall thickening or mass (Fig. 16.9), and can be differentiated from T3 tumors by the presence of periesophageal fat infiltration (Fig. 16.10). Exclusion of T4 disease, as indicated by the preservation of fat planes between the esophageal mass and adjacent structures, is the most important role of CT in T staging [21]. The CT findings suggestive of local invasion include (a) loss of the fat plane between the tumor and adjacent organs, and (b)

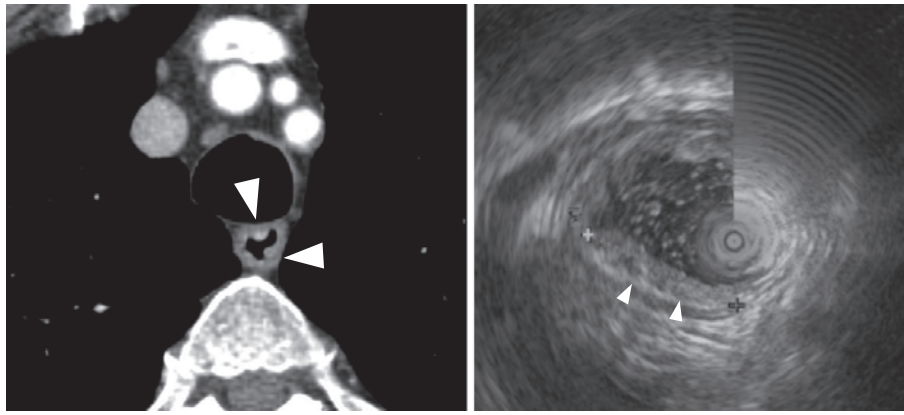

**Fig. 16.7** T1a tumor. (**a**) CT image at the level of aortic arch vessels shows a suspicious nodular wall thickening and mild enhancement (arrowheads), a finding later confirmed to be squamous cell carcinoma. (**b**) Endoscopic ultrasound image shows smooth wall thickening (cursors) and preservation of the hyperechoic third layer (submucosa) (arrowheads). The lesion was confirmed to be T1a squamous cell carcinoma by esophagectomy

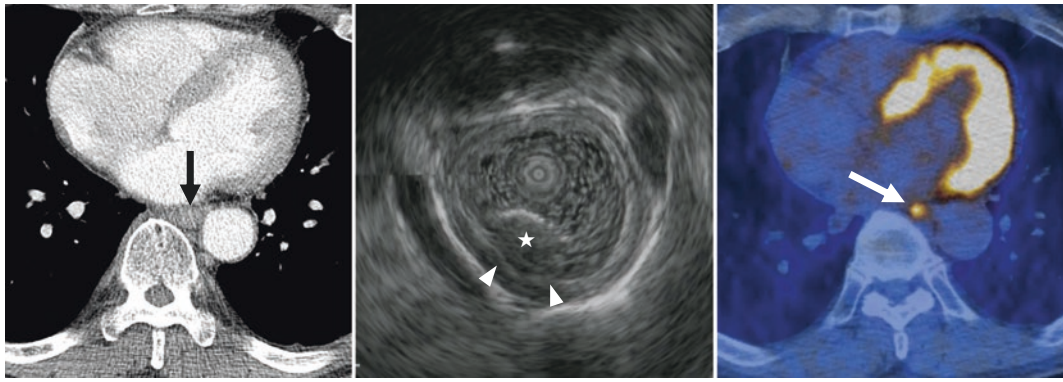

**Fig. 16.8** T1b tumor. (**a**) CT image at the level of left ventricle shows a suspicious wall thickening of the esophagus, a finding later confirmed to be squamous cell carcinoma (arrow). (**b**) Endoscopic ultrasound image shows a hypoechoic polypoid lesion (asterisk) with extension into the third hyperechoic submucosal layer (arrowheads). (**c**) PET/CT image clearly depicts a FDG-avid primary tumor (arrow)

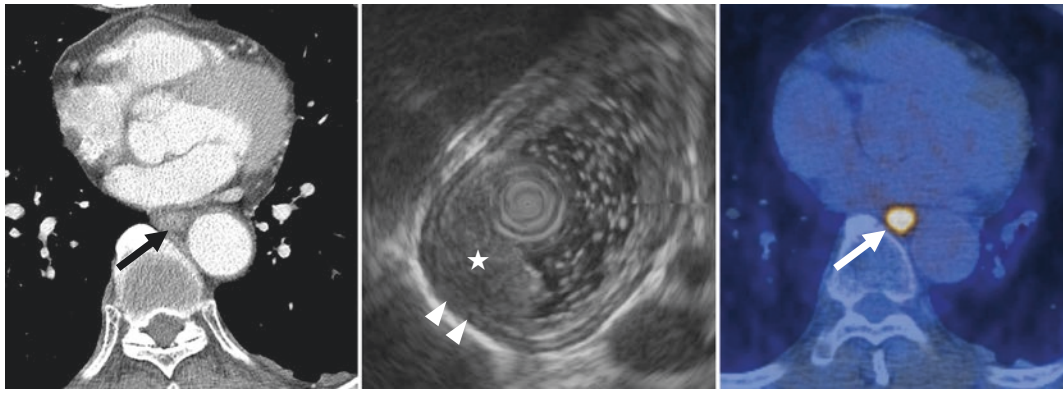

**Fig. 16.9** T2 tumor. (**a**) CT image at the level of the left atrium shows diffuse esophageal wall thickening (arrow), a finding later confirmed to be squamous cell carcinoma. (**b**) Endoscopic ultrasound image shows a mass (asterisk) with penetration into the fourth hypoechoic proper muscle layer (arrowheads). (**c**) PET/CT image shows a strong FDG uptake by the primary tumor (arrow)

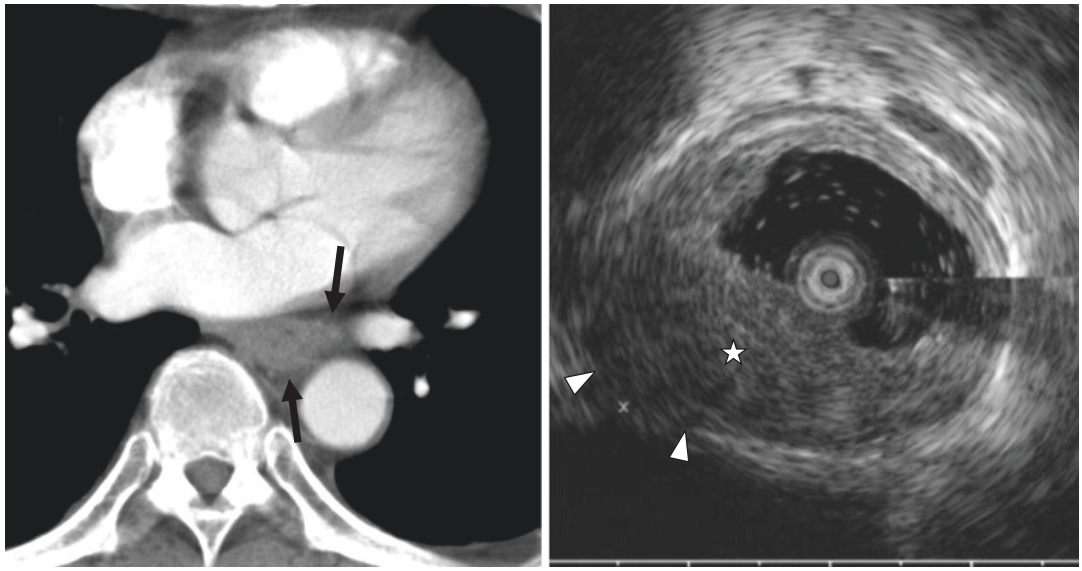

**Fig. 16.10** T3 tumor. (**a**) CT image at the level of the left atrium shows diffuse esophageal wall thickening in the lower thoracic esophagus and periesophageal fat infiltration (arrows), findings later confirmed to be T3 squamous cell carcinoma. (**b**) Endoscopic ultrasound image shows an echogenic mass (asterisk), with obliteration of the hyperechoic fifth layer (adventitia) (arrowheads)

displacement or indentation of the adjacent organs by the tumor. The fat plane may not be seen in cachectic patients or patients who have had previous radiotherapy or surgery; therefore, knowledge of the patient's prior medical history is important for CT evaluation [8, 17]. Pericardial invasion is suggested if there is pericardial thickening, pericardial effusion, or indentation of the cardiac chamber with loss of the pericardial fat plane [22, 23] (Fig. 16.11). Direct invasion of the peritoneum (T4a) is newly included in T staging in the 8th edition [1]. Aortic invasion is suggested when the tumor contacts the aorta at an angle of 90 degrees or more, or when the triangular fat plane between the esophagus, aorta, and vertebral body is obliterated (Fig. 16.12) [24]. Tracheobronchial invasion is highly suggested when there is a tracheobronchial fistula or formation of the endobronchial tumor. Displacement or posterior indentation of the trachea or left main bronchus is considered a reliable sign of airway invasion on CT, but must be differentiated from the normal expiratory collapse of the posterior wall of the trachea [23, 25] (Fig. 16.13).

With the advent of multidetector CT technology, MPR images have become valuable in the evaluation of the longitudinal extent of the esophageal cancer (Figs. 16.4 and 16.5). In the 8th edition, tumor location is determined by the epicenter of the tumor, which is typically evaluated by endoscopy, but can also be successfully determined using MPR CT images (Fig. 16.2). As the microscopic tumor spread is frequently more extensive than the extent of the gross tumor in esophageal cancer, a sufficient resection margin is important [26, 27]. The estimation of tumor length made using MPR images is more accurate than

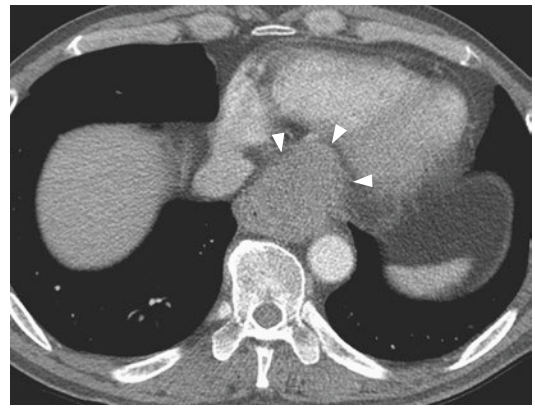

**Fig. 16.11** T4a tumor with pericardial invasion. CT image at the level of the liver dome shows a large esophageal mass with direct extension to the pericardium (arrowheads)

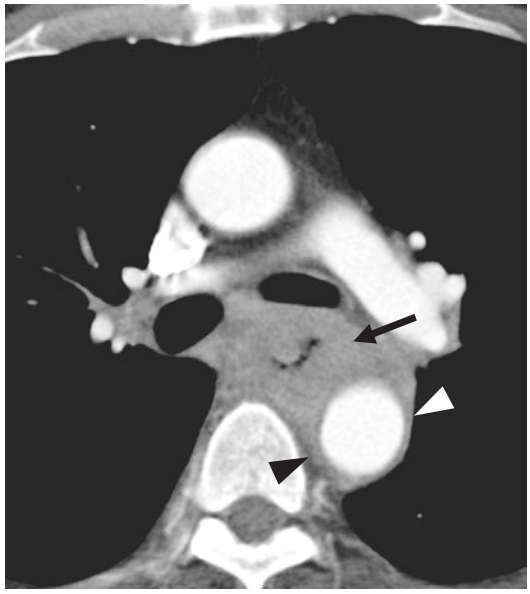

**Fig. 16.12** T4b tumor with aortic invasion. CT image at the level of the left main pulmonary artery shows a large esophageal mass with periesophageal fat infiltration, findings confirmed to be T4 squamous cell carcinoma. The tumor contacts the descending thoracic aorta at greater than 90° (arrowheads). Note the obliteration of triangular fat space between the esophageal mass and descending thoracic aorta (black arrowhead)

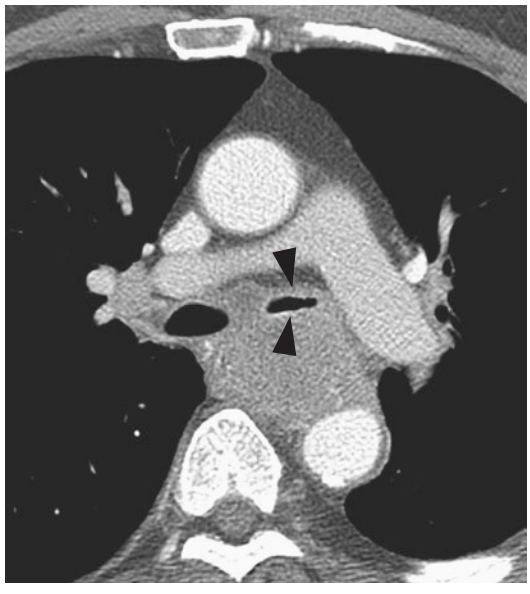

**Fig. 16.13** T4b tumor with tracheobronchial invasion. CT image at the level of the main stem bronchi shows a large esophageal mass, a finding later confirmed to be squamous cell carcinoma. Note diffuse wall thickening and luminal narrowing of the left main bronchus (arrowheads), findings consistent with bronchial invasion

that made using the axial image alone. MPR images are also useful for the evaluation of tumors in the esophagogastric junction, which is difficult to evaluate with axial scans alone [8] (Fig. 16.5).

2. EUS

EUS can differentiate the esophageal wall as five alternating layers of different echogenicities, and is currently considered the most accurate imaging modality for primary tumor staging in esophageal cancers [1]. The first layer is hyperechoic and represents the interface between the superficial mucosa and the balloon. The second layer is hypoechoic and represents the lamina propria and muscularis mucosae. The third layer is hyperechoic and represents the submucosa. The fourth layer is hypoechoic and represents the muscularis propria. The fifth layer is hyperechoic and represents the interface between the adventitia and surrounding tissues (Fig. 16.6). EUS is especially useful for the differentiation of T1, T2, and T3 diseases, which is important for neoadjuvant therapy [28]. EUS with a high-frequency probe is also useful to distinguish mucosal (T1a) from submucosal (T1b) tumors, which is critical for the identification of patients who are amenable to local ablative treatments such as endoscopic mucosal resection or photodynamic therapy [29, 30] (Figs. 16.7 and 16.8). The diagnostic accuracy of EUS ranges from 76 to 89%, which is superior to that of CT (49 to ~59%) and tends to improve as the T stage increases [31, 32].

3. N staging

The 7th edition of the AJCC Cancer Staging Manual, revised in 2009, was derived from World Esophageal Cancer Consortium (WECC) data, which showed that the nodal burden (number of positive nodes) was a significant contributor to patient outcome [33]. The N stage was determined based on the number of cancer-positive lymph nodes: N0 (no cancer-positive node), N1 (1 or 2 cancer-positive nodes), N2 (3–6 cancer-positive nodes), and N3 (7 or more cancer-positive nodes). Consequently, the N classification became similar to that of stomach cancer staging. However, this 7th edition staging system was problematic

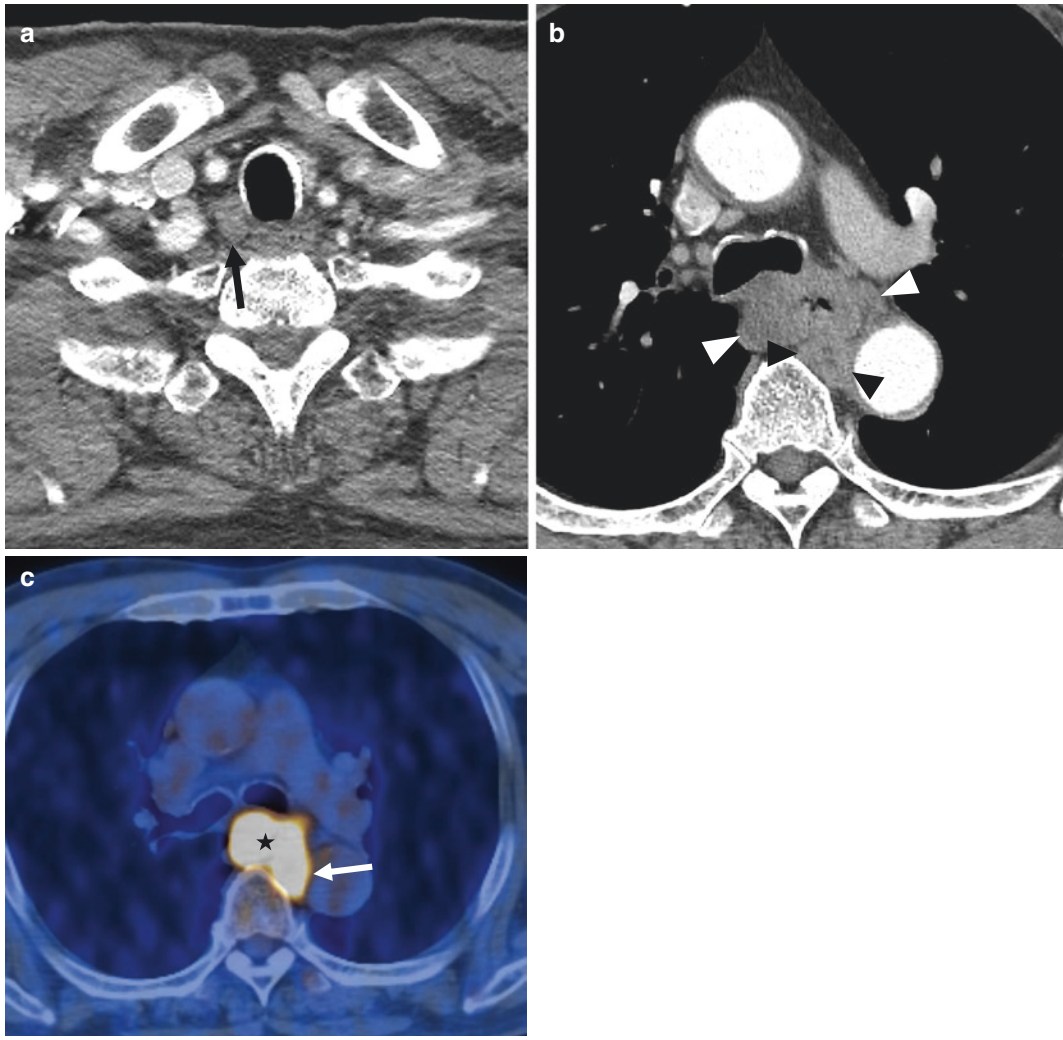


**Fig. 16.14** T3 mid-thoracic esophageal cancer with lymph node metastases. (**a**) CT image obtained at the level of thoracic inlet shows an enlarged recurrent laryngeal nerve lymph node (arrow), which was later confirmed to be metastatic lymph node. (**b**) CT image obtained at the level of the carina shows a large esophageal mass (white arrowheads) with a paraesophageal lymph node metastasis (black arrowheads). (**c**) PET/CT image obtained at the same level as B shows a large FDG-avid esophageal mass (asterisk). However, it is difficult to differentiate the FDG uptake by the paraesophageal lymph node (arrow) seen in B from the FDG uptake by the primary tumor (asterisk)

because of the non-regional lymph node stations, which are used in lung cancer staging. In the 8th edition, the regional lymph nodes, which are found in the periesophageal tissue from the upper esophagus to the celiac artery, are clarified for esophageal cancer in a new diagram [1].

1. CT

The sensitivity and specificity of CT in N staging vary with the definition of abnormally enlarged lymph nodes. In general, lymph nodes in the thoracic or abdominal cavity with a short-axis diameter greater than 1 cm are considered to be abnormally enlarged [34, 35]. Applying the common size criteria of 1 cm to define an enlarged node, CT sensitivity ranges

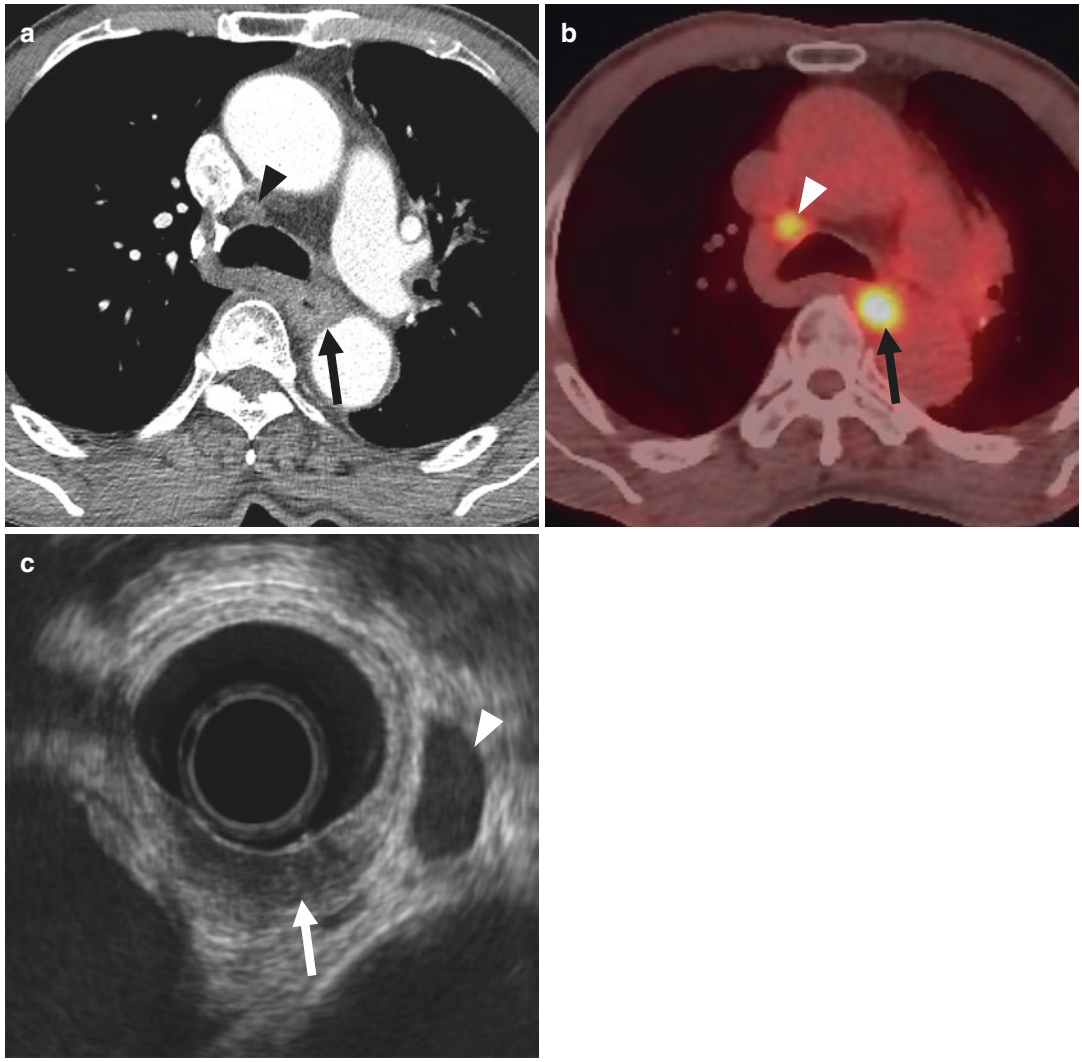


**Fig. 16.15** Pitfalls in N staging at CT and PET/CT. (**a**) CT image obtained at the level of the carina shows diffuse circumferential esophageal wall thickening (arrow) and a small right paratracheal lymph node (arrowhead). (**b**) PET/CT demonstrates strong FDG uptake in the primary tumor (arrow) and a FDG-avid small right paratracheal lymph node (arrowhead). (**c**) Endoscopic ultrasound image shows a T3 esophageal mass (arrow) with an enlarged paraesophageal lymph node, which was not identified on CT or PET/CT. At surgery, the right paratracheal lymph node was confirmed to be benign (false positive at PET/CT), whereas the paraesophageal lymph node was confirmed to be malignant (false negative at both CT and PET/CT)

from 30 to 60%, and the specificity ranges from 60 to 80% [36, 37] (Fig. 16.14). An important limitation of CT in N staging of esophageal cancer is the limited sensitivity for the detection of lymph node metastasis, because even a normal-sized lymph node may have microscopic foci of metastasis (Fig. 16.15). Picus et al. reported that most metastatic nodes less than 7 mm in size were indistinguishable from nonmetastatic nodes on CT [23]. Another limitation is the reduced specificity due to enlarged lymph nodes greater than 1 cm in size, such as benign reactive hyperplasia or granulomatous inflammation. In

addition, an accurate number of lymph node metastases cannot be counted if there are conglomerated lymph nodes or if periesophageal lymph is attached to the large primary tumor.

2. PET/CT

PET/CT is superior to CT for the detection of normal-sized metastatic lymph nodes due to FDG uptake by the small metastatic foci. PET/CT may have difficulty differentiating the primary tumor from the peritumoral lymph node due to the intense FDG uptake by the tumor [25] (Fig. 16.14). False-positive findings due to reactive lymph node hyperplasia or granulomatous inflammation are other limitations hampering the specificity of PET/CT (Fig. 16.15). Because of its good specificity, the main role of PET/CT in N staging is to confirm cN0 disease [38].

3. EUS

EUS shows higher accuracy (72–80%) for assessing lymph node metastases than CT (46–58%). EUS relies on various criteria for the assessment of lymph node metastasis, including the size criterion of a short-axis diameter greater than 1 cm, round shape, hypoechoic central echo pattern, and sharply demarcated borders [32] (Fig. 16.15). If all four EUS features are present, the accuracy of EUS for the detection of lymph node metastases has been reported as 100% [21]. However, a small number of metastatic nodes show all four malignant features, especially in the periesophageal region. The combined use of EUS and EUS-guided needle aspiration in the evaluation of lymph nodes has been shown to improve the accuracy more than EUS alone [39]. In a recent meta-analysis, EUS-guided needle aspiration showed a 92% sensitivity and a 93% specificity for lymph node metastasis, with a 100% positive predictive value and an 86% negative predictive value [40].

4. M staging

Early detection of distant metastases is very important to determine operability and plan appropriate treatment. Distant metastases on initial presentation have been reported in up to 20–30% of patients with esophageal cancers [25, 41]. In the 8th edition of the AJCC classification system, M staging is divided into M0 and M1 according to the presence or absence of distant

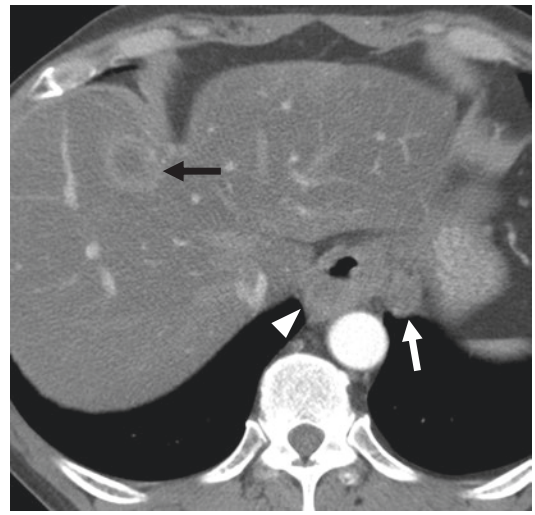

**Fig. 16.16** Hepatic metastasis in lower thoracic esophageal cancer. CT image shows a lower esophageal cancer (arrowhead) with a paracardial lymph node metastasis (white arrow). Metastatic nodule with internal necrosis is seen in the right lobe of the liver (black arrow)

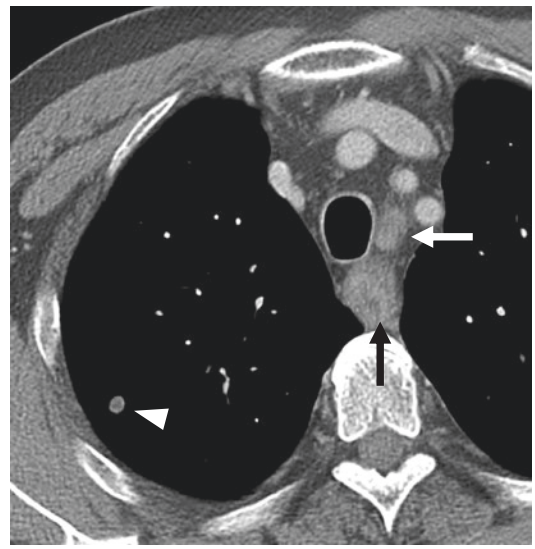

**Fig. 16.17** Pulmonary metastasis in upper thoracic esophageal cancer. CT image shows an upper thoracic esophageal cancer (black arrow) with a left recurrent laryngeal nerve lymph node metastasis (white arrow). A small noncalcified nodule (arrowhead) in the right upper lobe was confirmed to be a metastatic lesion at surgical excision

metastasis, and all distant metastases are classified as M1 [1]. The most common sites of distant metastases of esophageal cancers include the liver, lungs, bones, and adrenal glands [41] (Figs. 16.16 and 16.17).

1. CT

CT is the initial imaging modality used for detection of distant metastases in esophageal cancers. CT is useful in the triage of patients who are amenable to chemotherapy or multimodality treatments. Contrast-enhanced CT is the mainstay for imaging patients with esophageal cancer to rule out the three most common sites of distant metastases, including the liver, lungs, and adrenal glands (Figs. 16.16 and 16.17). Pulmonary metastases are usually round, well-defined, noncalcified nodules (Fig. 16.17). Given the high incidence of incidentally detected nodules on low-dose screening CT, suspected pulmonary nodules require pathological confirmation by either percutaneous biopsy or thoracoscopic biopsy, or a close imaging follow-up. Furthermore, because smoking is the shared risk factor for both esophageal and lung cancers, synchronous lung cancer should be considered in patients with esophageal cancer, especially when the pulmonary lesion is solitary [42].

2. PET/CT

The major role of PET/CT in esophageal cancer staging is the detection of distant metastasis. Similar to other gastrointestinal malignancies, PET/CT is the most accurate diagnostic for the determination of metastatic disease, and has better sensitivity and specificity. A systematic analysis revealed that the pooled sensitivity and specificity of distant metastases by PET/CT were 67% and 97%, respectively [43]. PET/CT can detect unsuspected metastases in 15% of patients with localized esophageal cancer based on findings on conventional diagnostic modalities [38, 44] (Fig. 16.18). Therefore, PET/CT is cost effective in futile surgery, as it can detect metastases not identified with other imaging modalities [20]. A drawback of PET/CT in M staging is the limited sensitivity for the detection of metastatic lesions in organs with intrinsic high glucose metabolism such as the liver, kidneys, and brain. This limitation can be addressed by using PET/MR or new PET tracers [45, 46].

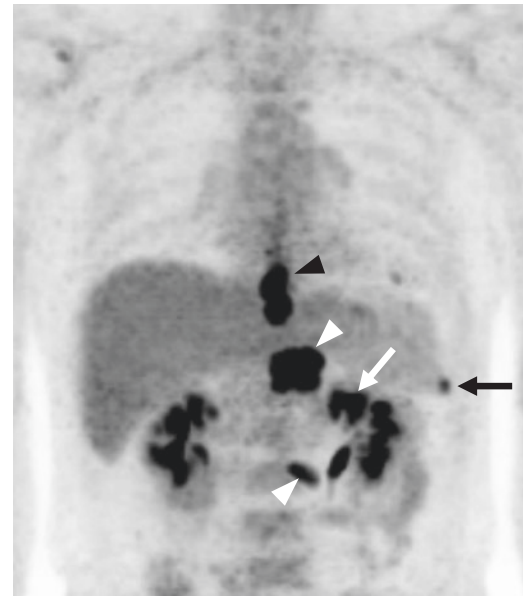

**Fig. 16.18** Unexpected distant metastasis detected by PET/CT. Coronal PET scan shows a FDG-avid esophageal tumor (black arrowhead) with multiple lymph node metastases (white arrowheads) and left adrenal metastasis (white arrow). Note the small FDG-avid peritoneal metastasis in the left upper abdomen (black arrow), which was not detected on chest CT

## 16.4 Nonanatomical Cancer Characteristics

1. Histologic cell type

Squamous cell carcinoma of the esophagus is closely correlated with smoking and alcohol consumption, and usually occurs in the upper two-thirds of the esophagus. Adenocarcinoma of the esophagus is most commonly found in the lower thoracic esophagus and esophagogastric junction and usually develops in association with Barrett's esophagus. Siewert et al. showed

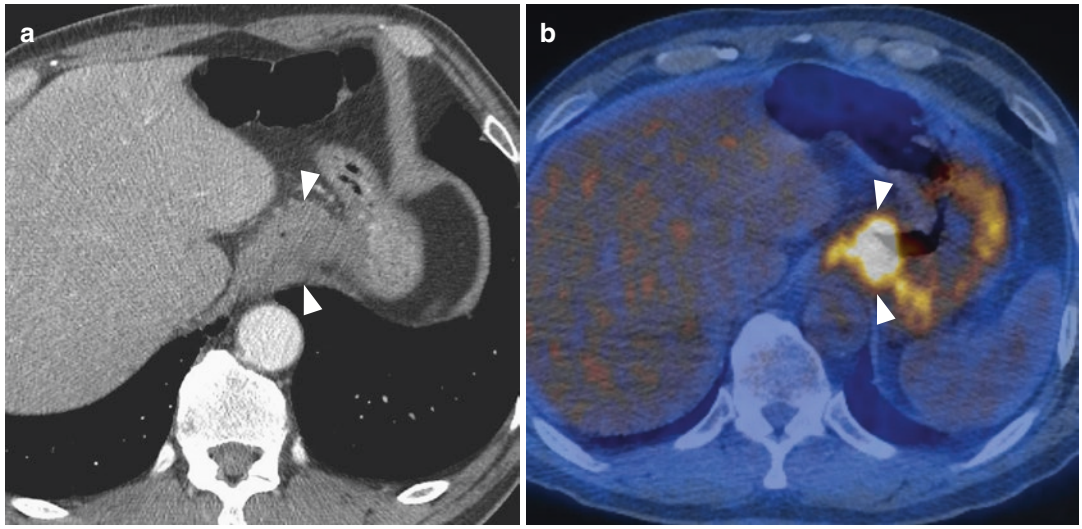


**Fig. 16.19** Cancers in the esophagogastric junction. (**a**) CT image shows diffuse wall thickening around the esophagogastric junction (arrowheads). (**b**) PET/CT shows strong FDG uptake in the tumor (arrowheads). At surgery, the findings were confirmed to be adenocarcinoma. Cancers of the esophagogastric junction that have the epicenter less than or equal to 2 cm from the esophagogastric junction are staged as esophageal cancer in the 8th edition of the TNM staging system

that the prognosis of squamous cell carcinoma of the esophagus was better than that of adenocarcinoma; the 5-year survival rate was 46% vs. 37%, respectively [47]. In addition, the results of recent studies assembled by the WECC suggest that the histologic cell type is one of the important factors for best survival rate [48]. According to the 8th edition of the AJCC staging system, esophageal cancer should be managed with separate stage groupings depending on the histologic cell type, specifically for stage I and II tumors (table) [1].

2. Histologic grade

According to the 8th edition of the TNM staging system, esophageal cancer is categorized as well: differentiated (G1), moderately differentiated (G2), or poorly differentiated (G3) based on the histologic grade, which represents the biologic activity of the tumor. If the histologic grade of the esophageal cancer cannot be assessed, the tumor is considered to be a G1 cancer. If the histologic grade is undifferentiated, the tumor is considered to be a G3 cancer. The undifferentiated histologic grade (G4) of the 7th edition has been removed. A higher histologic grade is associated with a poorer prognosis, especially for early-stage cancers. Therefore, the histologic grades are applied for stage groupings of T1–3N0M0 squamous cell carcinoma and T1–2N0M0 adenocarcinomas [1].

3. Cancer location

The cancer location is associated with the prognosis of the patient. The location of the primary cancer is included in the stage grouping of T3N0M0 squamous cell carcinoma in the 8th edition (upper and middle thoracic vs. lower thoracic) [1]. In general, adenocarcinomas around the esophagogastric junction have a poorer prognosis than other gastric adenocarcinomas [33]. Tumors arising at the esophagogastric junction, or arising in the stomach less than or equal to 2 cm from the esophagogastric junction and crossing the esophagogastric junction, are staged using the TNM system for esophageal adenocarcinomas (Fig. 16.19) [1].

## References


1. Rice TW, Kelsen D, Blackstone EH, et al. Esophagus and esophagogastric junction. In: Amin MB, Edge S, Greene F, et al, eds. AJCC Cancer Staging Manual 8th ed New York: Springer;2017:185-202.
2. Kobori O, Kirihara Y, Kosaka N, Hara T. Positron emission tomography of esophageal carcinoma using 11 C-choline and 18 F-fluorodeoxyglucose. Cancer. 1999;86(9):1638–48.
3. Desai RK, Tagliabue JR, Wegryn SA, Einstein DM. CT evaluation of wall thickening in the alimentary tract. Radiographics. 1991;11(5):771–83.
4. Noh HM, Fishman EK, Forastiere AA, Bliss DF, Calhoun PS. CT of the esophagus: spectrum of disease with emphasis on esophageal carcinoma. Radiographics. 1995;15(5):1113–34.
5. Ravenel JG, Erasmus JJ. Azygoesophageal recess. J Thorac Imaging. 2002;17(3):219–26.
6. Kim SH, Kim YJ, Lee JM, et al. Esophageal varices in patients with cirrhosis: multidetector CT esophagography—comparison with endoscopy. Radiology. 2007;242(3):759–68.
7. Umeoka S, Koyama T, Togashi K, et al. Esophageal cancer: evaluation with triple-phase dynamic CT—initial experience. Radiology. 2006;239(3):777–83.
8. Kim TJ, Kim HY, Lee KW, Kim MS. Multimodality assessment of esophageal cancer: preoperative staging and monitoring of response to therapy. Radiographics. 2009;29(2):403–21.
9. Swisher SG, Maish M, Erasmus JJ, et al. Utility of PET, CT, and EUS to Identify Pathologic Responders in Esophageal Cancer. Ann Thorac Surg. 2004;78(4):1152–60.
10. Westerterp M, van Westreenen HL, Reitsma JB, et al. Esophageal cancer: CT, endoscopic US, and FDG PET for assessment of response to neoadjuvant therapy—systematic review. Radiology. 2005;236(3):841–51.
11. Kelly S, Harris KM, Berry E, et al. A systematic review of the staging performance of endoscopic ultrasound in gastro-oesophageal carcinoma. Gut. 2001;49(4):534–9.
12. Rosch T. Endosonographic staging of esophageal cancer: a review of literature results. Gastrointest Endosc Clin N Am. 1995;5(3):537–47.
13. Souquet JC, Napoleon B, Pujol B, et al. Endoscopic ultrasonography in the preoperative staging of esophageal cancer. Endoscopy. 1994;26(9):764–6.
14. Zuccaro G, Rice TW, Goldblum J, et al. Endoscopic ultrasound cannot determine suitability for esophagectomy after aggressive chemoradiotherapy for esophageal cancer. Am J Gastroenterol. 1999;94(4):906–12.
15. Lightdale CJ, Kulkarni KG. Role of Endoscopic Ultrasonography in the Staging and Follow-Up of Esophageal Cancer. J Clin Oncol. 2005;23(20):4483–9.
16. Brown LM, Devesa SS, Chow W-H. Incidence of adenocarcinoma of the esophagus among white Americans by sex, stage, and age. J Natl Cancer Inst. 2008;100(16):1184–7.
17. Hong SJ, Kim TJ, Nam KB, et al. New TNM staging system for esophageal cancer: what chest radiologists need to know. Radiographics. 2014;34(6):1722–40.
18. Ell C, May A, Gossner L, et al. Endoscopic mucosal resection of early cancer and high-grade dysplasia in Barrett's esophagus. Gastroenterology. 2000;118(4):670–7.
19. Wakelin SJ, Deans C, Crofts TJ, Allan PL, Plevris JN, Paterson-Brown S. A comparison of computerised tomography, laparoscopic ultrasound and endoscopic ultrasound in the preoperative staging of oesophagogastric carcinoma. Eur J Radiol. 2002;41(2):161–7.
20. Wallace MB, Nietert PJ, Earle C, et al. An analysis of multiple staging management strategies for carcinoma of the esophagus: computed tomography, endoscopic ultrasound, positron emission tomography, and thoracoscopy/laparoscopy. Ann Thorac Surg. 2002;74(4):1026–32.
21. Rice TW. Clinical staging of esophageal carcinoma. CT, EUS, and PET. Chest Surg Clin N Am. 2000;10(3):471–85.
22. Daffner RH, Halber MD, Postlethwait RW, Korobkin M, Thompson WM. CT of the esophagus. II. Carcinoma. AJR Am J Roentgenol. 1979;133(6):1051–5.
23. Picus D, Balfe DM, Koehler RE, Roper CL, Owen JW. Computed tomography in the staging of esophageal carcinoma. Radiology. 1983;146(2):433–8.
24. Takashima S, Takeuchi N, Shiozaki H, et al. Carcinoma of the esophagus: CT vs MR imaging in determining resectability. AJR Am J Roentgenol. 1991;156(2):297–302.
25. Flanagan FL, Dehdashti F, Siegel BA, et al. Staging of esophageal cancer with 18F-fluorodeoxyglucose positron emission tomography. AJR Am J Roentgenol. 1997;168(2):417–24.
26. Mariette C, Castel B, Balon J, Van Seuningen I, Triboulet J. Extent of oesophageal resection for adenocarcinoma of the oesophagogastric junction. Eur J Surg Oncol. 2003;29(7):588–93.
27. Casson AG, Darnton SJ, Subramanian S, Hiller L. What is the optimal distal resection margin for esophageal carcinoma? Ann Thorac Surg. 2000;69(1):205–9.
28. Reed CE, Eloubeidi MA. New techniques for staging esophageal cancer. Surg Clin N Am. 2002;82(4):697–710.
29. Hasegawa N, Niwa Y, Arisawa T, Hase S, Goto H, Hayakawa T. Preoperative staging of superficial esophageal carcinoma: comparison of an ultrasound probe and standard endoscopic ultrasonography. Gastrointest Endosc. 1996;44(4):388–93.
30. Murata Y, Suzuki S, Ohta M, et al. Small ultrasonic probes for determination of the depth of superficial esophageal cancer. Gastrointest Endosc. 1996;44(1):23–8.
31. Hordijk ML, Kok TC, Wilson JH, Mulder AH. Assessment of response of esophageal carcinoma to induction chemotherapy. Endoscopy. 1993;25(9):592–6.

32. Tio TL, Cohen P, Coene PP, Udding J, den Hartog Jager FC, Tytgat GN. Endosonography and computed tomography of esophageal carcinoma. Preoperative classification compared to the new (1987) TNM system. Gastroenterology 1989;96(6):1478-1486.
33. Rice T, Rusch V, Apperson-Hansen C, et al. Worldwide esophageal cancer collaboration. Dis Esophagus. 2009;22(1):1–8.
34. Dorfman RE, Alpern MB, Gross BH, Sandler MA. Upper abdominal lymph nodes: criteria for normal size determined with CT. Radiology. 1991;180(2):319–22.
35. Fultz PJ, Feins RH, Strang JG, et al. Detection and Diagnosis of Nonpalpable Supraclavicular Lymph Nodes in Lung Cancer at CT and US. Radiology. 2001;222:245–51.
36. Block MI, Patterson GA, Sundaresan RS, et al. Improvement in Staging of Esophageal Cancer With the Addition of Positron Emission Tomography. Ann Thorac Surg. 1997;64(3):770–7.
37. Kato H, Kuwano H, Nakajima M, et al. Comparison between positron emission tomography and computed tomography in the use of the assessment of esophageal carcinoma. Cancer. 2002;94(4):921–8.
38. Flamen P, Lerut A, Van Cutsem E, et al. Utility of Positron Emission Tomography for the Staging of Patients With Potentially Operable Esophageal Carcinoma. J Clin Oncol. 2000;18(18):3202–10.
39. Parmar KS, Zwischenberger JB, Reeves AL, Waxman I. Clinical impact of endoscopic ultrasound-guided fine needle aspiration of celiac axis lymph nodes (M1a disease) in esophageal cancer. Ann Thorac Surg. 2002;73(3):916–20.
40. Van Vliet E, Heijenbrok-Kal M, Hunink M, Kuipers E, Siersema P. Staging investigations for oesophageal cancer: a meta-analysis. Br J Cancer. 2008;98(3):547–57.
41. Quint LE, Hepburn LM, Francis IR, Whyte RI, Orringer MB. Incidence and distribution of distant metastases from newly diagnosed esophageal carcinoma. Cancer. 1995;76(7):1120–5.
42. Margolis ML, Howlett P, Bubanj R. Pulmonary nodules in patients with esophageal carcinoma. J Clin Gastroenterol. 1998;26(4):245–8.
43. Van Westreenen H, Westerterp M, Bossuyt P, et al. Systematic review of the staging performance of 18F-fluorodeoxyglucose positron emission tomography in esophageal cancer. J Clin Oncol. 2004;22(18):3805–12.
44. Downey RJ, Akhurst T, Ilson D, et al. Whole body 18FDG-PET and the response of esophageal cancer to induction therapy: results of a prospective trial. J Clin Oncol. 2003;21(3):428.
45. Judenhofer MS, Wehrl HF, Newport DF, et al. Simultaneous PET-MRI: a new approach for functional and morphological imaging. Nat Med. 2008;14(4):459–65.
46. Pichler BJ, Kolb A, Nägele T, Schlemmer H-P. PET/MRI: paving the way for the next generation of clinical multimodality imaging applications. J Nucl Med. 2010;51(3):333–6.
47. Siewert JR, Stein HJ, Feith M, Bruecher BL, Bartels H, Fink U. Histologic tumor type is an independent prognostic parameter in esophageal cancer: lessons from more than 1,000 consecutive resections at a single center in the Western world. Ann Surg. 2001;234(3):360.
48. Rice TW, Rusch VW, Ishwaran H, Blackstone EH. Cancer of the esophagus and esophagogastric junction. Cancer. 2010;116(16):3763–73.

# Imaging of Nonneoplastic Esophageal Pathologies

17

Elena Lucia Indino, Alessandro di Gaeta, Gianmarco Andreoli, Maurizio Del Monte, and Valeria Panebianco

**Abstract**

The esophagus is an organ which consists of a fibromuscular tube which enables the passage of food. This transmission is aided by peristaltic contractions, from the pharynx to the stomach, where the process of digestion reaches the acme. Efficient transport through the esophagus requires the organ either to be patent and well canalized or to have adequate motility. This consists of coordinating sequential contraction that mobilizes the bolus from above and clears acid and bile reflux from below. Dysfunction of this integrated muscular motion reduces progression of bolus and causes a distressing sense of dysphagia, chest pain, and regurgitation, or leads to other severe conditions (i.e., ab ingestis pneumonia).

In this scenario modern imaging techniques, either invasive or noninvasive, concede an early and accurate diagnosis that radically changed the approach to those disorders. In fact a predominant role is played by contrast-enhanced computed tomography (CT) and magnetic resonance imaging (MRI), but conventional radiology (barium esophagography; endoscopic ultrasonography, EUS) is still essential. Among those techniques, dynamic MRI of the esophagus has developed a great potential, with the introduction of ultrafast MR sequences, which have decreased scan times, granting a minor exposure to ionizing radiation.

**Keywords**

Esophagus · Esophagus congenital malformation · Esophagus motility · Hiatus hernia · Esophageal trauma · Esophageal atresia · Achalasia · Esophagitis, reflux

## Abbreviations

| | |
|---|---|
| CES | Congenital esophageal stenosis |
| CT | Computed tomography |
| DES | Diffuse esophageal spasm |
| EA | Esophageal atresia |
| Gd | Gadolinium |
| GERD | Gastroesophageal reflux disease |
| HU | Hounsfield unit |
| IEM | Ineffective esophageal motility |
| MRI | Magnetic resonance imaging |
| NEMD | Nonspecific esophageal motility dysfunction |
| SE | Scleroderma of the esophagus |
| TEF | Tracheoesophageal fistula |
| UES | Upper esophageal sphincter |

E. L. Indino · A. di Gaeta · M. Del Monte
V. Panebianco (✉)
Department of Radiological, Oncological and Anatomopatological Sciences, Sapienza—University of Rome, Policlinico Umberto I, Rome, Italy
e-mail: valeria.panebianco@uniroma1.it

G. Andreoli
Hospital Policlinico Umberto I of Rome, Rome, Italy


M. Anzidei, M. Anile (eds.), *Diagnostic Imaging for Thoracic Surgery*,
https://doi.org/10.1007/978-3-319-89893-3_17

## 17.1 Congenital Anomalies of the Esophagus

### 17.1.1 Esophageal Atresia and Tracheoesophageal Fistula

Congenital esophageal anomalies represent a complex of anatomical alteration characterized by the uncomplete formation of esophagus and/or an abnormal communication between the esophagus and other anatomical structures. This combination of pathologies may occur in 1 per 3000–5000 births.

The rare defects of development of the esophagus must be corrected early after the birth because of incompatibility with life. They are often found because of an early regurgitation after feeding. The exact cause is still undefined. It is known that it occurs as a developmental disorder in formation and separation of the primitive foregut into trachea and esophagus. This results from the fusion of both lateral mesodermal ridges of the foregut approximately around fourth week of gestation.

If the lateral walls fail to meet, they result in tracheoesophageal fistula; if these lateral walls turn dorsally, and compress the esophageal lumen, it will result in atresia.

Other causes can be intrauterine anoxia (can lead to a focal reduced perfusion and necrosis resulting in fistulae or atresia).

The esophageal agenesia is the absence of the esophagus and is not compatible with life. While this condition is extremely rare, more common defects are the esophageal atresia and tracheoesophageal fistula, often present at the same time [1].

Those anomalies can be associated with other gastrointestinal malformations in 25% of cases, such as imperforate anus, pyloric stenosis, duodenal atresia, and annular pancreas. Less frequent are cardiac, genitourinary, and vertebral changes.

Five different types of atresia have been identified, depending on the presence or absence of tracheoesophageal fistula and its location (Fig. 17.1):

- Type A corresponds to pure esophageal atresia without fistula (8%).
- Type B is esophageal atresia and fistula from trachea to the proximal esophageal pouch (>1%).
- Type C is esophageal atresia with fistula between the trachea and the main bronchus to the distal segment; this is the most common type (84%).
- Type D is esophageal atresia with both proximal and distal fistulae (3%).
- Type E is tracheoesophageal fistula without atresia (4%); this type of anomaly must be suspected in feeding difficulties in infants, occasionally related with choking.

The inability to pass a rigid nasogastric tube from patient's mouth to the stomach is diagnostic of EA and/or TEF. However this finding should

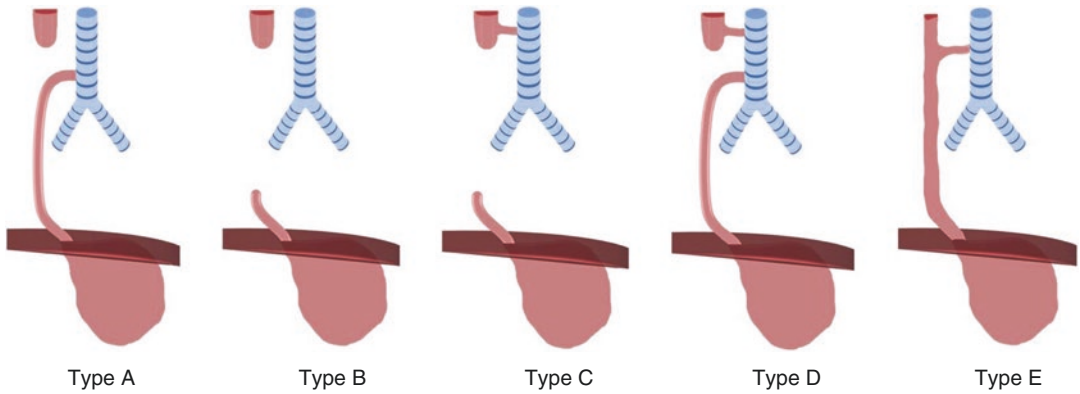


**Fig. 17.1** Esophageal atresia classification according to Gross

be confirmed with radiographic visualization of the tube coiled in the proximal esophageal segment.

The radiological diagnosis (Fig. 17.2a, b) is based on chest radiographs on the posteroanterior and lateral projection which reveal a blind proximal pouch distended with air. The radiograph should always include the abdomen, in order to demonstrate the presence of air in the gastrointestinal tract. In types A and B, there is complete absence of gas in the stomach and intestinal tract, although in types C and D the gastrointestinal tract is distended with air.

Confirmation of diagnosis is achieved by a contrast swallow study. Barium agents allow the best visualization of a fistula; however if TEF is suspected, barium is not indicated because of the risk of mediastinitis and chemical pneumonia. The contrast of choice is an isotonic, nonionic iodate contrast agent. Main findings are the demonstration of esophageal obstruction and fistula, together with opacification of the bronchus and distal airways.

CT scan is not typically used in the evaluation of EA and TEF; however, CT does allow 3-dimensional (3D) examination of the esophagus in relation to its adjacent structures. Axial images can be difficult to interpret, in which a fistula may be missed; however the sagittal reformation obtained from thin-section multidetector scans has been used in newborns to accurately diagnose EA and TEF. This method enables visualization of the entire length of the esophagus, complete with atresias, fistulas, and gap length.

Three-dimensional CT with virtual endoscopy facilitates the understanding of complex anatomic relationships and evaluation of transverse stenoses.

### 17.1.2 Esophageal Duplications

Duplication of the esophagus is the second most common duplication of the gastrointestinal tract after that of the ileum. Several theories have been proposed to explain the embryologic basis for gastrointestinal tract duplications.

The most held theory was proposed by Bremer, according to which at the fifth week of intrauterine life, the foregut epithelium produces secretions that form vacuoles. Those vacuoles line up longitudinally to form the new lumen; if

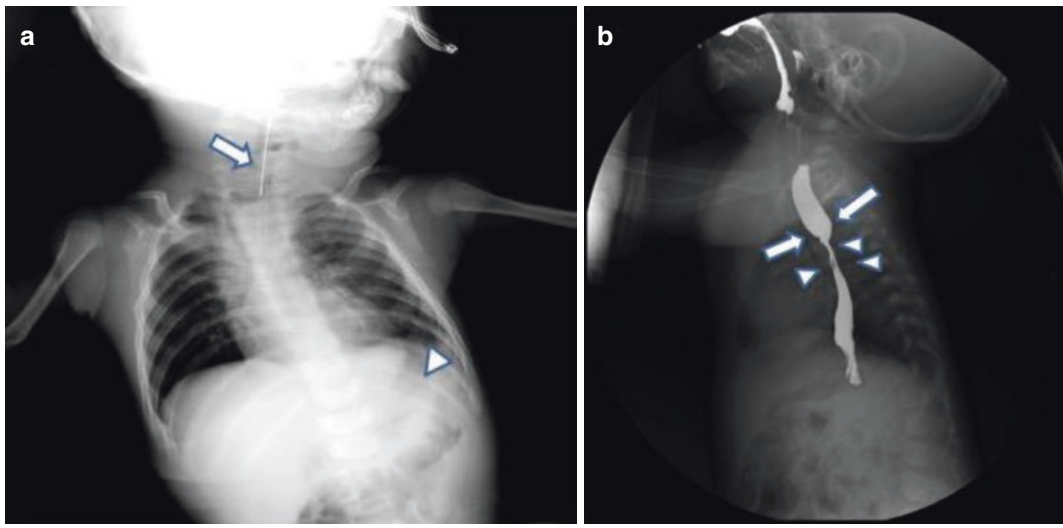


**Fig. 17.2** Esophageal atresia. Chest radiograph of a newborn child revealed esophageal atresia without tracheoesophageal fistula. Should be noted (in **a**) the Replogle tube in the upper pouch (arrows) and the absence of GI air below the diaphragm (arrowheads), which is an indirect sign of the absence of tracheoesophageal fistula. After barium swallow (in **b**) is seen a narrowing of the esophagus lumen (arrowheads) with a mild dilatation of the upper pouch (arrows)

some vacuoles fail to coalesce, it will result in a cyst that migrates into the esophageal wall and becomes surrounded by the muscular layers. The duplicated segment has a thick wall of smooth muscle and is lined with alimentary tract mucosa.

It is possible to distinguish a partial and a complete esophageal duplication; the former is the second most common gastrointestinal duplication after the ileum and the latter is a rare malformation, often associated with gastric duplication.

Most often, duplications are spherical cysts that rarely make an impression on the esophagus. On plain chest radiographs, they are usually seen as posterior mediastinal masses. Barium swallow shows the esophagus to be displaced to the cyst's opposite side or an intramural extramucosal mass. At CT, a duplication is sharply marginated, has a homogeneous near-water density (9–18 HU), and is not enhanced after intravenous contrast material injection.

The MRI shows relatively low signal intensity on T1-weighted images and high signal intensity on T2-weighted images (Fig. 17.3a, b), and no significant enhancement in postcontrast sequences.

Endoscopic sonography has proved to be a reliable method for the diagnosis of this lesion because it can demonstrate contiguity of the muscularis propria of the esophagus with the muscle layer of the cyst wall.

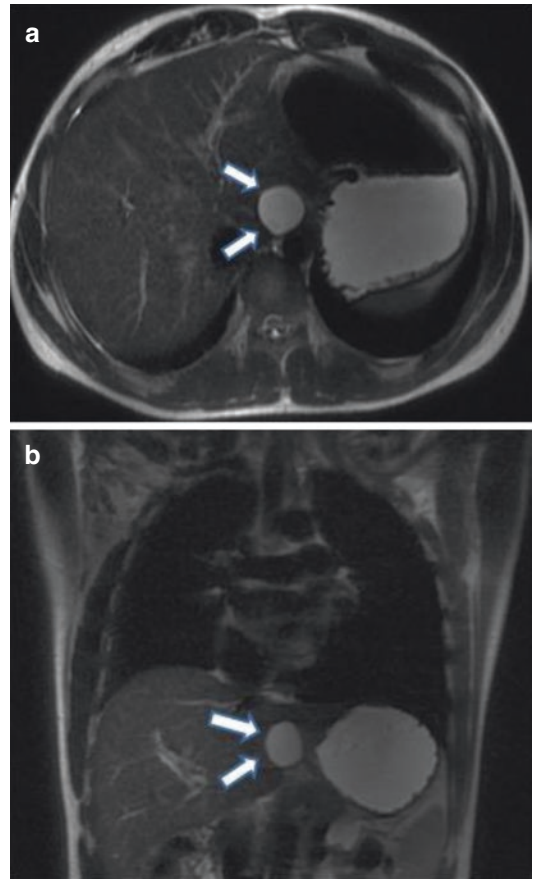


**Fig. 17.3** Esophageal duplication. Axial (**a**) and coronal (**b**) T2W image of the distal esophageal tract shows a well-circumscribed fluid-filled lesion with a thin wall (arrows) without communication with the esophageal lumen

### 17.1.3 Other Minor Congenital Anomalies

Less frequent congenital anomalies are diaphragm, stenosis, and congenital brachy-esophagus. Those alterations can be easily demonstrated with barium swallow:

- Diaphragms are incomplete endoluminal thin membranes that can be mostly seen in the upper tract of the esophagus; generally these membranes are seen in particular conditions such as Plummer-Vinson syndrome (esophagitis, sideropenic anemia, and gastric achlorhydria).
- Congenital stenosis (CES) is an esophageal benign lesion that narrows the organ; those lesions can easily be demonstrated by a barium swallow that demonstrates the narrowing.
- Brachy-esophagus is an incomplete enlargement of the esophagus that leads to a hiatal hernia.

## 17.2 Acquired Malformations

### 17.2.1 Esophageal Diverticula

Rings, webs, and diverticula are among the most common acquired anomalies of the esophagus.

Although these structural lesions are often asymptomatic, patients can develop significant problems with dysphagia, regurgitation, and aspiration.

Most well-known classifications of diverticula are by location in the esophagus: upper (pharyngoesophageal, Killian-Jamieson, or Zenker), middle, or lower (epiphrenic) and on the basis of histopathology in true diverticula (contain all layers of the intestinal tract wall) and pseudodiverticula (herniation of mucosa and submucosa through a defect in the muscular wall occurs). Of the diverticula, Zenker diverticula are the most common type to cause symptoms. Zenker diverticula are an acquired pulsion type of diverticula formed by the herniation of mucosa through an area of weakness in the Killian triangle of the hypopharynx.

A special type of pseudodiverticula, believed to represent dilated excretory ducts of esophageal submucosal glands, is observed in the condition of esophageal intramural pseudodiverticulosis.

Most esophageal diverticula occur in middle-aged adults and elderly people, in particular Zenker diverticula typically present in people older than 50. Oropharyngeal dysphagia to solids is the most common symptom. Regurgitation and aspiration may be related to large midesophageal and epiphrenic diverticula.

Most diverticula are caused by an underlying motility disorder of the esophagus. Structural lesions, including a noncompliant cricopharyngeus muscle (i.e., Zenker diverticulum), incomplete or uncoordinated relaxation of the lower esophageal sphincter, or strictures, may play a role as well.

### 17.2.2 Imaging Findings

Esophageal diverticula often are asymptomatic; therefore, radiographic studies detect many esophageal diverticula incidentally. On standard chest radiographs and CT scans, large diverticula of the esophagus and hypopharynx also may manifest as air-filled and/or fluid-filled structures communicating with the esophagus. Barium radiography is still considered the gold standard exam even because barium swallow also may provide clues to underlying motility disturbances that may be involved in diverticular formation. Diagnosis of esophageal intramural pseudodiverticulosis is made best using barium radiography. Diagnosis of Zenker diverticulum is made best using barium swallow, which should include lateral views of the pharyngoesophageal junction. Because of its location Killian-Jamieson diverticula could be detected on ultrasonography miming thyroid nodules. Also a Zenker diverticulum reportedly can be distinguished from a thyroid nodule on ultrasound by the sign of air in the diverticulum. There also has been a study of the use of swallow contrast-enhanced ultrasound to detect Zenker diverticulum that appeared as a pouch-shaped structure at the posterior pharyngoesophageal junction which retained ultrasound contrast agent for longer than 3 min. All patients underwent a barium esophagram as the gold standard. The authors explained that contrast-enhanced ultrasound provides advantages of bedside availability and no radiation exposure. When incidentally imaged on computed tomography (CT) and magnetic resonance imaging (MRI) scan, a Zenker diverticulum appears as a structure arising posteriorly from the hypopharynx and is filled with gas, fluid, oral contrast material, or a mixture of these [2, 3].

## 17.3 Dyskinesia

Esophageal motility disorders consist of a complex array of disturbances in normal esophageal function associated with dysphagia, gastroesophageal reflux, and noncardiac chest pain.

Primary motility disorders consist of achalasia, diffuse esophageal spasm (DES), "nutcracker esophagus," hypertensive lower esophageal sphincter, and nonspecific esophageal motility dysfunction (NEMD). A host of secondary and miscellaneous motility disorders also affect the esophagus, including scleroderma and other connective tissue diseases, diabetes mellitus, Chagas disease, chronic idiopathic intestinal pseudoobstruction, and neuromuscular disorders of striated muscle. Gastroesophageal reflux disease (GERD) may also be promoted by associated

motility disturbances. In this chapter will discuss imaging findings in patients with achalasia.

Deglutition is a neuromuscular act coordinated by neural centers located in the brainstem and controlled by a widespread network of cortical regions; it is a complex function coordinated by voluntary and involuntary muscles of the oropharynx, larynx, and upper digestive pathway. The swallowing process is generally divided into three phases: (1) the *voluntary phase*, the onset of deglutition; (2) the *pharyngeal phase*, consisting of bolus passage from the mouth to the superior esophageal sphincter through the pharynx; and (3) the *esophageal phase*, characterized by bolus progression to the stomach through the esophagus [4]. The last two phases are involuntary. The *esophageal phase* starts with the opening of the superior esophageal sphincter. The primary function of the esophagus is to transport and direct the bolus from the pharynx to the stomach. The sequence of the muscular contractions is known as *peristalsis*. In normal subjects, two types of peristaltic activity are described: primary and secondary peristalsis.

The identification of the deglutition phases has been described in dynamic MR studies [using the different dynamic sequences such us turbo-FLASH, TrueFISP, and EPI combined with an oral positive contrast agent]. Turbo-FLASH and echo planar (EPI) MRI sequences demonstrated a sufficient temporal resolution for dynamic imaging of the deglutition process. However, detailed analysis is still restricted, mainly by the significantly lower SNR of high-speed MRI compared with conventional MRI, and by the occurrence of shape distortions in regions of large susceptibility gradients. The temporal resolution provided by ultrafast MRI is essential for the analysis of deglutition. Hagen et al. obtained good-quality images using turbo-FLASH sequences for dynamic oropharyngeal evaluation with temporal resolution of 0.2 s/slice and 0.3 s/slice [5].

Gd-based oral contrast agents are used for MRI evaluation of bolus transit along the pharyngeal and esophageal tract. Gd-DTPA-based contrast agent provides optimum signal intensity, while its combination with semifluid yoghurt (1:100) offered barium-like physical properties, improving at the same time patient comfort and granting good compliance during the examination [6]. The bolus is injected in the patient's mouth by the doctor or technician before the start of the dynamic sequence by a syringe (20 mL) and oral silicone cannula [6–8].

**Esophageal motility** imaging protocol is divided into the following:

*Phase 1*: A breath-hold half Fourier single-shot turbo spin echo (HASTE) T2-weighted sequence orientated on coronal and axial planes is used to visualize the position of the esophagus and the gastroesophageal junction.

*Phase 2*: Dynamic examination is performed with a single-slice sagittal slab (10mm thickness) T1-weighted (turbo-FLASH) sequence. This slice is positioned at the center of the esophageal lumen, in order to depict the transit of contrast agent boluses through the esophageal lumen. The parameters of the turbo-FLASH sequence are modified to obtain a temporal resolution of approximately 3–4 images/s. Immediately before the sequence starts, a small amount of contrast agent (10–15mL) is administered directly into the oral cavity. Patients are instructed to swallow the entire bolus immediately after the onset of the gradient pulsations. Patients with severe deglutition disorders are at high risk for airway aspiration of oral contrast agent; in such situations oral contrast media should not be used. Five series of dynamic acquisitions are obtained: four acquired on the median sagittal and coronal plane to visualize esophageal motility and one on the oblique axial plane to depict gastroesophageal junction functionality.

### 17.3.1 Imaging Findings

In patients with achalasia, the main findings are the stenotic appearance of the distal esophagus with and/or without wall thickening and the dila-

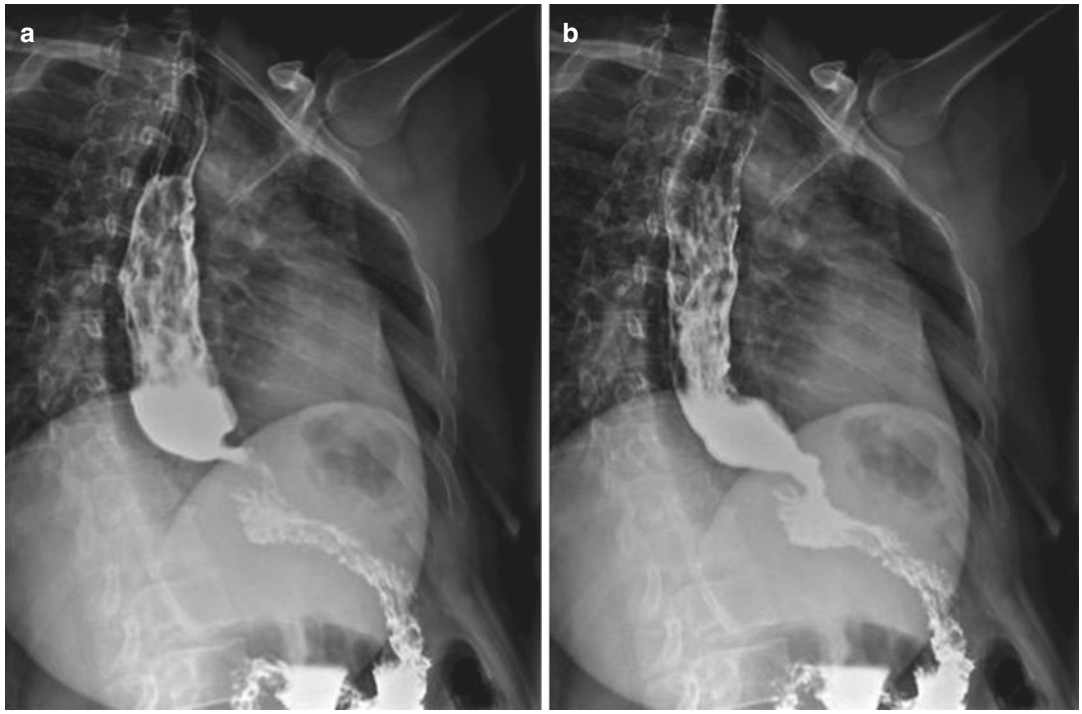


**Fig. 17.4** CRX of achalasia: the images show a conventional barium swallow on the oblique projection that demonstrated a mild dilatation of the lower esophageal tract. A narrowing progression of barium through the sphincter into the stomach is also seen

tation of the segments above (Fig. 17.4a, b); poor relaxation of the gastroesophageal junction; inefficient peristalsis replaced by "to-and-fro" movements (repeated upward/downward movement of the bolus in the esophageal lumen caused by abnormal peristalsis and unrelaxed gastroesophageal junction); and the increased bolus transit time (up to 20 s). In advanced stages, the main findings are represented by a marked and widespread distension of the esophageal lumen (maximum caliber >60 mm) with tertiary peristalsis that is unable for activity and to fully empty the organ [9–11].

MRI findings (Fig. 17.5a–f) in patients with esophageal body motility incoordination (EBMU) are intermittent progression of the contrast bolus along the lumen with tertiary peristalsis, increased transit time (12–15 s), and reduction with a "corkscrew" appearance [12, 13].

In ineffective esophageal motility (IEM)/scleroderma of the esophagus (SE), a weak peristaltic activity, enlarged diameter, and mildly reduced esophageal clearance are considered significant diagnostic features of gastroesophageal junction incontinence with reflux and diminished clearance with delayed cleansing time (>18 s) [14, 15].

An additional application of MR-fluoroscopy is the follow-up of patients affected by achalasia after conservative treatment such as balloon dilatation of the distal esophagus. In this patient, population dynamic MRI is also adequate in the posttreatment follow-up to evaluate the efficacy therapy [8, 16–18].

## 17.4 Esophagitis

Common forms of esophagitis include reflux esophagitis, infectious esophagitis, pill esophagitis, eosinophilic esophagitis, and radiation and chemoradiation esophagitis. Candida esophagitis

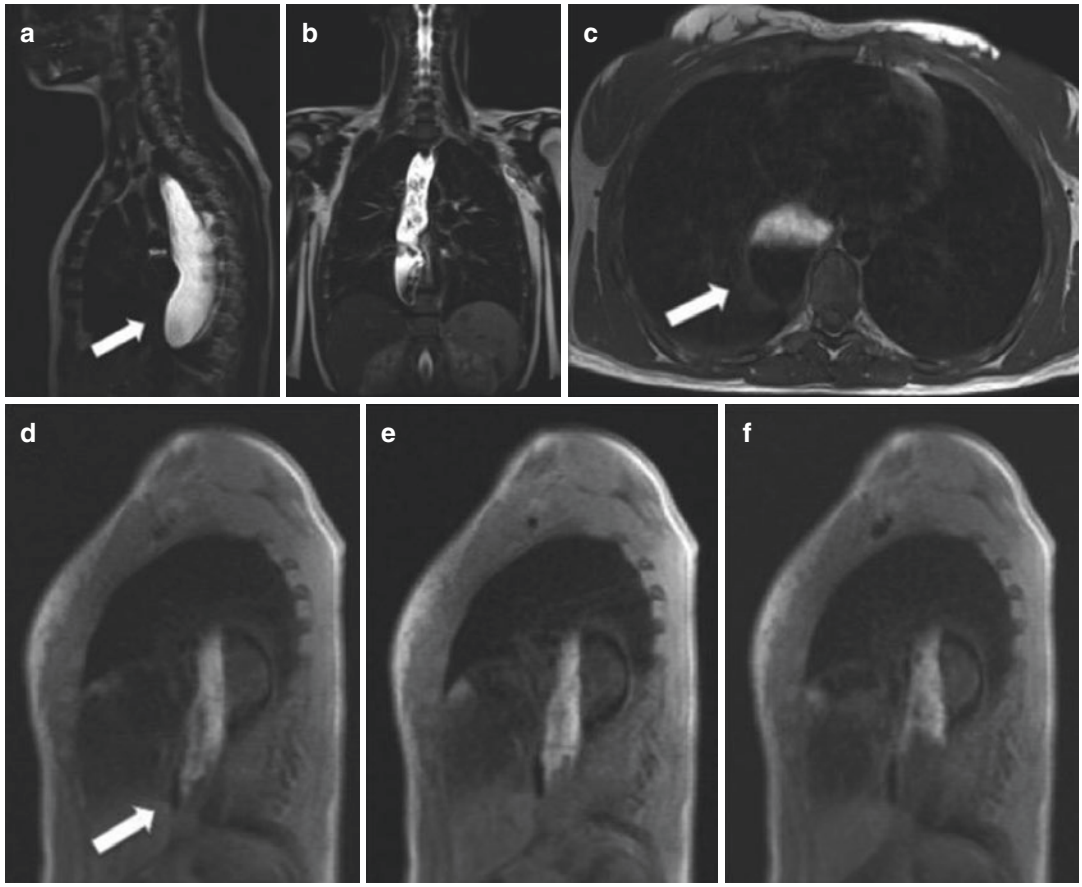


**Fig. 17.5** MRI of achalasia: T2W HASTE images acquired on axial (**a**), coronal (**b**), and sagittal (**c**) plane. The exam revealed distension of the esophageal lumen (40 mm), narrowing of the distal esophagus, and replacement of the normal peristalsis by tertiary activity. On T1W F.L.A.S.H. sequences, after contrast bolus administration the gastroesophageal junction is closed and the bolus cannot progress (**d**–**f**)

is the most common type of infectious esophagitis [19]. The prognosis is good with rapid diagnosis and proper treatment [16]. Although barium studies and endoscopy are more sensitive modalities for detecting this condition, the CT finding should suggest the diagnosis of esophagitis in the proper clinical setting. It has been suggested that 3 or 5 mm be considered the maximum normal values for esophageal wall thickness on CT and that a greater wall thickness may represent a sign of esophagitis. Wall thickening in esophagitis was concentric and circumferential in all patients and involved a relatively long segment of the esophagus. Esophageal wall thickening was found in all types of esophagitis, so a specific cause of esophagitis cannot be suggested on the basis of CT findings. Occasionally, malignant esophageal tumors may be manifested on CT by concentric wall thickening over relatively long segments so that further investigation with double-contrast esophagography or endoscopy may be required in patients who do not have typical clinical features of esophagitis.

## 17.5 Trauma

### 17.5.1 Perforation

Causes of perforations are divided into iatrogenic (75%: endoscopy and tracheal intubation are the most common causes) and non-iatrogenic (25%,

including compression, foreign bodies, and neoplastic expansion). The cricopharyngeal area (UES) is the narrowest part of the esophagus where the perforations occur during endoscopy. The second restricted area is located close to aortic button and left bronchus and is the seat of the perforations by foreign bodies. The third zone is defined esophagogastric junction, and is involved in perforation especially during expansion maneuvers.

Symptoms of traumatic injury are often not specific: sudden violent pain, dysphagia, dyspnea, fever, subcutaneous emphysema, and shock.

The diagnosis is clinical and instrumental. When perforation is suspected, the imaging evaluation should generally commence with esophagography while the patient swallows a water-soluble contrast material (Fig. 17.6a, b). If no extra-esophageal leakage is observed, esophagography should be repeated during the oral administration of barium, which has a greater sensitivity for the detection of small perforations. In patients with penetrating trauma to the neck or chest, CT should be performed before contrast-enhanced esophagography, given the significant risk of damage to critical vascular structures. CT may be useful also in patients who are too ill to cooperate in esophagography or as a complement to contrast-enhanced luminal studies, to further delineate the extent of disease, assess complications, and guide therapy. In patients with acute chest pain, CT is used to exclude serious conditions such as aortic dissection and pulmonary embolism. CT findings of esophageal injury include esophageal wall thickening, periesophageal gas and fluid collections (Figs. 17.7a–f and 17.8a–d), contrast material extravasation, mediastinal fluid collection, mediastinal inflammation, focal esophageal wall defect, and pleural effusion [20–22]. Therapy is always urgent and surgical; it includes where possible the esophagus raffia.

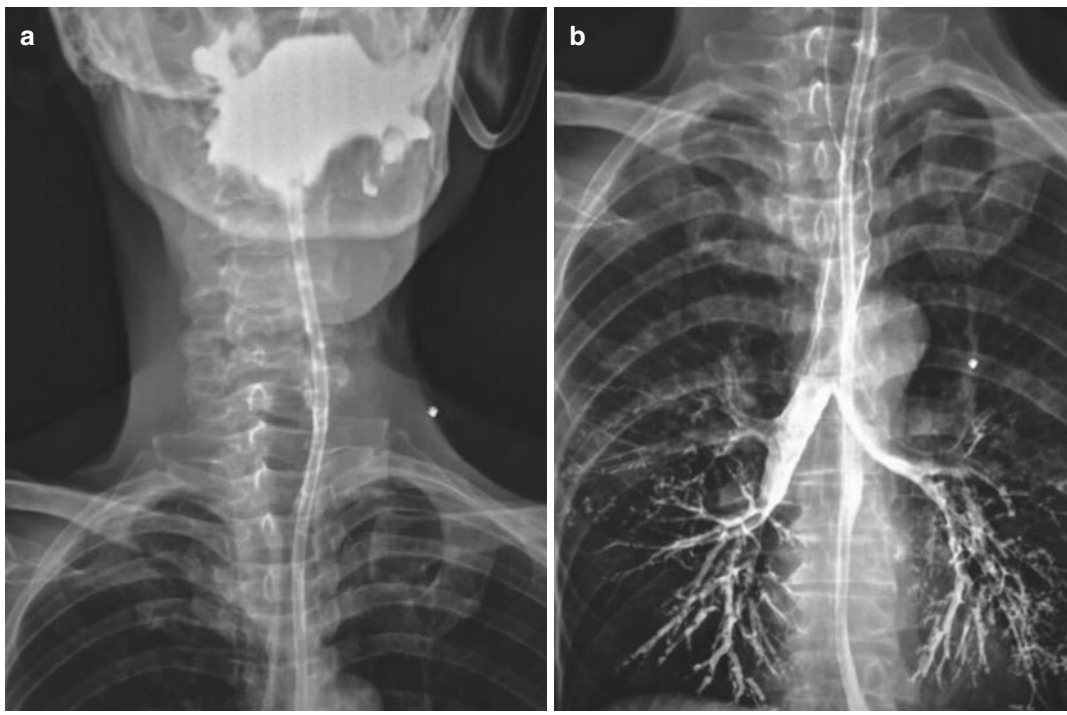


**Fig. 17.6** Barium swallow in a patient who experienced recurrent pneumonias. In figure (**a**) can be seen the soluble medium contrast in oral cavity and a nasogastric tube. In figure (**b**) is seen the aspiration of medium in pulmonary airways

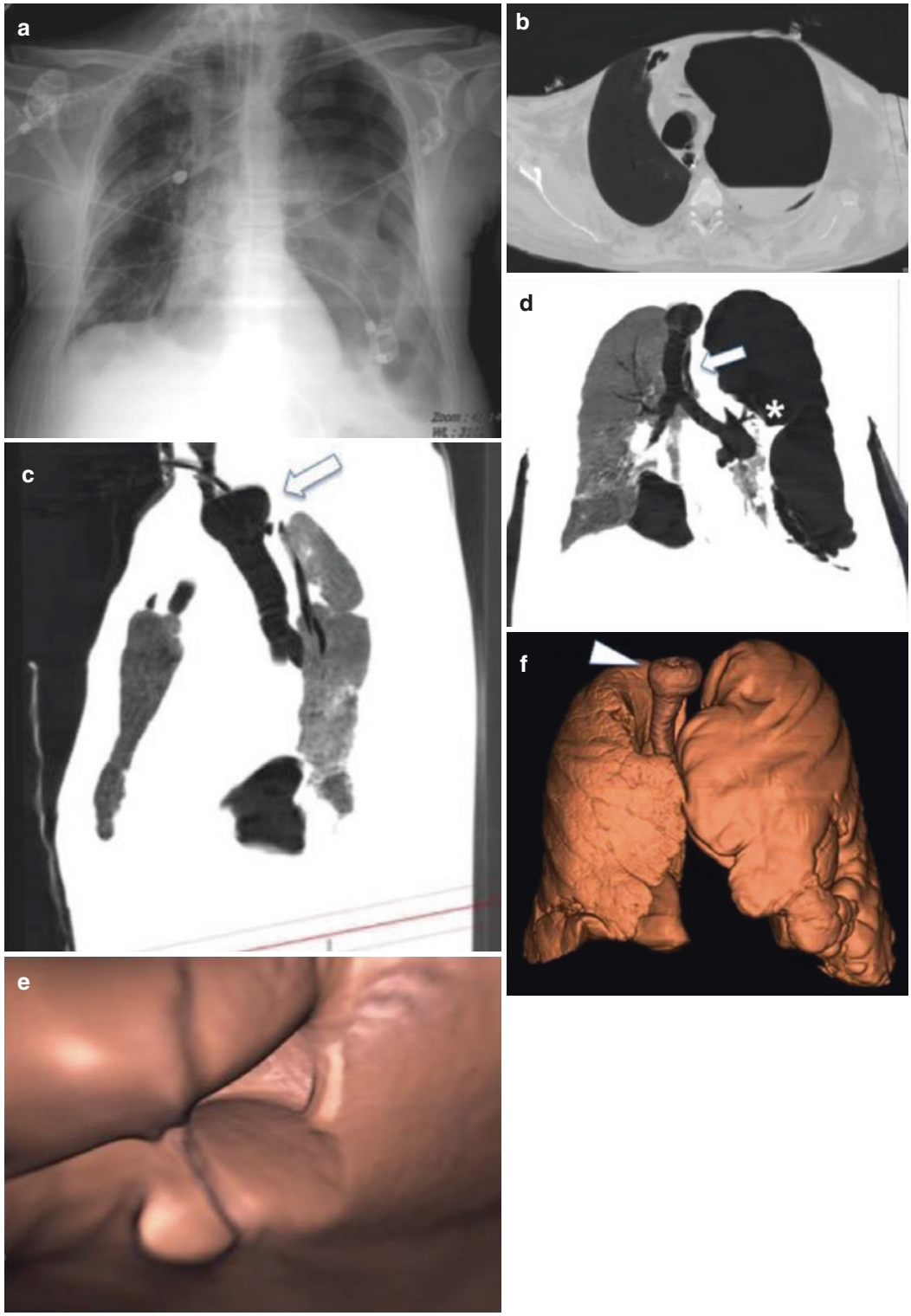


**Fig. 17.7** Tracheoesophageal fistula. A 43-year-old man was involved in a car accident and transferred to intensive care unit. A chest X-ray (**a**) demonstrated a tracheal tube and left hydropneumothorax. A thoracic CT scan on axial (**b**), sagittal (**c**), and coronal (**d**) planes showed a short fistula (arrow) located at the level of the fourth and fifth thoracic vertebrae, and left hydropneumothorax (*). In figure (**e**) is shown a 3D endoscopic reconstruction of the fistula (arrow). Figure (**f**) shows post-processed 3D reconstruction of lungs and tracheas with mild posttraumatic laryngocele (arrowhead)

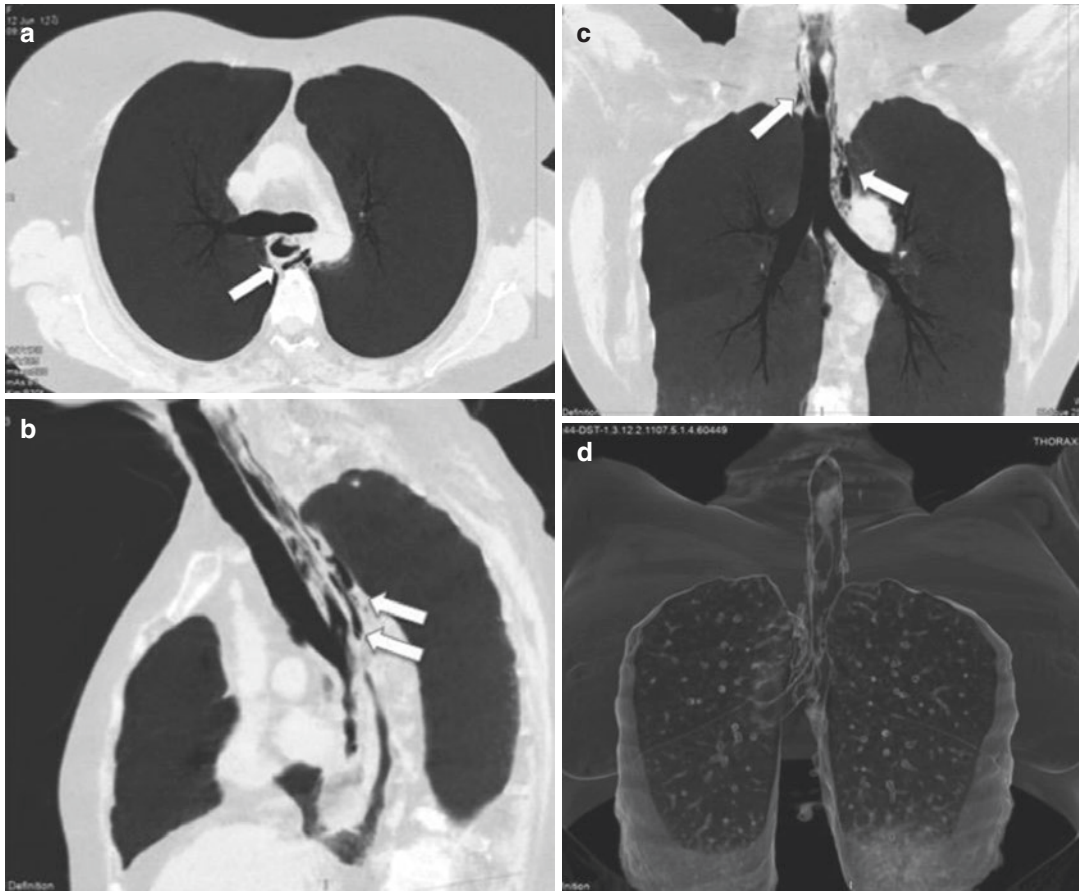


**Fig. 17.8** Esophageal rupture. Axial (**a**), sagittal (**b**), coronal (**c**), and volume-rendering (**d**) reconstruction of non-contrast CT of chest demonstrates perforation of the mid-thoracic esophagus with extra-luminal focus of gas (arrow) in the posterior mediastinum

### 17.5.2 Mallory-Weiss Tear and Other Mucosal Lacerations

A Mallory-Weiss tear is a longitudinal mucosal laceration observed in the distal esophagus or across the gastroesophageal junction. It occurs in the setting of retching or vomiting, frequently after excessive alcohol consumption or as a complication of endoscopy. Some degree of hematemesis is invariably present and is an indication for upper endoscopy. Similar linear mucosal lacerations occurring elsewhere in the esophagus as a result of forceful swallowing of an impacted foreign body or food bolus may pose a diagnostic dilemma. A mucosal laceration without transmural perforation is likely to be radiographically occult. However, to the attentive observer, CT images of the esophagus in patients with chest pain occasionally show evidence of hemorrhage or foci of extraluminal gas at a site of mucosal injury [23]. Unless bleeding persists, the treatment of a Mallory-Weiss tear, like that of other mucosal lacerations, is supportive.

### 17.5.3 Foreign Bodies

The inability of food to progress towards the stomach depends on the size of foreign bodies or on the presence of tips that favor anchor to the

esophagus wall. Most commonly foreign bodies stop in thoracic esophagus and preferably at the level of physiological narrowing. Symptoms could be pain, drooling, and dysphagia, and symptoms of perforation (if complicated). In cervical foreign body we could see phlegmon of the neck with subcutaneous emphysema and in chest foreign body an esophageal-mediastinal fistula with acute mediastinitis or esophageal-pleural. Diagnosis is by X-ray if the foreign body is metallic; if it is not radio-opaque examination with contrast reveals the location of the ingested body. Esophagoscopy allows to establish the seat of the foreign body and its removal and allows to detect the extent of a possible esophageal laceration. Once the presence of a foreign body is radiologically confirmed in the esophagus, but also in the clinical suspicion, it is necessary to intervene endoscopically early, regardless of location, size, and potential damaging [24]. Surgical excision, via cervicotomy or thoracotomy, is limited to cases where the endoscopy fails. The CT appearance of foreign-body impaction is variable, depending on the item ingested, site of impaction, and presence of an underlying pathologic esophageal process or associated complication. Axial and sagittal contrast-enhanced chest and upper abdomen CT image helps confirm the presence of a foreign body. Chronic impaction of a foreign body in the esophagus may produce erosion, fistula formation, and inflammatory reaction that are indistinguishable from those produced by a neoplastic process.

## 17.6 Esophageal Varices

Esophageal varices are abnormally enlarged veins, usually seen in lower part of the esophagus; these alterations are a spy of a portal hypertension that occurs in severe liver disease. These enlarged veins link the portal blood flow to the cava vein system, bypassing the liver. Esophageal varices are graded according to their size and appearance, as follows:

- Small (grade 1): small straight varices
- Medium (grade 2): enlarged tortuous varices occupying less than one-third of the lumen
- Large (grade 3): large coil-shaped varices occupying more than one-third of the lumen

The classification enlisted above is based on endoscopic appearance, which remains the gold standard in diagnosis, because of the direct visualization, and eventually for the possibility of treatment.

Diagnostic imaging can give an important support in the diagnosis, by using contrast imaging.

Nowadays, barium swallow technique is not considered the first-line exam to evaluate varices. However barium swallow may demonstrate large- and medium-grade varices as incidental finding. Those veins are not directly seen but images can demonstrate a serpiginous filling defects, involving the inferior third of the esophagus.

Better than barium swallow, contrast-enhanced CT (Fig. 17.9a–d) scanning and MRI are identical in their usefulness in diagnosing esophageal varices because of its direct visualization. These modalities have the advantage over endoscopy because of the possibility in evaluating the surrounding anatomic structures and the extent of esophageal varices, both above and below the diaphragm [25–27].

## 17.7 Hiatus Hernia

Hiatal hernia (or paraesophageal hernia) occurs when part of the stomach protrudes into the thoracic cavity through the esophageal hiatus of the diaphragm. A hernia may occur through a congenitally large esophageal hiatus; however, acquired hernias through the esophageal hiatus are more common. Approximately 99% of hiatal hernias are sliding, and the remaining 1% are paraesophageal, but it's very important to diagnose the last one because they are potentially life threatening because of the risk of volvulus and incarceration.

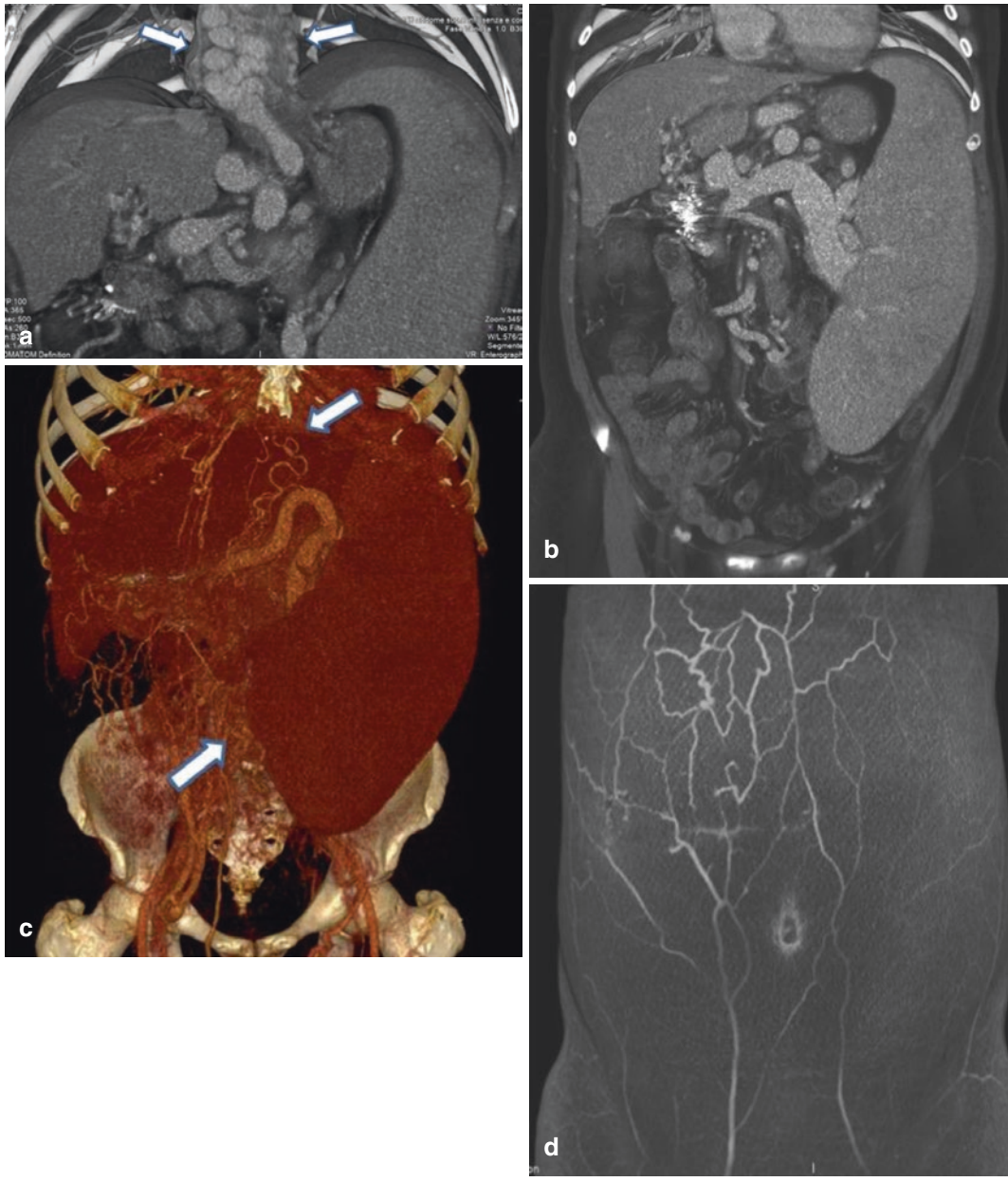


**Fig. 17.9** Esophageal varices. CT images of esophageal varices (**a**, arrows), in a patient with liver cirrhosis, splenomegaly, and portal hypertension with collateral circulation (**b**, **c**). Figure (**d**) shows subcutaneous collateral circulation as an effect of portal hypertension

### 17.7.1 Imaging Findings

Most hiatal hernias are found incidentally, and they are usually discovered on routine chest radiographs or computed tomography (CT) scans performed for unrelated symptoms. When symptomatic, patients may experience heartburn, dyspepsia, or epigastric pain.

An upper GI barium series is the preferred examination in the investigation of suggested hiatal hernia and its sequelae. CT scans are useful when more precise cross-sectional anatomic localization is desired and a hiatal hernia appears as a retrocardiac mass with or without an air-fluid level. The mass can usually be traced into the esophageal hiatus on sequential cuts. Herniation of omentum through the esophageal hiatus may result in an increase in fat surrounding the lower esophagus (Fig. 17.10a–c). CT scanning is particularly useful in the accurate anatomic depiction of a totally intrathoracic stomach, especially in patients in whom volvulus of the stomach is suspected. CT scanning is also useful for staging purposes in patients in whom a carcinoma complicates a hiatal hernia [28].

The use of magnetic resonance imaging (MRI) and radionuclide studies is anecdotal. MRI has helped to achieve a diagnosis of a paraesophageal omental hernia, in which a retrocardiac mass was shown as a fatty tumor, with contiguous blood vessels extending from the abdominal portion into the thoracic portion.

Ultrasonography is a sensitive means of diagnosing gastroesophageal reflux, and it is particularly attractive for use in young patients because it is noninvasive and does not require the use of ionizing radiation.

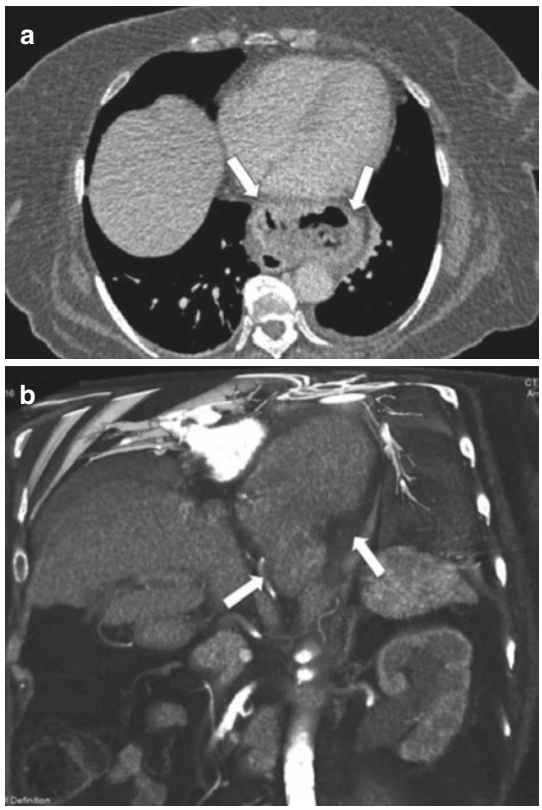


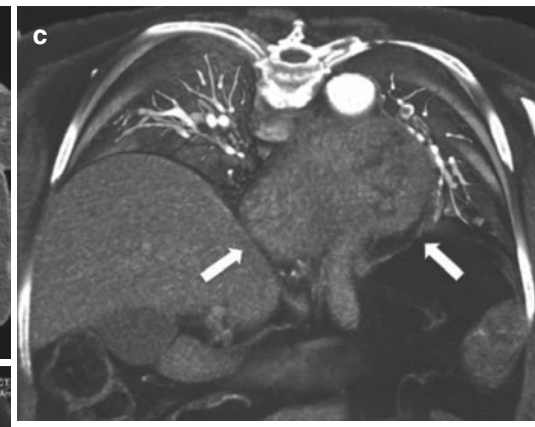


**Fig. 17.10** Hiatal hernia: 82-year-old woman referred to our department for a routine angio-CT scanner to study the abdominal aorta. As collateral finding marked distention and distortion of the stomach were seen with herniation of a portion of the fundus into the lower thorax. The hiatal hernia is seen on the axial (**a**), volume-rendering oblique reconstruction (**b**, **c**)

## References


1. Berrocal T, Madrid C, Novo S, et al. Congenital anomalies of the tracheobronchial tree, lung, and mediastinum: embryology, radiology, and pathology. Radiographics. 2003;24:e17. https://doi.org/10.1148/rg.e17.
2. Ekberg O. Normal anatomy and techniques of examination of the esophagus: fluoroscopy, CT, MRI, and scintigraphy. In: Freeny PC, Stevenson GW, editors. Margulis and Burhenne's alimentary tract radiology. 5th ed. St. Louis: Mosby; 1994. p. 168–85.
3. Herbella FA, Patti MG. Modern pathophysiology and treatment of esophageal diverticula. Langenbecks Arch Surg. 2012;397(1):29–35. Accessed Jan 2012.
4. Vaz M, Raj T, Anura K. Guyton & Hall textbook of medical physiology. 2nd ed. New Delhi: Elsevier; 2016. p. 747–8.
5. Mason RJ, Bremner CG, DeMeester TR, Crookes PF, Peters JH, Hagen JA, DeMeester SR. Pharyngeal swallowing disorders: selection for and outcome after myotomy. Ann Surg. 1998;228(4):598–608.
6. Panebianco V, Tomei E, Anzidei M, Habib FI, Catalano C, Lisi D, Laghi A, Passariello R. Functional MRI in the evaluation of oesophageal motility: feasibility, MRI patterns of normality, and preliminary experience in subjects with motility disorders. Radiol Med. 2006;111(7):881–9. Accessed 11 Oct 2006.
7. Covotta F, Piretta L, Badiali D, Laghi A, Biondi T, Corazziari ES, Panebianco V. Functional magnetic resonance in the evaluation of oesophageal motility disorders. Gastroenterol Res Pract. 2011;2011:367639. https://doi.org/10.1155/2011/367639. Accessed 29 Aug 2011.
8. Panebianco V, Habib FI, Tomei E, Paolantonio P, Anzidei M, Laghi A, Catalano C, Passariello R. Initial experience with magnetic resonance fluoroscopy in the evaluation of oesophageal motility disorders. Comparison with manometry and barium fluoroscopy. Eur Radiol. 2006;16(9):1926–33. Accessed 26 April 2006.
9. Vaezi MF, Richter JE. Duodenogastroesophageal reflux and methods to monitor nonacidic reflux. Am J Med. 2001;111(Suppl 8A):160S–8S.
10. Fiorentino E, Barbiera F, Runza G, Pangaro A, Rapisarda E, Latteri S, Valenti A, La Rocca A, Maiorana A, Mastrosimone A. Digital cineradiology in the diagnosis and surgical treatment of pharyngo-oesophageal junction motor disorders. Chir Ital. 2004;56(4):495–500.
11. Schima W, Ryan JM, Harisinghani M, Schober E, Pokieser P, Denk DM, Stacher G. Radiographic detection of achalasia: diagnostic accuracy of videofluoroscopy. Clin Radiol. 1998;53(5):372–5.
12. Schima W, Stacher G, Pokieser P, Uranitsch K, Nekahm D, Schober E, Moser G, Tscholakoff D. Esophageal motor disorders: videofluoroscopic and manometric evaluation—prospective study in 88 symptomatic patients. Radiology. 1992;185(2):487–91.
13. Prabhakar A, Levine MS, Rubesin S, Laufer I, Katzka D. Relationship between diffuse esophageal spasm and lower esophageal sphincter dysfunction on barium studies and manometry in 14 patients. AJR Am J Roentgenol. 2004;183(2):409–13.
14. Nelson JB, Castell DO. Esophageal motility disorders. Dis Mon. 1988;34(6):297–389.
15. Ipsen P, Egekvist H, Aksglaede K, Zachariae H, Bjerring P, Thommesen P. Oesophageal manometry and video-radiology in patients with systemic sclerosis: a retrospective study of its clinical value. Acta Derm Venereol. 2000;80(2):130–3.
16. Boyce HW Jr, Boyce G. Esophagus: anatomy and structural anomalies. In: Yamada T, editor. Textbook of gastroenterology. 4th ed. Philadelphia, PA: Lippincott Williams & Wilkins; 2003. p. 1148–65.
17. Bergeron JL, Long JL, Chhetri DK. Dysphagia characteristics in Zenker's diverticulum. Otolaryngol Head Neck Surg. 2013;148(2):223–8. Accessed Feb 2013.
18. James B, Nelson MD, Donald O, Castell MD. Esophageal motility disorders. (2015). http://www.uptodate.com/contents/. Accessed 19 Dec 2014.
19. Dellon ES, Gibbs WB, Fritchie KJ, Rubinas TC, Wilson LA, Woosley JT, et al. Clinical, endoscopic, and histologic findings distinguish eosinophilic esophagitis from gastroesophageal reflux disease. Clin Gastroenterol Hepatol. 2009;7(12):1305–13; quiz 1261. Accessed Dec 2009.
20. Wu JT, Mattox KL, Wall MJ Jr. Esophageal perforations: new perspectives and treatment paradigms. J Trauma. 2007;63(5):1173–84.
21. Port JL, Kent MS, Korst RJ, Bacchetta M, Altorki NK. Thoracic esophageal perforations: a decade of experience. Ann Thorac Surg. 2003;75(4):1071–4.
22. Rubesin SE, Levine MS. Radiologic diagnosis of gastrointestinal perforation. Radiol Clin North Am. 2003;41(6):1095–115.
23. Young CA, Menias CO, Bhalla S, Prasad SR. CT Features of esophageal emergencies. Radiographics. 2008;28:1541–53.
24. Società Italiana di Endoscopia Digestiva (S.I.E.D.). Linee guida per la rimozione endoscopica di corpi estranei. Clinical Guideline 1995.
25. De Macedo GF, Ferreira FG, Ribeiro MA, Szutan LA, Assef MS, Rossini LG. Reliability in endoscopic diagnosis of portal hypertensive gastropathy. World J Gastrointest Endosc. 2013;5(7):323–31. Accessed 16 Jul 2013.
26. Furuichi Y, Kawai T, Ichimura S, Metoki R, Miyata Y, Oshima T, et al. Flexible imaging color enhancement improves visibility of transnasal endoscopic images in diagnosing esophageal varices: a multicenter prospective blinded study. J Dig Dis. 2012;13(12):634–41.
27. Kim SH, Kim YJ, Lee JM, Choi KD, Chung YJ, Han JK, et al. Esophageal varices in patients with cirrhosis: multidetector CT esophagography—comparison with endoscopy. Radiology. 2007;242(3):759–68.
28. Kahrilas PJ, Kim HC, Pandolfino JE. Approaches to the diagnosis and grading of hiatal hernia. Best Pract Res Clin Gastroenterol. 2008;22(4):601–16.

# Diagnostic Imaging of Chest Wall Tumors

18

Ukihide Tateishi, Yusuke Ogihara, Yoshio Kitazume, Mitsuhiro Kishino, and Bae Hyeyeol

**Abstract**

There are several imaging devices routinely utilized for evaluation of chest wall tumors predominantly focused in determining the extent of tumor involvement and the potential for respectability. This comprises computed radiography (CR), ultrasound (US), computed tomography (CT), magnetic resonance imaging (MRI), [F-18] FDG positron-emission tomography (PET)/CT, and [F-18] FDG PET/MRI. CR, CT, and MRI are the first line; of these MRI allows tissue characterization, accurate assessment of tumor extent, differentiation from adjacent inflammation, information of blood flow, diffusion capacity, texture features, and specification of metabolites within tumors. Imaging devices are also noninvasive methods which have revolutionized oncological imaging by combination of metabolic activities and morphologic features. They are also useful in guiding biopsy, evaluating patient prognosis, staging the disease, monitoring therapeutic response, and detecting recurrences in chest wall tumors. This leads to the appropriate management of patients with these masses. In vivo morphologic and metabolic information obtained by these several modalities plays an important role to manage patients with chest wall tumors.

**Keywords**

Chest wall tumor · Imaging · CT · MRI PET/CT

U. Tateishi (✉)
Department of Diagnostic Radiology, Tokyo Medical and Dental University, Tokyo, Japan

Department of Diagnostic Radiology and Nuclear Medicine, Tokyo Medical and Dental University Graduate School of Medicine, Tokyo, Japan
e-mail: ttisdrnm@tmd.ac.jp

Y. Ogihara · Y. Kitazume · M. Kishino · B. Hyeyeol
Department of Diagnostic Radiology, Tokyo Medical and Dental University, Tokyo, Japan

## 18.1 Introduction

Chest wall tumors include a diverse group of neoplasm and nonneoplastic lesions presenting a wide variety of histologic lineages [1]. Various imaging devices are utilized for evaluation of chest wall tumors predominantly focused in determining the extent of tumor involvement and the potential for respectability [2]. This comprises computed radiography (CR), ultrasound (US), computed tomography (CT), magnetic resonance imaging (MRI), positron-emission tomography (PET)/CT, and PET/MRI.

## 18.2 Role of Diagnostic Imaging in Chest Wall Tumors

The recent progress in diagnostic and therapeutic methods has changed the clinical management of patients with chest wall tumors. The prognosis in



M. Anzidei, M. Anile (eds.), *Diagnostic Imaging for Thoracic Surgery*,
https://doi.org/10.1007/978-3-319-89893-3_18

patients with chest wall tumors has been improved by introducing wide resection and reconstruction. However, surgery in patients with chest wall tumor is an invasive procedure, and the postsurgical complications are still severe. It requires a cautious treatment decision in patients with chest wall tumor even if the perioperative management has been advanced. Anatomic imaging is the standard examination for investigating tumor extent, tumor invasion to the adjacent organs, and distant metastases.

CR can be used to determine the location, size, presence of calcification and/or ossification, bone destruction, and growth rate, but comprehensive assessment of the tumor is not fully allowed. Identification of incomplete border sign or tapering border sign is the first step for diagnosis of chest wall tumors (Fig. 18.1). Diagnostic flow of CR is presented (Fig. 18.2). CT allows more accurate assessment of tumor morphology, composition, location, and extent. Relevant anatomy is easily visualized on axial, coronal, and sagittal images as well as any oblique planes provided by multiplanar reconstruction or reformatting (MPR). Diagnostic performance of CT is summarized (Fig. 18.3). MRI allows tissue characterization, accurate assessment of tumor extent, differentiation from adjacent inflammation, information of blood flow, diffusion capacity, texture features, and specification of metabolites within tumors [3, 4]. MR evaluation of tumor extent provides critical anatomic information for treatment planning of initial surgical approach and chest wall reconstruction, and delineation of target tumor volume for adjuvant radiation therapy. Diagnostic performance of MRI is summarized (Fig. 18.3). Many investigators evaluate MRI of chest wall tumors and find that malignant tumors of chest wall reveal tumors with irregular margins and bone or vascular invasion representing heterogeneous signal intensity, with predominant hypointensity on T1-weighted images and isointensity or hyperintensity on T2-weighted images, relative to skeletal muscle. Data of MRI findings must be collected according to tumor size, location, types of margin and contours, internal architecture, tumor capsule,

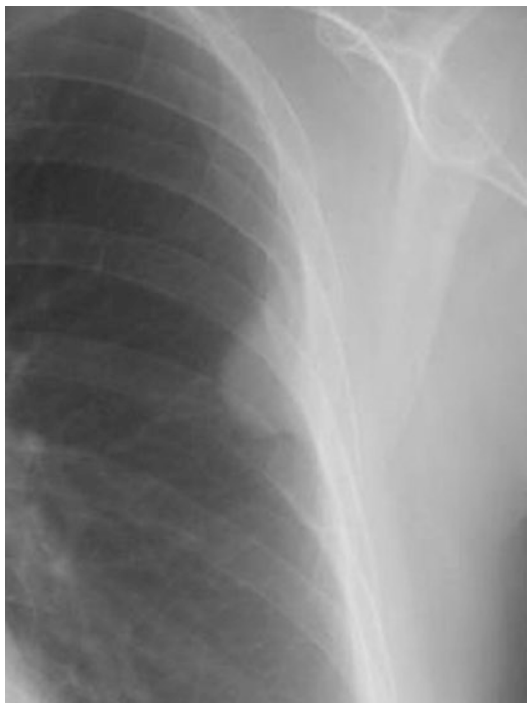

**Fig. 18.1** Incomplete border sign/tapering border sign. A 70-year-old female, plasmacytoma. Tumor margin is unclear on the surface of chest wall: incomplete border sign or tapering border sign

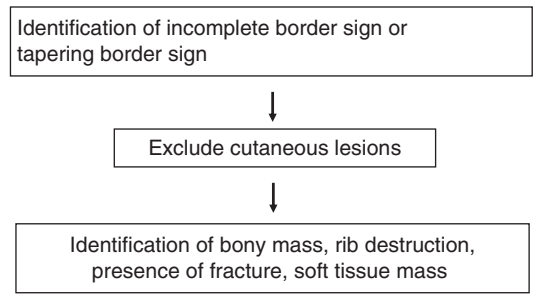


**Fig. 18.2** Diagnostic flow of computed radiography (CR)

- Specification of origin (bone or soft tissue)
- Differentiation of malignant and benign tumors
- Tumor extent (T factor)
- Interaction with surrounding tissue (organ, vessel, nerve)
- Tissue characterization (hemorrhage, cyst, fat)
- Recurrent tumor
- Response evaluation

**Fig. 18.3** Role of CT/MRI

signal characteristics, and heterogeneity [5]. The information of location that consists of anterior, lateral, and posterior chest wall is important for surgical resection and reconstruction. The presence or absence of axillary involvement is also noted for anterior and lateral chest wall malignant tumors [6]. The depth of the lesions is categorized into both superficial and deep distribution and assessed according to involved structures as follows: fascia, muscle, vessel, nerve, and bone. The presence or absence of bone involvement is usually categorized into cortical erosion and/or irregularity identified in the ribs, sternum, spines, and scapula. The signal characteristics are described as isointense or hyperintense relative to the signal intensity of adjacent skeletal muscle. On contrast-enhanced studies, the extent (none/weak or pronounced), pattern (punctate or diffuse), and homogeneity are also recorded for imaging evaluation. Punctate enhancement corresponded to spotty or nodular enhancement (ranging from 3 to 10 mm) within the mass on contrast-enhanced MR images is a major enhancement pattern of cartilaginous tumors. Septal structures are categorized as thin (uniform linear structures less than 2 mm) and thick (focally thickened linear structures thicker than 2 mm). Furthermore, dynamic contrast-enhanced MR images provide information of tumor vascularity and blood flow, i.e., k1–k4 and areas under the curve (AUC), being calculated by two- or three-compartment model. Diffusion-weighted MRI has been applied to assess macroscopic diffusion capacity within tumors because of the capability to characterize water proton mobility in tumor tissue. The apparent diffusion coefficient (ADC) reflects quantitative mobility of free water protons restricted by cell membranes, macromolecules, or fibers. Tumor tissues with high cellularity represent low ADC resulting from impeded mobility of protons by high amount of cell membranes, whereas necrotic tumor tissue exhibits high ADC as a result of rapid mobility of protons given by loss of membrane integrity [7]. Diffusion-weighted MRI can be affected by paramagnetic effect in the thorax; however, the air of the lung has little impact on tumors arisen from chest wall because of their location. The parameters of water proton mobility obtained by diffusion-weighted MRI can be used for response assessment of induction therapy. Most chest wall tumors exhibit heterogeneous features on a multimodal imaging modality. MRI is one of the promising tools for noninvasive exploration of intratumor heterogeneity at the macroscopic scale in anatomical dimension [8]. MRI also provides us to evaluate functional dimension by specification of metabolites in tumor tissue. MR spectroscopy using H-1 and P-31 has been known to be a valuable tool for noninvasive spectral analysis [9, 10].

Thus, CT and MRI provide helpful information regarding local extent and focal invasion by the tumor as well as tissue characterization. However, determination of tumor origin often seems to be difficult whether the tumor derives from bone or soft tissue of the chest wall even if using CT and MRI, because both primary benign and malignant tumors arising from the ribs may also cause a chest wall soft-tissue mass with associated rib destruction [1].

Conventional imaging (CI) modalities, such as CR, US, CT, and MRI, have been contributed to the diagnosis of chest wall tumors [2–4]. More recently, functional imaging methods, especially $^{18}$F-fluorodeoxyglucose-positron-emission tomography ([F-18] FDG-PET/CT), had played a pivotal role in the management of chest wall sarcomas, which can provide the information of metabolic activity in addition to morphologic features [6]. Diagnostic performance of MRI is summarized (Fig. 18.3). Malignant cells are frequently associated with increased metabolic activity. [F-18] FDG, which accumulates in proportion to the glucose metabolism, is the PET tracer most commonly used in oncology. [F-18] FDG uptake is generally higher in malignant lesions than benign ones, while it is also seen in inflammatory changes or fractures. The maximum standardized uptake value (SUVmax), which is an index semi-qualitatively measured by the intensity of [F-18] FDG uptake, can be used as one of the biomarkers [10]. Thus, metabolic information may help guide biopsy of more aggressive areas of chest wall tumors which are heterogeneous. Investigators have showed that

[F-18] FDG-PET/CT can differentiate benign lesions from malignant, has the greater accuracy for the detection and the staging of osseous and soft-tissue tumors compared with traditional anatomical imaging [11], may indicate the prognosis [12], and can be used to evaluate therapeutic response [13] or detect their recurrences [14]. Moreover, non-[F-18] FDG tracers and PET/MRI have developed to improve the utility of PET in oncology.

## 18.3 Role of PET/CT in Chest Wall Tumors

### 18.3.1 Differentiation Between Malignant and Benign Neoplasms

Role of [F-18] FDG PET/CT is summarized in Fig. 18.4. Of these, differentiation between malignant and benign chest wall tumors is important. Anatomical imaging may differentiate benign and malignant musculoskeletal neoplasms. However, final diagnosis can only be accomplished by biopsy or after operation because the morphologic characteristics may also be undefined.

[F-18] FDG-PET/CT cannot perfectly distinguish benign lesions from malignant ones, even if CT part is interpreted. In a study of 47 osseous tumors (27 benign, 20 malignant) and 44 soft tissue ones (19 benign, 25 malignant), the diagnostic accuracy of sarcomas in [F-18] FDG-PET/CT was 70% in bone sarcomas by using SUVmax 3.7 as a threshold and was 75% in soft-tissue sarcomas by using SUVmax 3.8 [15]. There were numerous false-positive and false-negative lesions. [F-18] FDG uptake is often high in some benign tumors, such as giant cell tumor, osteoid osteoma, and fibrous dysplasia [16].

Dual-time-point PET imaging is expected to improve the accuracy for the differentiation of chest wall tumors because [F-18] FDG uptake of malignancies can progress and become clear compared with background tissues for several hours. However, the use of the delayed-phase imaging may not be practical because of the extension for the examination time and no consensus on the optimal timing.

### 18.3.2 Staging of Chest Wall Tumors

Researchers clarified that [F-18] FDG PET/CT is helpful in the staging of bone and soft-tissue sarcomas. In a study of 117 patients with these malignancies, [F-18] FDG-PET/CT has the greater accuracy for nodal staging and metastatic staging compared with CI, although the difference in accuracy of local tumor staging was not significant [11]. Significance of [F-18] FDG PET/CT in staging or restaging will be applied to patients when stratified by chest wall sarcomas. Focused on the detection of pulmonary metastases, [F-18] FDG-PET/CT had a greater specificity but a less sensitivity compared with conventional imaging, because of the poor feasibility of full inspiratory PET/CT which took long time for examination. However, the acquisition time of PET became shorter recently. This may improve the sensitivity for detecting the metastases in lung.

Pediatric chest wall sarcoma contributes significantly to the burden of morbidity and mortality. Although introduction of aggressive therapy with multiagent chemotherapy and radiotherapy resulted in a significant improvement of the prog-

- Differentiation of malignant and benign tumors
- Tumor extent (M factor: skip metastasis, soft tissue metastasis)
- Grading
- Recurrent tumor
- Response evaluation
- Specification of primary tumor site

**Fig. 18.4** Role of [F-18] FDG PET/CT

nosis, children with dissemination or metastasis continue to have a poor prognosis. Diagnosis of nodal and distant metastases is crucial to determine the therapeutic plan and prognosis in patients with pediatric chest wall sarcomas [17]. Compared to the conventional imaging for initial staging of pediatric chest wall sarcomas, [F-18] FDG PET/CT can allow accurate anatomic localization of tumors, and thus has an important advantage over conventional imaging alone for the staging of tumors. Tateishi et al. demonstrated a significant difference in diagnostic accuracy for the detection of distant metastasis by PET/CT, PET, or CI in pediatric sarcomas and the improvement of diagnostic accuracy in detecting distant metastasis can affect tumor stage prior to treatment [18]. [F-18] FDG-PET is also useful for restaging or detection of the recurrence in chest wall tumors. In a study of 43 patients, [F-18] FDG-PET/CT has a higher accuracy (93%) in the diagnosis of the recurrence compared with contrast-enhanced CT (73%) [19].

Whole-body [F-18] FDG PET/CT has ignited interest in cancer screening. Tateishi et al. suggest that PET/CT study can detect unexpected bone and soft-tissue lesions at cancer screening setting [20]. From results of 62 subjects, there were abnormal findings at PET/CT study. Of these, 60% of lesions are derived from rib or thoracic vertebra. One case is diagnosed as having a non-Hodgkin's lymphoma of the bone which is localized in the vertebral centrum. The results may demonstrate the potential in unexpectedly detecting chest wall tumors by PET/CT study.

### 18.3.3 Monitoring of Therapeutic Response of Chest Wall Tumors

Chest wall sarcomas can usually be adequately encompassed by a wide, full-thickness excision to achieve negative margins. However, treatment of chest wall sarcoma has for years consisted of surgical resection, adjuvant chemotherapy, and/or radiation therapy. Attempts have been made to improve treatment by combination therapy. However, regimens of combination therapy often fail to improve survival over 3 years [21, 22]. Since the biologic behavior of soft-tissue sarcomas depends on the histologic grade, soft-tissue sarcomas are graded according to grading system on the basis of three histologic criteria: tumor differentiation, necrosis, and MIB-1 (Ki-67) score [23–25].

[F-18] FDG uptake expressed semiquantitatively by the SUV has been strongly associated with prognosis in patients with sarcomas. The degree of [F-18] FDG uptake in sarcomas is associated with histological tumor aggressiveness and glucose transporter protein 1 (Glut-1) expression [25–29]. Identification of PET findings affecting disease prognosis in chest wall sarcoma may be useful to determine preoperative value. Conventional methods to monitor treatment response are based on the size reduction on CT. However, the changes of tumor metabolism often occur early during therapy and precede size reduction of the tumor. The quantification of tumor glucose metabolism is highly accurate for monitoring effects of chemotherapy. [F-18] FDG PET is sensitive to detect prompt response to chemotherapy in many histologic types of malignant tumors. A few studies have demonstrated that [F-18] FDG-PET/CT can determine the histological responder to neoadjuvant chemotherapy (NAC) in soft-tissue sarcoma [26, 30]. This trend might be mirrored to chest wall tumors. The reduction of [F-18] FDG uptake between pre- and post-NAC has a relationship with histological change, often prior to morphologic changes on conventional imaging. However, despite the increasing use of PET in management of soft-tissue sarcomas, only a few studies to date have assessed the prognostic implication of PET in patients with chest wall sarcomas. Nishiyama et al. assessed prognostic implications of PET findings in patients with chest wall sarcomas [31]. The results were notable for three features. First, MIB-1 labeling index, Glut-1 expression, MIB-1 grade, and SUV were adverse prognostic factors in the univariate analysis (Fig. 18.5). Second, MIB-1 labeling index was independently associated with poor prognosis in the multivariate analysis. And third, there were significant correlations between MIB-1 labeling index, Glut-1 expression, MIB-1 grade, and SUV (Fig. 18.6). Therefore, the investigators confirm

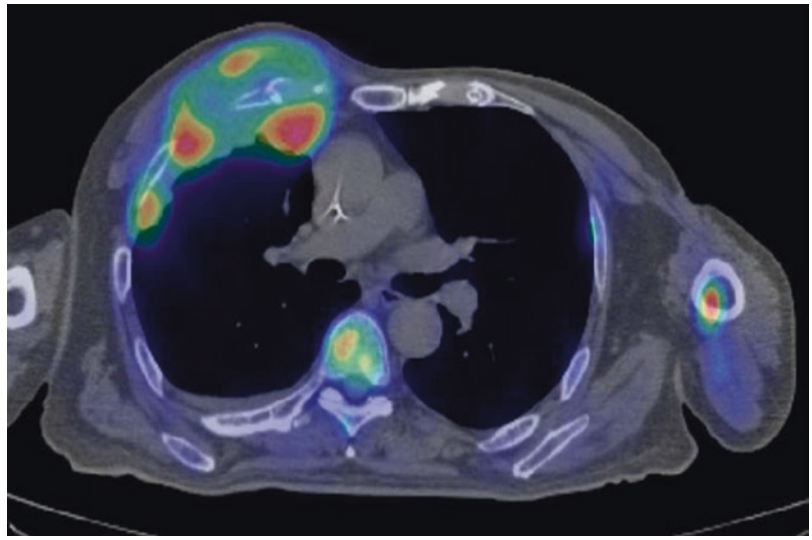

**Fig. 18.5** The SUV correlates with tumor grade and aggressiveness. In a case with 70-year-old male patient with undifferentiated pleomorphic sarcoma (grade 3, Glut-1 3+), tumor exhibits high SUV (12.9)

that PET imaging is a noninvasive method for evaluating patients' prognosis after treatment in chest wall sarcomas which are characterized as difficult tumors regardless of combination therapy.

## 18.3.4 Bone Tumors

### 18.3.4.1 Osteosarcoma

The age distribution of chest wall sarcoma in adolescents and adults is summarized in Fig. 18.7. Osteosarcoma (OS) is known to be the common primary bone chest wall sarcoma in adolescents. Initial stage and tumor necrosis rate after chemotherapy have the relationship with prognosis [32]. The response to treatment may determine whether amputation or limb-sparing resection should be done. Osteosarcoma often arises from rib, sternum, thoracic vertebra, and scapula (Fig. 18.8).

There are not many researches which concern the initial staging in OS with [F-18] FDG-PET. In a study of 20 osteosarcomas, [F-18] FDG-PET/CT had a little greater sensitivity in detecting malignant masses except lung ones than conventional imaging. The specificity between [F-18] FDG-PET/CT and CI was nearly equal. Regarding lung lesions, the specificity of [F-18] FDG-PET/CT is greater than CI (96% vs. 87%), but the sensitivity is less (80% vs. 93%) [17].

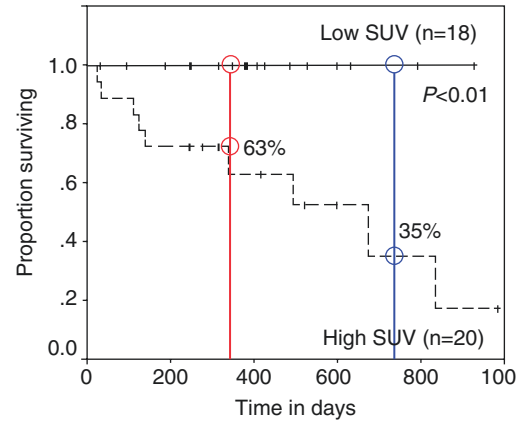


**Fig. 18.6** The SUV reflects prognosis after surgical resection in patients with chest wall sarcoma. Univariate analysis shows significant difference between tumors with high and low SUV

[F-18] FDG-PET/CT reported to be capable of indicating the prognosis in OS. In a study of 31 patients, the activity of glucose metabolism reflected progression-free survival, overall survival, and tumor necrosis [33].

While the histological necrosis after NAC can be assessed only after surgery, researchers have vigorously evaluated the tumor response in OS with [F-18] FDG-PET to overcome this limitation and they found that [F-18] FDG-PET/CT could contribute to monitoring this response [34]. Because the recurrence of OS often occurs

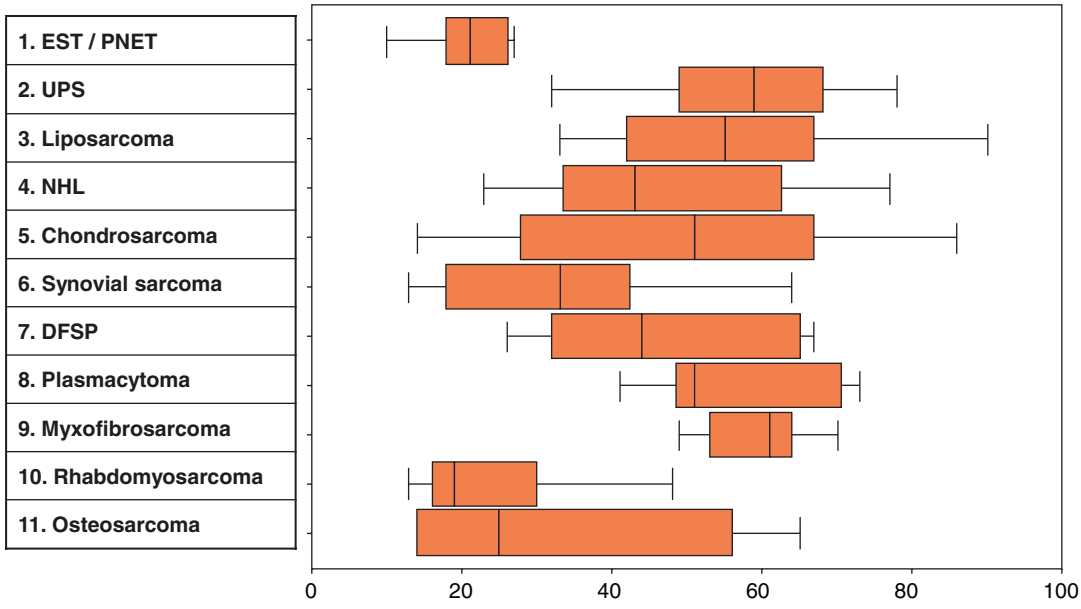


**Fig. 18.7** The age distribution of chest wall sarcoma in adolescents and adults in National Cancer Center Hospital for recent 20 years

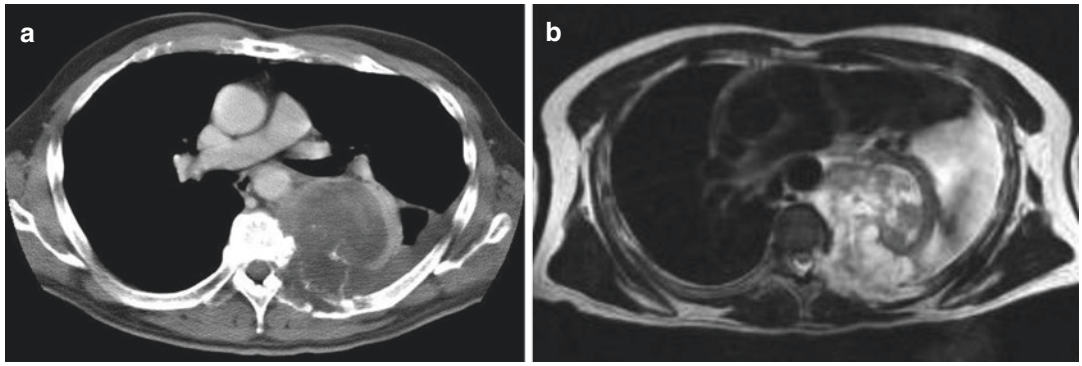


**Fig. 18.8** Chest wall osteosarcoma in a 20-year-old man. Axial contrast-enhanced CT image shows a large soft-tissue mass occupying left hemithorax with invasion of thoracic vertebra. A linear mineralization is observed in the center (**a**). Axial T2-weighted MR image demonstrates heterogeneous high signal intensity. Mineralization corresponds to low signal intensity (**b**)

in the lung, it can be diagnosed by plain radiography or CT.

#### 18.3.4.2 Ewing Sarcoma Tumor

Ewing sarcoma tumor (EST) is a frequently encountered chest wall sarcoma in children and adolescents (Fig. 18.9). The pivotal criteria for prognosis in EST are considered to be the size and the presence of metastases; however, the growth pattern identified in imaging studies also suggests prognosis in chest wall EST. Tumor with concentric growth pattern enlarges both to and from body center symmetrically. On the other hand, tumor with eccentric growth extends mostly to body center (Fig. 18.10). Tumor with eccentric growth shows poor prognosis compared to that with concentric growth (Fig. 18.11). The 5-year survival rate has been increased up to 65% by the development in treatment of the primary tumor

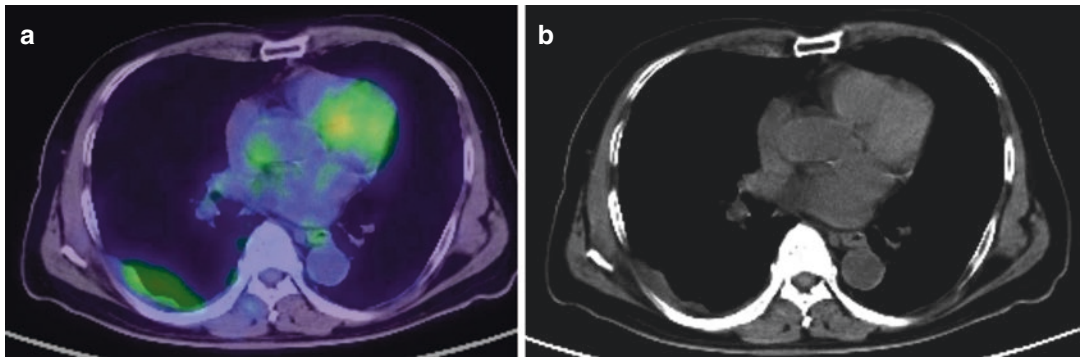


**Fig. 18.9** A 20-year-old male with EST of chest wall (**a**) fused image; (**b**) CT. Tumor shows eccentric growth pattern and high SUV on [F-18] FDG PET/CT

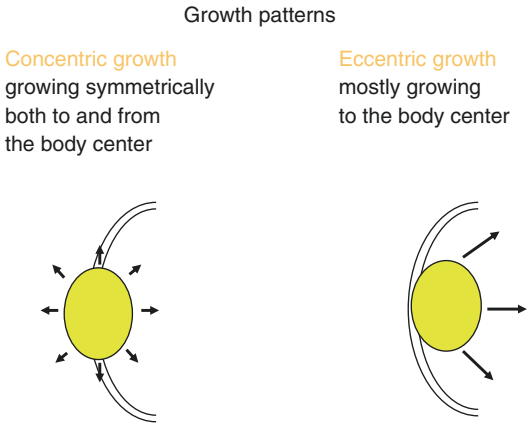


**Fig. 18.10** Growth pattern of chest wall EST on CT/MRI

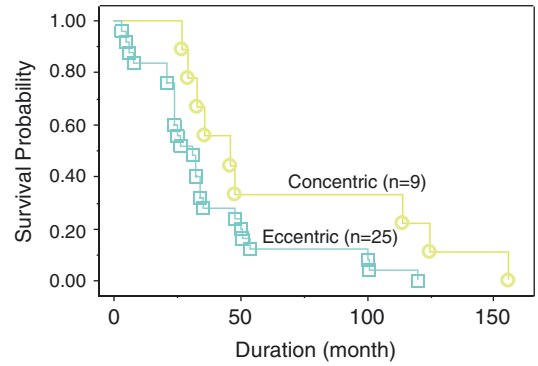


**Fig. 18.11** The Kaplan-Meier survival curves of EST. The significant difference was found between two groups by the log-rank test ($P < 0.05$)

[35]. [F-18] FDG-PET/CT may play a complementary role in the staging of EST [17].

[F-18] FDG-PET/CT is useful for the monitoring of therapeutic change. In a prospective study of 36 patients with EST, SUVmax less than 2.5 after NAC was correlated with progression-free survival [36]. However, the percentage reduction of SUVmax is a significant predictor of poor prognosis in chest wall sarcoma [31]. In addition, the percent change in metabolic tumor burden including metabolic tumor volume (MTV) or total lesion glycolysis (TLG) would be a much more reliable prognostic indicator. [F-18] FDG-PET/CT also has high diagnostic accuracy for the detection of recurrence in EST [37].

### 18.3.4.3 Chondrosarcoma

Chondrosarcoma accounts for about 20% of bone sarcoma and are common over the fifth decade (Fig. 18.12). It has been challenging to differentiate between benign cartilage masses and malignant ones radiologically and even histologically because of the wide spectrum of these lesions.

While the [F-18] FDG uptake is variable in chondrogenic lesions, some reports found that [F-18] FDG-PET may be helpful in evaluating their malignant potential. In a study of 31 chondrosarcomas, [F-18] FDG-PET could detect all masses. There was a significant difference in SUVmax of primary tumors between patients with disease progression and without recurrence. The sensitivity was 90% and specificity was 76% with cutoff SUVmax of 4.0 [38].

### 18.3.4.4 Giant Cell Tumors of Bone

Giant cell tumor (GCT) of bone makes up 5% for primary osseous tumors, is seen frequently from

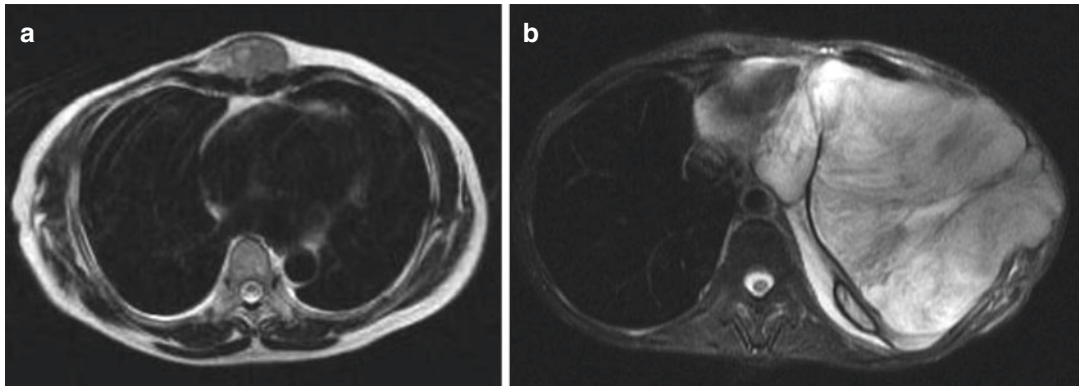


**Fig. 18.12** Well-differentiated chondrosarcoma of anterior chest wall in a 40-year-old man. Axial T2-weighted MR image shows heterogeneous mass arising from sternum being frequent site of origin in this histology (**a**). Extraskeletal myxoid chondrosarcoma of lateral chest wall in a 50-year-old man. Axial fat-saturated T2-weighted MR image demonstrates huge mass of high intensity occupying the entire hemithorax. Some spotty or linear low signal intensity is observed in the center corresponding to mineralization of tumor (**b**)

second to fourth decades, and is classified as intermediate lesions [39].

[F-18] FDG uptake with GCT is high [11], so [F-18] FDG-PET/CT cannot distinguish GCTs of the bone from osseous sarcomas. GCT can usually be diagnosed by its morphologic characteristics, such as nonsclerotic margin, occurring in near-physis or fluid-fluid level [40]. [F-18] FDG-PET/CT may be used for detection of multifocal GCTs and staging of sarcomatous degeneration. There is a case report that described GCT pulmonary metastases with [F-18] FDG uptake [41]. In this report, patient has a 30-year history of multiple recurrences of GCT in the knee. Two nodules in the lung were detected in the follow-up [F-18] FDG-PET/CT 26 and 28 years after the first surgical treatment. The SUVmax of them were 2.9 and 4.9. Both the two tumors were histologically proven to be the metastasis of GCT.

## 18.3.5 Soft-Tissue Tumors

### 18.3.5.1 Undifferentiated Pleomorphic Sarcoma

Undifferentiated pleomorphic sarcoma (UPS) is one of the undifferentiated/unclassified sarcomas, which is a new category and introduced in the 2013 WHO classification (Fig 18.13). UPS would have been called "malignant fibrous histiocytoma (MFH)" in the past.

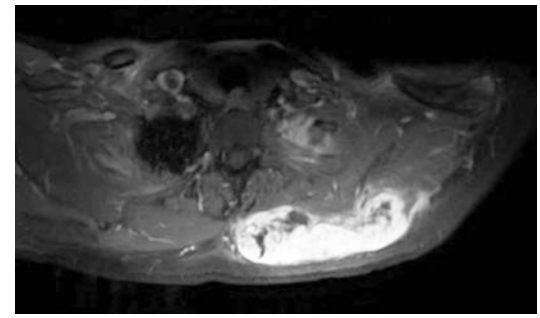

**Fig. 18.13** Undifferentiated pleomorphic sarcoma (UPS) of posterior chest wall in a 60-year-old man. Axial fat-saturated contrast-enhanced T1-weighted MR image shows heterogeneous enhancing mass with central necrosis

Although [F-18] FDG-PET/CT may be used for the management of patients with STS including UPS [11, 12], studies concerning especially about UPS have not been fully investigated to date (Fig. 18.5). In one case report, the patient with cardiac mass surgically proven UPS underwent [F-18] FDG-PET/CT 10 months after the first operation because local recurrence was suspected by echocardiography. PET/CT detected not only local recurrences (SUVmax 11.5) but also bone metastases (SUVmax 9.4) [41].

#### 18.3.5.2 Myxofibrosarcoma

Myxofibrosarcoma (MFS), known as a myxoid variant of MFH, is one of the common fibroblastic sarcomas occurring in chest wall of elderly patients (Fig. 18.14). This tumor tends to infiltrate surrounding tissues and often recurs after surgery.

Although the use of [F-18] FDG-PET for the staging or prognosis in STS including MFS has previously been evaluated [11, 12], there is a paucity of [F-18] FDG-PET data focused specifically on MFS. There are only a few case reports [18, 42]. However, MFS has been known to develop second primary malignancy in patients with multiple malignancies [20] (Fig. 18.15). Chest wall is one of the frequent origins.

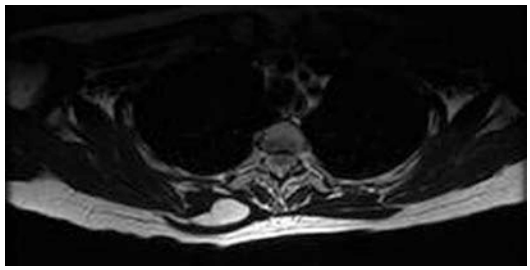

**Fig. 18.14** Myxofibrosarcoma of posterior chest wall in a 60-year-old man. Axial T2-weighted MR image shows localized high-intensity mass in deep posterior chest wall

#### 18.3.5.3 Liposarcoma

Liposarcoma represents the second most common type of soft-tissue sarcoma and is grouped into five types (well differentiated, dedifferentiated, myxoid, pleomorphic, and mixed). Errors in sampling masses and diagnosis of histological grade of this tumor may be seen because of this wide heterogeneousness. Therefore, radiologic assessment is important for appropriate management (Fig. 18.16).

The [F-18] FDG uptake of liposarcoma is lower in a well-differentiated type and greater in pleomorphic, myxoid, and dedifferentiated types [43]. In a study of 54 patients, [F-18] FDG-PET had the higher accuracy (75%) in predicting a recurrence with cutoff of SUVmax 3.6 than both tumor grade (50%) and tumor subtype (35%). Furthermore, there was a significant difference in disease-free survival (21 months vs. 44 months) by using the same threshold, but no difference in tumor grading and subtype [44]. PET/CT may be used for assessing the response to chemotherapy [12] or guiding biopsy of the most metabolically active areas to improve the diagnostic accuracy.

#### 18.3.5.4 Aggressive Fibromatosis

Aggressive fibromatosis (AF, known as extra-abdominal desmoid) is a proliferative disease and has a peak incidence between 20 and 50 years

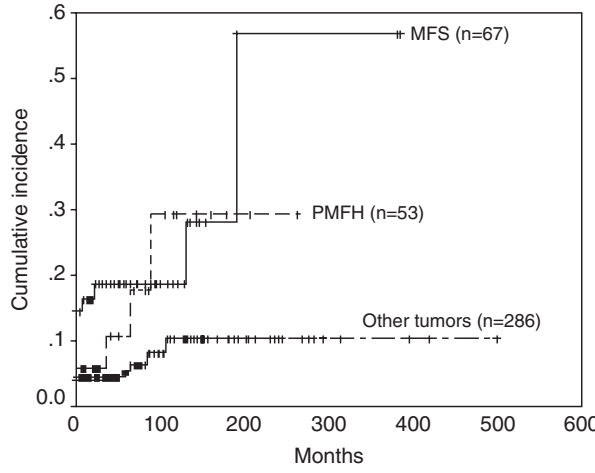


| Variables | HR | 95% CI | P Value |
|---|---|---|---|
| Age | 1.51 | 1.17-1.96 | 0.0019 |
| Tumor size | 1.03 | 0.99-1.07 | 0.18 |
| MFS | 2.34 | 1.01-5.41 | 0.048 |
| PMFH | 1.85 | 0.69-4.97 | 0.22 |
| Other tumors* | 1 | - | - |

**Fig. 18.15** Second primary myxofibrosarcoma is the most frequent histologic subtype in patients having multiple malignancies

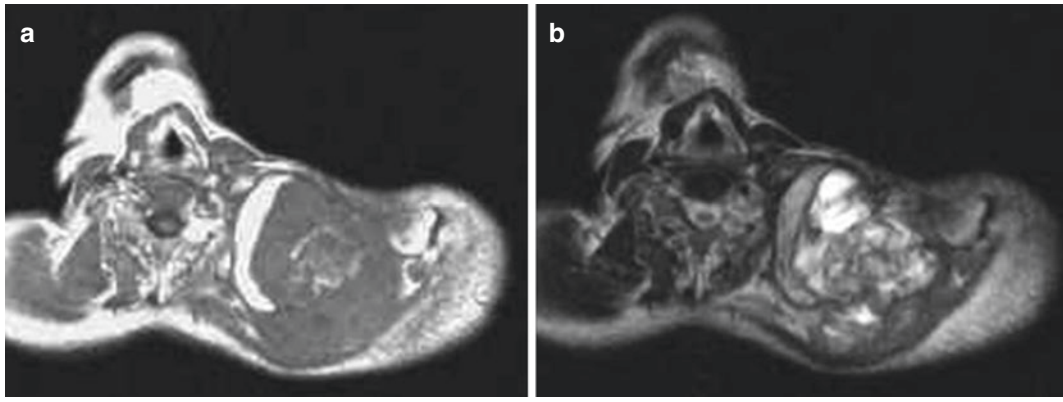


**Fig. 18.16** Myxoid liposarcoma of chest wall in a 50-year-old man. Axial T1-weighted MR image demonstrates heterogeneous mass with high signal intensity of fat within the tumor (**a**). Corresponding axial T2-weighted MR image shows heterogeneous signal intensity (**b**)

(Fig. 18.17). While AF rarely turns malignant, it can infiltrate into surrounding tissues and recurs frequently after operation. Radiation or pharmacotherapy is used to prevent disease progression which worsens the patient's quality of life by the pain and loss of function [45].

[F-18] FDG-PET may be used for staging [46] and monitoring of the therapeutic changes. In a pilot study of 9 AF patients treated with imatinib, the median SUVmax was 5.5 (range: 2.8–8.1) before treatment and 3.9 (range: 2.6–5.7) after. [F-18] FDG uptake did not increase in all the patients [47].

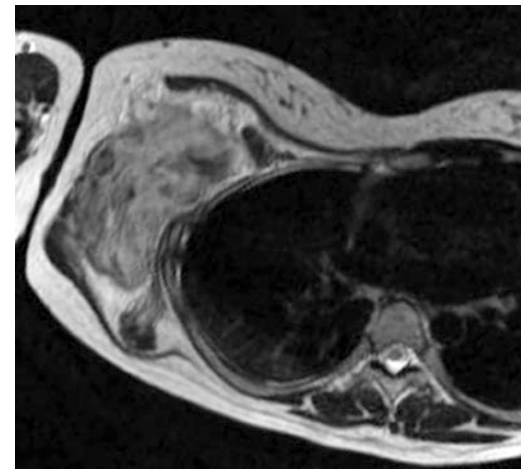

**Fig. 18.17** Aggressive fibromatosis of axillary region in a 20-year-old man, axial T2-weighted MR image shows heterogeneous high signal intensity relative to adjacent muscle

## 18.4 Non-[F-18] FDG Tracers

Molecular etiologies of tumor characteristics have been investigated, including the increased rate of proliferation, over- or underexpression of receptors/tumor antigens, presence of hypoxia and/or necrosis, increased metabolism of glucose, amino acids, phospholipid membrane precursors, DNA precursors, angiogenesis, bone metabolism, and accelerated rate of apoptosis. Each of the phenotypic features represents a possible target for tumor imaging with PET/CT, and some of these processes have been introduced to clinical use. PET/CT tracers other than [F-18] FDG have developed to improve the utility of PET/CT in oncology (Table 18.1).

Carbon-11 choline ([C-11] choline) has been introduced as oncological positron-emitting radiopharmaceutical for evaluation of a variety of malignant tumors. Choline is an essential component of the cell membrane, and choline uptake may be via a choline-specific transporter protein. Choline kinase alpha, which catalyzes the phosphorylation of choline, is upregulated in malignant cells. [C-11] choline uptake is significantly higher in malignant tumors than that in benign tumors and correlates well with the degree

**Table 18.1** PET probes for clinical use

| Probe | Trivial name | Half life | Molecular target | Cell target |
|---|---|---|---|---|
| [F-18]FDG | 2-Deoxy-2-(18F)fluoro-D-glucose | 110 min | Transporter (Glut) | Glucose utilization |
| [F-18]FLT | 3'-(18F)Fluoro-3'-deoxythymidine | 110 min | Thymidine kinase | DNA replication |
| [F-18]FHBG | 2-Amino-9-[3-[(18F) fluoromethyl]-4-hydroxybutyl]-1,6-dihydro-9H-purine-6-one | 110 min | HSV thymidine kinase | Gene therapy |
| [F-18]NaF | Sodium fluoride | 110 min | Hydroxyapatite | Bone reaction to tumor |
| [F-18]FMISO | α-(Fluoromethyl)-2-nitro-1H-imidazole-1-ethanol | 110 min | Radical anion | Hypoxia |
| [F-18]FAZA | 2-Nitro-1H-imidazole-1-yl 5-fluoro-5-deoxy-α-D-arabinofuranoside | 110 min | Radical anion | Hypoxia |
| [C-11]choline | [N-methyl-(11)C]choline | 20 min | Choline kinase | Phospholipid synthesis |
| [F-18] fluorocholine | [N-methyl-(18)F]choline | 110 min | Choline kinase | Phospholipid synthesis |
| [C-11] methionine | L-[methyl- 11C]methionine | 20 min | Transporter | Protein synthesis |
| [F-18] anti-FACBC | 1-Amino-3-[18F]fluorocyclobutane-1-carboxylic acid | 110 min | transporter | Protein synthesis |
| [F-18]FES | 16α-[18F]Fluoro-17β-estradiol | 110 min | Estrogen receptor | Hormone synthesis |
| [F-18] galactoRGD | 18F-galacto-arginine-glycine-aspartic-acid | 110 min | Integrin | Angiogenesis |

of [F-18] FDG uptake. [C-11] choline has little radiotracer activity in urinary tract. This is an advantage compared with [F-18] FDG, of which the urinary excretion interferes with the diagnosis in PET. In a study of 16 patients with bone and soft-tissue sarcomas, [C-11] choline-PET/CT was more accurate for the staging than CT, MRI, and bone scintigraphy [48]. The study of [F-18] choline has focused largely on prostate cancer. A systematic review indicated that choline-PET/CT (including [C-11] choline) seemed to be used also in musculoskeletal oncology [49].

[F-18] fluorothymidine (FLT) is a marker of proliferation. In a study of 22 patients with osseous and soft-tissue masses, FLT detected all malignancies. There was correlation between FLT uptake and tumor grade, although [F-18] FDG did not have this correlation [50].

[F-18] misonidazole (FMISO) is a marker of tumor hypoxia which imparts resistance to radiotherapy or chemotherapy. In a study of 19 patients with STS, FMISO uptake had no relationship with that of [F-18] FDG [51]. Regional hypoxia and glucose metabolism do not always correlate.

[C-11] methionine (MET)-PET is the most popular amino acid imaging. In a study of 31 neoplasms (3 bone tumors and 9 soft tissue ones), MET-PET had the sensitivity for detecting malignancies, nearly equal to [F-18] FDG-PET [52].

Further researches of musculoskeletal tumors with non-[F-18] FDG tracers will be expected.

## 18.5 PET/MRI

Recently, PET/MRI imaging has been introduced and used in the assessment of malignancies including musculoskeletal tumors. MRI has the advantages of the spatial resolution of soft-tissue lesions and the sensitivity for detecting bone marrow diseases compared with CT. [F-18] FDG-PET/MRI has reported to possess higher diagnostic performance in bone malignancies than PET/CT [53]. MRI also provides the reduction of radiation exposure, especially pivotal in younger patients. However, PET/MRI has the disadvantages of longer examination times, difficulty in evaluating lung lesions, and metallic artifacts.

Depending on the patient and the purpose of examination, it has to be carefully chosen whether to use whole-body PET/MRI or localized PET/MRI. The field of view may differ between these two techniques and influence delineation of the disease.

Although T2-weighed or fat-suppressed T2-weighed images are recommended for integrated PET/MRI, it can be changed if necessary. Contrast enhancement may be helpful for differentiating solid tumors from cystic lesions and determining the site for biopsy compared with PET images [54].

**Conclusion**

Current imaging devices are noninvasive methods which have revolutionized oncological imaging by combination of metabolic activities and morphologic features. They are useful in guiding biopsy, evaluating patient prognosis, staging the disease, monitoring therapeutic response, and detecting recurrences in chest wall tumors. In vivo morphologic imaging using CR, US, CT, and MRI as well as metabolic imaging using PET/CT or PET/MRI lead to the appropriate management of patients with these masses.

**Acknowledgments** This work was supported in part by grants from Scientific Research Expenses for Health and Welfare Programs; the Grant-in-Aid for Cancer Research from the Ministry of Health, Labor and Welfare, No. 15K09885; the Scientific Research Expenses for Health and Welfare Programs, No. 29-A-3 (Takashi Terauchi and Ukihide Tateishi: squad leaders); Practical Research for Innovative Cancer Control; and Project Promoting Clinical Trials for Development of New Drugs by Japan Agency for Medical Research and Development (AMED).

## References

1. Shah AA, D'Amico TA. Primary chest wall tumors. J Am Coll Surg. 2010;210:360–6.
2. Tateishi U, Gladish GW, Kusumoto M, Hasegawa T, Yokoyama R, Tsuchiya R, Moriyama N. Chest wall tumors: radiologic findings and pathologic correlation: Part 1. Benign tumors. Radiographics. 2003;23:1477–90.
3. Carter BW, Gladish GW. MR Imaging of chest wall tumors. Magn Reson Imaging Clin N Am. 2015;23:197–215.
4. Tateishi U, Gladish GW, Kusumoto M, Hasegawa T, Yokoyama R, Tsuchiya R, Moriyama N. Chest wall tumors: radiologic findings and pathologic correlation: Part 2. Malignant tumors. Radiographics. 2003;23:1491–508.
5. O'Sullivan P, O'Dwyer H, Flint J, Munk PL, Muller N. Soft tissue tumours and mass-like lesions of the chest wall: a pictorial review of CT and MR findings. Br J Radiol. 2007;80:574–80.
6. Carter BW, Benveniste MF, Betancourt SL, de Groot PM, Lichtenberger JP 3rd, Amini B, Abbott GF. Imaging evaluation of malignant chest wall neoplasms. Radiographics. 2016;36:1285–306.
7. Davnall F, Yip CS, Ljungqvist G, Selmi M, Ng F, Sanghera B, et al. Assessment of tumor heterogeneity: an emerging imaging tool for clinical practice? Insights Imaging. 2012;3:573–89.
8. Wang CK, Li CW, Hsieh TJ, Chien SH, Liu GC, Tsai KB. Characterization of bone and soft-tissue tumors with in vivo 1H MR spectroscopy: initial results. Radiology. 2004;232:599–605.
9. Negendank WG, Crowley MG, Ryan JR, Keller NA, Evelhoch JL. Bone and soft-tissue lesions: diagnosis with combined H-1 MR imaging and P-31 MR spectroscopy. Radiology. 1989;173:181–8.
10. Pauwels EK, Sturm EJ, Bombardieri E, Cleton FJ, Stokkel MP. Positron-emission tomography with [18F]fluorodeoxyglucose. Part I. Biochemical uptake mechanism and its implication for clinical studies. J Cancer Res Clin Oncol. 2000;126:549–59.
11. Tateishi U, Yamaguchi U, Seki K, Terauchi T, Arai Y, Kim E. Bone and soft-tissue sarcoma: preoperative staging with fluorine 18 fluorodeoxyglucose PET/CT and conventional imaging. Radiology. 2007;245:839–47.
12. Andersen KF, Fuglo HM, Rasmussen SH, Petersen MM, Loft A. Volume-based F-18 FDG PET/CT imaging markers provide supplemental prognostic information to histologic grading in patients with high-grade bone or soft tissue sarcoma. Medicine (Baltimore). 2015;94:2319.
13. Eary JF, Conrad EU, O'Sullivan J, Hawkins DS, Schuetze SM, O'Sullivan F. Sarcoma mid-therapy [F-18] fluorodeoxyglucose positron emission tomography (FDG PET) and patient outcome. J Bone Joint Surg Am. 2014;96:152–8.
14. Al-Ibraheem A, Buck AK, Benz MR, Rudert M, Beer AJ, Mansour A, Pomykala KL, Haller B, Juenger H, Scheidhauer K, Schwaiger M, Herrmann K. 18F-fluorodeoxyglucose positron emission tomography/computed tomography for the detection of recurrent bone and soft tissue sarcoma. Cancer. 2013;119:1227–34.
15. Shin DS, Shon OJ, Han DS, Choi JH, Chun KA, Cho IH. The clinical efficacy of 18F-FDG-PET/CT in benign and malignant musculoskeletal tumors. Ann Nucl Med. 2008;22:603–9.
16. Tateishi U, Yamaguchi U, Miyake M, Maeda T, Chuman H, Arai Y, Jurik AG, editors. Primary bone tumours. Imaging of the sternocostoclavicular region: Springer-Verlag; 2007. p. 207–28.

17. London K, Stege C, Cross S, Onikul E, Graf N, Kaspers G, Dalla-Pozza L, Howman-Giles R. 18F-FDG PET/CT compared to conventional imaging modalities in pediatric primary bone tumors. Pediatr Radiol. 2012;42:418–30.
18. Tateishi U, Hosono A, Makimoto A, Sakurada A, Terauchi T, Arai Y, Imai Y, Kim EE. Accuracy of 18F fluorodeoxyglucose positron emission tomography/computed tomography in staging of pediatric sarcomas. J Pediatr Hematol Oncol. 2007;29:608–12.
19. Al-Ibraheem A, Buck AK, Benz MR, Rudert M, Beer AJ, Mansour A, Pomykala KL, Haller B, Juenger H, Scheidhauer K, Schwaiger M, Herrmann K. 18F-fluorodeoxyglucose positron emission tomography/computed tomography for the detection of recurrent bone and soft tissue sarcoma. Cancer. 2013;119:1227–34.
20. Tateishi U, Hasegawa T, Terauchi T, et al. Incidence of multiple primary malignancies in a cohort of adult patients with soft tissue sarcoma. Jpn J Clin Oncol. 2005;35:444–52.
21. Yang JC, Chang AE, Baker AR, et al. Randomized prospective study of the benefit of adjuvant radiation therapy in the treatment of soft tissue sarcomas of the extremity. J Clin Oncol. 1998;16:197–203.
22. Wendtner CM, Abdel-Rahman S, Krych M, et al. Response to neoadjuvant chemotherapy combined with regional hyperthermia predicts long-term survival for adult patients with retroperitoneal and visceral high-risk soft tissue sarcomas. J Clin Oncol. 2002;20:3156–64.
23. Sobin LH, Gospodarowicz MK. International Union Against Cancer (UICC): TNM Classification of malignant tumours. 7th ed. New York, NY: Wiley; 2009.
24. Amin MB, Edge S, Greene F, et al. AJCC cancer staging manual. 8th ed. New York, NY: Springer; 2017.
25. Fletcher CDM, Bridge JA, Hogendoorn P, Mertens F. World Health Organization classification of tumours. Pathology and genetics of tumours of soft tissue and bone. 4th ed. Lyon: IARC Press; 2013.
26. Folpe AL, Lyles RH, Sprouse JT, et al. (F-18) fluorodeoxyglucose positron emission tomography as a predictor of pathologic grade and other prognostic variables in bone and soft tissue sarcoma. Clin Cancer Res. 2000;6:1279–87.
27. Schwarzbach MHM, Hinz U, Dimitrakopoulou-Strauss A, et al. Prognostic significance of preoperative [18-F]fluorodeoxyglucose (FDG) positron emission tomography (PET) imaging in patients with resectable soft tissue sarcomas. Ann Surg. 2005;241:286–94.
28. Tateishi U, Yamaguchi U, Seki K, et al. Glut-1 expression and enhanced glucose metabolism are associated with tumor grade in bone and soft tissue sarcomas: a prospective evaluation by [18F]fluorodeoxyglucose positron emission tomography. Eur J Nucl Med Mol Imaging. 2006;33:683–91.
29. Ito S, Nemoto T, Satoh S, et al. Human rhabdomyosarcoma cells retain insulin-regulated glucose transport activity through glucose transporter 1. Arch Biochem Biophys. 2000;3:72–82.
30. Nieweg OE, Prium J, van Ginkel RJ, et al. Fluorine-18 fluorodeoxyglucose PET imaging of soft-tissue sarcoma. J Nucl Med. 1996;37:257–61.
31. Nishiyama Y, Tateishi U, Kawai A, Chuman H, Nakatani F, Miyake M, Terauchi T, Inoue T, Kim EE. Prediction of treatment outcomes in patients with chest wall sarcoma: evaluation with PET/CT. Jpn J Clin Oncol. 2012;42:912–8.
32. Glasser DB, Lane JM, Huvos AG, Marcove RC, Rosen G. Survival, prognosis, and therapeutic response in osteogenic sarcoma. The Memorial Hospital experience. Cancer. 1992;69:698–708.
33. Costelloe CM, Macapinlac HA, Madewell JE, Fitzgerald NE, Mawlawi OR, Rohren EM, Raymond AK, Lewis VO, Anderson PM, Bassett RL Jr, Harrell RK, Marom EM. 18F-FDG PET/CT as an indicator of progression-free and overall survival in osteosarcoma. J Nucl Med. 2009;50:340–7.
34. Cheon GJ, Kim MS, Lee JA, Lee SY, Cho WH, Song WS, Koh JS, Yoo JY, Oh DH, Shin DS, Jeon DG. Prediction model of chemotherapy response in osteosarcoma by 18F-FDG PET and MRI. J Nucl Med. 2009;50:1435–40.
35. Ludwig JA. Ewing sarcoma: historical perspectives, current state-of-the-art, and opportunities for targeted therapy in the future. Curr Opin Oncol. 2008;20:412–8.
36. Hawkins DS, Schuetze SM, Butrynski JE, Rajendran JG, Vernon CB, Conrad EU 3rd, Eary JF. [18F] Fluorodeoxyglucose positron emission tomography predicts outcome for Ewing sarcoma family of tumors. J Clin Oncol. 2005;23:8828–34.
37. Sharma P, Khangembam BC, Suman KC, Singh H, Rastogi S, Khan SA, Bakhshi S, Thulkar S, Bal C, Malhotra A, Kumar R. Diagnostic accuracy of 18F-FDG PET/CT for detecting recurrence in patients with primary skeletal Ewing sarcoma. Eur J Nucl Med Mol Imaging. 2013;40:1036–43.
38. Brenner W, Conrad EU, Eary JF. FDG PET imaging for grading and prediction of outcome in chondrosarcoma patients. Eur J Nucl Med Mol Imaging. 2004;31:189–95.
39. Chakarun CJ, Forrester DM, Gottsegen CJ, Patel DB, White EA, Matcuk GR Jr. Giant cell tumor of bone: review, mimics, and new developments in treatment. Radiographics. 2013;33:197–211.
40. Makis W, Alabed YZ, Nahal A, Novales-Diaz JA, Hickeson M. Giant cell tumor pulmonary metastases mimic primary malignant pulmonary nodules on 18F-FDG PET/CT. Nucl Med Mol Imaging. 2012;46:134–7.
41. Uslu L, Asa S, Sager S, Halaç M. Multiple cardiac masses and distant metastatic foci in a patient with high grade pleomorphic sarcoma of the heart revealed by follow-up FDG PET/CT. Nuklearmedizin. 2014;53(2):8–9.
42. Enomoto K, Inohara H, Hamada K, Tamura M, Tomita Y, Kubo T, Hatazawa J. FDG PET imaging of myxofibrosarcoma on the sphenoid sinus. Clin Nucl Med. 2008;33:421–2.

43. Schwarzbach MH, Dimitrakopoulou-Strauss A, Mechtersheimer G, Hinz U, Willeke F, Cardona S, Attigah N, Strauss LG, Herfarth C, Lehnert T. Assessment of soft tissue lesions suspicious for liposarcoma by F18-deoxyglucose (FDG) positron emission tomography (PET). Anticancer Res. 2001;21:3609–14.
44. Brenner W, Eary JF, Hwang W, Vernon C, Conrad EU. Risk assessment in liposarcoma patients based on FDG PET imaging. Eur J Nucl Med Mol Imaging. 2006;33:1290–5.
45. Murphey MD, Ruble CM, Tyszko SM, Zbojniewicz AM, Potter BK, Miettinen M. From the archives of the AFIP: musculoskeletal fibromatoses: radiologic-pathologic correlation. Radiographics. 2009;29:2143–73.
46. Kleis M, Daldrup-Link H, Matthay K, Goldsby R, Lu Y, Schuster T, Schreck C, Chu PW, Hawkins RA, Franc BL. Diagnostic value of PET/CT for the staging and restaging of pediatric tumors. Eur J Nucl Med Mol Imaging. 2009;36:23–36.
47. Kasper B, Dimitrakopoulou-Strauss A, Strauss LG, Hohenberger P. Positron emission tomography in patients with aggressive fibromatosis/desmoid tumours undergoing therapy with imatinib. Eur J Nucl Med Mol Imaging. 2010;37:1876–82.
48. Tateishi U, Yamaguchi U, Maeda T, Seki K, Terauchi T, Kawai A, Arai Y, Moriyama N, Kakizoe T. Staging performance of carbon-11 choline positron emission tomography/computed tomography in patients with bone and soft tissue sarcoma: comparison with conventional imaging. Cancer Sci. 2006;97:1125–8.
49. Treglia G, Giovannini E, Di Franco D, Calcagni ML, Rufini V, Picchio M, Giordano A. The role of positron emission tomography using carbon-11 and fluorine-18 choline in tumors other than prostate cancer: a systematic review. Ann Nucl Med. 2012;26:451–61.
50. Buck AK, Herrmann K, Büschenfelde CM, Juweid ME, Bischoff M, Glatting G, Weirich G, Möller P, Wester HJ, Scheidhauer K, Dechow T, Peschel C, Schwaiger M, Reske SN. Imaging bone and soft tissue tumors with the proliferation marker [18F]fluorodeoxythymidine. Clin Cancer Res. 2008;14:2970–7.
51. Rajendran JG, Wilson DC, Conrad EU, Peterson LM, Bruckner JD, Rasey JS, Chin LK, Hofstrand PD, Grierson JR, Eary JF, Krohn KA. [18F]FMISO and [18F]FDG PET imaging in soft tissue sarcomas: correlation of hypoxia, metabolism and VEGF expression. Eur J Nucl Med Mol Imaging. 2003;30:695–704.
52. Inoue T, Kim EE, Wong FC, Yang DJ, Bassa P, Wong WH, Korkmaz M, Tansey W, Hicks K, Podoloff DA. Comparison of fluorine-18-fluorodeoxyglucose and carbon-11-methionine PET in detection of malignant tumors. J Nucl Med. 1996;37:1472–6.
53. Eiber M, Takei T, Souvatzoglou M, Mayerhoefer ME, Fürst S, Gaertner FC, Loeffelbein DJ, Rummeny EJ, Ziegler SI, Schwaiger M, Beer AJ. Performance of whole-body integrated 18F-FDG PET/MR in comparison to PET/CT for evaluation of malignant bone lesions. J Nucl Med. 2014;55:191–7.
54. Kaneta T. A brief review of Japanese guidelines for the clinical use of (18)F-FDG-PET/MRI 2012 (Ver 1.0). Ann Nucl Med. 2013;27:309–13.

# Imaging of Nonneoplastic Chest Wall Pathologies

19

Justin Stowell and Santiago Martínez-Jiménez

**Abstract**

The chest wall is commonly affected by nonneoplastic conditions including traumatic, infectious, arthritic, metabolic, and congenital lesions. Imaging plays a critical role in differentiating among these entities and other neoplastic mimics. Multimodality imaging evaluation including radiography, ultrasound (US), computerized tomography (CT), nuclear medicine, and magnetic resonance imaging (MRI) allows comprehensive evaluation of chest wall lesions and other ancillary findings. The radiologist plays an important role and is often be the first to identify abnormalities and alert clinicians and surgeons of both surgical and nonsurgical conditions. Thoracic surgeons and radiologists should work jointly in arriving at the imaging diagnosis and collaborate in the preoperative evaluation of patients who suffer from these conditions.

**Keywords**

Chest wall · Trauma · Hematoma · Fracture · Flail chest · Dislocation · Infection · Osteomyelitis · Septic arthritis · Inflammatory arthritis · Cellulitis · Abscess · Necrotizing fasciitis · Congenital chest wall disorders · Pectus excavatum · Osteoporosis · Renal osteodystrophy

## Abbreviations

| | |
|---|---|
| CT | Computed tomography |
| HIV | Human immunodeficiency virus |
| HU | Hounsfield unit |
| IV | Intravenous |
| MRI | Magnetic resonance imaging |
| SC | Sternoclavicular |
| TB | Tuberculosis |
| US | Ultrasound |

## 19.1 Trauma

Imaging plays a critical role in the evaluation and management of patients after chest trauma. Documentation of the extent of thoracic injury (extrathoracic and intrathoracic) is not only helpful to direct appropriate treatment but also provides prognostic information [1]. Risk factors for increased morbidity and mortality in the blunt chest trauma include advanced age (>65), three or more rib fractures, development of pneumonia, and preexisting chronic lung disease [2]. Delayed

J. Stowell (✉)
University of Missouri-Kansas City School of Medicine, Kansas City, MO, USA

S. Martínez-Jiménez
Saint Luke's Hospital of Kansas City & University of Missouri-Kansas City School of Medicine, Kansas City, MO, USA


M. Anzidei, M. Anile (eds.), *Diagnostic Imaging for Thoracic Surgery*,
https://doi.org/10.1007/978-3-319-89893-3_19

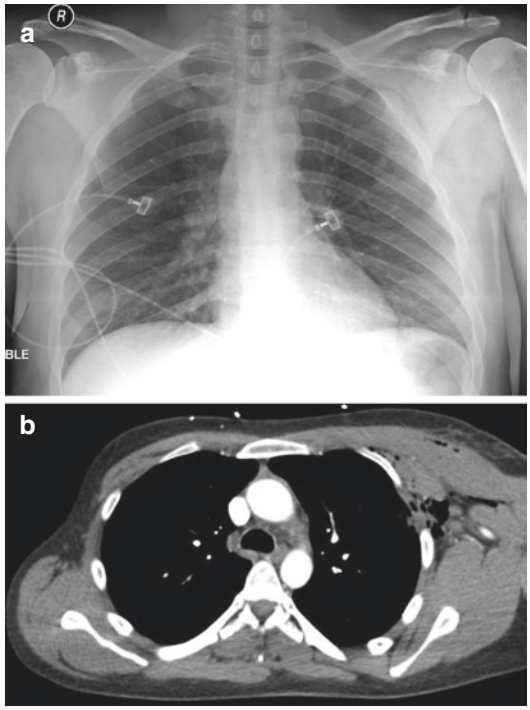


**Fig. 19.1** Portable anteroposterior chest radiograph (**a**) and contrast-enhanced CT (**b**) demonstrate the superior sensitivity and specificity of CT for detailing the extent of chest wall injury after blunt and penetrating trauma. The patient suffered a stab wound to the left anterior chest wall, which caused left chest wall hematoma, subcutaneous air, and left pectoral laceration. Left upper lobe laceration and pneumothorax were also seen using lung windows on the chest CT (not shown), but were only subtly present on radiography

**Table 19.1** Relative utility of commonly used imaging modalities in evaluation of the chest wall

| Modality | Pros | Cons |
|---|---|---|
| Chest radiography | Readily available<br>Fast and cost effective<br>Prognostic value | Limited sensitivity for rib fractures and pneumothorax |
| Chest CT | Fast scan times<br>Multi-planar imaging capabilities<br>High sensitivity for detection of rib fractures, pneumothorax, pulmonary contusion or laceration, as well as other solid-organ or vascular injury | Expensive<br>Radiation exposure<br>Time-intensive interpretation<br>Risk of adverse effects of iodinated contrast administration |
| Ultrasound | Fast and portable<br>Relatively inexpensive<br>Can be performed by clinicians<br>High sensitivity and specificity for identification of rib and sternal fractures, pleural effusion, or rib fractures<br>Dynamic exam with confirmation of site of maximal tenderness | Lacks sensitivity for small pleural space collections<br>Limited for evaluation of scapular injuries<br>Poor tissue penetration in obese patients or women with large breasts |

complications related to blunt chest trauma include occult pneumothorax or hemothorax.

Chest radiography is important as the initial imaging assessment in patients after trauma. Since chest radiography is readily available and rapidly performed, it allows identification of common life-threatening thoracic injuries that require immediate intervention (e.g., pneumothorax, hemothorax). Further, radiographic findings often prompt additional imaging evaluation with chest CT, which has better sensitivity and specificity for chest wall, vascular, and visceral traumatic injuries, and often alters initial management [3] (Fig. 19.1). The utility of various imaging modalities in the initial evaluation of blunt chest trauma is presented in Table 19.1 [2]. It is generally recommended that both symptomatic and asymptomatic patients who sustain even minor blunt chest wall trauma return for follow-up chest radiographs 2 weeks after injury to exclude delayed complications.

## 19.1.1 Osseous

### 19.1.1.1 Sternal, Rib, and Costochondral Fractures

Sternal fractures are found in 8–10% of patients who sustain blunt chest wall injury [3–6]. The combination of sternal, scapular, or rib fractures and associated sternoclavicular joint dislocation comprises the "seat-belt syndrome" of motor vehicle collisions, indicating an increased likelihood of internal organ injuries [3]. Some authors have concluded that isolated sternal fractures in the absence of cardiac injury or arrhythmia may be managed conservatively with surgery rarely required [2].

Chest radiography is insensitive for the initial detection of non-displaced sternal fractures [7], and lateral views of the sternum are seldom obtained in the trauma setting despite their increased sensitivity for fracture. Axial chest CT readily depicts displaced sternal fractures, as well as concomitant retrosternal hematoma or other associated injuries (e.g., acute traumatic aortic injury) [3].

Up to 50% of patients with blunt trauma exhibit rib fractures, most commonly involving the fourth through ninth ribs [6, 8]. Simple rib fractures are generally of no clinical consequence, but may be associated with more serious injuries such as pneumothorax, hemothorax, pulmonary contusion or laceration, great vessel injury, or solid-organ injury [1]. Unlike radiography, CT offers high sensitivity and specificity for detection of rib fractures, with the additional benefit of assessing other radiographically occult injuries [3].

Flail chest occurs in up to 20% of major trauma victims and is defined as greater than or equal to three segmental (greater than two fractures occurring in the same rib) or greater than five adjacent rib fractures, leading to paradoxical motion of the chest during respiration (Fig. 19.2). Paradoxical chest wall motion impairs adequate ventilation, which, in combination with lung injury, can progress to acute respiratory failure [6].

One challenge is the evaluation of radiographically occult costochondral fractures. While ultrasound has been proven to be very sensitive [8], it is usually not practical in the acute setting. In our practice, we routinely use coronal maximum intensity projection (MIP) reformations to assess for costochondral fractures (Fig. 19.3). Detection of this type of injury is important as it is associated with more serious injuries and entails increased mortality [9].

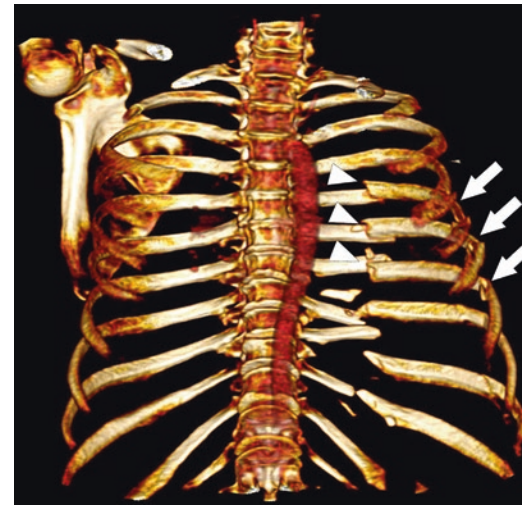

**Fig. 19.2** Flail chest. Multilevel displaced segmental rib fractures (*arrows* and *arrowheads*) contributed to paradoxical chest wall motion during respiration and flail-chest physiology in this 70-year-old male who sustained a motor vehicle collision. 3D volume-rendered CT can be performed to better highlight the extent of thoracic injury and assist the thoracic surgeon in presurgical planning

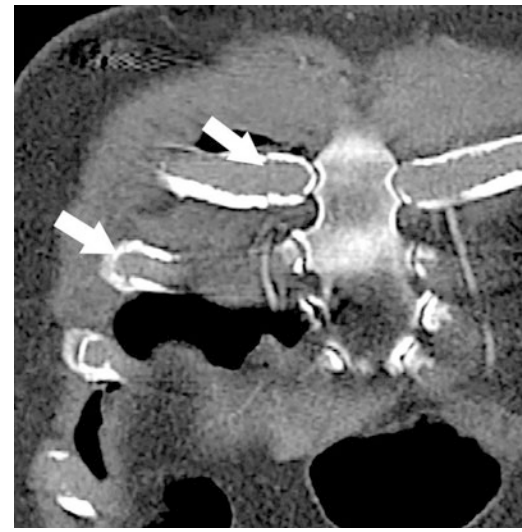

**Fig. 19.3** Costochondral fractures. Coronal CT with maximum intensity projection (MIP) reformations more readily depicts radiographically occult though clinically significant costochondral fractures (*arrows*)

### 19.1.1.2 Clavicle Fracture

Clavicle fractures represent up to 5% of all fractures. When describing a clavicular fracture, it is important to include the location (middle, distal, or proximal), degree of comminution or displacement, and likelihood of ligamentous injury [10]. Most (69–72%) clavicle fractures are mid-shaft in location, with distal and medial clavicle fractures representing 28% and 2–3% of the remaining fractures, respectively. Most clavicle fractures are non-displaced and extra-articular and can be managed conservatively. However, medial, posteriorly displaced fractures or associated sternoclavicular (SC) joint dislocations may cause injury to the great vessels, airway, or nerves within the superior medi-

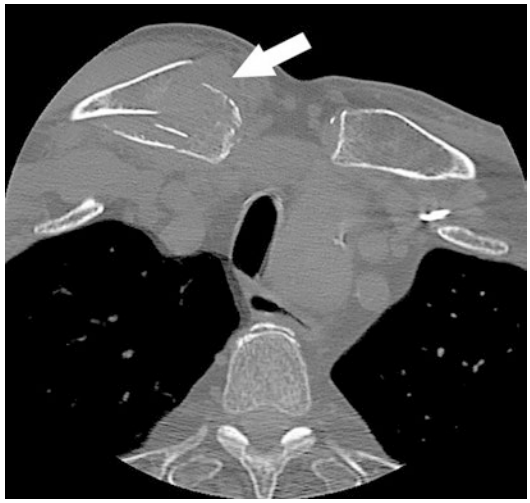

**Fig. 19.4** Clavicle fracture. A CT from a 68-year-old man who sustained a comminuted, mildly displaced medial right clavicular fracture with surrounding hematoma (*arrow*) after an all-terrain vehicle rollover highlights the importance of cross-sectional imaging in characterizing radiographically occult chest wall injury

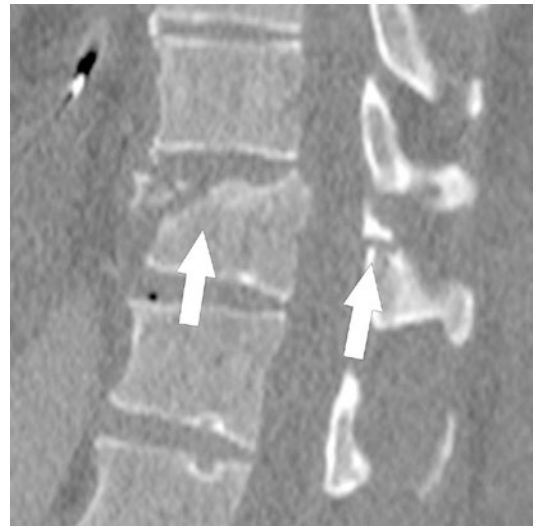

**Fig. 19.5** Coned-down sagittal CT reveals a flexion-distraction "seat-belt" pattern of injury at T11. Fractures of the vertebral body (Chance fracture) and spinous process of T11 indicate simultaneous anterior column compression and posterior column interspinous ligament avulsion injuries, respectively (*arrows*). This pattern has a high association with coexistent abdominal and spinal cord injuries

astinum and often have surgical implications. Most of these are radiographically occult and are best characterized on axial CT (Fig. 19.4). Multiplanar reformatted images and 3D reconstructions may be helpful to the surgeon in preoperative planning.

#### 19.1.1.3 Scapular Fracture

Because it is relatively protected by surrounded shoulder girdle and back musculature, the scapula is rarely injured in blunt trauma. The presence of scapular injury should raise suspicion for more extensive thoracic injury. Most scapular fractures are managed conservatively in the absence of involvement of the glenoid or scapular neck [6].

#### 19.1.1.4 Spinal Trauma

The thoracic spine should be carefully evaluated in the setting of blunt chest trauma, as injuries in this region can be complicated by devastating neurologic defects in up to 60% of patients [6]. Vertebral body (wedge, burst, and Chance-type) is typically located near the thoracolumbar junction [5, 6]. Wedge fractures typically spare the posterior aspect of the vertebral body. Burst fractures involve the posterior aspect of the vertebral body, which entails increased risk of cord injury. Finally, Chance fractures are defined by extension into the posterior elements or ligamentous structures. CT defines the extent of injury, including pedicle and spinous processes fractures, as well as paraspinal hematoma (Fig. 19.5). CT may also provide information of the integrity of the spinal canal and neural foramina. MRI is often required to assess for spinal cord injury, which may be present in up to 30% of traumatic spine injuries especially in the setting of burst and Chance fractures [11].

### 19.1.2 Joints

#### 19.1.2.1 Sternoclavicular and Manubriosternal Dislocation

Lateral compression injuries with medially directed force through the shoulder may lead to sternoclavicular dislocation. Patients present with anterior chest wall tenderness, impaired shoulder range of motion, and often visible deformity at the sternoclavicular joint. The direction of dislocation of the medial clavicular head in relation to the manubrium has prognostic implications. Most SC dislocations are anterior, with posterior dislocations less common but associated with worse prognosis as they are frequently associated with mediastinal injury (e.g.,

head/neck vessels and tracheal compression) [6]. SC dislocation is often occult on radiography; however, it may occasionally be seen as abnormal position of the clavicular head. CT readily demonstrates anterior or posterior position of the medial clavicle and allows for detailed assessment of the adjacent mediastinal structures [12] (Fig. 19.6).

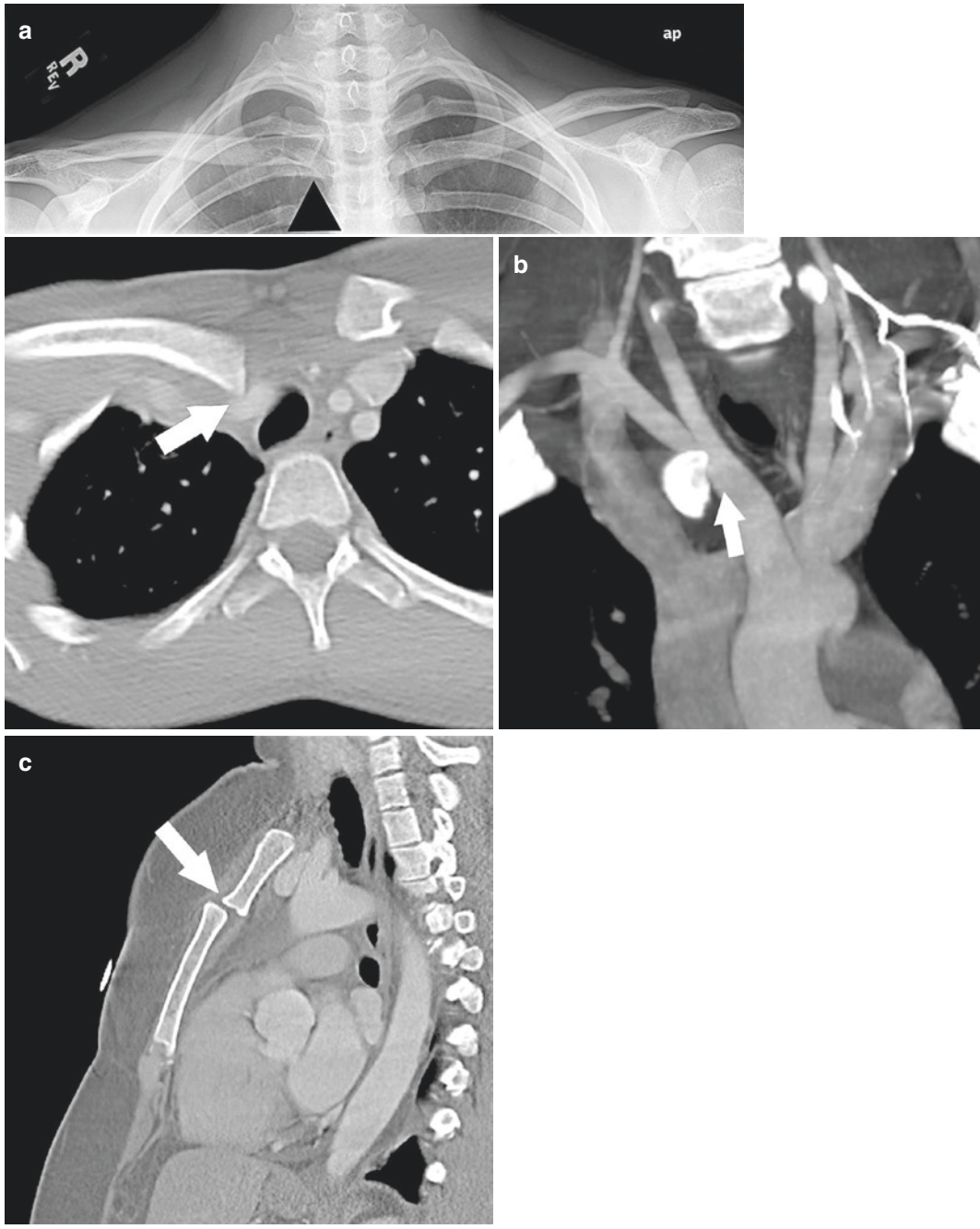


**Fig. 19.6** Sternoclavicular and manubriosternal dislocation. (**a**) Chest radiograph shows subtle asymmetric displacement of the medial right clavicle (*black arrowhead*). Contrast-enhanced axial (**b**) and coronal MIP (**c**) CT better characterizes the posterior displacement of the medial clavicle with compression of the right brachiocephalic artery (*arrows*). (**c**) Sagittal CT is best to characterize the degree of displacement in manubriosternal dislocations (*arrow*). Manubriosternal dislocations are rare and imply high-force injury mechanisms

Manubriosternal dislocation is rare, occurring most frequently in the setting of trauma or exaggerated kyphosis related to chronic diseases (e.g., osteoporosis and rheumatoid arthritis). Dislocations are classified as either type 1 or type 2 based on the posterior or anterior position of the sternum in relation to the manubrium, respectively [12].

#### 19.1.2.2 Costovertebral Fracture-Dislocations

Costovertebral dislocations involve ligamentous or osseous disruption of the costocentral and costotransverse constituents of the arthrodial joint structure. The costocentral joint spans a large portion of the posterolateral disk space. It is stabilized by a thin synovial capsule and ligaments (interarticular and radiate), which may not be visualized on CT. Costovertebral joints are comprised primarily of two thick ligaments which stabilize the neck and tubercles of the ribs to the transverse processes, oriented in a transverse plane. Collectively, these joints provide important stabilization and support to the thoracic spine [13].

While uncommon, costovertebral joint injuries are often overlooked as they are generally radiographically subtle. Their presence suggests serious radiographically occult injuries of the chest and thoracic spine and should be further evaluated with cross-sectional imaging. Costocentral articulations are well defined on chest radiographs, where the costal head can be seen articulating with the vertebral pedicle. The joints are best evaluated in the axial plane on CT bone window settings. While traumatic costovertebral fracture-dislocations are most common, dislocation with penetration of the rib into the spinal canal or neuroforamen may be seen in patients with scoliosis or neurofibromatosis [13, 14].

### 19.1.3 Soft Tissues

#### 19.1.3.1 Direct Injury

##### Blunt and Penetrating Trauma

Direct muscle and soft-tissue injury results in hemorrhage that ranges from intramuscular interstitial bleed to frank hematoma. Additionally, penetrating trauma (e.g., stab wounds) may disrupt the muscle fibers and result in denervation atrophy.

Hematomas may be the result of arterial (intercostal, internal mammary, or subclavian artery) or venous bleeding. Extrapleural hematomas collect between the endothoracic fascia and parietal pleura, which on CT appear as a convex, hyperdense collection with characteristic displacement of the extrapleural fat from the chest wall with mass effect on the adjacent lung [5]. Occasionally, sites of active bleeding may be detected if intravenous contrast is utilized; this may be facilitated by using MIP reformations. Subcutaneous fat stranding is another common finding. Acute hemorrhage is typically hyperdense, and the affected musculature may be focally enlarged. CT is helpful to detect radiographically occult injuries which include pneumothorax (15%), hemothorax (11%), and combined hemopneumothorax (9%), as well as hemopericardium [15] (Fig. 19.1).

Hematomas have variable appearance on MR, depending on the extent and age of the blood products (Table 19.2). Fat-suppression

**Table 19.2** Variability of imaging features in chest wall soft-tissue injury

| Classification | MRI appearance |
|---|---|
| Type 1 (seroma) | Homogenous hypointense T1, hyperintense T2; no capsule formation |
| Type 2 (subacute hematoma) | Homogenous hyperintense T1 (methemoglobin) and T2, becoming heterogeneous with time; +/− hemosiderin capsule; +/− internal fat, fluid–fluid levels, or septations; patchy enhancement from neovascularity |
| Type 3 (chronic organizing hematoma) | Hypointense T1 and heterogeneous hypo- to isointense T2 signal; internal enhancement from neovascularization and granulation tissue; hypointense ring from hemosiderin and fibrous pseudocapusle |
| Type 4 (closed laceration) | No capsule; T1 hypointense, T2 hyperintense, variable enhancement |
| Type 5 | Pseudonodular appearance with variable T1 and T2 signal; variable internal or peripheral enhancement |
| Type 6 (infected hematoma) | Thick enhancing capsule +/− sinus tract formation |

techniques distinguish fat from subacute blood product on T1-weighted images. Hematomas typically resolve in 6–8 weeks after injury.

Soft tissues occasionally react to blunt trauma by the formation of a circumscribed mass of granulation tissue which may eventually form new bone (heterotopic ossification) due to activation of osteoblast progenitor cells in damaged tissue. Radiography and CT vary in time, progressing from early nonspecific soft-tissue swelling (0–2 weeks) to heterogeneous soft-tissue enhancement and periosteal reaction in adjacent bone with formation of amorphous osteoid (3–4 weeks). Beyond 6 weeks, a characteristic zoning phenomenon occurs wherein mature cortical bone forms around the periphery of the immature osteoid centrally [16]. MR imaging features also evolve over time from injury, manifesting initially as heterogeneous increased T2 signal (edema), with progression to an enhancing mass-like high T2 signal intensity lesion which mimics a soft-tissue sarcoma. In many cases, patients may be referred to the thoracic surgeon for suspicion of underlying tumor. With increasing age of injury beyond 6–8 weeks, peripheral ossification begins, leading to low signal on T1- and T2-weighted images, as well as dark signal on gradient echo sequences [16, 17] Unlike sarcomas, the overall lesion of heterotopic ossification tends to decrease in size over time.

#### 19.1.3.2 Indirect Injury

##### Muscle Strain and Tendon Injury

Musculotendinous injury (muscle strains, ruptures, and hematoma) occurs most frequently in active individuals, with higher risk in weightlifters, football players, and wrestlers [4]. Pectoralis major is by far the most commonly injured chest wall muscle, followed successively in frequency by pectoralis minor, internal oblique, or external oblique. Muscle strains represent either partial or complete tears of the muscle fibers at the musculotendinous junction, often resulting from sudden forceful loads applied during eccentric contraction. Most indirect muscle injuries are not imaged and may be conservatively managed. Imaging appearance of indirect muscle injury is dependent on the grade of injury.

Ultrasound may be used in the evaluation of musculotendinous injury, manifesting as hypoechoic signal or non-visualization of a tendon and loss of the normal fibrillary pattern. In full-thickness tendon tears, a gap may be seen in the disrupted tendon with a blunt-ending, retracted tendon fragment, which may produce a refractive shadow. Adjacent fluid collections or hematomas may also be seen. Imaging features of muscle injury are identical to other soft-tissue hematomas, with progressive liquefaction of the blood product over the healing process. Once liquefied, the collection may undergo ultrasound-guided aspiration.

CT is inferior to MRI and US in characterization of soft-tissue injury. CT may show ill-defined heterogeneous density near the insertion or origin of the involved muscle, with varying degrees of perimuscular fluid or hemorrhage. Bony avulsion fractures may be detected using bone windows. MRI readily depicts all degrees of traumatic soft-tissue injury.

## 19.2 Infection

Primary spontaneous infection of the chest wall is rare but may occur in the certain scenarios such as altered immunity, intravenous drug abuse, diabetes mellitus, or previous trauma or surgery [18]. Secondary chest wall infections (i.e., osteomyelitis) are usually related to pulmonary or pleural infections (e.g., *Actinomyces*, tuberculosis, or fungal infection, discussed subsequently) or recent surgery (e.g., sternotomy). *Staphylococcus aureus* and *Pseudomonas aeruginosa* are the organisms most commonly responsible for pyogenic infection of the chest wall. *Salmonella* species may be responsible for chest wall infections in a subset of patients (i.e., sickle cell) [19]. Imaging is integral to evaluation, as clinical and laboratory evaluations are often nonspecific. Despite inherent limitations in evaluation of the chest wall, chest radiography is often the first modality employed. CT and MRI provide better detail of the extent of infection, as well as vital anatomic information related to bone destruction (CT) and soft-tissue complications (MR). Cross-sectional imaging is a necessary component of

presurgical planning prior to chest wall resection. Furthermore, CT and ultrasound may be utilized in drainage procedures or percutaneous biopsy.

## 19.2.1 Osseous

### 19.2.1.1 Osteomyelitis

#### Pyogenic Infection

Osteomyelitis is defined as infection of the bone and marrow space by various microorganisms. Primary chest wall infections are rare, with most occurring in the setting of diabetes, immunosuppression (chronic immunosuppressive therapy or HIV), or trauma (including surgery). Osteomyelitis of the sternum, ribs, clavicles, or spine occurs most commonly from contiguous spread of infection from pulmonary or pleural processes [19]. Hematogenous involvement may also occur in the setting of intravenous drug abuse, severe immune suppression (AIDS), hemoglobinopathies, and other immune-suppressed states [20]. Responsible organisms in pyogenic osteomyelitis most commonly include *Staphylococcus aureus* and *Streptococcus* species. However, other organisms may be implicated in particular populations (Table 19.3) [18–23]. Early recognition and initiation of treatment are important to prevent progression of infection to subacute or chronic stages, and to prevent complications of sepsis.

Osteomyelitis is characterized histologically by marrow edema and cellular infiltration, with contiguous intramedullary spread of infection via Haversian and Volkmann canals, leading to eventual cortical destruction and spread to adjacent soft tissues or joints [20]. Intramedullary pressures increase with cellular proliferation and progressive edema, which may lead to intramedullary vascular compromise, ischemia, and necrosis. Over time, the bone may react by activation of osteoclasts and formation of sclerotic bone in an attempt to sequester or wall off the offending organism, producing an interosseous abscess and eventual sequestrum.

Primary sternal osteomyelitis is uncommon. Sternal and rib osteomyelitis typically occur as complications of recent trauma, surgery, or contiguous chest wall or mediastinal infection. Postoperative sternal osteomyelitis is associated with a mortality rate as high as 50% [22] and should be aggressively treated. While radiography is often insensitive, CT highlights osseous destruction, erosion, periosteal reaction, and soft-tissue abscess (Fig. 19.7). Pyogenic infections tend to involve the opposing ends of the rib, at the costochondral and costovertebral junctions [22] (Fig. 19.8). MRI has high sensi-

**Table 19.3** Implicated organisms in chest wall infections affecting particular patient populations

| Patient condition | Associated organisms |
|---|---|
| Immunocompetent | *Staphylococcus aureus, Streptococcus pyogenes* |
| IV drug abusers | *Pseudomonas aeruginosa* |
| Median sternotomy | *Staphylococcus aureus, Pseudomonas, Serratia, Klebsiella* |
| HIV and AIDS | Usual bacterial organisms, *M. tuberculosis*, *Nocardia* |
| Lung or heart transplant | Fungal (*Aspergillus*, *Actinomyces*, *Blastomyces*) |

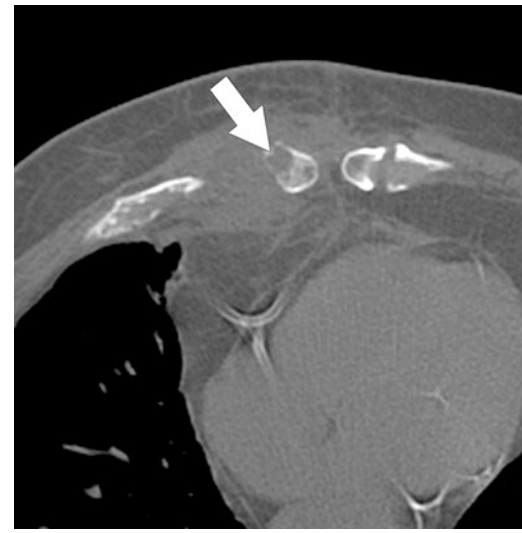

**Fig. 19.7** Sternal osteomyelitis extending into the anterior mediastinum after median sternotomy. CT depicts sternal erosion (*arrow*) and the extent of surrounding phlegmon in a patient who had recent sternotomy for coronary artery bypass graft surgery. CT is the preferred modality for evaluating complications of sternal osteomyelitis, which include mediastinitis and abscess

tivity for early marrow edema and characterizes abscesses or fistulae. The radiologic findings of more extensive infection are nonspecific and overlap with other entities such as plasmacytoma and metastases. Therefore, clinical context and histologic correlation is required.

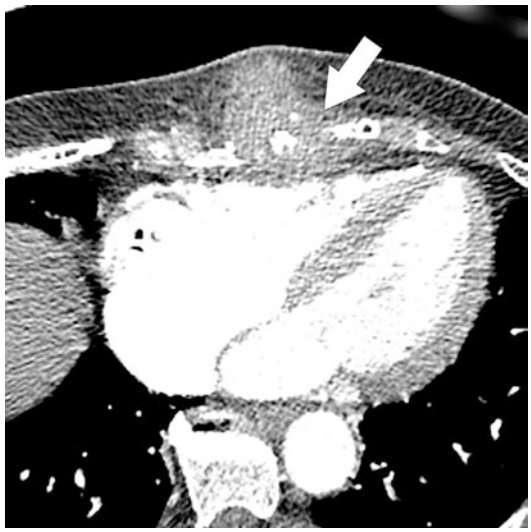

**Fig. 19.8** Costochondral osteomyelitis. Extensive soft-tissue inflammation surrounds an area of costochondral and rib destruction (*arrow*) from contiguous spread of pyogenic infection after recent sternotomy

Multi-modality imaging is often required when osteomyelitis is clinically suspected [20]. Radiographic findings include soft-tissue swelling and thickening of septae in subcutaneous fat (edema), often before osseous changes are present. Air-fluid levels in the soft tissues may indicate abscess [18]. Osseous changes include cortical erosion or sclerosis, osseous destruction, and periosteal reaction, which generally suggests that the infection has been present for 1–2 weeks. Regional hyperemia and marrow infiltration will lead to localized osteoporosis and eventual trabecular destruction/osteolysis [20]. Normal radiographs do not exclude the presence of osteomyelitis.

MRI is the most sensitive and specific modality for detection of early osteomyelitis, ranging from 82 to 100% and 75 to 96%, respectively [20, 24]. Fat-suppressed T2-weighted and short tau inversion recovery (STIR) sequences are sensitive to the presence of marrow edema, manifesting as areas of hyperintensity (Figs. 19.9 and 19.10). Replacement of the normal hyperintense signal of marrow fat on T1-weighted sequences

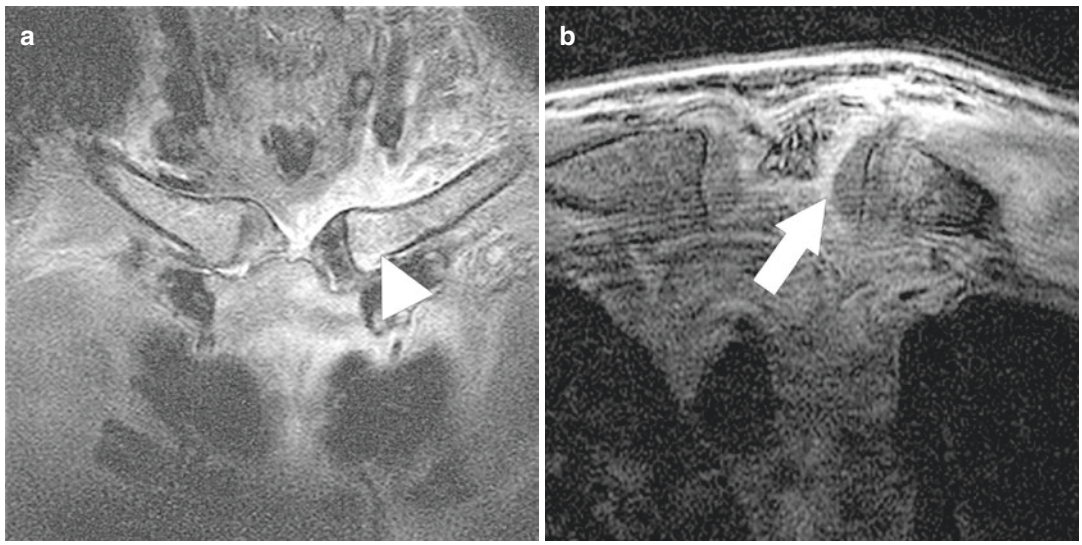


**Fig. 19.9** Sternoclavicular septic arthritis. (**a**) Coronal short tau inversion recovery (STIR) MR reveals expected periarticular inflammation and clavicular marrow edema (*arrowhead*) surrounding the left SC joint. (**b**) Axial T1 fat-suppressed MR after intravenous gadolinium contrast material shows corresponding enhancement of the left SC joint (*arrow*) and periarticular soft tissue

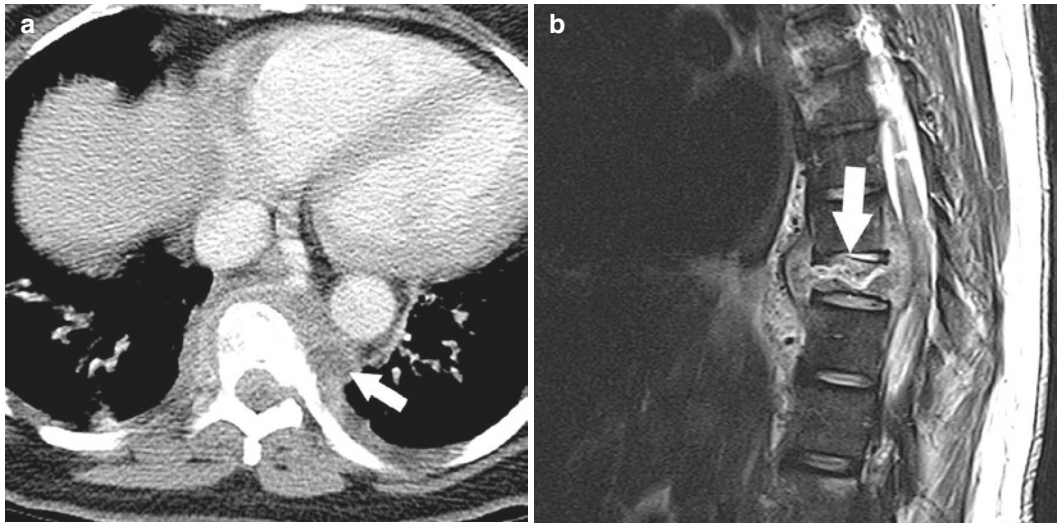


**Fig. 19.10** Pott disease. (**a**) CT reveals low-attenuation paravertebral soft-tissue masses and fluid collections (*arrow*) in a young patient with spinal TB. Paravertebral masses are present in 95% of cases, often with calcification. Other CT findings include anterior endplate erosion without significant reactive sclerosis, and wedge deformities. (**b**) Sagittal MRI STIR sequence shows marrow edema as increased signal and a linear hyperintense cleft in the involved vertebral body (*arrow*), indicating a pathologic fracture. MRI STIR sequence also delineates the craniocaudal spread of the paraspinal infectious material, as well as anterior spread into the lower mediastinum. Marked cord compression is seen to better advantage with MRI

by intermediate to low signal indicates an infiltrative process. The clinician must be aware that imaging findings in acute osteomyelitis are nonspecific, as similar findings may be seen in noninfectious processes, including trauma, fracture, ischemia, and tumor [24]. MR features of the various stages of osteomyelitis are summarized in Table 19.4.

Despite its inferior sensitivity (73%) and specificity, scintigraphy may be considered as an adjunct modality, particularly for evaluating patients who have contraindications to MRI. Three-phase bone scans using technetium-99m-labeled methylene diphosphonate (MDP) reveal increased radiotracer uptake in arterial flow, blood pool, and 3-hour delayed imaging [20, 25]. The intensity of uptake localizes to the areas of infection. Specificity of bone scintigraphy is reduced in the presence of complicating conditions (i.e., trauma, surgery, orthopedic hardware, and diabetes). Other nuclear medicine techniques utilizing various radiopharmaceuticals (technetium-99m hexamethylpropylenamine oxime (HMPAO)-labeled white blood cells, murine immunoglobulin-M monoclonal antigranulocyte antibodies, or ciprofloxacin-labeled moi-

**Table 19.4** Expected evolution of osteomyelitis on MRI

| Stage of infection | MRI appearance |
|---|---|
| Acute: edema and exudate | Ill-defined low T1 signal<br>High signal T2, STIR<br>Ill-defined soft-tissue planes<br>Disruption of dark cortical signal<br>+ enhancement<br>Rim enhancement = abscess<br>Intramedullary fat globules (marrow necrosis) |
| Subacute: intraosseous abscess formation | Low T1 signal surrounding abscess (granulation tissue)<br>High T2 signal within abscess and in surrounding marrow (edema)<br>"Double-line effect" or "target" appearance = concentric enhancing granulation tissue with low signal band of sclerosis and peripheral rim enhancement<br>Cortical thickening |
| Chronic | Low T1<br>Low T2 (scarring and bony sclerosis)<br>Sharp zone of transition between normal and infected marrow<br>"Rim sign" = peripheral low signal on all sequences corresponds to fibrotic changes and reactive bone<br>Areas of non-enhancement (devitalized bone, sequestrum)<br>Cortical thickening<br>+/− sinus tracts |

eties) may also be considered [20, 24]. However, false-negative scans may occur in the setting of chronic or partially treated osteomyelitis.

### Tuberculosis

The spine is the most common site of musculoskeletal *Mycobacterium tuberculosis* infection, also known as Pott disease [26] (Fig. 19.10). The thoracic spine is most commonly affected. The chest wall is affected in up to 10% of extrapulmonary TB [21]. Infections manifest with osteitis of the ribs, sternum, vertebrae, as well as costochondral and costovertebal articulations. A strong predilection for the sternal margins has been associated with TB, possibly a result of secondary infection from infected internal mammary chain lymph nodes [21, 27]. Nevertheless, the sternum is affected in less than 1% of all cases of tuberculous osteomyelitis [28]. Others report a predilection for the rib shaft (unlike pyogenic infection) with osseous destruction and adjacent abscess formation [22, 29]. Radiographs will be normal. Osseous changes (cortical erosions or expansile osteolytic mass) occur secondary to direct infection or pressure necrosis from inflammatory granulation tissues and are better depicted on CT and MR. Signs of bone repair (periosteal reaction or sclerosis) are less frequently seen in TB than in pyogenic osteomyelitis [22, 29]. Necrotic lymph nodes may form subpleural collections referred to as "cold abscesses," which can extend from the chest wall and ultimately require wide surgical resection in addition to multidrug therapy [21, 27]. Cutaneous fistulae may also develop [27, 30]. CT reveals expansile, destructive lytic lesions with adjacent sclerosis with nearby soft-tissue thickening and enhancement. The soft-tissue component often is in continuity with mediastinal or internal mammary lymphadenopathy [29]. Ultrasound and CT are useful for diagnosis and sampling.

### Actinomyces

Of the five major forms of actinomycotic infections, the thoracic form is quite common (15%) [21, 22, 31]. *Actinomyces israelii* is a gram-positive anaerobic inhabitant of the oral cavity, which explains its predilection to involve the cervicothoracic and abdominal regions. Isolated actinomycotic chest wall infection is rare, and usually occurs secondary to a pulmonary infection. Aspiration of oral flora leads to parenchymal infection, with subsequent spread through the pleura and into the chest wall. Complications of actinomycosis infection include empyema and empyema necessitatis, chronic pleurocutaneous fistula, and systemic dissemination [21, 31]. Radiographic manifestations include nonspecific osteolysis with or without periostitis, or subpleural consolidations with or without pleural effusion [31, 32]. Bone scintigraphy may show focal radiotracer uptake in the region of bony involvement and periosteal new bone formation [31]. CT and MRI show to better advantage the extent of thoracic and soft-tissue involvement. Intravenous contrast highlights the enhancing inflamed tissue and rim-enhancing abscesses, if present [21, 31, 32]. MRI features include nonspecific T1 hypointense as well as T2 and STIR hyperintensity, often with enhancement [31]. Ultrasound of the chest wall may assist in diagnosis or drainage of soft-tissue abscesses (complex fluid collection with surrounding hyperemia), empyema, and soft-tissue mass, but generally underestimates the extent of disease.

### Fungal and Hydatid Infection

Fungal organisms are rare but increasingly recognized sources of chronic infections of the ribs and sternum, especially in the setting of immunosuppression. Sternal osteomyelitis and costochondritis often result from hematogenous dissemination or contiguous spread of pulmonary infections. Costal cartilages, especially after perichondrial damage, are particularly susceptible to infection. While *Aspergillus* infection as a complication of surgery is well described, primary *Aspergillus* infections occur in the setting of immune compromise (diabetes, alcoholism, prolonged antibiotic therapy, immunosuppressive therapy, neutropenia, and HIV) or IV drug abuse [23, 33]. Other fungal infections (histoplasmosis, blastomycosis, cryptococcosis, and coccidioidomycosis) are rare, occurring most often in the immunocompromised patient, and share similar imaging features. Radiographic manifes-

tations include nonspecific osseous destruction and soft-tissue masses [22]. Histocytopathologic sampling must confirm the diagnosis. Treatment often requires radical debridement of chronically inflamed tissues, with potential necessity of chest wall defect reconstruction [21, 22, 33].

Hydatidosis represents human parasitic infection with the larval form of the *Echinococcus granulosus*. Although rare in the United States, the parasite is very common among rural populations in Mediterranean countries, Australia, and South America, with increasing incidence in China [34]. Both costovertebral and primary rib hydatidosis have been described with rib involvement in 22–72% of cases [22, 34]. Radiographic manifestations include a permeative, multiloculated expansile predominantly lytic bony destruction, adjacent soft-tissue swelling, and pleural thickening. Periosteal new bone formation and sclerosis are uncommon. Calcified extraosseous cysts may be present in over 1/3 of cases. Ultrasound may be helpful to determine cystic appearance of lesions. CT and MRI are useful in presurgical planning, showing extraosseous disease and potential spinal involvement. The MRI appearance of the cysts includes hyperintense T1 (high protein content) and T2 signal. Daughter cysts may be less proteinaceous, manifesting with lower T1 and higher T2 signal. There is faint, thin cyst wall enhancement after gadolinium contrast administration. Histologic confirmation must exclude other mimics including metastasis, plasmacytoma, aneurysmal bone cyst, or cystic neurogenic tumors. Treatment typically involves radical surgical resection to avoid recurrence or inadvertent cyst rupture. Cyst rupture may lead to dissemination of infection or even anaphylaxis, and thus needle biopsy is contraindicated [22, 34, 35]. However, in poor surgical candidates, percutaneous needle aspiration of cyst contents with injection of antiprotoscolicidal has been described [34].

## 19.2.2 Joints

### 19.2.2.1 Primary septic arthritis

Septic arthritis is defined by direct invasion of microorganisms into the joint space. Sternoclavicular joints comprise only 2% of all pyogenic arthritis, but are frequently complicated by periarticular abscess because of the capsule limitations to distention [36]. The joint may become secondarily affected by spread of infection from adjacent sternal osteomyelitis or mediastinal abscess [37]. Most pyogenic SC joint infections are unilateral, with slight predilection for the right side. Primary manubriosternal infections occur almost exclusively in the setting of IV drug abuse, and share similar imaging features. Close anatomic relationship of these joints to the pleural space, mediastinum, and great vessels explains associated infectious involvement of vital structures. The superficial location of the joints allows for easy palpation to elicit physical findings of focal tenderness, cutaneous erythema and induration, and joint capsular swelling. Referred pain to the shoulder may be found in 25% of cases. Surgical intervention (incision and drainage, debridement, or en bloc chest wall resection) is indicated in the presence of failed antibiotic therapy, periarticular fluid collections/abscess, and osseous destruction.

Cross-sectional imaging is the cornerstone of diagnosis and should be performed routinely in all cases of suspected SC joint septic arthritis to confirm the diagnosis and determine possible complications, especially the presence of retrosternal or mediastinal abscess [36]. CT findings include periarticular inflammation, osseous erosion, sclerosis, and periosteal reaction of the surrounding bone (Fig. 19.9). However, osseous changes may not be apparent at early stages (i.e., first 1–2 weeks). Degenerative changes of the joints can simulate infection on radiography, but CT findings of periarticular osteophytes, subchondral sclerosis, and occasional intra-articular gas in the absence of soft-tissue inflammation are essentially diagnostic [22]. Radiographs and ultrasound findings may be absent despite the presence of SC joint infection. Ultrasound may readily characterize periarticular soft-tissue fluid collections (joint effusions, abscess), synovial thickening and hyperemia (synovitis), and presence of soft-tissue collections [22, 38]. MRI can detect early inflammatory changes of bone, joint, and soft tissues, depicted as heterogeneous low

T1 signal and high signal intensity (edema) on T2-weighted sequences. Intravenous gadolinium further characterizes inflamed soft tissues and can outline areas of non-enhancing, devitalized tissue [22] (Fig. 19.9).

SC joint infections with atypical organisms are rare and exhibit unique clinical and imaging manifestations. Nearly 3% of TB extraspinal arthritis involves the SC joint, manifesting with extensive osteolysis, periarticular inflammatory soft-tissue mass, abscess with rim enhancement and mural calcifications, and lack of periosteal reaction in adjacent bone [22]. Manubriosternal joint involvement is very rare [39]. US and CT may reveal bony sequestra within areas of smoldering osteolysis. Radiography is insensitive and nonspecific, and may demonstrate the presence of a presternal soft-tissue mass with or without osseous changes. Most systemic infections with *Brucella* involve the musculoskeletal system, and 2–5% affect the SC joint. Most brucellar SC joint infections are treated with long-term antibiotic therapy, and surgical control is seldom necessary. CT may show subchondral erosion and joint space enlargement. Healing changes include bony sclerosis and new bone formation [22, 29].

In the setting of chronic relapsing sternoclavicular inflammation, hyperostosis, and osteitis, a common mimicker of pyogenic SC arthritis—synovitis, acne, pustulosis, hyperostosis, and osteitis syndrome (SAPHO)—should be raised. SAPHO is an inflammatory disorder of the skin and musculoskeletal system, occurring in otherwise healthy young adults in the absence of immune suppression or infectious etiology. The sternoclavicular joints are involved in 60–90% of cases, with concomitant sacroiliitis and spondylitis [22]. Cultures from joint aspiration and bone biopsies may be negative or may isolate *Propionibacterium acnes*, and patients may have undergone treatment with prolonged antibiotics and prior surgical debridement. Sternocostoclavicular hyperostosis (Fig. 19.11), along with erosion, subchondral sclerosis, and ankylosis, is a radiologic and CT feature. T2-weighted MR sequences additionally may reveal active marrow edema [12]. Classically, technetium-99m bone scintigraphy reveals uptake in the sternocostoclavicular and manubriosternal joints in a highly specific "bulls horn" configuration [40] (Fig. 19.11). CT and MRI features are nonspecific and do not reliably differentiate SAPHO-related osteitis and hyperostosis from those of other infectious etiologies. Nonsteroidal anti-inflammatories (NSAIDs) are the mainstay of treatment. Surgical intervention is rarely indicated.

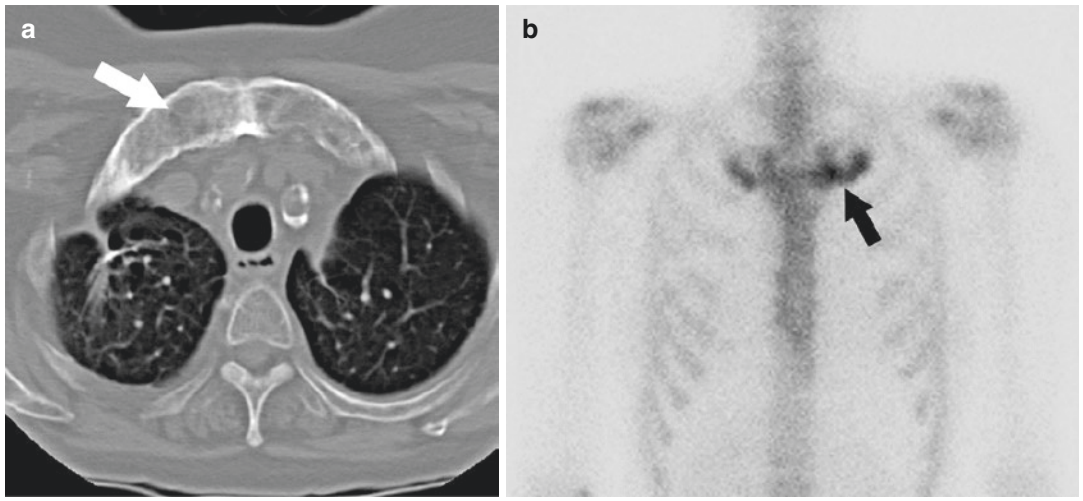


**Fig. 19.11** Synovitis, acne, pustulosis, hyperostosis, and osteitis syndrome (SAPHO). (**a**) CT shows hyperostosis, expansion, and ankylosis of the sternoclavicular joints (*arrow*). (**b**) Technetium-99m bone scan in the same patient manifests the classic "bull's horn" appearance of increased radiopharmaceutical uptake in the involved sternoclavicular joints (*arrow*)

### 19.2.3 Soft Tissues

#### 19.2.3.1 Cellulitis, Pyomyositis, and Abscess

Cellulitis refers to an infection of the dermis and subcutaneous fat related to bacterial inoculation from small traumatic defects in the skin; contiguous spread from adjacent infected bones or joints; or hematogenous spread. Recurrent cellulitis may occur in the setting of postoperative vascular and lymphatic damage (e.g., breast surgery or lymph node dissection), intravenous drug abuse, or radiation therapy. Clinical presentation includes fever and malaise with warm, tender, erythematous areas of skin. Extreme cases may manifest with edema, pustules, vesicle and bulla formation, necrosis, or lymphangitis. Common causative microorganisms in the immunocompetent adult patient are *Staphylococcus aureus* or *Streptococcus pyogenes*. Anaerobes should be considered in patients with peripheral vascular disease, venous insufficiency, or diabetes. In the setting of immunosuppression (e.g., diabetes, HIV, long-term corticosteroid therapy, neutropenia, leukemia), the concern for infection with atypical or opportunistic organisms (e.g., *Nocardia*, *Cryptococcus*, or atypical mycobacteria) should be raised. While most cases can be managed medically, some patients may require surgical debridement [41].

The full extent of cellulitis is best characterized with MRI given the sensitivity of MR in depicting high T2 signal (edema) within the involved subcutaneous tissues. On T2-weighted images, a lacelike reticular pattern of hyperintense signal is often present in the subcutaneous fat [4, 42]. Small fluid collections and variable tissue enhancement can be seen after intravenous gadolinium. MRI may characterize involvement of deeper chest wall structures (e.g., muscles, joints, bones, or even pleura and lung) [4].

Bacterial infection of skeletal muscle (i.e., pyomyositis) is increasing in incidence, especially in susceptible populations (e.g., patients with diabetes or HIV). Responsible organisms are similar to those seen in cellulitis. CT and MRI reveal muscle enlargement, edema, enhancement, and frequently intramuscular abscess formation [4] (Fig. 19.12).

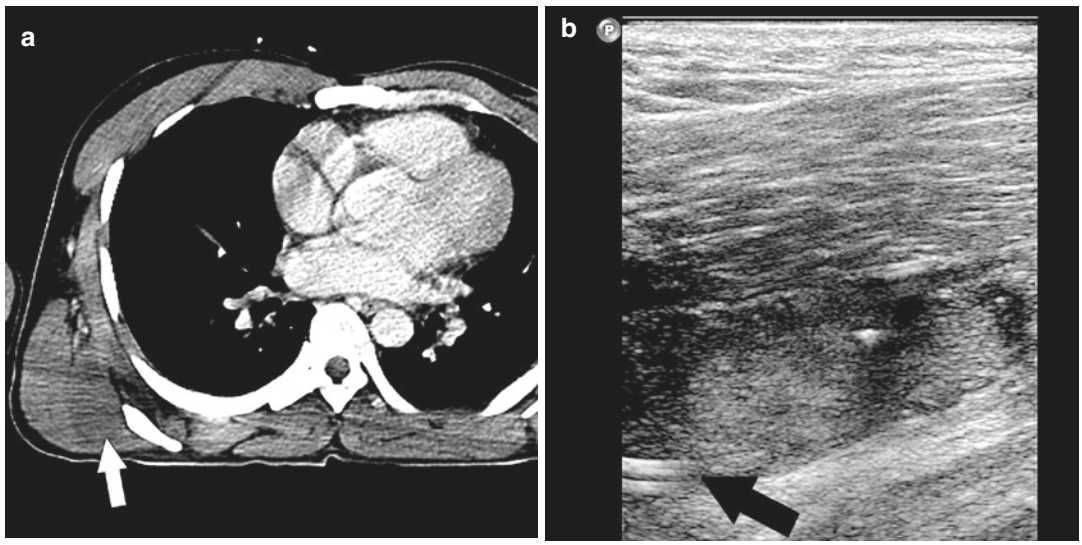


**Fig. 19.12** Pyogenic intramuscular abscess. A 34-year-old male immigrant from Uganda was hospitalized with protracted fevers, chest wall pain, and leukocytosis. Admission CT (**a**) revealed subtle enlargement and hypoattenuation in his right latissimus dorsi muscle (*white arrow*). Targeted US in this region revealed a complicated intramuscular fluid collection (*arrowhead*), consistent with abscess, which was successfully treated with antibiotics and ultrasound-guided percutaneous drainage (*arrow*, **b**). Gram stain and culture of the fluid grew methicillin-sensitive *Staphylococcus aureus* (MSSA)

Radiography frequently lacks adequate sensitivity for soft-tissue infection, but uncomplicated cellulitis may appear nonspecific soft-tissue swelling or fullness. Evidence of prior trauma or surgical intervention may be present. Retained radiopaque foreign bodies serve as a nidus for infection. Air-fluid levels within soft tissues on radiography often indicate abscess [42].

CT is frequently used instead of MRI given its availability and short imaging time, as well as for patients in whom MRI is contraindicated. While inferior to MRI, resolution of CT allows determination of the extent of infection and structures involved. Imaging features of soft-tissue infection on CT include hazy or indistinct soft-tissue planes with variable heterogeneous enhancement after intravenous contrast administration (Fig. 19.13). Phlegmon is defined as soft-tissue infiltration by purulent material. Abscesses represent discrete collections of pus within the soft tissues and are depicted as rim-enhancing, thick-walled, often complex, fluid collections. Percutaneous drainage procedures may be performed under CT or US guidance [41, 43, 44] (Fig. 19.12).

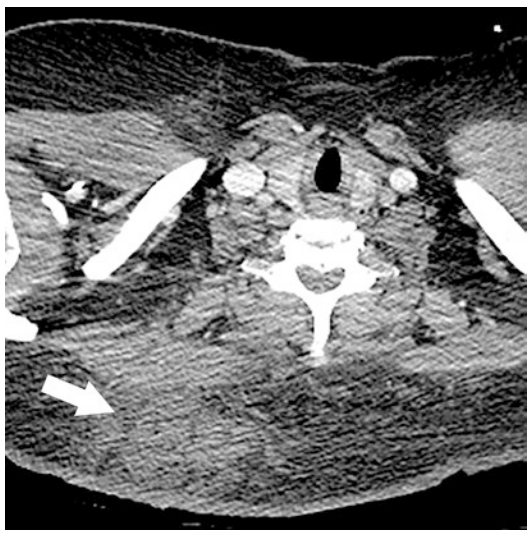

**Fig. 19.13** Cellulitis and phlegmon. CT reveals nonspecific skin thickening and inflammatory change in the posterior soft tissues of the back in this 54-year-old diabetic patient. There is no appreciable rim enhancement to suggest abscess formation

### Necrotizing Infection

Necrotizing fasciitis—a rapidly progressive deep-tissue infection—most commonly affects the perineum or abdominal wall, with rare involvement of the thorax. In most cases, chest wall-necrotizing infections occur as a complication of empyema and chest drainage procedures. Patients with these aggressive, often lethal, infections present with severe systemic infection and sepsis. Physical exam reveals dramatic chest wall pain beyond that expected by the wound's external appearance. Erythema, swelling, blistering, crepitus, and watery drainage may also be present. While no risk factors have been identified, the association of such infection is highest in patients with diabetes and other immune-compromised states [17, 45]. Most infections are polymicrobial and synergistic, with *Clostridium perfringens* and *Streptococcus* species frequently implicated. Fatal toxin release from these organisms may lead to circulatory collapse. The aggressive course of these infections explains the rate of complications, such as extension into the pleural space. Widespread involvement may also contribute to respiratory compromise and death. Rapid surgical debridement and early broad-spectrum antibiotic therapy are the mainstays of treatment. Daily debridement may be indicated until adequate source control is obtained.

Imaging features of necrotizing fasciitis are often indistinguishable from cellulitis. CT and MRI are essential in identifying deep fascial involvement or other complications of infection (vascular thrombosis, mediastinitis). CT is the most sensitive modality for the detection of deep-tissue inflammation and soft-tissue gas (Fig. 19.14). Signal voids within soft tissue on all MRI pulse sequences and areas of susceptibility on gradient echo sequences can suggest the presence of gas—a classic but variably present feature of necrotizing infection [4, 17, 42]. Importantly, the absence of soft-tissue gas does not reliably exclude necrotizing infection. Otherwise, MR findings include increased T2 signal with extension along deep fascial planes, indistinct fascial and fat planes, and tissue enhancement on T1 fat-suppressed sequences after intravenous gadolinium administration [17, 42] (Fig. 19.14). Tissue necrosis and hypoperfusion would manifest as areas of lack of enhancement.

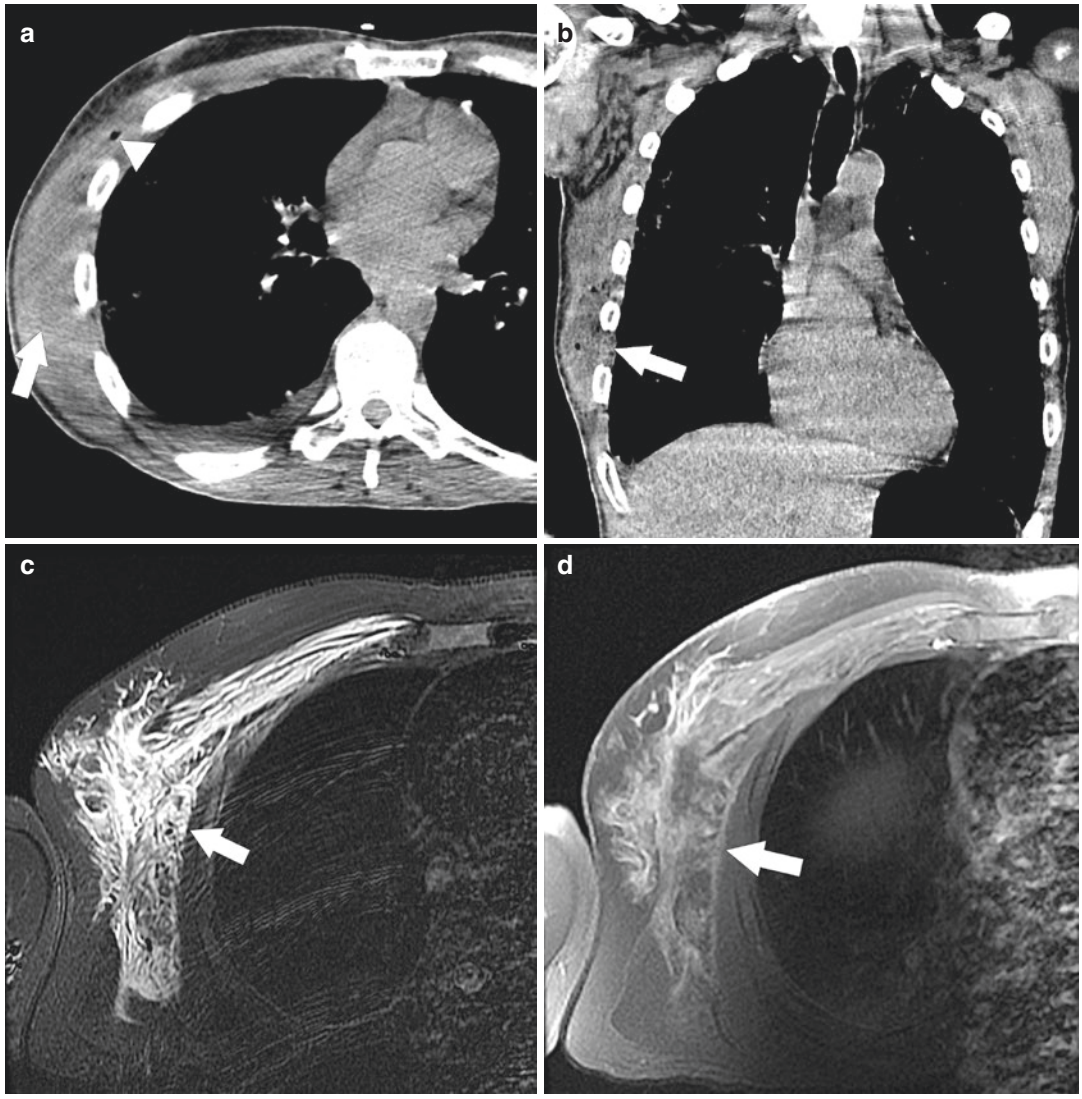


**Fig. 19.14** Necrotizing fasciitis. Axial (**a**) and coronal (**b**) CT shows nonspecific soft-tissue swelling and inflammation involving the deep fascial planes in a septic, obtunded 45-year-old male with untreated HIV and IV drug use who presented with CD4 34 cells/μL and HIV PCR viral load 166 copies/mL. Bubbles of gas were present in the inflamed deep fascia (*arrowhead*). Axial STIR (**c**) and T1-weighted, fat-suppressed post-contrast (**d**) MR in a different patient who suffered extreme immunosuppression revealed extensive edema, fascial thickening, and enhancement (*arrows*, **c** and **d**) in the deep soft tissues of the right chest wall and raised concern for necrotizing infection and the patient was ultimately treated with fasciotomy

## 19.3 Arthritides

The chest wall architecture comprises several unique articulations, each with somewhat unique anatomic and functional features. The sternoclavicular, manubriosternal, costochondral, acromioclavicular, and glenohumeral joints are comprised of variable histologic elements and are subject to several degenerative or inflammatory diseases as in other parts of the axial and appendicular skeleton. The sternoclavicular and manubriosternal joints are often overlooked on imaging, but may come to the attention of the thoracic surgeon in the perioperative assessment

prior to sternotomy, or in patients presenting with abnormalities in these regions.

### 19.3.1 Osteoarthritis

The normal manubriosternal joint undergoes histologic progressive degenerative change over the life span, beginning with conversion of manubriosternal hyaline cartilage to fibrocartilage and later ossification [37]. The fibrocartilaginous components of the joint may become variably absorbed and replaced with synovial tissue. Synostoses may form when the disk ossifies, increasing in incidence with age. The second sternocostal joint is a synovial joint which contacts the lateral aspects of the manubriosternal joint. Varying degrees of joint narrowing, sclerosis, and irregularity have been described in normal manubriosternal joints.

Degenerative changes are the most common arthritic changes of the sternoclavicular and manubriosternal joints. Many radiographic and CT features are similar with the expected normal joint changes with aging, including joint space narrowing, subchondral sclerosis and cystic change, irregularity, and ankyloses [12]. Osteophyte formation and sclerosis predominate in osteoarthrosis. Intra-articular gas—the so-called—vacuum phenomenon may be detected radiographically or on CT. Similarly, patients with diffuse idiopathic skeletal hyperostosis (DISH) may demonstrate exuberant, large osteophytes and joint space flaring and wedging [37].

Lateral and oblique radiographs depict the joint to some advantage, but may be limited by rotation. Multiplanar CT in the sagittal and coronal planes is superior to radiography in depicting the joint (Fig. 19.15). Ultrasound findings of osteoarthritis of the sternoclavicular, manubriosternal, and costochondral junctions include most commonly capsular thickening, as well as echogenic marginal osteophyte and joint space narrowing [38]. Bone scintigraphy is less reliable in assessment of the sternum, as increased radiotracer uptake can be seen in non-inflamed sternoclavicular and manubriosternal joints [37]. MRI is less useful in depicting the normal anatomy of the joint, but is very sensitive to detection of bone marrow changes and surrounding soft-tissue involvement by inflammatory processes.

### 19.3.2 Inflammatory

#### 19.3.2.1 Costochondritis

Costochondritis (inflammation of the costal cartilages) may be from sterile inflammation or infectious agents (*Staphylococcus, Streptococcus, Candida,* or Aspergillus species). Its incidence is increasing with the widespread abuse of IV drugs [46]. Painful chest wall abnormalities are easily evaluated with targeted ultrasound, where costochondritis may manifest as ill definition and swelling of the affected cartilage with some perichondral fluid signal (edema) [38]. Radiographic features included cartilaginous expansion, fragmentation, or adjacent bone destruction. CT findings include low attenuation of the cartilage with or without adjacent soft-tissue inflammatory changes often with localized peripheral calcification [46, 47]. Bone scintigraphy may also be used to define the extent of radiographically occult costochondritis. Tietze syndrome is a unique painful costochondritis appearing as swelling, dystrophic calcification, degenerative change, and osteophytosis of upper costochondral junctions, likely a result of recurrent anterior chest wall microtrauma.

##### Rheumatoid Arthritis (RA)

Imaging features of RA of the sternoclavicular and manubriosternal joints may be indistinguishable from osteoarthritis, but are generally more severe. Patients may be asymptomatic but exhibit markedly abnormal imaging findings. Typically, erosions along the articular surfaces predominate (Fig. 19.15), primarily affecting the synovium of the second sternocostal or manubriosternal joints [37]. These features are also indistinguishable from those in patients with reactive arthritis and other seronegative spondyloarthropathies. Contrast-enhanced MRI using fat-suppressed T1-weighted sequences allows for quantification of synovial volume and enhancement. MR

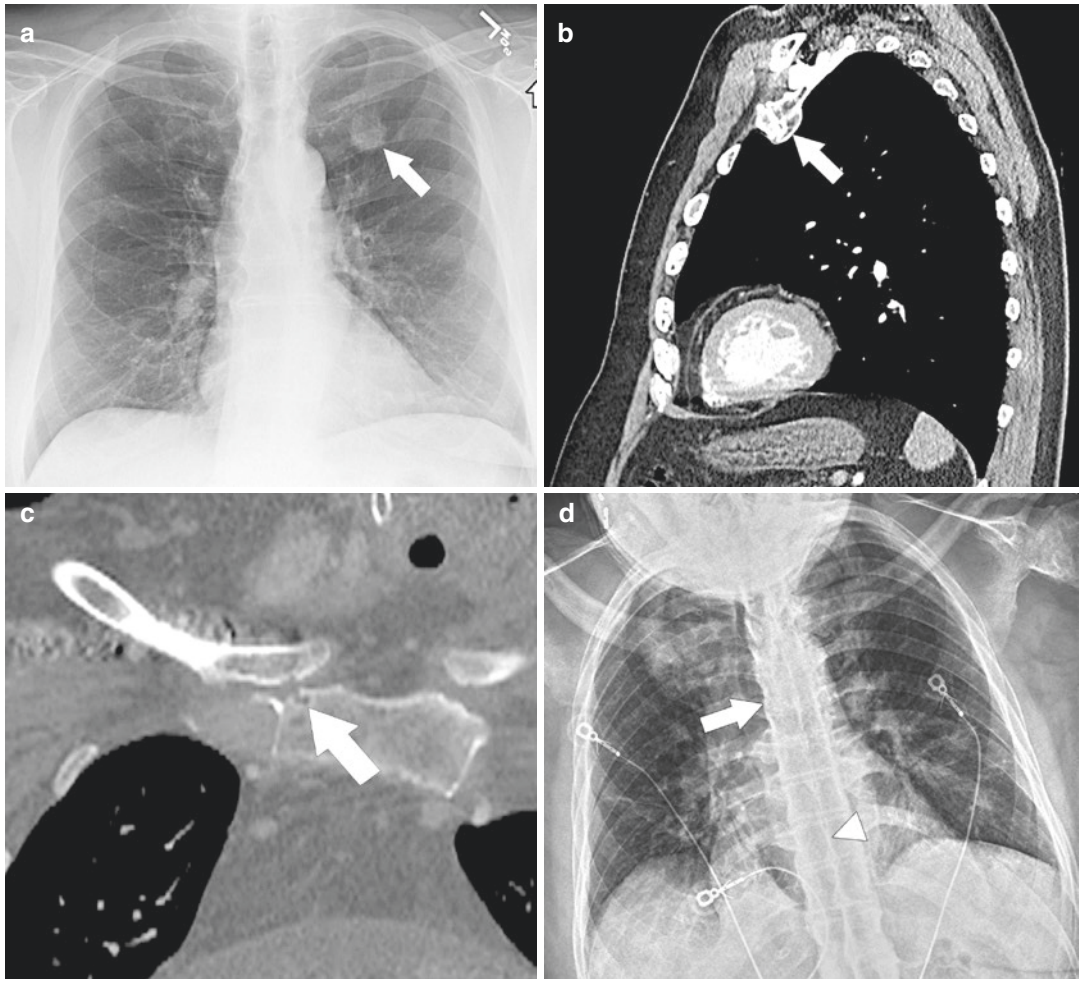


**Fig. 19.15** Chest wall arthritides. (**a**) Posterior-anterior chest radiograph reveals a dense rounded opacity projecting over the left upper lung zone (*arrow*), which raised concern for an underlying lung cancer. (**b**) Sagittal contrast-enhanced CT showed no lung mass, but detailed marked degenerative osteoarthritis and osteophyte formation involving the left costochondral articulation (*arrow*). (**c**) Joint space erosion (*arrow*) and periarticular inflammation is present in the right sternoclavicular joint in the patient with long-standing rheumatoid arthritis. (**d**) Anterior–posterior chest radiograph reveals bridging syndesmophytes (*arrow*) and interspinous ligament calcification (*arrowhead*), which respectively create the "bamboo spine" and "dagger sign" radiographic descriptors associated with ankylosing spondylitis. (**e**) Sagittal CT in a different patient depicts the thin syndesmophytes (*arrow*) formed in the spine, a specific feature of ankylosing spondylitis. (**f**, **g**) Sheetlike chest wall calcifications (*arrows*) involve the deep fascia in this patient with dermatomyositis

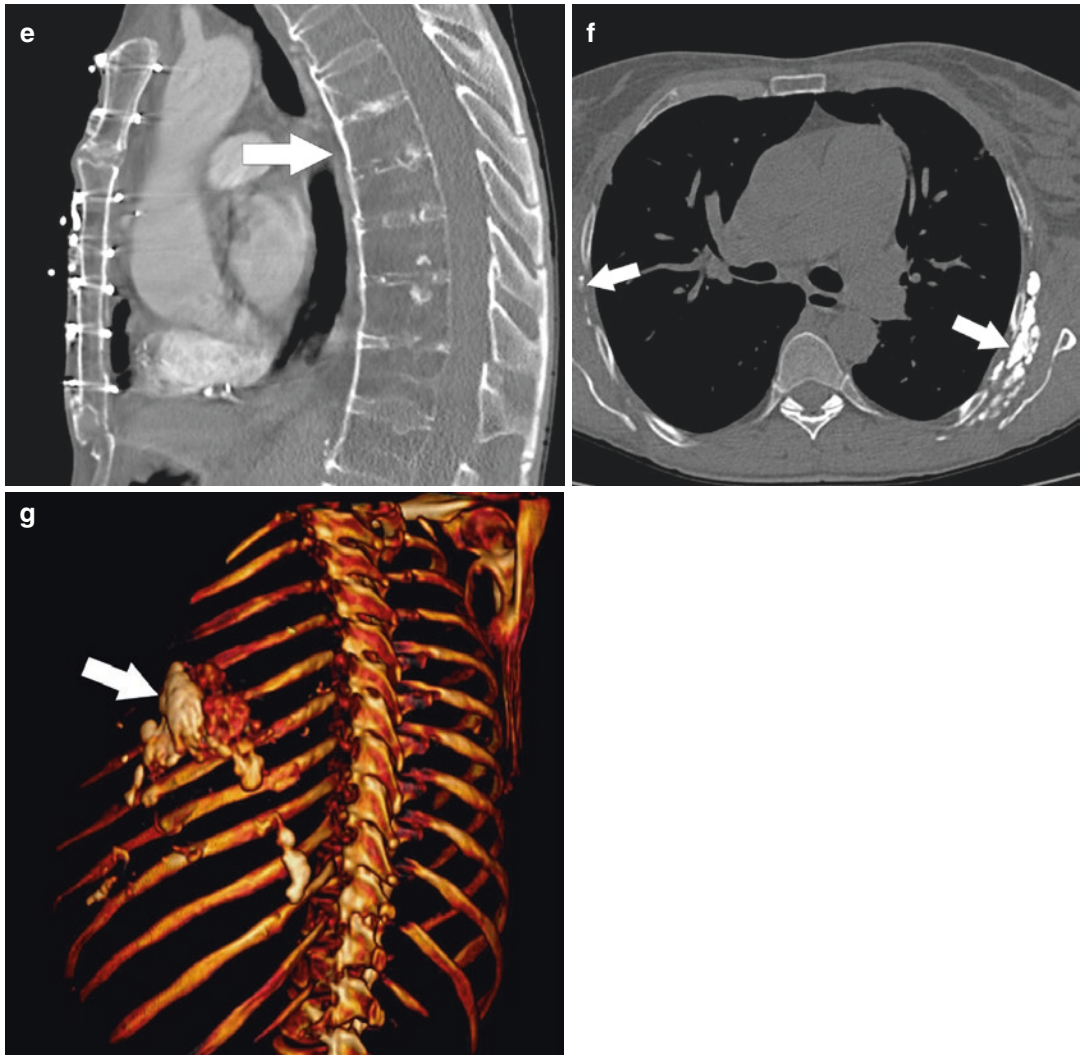


**Fig. 19.15** (continued)

best depicts associated findings of bone marrow edema and enhancement [12].

### Ankylosing Spondylitis, Dermatomyositis

Imaging features of ankylosing spondylitis include osseous expansion, joint erosion, and ankylosis, with ankylosis as a predominant feature [37]. Bridging syndesmophytes and ankylosis of facets are consistent features of ankylosing spondylitis (Fig. 19.15) forming a rigid spine, often referred as the bamboo spine, which is at increased risk for fractures, even from minor trauma. Fusion and erosion are the most common imaging features of psoriatic arthritis of the sternal joints, occurring in nearly 100% of cases. In addition to joint erosions, a characteristic manifestation of dermatomyositis is the formation of sheets of calcification along fascial planes (Fig. 19.15).

### 19.3.3 Crystalline Deposition Disease

#### 19.3.3.1 Gout

Gout rarely affects the sternum, and imaging findings are often nonspecific, overlapping with those of degenerative change [37]. Rarely, gouty tophus may be seen. Imaging features include juxta-articular erosion and marginal bony deposition creating the classically described "overhanging edge" [12]. Acute inflammation is shown on MRI as increased periarticular T2 signal with enhancement.

#### 19.3.3.2 Calcium Pyrophosphate Dehydrate Deposition Disease (CPPD)

CPPD may be deposited in the joint capsules of the sternum or ribs, with imaging features similar to those of osteoarthritis [37]. Calcifications within the cartilage (chondrocalcinosis) and articular disks of the sternoclavicular joints may be present on radiographs or CT. Rarely, periarticular soft-tissue calcifications (pseudogout) may be present [12].

## 19.4 Metabolic Disorders

### 19.4.1 Osteopenia and Osteoporosis

Low bone density is common among the elderly, as well as patients with predisposing conditions (inactivity, chronic inflammatory conditions, chronic renal failure, chronic corticosteroid therapy, COPD, estrogen deficiency, among others). Bone density is routinely measured with dual-energy X-ray absorptiometry (DXA) scans in at-risk populations. Loss of bony trabeculae is the histologic hallmark of osteoporosis, which leads to weakening of the bone and predisposition to insufficiency fractures. Sternal insufficiency fractures (SIF) have been described in the setting of osteoporosis, thought related to a combination of low bone mass and abnormal stresses on the sternum from exaggerated thoracic kyphosis (also found commonly in osteoporotic patients) (Fig. 19.16). Forceful coughing may also result in SIF [48–50]. Radiographic and CT evaluations classify SIF as either buckling or non-buckling based on absent cortical disruption, callus formation, or localized bone resorption in the former and posterior position of the upper part of the sternum in the latter [48] (Fig. 19.16). Non-buckling fractures are further subdivided into displaced (cortical offset of >25% of the width of the sternum on lateral radiographs) or non-displaced. Chest pain is the most common symptom at presentation. However, patients with buckling SIF are frequently asymptomatic.

### 19.4.2 Renal Osteodystrophy

Renal osteodystrophy refers to musculoskeletal alterations that are found in association with chronic renal insufficiency and treatments thereof, all of which involve complex metabolic alterations of calcium, phosphate, and vitamin D. Modern advances in the care related to chronic renal disease (i.e., hemodialysis and renal transplantation) have led to an increase in the incidence of these disorders on routine thoracic imaging. Radiographic manifestations classically include subperiosteal, subchondral, and subligamentous bone resorption/osteolysis which commonly occur in the sternoclavicular and acromioclavicular joints, as well as intervertebral disks and coracoclavicular ligamentous insertions [51]. Diffuse osteosclerosis results from a combination of effects from renal osteodystrophy and secondary hyperparathyroidism, frequently visualized in the axial skeleton as subendplate osteosclerosis with normal density of the middle of the vertebral body, the so-called rugger-jersey spine (Fig. 19.16). Osteoporosis is frequently found in patients with chronic renal disease, predisposing to thoracic vertebral compression fractures.

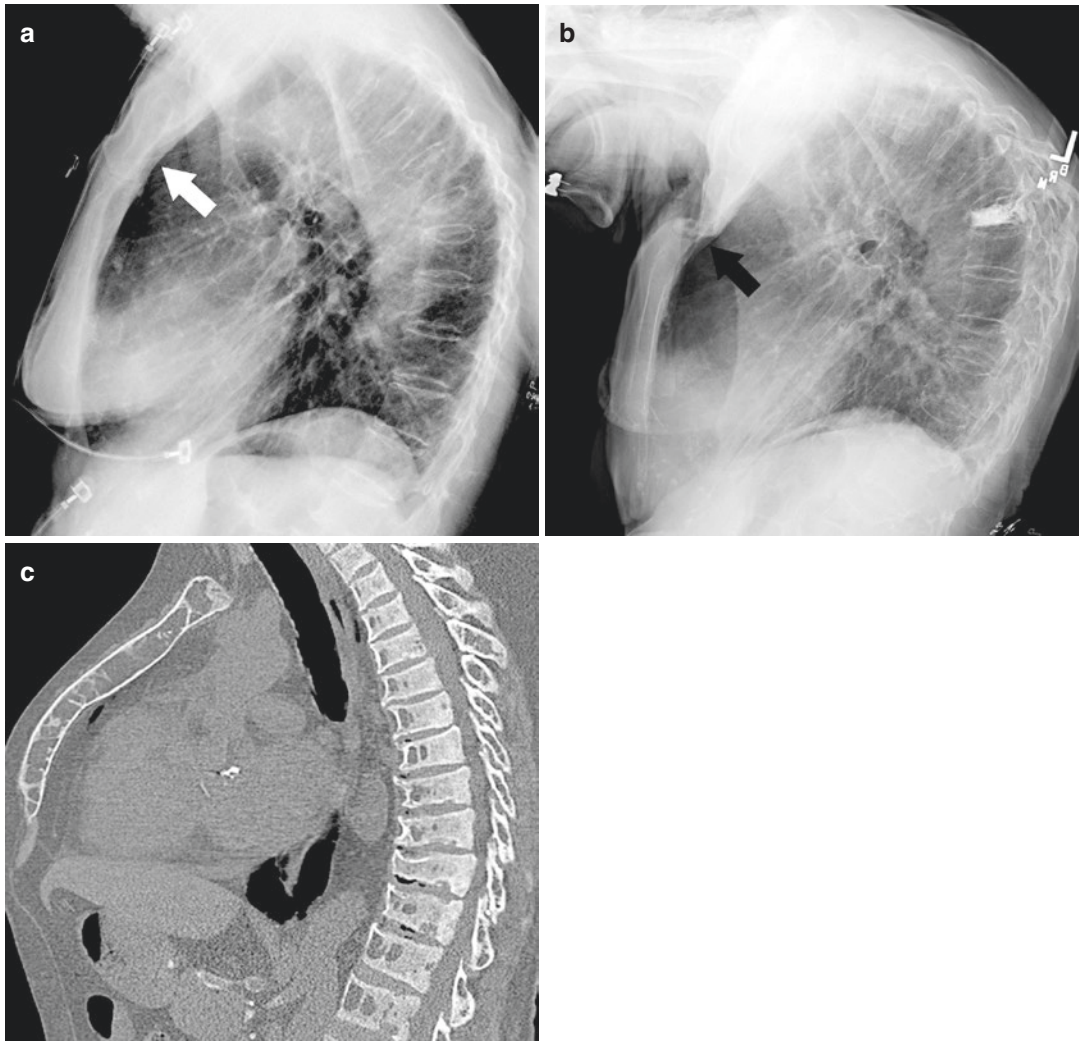


**Fig. 19.16** Metabolic disorders of the chest wall. (**a**) Lateral chest radiograph in an 80-year-old patient with chest pain reveals diffuse osteopenia and an acute compression deformity of a midthoracic vertebral body. The patient's sternum is intact (*white arrow*). (**b**) Lateral chest radiograph from the same patient performed 2 years later shows vertebral augmentation of the compressed vertebral body, new compression deformities, progressive kyphosis, and development of a posteriorly displaced nonbuckling fracture of the manubrium (*black arrow*) and subtle buckling fracture of the upper sternal body. (**c**) Sagittal chest CT reveals diffuse osteosclerosis involving the vertebral bodies, as well as marrow expansion in the sternum in a patient on hemodialysis for chronic renal failure, consistent with renal osteodystrophy

## 19.5 Congenital

Congenital malformations of the chest wall and ribs are often found in association with spinal anomalies, most commonly scoliosis [52]. Most occur in succession of a failure of embryologic segmentation and formation of ribs from developing somites. Embryological development of the ribs, scapulae, and spine is closely linked with the scapulae and arms developing from primitive arm buds—lateral swellings along the C5 through T1 vertebral bodies during the third week of gestation. The scapulae form from the arm bud mesenchyme and migrate inferiorly to their posterolateral locations behind the second through eighth ribs.

### 19.5.1 Sternum

The origins of developmental anomalies of the sternum are generally regarded as sequelae either of (1) dysmorphic costal cartilage growth (pectus excavatum and pectus carinatum) or (2) an embryologic failure of the developing sternum (sternal cleft, sternal foramen, etc.).

#### 19.5.1.1 Pectus Excavatum (Funnel Chest, Trichterbrust)

Pectus excavatum is the most common developmental sternal deformity, present in up to 1:400 live births [12, 53], with a marked male predominance of 5:1. It occurs as a result of rapid overgrowth of the lower costal cartilages, resulting in posterior displacement of the sternum and anterior positioning of the ribs. The retrosternal space is often markedly reduced with leftward displacement and rotation of the heart and reduced left lung volumes from mass effect. Pectus excavatum is often an isolated finding without a known genetic causation, but up to 45% show a familial pattern. The condition is found in association with other genetic disorders such as Marfan, Ehlers-Danlos, Loeys-Dietz, Poland, and Klippel-Feil syndromes. Also, it is not uncommon to encounter pectus excavatum in patients with bronchiectatic non-tuberculosis mycobacterial infection. Other conditions may coexist such as syndactylism, club foot, scoliosis, osteogenesis imperfecta, mitral valve prolapse, and other congenital heart diseases.

Besides the obvious cosmetic and psychological effects of pectus excavatum, there remains controversy as to the physiologic effect of sternal depression on cardiopulmonary function [12, 53]. Patients may present with exertional dyspnea, reduced exercise tolerance, angina, palpitations, wheezing, and recurrent upper respiratory infections. Pulmonary function testing (PFT) in these patients may reveal a restrictive pulmonary pattern, with diminished total lung capacity, forced vital capacity, and vital capacity—the severity of which may increase with more severe sternal depression. Several studies have suggested that exercise intolerance may be related to sternal compression, impaired filling of the right heart chambers, and reduced stroke volume [53].

The degree of sternal depression can be classified based on physical appearance as localized and symmetric (type I), diffuse and symmetric (type II), and asymmetric diffused or localized (type III). When surgery is contemplated, imaging remains a useful tool for pectus excavatum characterization and surgical planning. Chest radiographs (posteroanterior and lateral) and CT are usually sufficient. A fronto-sagittal thoracic index ("Welch index") can be measured radiographically. Others report utility of the lateral radiograph in establishment of a configuration index—a ratio of the lower vertebral index (depth of the thorax at the xiphisternal junction) and the upper vertebral index (thoracic depth at the sternomanubrial junction). CT is frequently employed for presurgical planning for pectus excavatum, with measurement of the Haller index. The Haller index is derived from an axial CT image through the deepest part of sternal depression. A ratio of the transverse thoracic diameter (width of chest between the lateral ribs) is divided by the anteroposterior diameter (anterior part of spine to lowest part of sternal depression) at the same level [53, 54]. A normal index is $2.56 \pm 0.35$. Ratio of more than 3.25 is associated with an increased need for operative intervention (Fig. 19.17).

#### 19.5.1.2 Pectus Carinatum (Pigeon Breast, Chicken Breast, Pouter Chest, Pyramidal Chest)

In pectus carinatum (PC), the sternum is displaced anteriorly, and occurs five to six times less frequently than pectus excavatum. Like pectus excavatum, there is a strong male predominance, and the defect is usually isolated. However, a family history of chest wall anomalies may be present. Furthermore, pectus carinatum may coexist with cardiac anomalies and scoliosis. Patients are usually asymptomatic, but may complain of angina, exertional dyspnea, and poor exercise tolerance. The effects of pectus carinatum on pulmonary function are less clear than in pectus excavatum, but poor exercise tolerance is believed to result from

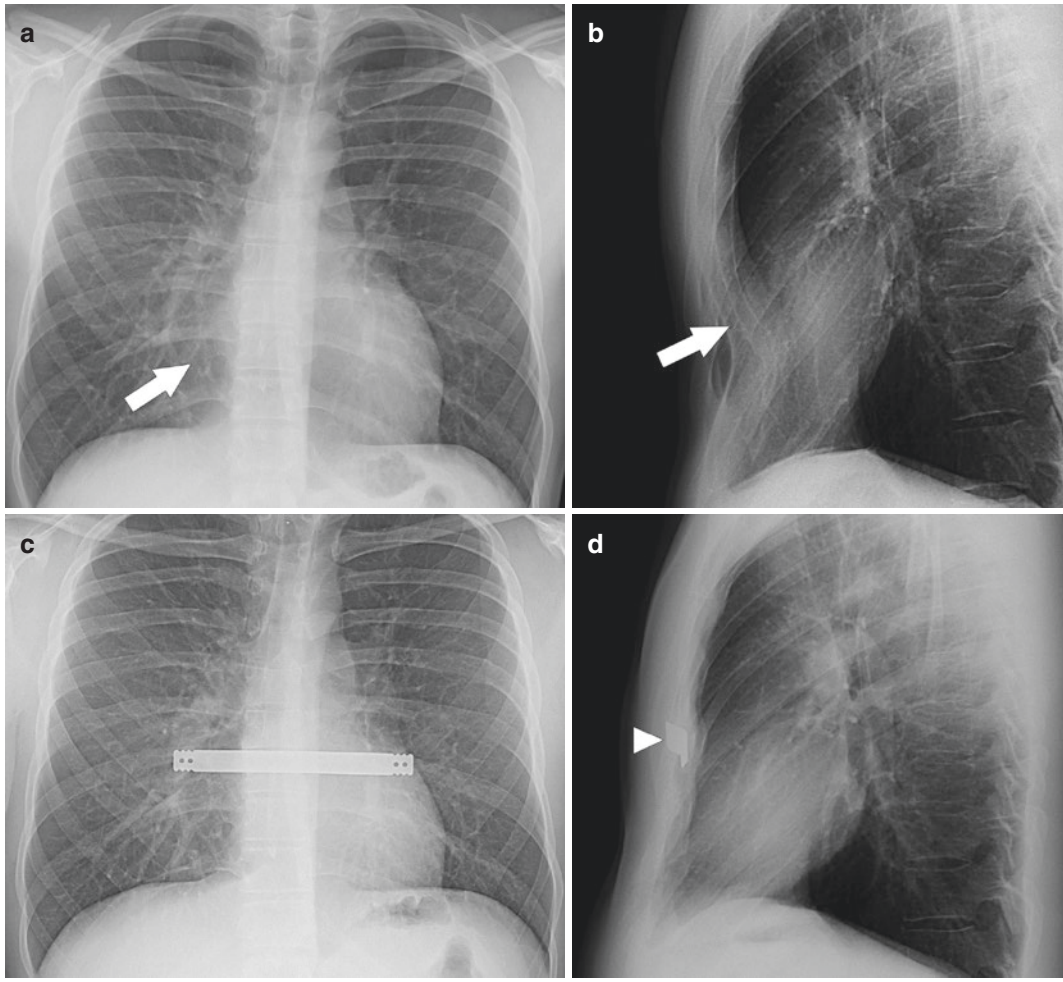


**Fig. 19.17** Pectus excavatum and pectus carinatum. A 26-year-old male United States Air Force recruit presented with intermittent pleuritic anterior chest pain and dyspnea on exertion. (**a**) Posterior-anterior chest radiograph shows obscuration of the right-heart border (*arrow*), simulating right middle lobe airspace disease. (**b**) Lateral chest radiograph in the same patient shows marked xiphisternal depression with compression of the heart (*arrow*). The patient underwent subsequent Nuss procedure with placement of an Adkins strut (*arrowhead*, **d**), which improved the degree of sternal depression and mass effect on the heart (**c**, **d**). (**e**) A preoperative chest CT was performed to measure the degree of sternal depression (Haller index = 3.9). (**f**) Lateral chest radiograph depicts marked sternal protrusion (*arrow*), consistent with pectus carinatum. (**g**) Marked anterior bowing of the upper sternal body and manubriosternal joint (*arrow*) in this dyspneic 19-year-old female is consistent with the pouter chest variant of pectus carinatum.

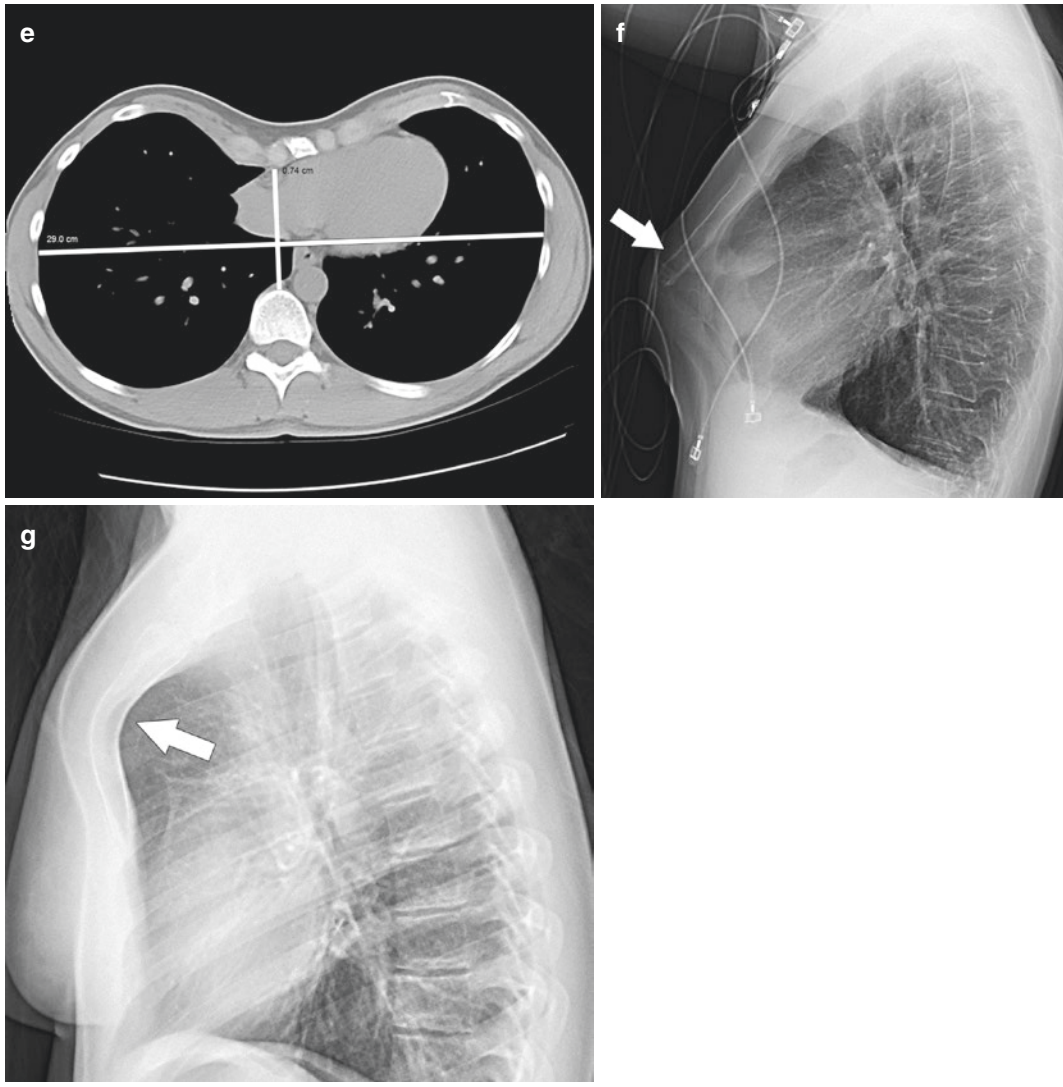


**Fig. 19.17** (continued)

abnormal thoracic movement during the respiratory cycle, leading to tachypnea and diaphragmatic breathing, and eventually to fatigue [53].

A rare subtype of pectus carinatum manifests with marked enlargement and protrusion of the second costal cartilages and sternomanubrial joint (the so-called pouter chest) (Fig. 12.17). Elevation of the adjacent costal cartilages on either side of the sternomanubrial joint contributes to a U-shaped deformity of the anterior chest wall [54].

Physical examination usually reveals the defect pattern, classified as chondrogladiolar (type I, keel chest)—protrusion of the gladiolus and inferior cartilages; chondromanubrial (type II, pigeon breast)—prominence of the superior costal cartilages; and lateral PC (type III)—asymmetric deformity with unilateral sternal protrusion or rotation [53]. Chest radiography and CT can further document the severity of PC with pectus severity index of 1.2 to 2 being associated with operative repair [12].

#### 19.5.1.3 Tilted Sternum

When the longitudinal orientation of the sternum deviates to the right or left of midline it is referred to as tilted. The resultant chest wall deformity can be found in association with anterior convex ribs or an anteriorly subluxed sternoclavicular joint [12]. Depending on the severity of tilt, these anomalies are usually incidental, and surgical consultation is usually reserved for cosmetic purposes. CT is the preferred modality for evaluation of the tilted sternum, primarily for presurgical planning and excluding underlying neoplasm as a cause for the palpable abnormality.

#### Sternal Bands and Clefts

The sternum is formed from enchondral ossification and midline fusion of two longitudinal bars of lateral plate mesoderm (sternal bars) oriented in a craniocaudal direction. The more common sternal band appears as a line of sclerosis along the midline embryologic cleavage plane and is usually of no clinical significance (Fig. 19.18). Bands may be seen in association with sternal clefts, which are midline defects in the sternum from failure of osseous fusion. Seventy-five percent of sternal clefts were found in female subjects in one large series [53]. Unlike bands, sternal clefts are more often found in association with other congenital abnormalities such as ectopia cordis and pentalogy of Cantrell. Clefts may result in paradoxical movement of the chest during respiration, which some believe to contribute to symptoms of dyspnea, cyanosis, and recurrent pneumonia, which justifies their frequent surgical repair. Sternal bands and clefts may be found in any part of the sternum, except that bands are not found in the xiphoid process. Axial and coronal CT best characterizes these anomalies as incomplete or complete, and their associations with orthotopic heart and ectopia cordis, respectively. Sternal clefts may rarely be seen in association with various vascular malformations such as craniofacial hemangioma, aneurysm of the ascending thoracic aorta, or obliteration of the brachiocephalic artery.

#### Sternal Foramen

Sternal foramina are found in 5% of the population, and appear as a "bow-tie" osseous defect on axial CT [12] (Fig. 19.18). Associated sternal bands and clefts may also be present. Radiologists should alert surgeons to the presence of sternal foramina in patients who may undergo sternal intervention (e.g., interosseous access or bone marrow aspiration) as fatal hemorrhage and cardiac tamponade may result.

#### 19.5.1.4 Episternal Ossicles

Supernumerary ossification centers about the manubrium may result in the presence of unilateral or bilateral, pyramid-shaped accessory bones, usually 2–15 mm in size (Fig. 19.18). These are detected in 1.5% of the population, and most commonly found on CT [12]. These should be differentiated from mimics such as atherosclerotic vascular calcifications, calcified lymph nodes, fractures, and foreign bodies. As other bones, they typically exhibit a well-defined and sclerotic cortex.

### 19.5.2 Ribs

Rib anomalies may be classified as *simple* or *complex* relative to the extent and number of rib fusions, rib absence, chest wall defects, or general pattern of rib anomalies [52]. Most rib anomalies are simple (80%), manifest as localized fusion of 2–3 ribs. Complex rib anomalies frequently coincide with large chest wall defects. Rib anomalies are found in nearly 20% of patients with congenital deformities of the spine, and occur more commonly in females (2.5:1). Both simple and complex rib anomalies tend to occur on the concave side of associated thoracic or thoracolumbar scoliosis, most commonly associated with unilateral vertebral segmentation failure. Early detection of rib anomalies is important, as such deformities might lead to scoliotic curve progression and may assist in early planning of prophylactic treatment for these patients.

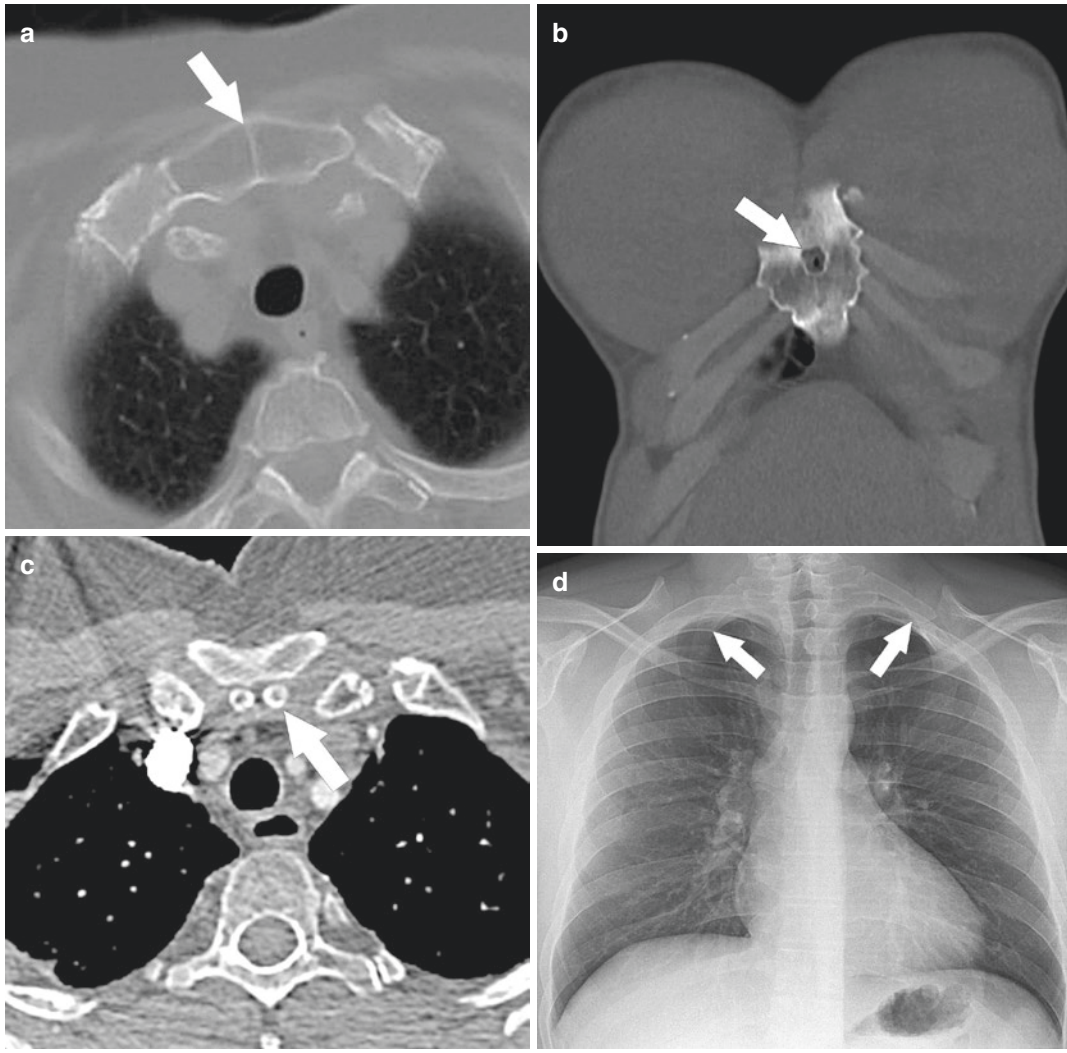


**Fig. 19.18** Congenital chest wall deformities. (**a**) Incidentally detected sternal band on CT shows a line of sclerosis along the embryologic fusion plane. (**b**) Variably sized sternal foramina (*arrow*) are common. The presence of a sternal foramen should be known prior to intraosseous access or bone marrow aspiration procedures to prevent life-threatening cardiac injury. (**c**) Episternal ossicles (*arrow*) are normal structures occasionally seen near the manubrium on routine chest CT, and are of no clinical significance, but may simulate other processes. (**d**) Variably sized supernumerary (cervical) ribs (*arrows*) may be found incidentally on routine chest imaging, but can occasionally contribute to symptoms of thoracic outlet syndrome, which may require surgical intervention. (**e**) Coronal MIP and (**f**) 3D volume-rendered contrast-enhanced CT delineates extensive right shoulder venous collaterals from chronic compression of the right subclavian vein (*arrows*). (**g**) Frontal chest radiograph depicts complete absence of the clavicles (*arrows*) in this patient with cleidocranial dysostosis. (**h**) Asymmetric elevation of the right scapula (*arrow*) was detected incidentally in this patient with Sprengel deformity. An omovertebral fibro-osseous connection, though classically described, was absent in this patient and is only present in 25% of cases. (**i**) Complete absence of the right pectoral muscle (*arrow*) was detected on chest CT in this patient with Poland syndrome

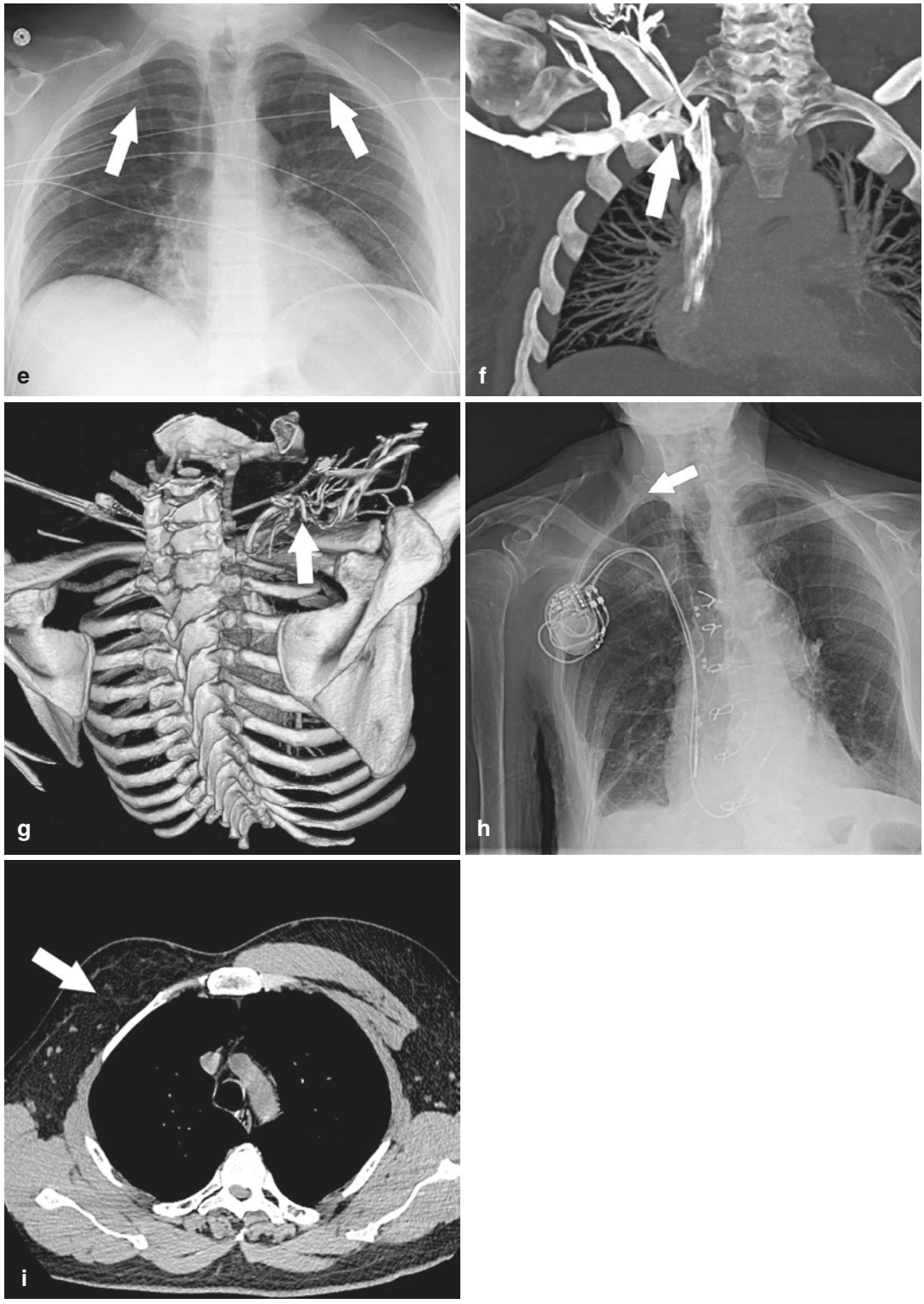


**Fig. 19.18** (continued)

*Cervical rib (anomalous accessory rib, "Eve's rib")*. Supernumerary ribs may develop from the C7 vertebrae, and are defined as the presence of a rib with a distinct articulation with a horizontally oriented (cervical type) transverse process. The size of the rib is variable, and larger ribs may cause thoracic outlet syndrome from compression of the neurovascular structures along the thoracic outlet, leading to symptoms of arm pain and weakness, hand swelling, and positional variation in pulse intensity between the upper extremities. Cervical ribs may be detected on chest radiography and must be distinguished as supernumerary by identification of the true second rib and its reliable anterior articulation with the manubriosternal junction (Fig. 19.18). CT angiography can provide noninvasive anatomic detail related to thoracic outlet anatomy and anomalous rib (Fig. 19.18). Dynamic fluoroscopic angiography and Doppler US can document compression of the subclavian artery by the cervical rib between upper extremity adduction and abduction, confirming the diagnosis [19, 55].

### 19.5.3 Clavicle

*Cleidocranial dysostosis* Cleidocranial dysostosis is the most common congenital anomaly of the clavicle. It manifests as incomplete ossification, with associated defects in vertebral, long bone, and pubic bone development. The clavicles are usually underdeveloped, with residual hypoplastic segments, but may be completely absent [19, 56] (Fig. 19.18).

### 19.5.4 Scapulae

*Sprengel deformity*. Congenital elevation of the scapula (Sprengel deformity) is a rare consequence of congenital interruption in the caudal descent of the scapula in early development. The presence of an omovertebral fibro-osseous connection between the cervical spine and scapula is classically associated, occurring in 20–25% of cases. A hypoplastic, elevated scapula (Fig. 19.18) results in altered range of motion to the affected extremity in addition to cosmetic consequences that may worsen with continued growth of the child [57]. Sprengel deformity may be seen in association with other vertebral and rib anomalies, and is present in 20-42% of patients with Klippel-Feil syndrome [58]. This condition is generally surgically repaired early in life (2–5 years) using various techniques. The degree of scapular deformity may be graded radiographically using the Rigault classification, using the craniocaudal position of the superomedial angle of the clavicle on AP radiographs. The deformity is considered grade 1 when the superomedial angle of the scapula projects above the T4 transverse process, grade 2 when located between C5 and T2, and grade 3 when positioned above C5 [57, 59]. 3D CT reformations may assist the surgeon in preoperative planning.

### 19.5.5 Soft Tissues

#### 19.5.5.1 Poland Syndrome

Rarely, the sternal portion of the pectoralis major muscle may be congenitally absent or hypoplastic from failed mesodermal development in a quadrant of the fetus, the so-called Poland syndrome. The clavicular portion of the pectoralis muscle is typically spared. The anomaly is most commonly right sided. Other associations in this syndrome include ipsilateral syndactyly, ipsilateral simian crease, aplastic ipsilateral breast tissue, absence or hypoplasia of the pectoralis minor muscle, and absence or hypoplasia of the ipsilateral second through fifth ribs [19]. Relative hyperlucency of the affected hemithorax is found on chest radiography, while CT better defines the extent of musculoskeletal involvement [54] (Fig. 19.18).

**Conclusion**

Nonneoplastic chest wall lesions often come to the attention of the thoracic surgeon. Comprehensive imaging of any chest wall lesion is integral to lesion characterization, detection of concomitant intrathoracic conditions, and direction of operative or nonoperative patient management.

## References


1. Lomoschitz FM, Eisenhuber E, Linnau KF, Peloschek P, Schoder M, Bankier AA. Imaging of chest trauma: radiological patterns of injury and diagnostic algorithms. Eur J Radiol. 2003;48:61–70. https://doi.org/10.1016/S0720-048X(03)00202-X.
2. Battle C, Hutchings H, Evans PA. Blunt chest wall trauma: a review. Dent Traumatol. 2013;15:156–75. https://doi.org/10.1177/1460408613488480.
3. Sangster GP, González-Beicos A, Carbo AI, Heldmann MG, Ibrahim H, Carrascosa P, Nazar M, D'Agostino HB. Blunt traumatic injuries of the lung parenchyma, pleura, thoracic wall, and intrathoracic airways: multidetector computer tomography imaging findings. Emerg Radiol. 2007;14:297–310. https://doi.org/10.1007/s10140-007-0651-8.
4. Lee TJ, Collins J. MR imaging evaluation of disorders of the chest wall. Magn Reson Imaging Clin N Am. 2008;16:355–79. https://doi.org/10.1016/j.mric.2008.03.001.
5. Palas J, Matos AP, Mascarenhas V, Herédia V, Ramalho M. Multidetector computer tomography: evaluation of blunt chest trauma in adults. Radiol Res Pract. 2014;2014:1–12. https://doi.org/10.1155/2014/864369.
6. Peters S, Nicolas V, Heyer CM. Multidetector computed tomography-spectrum of blunt chest wall and lung injuries in polytraumatized patients. Clin Radiol. 2010;65:333–8. https://doi.org/10.1016/j.crad.2009.12.008.
7. Rainer TH, Griffith JF, Lam E, Lam PKW, Metreweli C. Comparison of thoracic ultrasound, clinical acumen, and radiography in patients with minor chest injury. J Trauma Inj Infect Crit Care. 2004;56:1211–3. https://doi.org/10.1097/01.TA.0000075800.65485.48.
8. Turk F, Kurt AB, Saglam S. Evaluation by ultrasound of traumatic rib fractures missed by radiography. Emerg Radiol. 2010;17:473–7. https://doi.org/10.1007/s10140-010-0892-9.
9. Nummela, M.. The incidence and effect on mortality of costochondral fractures in blunt polytrauma patients-a review of 1461 consecutive whole body CT studies for trauma. Radiological Society of North America 2016 Scientific Assembly and Annual Meeting, Chicago, IL; 2016. archive.rsna.org/2016/16002567.html.
10. Melenevsky Y, Yablon CM, Ramappa A, Hochman MG. Clavicle and acromioclavicular joint injuries: a review of imaging, treatment, and complications. Skeletal Radiol. 2011;40:831–42. https://doi.org/10.1007/s00256-010-0968-3.
11. Groves CJ, Cassar-Pullicino VN, Tins BJ, Tyrrell PNM, McCall IW. Chance-type flexion-distraction injuries in the thoracolumbar spine: MR imaging characteristics. Radiology. 2005;236:601–8. https://doi.org/10.1148/radiol.2362040281.
12. Restrepo CS, Martinez S, Lemos DF, Washington L, McAdams HP, Vargas D, Lemos JA, Carrillo JA, Diethelm L. Imaging appearances of the sternum and sternoclavicular joints. Radiographics. 2009;29:839–59. https://doi.org/10.1148/rg.293055136.
13. O'Brien SD, Bui-Mansfield LT. Costovertebral fracture dislocations: important radiographically difficult diagnosis. J Comput Assist Tomogr. 2009;33:748–51.
14. Kishen TJ, Mohapatra B, Diwan AD, Etherington G. Post-traumatic thoracic scoliosis with rib head dislocation and intrusion into the spinal canal: a case report and review of literature. Eur Spine J. 2010;19:183–6. https://doi.org/10.1007/s00586-010-1321-1.
15. Nguyen BM, Plurad D, Abrishami S, Neville A, Putnam B, Kim DY. Utility of chest computed tomography after a "normal" chest radiograph in patients with thoracic stab wounds. Am Surg. 2015;81:965–8.
16. McCarthy EF, Sundaram M. Heterotopic ossification: a review. Skeletal Radiol. 2005;34:609–19. https://doi.org/10.1007/s00256-005-0958-z.
17. Hayeri MR, Ziai P, Shehata ML, Teytelboym OM, Huang BK. Soft-tissue infections and their imaging mimics: from cellulitis to necrotizing fasciitis. Radiographics. 2016;36:1888–910. https://doi.org/10.1148/rg.2016160068.
18. Kuhlman JE, Bouchardy L, Fishman EK, Zerhouni EA. CT and MR imaging evaluation of chest wall disorders. Radiogr Rev Publ Radiol Soc N Am Inc. 1994;14:571–95. https://doi.org/10.1148/radiographics.14.3.8066273.
19. Jeung MY, Gangi A, Gasser B, Vasilescu C, Massard G, Wihlm JM, Roy C. Imaging of chest wall disorders. Radiogr Rev Publ Radiol Soc N Am Inc. 1999;19:617–37. https://doi.org/10.1148/radiographics.19.3.g99ma02617.
20. Restrepo CS, Giménez CR, McCarthy K. Imaging of osteomyelitis and musculoskeletal soft tissue infections: current concepts. Rheum Dis Clin North Am. 2003;29:89–109.
21. Blasberg JD, Donington JS. Infections and Radiation Injuries Involving the Chest Wall. Thorac Surg Clin. 2010;20:487–94. https://doi.org/10.1016/j.thorsurg.2010.06.003.
22. Chelli Bouaziz M, Jelassi H, Chaabane S, Ladeb MF, Ben Miled-Mrad K. Imaging of chest wall infections. Skeletal Radiol. 2009;38:1127–35. https://doi.org/10.1007/s00256-008-0636-z.
23. Elahi MM, Mitra A, Spears J, Tariq GB, McClurken JB. Aspergillus chest wall osteomyelitis: surgical and medical management. Eur J Plast Surg. 2004;26:425–9. https://doi.org/10.1007/s00238-003-0584-8.
24. Pineda C, Vargas A, Rodríguez AV. Imaging of osteomyelitis: current concepts. Infect Dis Clin North Am. 2006;20:789–825. https://doi.org/10.1016/j.idc.2006.09.009.
25. Hsu P-K, Hsu W-H. Chest wall mass caused by salmonella enteritidis-a pitfall of pet imaging interpretation. Thorac Cardiovasc Surg. 2008;56:239–40.
26. Varanauskienė E, Mašanauskienė E. Tuberculosis complications after bcg treatment for urinary bladder cancer. Med Kaunas. 2012;48:563–5.

27. Gözübüyük A, Özpolat B, Gürkök S, Çaylak H, Yücel O, Kavaklı K, Dakak M, Genç O. Surgical management of chest wall tuberculosis. J Cutan Med Surg. 2009;13:33–9. https://doi.org/10.2310/7750.2008.07084.
28. Saifudheen K, Anoop TM, Mini PN, Ramachandran M, Jabbar PK, Jayaprakash R. Primary tubercular osteomyelitis of the sternum. Int J Infect Dis. 2010;14:e164–6. https://doi.org/10.1016/j.ijid.2009.03.021.
29. Grover SB, Jain M, Dumeer S, Sirari N, Bansal M, Badgujar D. Chest wall tuberculosis - a clinical and imaging experience. Indian J Radiol Imaging. 2011;21:28–33. https://doi.org/10.4103/0971-3026.76051.
30. Catano J, Perez J. Tuberculosis abscess of the chest wall. Am J Trop Med Hyg. 2014;91:663. https://doi.org/10.4269/ajtmh.14-0063.
31. Lopez-Menendez C, Ruiz-Martinez R, Molino-Trinidad C, et al. Pulmonary actinomycosis with thoracic soft tissue mass: a rare onset form. Eur J Radiol. 2001;37:195–9.
32. Yeung VHW, Wong QHY, Chao NSY, Leung MWY, Kwok WK. Thoracic actinomycosis in an adolescent mimicking chest wall tumor or pulmonary tuberculosis. Pediatr Surg Int. 2008;24:751–4. https://doi.org/10.1007/s00383-008-2155-3.
33. Walker WA, Pate JW. Primary Aspergillus osteomyelitis of the sternum. Ann Thorac Surg. 1991;52:868–70.
34. Boudaya M-S, Mlika M, Chaari Z, Zribi H, Aouadi S, Marghli A, Kilani T. Chest wall hydatidosis: A single institution experience. Arch Clin Infect Dis. 2016;11. https://doi.org/10.5812/archcid.35134.
35. Topuzlar M, Eken C, Ozkurt B, Khan F. Possible anaphylactic reaction due to pulmonary hydatid cyst rupture following blunt chest trauma: a case report and review of the literature. Wilderness Environ Med. 2008;19:119. https://doi.org/10.1580/07-WEME-CR-1561.1.
36. Tanaka Y, Kato H, Shirai K, Nakajima Y, Yamada N, Okada H, Yoshida T, Toyoda I, Ogura S. Sternoclavicular joint septic arthritis with chest wall abscess in a healthy adult: a case report. J Med Case Reports. 2016;10. https://doi.org/10.1186/s13256-016-0856-0.
37. Ehara S. Manubriosternal joint: imaging features of normal anatomy and arthritis. Jpn J Radiol. 2010;28:329–34. https://doi.org/10.1007/s11604-010-0438-9.
38. Lee RKL, Griffith JF, Ng AWH, Sitt JCM. Sonography of the chest wall: a pictorial essay: sonography of the chest wall. J Clin Ultrasound. 2015;43:525–37. https://doi.org/10.1002/jcu.22286.
39. Gorospe L, Ayala-Carbonero AM, Rodríguez-Díaz R, García Latorre R, Muñoz-Molina GM, Cabañero-Sánchez A. Tuberculosis of the manubriosternal joint and concurrent asymptomatic active pulmonary tuberculosis in a patient presenting with a chest wall mass. Clin Imaging. 2015;39:311–4. https://doi.org/10.1016/j.clinimag.2014.08.006.
40. Sallés M, Olivé A, Perez-Andres R, Holgado S, Mateo L, Riera E, Tena X. The SAPHO syndrome: a clinical and imaging study. Clin Rheumatol. 2011;30:245–9. https://doi.org/10.1007/s10067-010-1560-x.
41. Kroshinsky D, Grossman ME, Fox LP. Approach to the patient with presumed cellulitis. Semin Cutan Med Surg. 2007;26:168–78. https://doi.org/10.1016/j.sder.2007.09.002.
42. Turecki MB, Taljanovic MS, Stubbs AY, Graham AR, Holden DA, Hunter TB, Rogers LF. Imaging of musculoskeletal soft tissue infections. Skeletal Radiol. 2010;39:957–71. https://doi.org/10.1007/s00256-009-0780-0.
43. Bailey E, Kroshinsky D. Cellulitis: diagnosis and management. Dermatol Ther. 2011;24:229–39.
44. Swartz MN. Cellulitis. N Engl J Med. 2004;350:904–12.
45. Birnbaum DJ, D'Journo XB, Casanova D, Thomas PA. Necrotizing fasciitis of the chest wall. Interact Cardiovasc Thorac Surg. 2010;10:483–4. https://doi.org/10.1510/icvts.2009.222323.
46. Meyer CA, White CS. Cartilaginous disorders of the chest. Radiographics. 1998;18:1109–23.
47. Ontell FK, Moore EH, Shepard JA, Shelton DK. The costal cartilages in health and disease. Radiogr Rev Publ Radiol Soc N Am Inc. 1997;17:571–7. https://doi.org/10.1148/radiographics.17.3.9153697.
48. Chen C, Chandnani V, Kang HS, Schils JP, Resnick D, Bjorkengren AG, Kaplan P. Insufficiency fracture of the sternum caused by osteopenia: plain film findings in seven patients. AJR Am J Roentgenol. 1990;154:1025–7.
49. Cooper KL. Insufficiency fractures of the sternum: a consequence of thoracic kyphosis? Radiology. 1988;167:471–2. https://doi.org/10.1148/radiology.167.2.3357957.
50. Min J-K, Sung M-S. Insufficiency fractures of the sternum. Scand J Rheumatol. 2003;32:179–80.
51. Degrassi F, Quaia E, Martingano P, Cavallaro M, Cova MA. Imaging of haemodialysis: renal and extrarenal findings. Insights Imaging. 2015;6:309–21. https://doi.org/10.1007/s13244-015-0383-3.
52. Tsirikos AI, McMaster MJ. Congenital anomalies of the ribs and chest wall associated with congenital deformities of the spine. J Bone Joint Surg Am. 2005;87:2523–36. https://doi.org/10.2106/JBJS.D.02654.
53. McGuigan RM, Azarow KS. Congenital chest wall defects. Surg Clin North Am. 2006;86:353–70. https://doi.org/10.1016/j.suc.2005.12.012.
54. Colombani PM. Preoperative assessment of chest wall deformities. Semin Thorac Cardiovasc Surg. 2009;21:58–63. https://doi.org/10.1053/j.semtcvs.2009.04.003.
55. Chang KZ, Likes K, Davis K, Demos J, Freischlag JA. The significance of cervical ribs in thoracic outlet syndrome. J Vasc Surg. 2013;57:771–5. https://doi.org/10.1016/j.jvs.2012.08.110.

56. Kumar R, Madewell JE, Swischuk LE, Lindell MM, David R. The clavicle: normal and abnormal. Radiographics. 1989;9:677–706.
57. Andrault G, Salmeron F, Laville JM. Green's surgical procedure in Sprengel's deformity: Cosmetic and functional results. Orthop Traumatol Surg Res. 2009;95:330–5. https://doi.org/10.1016/j.otsr.2009.04.015.
58. Radmore L, Thomas W, Tasker A, Diamond D, Amirfeyz R, Gargan M. Sprengel's deformity. Orthop Trauma. 2011;25:131–4.
59. Bhatia D, DasGupta B, Kadavkolan A, Bhosale P. Sprengel′s deformity of the shoulder: Current perspectives in management. Int J Shoulder Surg. 2011;5(1). https://doi.org/10.4103/0973-6042.80459.

# Pulmonary Imaging Findings After Surgery, Chemotherapy and Radiotherapy

20

Roberto Scipione, Fabrizio Boni, Renato Argirò, and Michele Anzidei

**Abstract**

Imaging plays a central role in the management of patients undergoing lung surgery and/or chemo- and radiotherapy, allowing both to assess the efficacy of the procedures and to identify possible treatment-related complications. The radiologist should be familiar with surgical procedures and postoperative radiological evolution, mechanisms of action of main chemotherapy drugs, and modern applications of radiotherapy, in order to differentiate "normal" anatomy from pathologic treatment-related presentations.

Early post-surgery monitoring is usually managed by chest X-ray, since it is a fast, easy, and cheap tool that allows the assessment of intrathoracic device positioning and the identification of the more frequent intervention-related complications (such as pleural effusion, pneumothorax, and pneumonia), with limited radiation exposure. On the other hand, the evaluation of more complex treatment-related complications unavoidably requires CT imaging.

In this chapter, we focus on the main radiological findings after thoracic surgery, focusing on the "normal" anatomic evolution and on the pathological changes observed in early and late complications.

**Keywords**

Lung surgery · Chemotherapy · Radiotherapy · Chest X-ray · CT · Postsurgical complications

## 20.1 Introduction

Imaging has a central role in the management of patients undergoing lung surgery and/or chemo- and radiotherapy, providing both the assessment of the procedure efficacy and the identification of possible treatment-related complications.

Chest X-ray is particularly recommended in early post-surgery monitoring, since it allows the identification of pathological intervention-related alterations such as pleural effusion, pneumothorax, and pneumonia, and the assessment of the correct positioning of intrathoracic devices (drainage tubes, vascular catheters, etc.).

On the other hand, the evaluation of more complex peri- and post-procedural complications and the assessment of the response to surgical treatment require CT imaging.

In order to have a proper and accurate diagnosis, the radiologist should have an extensive

R. Scipione (✉) · F. Boni · M. Anzidei
Department of Radiological, Oncological and Pathological Sciences, Policlinico Umberto I, Sapienza University of Rome, Rome, Italy
e-mail: roberto.scipione@uniroma1.it

R. Argirò
Department of Radiology, Policlinico Universitario Campus Bio-Medico, Rome, Italy


M. Anzidei, M. Anile (eds.), *Diagnostic Imaging for Thoracic Surgery*,
https://doi.org/10.1007/978-3-319-89893-3_20

technical knowledge of surgical procedures, mechanisms of action of main chemotherapy drugs, and modern applications of radiotherapy, including a wide iconography of both "normal" anatomy and pathologic aspects due to treatment-related complications.

## 20.2 Pulmonary Surgery

### 20.2.1 Pneumonectomy

Post-pneumonectomy imaging shows a dramatic change in normal thorax anatomy [1]: therefore, it is essential to be familiar with such variations and their chronological evolution, in order to have an early recognition of complications and also not to confuse the phases of normal postsurgical evolution as pathological presentations.

The evolution of patients after pneumonectomy can be efficiently monitored with X-rays [2] which, in early phases, shows a medially placed tracheal shadow, mild signs of hilar congestion, and the filling of surgical recess with fluid and gas; the extent of air accumulation is highly variable, even though during the first 4–5 days approximately a half of the hemithorax is occupied, and after a week the classical sign of air-fluid levels can be observed. Subsequently, there is a gradual shift of mediastinal structures towards the treated side, due to the coexistent compensatory hyperexpansion of the contralateral lung and the initial reabsorption of gas in the surgical site (the progressive shift during following weeks should show the continuous reabsorption of gas). The complete obliteration of surgical site occurs within a period of weeks or months. Once the obliteration has occurred, the heart rotates posteriorly and the contralateral lung herniates beyond the median line, anteriorly to the heart and the aorta.

Therefore, it appears clear that a fast mediastinal shift towards residual lung during early post-operatory period has to be considered as pathologic and highly suggestive of contralateral lung atelectasis or of massive accumulation of air and/or fluid within the surgical recess (due to hemorrhage, fistulas, empyema, etc.). During subsequent phases, a mediastinal shift towards residual parenchyma will be suggestive of possible late complications.

### 20.2.2 Lobectomy and Limited Pulmonary Resections

Similarly to what is previously described for pneumonectomy, even after lung resection radiological appearance changes drastically, even though less impressively [3]; even in this case, chest X-ray allows a reasonable evaluation of postoperative evolution (Fig. 20.1).

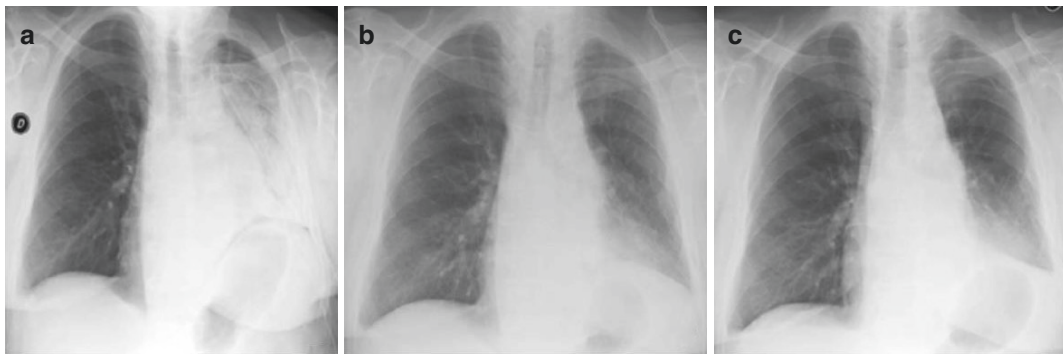


**Fig. 20.1** Evolutive phases after lobectomy. The first early radiogram (**a**) shows a surgical site mainly occupied by fluid, with a pleural drainage tube; the left hemidiaphragm is lifted up. In the following two controls (**b** and **c**), there is re-expansion of residual parenchyma, with obliteration of surgical recess

### 20.2.3 Pleural Surgery

The most common pleural intervention is represented by pleurodesis [4]. In this case, chest X-ray has scarce specificity, showing pleural thickening, nodularity, and sometimes effusions that may also mimic malignancies. The mediastinum may shift to the side of treatment because of constriction of the lung. Usually pleurodesis talc shows high attenuation and tends to be distributed in the posterior costophrenic angles or apical regions.

CT allows a more accurate identification of pleurodesis material and pleurodesis-related lesions; the latter may appear as diffuse pleural thickening or one or more focal plaque-like or nodular pleural lesions.

## 20.3 Postsurgery Complications

As previously said, the knowledge of normal postoperative course and its variations allows a careful identification of possible complications that can be distinguished early and late.

### 20.3.1 Early Complications

*Pulmonary Edema*: It is a potentially lethal condition that may complicate a pneumonectomy, with a prevalence rate of 2.5–5% (less frequent in case of bi-lobectomy, rare in case of lobectomy, <1% of cases) and a mortality rate of 80–100% [5]. Pathogenesis remains unclear, even though it is thought that an increase in hydrostatic pressure and an alteration in capillary permeability could have a key role. Other potential contributory causes are represented by overhydration during intervention, left ventricle failure, hypoproteinemia, septic capillary damage, and prolonged exposition to oxygen at high concentrations. Patients after right pneumonectomy are more likely to develop pulmonary edema, probably because fluid collection within the surgical recess leads to an increase in blood flow towards the left lung that in normal conditions only receives 45% of cardiac output and only contains 45% of the whole pulmonary lymphatic system.

The diagnosis of post-pneumonectomy pulmonary edema is usually based on clinical and radiological exclusion of infective causes (including aspiration pneumonia), thromboembolism, bronchopleural fistulas, and other causes of ARDS. In more severe cases, serial chest X-rays show the typical appearance of parenchymal opacities, whose aspect is completely superimposable to other forms of ARDS. Mild cases usually show more classic signs of pulmonary edema, with Kerley lines, thickening of peri-bronchovasal interstitium, and vascular hila prominence [6].

If CT scan is needed, salient aspects are the thickening of interlobular septa and peribronchovasal interstitium, and diffuse lung opacities; only if fluid accumulation overcomes the lymphatic circulation reabsorption rate, pleural effusion will be present [6].

*Hemothorax*: Although a small extent of blood may be normally seen in early post-operatory periods, due to small-vessel damaging during intervention, wider bleeding may represent a dramatic complication and is due to a nonadequate hemostasis on a bronchial artery or on thoracic wall (much less likely the bleeding originates from pulmonary ligatures). However, mortality from uncontrolled bleeding is inferior to 0.1%. Hemothorax appears as a rapid progression of pleural effusion; CT imaging also allows to assess the increased density of this finding, both qualitatively and quantitatively. The tendency for coagulation of hemothorax may determine the apposition of fibrin deposits in subpleural regions, with the appearance of pseudo-masses, easily distinguishable from pleural thickening of other nature because of the high density values detected at unenhanced CT [7].

*Chylothorax*: Chylothorax is defined by chyle collection within the pleural space due to the lesion of the thoracic duct or one of its main branches. The fast filling of pleural space after pneumonectomy represents a characteristic radiographic sign, even though it does not allow a sure differentiation from other causes of effusion. Even CT (Fig. 20.2) cannot provide a sure

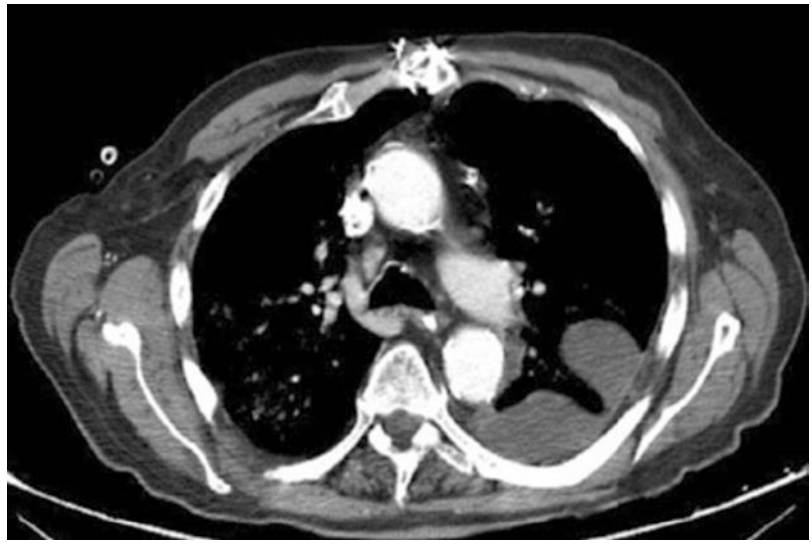

**Fig. 20.2** A case of chylothorax after pulmonary surgery; the polylobate morphology of the effusion can be easily recognized

diagnosis of the nature of the effusion, given the variable density of chylothorax; the polylobate profile of the effusion may be an important clue [7]. Currently, among different diagnostic tools, lymphangiography remains the gold standard, even though the integration with laboratory data can provide a definitive diagnosis, too (triglyceride concentration > 110 mg/dL).

*Bronchopleural fistula*: Bronchopleural fistula is a potentially lethal complication, with a prevalence of 2–13% and a mortality rate of 16–23%; the cause of death in these patients is generally due to associated aspiration pneumonias, with consequent ARDS. It is more common after right pneumonectomy, because of different anatomical characteristics of the right bronchial tree (mainly represented by the different caliber). Actually, this complication can be considered both as early and late: in the first case it is due to a suture dehiscence, and in the latter due to a relapse or a peri-anastomotic infection [8].

Radiological signs may be represented by a continuous increase of air collection within the pleural space, the appearance of an air-fluid level or alterations in an already existing air-fluid level, the development of a hypertensive pneumothorax, and a lowering of the air-fluid level greater than 1.5–2 cm inside the surgical recess. Since an increase of air collection and a reduction of fluid are both important signs of bronchopleural fistula, it is fundamental to monitor air-fluid levels in patients after pneumonectomy [9]. HRCT has a key role in these patients, not only for the diagnosis, but also for treatment planning, often allowing the direct visualization of the fistula between the bronchus lumen and the surgical recess, thanks to multi-planar reconstructions (MPR) (Fig. 20.3).

*Empyema*: Empyema is a serious but uncommon complication, with an incidence of 2–16% (more frequent in case of pneumonectomy after a prior lobectomy) and a mortality rate of 16–71% (mortality reaches greater values if this complication is associated with bronchopleural fistulas). Even though it is mainly an early condition, empyema may sometimes occur after months or years from the intervention [10].

At X-ray, empyema may present with the appearance of multiple air-fluid levels within the surgical recess; however, in cases where these initial alterations are absent, X-ray cannot be diagnostic. CT (Fig. 20.4) is certainly superior in the evaluation of patients with clinical suspect of empyema, highlighting an expansion of the surgical recess (actually, its behavior is similar to an expansive process); other signs are represented by complicated effusion, irregular thickening of residual parietal pleura (with wall enhancement in case of contrast agent adminis-

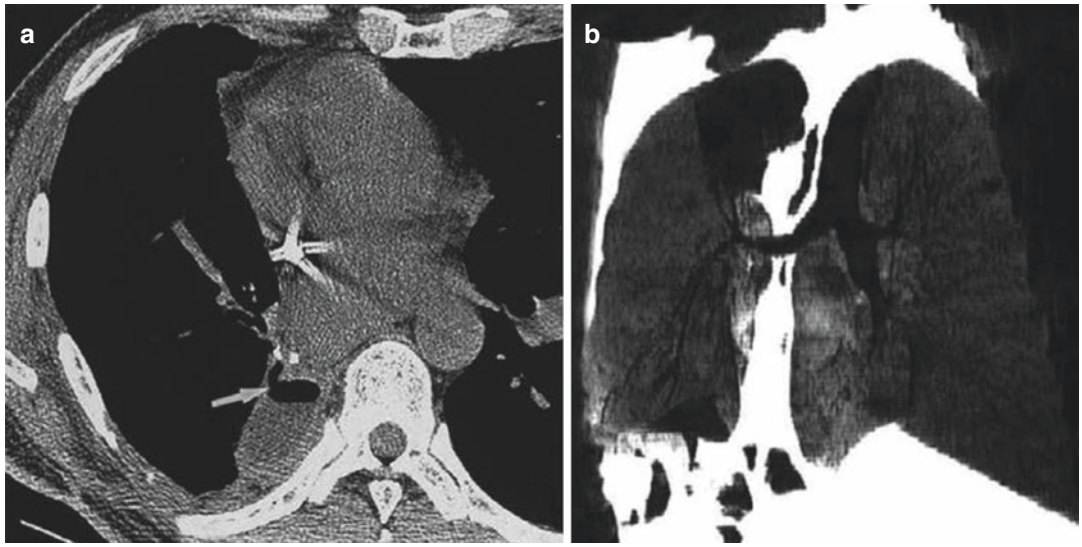


**Fig. 20.3** After superior right lobectomy in this patient, postoperative CT scan shows a bronchopleural fistula (**a**, *arrow*); MinIP reconstruction confirms the presence of an air recess (**b**)

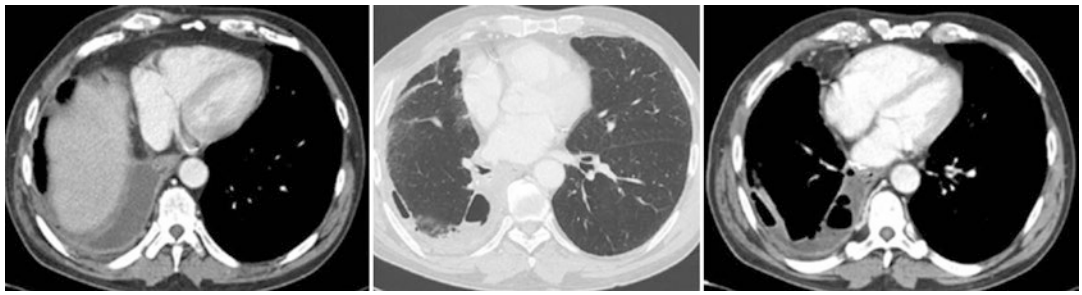

**Fig. 20.4** Loculated pleural effusion in a patient after inferior right lobectomy. Major findings are represented by pleural thickening associated with post-contrast enhancement; within the collection there are multiple air-fluid levels. This appearance is highly suggestive of empyema

tration), convexity or partial loss of the normal concavity of the surgical recess on its mediastinal contour, and bronchopleural recess (that may be associated).

*Persistent air leak*: After lobectomy or segmentectomy, all patients are likely to develop a modest postoperative air leak (even more likely in case of incomplete or absent fissures) that tends to resolve spontaneously. In case of leaks with greater extent, X-ray and CT (Fig. 20.5) show signs of persistent pneumothorax, possibly associated with pneumomediastinum or subcutaneous emphysema [11]. Almost all leaks originating from the periphery of the lung have a spontaneous resolution within 24–48 h, when residual parenchyma completely fills pleural recess; a leak is defined persistent if it is still present at the seventh postoperative day. This condition does not show any significant impact on post-surgery mortality.

*ARDS*: It is recognized as a fatal complication, with a prevalence of about 5% (in case of pneumonectomy) and a mortality rate of 80% (versus 65% of ARDS in non-operated patients). In case of a coherent clinical presentation, diagnosis is usually obtained through serial chest X-rays that demonstrate the fast development of diffuse opacities within residual parenchyma; CT allows the identification of "ground-glass" areas, and interlobular septa thickening, with a typical

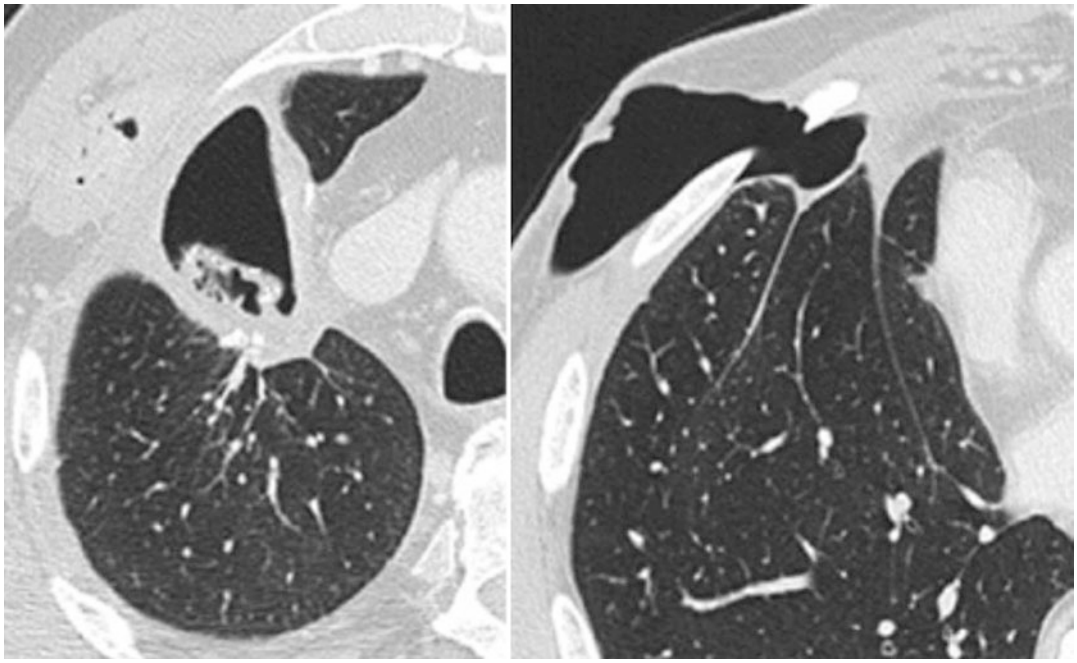

**Fig. 20.5** Persistent air leak in a patient after superior right lobectomy, during the 30th postoperative day; the fistulose communication between the pleural recess and subcutaneous space can be easily seen

development gradient along an anteroposterior direction [12]. ARDS can appear alone or can coexist with other complications, such as pneumonia and bronchopleural fistula with or without empyema.

*Pneumonia*: After pneumonectomy, pneumonia shows a prevalence between 2 and 22% and is associated with mortality rates up to 25%. Most common etiologies are represented by aspiration of gastric secretions and bacterial colonization of atelectatic parenchyma; intubation and invasive ventilation are predisposing factors (especially for aspiration pneumonia) [13].

In operated patients, the radiographic pattern, together with signs and symptoms, may lead to postoperative pneumonia overdiagnosis; on the other hand, the opposite mistake (misdiagnosed pneumonia) may be fatal. Furthermore, sometimes a negative X-ray cannot exclude with certainty a pneumonic process, since it could be detected at imaging only after the appearance of first symptoms. Radiological signs may be variable, ranging from foci of increased density to bronchopneumonia and to lobar pneumonia (less common). Aspiration pneumonia may associate to necrotizing phenomena, with abscess formation.

*Gossypiboma*: This term describes an iatrogenic mass, represented by granulation tissue surrounding surgical gauzes. CT images show a mass with parietal enhancement and a hyperdense inner core; air collection can often be seen within the lesion (Fig. 20.6).

In early postoperative period, gossypiboma can be mistaken at imaging with an abscess, a loculated empyema, a complicated hematoma, or a seroma [14]. In case of late detection, differential diagnosis includes chronic infections, granulomatous processes, or neoplastic tissue.

*Atelectasis*: Atelectasis may result from an insufficient ventilation of residual parenchyma in case of partial pulmonary resections; it occurs in 5–10% of sleeve resections and may be due to edema formation at the anastomosis site, interruption of ciliary epithelium and lymphatic vessels, or partial lobe denervation [15].

CT shows areas with "ground-glass" opacity or proper consolidation.

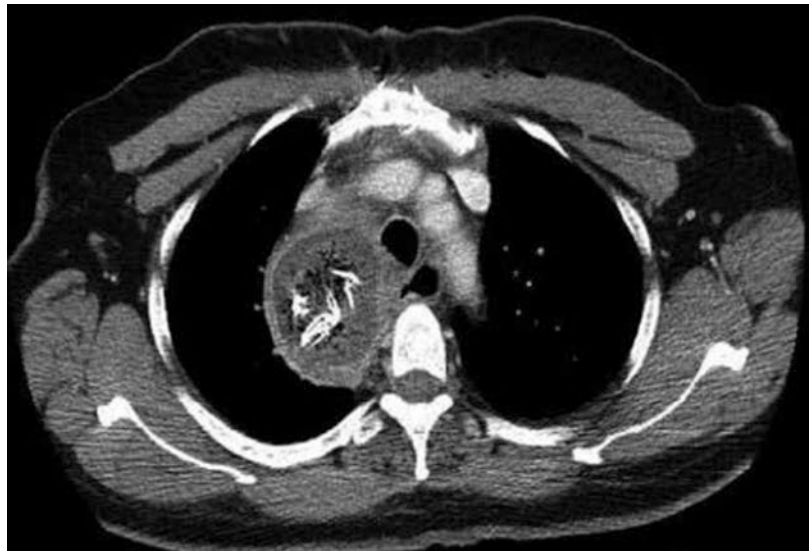

**Fig. 20.6** A case of gossypiboma after thoracic surgery; the surgical gauze can be easily seen close to the trachea, surrounded by a fluid collection, in which air components can be observed

*Others*: Among other possible early complications, some are worthy of consideration, even if uncommon: pulmonary torsion, cardiac herniation, or anastomotic dehiscence.

### 20.3.2 Late Complications

*Post-pneumonectomy syndrome*: This complication is characterized by the compression of main intrathoracic airways, as a consequence of an excessive compensatory response after pulmonary resection; being more responsive, younger patients are more likely to be affected. Bronchial stenosis determines pulmonary stridor and facilitates infection development [16].

Chest X-ray may show the shift of trachea, mediastinum, and heart towards the surgical recess. CT and bronchoscopy provide an excellent documentation about the compressed area; moreover, thanks to its panoramic view, CT also gives specific information about the site of bronchial obstruction.

*Esophageal-pleural fistula*: This potentially devastating complication approximately occurs in 0.2–1% of patients after pneumonectomy. Although it may also develop as an early complication (because of iatrogenic damages or arterial flow compromising), more frequently esophageal-pleural fistula is a late complication due to esophageal or peri-anastomotic chronic inflammation, or due to illness relapse [17] (Fig. 20.7).

X-ray is often inadequate and insufficient for the diagnosis; esophagography can highlight the presence of the fistula. However, CT represents the best diagnostic tool, since it allows to detect the fistula and also the underlying cause and the possible associated empyema, at the same time.

*Bronchial anastomosis stenosis*: This is the most common complication after sleeve resections (more than 18% of cases) and may lead to potentially serious conditions. It is due to blood flow interruption at the distal bronchial segment and due to the consequent partial anastomosis dehiscence, with granulation tissue formation [18].

CT is a much more precise exam than X-ray and can directly highlight the stenosis of the anastomotic tract.

*Infections*: Even though less frequent than during early phases, late infections can show as bronchopleural fistulas or as pleural empyema.

*Relapse*: Illness relapse may be represented by pathological localizations within residual parenchyma, homolateral mediastinal lymphadenopathies, involvement of thoracic wall or parietal pleura, and localization along surgical margins (even in case of margins with sufficient distance from the primary illness and with no

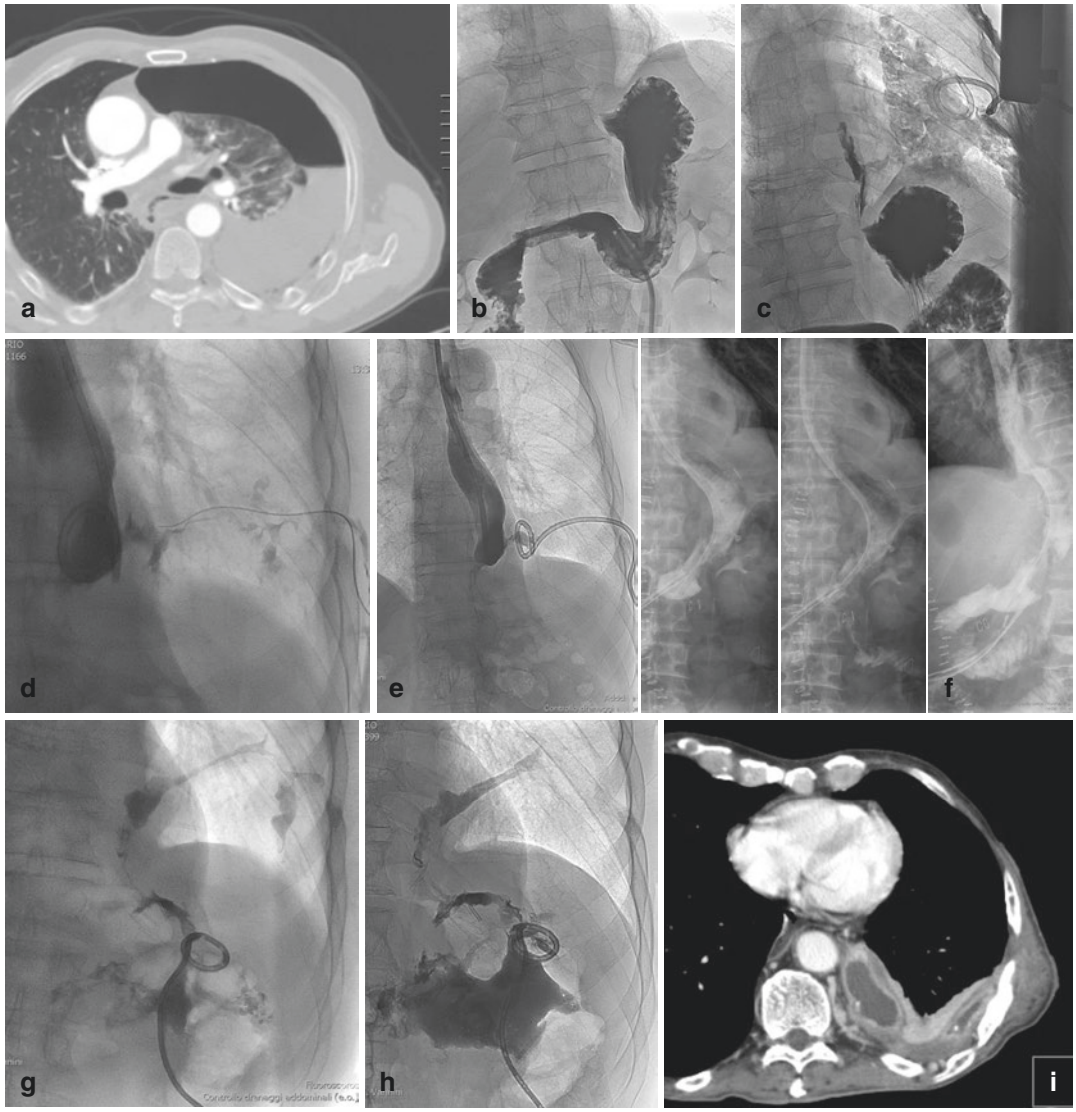


**Fig. 20.7** CT scan of a patient with spontaneous esophageal rupture with hydro-pneumothorax and posterior mediastinal fluid collection (**a**). A conservative surgery treatment was performed with cardiac suture, transcutaneous PEG positioning, and esophageal cervicostomy. Contrast injection from the PEG demonstrates no leak at the anastomotic tract (**b**). Injection of c.m. from the pleural drainage demonstrates opacification of distal esophageal lumen for an esophageal-pleural fistula (**c**). Further examination demonstrates the progression of the fistula within subcutaneous tissue and skin (**d**); therefore, another 10Fr pigtail drainage was positioned close to the esophageal leak (**e**). After 2 months, a reconstruction of the esophageal tract was performed with colon interposition; (**f**) image demonstrates no extra-luminal c.m. collection. Patient presented an abdominal fluid collection that demonstrates transdiaphragmatic communication and persistency of pleuro-cutaneous fistula collection (**g**, **h**) with pleura. CT scan demonstrates two fluid collections with ticked wall (**i**); the patient has been scheduled for a pleural cavity revision

interruption recognizable at histology) [19]. CT is the current standard for the evaluation of relapses (Fig. 20.8); however, in case of relapses with small dimensions, with scarcely defined borders and without architectural distortion of surrounding structures, the differentiation from postsurgical fibrosis could not be easy; the association with bronchoscopy and PET-CT, and/or the evaluation during serial follow-ups, may be helpful.

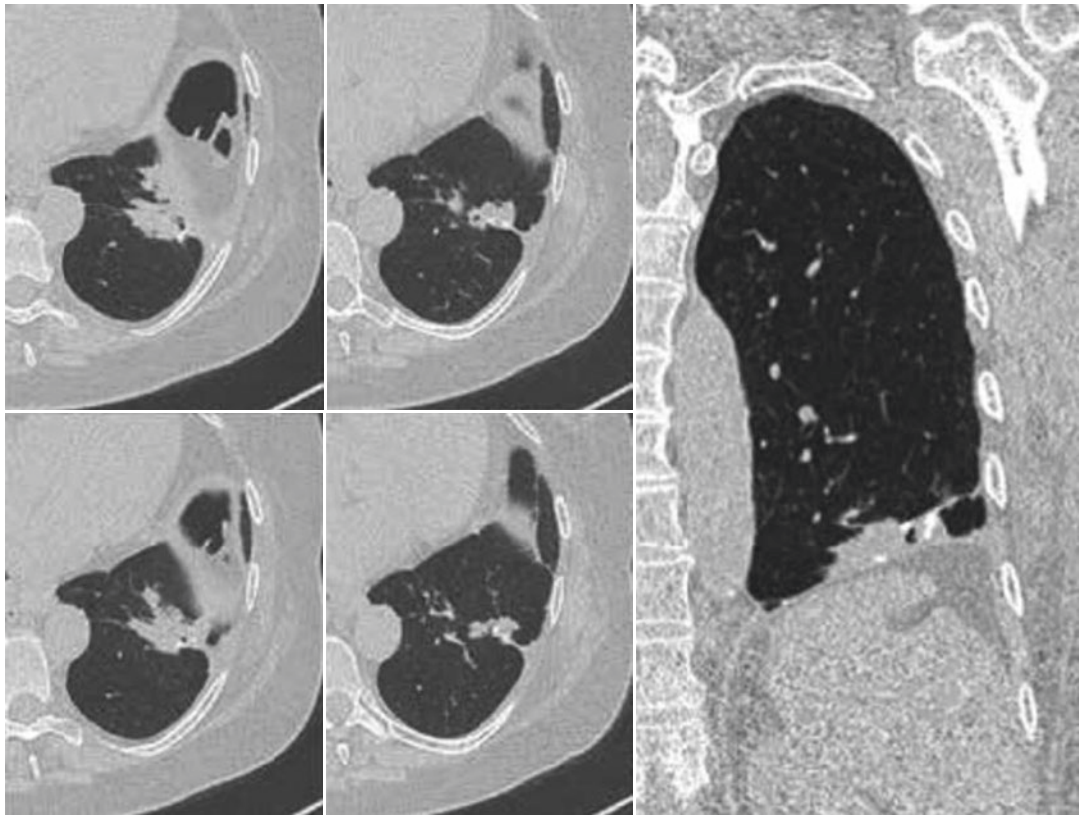

**Fig. 20.8** A case of relapse in a patient after atypical resection; a nodular thickening with irregular margins along the metallic surgical staple line can be noticed

## 20.4 Pulmonary Radiotherapy

Radiotherapy (RT) represents a viable therapeutic option in patients with lung cancer and may be proposed with different aims: curative aim (stage I–II that cannot be treated with surgery for other reasons), adjuvant or neoadjuvant therapy (stage IIIa), and palliative aim [20].

Classical RT techniques determined a significant administration of radiation dose beyond tumor margins, with consequent significant risk of radiation-induced lung disease (RILD) on surrounding parenchyma. In order to reduce toxic effects of radiation exposure, other innovative techniques have been developed, such as 3D-conformal radiation therapy (CRT) and stereotaxic therapy (SBRT); both techniques use multiple radiation beams that determine a distribution of dose strictly limited to the target.

Despite significant benefits deriving from these new approaches, radiation-induced parenchymal damages still represent a concrete possibility in patients undergoing RT; the risk of radiation-induced damage is strictly related to radiation dose, tumor site, and specific patient-related factors (such as a contextual chemotherapy treatment, since drugs like actinomycin D, bleomycin, and busulfan may further empower actinic damaging). The relationship between dose and radiation damage is not linear, but usually there is a sudden increase of prevalence beyond a certain cutoff. Hardly pulmonary parenchyma can be damaged by overall radiation doses inferior to 20Gy (subcritical dose), while structural alterations are commonly observed for doses between 30 and 40Gy, and damages are always observed for overall doses greater than 40Gy.

Radiation-induced pulmonary damage can be an immediate potential toxic effect, but may also appear

with two different clinical-pathological-radiological presentations, with different distance from treatment time: an early phase (early radiation pneumonia), usually between 1 and 6 months after therapy conclusion, and a chronic phase (chronic radiation fibrosis), 6 and 12 months after treatment conclusion.

### 20.4.1 Acute Pulmonary Damage

Radiological appearances of acute lung injury after standard radiotherapy generally include "ground-glass" opacities, parenchymal consolidation, or both (usually on treated lung regions); sometimes, radiation pneumonia can be associated with pleural effusion and atelectasis (Fig. 20.9).

The development of new techniques as CRT and SBRT has changed radiological presentation of pulmonary radiation-induced damages; therefore anamnestic data about the type of treatment are fundamental for the radiologist during reporting. Since these innovative techniques deliver therapeutic dose in the tumor through different beams, possible radiation injury differs from classic RT in terms of morphology, characteristics, localization, extension, and distribution; radiation damages after CRT and SBRT are described as unusual or atypical.

After CRT, radiation pneumonia may manifest with focal or nodular "ground-glass" opacity, parenchymal consolidation, or both patterns, but limited to treated tumor area and to the healthy lung parenchyma strictly adjacent to the target; however, some reports from literature also describe CRT damages distant from treated sites and/or to contralateral lung.

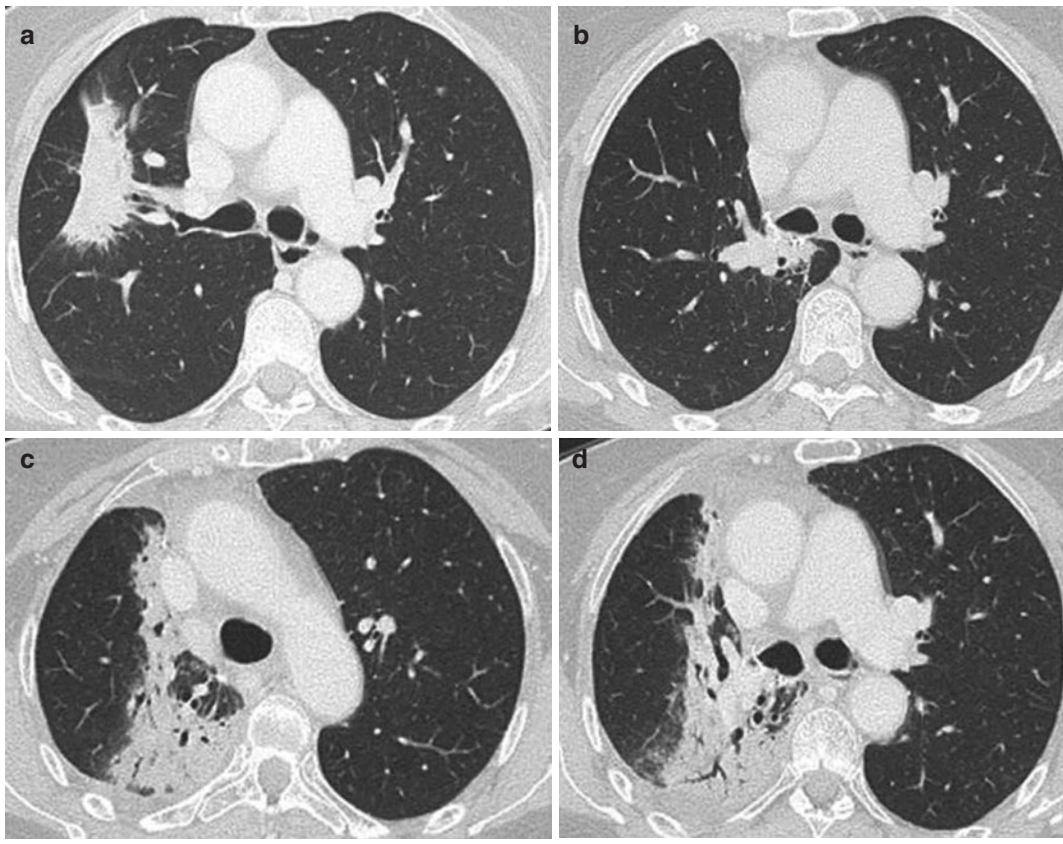


**Fig. 20.9** Neoplastic lesion on superior right lobe (**a**); this patient underwent lobectomy (**b**) with subsequent adjuvant conventional radiotherapy. After 1 month a parenchymal consolidation with air bronchogram sign and peripheral ground-glass areas can be observed (**c**, **d**); these findings are coherent with radiation-induced acute pulmonary injury

After SBRT, no distant alterations from treated site are commonly observed; because of the steep gradient of dose between the periphery of target area (high-dose area) and healthy surrounding tissues (low-dose areas), post-SBRT damages are usually limited to treated region and typically retrace the lesion shape. This kind of radiation damages has been classified by Ikezoe in four different patterns: diffuse consolidation, diffuse ground-glass opacities, patchy consolidation, and patchy ground-glass opacities.

### 20.4.2 Chronic Pulmonary Fibrosis

Usually, after conventional RT, classical alterations from radiation pneumonia gradually resolve within the following 6 months; in case of limited damage, no radiological sequelae are observed, while in case of more extended damage there is a progression towards fibrosis. The radiological aspect of chronic pulmonary fibrosis appears as a well-circumscribed area of volume loss, with a linear scar or a parenchymal consolidation; areas of parenchymal distortion or traction bronchiectasis are associated. Fibrosis may establish or even progress for over 24 months. Further modalities of damage evolution are represented by the reduction of consolidation dimensions or the appearance of a clear demarcation from surrounding healthy tissue. Occasionally, these signs may associate with an ipsilateral mediastinal shift or surrounding pleural thickening/effusion (Fig. 20.10).

After CRT and SBRT, chronic pulmonary fibrosis may develop according to one of these different patterns:

– Conventional modified: A well-circumscribed area of parenchymal consolidation with volume loss and traction bronchiectasis; it is similar to the radiological pattern that follows classical RT, even though it shows a minor extension.

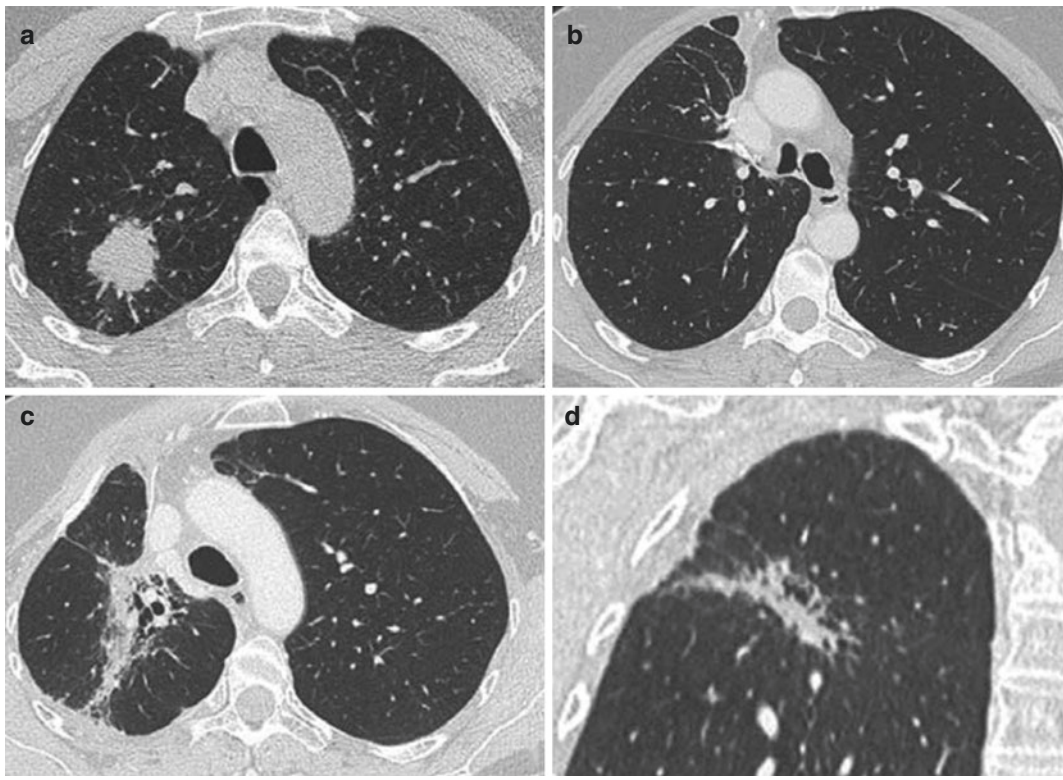


**Fig. 20.10** Neoplastic lesion on posterior segment of right superior lobe (**a**); this patient underwent lobectomy (**b**) with adjuvant radiotherapy. After 8 months, a parenchymal consolidation with volume loss and traction bronchiectasis is observed (**c**, **d**); these findings are suggestive of chronic radiation-induced fibrosis

– Mass-like: It is a variant of the previous pattern; in fact, when previously described characteristics are focal and confined within a 2 cm area around the treated lesion, the term mass-like pattern is used. Usually, mass-like alteration shows greater dimensions than original treated lesion.
– Scar-like: It is a linear opacity whose thickness is minor than 1 cm, associated with moderate/severe volume loss; this alteration remains on treated tumor location, even if the original lesion cannot be observed any more at all (or almost). It represents the radiological pattern that differs more considerably from classical presentations described for conventional treatment.

### 20.4.3 Differential Diagnosis

Radiation toxicity is often difficult to diagnose with certainty, since infections or tumor recurrences may present with similar clinical and radiological patterns. The exact knowledge of radiation treatment timing, type, and dose is fundamental to ensure diagnostic accuracy.

– *Pneumonia*: Infections should be suspected in case of pulmonary opacities detected at CT before RT completion, or diffuse or bilateral parenchymal anomalies. Other suspicious signs of infection may be centrilobular nodules, suggestive of bronchiolitis (tree-in-bud), sometimes associated with consolidations or cavitations (common in case of TBC). Sometimes a superinfection can complicate an injury from radiation toxicity; in these cases cavitation phenomena often appear. It is important to point out that radiation pneumonia has a more indolent course than infective processes: a sudden outset of symptoms (and radiological findings) is more indicative for an infective pneumonia.
– *Lymphangitic carcinomatosis*: Clinically, it may mimic an abnormality from RT, determining dyspnea; however, lymphangitic carcinomatosis shows a greater severity and a faster progression of symptoms, with a radiological pattern characterized by irregular thickening of interlobular septa and peribronchial interstitium, pleural effusion, and mediastinal lymphadenopathies.

*Recurrence*: Usually recurrences occur within 2 years from treatment time and depend on treated lesion dimensions, stage, and histotype, and on treatment type. At CT, recurrence diagnosis is often difficult in patients who developed post-RT fibrotic alterations, especially with mass-like patterns. A parenchymal consolidation with regular margins and air bronchogram is a classical CT sign of stable radiation-induced fibrosis; an alteration in margins and/or in dimensions of the fibrotic area and the appearance of a homogeneous opacity without air bronchogram and with convex margins are suspicious signs of a local recurrence. Obviously, in association with other signs of illness recurrence (nodules in other locations of contralateral/ipsilateral parenchyma, pleural effusion, mediastinal lymphadenopathies, etc.) diagnosis becomes more simple. In some cases, X-ray, CT, nor MRI does not allow a sure distinction between illness residual/recurrence and radiation-induced damage. In these cases, 18-FDG PET represents a valid diagnostic tool, allowing the differentiation between tumor tissue (with active metabolism) and post-RT fibrosis (with no active metabolism). Since radiation pneumonia may determine a local increase in FDG uptake that could be misunderstood as illness residual/recurrence, PET should be performed only at least 3 months after RT completion, in order to reduce the possibility of false positives. Rarely, an increased uptake may be observed until the 15th month after treatment conclusion, in the absence of actual tumor recurrence; in these cases, biopsy is mandatory.

## 20.5 Pulmonary Chemotherapy

Chemotherapy (CHT) has a central role in the management of a patient with lung cancer; in fact, almost every class of patients can undergo CHT, with either neoadjuvant (stages IIIa, IIIb) or adjuvant aim (stages I, II, and III) [21].

Classical drugs inhibit mitosis and then target cells with high proliferation rate; on the contrary, new class of drugs (target therapy) are directed against specific molecules responsible for cell activity.

Cytotoxic agents interfere with DNA and RNA synthesis or with cell division, inhibiting cellular growth with various mechanisms. If drug-induced damage is too great to be repaired, it will induce cell necrosis and apoptosis; the aim is to obtain a greater effect on tumor rather than healthy tissue.

Molecular therapies have developed thanks to increasing knowledge on tumor biology; their target is represented by antigens (in case of monoclonal antibodies) or signal molecules (in case of kinase inhibitors). The knowledge of basilar mechanisms of these drugs allows the assessment of therapy outcomes and the identification of possible adverse events.

In a patient under chemotherapy, the appearance of pulmonary parenchyma alterations may depend on drug toxicity, infections, or primitive illness. Among drug-induced alterations, three different patterns can be identified:

– *Pulmonary infiltrations*: They may either have an early appearance with parenchymal infiltrations, pulmonary edema, and hypersensibility reactions or pleural effusion or a late appearance (2 or more months after therapy) with infiltrations and fibrosis. At CT, four different patterns of drug-related pulmonary infiltration may be distinguished: specific areas of ground-glass opacity, multiple areas of parenchymal consolidation, scattered area of ground-glass opacity with interlobular septa thickening and spread bilateral areas of ground-glass opacities, or parenchymal consolidation with traction bronchiectasis (Fig. 20.11). Most common pattern is represented by specific areas of ground-glass opacity, while the pattern with greater mortality rates is represented by spread bilateral areas of ground-glass opacities, suggestive of diffuse alveolar injury.
– *Pulmonary Hemorrhage*: It is a potentially lethal condition reported in patients with NSCLC under treatment with bevacizumab (incidence <5%). The mechanism of hemorrhage is not clear, but several studies identified necrosis and intra-lesion cavitation as potential risk factors. Moreover, squamous cell carcinoma seems to be the most common type associated with this complication; thus it is considered as an exclusion criterion for treatment.
– *Capillary leak syndrome*: This syndrome is characterized by generalized edema, hypotension, dehydration, and hypoproteinemia. The cause is a sudden increased permeability, with plasma extravasation from intravascular to extravascular space. Radiological pattern is due to the increased vascular permeability that determines interstitial edema with multiple confluent ground-glass opacities (Fig. 20.12). The evolution to ARDS and to non-cardiogenic pulmonary edema is common; differential diagnosis with other forms of pulmonary toxicity is important, because this condition often requires diuretics (combined with drug interruption and cortisone). Most common drug responsible for this syndrome is gemcitabine.

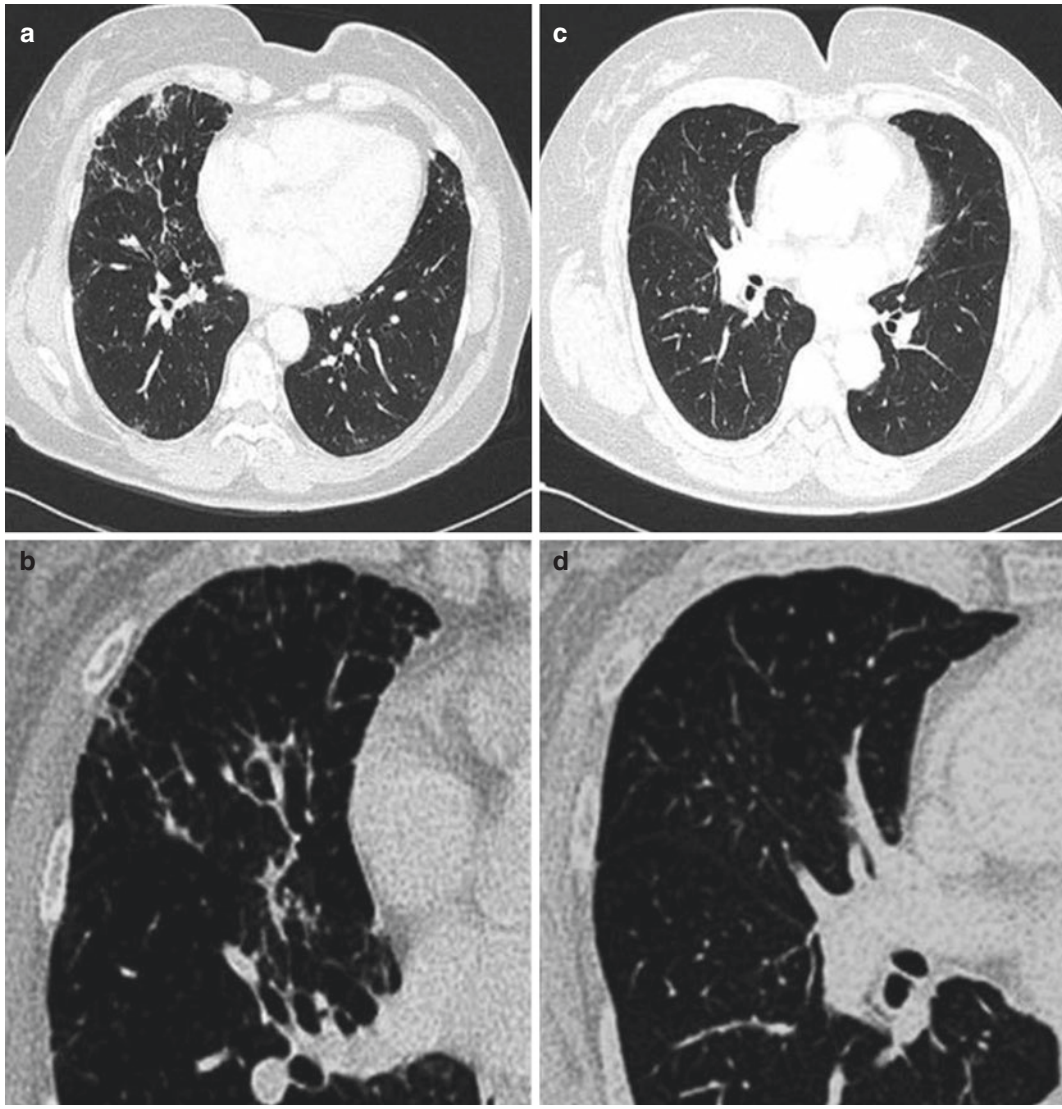


**Fig. 20.11** Pulmonary infiltrates on the middle lobe (**a**, **b**) in a patient with lung cancer under treatment with bleomycin; nearly complete resolution of the infiltrates 3 months after drug interruption (**c**, **d**)

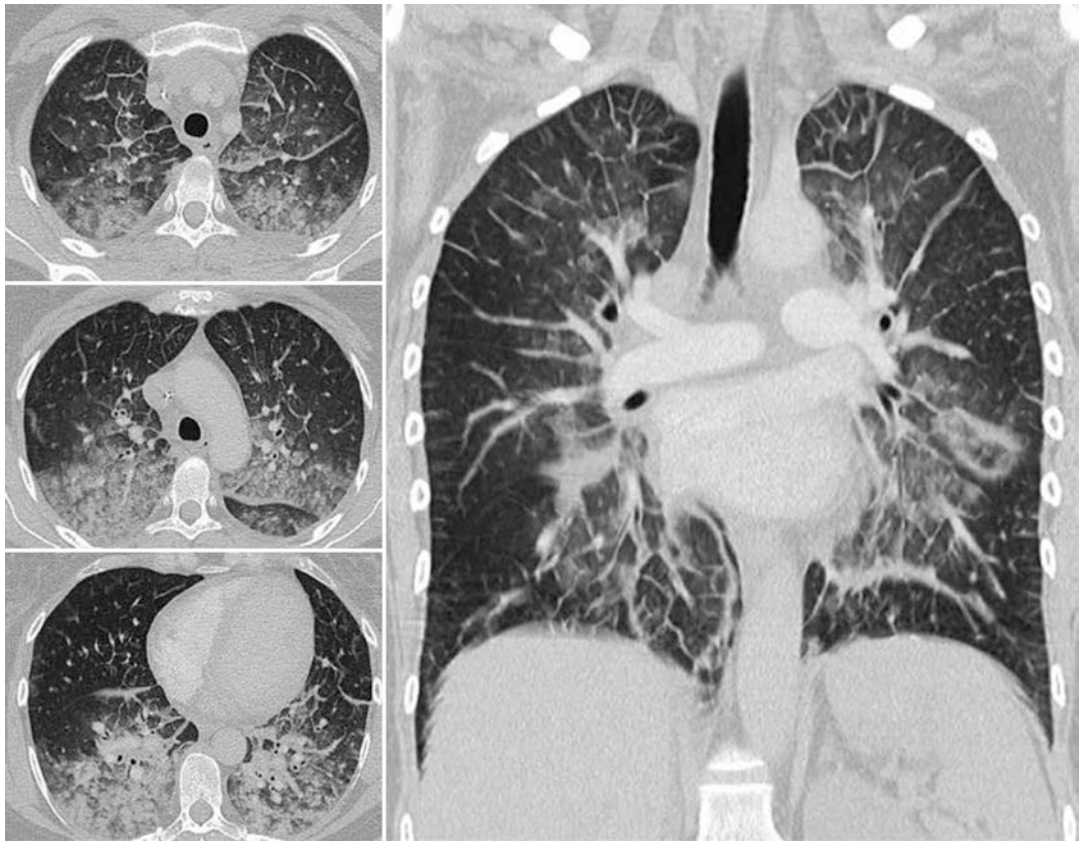

**Fig. 20.12** Patient treated with gemcitabine: bilateral ground-glass opacities, with prevalent peri-hilar distribution, widely confluent; diffuse interlobular septa thickening. These findings are compatible with capillary leak syndrome

## Bibliography


1. Shields TW, Locicero J, Reed CR, et al. General thoracic surgery. Philadelphia, PA: Lippincott Williams & Wilkins. ISBN:0781779820
2. Chae EJ, Seo JB, Kim SY, et al. Radiographic and CT findings of thoracic complications after pneumonectomy. Radiographics. 2006;26:1449–67.
3. Kim EA, Lee KS, Shim YM, et al. Radiographic and CT findings in complications following pulmonary resection. Radiographics. 2002;22:67–86.
4. Sonoda A, Jeudy J, White CS, et al. Pleurodesis: indications and radiologic appearance. Jpn J Radiol. 2015;33(5):241–5.
5. Deslauriers J, Aucoin A, Grégoire J. Postpneumonectomy pulmonary edema. Chest Surg Clin N Am. 1998;8:611–31.
6. Gluecker T, Capasso P, Schnyder P, Gudinchet F. Clinical and radiologic features of pulmonary edema. Radiographics. 1999;19:1507–31.
7. Kuhlman JE, Singha NK. Complex disease of the pleural space: radiographic and CT evaluation. Radiographics. 1997;17:63–79.
8. Lois M, Noppen M. Bronchopleural fistulas: an overview of the problem with special focus on endoscopic management. Chest. 2005;128(6):3955–65.
9. Westcott JL, Volpe JP. Peripheral bronchopleural fistula: CT evaluation in 20 patients with pneumonia, empyema, or postoperative air leak. Radiology. 1995;196(1):175–81.
10. Kirsh MM, Rotman H, Behrendt DM, Orringer MB, Sloan H. Complications of pulmonary resection. Ann Thorac Surg. 1975;20:215–36.
11. Venuta F, Rendina EA, Giacomo TD, et al. Technique to reduce air leaks after pulmonary lobectomy. Eur J Cardiothorac Surg. 1998;13:361–4.
12. Zompatori M, Ciccarese F, Fasano L. Overview of current lung imaging in acute respiratory distress syndrome. Eur Respir Rev. 2014;23(134):519–30.
13. Ferdinand B, Shennib H. Postoperative pneumonia. Chest Surg Clin N Am. 1998;8:529–39.

14. Sheehan RE, Sheppard MN, Hansell DM. Retained intrathoracic surgical swab: CT appearances. J Thorac Imaging. 2000;15:61–4.
15. Massard G, Wihlm JM. Postoperative atelectasis. Chest Surg Clin N Am. 1998;8:503–28.
16. Mehran RJ, Deslauriers J. Late complications: post-pneumonectomy syndrome. Chest Surg Clin N Am. 1999;9:655–73.
17. Massard G, Ducrocq X, Hentz JG, et al. Esophagopleural fistula: an early and long-term complication after pneumonectomy. Ann Thorac Surg. 1994;58:1437–40.
18. Tsang V, Goldstraw P. Endobronchial stenting for anastomotic stenosis after sleeve resection. Ann Thorac Surg. 1989;48:568–71.
19. Miura HM, Konaka C, Kato H, Kawate N, Taira O. Recurrence at the bronchial stump after resection of lung cancer. Ann Surg. 1994;219:306–9.
20. Larici AR, et al. Lung abnormalities at multimodality imaging after radiation therapy for non–small cell lung cancer. Radiographics. 2011;31:771–89.
21. Diederich S, et al. Chest CT for suspected pulmonary complications of oncologic therapies: how I review and report. Cancer Imaging. 2016;16(1):7.